POLARIZATION STUDIES OF BL LAC OBJECTS

Christopher David Impey

B.Sc. , A.R.C.S.

Presented for the Degree of Doctor of Philosophy

at the University of Edinburgh

January , 1981

This thesis is my own composition,

except where reference is made to the work of others

January , 1981

ABSTRACT

The polarization properties of BL Lac objects have been studied in two ways. First, a search for BL Lac objects has been conducted on the basis of their linear polarization properties alone, using a rotating Polaroid filter on the UK Schmidt Telescope in Australia. The large field and faint limiting magnitude of the Schmidt and the measuring capability of the COSMOS machine make a large-scale survey feasible. After a test object was calibrated on short exposure plates, a series of deep exposures of a high latitude field were taken. The calibration was photoelectric down to B $\sim$ 16, with a photographic extension down to B $\sim$ 19 using the sub-beam prisms of the Schmidt and the AAT. Calibrated polarizations and their errors are discussed, as is the senstivity of a simple differential technique to detect high degrees of polarization. Finally a detection limit is derived and candidate BL Lac objects are selected. Implied limits on the surface density of BL Lacs are related to current ideas of their relationship to QSO's.

Second, a sample of BL Lac objects have been investigated with infrared polarimetry in the J, H and K wavebands using the UKIRT. The instrument and calibration procedures are described. The timescales of polarization variability from days to several months have been analysed for the most violent examples of this class. Several unusual kinds of polarization behaviour are seen. Wavelength dependent polarization appears to be a property of two of these objects. This dependence is intrinsic to the non-thermal source and is not caused by dilution due to an underlying galaxy. Second, there is no obvious correlation between polarized and unpolarized flux. In particular, examples of large changes in the degree of polarization with little change in the total flux are seen. Variable polarization on short timescales is a property of all objects observed, and there is also evidence for position angle rotations. The implications of these features for current models of BL Lac objects are discussed.

CONTENTS

Page

Page

CHAPTER ONE

1.1 BL Lac Objects and Active Nuclei

Recent observational evidence indicates that BL Lac objects are one of the most direct links with the energy source of all active galactic nuclei. BL Lac objects have a continuity of properties with quasars and compact radio sources, and also with less energetic activity in relatively nearby galaxies. They emit the purest form of the non-thermal radiation which comes from the heart of quasars, Seyferts, N galaxies, radio galaxies and other active nuclei. BL Lac objects also include the most extreme examples of nuclear activity, where the luminosity, compactness and variability exceed that of any other extragalactic object. These properties pose severe problems both for theories of the ultimate power source and the emission mechanism. It is the physics of their non-thermal emission and their close link with quasars which make the BL Lac objects so important.

The variable star BL Lacertae had been known for 50 years when Schmitt (1968) identified it with the radio source VRO 42.22.01 (MacLeod & Andrew, 1968). It was subsequently found to have rapidly variable radio flux (Biraud & Veron, 1968; Andrew *et al.*, 1969) and polarization (Olsen, 1969), and a featureless optical spectrum (Oke *et al.*, 1969; Du Puy *et al.*, 1969). Visvanathan (1969) found a high degree of linear polarization in the optical continuum. The object was non-stellar on the Palomar Sky Survey plates, and Miller *et al.* (1978a) eventually demonstrated that the nucleus was in an elliptical galaxy with $z = 0.07$. Since the classification of BL Lac, many more objects with similar properties have been discovered, though they still form a small fraction of the number of known quasars. The review by Stein *et al.* (1976) quoted 32 BL Lac objects and the recent article by Angel and Stockman (1980) contains 56 with the number increasing every year. The definition of a BL Lac object has become looser as the barriers between classes of extragalactic objects are eroded, but it includes several of the following properties:

(i) strong, non-thermal radiation from optical to radio frequencies,

(ii) large amplitude and often rapid flux variations at all frequencies.

(iii) strong and variable linear polarization at optical/infrared frequencies.

(iv) power-law flux distribution rising steeply into the infrared.

(v) generally smooth optical continuum with weak or undetected emission and absorption features.

(vi) usually a stellar image, sometimes with surrounding nebulosity (whenever a galactic component can be detected, it is due to an elliptical galaxy).

It is becoming accepted as a working hypothesis (Stein, 1978) that the non-thermal BL Lac properties are a basic component of the quasar phenomenon. Consequently, the property of a featureless spectrum is of secondary importance because the emission and absorption-line regions are well-removed from the central 'engine'. Many BL Lac objects in fact have weak lines; spectroscopy at higher resolution and with good signal-to-noise has led to redshifts for over half the current sample. The absence of strong emission lines in BL Lac objects can be explained by a lack of gas rather than a lack of soft X-ray or UV ionizing flux (Schwartz, 1979; Shields, 1978). The class of OVV (optically violent variable) quasars seem to be transitional between BL Lac objects and normal quasars. OVV quasars have strong emission lines, but share the properties of the BL Lac compact source: rapid variability and high polarization (Visvanathan, 1973;Miller,J., 1978). There are also transitional cases between nearby, nebulous BL Lac objects and elliptical galaxies which are only mildly non-thermal (Miller J., 1975). Unfortunately, it is not yet possible to decide whether the various types of object are related in an evolutionary way or represent a common power source in different environs.

1.2 Properties of BL Lac Objects

1.2.1 Radio Properties

Selection techniques for BL Lac objects heavily favour radio-emitters. The techniques of slitless spectroscopy and UV-excess searches are not appropriate for BL Lacs, so most have been found by identifications with the accurate radio positions of flat spectrum radio sources (i.e. from the Parkes 2700 MHz survey or from Ohio survey positions remeasured with the NRAO interferometer). The great majority of BL Lac objects in the literature were selected for further study simply on the basis of positional agreement with a radio source. It is natural to wonder whether BL Lac objects have analogues to the radio-quiet quasars, which greatly outnumber the radio-emitting quasars (Murdoch & Crawford, 1977; Katgert et al., 1973). Despite the selection effects, it seems likely that radio-quiet BL Lacs are very rare. The few BL Lac objects which have been selected by optical methods are also radio sources. I Zw 186 and Mk 501 were discovered in compact galaxy surveys and both turned out to be flat spectrum radio sources (Altschuler & Wardle, 1976; Khachakian & Weedman, 1974). Similarly 2155-304 and 1218+304 were discovered in X-ray surveys and were subsequently found to be radio-emitters (Agrawal & Riegler, 1979; Wilson et al., 1979; Cooke et al., 1978), although 1218+304 is the weakest known radio-emitting BL Lac: 57 mJy at 1.4 GHz (Ledden et al., 1980). The only one of 17 highly polarized QSOs which is radio quiet is PHL 5200, and there is doubt in this object as to whether the polarized continuum is non-thermal synchrotron emission. The alternatives are scattering by dust or free electrons in the broad absorption trough region (Stockman et al., 1980). Finally, the claim that 1210+121 and 1620+103 are radio quiet BL Lacs must await confirmation of the single, low S/N polarization measurement of each object (McIlwrath & Stannard, 1980). To date, there is no compelling candidate for a radio quiet BL Lac object. One optical search technique based on high linear polarization is described in the second part of this thesis.

The radio properties of BL Lac objects have been summarized by Altschuler and Wardle (1975), Weiler and Johnson (1980) and Condon (1978). Most of the objects have a very compact radio core, with the majority of the flux contained within milli-arc second regions. VLBI detections have been reviewed by Shaffer (1978a). Wardle (1978) has also found extended structure (10 - 200 arc seconds) in half of a sample of 27 BL Lac objects studied at 11.1cm and 3.7cm. 3C390.3 and 1400+162 have extended double structure, though no BL Lac object has been found with classical D2 double-lobed structure. There is a range of components from the compact self-absorbed cores of a few parsecs to the regions of extended emission up to a hundred kiloparsecs in size. BL Lac objects therefore have the same range of scale sizes as quasars and radio galaxies. Although the range is large, the typical radio spectrum in a centimetre survey differs from the typical quasar spectrum. Quasars have a median radio spectral index of $\alpha = 0.2$ below 5 GHz and are optically thin above 10 GHz (Kellerman & Pauliny-Toth, 1972). BL Lac objects have flatter spectra, $\alpha = 0$ and remain optically thick up to 90 GHz (O'Dell et al., 1978a). Both classes turn over with a spectral index of about $\alpha = 0.7$ down to 10^{14} Hz (Condon et al., 1978). Many BL Lacs are flat over a very large range of radio frequency (Owen et al., 1978), and can be interpreted as the superposition of incoherent synchrotron radiation from several separate, homogenous components (Cotton et al., 1980). In some of these objects the spectra are far from 'flat', and the term is used here to mean sources with GHz spectral indices $\alpha < 0.5$. The luminosity of the compact components covers the range 10^{42} - 10^{46} erg s^{-1} (assuming isotropic emission), which is again the same range covered by quasars and radio galaxies. As at optical/infrared frequencies, the strongest BL Lacs are among the brightest radio sources in the sky.

Rapid and strong variability of the radio flux is one of the most important properties of BL Lac objects. For homogenous samples, BL Lacs show a much larger degree of variability than quasars (Wardle, 1978), though there are exceptions and the OVV quasars 3C454.3, 3C446 and CTA 102 have rather steady radio flux.

Not only is the amplitude larger, but the variability timescale is shortest for BL Lac objects. The high frequency variability timescale is often days or weeks, while quasars vary over months or years (Altschuler & Wardle, 1977). For the most extreme high frequency variables (AO 0235+164, BL Lac, 0735+178), the rapid variability presents problems for conventional synchrotron theory if the sources are at the cosmological distances indicated by their redshifts. If the radiation mechanism is incoherent synchrotron radiation, then self-absorption limits the source brightness temperature to $\sim 10^{12}$K (Jones & O'Dell, 1974). The light travel radius of AO 0235+164 from rapid 2.8cm variability implies a brightness temperature $>10^{15}$K which can only be avoided if the emission is coherent or if the emitting region is moving relativistically towards the observer (Ledden et al., 1976). The absence of interstellar scintillation in AO 0235+164 requires that $T_B < 10^{15}$K and rules out coherent radiation at least for that object (Scheuer, 1976).

Variability at low radio frequencies is even harder to reconcile with the canonical synchrotron model. Since the early Molonglo observations by Humstead (1972), the evidence for sub-GHz variability has become more convincing. Simultaneous 408 MHz monitoring at Molonglo (McAdam, 1979) and Bologna (Fanti et al., 1979) has confirmed several cases of variability on timescales of less than a year. The BL Lac objects 0736+017 and 0537-441 have inferred brightness temperatures of 2×10^{16}K and 2×10^{17}K respectively. It is most likely that relativistic effects are responsible for the apparent superluminal flux variations. Since BL Lac, which has been demonstrated to lie within an elliptical galaxy, also displays super-luminal variations, the problem is not eased by assuming non-cosmological redshifts.

1.2.2 Optical/Infrared Continuum

The optical and infrared continua of BL Lac objects are well represented by a power law with a spectral index in the range $0.8 < \alpha < 2.2$ (Tapia et al., 1976; O'Dell et al., 1977a,1978). The continuum slopes are generally steeper than those of quasars ($0 < \alpha < 1.6$ from Neugebauer et al., 1979) with OVV quasars once again being transitional

objects between the two classes. A power law is a noticeably better approximation to the continuum for BL Lac objects than for quasars, implying that the optical infrared flux is predominantly non-thermal. In objects such as AO 0235+164, 1308+325 and 0735+178 the smooth power law steepens at optical frequencies, and this can be interpreted as high energy losses among the synchrotron-emitting electrons (Rieke & Lebofsky, 1979; Rieke & Kinman, 1974; Puschell et al., 1979). Such steeply rising flux into the infrarad means that the bulk of the emission is emitted from 1-20μm. The most luminous BL Lac objects have an integrated optical/infrared flux of $>10^{48}$ erg s^{-1}, making them among the luminous objects in the universe. The infrared is therefore a very important wavelength range for the study of BL Lac objects, especially when there are selection effects against strong infrared emitters. Rieke and Lebofsky (1979) have pointed out that the volume of space sampled in searches to a given visual magnitude is a strong function of α, and by studying the fields of flat spectrum radio sources without regard to optical morphology Rieke et al. (1979) have discovered objects with $2.5 < \alpha < 3.0$. These infrared sources have the BL Lac property of variability and are among the reddest extragalactic objects known.

1.2.3 Optical/Infrared Variability

Most BL Lac objects are strongly variable at optical and infrared wavelengths. Substantial flux variations on a timescale of 1 day have been reported by many observers, e.g. Miller (1977), Liller and Liller (1975), Veron (1975) and Pica et al. (1980). The evidence for variability on a timescale of hours is less convincing, but isolated examples exist: Synder (1980), Puschell et al. (1979), Wolstencroft et al. (1980). The maximum rate of change is one magnitude in 24 hours for BL Lac itself (Wolfe, 1978), and there is no evidence for periodicity in the flux variations of any BL Lac object or quasar. Over longer periods of weeks or months, flux changes of $\Delta m = 5$-6 magnitudes have been seen. The flux variations of OVV quasars are comparable with this, but the variations in most quasars and Seyfert nuclei are much more modest - only 10-20%. During the long-term changes, the shape of the optical/infrared continuum is usually constant (Kikuchi et al., 1976; Smith et al., 1975; Rieke

et al., 1976), though short-term changes in α have occured in some sources (Oke, 1966; Visvanathan, 1973; Craine et al., 1975). Most of the monitoring programs cover only the optical variability, but the infrared variations have the same characteristic timescale and amplitude. The widespread correlation of infrared and optical variations supports the idea that all the radiation in that wavelength band comes from the same emitting volume. More significantly, BL Lac objects are the only class of extragalactic object (with OVV quasars) to show correlated radio and optical/infrared variability. Simultaneous radio and optical outbursts have been observed in OJ287 (Rieke & Kinman, 1974), AO 0235+164 (Rieke et al., 1976) and 1921-293 (Gilmore, 1980a), with the high frequency variations occuring much more rapidly than the radio variations. It appears that the radio and infrared/optical fluxes are closely related in some BL Lac objects, and are all produced by the synchrotron mechanism. The few sub-millimeter observations indicate that there is little deviation from a simple extrapolation between the high frequency radio and near infrared points.

1.2.4 Linear Polarization

The most distinctive property of BL Lac objects is their strong and variable linear polarization. Polarization has been observed in a variety of extragalactic objects, and can be caused by several physical mechanisms. Visvanathan (1974) and Hagen-Thorn (1974) have summarized polarization by scattering in normal galaxies, and Maza et al. (1979) have surveyed the polarization of 47 Seyfert galaxies where 8 of the sample had polarizations greater than 1.5%. The optical and infrared polarization of Seyferts is predominantly due to dust scattering, since spectropolarimetry shows the emission lines and continuum to have the same degree of polarization (Stockman et al., 1976; Thompson et al., 1980; Martin, 1979). Stockman and Angel (1978) measured the optical linear polarization of 44 optically bright quasars, and the large majority have low ($p \sim 1\%$) intrinsic polarizations. The sample was later extended to 102 objects with no difference between the polarization distribution of the optical and radio-selected quasars (Stockman, 1978). BL Lac objects and OVV quasars have much stronger optical polarization ($p > 5\%$) which is attributed to synchrotron emission. These

objects do not form a simple continuation of the polarization distribution of quasars; the distribution is bi-modal with the majority having $p < 2\%$ and a small tail of highly-polarized objects. High polarization is a good discriminant between BL Lac-type objects and 'normal' quasars.

BL Lac objects show substantial linear polarization at all wavelengths. At radio wavelengths, the polarizations are lower and the fluctuations less rapid than at optical wavelengths. Wardle (1978) surveyed the polarization of 27 BL Lac objects at centimeter wavelengths and nearly half the objects had $p > 10\%$. Conversely, the highest degree of polarization in a variable quasar was 6.5%, so there is a demarcation between quasars and BL Lac objects in terms of radio as well as optical polarization. Aller et al. (1980) have extensively monitored the polarization of fourteen variable radio sources, including seven BL Lac objects, at 4.8, 8.0 and 14.5 GHz. The degree of polarization and position angle vary on the same timescale as the total flux, and the detailed behaviour varies from object to object. There is no correlation of flux, polarization and position angle (Seielstad & Berge, 1975) or of polarization position angle with the orientation of VLBI structure (Altschuler & Wardle, 1977). The polarization behaviour is probably complex because of the complicated spectral structure of most BL Lac objects; several self-absorbed components may be contributing to the resultant polarization. Nevertheless, some very simple and important variations have been observed. BL Lac, OV-236 and OX 036 have shown rapid, large amplitude variations in position angle, always returning to the value before the burst (Aller et al., 1980). The position angle of OJ 287 rotated systematically by $\sim$100 degrees over two years, similar to the change expected when a synchrotron source evolves from being opaque to transparent. This interpretation was supported by the fact that the rotation propagated from high (8 GHz) to low(2.7 GHz) frequencies, which presumably became transparent at successively later times (Aller & Ledden, 1978). Even more striking are the linear position angle rotations which have been detected as the amount of systematic

monitoring increases. Ledden and Aller (1978) observed a remarkable 130 degrees rotation over 40 days during an epoch of otherwise random variations in AO 0235+164. The most reasonable explanation is a rotation of the magnetic field in the emitting region.

Most of the radio flux, polarization and position angle variations are consistent with the injection of populations of synchrotron-emitting electrons in a relatively small volume of the source. The high polarization and long-term position angle stability imply that the magnetic field structure is not disrupted by the bursts. The spectra of the polarized emission as it develops suggests that the absorption depth is near unity at lower frequencies, probably due to synchrotron self-absorption by the emitting particles themselves. It is significant that neither the position angle rotations nor the low (compared with the optical) polarizations can be due to Faraday effects. Faraday rotation outside the source is small; there is little rotation in the intergalactic medium (Kronberg, 1977) and little rotation in our own galaxy for $|b^{II}| > 25^{o}$. Unless the source has a special geometry or large amounts of electron-position plasma, the limits on "front-back" Faraday depolarization restrict the proportion of thermal to relativistic electrons to be very small, $n_e/n_{rel} < 10^{-2}$ (Altschuler & Wardle, 1977). This limit is improved by looking for variable Faraday rotation between wavelengths, since the rotation is proportional to 1/(wavelength squared). The lack of observed Faraday rotation in some sources sets limits of $n_e/n_{rel} < 10^{-4}$ (Wardle, 1977). These limits are so severe that some Faraday rotation might be expected due to the relativistic electrons themselves. Not only must there by very little thermal plasma in the source, but the power-law distribution of the relativistic electrons must cut off below a Lorentz factor of $\sim$10 (Jones & O'Dell, 1977a).

The polarization of BL Lac objects in the optical and infrared bands is generally higher than at radio frequencies. There are four BL Lacs with maximum polarizations greater than 30% and another nine with values greater than 20%. The observations and current theoretical models have been reviewed in a comprehensive article by Angel and Stockman (1980). Characterising the polarization

behaviour is difficult, because the most dramatic and highly polarized objects are often those which have been most frequently observed. The highest polarizations (44% - see figure 3.5b) are a sizeable fraction of the maximum degree of polarization for synchrotron emission in a uniform magnetic field. This indicates that there is very little inhomogeneity in the source emitting region. Optical monitoring by Angel et al. (1978) shows that the power spectrum of variability drops off on timescales of less than a day; large hourly changes are very rare. At the other extreme, Kinman (1977, 1978) has discovered systematic changes in the annual means of the normalized Stokes parameters for 3C 345 and OJ 287. Polarization is usually independent of wavelength across the optical and infrared (Knacke et al., 1976; Tapia et al., 1977), but there are examples of polarization decreasing (figure 3.5) and increasing (Knacke et al., 1979) with wavelength. BL Lac objects split into two groups with respect to position angle rotations. One group has position angles which cover 2π radians and can be wildly variable; they are nearly all very luminous. The other group have preferred angles and are generally less luminous. Despite the range of properties in BL Lac objects, there is nearly a 1:1 correspondence between high optical polarization, optical variability and the presence of strong radio emission. Therefore, highly polarized objects are invariably those active nuclei with extreme non-thermal emission.

1.3 Infrared Polarimetry

The first infrared polarimetry of a BL Lac object consisted of 2.2μm and 3.5μm polarimetry of the prototype BL Lacertae by Knacke et al. (1976). The polarization was independent of wavelength from 0.44 - 3.5μm and substantial dust emission was ruled out. Since then, 2.2μm polarimetry has been published for AP Lib (Capps & Knacke, 1978), OJ 287 (Rudnick et al., 1978), OI 090.4, 0735+178, Mk 421 (Rieke et al., 1977), 1308+326 (Moore et al., 1980; Puschell et al., 1979) and 3C345 (Knacke et al., 1979). Where simultaneous optical and infrared polarimetry is available, the variations are

similar at all wavelengths (1308+326: Moore et al., 1980). Rieke et al. (1977) observed position angle rotations between the optical and the infrared in 0735+178 and OI 0904. In contrast to the first published observations of BL Lac, Puschell and Stein (1980) found wavelength-dependent polarization with the polarization increasing with decreasing wavelength. Knacke et al. (1979) observed the opposite dependence in 3C345, with the polarization increasing towards the infrared. Their measured infrared polarization is one of the highest ever recorded, 23.8% at 2.2μm. The near infrared is a productive wavelength range for polarimetry of BL Lac objects. Not only are the maximum polarizations as high and the variability timescales as short as at optical wavelengths, but the infrared excess means that most of the energy is emitted beyond 1μm. Therefore, infrared measurements give the most severe limits on the energy density in the compact source.

In Chapter Two, the design and use of the infrared polarimeter is discussed and the instrumental parameters and data reduction algorithms are derived. Chapter Three presents the observations. The observations are interpreted in terms of current theories for the power source and emission mechanism in Chapter Four, and in Chapter Five simple models of the magnetic field geometry in BL Lac objects are presented, with the aim of understanding their polarization properties.

CHAPTER TWO

This chapter describes the configuration of the polarimeter, detector and telescope used in all the observations. It also contains a description of the observing, calibration and reduction procedures. All of the observations were made using the 3.8m United Kingdom Infrared Telescope between December 1979 and August 1980. Because of the developing state of the telescope and instrumentation during that period, the experimental configuration was not the same for each observing run. The special techniques of infrared photometry and polarimetry demand a discussion of several parts of the telescope system in addition to the polarimeter.

The infrared polarimeter used for these observations was designed, constructed and tested during a seven day period in December 1979. It was anticipated that various aspects of the early UKIRT instrumentation might contribute systematic errors to the measurements, so the aims of the polarimeter were modest. It was designed to measure the high linear polarizations shown by BL Lac objects with a polarimetric precision of $\sim$ 1%. The principal merit of the polarimeter is its simplicity.

2.1 Equipment

2.1.1 Polarimeter.

The polarimeter consists of a circular plate in which is mounted a circular hollow bearing rotated by a stepper motor. A teflon belt drives the bearing from the stepper motor via reduction gearing of 3:1. A 2 inch square of HR Polaroid is mounted in the hollow bearing. On the rim of the bearing is a projection which trips a switch and acts as a repeatable top dead centre for the rotating analyzer.

In December 1979, the polarimeter was mounted upstream of the dichroic mirror between the two castings of the f/9 configuration. In April, July and August 1980 the polarimeter was mounted downstream of the dichroic on one of the ports of the photometer cage. In December, April and July the telescope was operated at the f/9 Cassegrain focus using focal plane chopping. In August 1980, the f/35 focus with chopping secondary was employed. The position of the polarimeter in the light path has a significant effect on the instrumental polarization, and is discussed later in Chapter 2 (see Fig. 2.1).

2.1.2 Detector

The infrared detector used is a 0.5mm piece of indium-antimonide which is a photoconductive material and electronically acts like a diode. The detector has a high impedance and two values of feedback resistor (Rs) are used to maintain the bias conditions under varying ranges of light intensity ($L_oR_f = 5 \times 10^9\Omega$; $H_iR_f = 2 \times 10^{11}\Omega$). For faint objects or long wavelengths (L and longer), H_iR_f is used; for standards and bright stars, L_oR_f is used. Since $L_oR_f << H_iR_f$, the two resistors in parallel effectively equal L_oR_f. To use H_iR_f, L_oR_f is simply switched out of circuit. The two feedback resistors must be very stable and carefully isolated from the rest of the circuitry to prevent stray capacitances from altering their effective impedance. The balance potentiometer controls two back-to-back F.E.T.'s and must be adjusted to optimize noise. The offset potentiometer controls the biassing condition by routing a highly linear fast-slewing opamp through R_f into the FET chain. Saturation voltage for the circuit is 1.1 volts (Fig. 2.2).

2.1.3 Cryostat

The InSb detector and preamp circuitry are mounted inside an Oxford Instruments Dewar. To prevent thermal noise and microphonics the electronics are thermally and mechanically isolated from the inner walls of the cryostat. The entry port (side-looking) has a mica window, followed by the filter wheel, the aperture wheel and a Fabry lens imaging onto the detector. The filters used in this work were the J, H and K filters, and the only apertures those of diameter 10, 15 and 19 arc seconds.

The inner and outer jackets of the cryostat are filled with liquid nitrogen (T = 77K) and the inner nitrogen is pumped solid on the telescope so the actual temperature is approximately 65K. The outer jacket is topped up periodically during the night to keep the detector temperature nearly constant. Every three or four days the inner jacket is brought up to ambient pressure, back-filled with Helium, and refilled with Nitrogen. The Nitrogen cooling reduces the detector noise, as does a technique called "flashing". It has

been discovered empirically that the unlikely procedure of shining a torch directly onto the InSb crystal decreases the detector noise by a factor of 3 or greater. The size of the effect varies from detector to detector but usually persists for a couple of days, and there appear to be no short term changes in sensitivity.

The mechanism for this noise reduction is not properly understood, but it is possible that the influx of light creates a quasi-stable population of electrons in the conduction band of the crystal which increase the conductivity but not the sensitivity. However poorly understood it is, "flashing" has become a standard technique in infrared astronomy (Soifer & Pipher, 1978).

2.1.4 Phase Sensitive Detection

One of the characteristics of infrared observations of faint sources is that the signal is often very much smaller than the noise contribution from the sky. Therefore star/sky chopping is a commonly employed technique where the object signal is subtracted from the signal due to object + sky at a rate faster than the variations in sky brightness. There are normally two ways of subtracting the stellar signal. With focal plane dropping, the angled dichroic is mounted on a Ling vibrator which performs a square wave motion of variable frequency, and throws the beam a specified amount in the focal plane. The throw required clearly depends on the aperture used but has a maximum of ~19 arc seconds, and the normal chopping frequency is between 6 and 10Hz. The second way of performing the subtraction is using a chopping secondary mirror, which on UKIRT is driven hydraulically. This has several advantages over focal plane chopping, including a much larger throw (2 arc minutes), variable orientation of throw and less microphonics because the mechanical vibration is well removed from the cryostat.

Phase sensitive detection of the signal uses a half-wave rectifier tuned to the mirror chopping frequency. The input to the P.S.D. is an alternating signal of star and star + sky, and the P.S.D. inverts the sky signal so that the net signal is star only. Therefore the output of the P.S.D. is a D.C. voltage, and if the object is faint, the D.C. level will hardly be distinguishable from noise fluctuations

about zero. This voltage goes to a V-F converter which is linear over a large bandwidth and can adequately digitize bright and faint objects and accurately represent the noise fluctuations. The output of the V-F is a series of pulses produced at a rate proportional to the D.C. input level. The pulses are registered in 1 second bins and integrated for a time determined by the observer (these are instrumental pulses, and there is no analogy with photon counting). In addition to sky chopping, there is a much slower beam switching or "nodding" where the star is alternately placed in each of the two chopping positions. In this way the effect of sky brightness gradients in the vicinity of the object is removed. Beam switching is normally done every 10 to 20 seconds. The data acquisition system is shown in Figure 2.3.

2.1.5 System Software

The pulse trains from the V-F converter are counted over a fixed interval by the LSI 11 software. One beam switch pair (left and right) is used as one observation to estimate a probable error and calculate an instrumental magnitude. If a standard star has previously been observed, instrumental magnitude offsets can be used to calculate the true magnitude of a program star. Each left-right pair is multiplied by the range on the amplifier, which has been calibrated to <0.1%. Data files are labelled and stored on disc and can be manipulated and displayed on a Tektronix scope. The LSI 11 drives the filter wheel and counts and times the integrations through a CAMAC interface.

2.1.6 Polarimetry Software

The polarimeter uses the CVF mode of the LSI 11 system. By using the CAMAC port normally assigned to the filter drive unit, the observer drives the analyzer as if it were a CVF. A polarization scan consists of integrations at 8 positions separated by 45^{o}; successive scans are co-added and the integration time at each position can be set by the observer. After each scan (or "8 wavelength

spectrum"), the Polaroid is returned to the top dead centre position with a precision of one stepping motor step or 0.3^{o}. There is no chance of a cumulative position angle error with this procedure. As data is acquired, it can be reduced in real time using an instrumental parameter file which is stored on disc. At the end of an observation, it is possible to print out the magnitude, polarization and position angle of the object plus the relevant instrumental polarization parameters. The reduction software is outlined in Figure 2.5.

2.2 Observing Procedures

2.2.1 Configuration of the Polarimeter

The position of the polarimeter in the light train of the telescope was dictated by the need to accurately guiding on optically faint objects. During the period of the observations, the limiting magnitude of the UKIRT T.V. guiding system was brighter than all but one of the program objects. Therefore object guiding was impossible. In December 1979, the polarimeter was mounted upstream of the focal plane chopper (dichroic); however, the attenuation of light reaching the T.V. by the Polaroid prevented even the use of offset stars for guiding. So a flip-in mirror and graticule were used to position the object in the left and right beams by eye. This observing procedure was very inefficient. In April and July, 1980 the polarimeter was placed downstream of the dichroic on the entry port of the cryostat. This permitted use of the T.V. system to offset guide on a bright star. At f/9, the travel on the X-Y crosshold for the T.V. camera was $\pm$ 12" and an SAO star could be found near most of the BL Lac objects. For the remainder, a bright star in the field was measured on an X-Y machine to about 2" . However, it is a polarimetric principle that there should be no optical component above the analyzer because it may alter the Stokes parameters of the incoming light. To understand the effect of the dichroic mirror, a series of tests had to be made on the telescope.

These are described in the next section. In August 1980, a further complication was added by working at f/35 with a chopping secondary. The reduction in the size of the offset field from f/9 to f/35 scaled the offset stars for most objects beyond the reach of the crosshead, and since the T.V. limiting magnitude was only $n_v = 14$, observations were restricted to BL Lac objects with bright, nearby guide stars. Because of the different configurations of the polarimeter, the instrumental parameters were expected to change from run to run. In particular, a different reduction procedure was required for measurements made with the analyzer before and after, the dichroic mirror (Table 2.1).

2.2.2 Observing Procedures

On each night, the inner and outer jackets of the cryostat were topped up with liquid Nitrogen and the detector was given a 2-3 minute "flash" with a torch through the J filter (the length and intensity of the flash did not appear to be critical, although some InSb systems do not respond to "flashing"). After adjusting the balance pot, the detector noise was measured with a blank aperture in position and the bias voltage on. The next checks, both critical for good photometry, were the focus and beam profiles. The infrared focus is normally linked to the T.V. focus, but with the thermal inertia of the telescope being significant, it can change and must be checked more than once in a night. Optimum focus is essential when the beam is being imaged onto a $\frac{1}{2}$mm detector. Beam profiles were mapped by drifting a bright star through the left and right beams. First, the profiles should be flat-topped and steep-sided; if they are not then signal can be lost by small deviations in guiding. The diagnosis for peaked beam profiles is usually poor Fabry optics. Second, the beam separation must be adequate. Unless the chopping throw is larger than the aperture being used, there will be no plateau of zero signal between the right and left beams. When the T.V. was being used for guiding, the half-power points on four sides of each beam were marked on the T.V. screen as an aid to guiding.

Since flexure in the telescope, dichroic mounting and T.V. mounting can change the beam positions substantially, they were checked repeatedly, especially after moving through the zenith.

After acquiring and centering an object, the observing routine began by choosing an integration time for each position angle in a polarization scan. For most of the observations, that ranged from 5 to 10 seconds and a complete scan took from ¾ to 1½ minutes. Although rapid rotation would have allowed the advantage of working through thin cloud such as cirrus, it was impractical to drive the analyzer any faster than 1Hz and the resolution would have been considerably degraded* All the observations were made in the step-and-integrate mode, with the facility to pause between individual integrations or between complete scans. Occasionally a noise spike or "glitch" contaminated a point in a scan, and with the LSI 11 software it was possible to redo that point. Meanwhile, the offset star was kept in the centre of the appropriate beam using the analogue guiding mode operated through a joystick. With analogue guiding, any tendency for PA oscillations was considerably reduced. Polarization scans were coadded and displayed until sufficient precision had been achieved. Data files were written to disc as they were acquired, and a separate observing log was kept to record housekeeping information and weather conditions. Notes were written on the computer output and on the chart recorder output to diagnose glitches, noise and amplifier gain settings.

During each night, photometric and polarimetric standards were observed, with photometric standards serving as extra checks on the instrumental polarization. The standard stars used during the observations are listed in Table 2.2. A second piece of HR Polaroid was used for tests of Polaroid efficiency and the polarization properties of the dichroic. In July and April, objects of known polarization were observed. In December, a faint unpolarized source was observed to check for magnitude-dependent effects in the

---

* The duty cycle of integration/rotation with 10 seconds/angle was >90%.

instrument. Observations of an unpolarized standard were made with the photometer cage rotated through 90°, to measure any polarization due to the telescope optics. The instrumental parameters were checked during each run.

2.2.3 Sources of Error

The sources of error in the photometry and polarimetry are noted here in principle and are quantified in Section 2.4. It was recognized that because of imperfections in the polarimeter, problems with guiding, non-ideal beam profiles and other systematic errors, the strict photon-error was unlikely to be the dominant contribution to the precision of an observation. Since the offset crosshead could not move reliably onto an object viewed through a 10" or 15" aperture, the position of the object in a beam was always checked by peaking up on the half-power points of the infrared signal. This limited observations to BL Lac objects whose signal could be seen on the strip chart; in general more than 3 magnitudes above the detection limit of the system. Blind offsetting onto faint sources was not possible. Once centred, the object was kept within the infrared beam by guiding the appropriate bright offset star on the T.V. screen. 10",15" & 19" apertures were used throughout and no correction was needed between them because the sources were stellar and observations at 2μm were not background limited. In July and August, the beam profiles were poor with peaked tops and a reduction in signal within the extent of the aperture. Therefore guiding to better than 2" was needed to maintain the integrity of the signal to a few percent. In general, this was not a problem; but in the presence of a strong wind and at large zenith distances, telescope oscillations of 1-3" were observed and contributed errors to the photometry.

During parts of the April, July and August runs, observations were made in non-photometric conditions. Without fast rotation of the analyzer, the polarimetry is contaminated by changes in transparency. Weather conditions were monitored by standard observations

at the beginning, middle and end of the night and the photometric error within a night was characterized by the agreement of standard magnitudes with published values. It is noted that one potential problem was avoided by step-and-integrate polarimetry. The presence of a stepping motor near the beam is a possible source of heat contamination. However, by being run only intermittently, the stepper motor never reached its operating temperature and did not contribute to the thermal noise.

In the reduction of the observations a three tier system of error determination was used. First, the formal photon error was calculated based only on the intensity of the source. Second, a standard error was calculated based on the goodness of the least square fit to the data points. The standard error uses the reduction algorithm and includes the uncertainties in the instrumental polarization parameters. Finally, a representative error was calculated. This includes the agreement of the standard observations (photometric, unpolarized and polarized), with published values and the consistency of measurements within a night, within a run and between runs. The representative error also reflects the correctness of the reduction algorithm and includes sources of systematic error such as guiding errors, imperfections and dust on the analyzer and optics, reflected light in the photometer cage, beams wander on the detector, flexure of the telescope and poor transparency. In general the three errors increase in magnitude, and in this study the largest will be adopted as the true error.

2.3 Calibration

2.3.1 Definitions

A polarized beam of light can be described in terms of the ellipse swept out by the electric field vector, with four parameters corresponding physically to the shape, size, orientation of the major axis and sense of rotation of the electric vector. The four parameters are the semi-major axis E_a, the semi-minor axis E_b, the angle θ between the semi-major axis and x-axis of an arbitrary Cartesian coordinate system, and the sense of rotation of the electric vector as viewed down the Z-axis of the coordinate system (Fig. 2.4). A beam

composed of unpolarized light of intensity I_u and polarized light of intensity I_p (where $I_p^2 = E_a^2 + E_b^2$) is described by four quantities known as the Stokes Parameters (I, Q, U and V), which are defined by

$$I = I_u + P_p \tag{2.1a}$$

$$Q = I_p \text{ Cos } 2\xi \text{ Cos } 2\theta \tag{2.1b}$$

$$U = I_p \text{ Cos } 2\xi \text{ Sin } 2\theta \tag{2.1c}$$

$$V = I_p \text{ Sin } 2\xi$$

where

$$I_p = \sqrt{Q^2 + U^2 + V^2} \tag{2.2}$$

and

$$\tan 2\xi = E_b/E_a \tag{2.3}$$

The linear polarization p is defined as

$$p = I_p \text{ Cos } 2\xi/I \tag{2.4a}$$

and the circular polarization is given by

$$q = I_p \text{ Sin } 2\xi/I \tag{2.4b}$$

The advantage of using Stokes parameters is that although they were formulated to describe perfectly polarized light, they can be used for any partially polarized light beam. A generalized light beam has two components with the following Stokes parameters.

Unpolarized component : I_u, 0, 0, 0

Polarized component : I_p, Q, U, V

The Stokes parameters of a light beam will alter as they pass through an optical element, and are dealt with using the Meuller calculus (Meuller, 1948). This formalism treats the Stokes parameters as a column vector and the optical component as a suitable matrix. The emergent light after passing through N elements is given by

$$\begin{pmatrix} I^* \\ Q^* \\ U^* \\ V^* \end{pmatrix} = \{X_i\}\{X_{i+1}\}\{X_{i+2}\} \ldots \{X_N\} \begin{pmatrix} I \\ Q \\ U \\ V \end{pmatrix} \tag{2.5}$$

Each element must have its axes transformed into the same reference frame and particular care must be taken to apply the elements in their right order, as matrix algebra is non-commutative. The elements used in this analysis represent partial polarizers and retarders. The telescope and analyzer are assumed to be partial polarizers and the dichroic mirror is assumed to be a partial polarizer and retarder. All angles and rotations are taken with respect to polarization on the sky, i.e. North-South is zero and angles increase measured North through East. The matrix elements which will be frequently used in the reduction are derived in Appendix A. The Meuller matrix for a partial polarizer is given by

$$\{P'\} = \tfrac{1}{2}\begin{pmatrix} (K_1+K_2) & (K_1-K_2) & 0 & 0 \\ (K_1-K_2) & (K_1+K_2) & 0 & 0 \\ 0 & 0 & 2(K_1K_2)^{\frac{1}{2}} & 0 \\ 0 & 0 & 0 & 2(K_1K_2)^{\frac{1}{2}} \end{pmatrix} \tag{2.6}$$

where K_1 and K_2 are the principle transmission coefficients in orthogonal directions bounded by

$$0 < K_2 < K_1 < 1 \tag{2.7}$$

For an ideal analyzer $K_1 = 1$ and $K_2 = 0$. The matrix element for a pure retarder is given by

$$\{R\} = \begin{pmatrix} 1 & 0 & 0 & 0 \\ 0 & 1 & 0 & 0 \\ 0 & 0 & \cos\delta & \sin\delta \\ 0 & 0 & -\sin\delta & \cos\delta \end{pmatrix} \tag{2.8}$$

where δ is the differential retardation or retardance. The matrix element for rotation of axes is given by

$$\{\Delta\} = \begin{pmatrix} 1 & 0 & 0 & 0 \\ 0 & \text{Cos } 2\Delta & \text{Sin } 2\Delta & 0 \\ 0 & -\text{Sin } 2\Delta & \text{Cos } 2\Delta & 0 \\ 0 & 0 & 0 & 1 \end{pmatrix} \qquad (2.9)$$

where Δ is the angle between the principal axis of the optical component and the reference frame of position angles on the sky. The matrix with $\Delta = -\Delta$ is called $\{\Delta'\}$ and $\{\Delta\}\{\Delta'\} = \{I\}$, the unit matrix. Therefore the full matrix operator used to incorporate an element X into the optical train is

$$\{\Delta'\}\{X\}\{\Delta\} \qquad (2.10)$$

and from eqn. (2.5)

$$\begin{pmatrix} I^* \\ Q^* \\ U^* \\ V^* \end{pmatrix} = \{\Delta'\}\{X\}\{\Delta\} \begin{pmatrix} I \\ Q \\ U \\ V \end{pmatrix} \qquad (2.11)$$

2.3.2 Instrumental Parameters

For this telescope-polarimeter combination, there are eight instrumental parameters to determine (seven of them at three wavelengths each). They are:

- S - instrumental sensitivity
- $\underline{\beta}$ - efficiency of the HR Polaroid
- β', ω - polarization and position angle of the telescope
- β, α - polarization and position angle of the dichroic mirror
- γ - effective retardance of the dichroic mirror
- ε - conversion angle for position angle zero point.

The 22 parameters are determined by various tests on the telescope, with as much multiplicity as possible to ensure reliable answers. Three of the parameters were only calculated during one run and were assumed to remain constant.

(a) β', ω : the linear polarization of a Cassegrain telescope does not usually exceed 0.1%, so β' would be expected to make a negligible contribution to the analysis. To check this, an unpolarized star from Serkowski's list(1974a)was observed. These stars have been observed with rotatable tube telescopes and are therefore reliable standards. Scans were taken with photometer cage at 0° and 90°, and reduced according to the equations (C4) and (C5). The results were,

$$\beta_J < 0.3\% \ , \quad \beta_H < 0.2\% \qquad (2.12)$$

In view of the errors introduced by other parts of the polarimeter, it was clear that the telescope polarization could be taken as zero since the errors on these measurements were $\sim$0.2%. The result was applied to the K waveband too, and in all the subsequent analysis,

$$\beta_{J,H,K} = 0 \ , \quad \omega_{J,H,K} = 0 \qquad (2.13)$$

(b) $\underline{\beta}$: The published efficiency curve for HR Polaroid (Polaroid U.K. Ltd.) shows that it becomes 'leaky' longward of 2.2μm. Since the efficiency $\underline{\beta}$ is a factor as in all the reduction equations, it must be calculated very carefully, especially across the K waveband. First, it was calculated by convolving the transmittance of the UKIRT filters with the principal transmittances of the HR Polaroid as a function of wavelength and considering various incident flux distributions. This calculation is presented in Appendix E, and the results were,

$$\underline{\beta}_J = 0.9986, \quad \underline{\beta}_H = 0.996, \quad \underline{\beta}_K = 0.916 \qquad (2.14)$$

There is a $\sim$10% leakage of unpolarized light across the K waveband. Although a uniform flux distribution with wavelength was assumed, using power law flux distribution of slope $\alpha = 2$ (typical for a BL Lac object) makes less than 1% difference in $\underline{\beta}_K$. A second determination came from a telescope test involving crossed, identical HR Polaroids. From equation (C 14),

$$\underline{\beta}_J = 0.991, \quad \underline{\beta}_H = 0.994, \quad \underline{\beta}_K = 0.881 \qquad (2.15)$$

The agreement is good: less than 0.5% at J and H, and 3.5% at K. The published curves for Polaroid materials are not guaranteed to better than a few percent. The experimental values (2.15) for $\underline{\beta}$ were adopted (see Table 2.8 for summary).

The other quantities, which refer to the dichroic mirror and the sensitivity of the InSb detector, were determined on every night. The instrumental sensitivity S was measured by observing photometric standards from the UKIRT, Glass and AAO lists. These stars are usually brighter than K = 4 and often had to be observed with a divide-by-10 circuit to reduce the signal below the saturation level. The scaling circuitry has been calibrated to 0.1%, so no systematic errors were caused by calibrating faint objects with bright standards. During some nights the transparency was poor and the accuracy of the photometry was determined by (a) the consistency between closely spaced scans of the same star (Table 2.4) and (b) differences between the instrumental sensitivity on successive nights (Table 2.5). Changes in sensitivity between runs may be expected since a different detector was used in December and in April-July. In August, a different telescope f-ratio and cryostat were used and the sensitivity is likely to be different again. The values of S are presented in Table 2.3 and Figures 2.6-2.8.

The sensitivity is calculated in terms of the magnitude of the standard (m) by,

$$S = \exp\left[\frac{-\log_e 10 m}{2.5}\right]/\bar{I}_K = \exp\left[\frac{-\log_e 10 m}{2.5}\right]/K \qquad (2.16)$$

the object magnitude is therefore calculated by,

$$m = \frac{-2.5}{\log_e 10} \log_e(S.K) = -2.5 \log_{10}(S.K) \qquad (2.17)$$

The transmission curves of the broadband interference filters are plotted in Figures E2, E3 and E4. The effective wavelengths are 1.25μm(J), 1.65μm(H) and 2.2μm(K). The flux calibrations were taken from Neugebauer et al., (1979) and Beckwith et al., (1976), and are based on the model of αLyr by Schild et al., (1971) and absolute measurements of αLyr by Oke and Schild (1970). The spectral flux calibrations and typical telluric extinction coefficients for Mauna Kea are

listed in Table 2.1. BL Lac objects are significantly redder than the stars used as calibration standards and the effect of mapping the energy distribution with broadband filters means that the calibration will only be accurate to ~5%. It is worth noting that the general lack of emission and absorption features means that the colours are insensitive to changes in z, and that differential flux measurements are considerably more accurate than 5% and usually limited by other systematic errors. For conversion from the broad band filter system to flux units, a correction for each waveband must be derived from the transmission functions of the filters and the polaroid, the spectral sensitivity of the detector and the flux distribution of the object. This calculation is presented in Appendix E(ii) and the fluxes in Table 3.4 have been corrected appropriately.

The general effect of mounting the polarimeter above and below the dichroic is now discussed. Each set-up has its own disadvantages for accurate polarimetry. Only by carefully considering the polarizing properties of each element in the light path can consistent results be obtained. In December 1979, the polarimeter was mounted upstream of the dichroic mirror and was therefore the first optical element (the telescope having insignificant polarization). The next element was the dichroic, which consists of a metallic film plus optical anti-reflection coating on a dielectric substrate. The optical radiation passes straight through to the T.V. guider and the infrared beam is reflected at 45°. In general, a tilted mirror will introduce both linear polarization and linear-to-circular conversion to a partially polarized incident beam. Therefore the dichroic is characterized by an instrumental linear polarization and position angle (β,α) and a retardance (δ). The characteristics of metallic reflection are discussed in Appendix D. In this treatment, the only assumption made about the action of the dichroic is that the principle axes of retardance and partial polarizance are identical (In fact, a difference of 5° would make a difference of <3% in the terms of matrix element {D} - see Appendix A(iv) and (v)). It can be shown that the two actions of the dichroic are independent - see Appendix A(iv). The problem with having a partial polarizer between the rotating analyzer and the detector is that the signal is modulated at four times the rotation frequency of the analyzer (Appendix C(v)). There are terms in 4Ø in

equation (C.16), where $\emptyset$ is the rotation frequency. Since there are only sampled intensities at 45° intervals, a sampling frequency of $8\emptyset$, Fourier components at $4\emptyset$ are aliassed and that information cannot be retrieved. However the Fourier components at $2\emptyset$ contain the polarization information of the source, and the polarization can be computed exactly (C.20)(C.21). The consequence of power in a higher order component is that signal-to-noise is degraded in the $2\emptyset$ components fitted by least squares. One solution would be to sample more frequently, another would be to use a (wavelength integrating) depolarizer in between the analyzer and dichroic. With a depolarizer, unmodulated radiation would be incident on the dichroic and the $2\emptyset$ modulation produced at the detector could be subtracted off by observing an unpolarized star.

With the dichroic above the analyzer, both the linear polarization and the retardance of the dichroic become important. The Stokes parameters of the dichroic as a partial polarizer will just add vectorially with the Stokes' Parameters of the incoming light, and can be subtracted away using an unpolarized star. However the action of the dichroic as a retarder will depend on the phase of the incoming light, and the retardance can only be calibrated by observing a star of known polarization and position angle. The effect of retardance can be seen in equation (B.7), where for convenience the quantity γ is used ($\gamma = \sqrt{1-\beta^2}\cos\delta$). At reflection, the E vector parallel to the principle axis of the dichroic suffers a phase change δ. The effect is equivalent to linear-to-circular conversion. In equation (B.7), the effect is to reduce the modulation on the term $\sin 2(\emptyset-\alpha)$, i.e. the term parallel to the principle axis. If $\delta = 0$, there is no demodulation and if $\delta = 90^{\circ}$, the E vector is rotated to be perpendicular to the principle axis and the term in $\sin 2(\emptyset-\alpha)$ is zero. In general, if linearly polarized light passes through a retarder, the emergent light will have two components differing in phase by δ. Since the tip of the E vector describes an ellipse, linear polarization will be converted into elliptical polarization.

β, α and δ must carefully be calculated. Since the demodulation by δ depends on the incoming Stokes parameters, it should be derived

for several incident position angles otherwise a small error in the angle can make a substantial error in the determination of δ. Similarly, in (C.22) the angles fitted by least squares involve $(\emptyset-\alpha)$, so α must be well-determined. Since the dichroic is so important to the polarization properties of the instrument, the physics of its action is discussed in Appendix D.

(c) β,α : The values of β and α derived from observations of unpolarized stars are given in Table 2.6. The reduction formulae are given by equations (C.9) and (C.10). It is noted that for observations of an unpolarized star, there is no difference between the two situations with the dichroic above and below the analyzer. Table 2.6 shows that the metallic reflection of the dichroic has introduced significant instrumental polarization which increases with decreasing wavelength. The magnitude and wavelength dependence of β and α are in agreement with the theoretical calculations of Appendix D. On many occasions, the photometric standard serves as a secondary check on the instrumental polarization. It can be seen that β and α change their mean values between runs, which can be expected due to deterioration of the dichroic or a different light path of the reflection. The value of β increases from Run 1 to Runs 2 and 3, and again to Run 4. The two runs (2 and 3) which took place with the same optical train show good agreement indicating that the optical configuration is more important than deterioration of the dichroic in determining β. The same dichroic material was used in Runs 1, 2 and 3 with a different piece in Run 4, and there is much larger dispersion in β and α during Run 4. There are also changes in the mean value of α, the position angle, between runs. If the dichroic is mounted North-South, α will be 90°. However, the procedure of aligning the optical and infrared axes of the telescope and imaging the beam on to the detector usually involves moving the dichroic on its triaxial mount. In Runs 2 and 3 it was clear from visual inspection that the dichroic was not in the North-South plane, hence α was not exactly 90°. In the case of focal plane chopping, the displacement would not be truly vertical and this was confirmed on the T.V. monitor. The dispersion of β and α between nights was always less than the changes between runs. β and α are plotted in Figures 2.9 - 2.11.

(d) γ : As discussed in Appendix D, metallic reflection generally introduces a phase lag between the components of the E vector parallel and perpendicular to the plane of incidence. The effect of the retardance depends on the Stokes parameters of the incident light, but generally δ will reduce the measured degree of linear polarization and rotate the plane of polarization. Equation (B.6) demonstrates that the retardance of the dichroic is not important when the analyzer comes first in the optical train. Therefore the reduction of data taken in December 1979 (Run 1) does not involve γ. For the remaining runs, the retardance and its effect on calculated polarizations is shown in equations (C.22)-(C.26).

γ was calculated by observing an object with known polarization and position angle. Since the dichroic may deteriorate between runs, γ was determined during each run with the dichroic ahead of the analyzer. The first measure of γ came from observing the Becklin-Neugebauer Object in Orion which has the following polarizations,

$$p_K = 17.5\% \quad , \quad \theta_K = 113^o \tag{2.18}$$

$$p_H = 34\% \quad , \quad \theta_H = 116^o \tag{2.19}$$

The object is too faint at J to have a measured polarization. When γ is calculated according to equation (C.23),

$$\gamma_K = 0.757 \quad , \quad \gamma_H = 1.07 \tag{2.20}$$

When the polarization of the object is calculated using (C.25) and assuming that $\gamma = 1$ (no retardance),

$$p_K = 16.2\% \quad , \quad p_H = 39.5\% \tag{2.21}$$

The result of (2.21) where the polarization comes within 1.5% of the true K value with $\gamma = 1$, shows that γ is close to one. However, the H polarization is higher than the true value implying $\gamma_H > 1$ which is obviously a non-physical result. Although the B-N test gives an indication of γ, it has several disadvantages. First, it is not

possible at all at J and at H B-N is over four magnitudes fainter than at K so the signal-to-noise on the H measurement is degraded. Second, the form of equation (C.23) shows that for angles where $\theta=\alpha$ there is an infinite discontinuity,

$$\gamma_{J,H,K} = \frac{B_2(1+\beta p \text{ Cos } 2(\theta-\alpha))}{p\underline{\beta} \text{ sin } 2(\theta-\alpha)} \qquad (C.23)$$

At values of θ near α, γ will be highly sensitive to errors in p, θ and α. For B-N, $\sigma(p_K) \sim 1\%$ and $\alpha(\theta_K) \simeq 2^o$ and from Table 2.6 $\alpha \simeq 80^o$; therefore a 2^o change in θ can alter γ by as much as 0.1. In contrast, equations (C.22) and (C.24) show that the fitted parameters A_2 and B_2 and the object Stokes parameters p_1 and p_2 are smoothly varying functions of θ and α. Determining γ is very sensitive to discontinuities in equation (C.22), but once γ is determined polarizations can be calculated from the smoothly varying reduction formulae. The danger is that the observation of a polarized object might correspond to a discontinuity, and γ must be found in a way that is less dependent on the errors in p, θ and α.

A second piece of HR polaroid was mounted above the dichroic, giving an arrangement of polaroid-dichroic-polaroid. The top analyzer was rotated through 180^o in 15^o steps; and for each position of the top analyzer, the bottom analyzer rotated once and a scan was stored. 12 positions from 0^o to 165^o were used, which is a sample of one full modulation period. The reduction is given by equations (B.4) and (C.11), which are identical to (B.7) and C.22) except that $\underline{\beta}$ replaces p. The polarized source is now a sheet of HR polaroid. In Figure 2.12, A_2, B_2 and γ are plotted against the angle of the top analyzer. These results map out the response of the instrument to <u>all</u> incident Stokes parameters. γ can be calculated by fitting this curve, which is much less sensitive to errors in angle than the B-N method. From (C.22),

$$A_2 = \frac{\underline{\beta}(\beta+\underline{\beta} \cos 2(\phi'-\alpha))}{(1+\beta\underline{\beta} \cos 2(\phi'-\alpha))} \quad , \quad B_2 = \frac{\gamma\underline{\beta}^2 \sin 2(\phi'-\alpha)}{(1+\beta\underline{\beta} \cos 2(\phi'-\alpha))} \qquad (C.22)$$

When $(\phi'-\alpha) = \pm 90^o$,

$$B_{MAX} = \gamma_1 \underline{\beta}^2 \quad ; \quad B_{MIN} = -\gamma_2 \underline{\beta}^2 \tag{2.22}$$

Also, from (C.11), when $A_2 = B_2$, $(\phi'-\alpha)$ can be measured off the graph,

$$\underline{\beta}(\beta+\underline{\beta} \cos 2(\phi'-\alpha)) = \gamma \underline{\beta}^2 \sin 2(\phi'-\alpha) \tag{2.23}$$

$$\therefore \quad \gamma_3 = \frac{(\beta+\underline{\beta} \cos 2(\phi'-\alpha))}{\underline{\beta} \sin 2(\phi'-\alpha)} \tag{2.24}$$

When $(\phi'-\alpha) = \pm 45^\circ$, $\quad \gamma_3 = \dfrac{\beta-\underline{\beta}\sqrt{2}/2}{\sqrt{2}\underline{\beta}/2}$ (2.25)

B_{MAX} and B_{MIN} are calculated from a least squares fit to the curves in Figure 2.12. Using $\underline{\beta} = 0.881$ and $\beta = 3.5\%$,

$$\gamma_1 = 0.95 \ , \quad \gamma_2 = 0.94 \ , \quad \gamma_3 = 0.95 \tag{2.26}$$

The agreement between these values indicates a value of γ around 0.95, with very little demodulation of the signal. As a check, p and θ are calculated from equations (C.24)-(C.26) to confirm that the calculated value of $\gamma = 0.95$ is correct. The mean value is 86.2% compared to $\underline{\beta} = 88.1\%$. Since γ is multiplicative, the error scales with the polarization and this implies a degree of polarization accurate to within 2-3% of its value. Some of this error can be attributed to an uncertainty of $\sim 2^\circ$ in measuring the position angle of the top analyzer. An estimate of γ_H and γ_J comes from two single measurements that were made at the last position of the top analyzer (165°). The analyzer was not moved between the J, H and K measurements, so they are directly comparable.

Now, $$\left(\frac{B_{165^\circ}}{B_{MAX}}\right)_K = \left(\frac{B_{165^\circ}}{B_{MAX}}\right)_H = \left(\frac{B_{165^\circ}}{B_{MAX}}\right)_J \tag{2.27}$$

$$\therefore \quad \gamma_H = \left(\frac{B_{MAX}}{B_{165^\circ}}\right)_K \frac{(B_{165^\circ})_H}{\underline{\beta}_H^2} \tag{2.28}$$

$$\gamma_J = \left(\frac{B_{MAX}}{B_{165^o}}\right)_K \frac{(B_{165^o})_J}{\underline{\beta}_J^2} \tag{2.29}$$

$$\rightarrow \gamma_H = 0.96 \ , \quad \gamma_J = 0.99 \tag{2.30}$$

In April, it was only possible to scan three angles of the top analyzer, but the numbers agree well with those obtained in July (Fig. 2.13). The first angle corresponds to B_{MAX}, so from (2.22),

$$\gamma_K = 0.96 \tag{2.31}$$

In the August run, the positions angles from 0^o to 165^o were mapped again in 15^o increments. In addition, there was a static piece of HR polaroid between the top analyzer and the dichroic, making the arrangement polaroid-polaroid-dichroic-polaroid. The modulation is given by (B.9) for the parallel polaroid case and (B.10) for crossed polaroids. From (B.10) and (C.28),

$$\gamma_K = 0.94 \tag{2.32}$$

The value was obtained from the 0^o position of the top analyzer. The H and J measurements were made at 165^o, but in analogy to (C.26) and (C.27),

$$\gamma_H = \left(\frac{B_{0^o}}{B_{165^o}}\right)_K \frac{(B_{165^o})_H}{\underline{\beta}_H^2} \tag{2.33}$$

$$\gamma_J = \left(\frac{B_{0^o}}{B_{165o}}\right)_K \frac{(B_{165^o})_J}{\underline{\beta}_J^2} \tag{2.34}$$

$$\rightarrow \gamma_H = 1.10 \ , \quad \gamma_J = 1.01 \tag{2.35}$$

In summary, the determinations of γ indicate a small retardance. The observation with most weight is the July P-D-P test because all possible incident Stokes' parameters were covered. Intuitively, the small amount of demodulation implies a value of γ near unity. Within

the errors, all estimates of γ_J and γ_H are consistent with unity, while $\gamma_K = 0.95$. The experimental tests are collected in Table 2.8.

The way to avoid linear-to-circular conversion by a tilted plane mirror is to place a rotatable retarder in front of it. The retarder modulates the three Stokes parameters Q, U and V, while reflection from the mirror changes only U and V (if angles are described by (2.1) and measured from the plane of incidence on the mirror). The modulated Q parameter is only multiplied by a constant factor near unity by the mirror. The reflected light then passes through a Wollaston prism in a fixed orientation such that the intensities of the transmitted beams depend only on Q. In this way it is possible to measure linear and circular polarization with the effects of metallic reflection removed.

(e) $\underline{\varepsilon}$: ε is an arbitrary constant angle that relates the position angle of the analyzer to the celestial coordinate frame. The celestial system is taken to have a zero point at North-South on the sky with angles being measured North through East. The analyzer is driven by a stepping motor which has 200 steps per revolution but 3:1 reduction gearing makes 600 steps equivalent to one revolution of the analyzer. A hardware datum is provided by a microswitch which is tripped by a lug on the rim of the rotating analyzer. At the beginning of a scan the computer searches for the datum, then steps 22.5° and integrates successively until 8 positions have been covered. After each scan the datum is found again, so the phase of the position angles is locked. The software takes the first position as the zero point, so ε relates that position to North-South on the sky. ε was different between December 1979 and the other three runs. In December, the position of the analyzer in the polarimeter assembly was checked with a second piece of polaroid (Fig. 2.14). The 2nd polaroid was suspended so that its fast axis (maximum transmission) was vertical. Then the polarimeter was suspended by its North bolt-hole, and the rotating analyzer was stepped around until minimum transmission was reached. This position labelled East-West for the

analyzer and could be interpolated to a precision of better than 1°. Then the angle between that position and the microswitch tripping position was measured. By counting stepping motor pulses, this could be done accurately to 0.3°. From these measurements $\varepsilon = 11.5^{\circ}$. The bolt holes for attaching the polarimeter were aligned East-West to $<0.5^{\circ}$ and the rotating instrument mount was locked to zero degrees. In the reduction software,

$$\xi_{TRUE} = \xi_{MEAS} + 11.5^{\circ} \tag{2.36}$$

For subsequent runs the instrument was seated on different bolt holes, but the position of the microswitch was unaltered. The only difference was that the rotation of the analyzer with respect to the sky was reversed (rotating North through West) giving,

$$\xi_{TRUE} = 258.5^{\circ} - \xi_{MEAS} \tag{2.37}$$

2.3.3 Errors

Errors in any of the instrumental parameters propagate through to the final results, so it is important to have a consistent scheme to quantify the errors. For the quantities that are only calculated once and used throughout the reduction:

(a) $\underline{\varepsilon}$: The error is a measuring error of 0.5° and is dominated by the systematic errors: $\sigma(\varepsilon) \sim 0.5^{\circ}$.

(b) $\underline{\beta', \omega}$: The upper limits on β' are the same order of magnitude as the photon error, and are consistent with $\beta'_{J,H,K} = 0$ with $\sigma(\beta') \sim$ 0.4% (photon error).

(c) $\underline{\underline{\beta}}$: An estimate of the precision of β is the agreement between the values measured on the telescope and the values calculated in Appendix E:

$$\sigma(\underline{\beta}_K) = 0.025 \ , \quad \sigma(\underline{\beta}_H) = 0.005 \ , \quad \sigma(\underline{\beta}_J) = 0.007.$$

(d) $\underline{S}$: During a single run on the telescope there is no reason to expect the instrumental sensitivity to change. The dewar is kept at

liquid nitrogen temperature and is sometimes pumped solid for the duration of a run. It is taken off the telescope only to flash the detector, and experience has shown that this does not change the sensitivity. The values of S below are a check on the stability of the InSb system and weather changes from night to night. For each run, S can be characterized by the r.m.s. and the mean deviation in each waveband:

$\alpha(\underline{S})/\frac{S_{MAX}-S_{MIN}}{2}$

	K	H	J
Run 1	0.40/1.30	0.99/3.16	2.84/5.61
Run 2	0.74/0.37	2.41/1.84	4.81/4.78
Run 3	0.66/0.63	5.70/7.85	1.09/1.67
Run 4	2.49/2.62	5.12/2.75	3.88/2.59

(in %)

Measurements at K have much less dispersion than at H and J; the sensitivity is greatest at K. On the 11th August 1980, the sensitivity changed abruptly in all three wavebands by ∿25% and there was no obvious cause or explanation for this behaviour. The averages for Run 4 exclude this night. All the changes in S between nights are systematic; they occur in the same sense for all three wavebands. The two explanations for systematic changes are poor transparency and real variations in sensitivity. Either way the photometric measurement only refers to the system at the time of measurement; no guess can be made as to how S changes between standard observations. However, an idea of the contribution due to transparency changes comes from Table 2.4, which shows the repeatability of consecutive scans as a function of the photon error of an individual scan. There are virtually no cases where the measurement is photon limited. The repeatability can be a diagnostic for sensitivity changes: in Run 1 the second night has a discrepant sensitivity in Table 2.3 and the repeatability in Table 2.4 shows that the transparency was poor. Conversely, the sensitivity changes during Run 4 do not show up as large repeatability errors. The two scans are usually separated by ∿1 minute, which is sufficient to sample the variations of all but the slowest-moving cirrus. Since the two effects (along with any other systematics) cannot be disentangled,

the representative error in S for a given night will be taken as the larger of the two quantities R, and the deviation $(S_{MAX}-S_{MIN})/2$ (Table 2.5),

$$\sigma(S) = R \text{ or } (S_{MAX}-S_{MIN})/2 \qquad (2.38)$$

$\sigma(S)$ is a useful parameter for the photometric precision during a run, but the observations will be used to study variability in BL Lac objects over longer timescales. The sensitivity changes between runs range up to a factor of two, but photometric standards cannot be used to check the photometry over these timescales because they are used to set up the values of S. BL Lacs themselves can vary by factors of greater than 2 in several months, so no continuity can be expected between consecutive sessions. However, polarimetric standards are non-variable and are used across consecutive runs, so they can serve as secondary photometric standards. The magnitudes the polarimetric standards common to two runs are listed below:

Run	Star	K	H	J
1	λ Psc	3.84	3.87	4.08
2	χ Her	3.13	3.15	3.38
2	λ Psc	3.81	3.87	4.06
3	χ Her	3.19	3.13	3.42
3	β Aql	1.67	1.70	2.09
4	χ Her	3.10	3.18	3.46
4	β Aql	1.58	1.66	2.01

There is no case in which the disagreement between any two runs in any waveband is >10%, indicating that the large sensitivity changes are a real instrumental effect.

(e) β, α : If the telescope alignment is only carried out once per run, the instrumental polarization should be constant during a single observing session. For both the degree of polarization and position angle, the r.m.s. deviation and dispersion are,

$\sigma(\beta)/\beta_{MAX}-\beta_{MIN}$	K	H	J	
Run 1	0.03/0.21	0.09/0.37	0.09/0.77	
Run 2	0.19/1.28	0.09/0.43	0.23/1.51	(in %)
Run 3	0.11/0.69	0.22/1.25	0.20/1.01	
Run 4	0.32/2.49	0.56/3.79	0.49/4.41	

$\sigma(\alpha)/\alpha_{MAX}-\alpha_{MIN}$	K	H	J	
Run 1	1.3/13.6	0.6/6.5	0.6/5.9	
Run 2	1.3/8.1	0.5/3.0	0.3/2.2	(in degrees)
Run 3	0.6/4.0	0.9/4.9	0.7/4.2	
Run 4	1.6/15.4	2.2/16.7	1.1/9.0	

In this and the previous section, the r.m.s. error does not represent a true error on an individual observation. Use of root-mean-square assumes that the mean represents the best estimate of the true value and that the residuals are distributed normally about the mean. The argument used here is that the variations in S, β and α are real, systematic variations (only in the photon limited case does the r.m.s. take on any physical meaning). In this context the r.m.s. represents a figure of merit for the run, or a degree of consistency. The errors adopted for the individual measures of β and α are residuals between the value for one night and the mean for an entire run (Table 2.7).

$$\sigma(\beta) = |\bar{\beta}-\beta_i| \ , \qquad \sigma(\alpha) = |\bar{\alpha}-\alpha_i| \tag{2.39}$$

One of the polarization standards, the 'OJ' Star, is not taken from a published list; but is a field star near the BL Lac object OJ287. It was measured to check for possible magnitude dependent instrumental effects, it is $\sim$8 magnitudes fainter than most of the standards at 2.2μm. Since the field is unobscured and at medium latitude, the 'OJ' Star is likely to have very small interstellar polarization. The error on each polarization is $\sim$2% and the result is consistent with the other bright star measurements of β and α. Therefore there are no significant magnitude dependent contributions to the instrumental polarization.

(f) $\underline{\gamma}$: The standard error in a single determination of γ at a single position angle is given by error propagation through equation (C.23),

$$\sigma^2(\gamma) = \sigma^2(\underline{\beta})\left(\frac{\gamma^2}{\underline{\beta}^2}\right)+\sigma^2(\beta)\left(\frac{B_2 pC}{\underline{\beta} pS}\right)^2 +\sigma^2(B_2)\gamma^2$$

$$+\sigma^2(p)\left((C^2+\frac{S^2}{4})\left(\frac{B_2 pC}{\underline{\beta} pS}\right)^2 +(S^2+\frac{C^2}{4})\left(\frac{\gamma}{pS}\right)^2\right) \qquad (2.40)$$

where $C = \cos 2(\theta-\alpha)$

$S = \sin 2(\theta-\alpha)$

As mentioned before, both (C.23) and 2.40) are sensitive to the value of $(\theta-\alpha)$ and the calculation becomes very unreliable as $\theta \to \alpha$. This is purely an artifact of the reduction algorithm, there is no physical reason why the exact value of α should be significant. By mapping all angles ofθ, the dependence of the calculation on any other angles is removed. The accuracy is determined by the least squares fit of a maximum and a minimum to Figure 2.12; and from equation (2.22),

$$\sigma^2(\gamma) = \frac{1}{\underline{\beta}^4}\left\{\sigma^2(B_{MAX})+\sigma^2(\underline{\beta})\left(\frac{2}{\underline{\beta}}\right)^2\right\}=\left\{\frac{1}{\underline{\beta}^4}\sigma^2(B_{MIN})+\sigma^2(\underline{\beta})\left(\frac{2}{\underline{\beta}}\right)^2\right\} \qquad (2.41)$$

From (2.38) and 2.39),

$$\gamma_1 = 0.95 \pm 0.08, \quad \gamma_2 = 0.94 \pm 0.08, \quad \gamma_3 = 0.95 \pm 0.04 \qquad (2.42)$$

$$\gamma_H = 0.96 \pm 0.10, \quad \gamma_J = 0.99 \pm 0.09$$

All these values are in good agreement with the physical arguments in Appendix D. If $\gamma = 0.95$ and $\beta = 3.5\%$, the retardance is $\sim 18^\circ$ which is within the range expected for a reflecting silver film. The expected wavelength dependence is not seen, but lies within the errors.

There is no evidence for any noticeable change in γ between runs, although it was not measured at J and H on all three runs. The adopted values of γ are therefore applied to all the data with the dichroic ahead of the analyzer, since they agree to within 1.5σ with all the measurements of γ:

$$\gamma_K = 0.95 \pm 0.07, \quad \gamma_H = 1.0 \pm 0.10, \quad \gamma_J = 1.0 \pm 0.09 \tag{2.43}$$

2.3.4 Systematic Effects

There are two aspects of the polarimetric throughout of the instrument which in principle affect the reduction algorithms, but which in practice can be shown to be negligible.

(a) Birefringence of the Analyzer: In general, a dichroic material will also be a birefringent material. Obviously a perfect analyzer is not birefringent because only one orientation of the E vector is transmitted. However, at 2.2μm the analyzer transmits orthogonal beams of radiation, and if the refractive indices in the material for the two orthogonal directions are not identical, the dispersion relation will lead to a retardance. The relationship between dichroism and birefringence has been calculated for interstellar grains by Shapiro (1975). Birefringence is very important in media with different refractive indices for the orthogonal directions of the E vector, but similar (usually negligible) absorption coefficients. In Polaroid material, the absorption coefficients are larger but birefringence can be substantial since the long polymers imbedded in the Polaroid sheet make it very anisotropic. This is called 'form' birefringence. The amount of retardance is highly sensitive to the composition and thickness of the HR Polaroid and is impossible to accurately predict. If the long polymers are approximated by aligned plates then the result of Born and Wolf (1959) will be valid,

$$n_e^2 - n_o^2 = \frac{f_1 f_2 (n_1^2 - n_2^2)^2}{f_1 n_2^2 + f_2 n_1^2} \tag{2.44}$$

where n_e and n_o are the ordinary and extraordinary refractive indices,

f_1 and f_2 are the volume filling factors of the polymer and inter-polymer regions, and n_1 and n_2 are the refractive indices of the two regions. The retardance is then given by,

$$\delta = \frac{\pi t}{\lambda} (n_e - n_o) \qquad (2.45)$$

where t is the thickness of the Polaroid film (50-100μm). Polaroid can not be modelled in such an ideal way and δ may be many cycles. The retardance due to dichroic birefringence is therefore not as easy to evaluate as the retardance due to metallic reflection (Appendix D). It is likely that the long-wavelength side of the K band the birefringence is strong because there is an absorption edge in the Polaroid material. Where the absorption coefficient changes rapidly, the refractive index will also change rapidly and dispersion will be important. The whole class of Reststrahlen filters exists to make use of this effect (Driscoll & Vaughan, 1978). Fortunately the uncertainty over δ does not affect the reduction formulae, because as shown in Appendix F the terms in cos δ and sin δ drop out of the crucial terms in the matrices. The dominant imperfection in the analyzer at 2.2μm is the leakiness not the birefringence.

(b) Circular Polarization in the Source. It has been assumed throughout that none of the sources observed have any intrinsic circular polarization. A component of V would introduce extra modulation into the equations in Appendix B. The BN object is known to have a small amount of circular polarization at 2.2μm, and the effect of this is calculated in Appendix F. In the configuration with the dichroic ahead of the analyzer, any significant circular polarization in the BL Lac objects would lead to systematic errors in the degree of linear polarization. Searches for circular polarization in objects with high linear polarization (optical) have always been negative (Landstreet & Angel, 1972; Nordsieck, 1972; Kemp et al., 1972; Maza, 1979). No search has ever revealed circular polarization at anywhere near the 1% level. Although not conclusive, this is the basis for the assumption of zero circular polarization in BL Lac objects.

2.4 Reduction

2.4.1 Derivation and Errors

All the data was reduced using a least squares algorithm which fitted the eight points in a complete scan by a function of the form

$$I_k = K + a_1 \cos \phi_k + b_1 \sin \phi_k + a_2 \cos 2\phi_k + b_2 \sin 2\phi_k \qquad (2.46)$$

All of the experimental parameters and object polarizations can be expressed in terms of the coefficients of the two double modulating terms $\cos 2\phi_k$ and $\sin 2\phi_k$. The coefficients are calculated in Appendix C. The terms in $\cos \phi_k$ and $\sin \phi_k$ are included as a diagnostic of systematic errors and the noise in an individual observation.

The analysis of least squares assumes that the deviation of the treasured quantity from its true value follows a Gaussian distribution. A model for the observations is chosen and the parameters are fitted to minimize the deviation from that model. The condition of least squares is

$$\sum_{k=1}^{n} \left\{ I_k - (K + a_1 \cos \phi_k + b_1 \sin \phi_k + a_2 \cos 2\phi_k + b_2 \sin 2\phi_k) \right\}^2 = \text{minimum} \qquad (2.47)$$

$$\text{Let, } v_k = I_k - (K + a_1 \cos \phi_k + a_2 \cos 2\phi_k + b_2 \sin 2\phi_k + b_1 \cos \phi_k) \qquad (2.48)$$

$$\sigma_v^2 = \bar{I}_k^2 - (K^2 + \tfrac{1}{2}(a_1^2 + b_1^2 + a_2^2 + b_2^2)) \qquad (2.49)$$

It is assumed that the deviation V_k is normally distributed with mean zero, and the probability is defined as

$$P(a_1, b_1, a_2, b_2) = \Pi \left[\frac{1}{\sigma_v \sqrt{2\pi}} \right] \exp \left[\frac{-1}{2} \sum \left(\frac{V_k}{\sigma_v} \right)^2 \right] \qquad (2.50)$$

Maximizing this quantity is equivalent to minimizing the sum of the exponential. The coefficients are given by

$$K = \frac{1}{n}\Sigma I_j, \quad a_1 = \frac{2}{n}\Sigma I_j \cos \phi_j, \quad b_1 = \frac{2}{n}\Sigma I_j \sin \phi_j,$$

$$a_2 = \frac{2}{n}\Sigma I_j \cos 2\phi_j, \quad b_2 = \frac{2}{n}\Sigma I_j \sin 2\phi_j \tag{2.51}$$

Therefore,

$$V_k = I_k - \frac{1}{n}\Sigma I_j - \frac{2}{n}\Sigma \cos \phi_j I_j \cos \phi_k - \frac{2}{n}\Sigma \sin \phi_j I_j \sin \phi_k$$

$$- \frac{2}{n}\Sigma \cos 2\phi_j I_j \cos 2\phi_k - \frac{2}{n}\Sigma \sin 2\phi_j I_j \sin 2\phi_k \tag{2.52}$$

$$V_k = I_k - \frac{1}{n}\sum_{j=1}^{\infty}\Sigma \left\{1+2(\cos(\phi_j-\phi_k) + \cos 2(\phi_j-\phi_k)\right\} I_k \tag{2.53}$$

$$\therefore \quad \sigma_v^2 = \sigma_I^2 - \frac{1}{n^2}\sum_{j=1}^{\infty}\Sigma \left\{1+4\cos^2(\phi_j-\phi_k)+4\cos^2 2(\phi_j-\phi_k)\right.$$

$$\left. +8\cos(\phi_j-\phi_k)\cos 2(\phi_j-\phi_k)+4\cos(\phi_j-\phi_k)+4\cos 2(\phi_j-\phi_k)\right\}\sigma_I^2 \tag{2.54}$$

After summing terms,

$$\sigma_v^2 = \sigma_I^2\left(1 - \frac{5}{n}\right) \tag{2.55}$$

Therefore, substituting in (2.49)

$$\sigma_k = \left\{ \bar{I}_k^2 - K^2\left(1+\tfrac{1}{2}(A_1^2+B_1^2+A_2^2+B_2^2)\right)/3\right\}^{\frac{1}{2}} \tag{2.56}$$

where $A_1 = a_1/K, \quad A_2 = a_2/K$

$$B_1 = b_1/K, \quad B_2 = b_2/K$$

σ_k is the standard error in the mean intensity K. The errors in the fitted coefficients A_2 and B_2 can also be calculated,

$$\sigma_A^2 = (2+A_2^2)\left(\frac{\sigma_k}{K}\right)^2 \tag{2.57}$$

$$\sigma_B^2 = (2+B_2^2)\left(\frac{\sigma_k}{K}\right)^2 \tag{2.58}$$

Equations (2.56), (2.57) and (2.58) define the standard photometric errors in terms of the fitted coefficients. Another possible source of error in the algorithm is computational error. The reduction formulae are complicated enough that it is difficult to have an intuitive feel for the correctness of the answer. To test the self-consistency of the algorithm, programmes were written to generate test data according to all the experimental set-ups in Appendix B. These scans were fed into the appropriate reduction formulae in Appendix C. A comprehensive matrix of test data was created, with assigned values of the instrumental parameters β', ω, β, α, $\underline{\beta}$ and γ. Since the presence of many trigonometric functions can lead to ambiguity, the test data covered 2π rotations in ω and α and the full range of γ, $\underline{\beta}$, β and β' from 0 to 1. The result of analyzing this test data was that in no case was the calculated parameter in error by more than 1 part in 10^4. Double precision variables are used throughout the reduction programmes. Therefore the computational error has an upper limit of 0.01%.

The standard errors in polarization and position angle are calculated according to the two reduction schemes for the analyzer before and after the dichroic mirror. For Run 1 (polaroid before dichroic; P-D), the coefficients A_2 and B_2 are given by (C.17),

$$A_2 = \frac{\underline{\beta}(p\cos 2\theta+\beta\cos 2\alpha)}{1+\frac{\beta p}{2}(1+\sqrt{1-\underline{\beta}^2})\cos 2(\alpha-\theta)} \quad , \quad B_2 = \frac{\underline{\beta}(p\sin 2\theta+\beta\sin 2\alpha)}{1+\frac{\beta p}{2}(1+\sqrt{1-\underline{\beta}^2})\cos 2(\alpha-\theta)} \qquad (C.17)$$

For all situations: $\beta < 4\%$, $p < 25\%$ denominator = 1 to better than 0.5%

$$\therefore \quad p_1 = \frac{A_2}{\underline{\beta}} - \beta_1 \quad , \qquad p_2 = \frac{B_2}{\underline{\beta}} - \beta_2 \qquad (2.59)$$

where $p\cos 2\theta = p_1$, $\beta\cos 2\alpha = \beta_1$

$p\sin 2\theta = p_2$, $\beta\sin 2\alpha = \beta_2$

Therefore, $p = (p_1^2+p_2^2)^{\frac{1}{2}}$ and $\theta = \frac{1}{2}\arctan(p_2/p_1)$ (2.60)

By propagating errors,

$$\sigma^2(p) = \left[\frac{p_1}{p}\right]^2\left\{\left(\frac{1}{\underline{\beta}}\right)^2\sigma^2(A_2)+\left(\frac{A_2}{\underline{\beta}^2}\right)^2\sigma^2(\underline{\beta})+\sigma^2(\beta_1)\right\}$$

$$+\left[\frac{p_2}{p}\right]^2\left\{\left(\frac{1}{\underline{\beta}}\right)^2\sigma^2(B_2)+\left(\frac{B_2}{\underline{\beta}^2}\right)^2\sigma^2(\underline{\beta})+\sigma^2(\beta_2)\right\} \qquad (2.61)$$

and using the fact that if $f(x) = \arctan(\frac{x}{a})$, $f'(x) = a/(a^2+x^2)$

$$\sigma^2(\theta) = \left[\frac{p_1}{p^2}\right]^2\left\{\left(\frac{1}{\underline{\beta}}\right)^2\sigma^2(A_2)+\left(\frac{A_2}{\underline{\beta}^2}\right)^2\sigma^2(\underline{\beta})+\sigma^2(\beta_1)\right\}$$

$$+\left[\frac{p_2}{p^2}\right]^2\left\{\left(\frac{1}{\underline{\beta}}\right)\sigma^2(B_2)+\left(\frac{B_2}{\underline{\beta}2}\right)^2\sigma^2(\underline{\beta})+\sigma^2(\beta_2)\right\} \qquad (2.62)$$

which reduces to the simple result,

$$\sigma(\theta) = \frac{\sigma(p)}{p} \quad \text{radians} \qquad (2.63)$$

For runs 2, 3 and 4 the analyzer was after the dichroic and the coefficients A_2 and B_2 are given by (C.22),

$$A_2 = \frac{\underline{\beta}(\beta+p\cos 2(\theta-\alpha))}{(1+\beta p\cos 2(\theta-\alpha))} \quad , \quad B_2 = \frac{\gamma p\,\underline{\beta}\sin 2(\theta-\alpha)}{(1+\beta p\cos 2(\theta-\alpha))} \qquad (C.22)$$

giving,

$$p_1 = \frac{A_2-\underline{\beta}\beta}{(\underline{\beta}-A_2\beta)} \quad , \quad p_2 = \frac{B_2(1-\beta^2)}{\gamma(\underline{\beta}-A_2\beta)} \qquad (2.64)$$

where $p\cos 2(\theta-\alpha) = p_1$,

$p\sin 2(\theta-\alpha) = p_2$

Therefore, $p = (p_1^2+p_2^2)^{\frac{1}{2}}$ and $\theta = \frac{1}{2}\arctan(p_2/p_1)+\alpha$ (2.65)

By propagating errors,

$$\sigma^2(p_1) = \left(\frac{(A-\underline{\beta}\beta)\beta-(\underline{\beta}-\beta A_2)\underline{\beta}\beta}{(\underline{\beta}-\beta A_2)^2}\right)^2 \sigma^2(A_2) + \left(\frac{(A_2-\underline{\beta}\beta)+(\underline{\beta}-\beta A_2)\beta}{(\underline{\beta}-\beta A_2)^2}\right)^2 \sigma^2(\underline{\beta})$$

$$+\left(\frac{(A_2-\underline{\beta}\beta)A_2-(\underline{\beta}-\beta A_2)\underline{\beta}}{(\underline{\beta}-\beta A_2)^2}\right)^2 \sigma^2(\beta) \qquad (2.66)$$

$$\sigma^2(p_2) = \left(\frac{(1-\beta^2)}{(\underline{\beta}-\beta A_2)^2}\frac{\beta}{\gamma}\right)^2 \sigma^2(A_2) + \left(\frac{1-\beta^2}{\gamma(\underline{\beta}-\beta A_2)}\right)^2 \sigma^2(B_2) + \left(\frac{(1-\beta^2)B_2}{(\underline{\beta}-\beta A_2)\gamma^2}\right)\sigma^2(\gamma)$$

$$+\left(\frac{(1-\beta^2)A_2B_2\gamma - 2(\underline{\beta}-\beta A_2)\beta B_2\gamma)}{\gamma(\underline{\beta}-\beta A_2)^2}\right)\sigma^2(\beta) + \left(\frac{(1-\beta^2)B_2}{(\underline{\beta}-\beta A_2)^2\gamma}\right)\sigma^2(\underline{\beta}) \qquad (2.67)$$

Hence,

$$\sigma^2(p) = \sigma^2(p_1)\left(\frac{p_1}{p}\right)^2 + \sigma^2(p_2)\left(\frac{p_2}{p}\right)^2 \qquad (2.68)$$

and as before, the equation generated for $\sigma(\theta)$ reduces to

$$\sigma(\theta) = \frac{\sigma(p)}{p} \text{ radians} \qquad (2.69)$$

Equations (2.66), (2.67) and (2.69) represent the standard error in p and θ calculated in terms of the uncertainties in the instrumental parameters and the fitted coefficients A_2 and B_2. There is another effect which must be taken into account at low signal-to-noise, and which can lead to systematic errors in calculating p and θ. The problem is equivalent to measuring a polarization vector $\underline{S} = p\, e^{2i\theta}$ in the presence of random, additive noise. Neither the amplitude or the phase of the resultant vector S´ will follow a Gaussian distribution, except at large values of signal-to-noise. On faint objects, the degree of polarization p will be systematically overestimated. This effect has been considered by Vinokur (1965)

and Wardle & Kronberg (1974). If a signal vector S has random Gaussian noise with a variance σ^2 added to it vectorially, the resultant amplitude is given by

$$P(S') = \frac{S'}{\sigma^2} I_o\left(\frac{SS'}{\sigma^2}\right) \exp\left[\frac{-S^2+S'^2}{2\sigma^2}\right] \qquad (2.70)$$

where $I_o(x)$ is the modified Bessel function of first order. For large signal-to-noise ratios, $P(S')$ tends to a Gaussian centred on $S' = S$ with a variance σ^2. However for low signal-to-noise ($\sim$1), the most probable value of $P(S')$ is given by the peak in the $P(S')$ distribution. Solving (2.70) for a maximum gives

$$S \sim S'\left\{1- \left(\frac{\sigma'}{S'}\right)^2\right\}^{\frac{1}{2}} \qquad (2.71)$$

Assuming $\sigma' = \sigma$,

$$p = p'\left\{1- \left(\frac{\sigma(p)}{p}\right)^2\right\}^{\frac{1}{2}} \qquad (2.72)$$

The probability distribution of the phase of S' is also given by Vinokur,

$$P(\theta') = \exp\left(\frac{-S^2 \sin^2(\theta'-\theta)}{2\sigma^2}\right)\left\{\frac{S\cos(\theta'-\theta)}{\sigma\sqrt{2\pi}}\left[\tfrac{1}{2}+K\,\frac{S^2\cos^2(\theta'-\theta)}{\sigma}\right]\right.$$

$$\left. + \frac{1}{2\pi}\exp\left[\frac{-S^2\cos^2(\theta'-\theta)}{2\sigma^2}\right]\right\} \qquad (2.73)$$

$$\text{where } K(u) = \frac{1}{\sqrt{2\pi}}\int_o^u \exp\left(\frac{-z^2}{z}\right) dz \qquad (2.74)$$

There is no systematic error in θ, because $P(\theta')$ is symmetric about $\theta = \theta'$. However, for a signal-to-noise of less than 1.5 the error in θ given by equation (2.69) is an underestimate. The definition of $\sigma(\theta)$ used by Wardle and Kronberg was

$$\int_{\theta-\sigma(\theta)}^{\theta+\sigma(\theta)} P(\theta')\,d\theta' = 0.68 \tag{2.75}$$

From their graphical solution, a good approximation of $\sigma(\theta)$ at $S/\sigma(S) < 2$ is,

$$\sigma(\theta) = 2\sigma(\theta') \frac{\sigma(S')}{S'} \tag{2.76}$$

In practice, these corrections apply to only a small fraction of the results described here, because the signal-to-noise is generally large. The limit on the precision of the data comes from systematic errors, which are discussed in the next section.

Two types of error can be defined from the preceding analysis. The first is a photon error defined by Poisson statistics

$$\text{(a)} \quad \sigma_k^2 = \frac{1}{n^2} \Sigma\sigma_I^2 \quad , \qquad \sigma_k^2 = \bar{I}_k = K \tag{2.77}$$

$$\therefore \quad \frac{\sigma_k}{K} = \frac{1}{\sqrt{K}} \tag{2.78}$$

Note that this is not a real photon error since photons are not being individually counted. In the regime where shot noise is negligible, σ_p represents the fluctuations in the current from the detector due to fluctuations in the arrival rate of photons at the detector surface. This is substituted into (2.57) and (2.58) and yields the errors described by (2.66), (2.67) and (2.69). The photon errors are designated by $\sigma_p(p)$ and $\sigma_p(\theta)$.

(b) The second error is determined by the goodness of the least-squares fit,

$$\frac{\sigma_k}{K} = \left\{ \frac{\bar{I}_k^2}{K^2} - (1+\tfrac{1}{2}(A_1^2+B_1^2+A_2^2+B_2^2))/3 \right\}^{\frac{1}{2}} \tag{2.79}$$

This is also substituted into (2.57) and (2.58) and yields errors of the same form. The standard errors are designated by

$\sigma_s(p)$ and $\sigma_s(\theta)$. Generally, $\sigma_s(p)$ is larger than $\sigma_p(p)$ and the ratio $\sigma_s(p)/\sigma_p(p)$ is plotted for all the observations (Fig. 2.15). The larger of the two is always adopted. In this study there is a third class of errors which can dominate: the systematic and non-normally distributed errors.

2.4.2 Systematic Errors

There are several sources of error in the data which are not adequately described by an analysis which assumes a Gaussian distribution of errors. These include

(i) Poor transparency
(ii) Bad guiding and imperfect beam profiles
(iii) Blemishes in the analyzer
(iv) Movement of the image on the detector (flexure, etc.)
(v) Scattered light in the photometer
(vi) Polarization due to the night sky

Taking the last first, the polarization of night sky can be a significant contributor to the measurement of p for a weak source. In those cases the flux from the sky is often 10^2 times that of the object, so obviously a small degree of polarization due to the sky leads to Stokes parameters Q and U similar in size to those of the object. However all of the observations were made in dark time or with very little moon. The advantage of star/sky chopping in the infrared is that both flux and polarization from the sky are subtracted away from the object signal. Only changes in sky polarization faster than the chopping frequency (6-8Hz) will be important, and these are expected to be negligible.

Several types of error have the mechanical modulation period of the analyzer, including movement of the image on the detector and spurious reflections from the surface of the analyzer. It is a general property of polarimeter design that mechanical and polaroid rotations should be separated in frequency space. In the expression

$$I_k = K(1+A_1 \cos \phi_k + B_1 \sin \phi_k + A_2 \cos 2\phi_k + B_2 \sin 2\phi_k) \qquad (2.80)$$

The coefficients A_2 and B_2 contain the polarimetric information and A_1 and B_1 contain mechanical modulation noise. In a perfect polarimeter $A_1 = B_1 = 0$.

Bad guiding can contribute to systematic errors, especially when the beam profiles do not have wide, flat tops. If the signal is considered to drop off linearly with time due to the object wandering out of the aperture,

$$I(t) \alpha mt \quad \text{or} \quad I(x) = m(x-a) \tag{2.81}$$

Considering Fourier components,

$$I(x) = \frac{a_o}{2} + \sum_{n=1}^{\infty} a_n \cos nx + \sum_{n=1}^{\infty} b_n \sin nx \tag{2.82}$$

where $a_o = \frac{1}{\pi} \int_{\pi}^{\pi} I(x)dX$, $a_n = \frac{1}{\pi} \int_{\pi}^{\pi} I(x) \cos nxdx$,

$$b_n = \frac{1}{\pi} \int_{\pi}^{\pi} I(x) \sin nxdx$$

and $I(x) = m(x-a) = mx$ by the Shift Theorem

$$\therefore \quad I(x) = \sum_{n=1}^{\infty} \frac{2m}{n}(-1)^{n+1} \sin nx$$

$$= 2m(\sin x - \frac{\sin 2x}{2} + \frac{\sin 3x}{3} \ldots.) \tag{2.83}$$

Drift out of the aperture will contribute power to coefficients B_1, B_2, B_3, etc., with decreasing power in higher harmonics. Since some of the power is in the polarimeter harmonic ($2\phi_K$), it is impossible to deconvolve the polarization component from the drift component. The form of I(x) is simplistic and in general the function will have power in the even harmonics (A_1, A_2, A_3, etc.) too.

The remaining sources of systematic error will have noise power spectra that are difficult to model. There is likely to be power in both the $\emptyset_K$ and $2\emptyset_K$ harmonics. Harmonics higher than $2\emptyset_K$ are accounted for by the standard error $\sigma_s(p)$ because it incorporates the residuals V_K given by (2.48). Therefore the noise power in the first harmonic $\emptyset_K$ is likely to be a good diagnostic of systematic errors in the data. It must be emphasized that although the noise power has a component in the $2\emptyset_K$ harmonic, it is not possible to subtract this power off because the phase is not known. Power in the first harmonic does not therefore introduce a bias into p but characterizes the noise $\sigma(p)$. $\sigma(p)$ is assumed to be orientated randomly in phase, but not with a Gaussian amplitude distribution. $\sigma_c(p)$ is the third type of error used in this treatment and is called the characteristic error.

$$\sigma_c(p) = \left(\frac{A_1^2+B_1^2}{2}\right)^{\frac{1}{2}} \qquad (2.84)$$

$\sigma_c(p)$ is usually the largest of the three errors: $\sigma_p(p)$, $\sigma_s(p)$ and $\sigma_c(p)$ and in each case the largest of the three is adopted as the probable error of an observation. The distribution of $\sigma_c(p)/\sigma_s(p)$ is shown in Figure 2.16; there is a tail of very noisy points which represents observations where the systematic errors due to guiding or thin cirrus have swamped the polarization signal. If the magnitude distribution of the objects with a given $\sigma_c(p)$ is plotted (Figs. 2.17 - 2.19), the noisy tail corresponds to observations of faint objects. This argues against a large component of $\sigma_c(p)$ being due to transparency variations, because a magnitude independent diagram would be produced. The form of Figure 2.17 indicates that $\sigma_c(p)$ is primarily a signal-to-noise effect. There is a very sharp blow-up of errors at the faint end of the distribution, and some observations must be discarded because the signal-to-noise is so poor. However for the rest, the relative values of $\sigma_p(p)$, $\sigma_s(p)$ and $\sigma_c(p)$ give a highest value which is adopted in the results.

2.4.3 Reduction Programs

On-line reduction of the telescope allowed p and θ to be calculated at the end of each observation. Instrumental parameters were written to a disc file and could be called back, edited, overwritten or used to reduce an observation. Each data file consists of eight intensities corresponding to the eight positions of the analyzer, and housekeeping information such as the object name, data, waveband, and voltage setting on the preamplifier. All this information, along with the Universal Time, was logged on a lineprinter as observations were being made. The third record was the chart recorder output, which was annotated with the weather conditions, integration times, chopping frequency and throw, and beam positions. A single scan consists of eight integrations (usually ten seconds per point), and a typical observation consists of several scans coadded.

A series of interactive programs was built up to fully reduce the data. Subroutines took the data from a standard observation, and calculated an instrumental parameter which was stored in an array. When the full set of instrumental parameters for that night was determined, the BL Lac files were reduced. There was a facility to examine, edit and coadd each individual file. The edit facility was used on the occasions when a noise spike in the detector corrupted a point in a scan. This could be diagnosed from the stripchart and the discrepant point was removed; it was rare for this to happen more than once per observation. BL Lac object files were always reduced using the instrumental parameters acquired on that night. The reduction procedure is shown in flowchart form in Figure 2.5 and is summarized below:

(a) The instrumental parameters for a given night were calculated. β and α were determined by observing an unpolarized star, γ by measuring a source of known polarization and position angle, and S by observing a photometric standard.

(b) p and θ were deduced using the reduction formulae appropriate to the polarimeter (i.e. polaroid-dichroic or dichroic-polaroid).

(c) The errors $\sigma_p(p,\theta)$, $\sigma_s(p,\theta)$ and $\sigma_c(p,\theta)$ were calculated and the largest was adopted as the error of a single observation.

TABLE 2.1 Details of the Observations/Filters

Run No.	Dates (U.T.)	Focus	Polarimeter Configurations	Chopping	Cryostat	Apertures Used
1	18-22 Dec. 1979	f/9	P-D	focal plane	UKT 0	10"
2	19-21 Apr. 1980	f/9	D-P	focal plane	UKT 1	10", 15"
3	9-11 July 1980	f/9	D-P	focal plane	UKT 1	10", 15"
4	9-12 Aug. 1980	f/35	D-P	secondary	f/35	10", 19"

P-D indicates polarimeter upstream of dichroic mirror

D-P indicates polarimeter downstream of dichroic mirror

Waveband	λ_{eff} (μm)	flux (0^m) in J_y	Extinction/airmass
J	1.25	1520	0.05
H	1.65	980	0.06
K	2.2	620	0.10

TABLE 2.2 Photometric and Polarimetric Standard Stars

Photometric Std.	R.A. (1975.0)			Dec.			V	J	H	K
BS 4550	11^h	50^m	06^s	$+38^o$	04'	39"	6.45	4.89	4.43	4.37
BS 4689	12	17	20	-00	23	21	3.82	-	3.73	3.75
BS 5447	14	32	30	+29	57	41	4.47	3.65	3.50	3.49
BS 6147	16	28	16	-16	30	19	4.27	2.68	2.33	2.27
BS 8143	21	15	27	+39	11	03	4.23	3.86	3.82	3.78
BS 8278	21	38	42	-16	46	33	3.67	3.19	3.09	3.02
BS 8551	22	26	35	+04	34	18	4.79	3.01	2.43	2.35

Polarimetric Std.	R.A. (1975.0)		Dec.		V	Spectral Type
107 Psc	01^h	41.2^m	$+20^o$	10'	5.2	K1 1V
χ Ori	05	52.9	+20	16	4.4	G0 V
λ Psc	08	06.3	+21	39	5.4	G2 IV
χ Her	15	51.9	+42	30	4.6	F9 V
β Aql	19	54.1	+06	20	3.7	G8 IV
i Peg	22	05.9	+25	13	3.8	F5 V

TABLE 2.3 Instrumental Sensitivity

Date	Star Name	Sensitivity ($\times 10^{-7}$) K	H	J	
Run 1					
18-12-79	CIT 4550	3.532	2.297	1.699	P
19-12-79	CIT 4550	3.625	2.304	-	P
20-12-79	χ Ori	3.552	2.271	1.642	S
21-12-79	107 Psc	3.559	2.419	1.837	S
22-12-79	CIT 4689	3.554	2.313	1.730	P
Run 2					
18-04-80	λ Psc	3.822	2.611	1.993	S
20-04-80	CIT 6147	3.824	2.591	2.192	P
21-04-80	CIT 4550	3.850	2.688	2.053	P
Run 3					
09-07-80	BS 8551	2.208	1.663	1.294	P
10-07-80	CIT 5447	2.221	1.540	1.328	P
11-07-80	BS 8278	2.236	1.421	1.338	P
Run 4					
09-08-80	CIT 8143	6.021	3.909	2.803	P
10-08-80	CIT 8143	5.879	3.856	2.791	P
11-08-80	CIT 8143	6.195	3.700	2.939	P
12-08-80	CIT 8143	4.502	3.134	2.103	P

P indicates primary standard

S indicates secondary standard

TABLE 2.4 Scan Repeatability

Date	Star Name	Repeatability/Photon Error (%) K	H	J
Run 1				
18-12-79	CIT 4550	1.05/0.45	1.42/1.16	2.01/0.88
19-12-79	λ Psc	2.52/0.40	2.49/0.32	2.98/0.87
20-12-79	107 Psc	1.28/0.89	-	-
21-12-79	107 Psc	0.70/0.87	2.53/0.73	1.68/0.77
22-12-79	107 Psc	0.52/0.27	-	-
Run 2				
18-04-80	λ Psc	1.81/0.36	4.32/0.95	1.80/0.96
20-04-80	CIT 6147	0.18/0.18	0.01/0.15	1.55/0.16
21-04-80	CIT 4550	1.76/0.47	2.65/0.20	1.51/0.43
Run 3				
09-07-80	BS 8551	0.64/0.28	0.95/0.25	0.36/0.29
10-07-80	CIT 5447	0.49/0.74	2.51/0.62	-
11-07-80	BS 8278	0.45/0.60	0.67/0.50	-
Run 4				
09-08-80	CIT 8143	0.70/0.44	0.16/0.36	0.14/0.99
10-08-80	CIT 8143	0.66/0.42	0.55/0.37	0.33/0.95
11-08-80	CIT 8143	2.21/0.25	0.29/0.20	4.42/0.56
12-08-80	CIT 8143	1.39/0.38	0.25/0.32	0.16/0.86

TABLE 2.5 Errors in S

Date	Star Name	σ(S) (in %) K	H	J	
Run 1	CIT 4550	0.91	1.03	1.62	P
19-12-79	CIT 4550	1.70	0.72	-	P
20-12-79	χ Ori	0.35	2.15	4.92	S
21-12-79	107 Psc	0.15	4.23	6.37	S
22-12-79	CIT 4689	0.29	0.34	0.17	P
Run 2					
18-04-80	λ Psc	0.26	0.71	4.15	S
20-04-80	CIT 6147	0.21	1.47	5.42	P
21-04-80	CIT 4550	0.47	2.22	1.27	P
Run 3					
09-07-80	BS 8551	0.62	7.90	1.97	P
10-07-80	CIT 5447	0.03	0.00	0.61	P
11-07-80	BS 8278	0.65	7.80	1.36	P
Run 4					
09-08-80	CIT 8143	6.58	7.10	5.42	P
10-08-80	CIT 8143	4.07	5.65	4.96	P
11-08-80	CIT 8143	9.66	1.38	10.53	P
12-08-80	CIT 8143	20.31	14.13	20.91	P

TABLE 2.6 Instrumental Polarization

Date	Star Name	Polarization (%)/Position Angle (°) K	H	J	
Run 1					
18-12-79	λ Psc	2.19/80.2	2.82/84.4	3.50/87.2	P
18-12-79	CIT 4550	2.02/87.1	2.45/88.4	3.47/90.2	S
19-12-79	λ Psc	1.90/84.6	3.09/88.7	3.40/89.3	P
19-12-79	'OJ' Star	4.05/87.6	4.26/88.2	4.47/87.6	S
19-12-79	CIT 4550	1.99/88.8	2.55/86.7	3.60/89.4	S
20-12-79	χ Ori	1.92/93.3	2.51/0.0	3.46/87.7	P
21-12-79	107 Psc	1.94/93.8	2.18/86.7	4.23/93.1	P
22-12-79	CIT 4689	2.11/85.9	2.53/86.7	3.81/87.4	S
22-12-79	χ Ori	2.04/86.0	2.40/90.9	3.56/87.7	P
Run 2					
18-04-80	λ Psc	3.65/82.4	4.16/82.7	6.97/81.7	P
20-04-80	χ Her	3.45/81.8	4.55/80.8	6.06/81.3	P
20-04-80	CIT 6147	3.54/80.6	4.57/83.6	5.46/82.4	S
21-04-80	χ Her	4.44/74.3	4.14/83.3	5.76/80.8	P
21-04-80	CIT 4550	3.16/77.5	4.61/83.8	6.09/80.2	S
Run 3					
09-07-80	χ Her	3.86/80.8	4.87/82.0	6.13/78.2	P
09-07-80	BS 8551	3.20/84.8	3.64/83.5	5.65/82.2	S
10-07-80	β Aql	3.47/81.4	4.82/83.9	6.66/82.4	P
10-07-80	CIT 5447	3.17/82.1	4.89/79.2	5.32/81.3	S
11-07-80	BS 8278	3.58/82.8	4.92/79.0	-	S
Run 4					
09-08-80	χ Her	3.51/82.6	6.19/83.2	7.57/79.0	P
09-08-80	CIT 8143	3.65/85.8	5.28/83.5	6.98/81.8	S
10-08-80	β Aql	1.58/89.1	1.49/66.8	3.16/80.7	P
10-08-80	CIT 8143	4.02/78.8	4.62/86.8	6.70/76.4	S
11-08-80	i Peg	3.78/80.5	4.79/81.5	7.18/82.1	P
11-08-80	CIT 8143	3.10/77.1	2.52/53.3	6.10/73.1	S
12-08-80	χ Her	2.67/73.7	2.82/79.8	5.39/82.0	P
12-08-80	CIT 8143	1.53/83.5	2.26/80.1	4.71/80.1	S

TABLE 2.7 Errors in β, α

Date	Star Name	σ(β)/σ(α) in (%)/(°) K	H	J	
Run 1					
18-12-79	λ Psc	0.18/7.3	0.25/3.5	0.13/1.6	P
18-12-79	CIT 4550	0.01/0.4	0.12/0.5	0.16/1.4	S
19-12-79	λ Psc	0.11/2.9	0.52/0.8	0.23/0.5	P
19-12-79	'OJ' Star	2.02/0.1	1.69/0.3	0.84/1.2	S
19-12-79	CIT 4550	0.02/1.3	0.02/1.2	0.10/0.6	S
20-12-79	χ Ori	0.09/5.8	0.06/2.1	0.04/1.1	P
21-12-79	107 Psc	0.07/6.3	0.39/0.8	0.73/4.3	P
22-12-79	CIT 4689	0.10/1.6	0.04/0.8	0.31/1.4	S
22-12-79	χ Ori	0.03/1.5	0.17/3.0	0.06/1.1	P
Run 2					
18-04-80	λ Psc	0.00/3.1	0.25/1.0	0.10/0.4	P
20-04-80	χ Her	0.20/2.5	0.14/2.9	0.01/0.0	P
20-04-80	CIT 6147	0.11/1.3	0.16/0.1	0.61/1.1	S
21-04-80	χ Her	0.79/5.0	0.27/0.4	0.31/0.5	P
21-04-80	CIT 4550	0.50/1.8	0.20/0.1	0.02/1.1	S
Run 3					
09-07-80	χ Her	0.40/1.6	0.24/0.5	0.19/2.8	P
09-07-80	BS 8551	0.26/2.4	0.99/2.0	0.29/1.2	S
10-07-80	β Aql	0.01/1.0	0.19/2.4	0.72/1.4	P
10-07-80	CIT 5447	0.29/0.3	0.26/2.3	0.62/0.3	S
11-07-80	BS 8278	0.12/0.4	0.29/2.5	-	S
Run 4					
09-08-80	χ Her	0.53/1.2	2.44/3.0	2.60/0.4	P
09-08-80	CIT 8143	0.67/4.4	1.53/3.3	1.01/2.4	S
10-08-80	β Aql	1.40/7.7	2.26/13.4	2.81/1.3	P
10-08-80	CIT 8143	1.04/2.6	0.87/6.6	0.73/3.0	S
11-08-80	i Peg	0.80/0.9	1.04/1.3	1.21/2.7	P
11-08-80	CIT 8143	0.12/4.3	1.23/26.9	0.13/6.3	S
12-08-80	χ Her	0.31/7.7	0.93/0.4	0.58/2.6	P
12-08-80	CIT 8143	1.45/2.1	1.49/0.1	1.26/0.7	S

TABLE 2.8 Instrumental Parameters

Date	Star Name	Test	Waveband	Result
09-07-80	BS 8551	0^{o}-90^{o}	K	β<0.30%
09-07-80	BS 8551	0^{o}-90^{o}	H	β= 0.20%
09-07-80	BS 8551	0^{o}-90^{o}	J	β= 0.31%
21-04-80	CIT 6147	D-P-P	K	$\underline{\beta}$= 0.881 ± 0.025
21-04-80	CIT 6147	D-P-P	H	$\underline{\beta}$= 0.994 ± 0.005
21-04-80	CIT 6147	D-P-P	J	$\underline{\beta}$= 0.991 ± 0.007
20-04-80	BN Object		K	γ= 0.757 ± 0.15, p = 16.2%
20-04-80	BN Object		H	γ= 1.07 ± 0.12, p = 39.5%
21-04-80	χ Her	P-D-P	K	γ= 0.96 ± 0.09
10-07-80	β Aql	P-D-P	K	γ_1= 0.95, γ_2=0.94, γ_3=0.95
			H,J	γ_H= 0.96, γ_J=0.99
09-08-80	CIT 8143	P-P-D-P	K	γ= 0.94 ± 0.05
			H,J	γ_H=1.10 ± 0.11, γ_J=1.01 ± 0.13
18-12-80	Lab	Position Angle	-	ε= 11.5^{o}
18-04-80	Lab	Position Angle	-	ε= -258.5^{o}

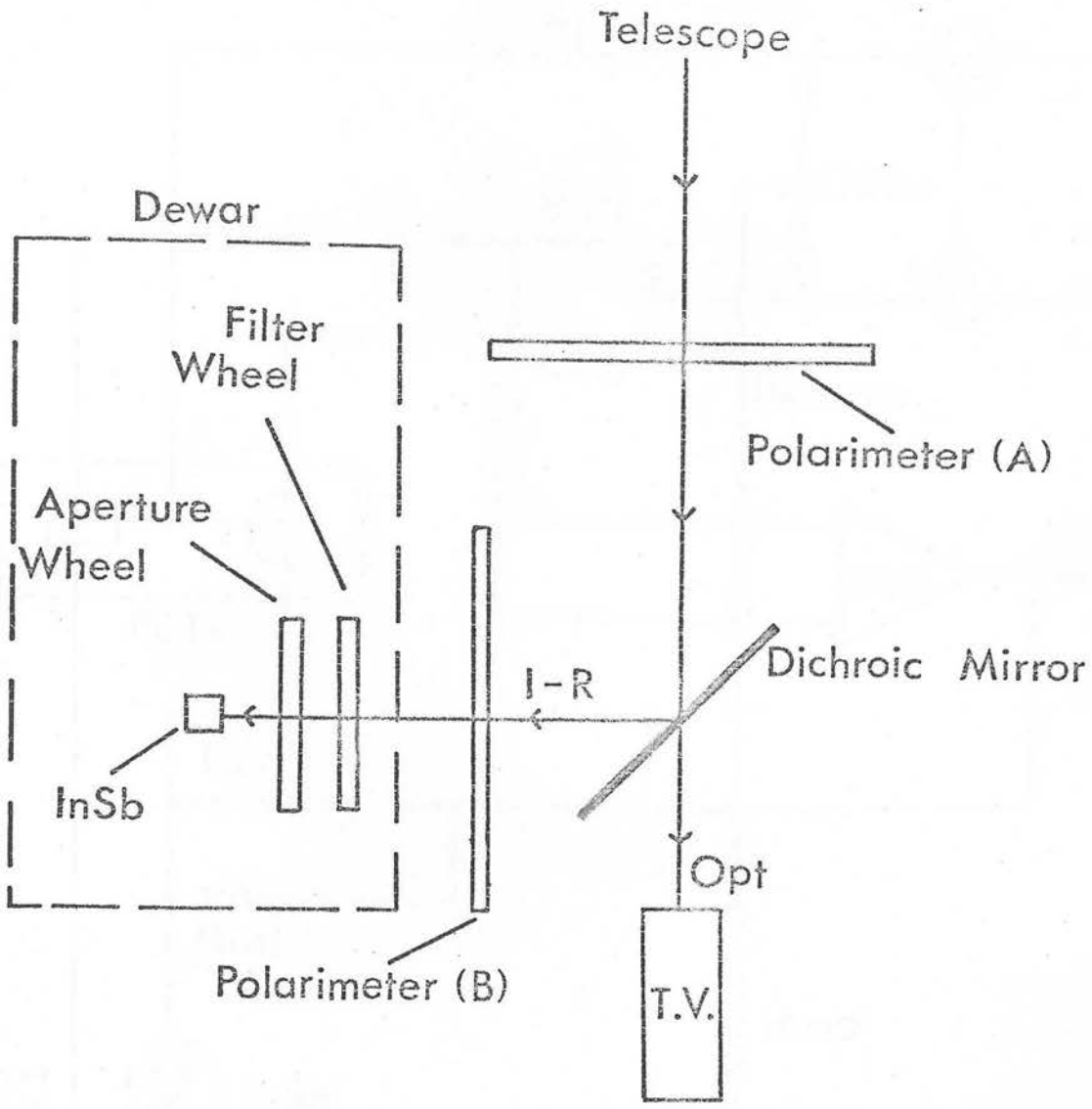

Figure 2.1 Schematic lay-out of the instrument. Polarimeter position (A) corresponds to the instrument during Run 1 (Dec.,1979). Polarimeter position (B) corresponds to the instrument during Runs 2,3,4 (April, July,August, 1980).

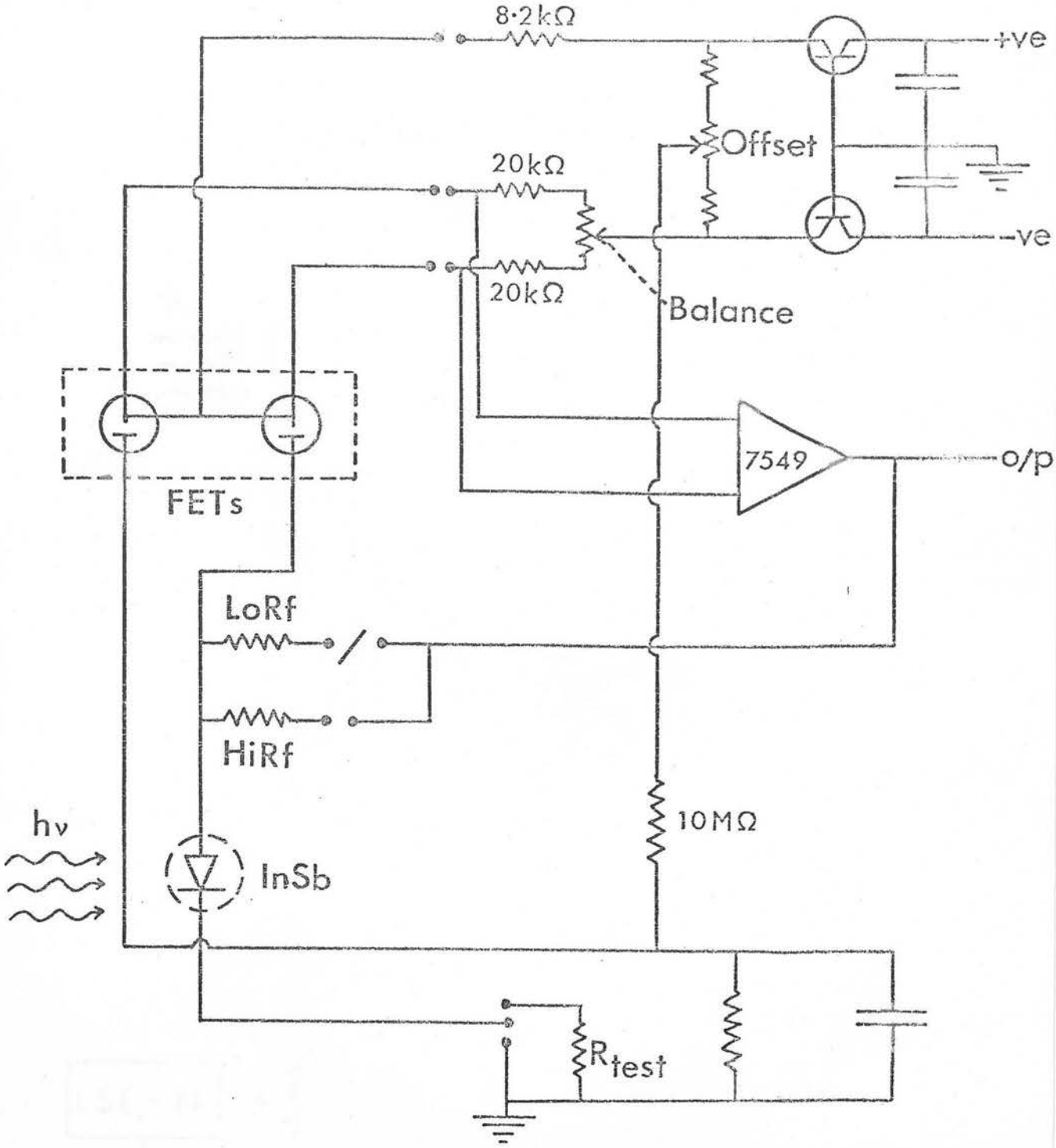

Figure 2.2 Circuit diagram of cooled preamplifier for InSb detector. For observing faint objects, HiRf $\simeq 2\times10^{11}\Omega$.

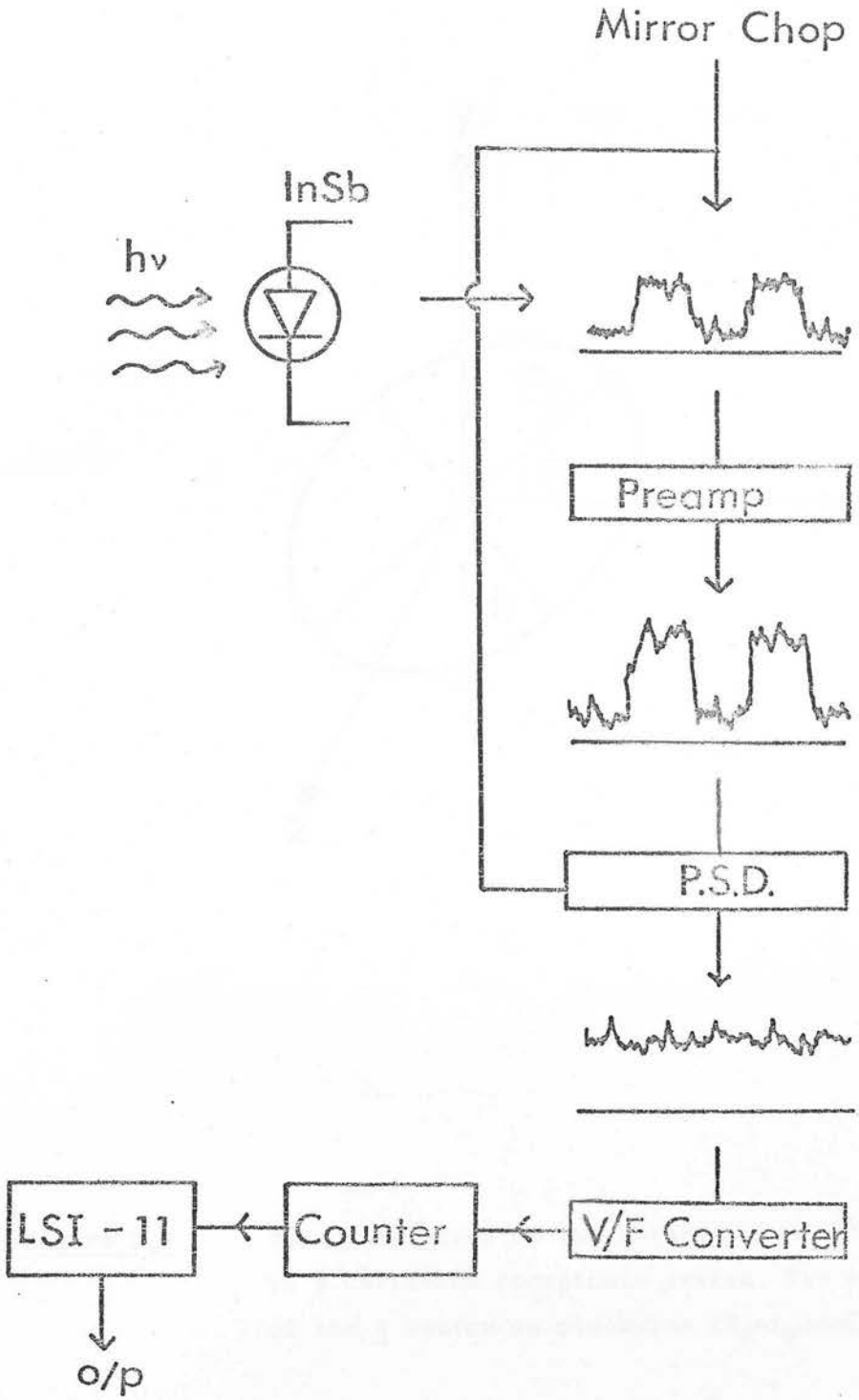

Figure 2.3 Schematic lay-out of the data acquisition system.

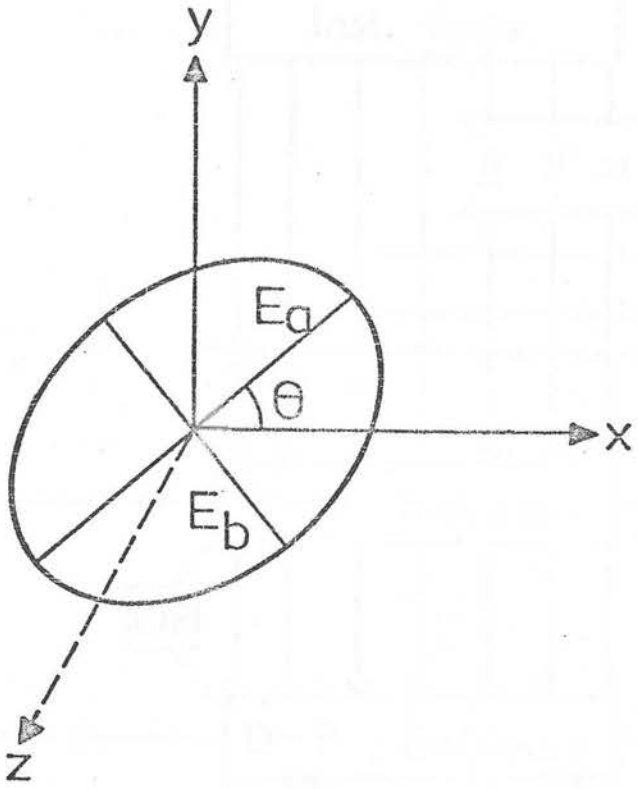

Figure 2.4 The orientation of the polarization ellipse relative to a Cartesian coordinate system. The sense of rotation of the $\underline{E}$ vector is clockwise ($E_a=I_p\cos\xi$, $E_b=I_p\sin\xi$).

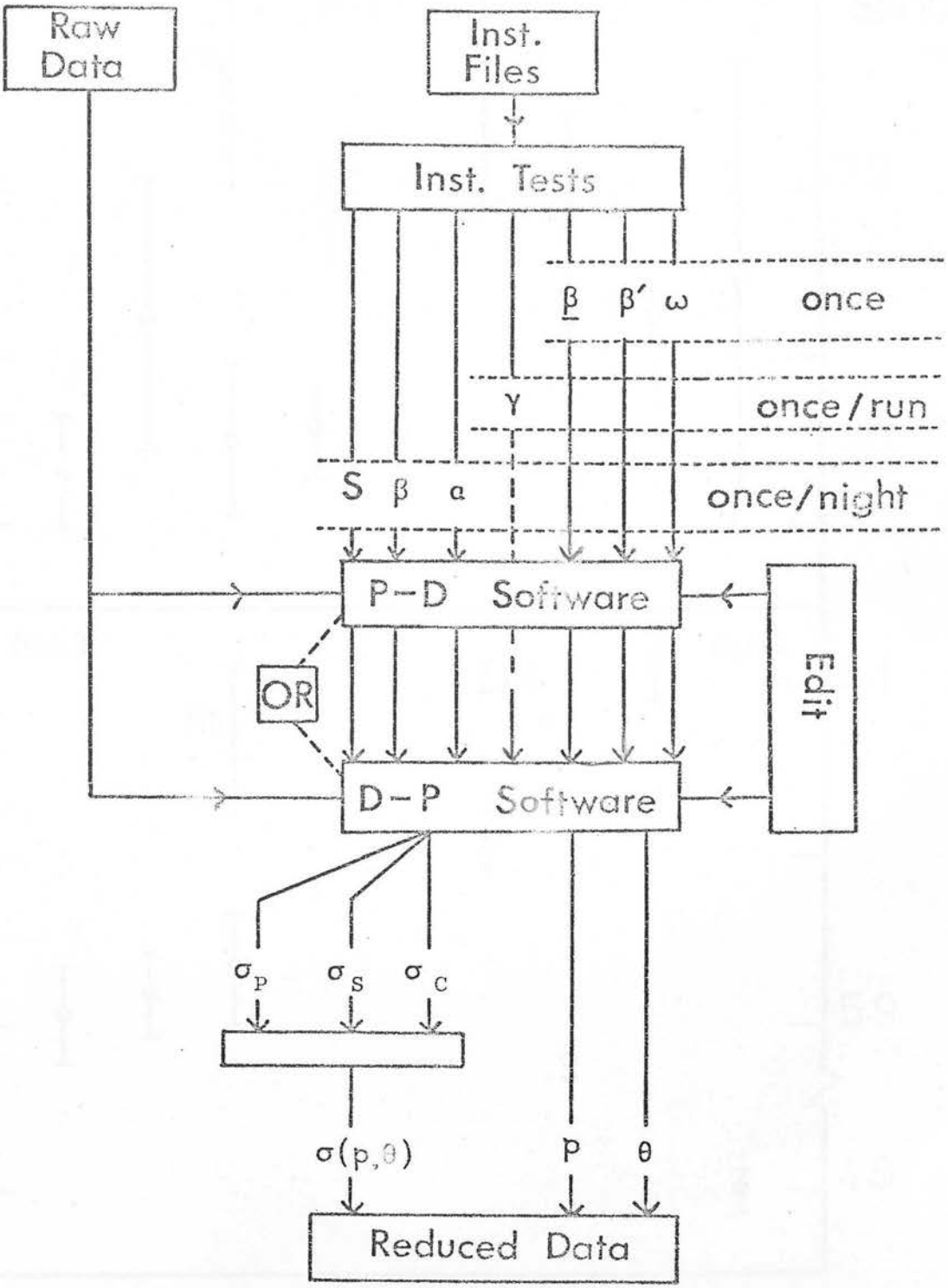

Figure 2.5 Schematic diagram of the data reduction procedure. P-D corresponds to Run 1, D-P corresponds to Runs 2,3,4.

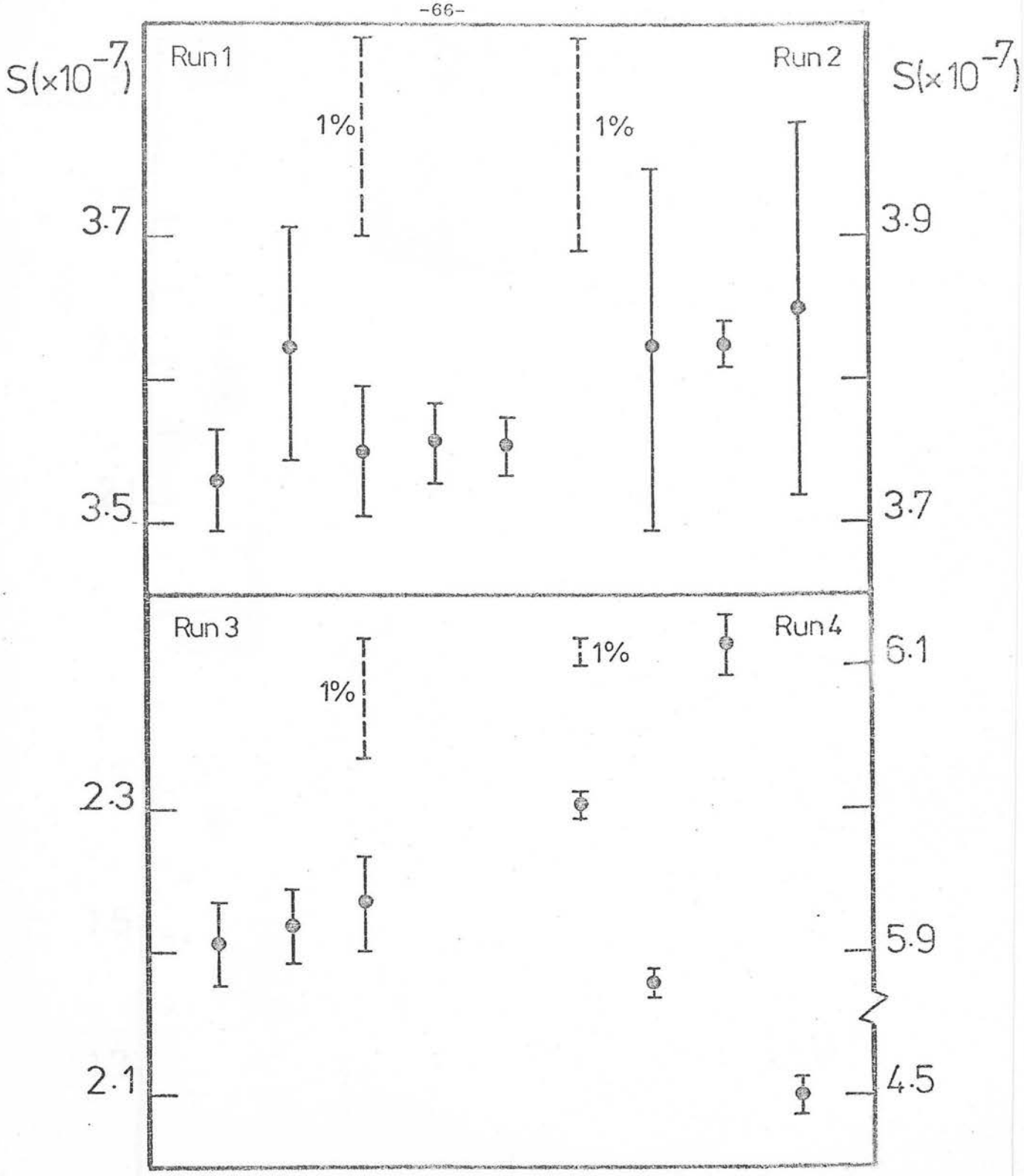

Figure 2.6 Instrumental sensitivity at K (2.2μm). The error bars are taken from the scan repeatability measurements. A 1% error bar is also shown.

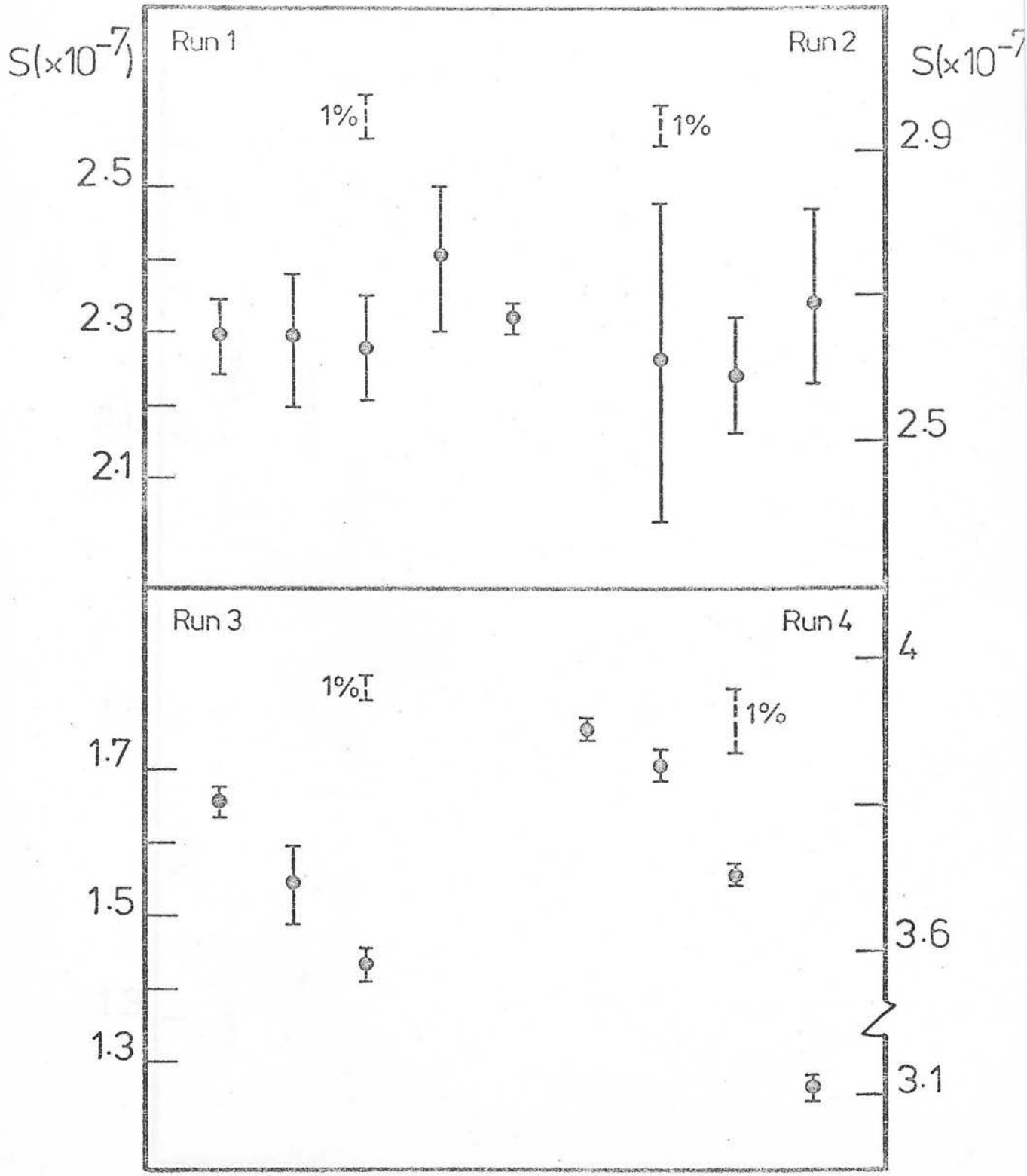

Figure 2.7 Instrumental sensitivity at H (1.65μm). The error bars are taken from scan repeatability measurements. A 1% error is also shown.

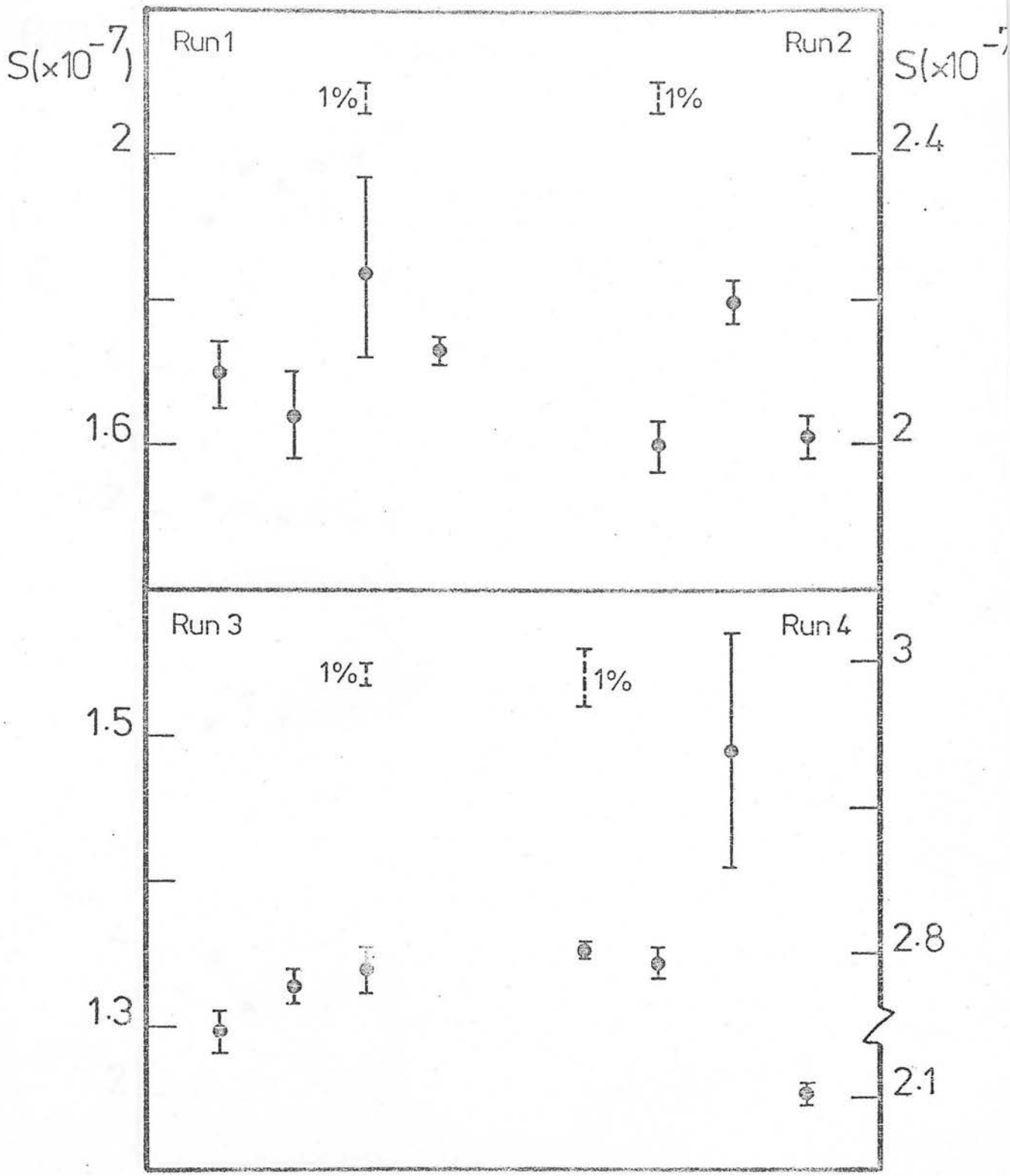

Figure 2.8 Instrumental sensitivity at J (1.25μm). The error bars are taken from scan repeatability measurements. A 1% error bar is also shown.

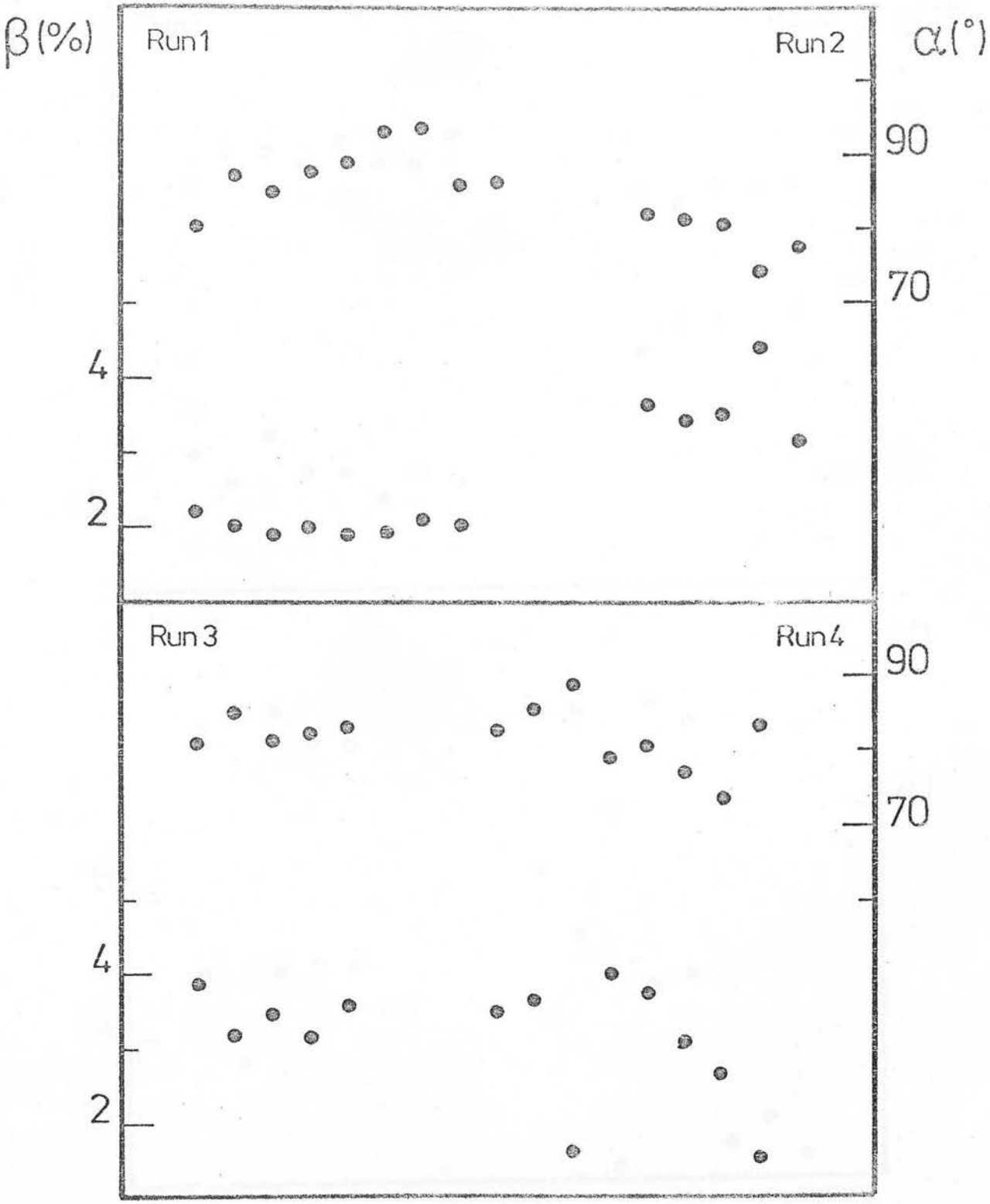

Figure 2.9 Instrumental polarization at K (2.2μm). All measures of β and α are shown, from photometric and polarimetric standards.

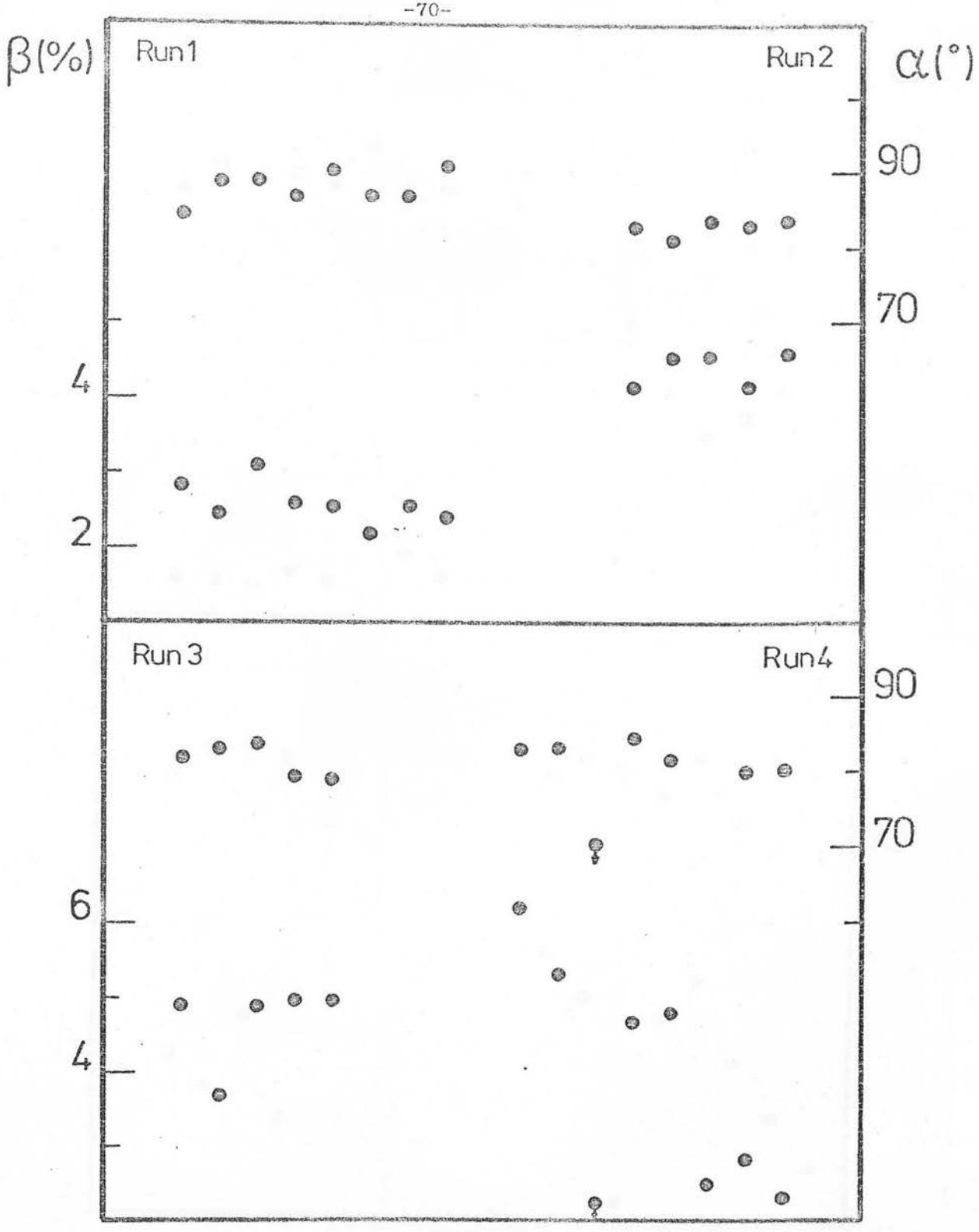

Figure 2.10 Instrumental polarization at H (1.65μm). All measures of β and α are shown, from photometric and polarimetric standards.

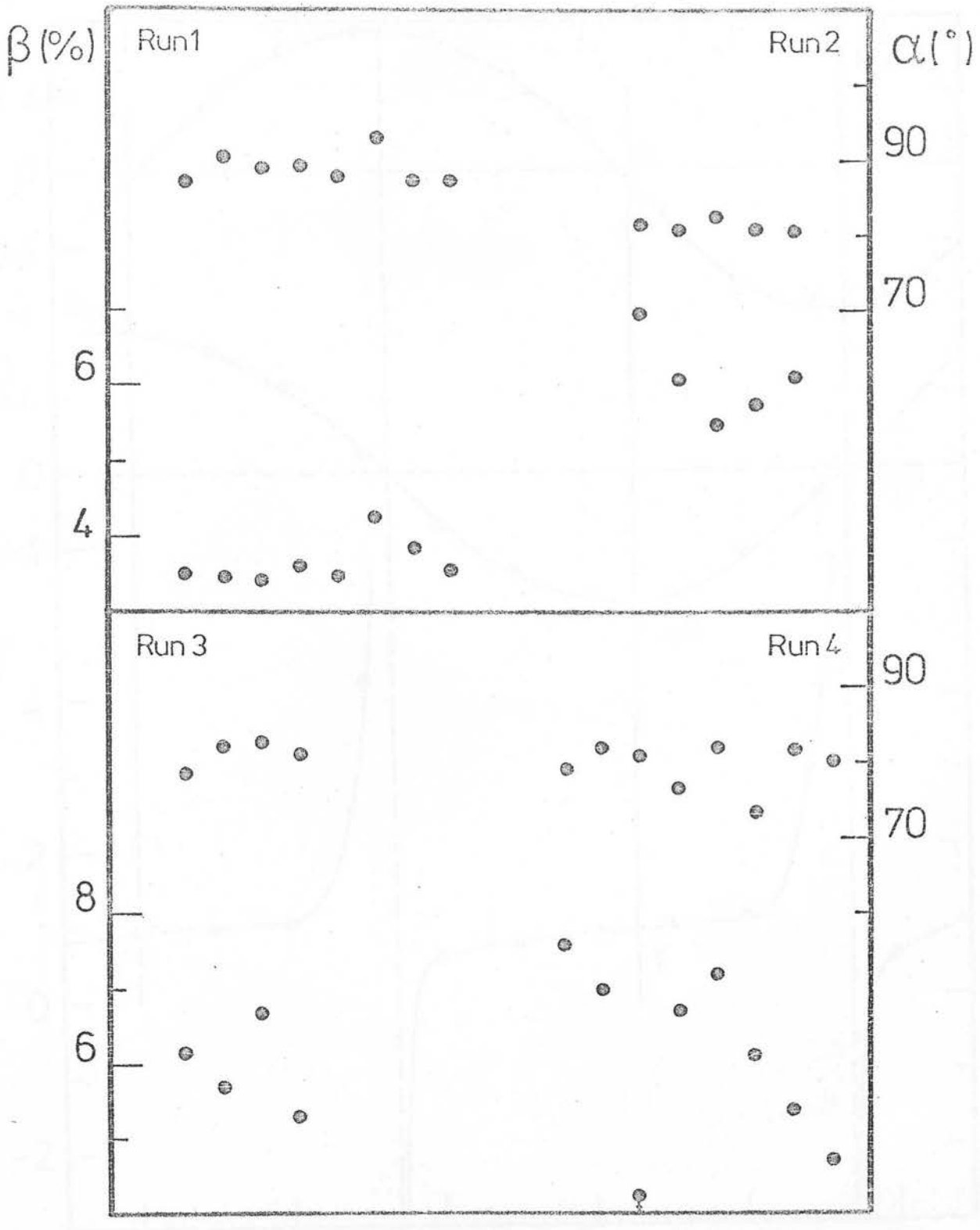

Figure 2.11 Instrumental polarization at J (1.25μm). All measures of β and α are shown, from photometric and polarimetric standards.

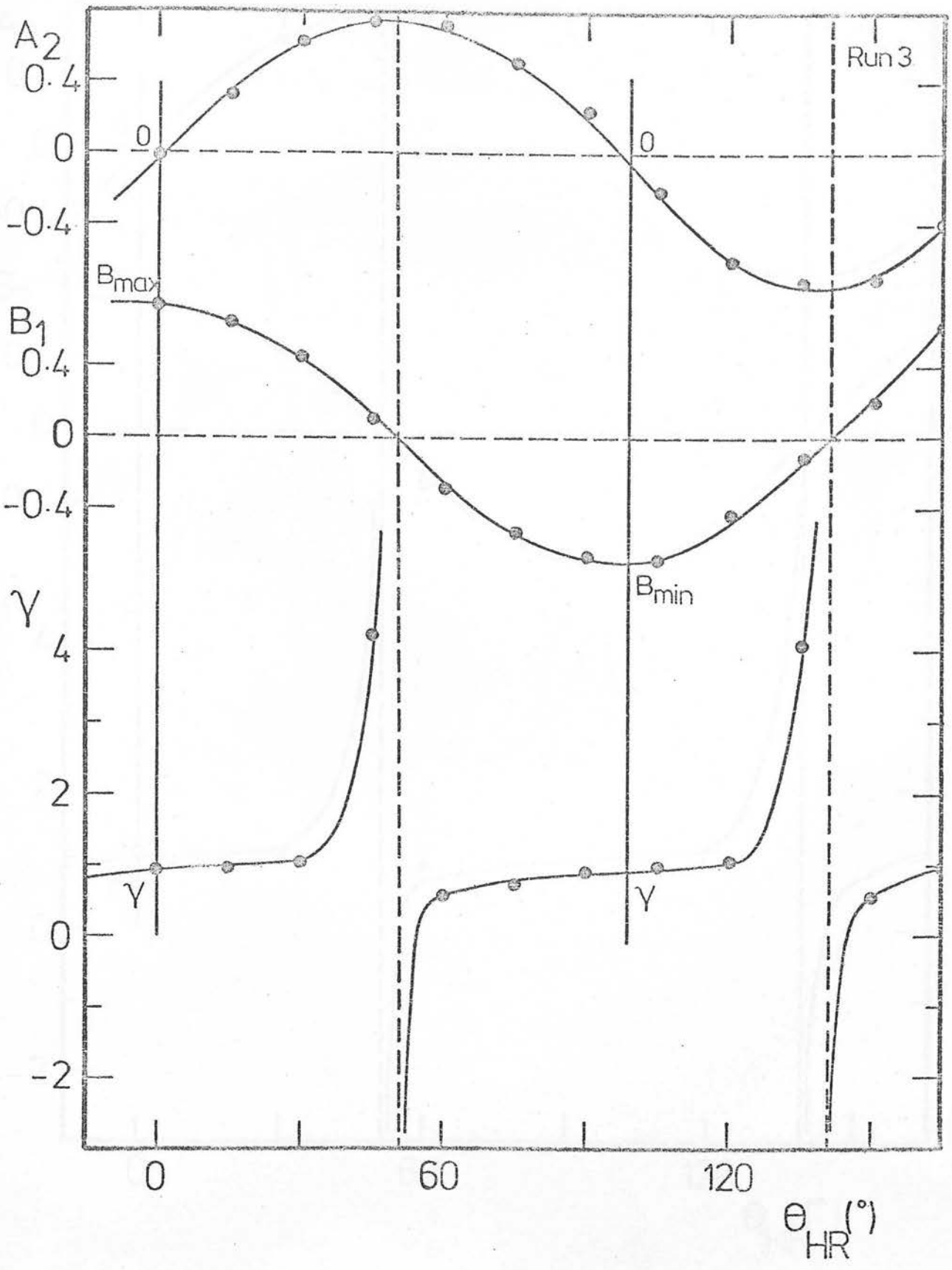

Figure 2.12 Fitted parameters A_2, B_2 and γ plotted against position angle of polarized source (in this case - HR Polaroid). There is a discontinuity at $B_2=0$, corresponding to $\sin 2(\phi'-\alpha)=0$.

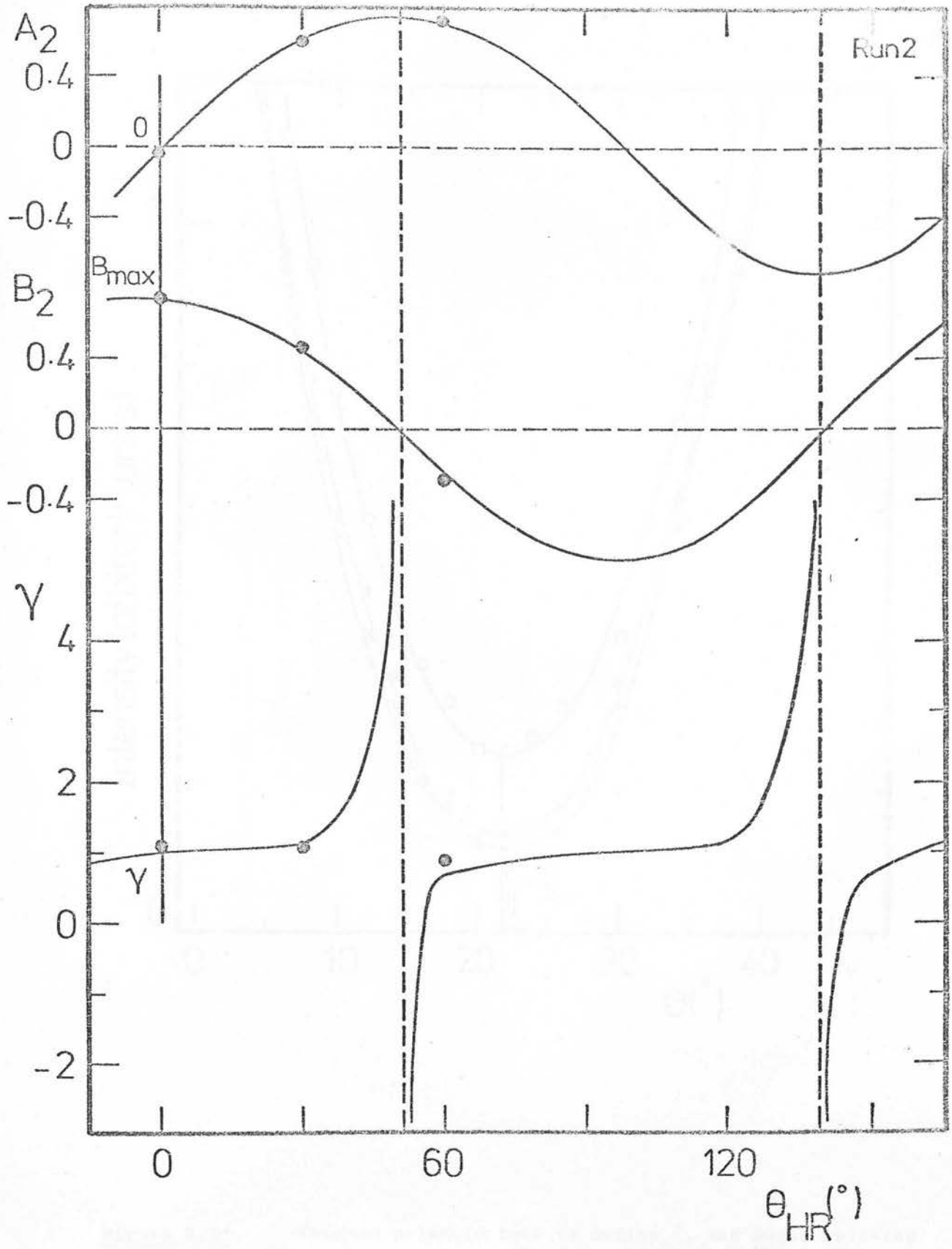

Figure 2.13 Fitted parameters A_2, B_2 and γ plotted against position angle of polarized source. Smooth curves are fit to data fron Run 3 (figure 2.12), dots are data points.

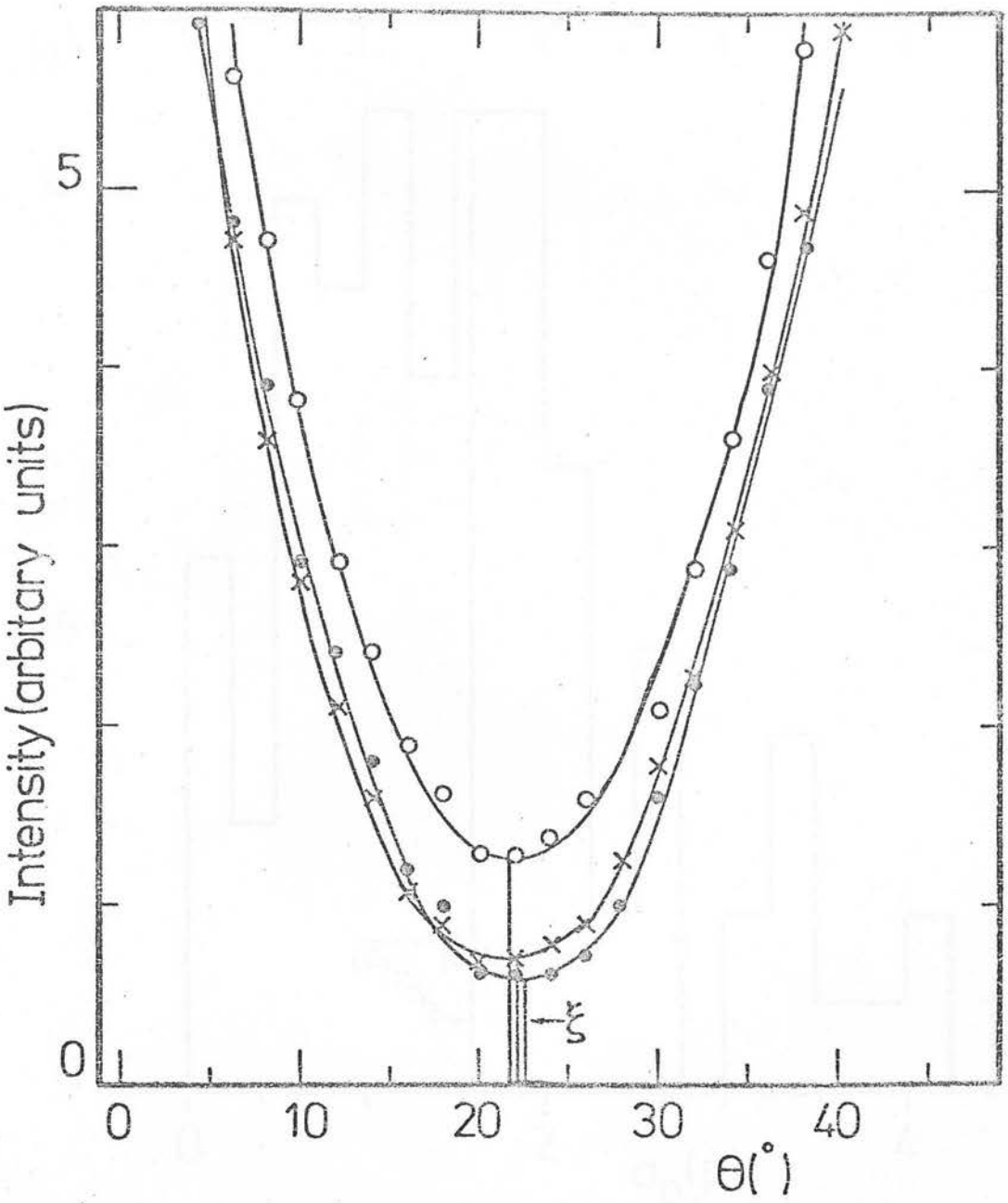

Figure 2.14 Crossed polaroid test to define ξ, the angle relating polaroid fast axis to celestial coordinate system. ξ is determined to a precision of $\sigma(\xi)<1^{o}$.

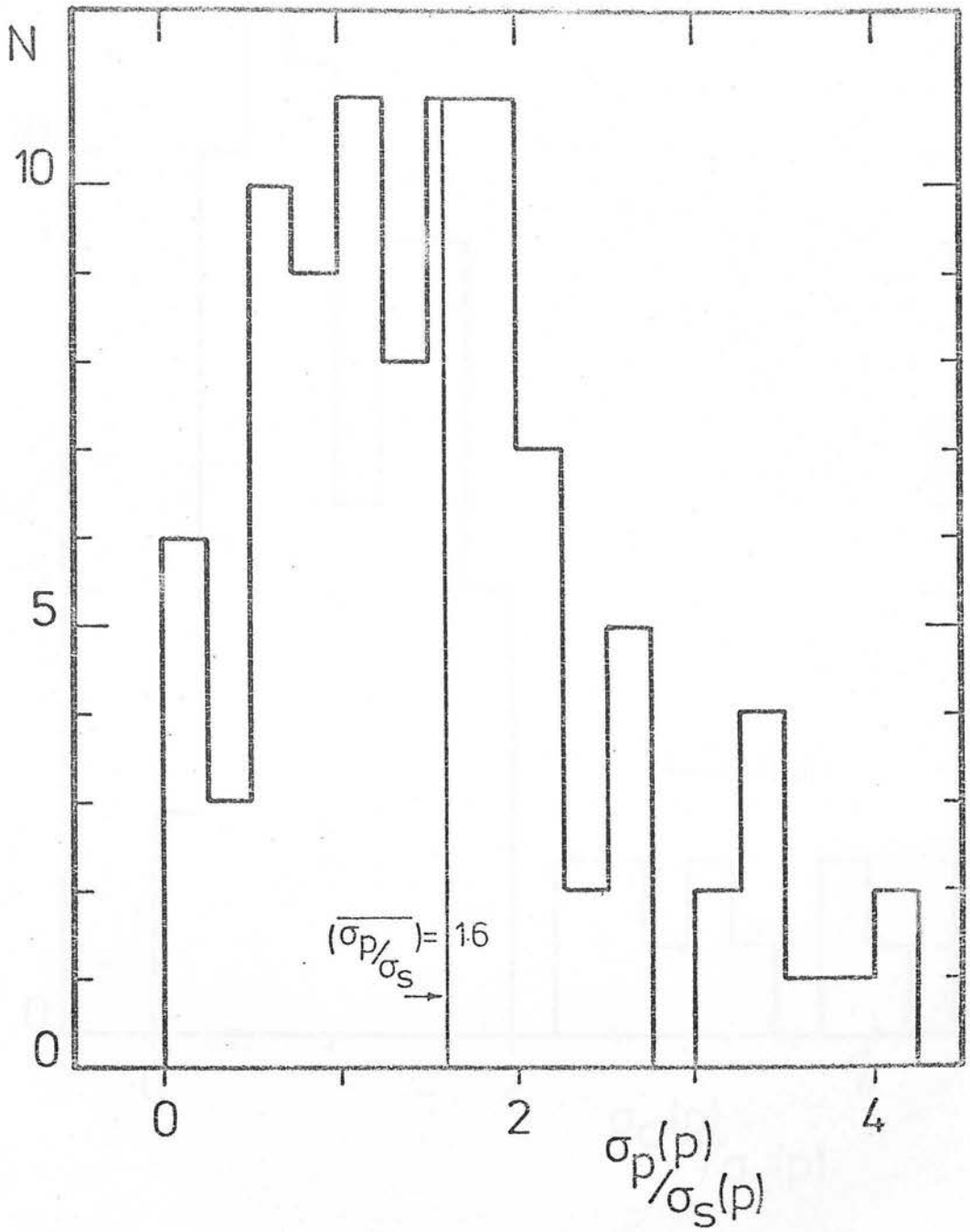

Figure 2.15 Histogram of the ratio of photon to standard errors for polarization observations. $\overline{(\sigma_p/\sigma_s)}$=1.6.

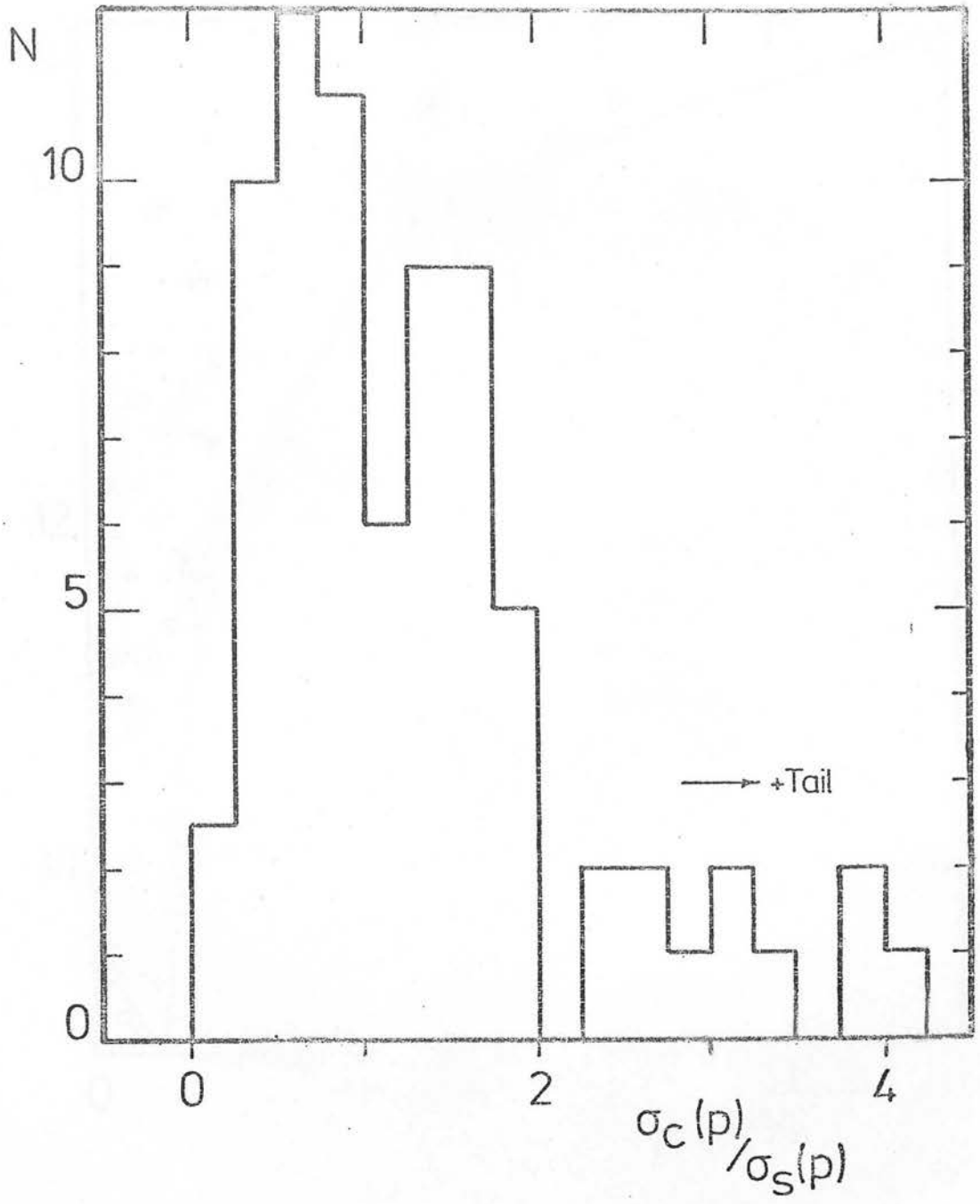

Figure 2.16 Histogram of the ratio of characteristic to standard errors for polarization observations. There is a tail of 15 observations with $\sigma_c(p)/\sigma_s(p)>5$.

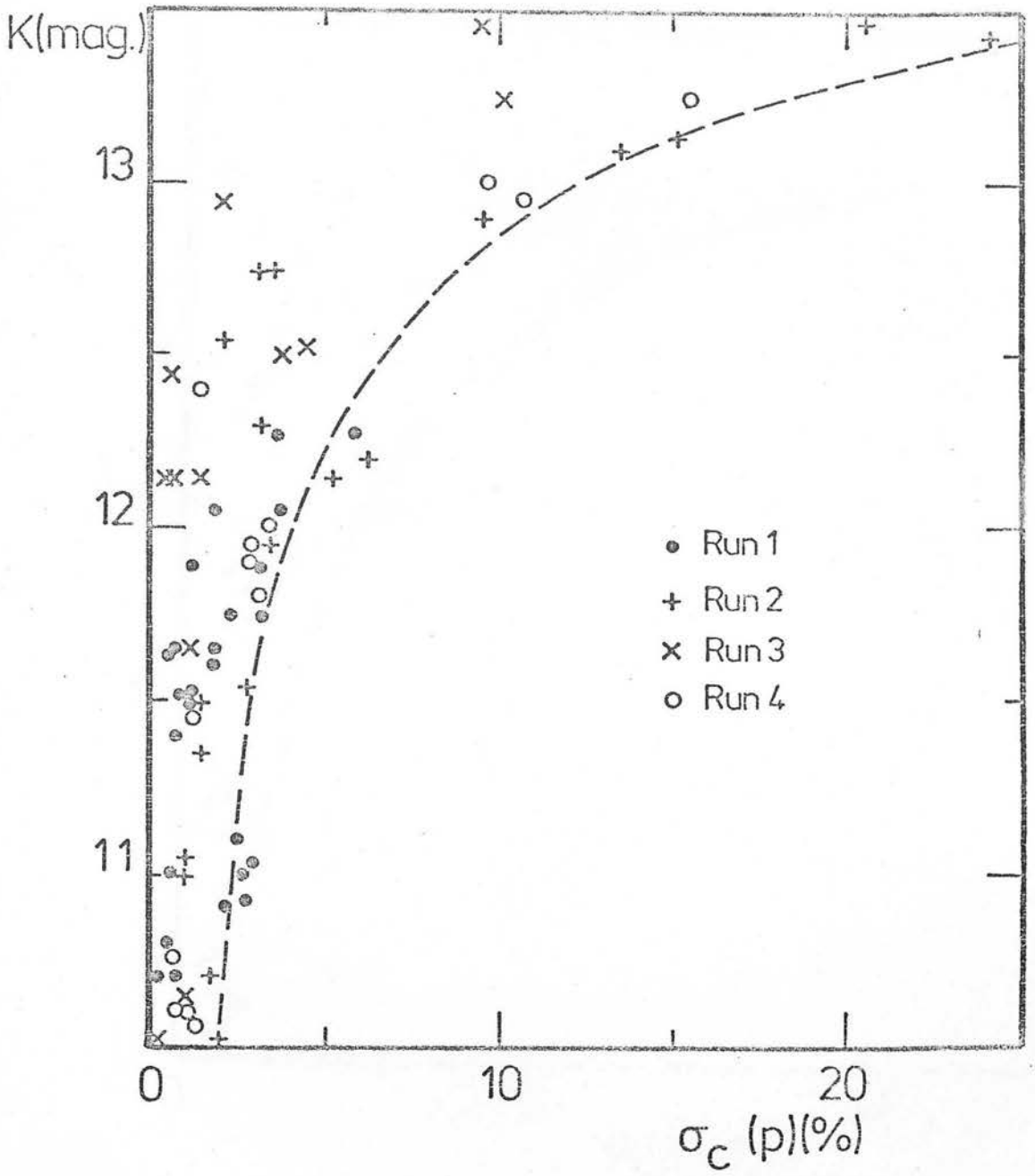

Figure 2.17 Distribution of characteristic error with K magnitude. $\sigma_c(p)$ corresponds roughly to polarization noise.

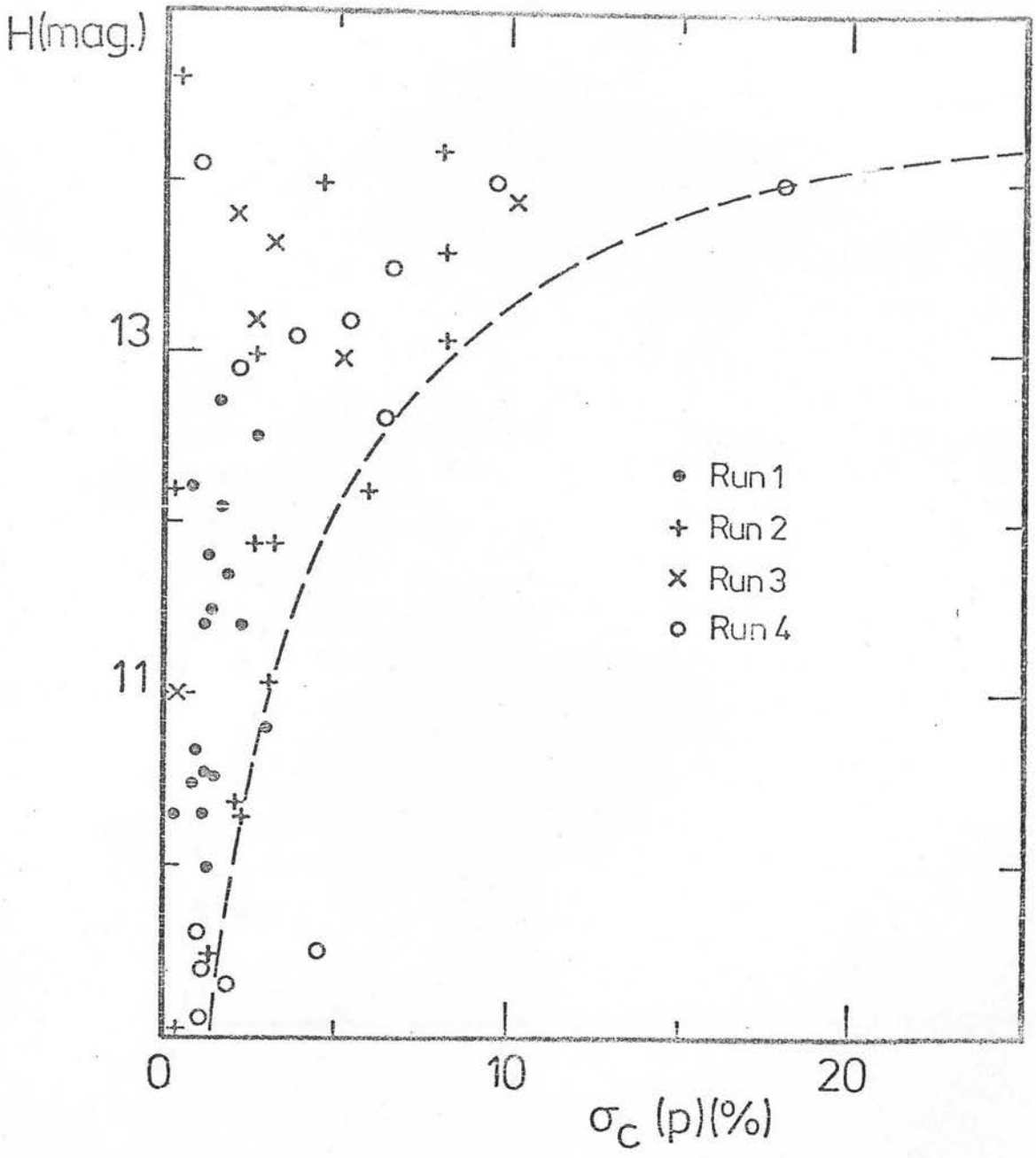

Figure 2.18 Distribution of characteristic error with H magnitude. $\sigma_c(p)$ corresponds roughly to polarization noise

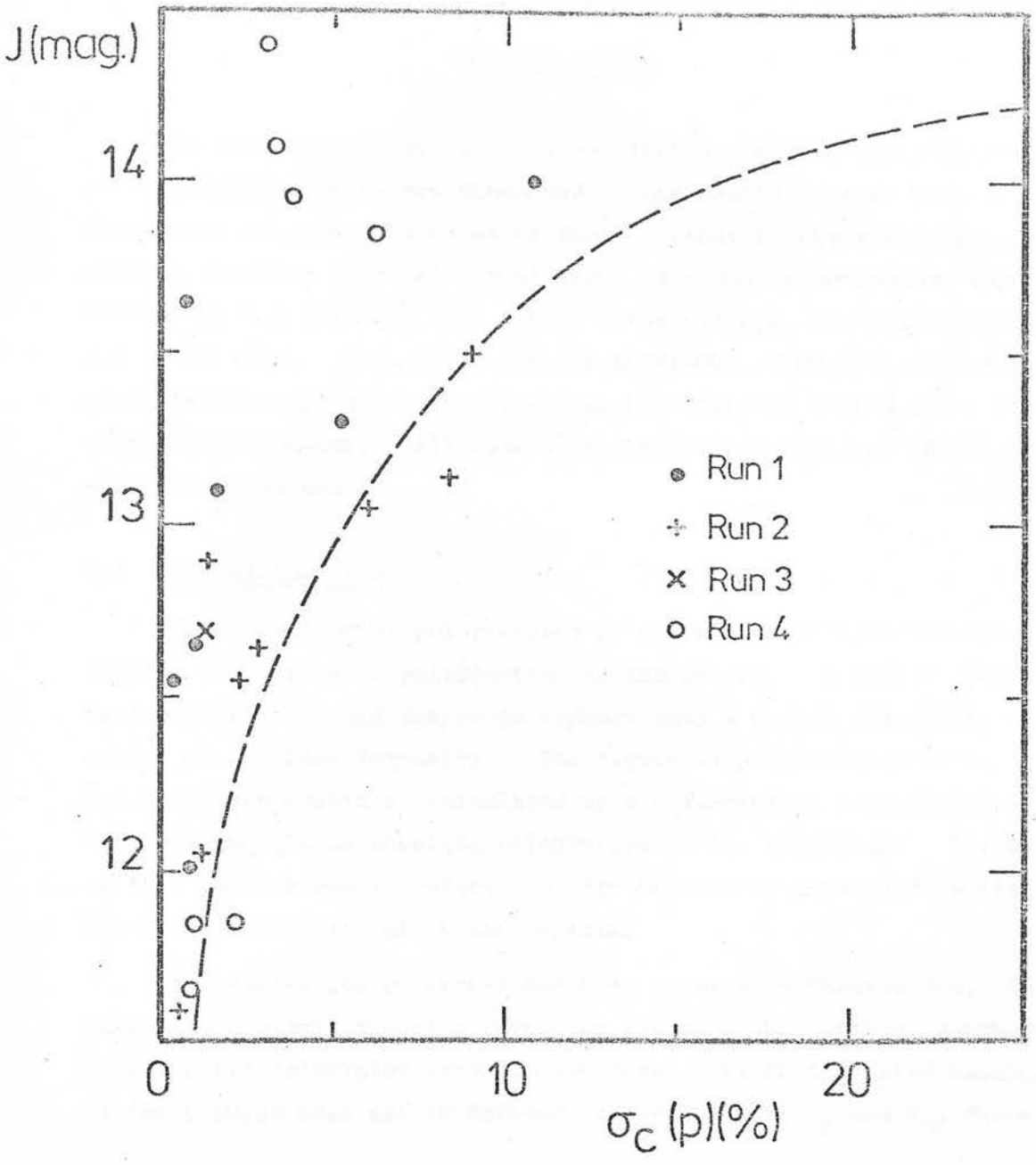

Figure 2.19 Distribution of characteristic noise with J magnitude. $\sigma_c(p)$ corresponds roughly to polarization noise.

CHAPTER THREE

In this Chapter the results are listed, and the observations of individual objects are discussed. The Chapter starts with a discussion of signal-to-noise in the polarimetric observations. Between December 1979 and August 1980, 17 BL Lac objects were observed. Photometry was obtained for all of these objects, and polarimetry for 13 of them. Five other sources (0048-097, 0109+220, 0219+428, 0818-128 and 2254+074) were observed, but found to be too faint for reliable photometry. All data were obtained in the J, H and K photometric wavebands.

3.1 Signal-to-Noise

The detection of polarization is a function of both the intensity and degree of polarization of the source. A highly polarized source is always easier to measure than a weakly polarized source of the same intensity. The degree of polarization is a dimensionless quantity, calculated by a differential measurement and does not require an absolute calibration of the intensity. The aim of this project was to detect the high degrees of polarization that are a characteristic of BL Lac objects.

The derivation of errors has been treated in Chapter Two. To calculate a signal-to-noise parameter for each observation, another quantity was calculated from the raw data. It is the third harmonic of the 8 point scan and is defined by coefficients A_3 and B_3, where

$$I_K = K(1+A_1\cos\phi_K+B_1\sin\phi_K+A_2\cos2\phi_K+B_2\sin2\phi_K+A_3\cos3\phi_K+B_3\sin3\phi_K) \qquad (3.1)$$

in analogy with equation (2.69)

The third harmonic has no physical significance, but power in A_3 and B_3 represents noise, imperfections in the polarimeter, and the same systematic errors which contribute to A_1 and B_1. The third harmonic plays no part in the formal error analysis, because it is not modelled in equations (2.69) and on. For "well-behaved" data, it would be expected that

$$(A_1^2+B_1^2)^{\frac{1}{2}} > (A_3^2+B_3^2)^{\frac{1}{2}} \qquad (3.2)$$

i.e. that the power spectrum converges at higher frequencies. Therefore the signal-to-noise for an observation has been defined as

$$\frac{S}{N} = \frac{(A_2^2 + B_2^2)^{\frac{1}{2}}}{(A_1^2+B_1^2)^{\frac{1}{2}} + (A_3^2+B_3^2)^{\frac{1}{2}}} \qquad (3.3)$$

This quantity is not as simple as the signal due to polarization of the object divided by the noise (systematic, photon, etc.) signal, because the coefficients A_2 and B_2 contain the instrumental polarization as well as the object polarization. However, β is determined quite accurately (to $\sim$0.3%), so the vector sum $\underline{\beta}+\underline{p}$ is dominated by the uncertainty in p and A_2 and B_2 are good measures of p. The observations form a continuous distribution of (S/N), from cases where the signal is buried in the noise (S/N < 1) to cases of bright objects with high polarizations (S/N > 100). A low (S/N) can be caused by low polarization, faint object, poor transparency or many other effects, therefore (S/N) is a good measure of the reliability of an observation. Because of the imperfect nature of the polarimeter and the effects of thin cloud on some of the data, polarimetric data was discarded if either of the following held,

$$(S/N) < 5 \qquad \text{or} \qquad (A_3^2+B_3^2)^{\frac{1}{2}} > (A_1^2+B_1^2)^{\frac{1}{2}} \qquad (3.4)$$

Figure 3.1 shows that $\sim$44% of the observations were considered of too low signal-to-noise to calculate a polarization. This is not surprising because polarimetry of BL Lac objects pushes against the limits of the UKIRT InSb system. It can be seen in Figures 2.17 - 2.19 that the errors increase drastically beyond a certain flux level, and the large number of observations with (S/N) < 5 in Figure 3.1 is just a reflection of this fact. If the measurements of faint objects are photon limited, then a longer integration time should increase (S/N). The longest integration used was $\sim$30 minutes, and it was felt that after that the contribution of errors in guiding could become

important. Therefore the effective magnitude limit for polarimetry had to be accepted. Note that the limiting magnitude for photometry is not nearly so severe. Figure 3.2 illustrates the effect of signal-to-noise; the signal coefficients (A_2, B_2) and noise coefficients (A_1, B_1) are shown for each individual scan and for the coadded totals in an observation. In the lower example, although the scatter in A_1 and B_1 is similar to the top case, the polarization signal is considerably stronger and the signal-to-noise is improved.

An important question is whether poor transparency can mimic high polarization in a faint object. In that case, some observations with large (S/N) would actually represent bad measurements. The worst contamination due to cirrus and the largest dispersion in the night-to-night values of instrumental parameters occurred during Run 4 in August 1980. By the criterion of equation (3.4) only 1 out of 29 observations has a large enough (S/N) for a polarization to be deduced. Undoubtedly, the quiescent state of the BL Lacs observed in August also had something to do with this low acceptance rate. By contrast, in December 1979 when the sky was excellent and several of the BL Lacs highly polarized, the (S/N) ratios were much higher. Therefore, (S/N) is a good reliability figure and when looking through the individual observations, there was no case when the instrumental parameters were bad but the (S/N) factor indicated a good measurement.

3.2. Results

There are approximately 80 BL Lac objects in the literature, although the number is increasing rapidly and the demarcations between quasars and BL Lac objects are being broken down. The objects in this sample are all confirmed BL Lacs in the sense that they have two or more of the defining properties of the class: non-thermal continuum, infrared excess, rapid or large amplitude variability and a high and variable degree of optical polarization. The objects were chosen where possible to have stellar images and large redshifts,

with the aim of setting up a data-base for a subset of the most extreme sources. The known BL Lac objects are a very heterogenous sample, so no attempt at completeness was possible. A practical consideration that dominated the selection was that the sources had to be bright enough in the near-infrared for polarimetry. The sample is listed in Table 3.1.

Nearly all of the sample have published optical polarizations, but only four (0735+178, 0754+101, 0851+202, and 1641+399) have published infrared polarimetry (Table 3.2). This work doubles the number of BL Lac objects whose infrared polarization has been monitored. Apart from expanding the sample, this work investigates the wavelength dependence of polarization between the J, H and K bands and probes the variability of these sources from timescales of 1 day to several months. Of the 13 BL Lacs studied polarimetrically, 9 were observed in more than one waveband and 10 were monitored on more than one night. The reduced data with appropriate errors are given in Table 3.3 and Table 3.4 Table 3.3 lists all the polarimetric measurements, including the photometry derived from the same measurement. Table 3.4 lists the flux measurements for all the sources; including the observations in Table 3.3 but with extra photometric observations in cases where (S/N) < 5 but the photometry was still reliable. Several features are obvious in the data as a whole. First, the tendency for BL Lac objects to have high and variable linear polarization on all timescales is confirmed. 9 out of the 13 BL Lacs with polarimetry have values >10%, ranging up to $\sim$35% for AO 0235+164. The changes in degree of polarization are often quite rapid; in 4 cases changes of $\sim$5% were seen between successive nights. Wavelength dependence of polarization is seen in 2 of the sources, with the degree increasing towards shorter wavelengths. This was not previously thought to be a common characteristic of BL Lac objects. Several examples of position angle rotation with time and wavelength were observed. One of the most interesting features of the data is the relationship between polarization and flux; this will be discussed in more detail later in the chapter. Results for the individual objects are now discussed.

3.3 Details of the Observations

3.3.1 0235 + 164

The Arecibo Occultation source 0235+164 is one of the most spectacular examples of a high luminosity BL Lac object, known to be both an optical and radio variable (Spinrad & Smith, 1975). The emission lines are very weak, but two absorption line redshifts have been detected at $z = 0.524$ and $z = 0.852$ (Rieke et al., 1976; Burbidge et al., 1976), and 21cm absorption has been detected in the lower redshift system (Roberts et al., 1976). Recent observations indicate that the 21cm absorption is variable (Wolfe, 1980). The source underwent a 5 magnitude outburst in 1975, and rose to the same flux level in 1979 (Pica et al., 1980a). On both occasions there was evidence for correlated radio/optical activity (Ledden et al., 1976; Balonek & Dent, 1980). Large and variable optical polarization has been observed in AO 0235+164, with a range of 5-26% (Rieke et al., 1976; Angel & Stockman, 1980). In 1975, the radio polarization position angle showed an extraordinary linear rotation of 130° during a sequence of otherwise stochastic variations (Ledden & Aller, 1979). The rotation occurred at two radio frequencies, and the lack of any differential rotation rules out Faraday rotation as causing the effect. No infrared polarimetry of this object has been published.

Figure 3.3a shows that AO 0235+164 has large and variable polarization at 2.2μm. In December, the object underwent a polarization burst during which the 2.2μm polarization rose from 17.5% to 28.7% and fell by a factor of two in 24 hours. At its peak the H (1.65μm) polarization was 34.6%, the largest infrared polarization yet observed in a BL Lac object. Over five nights, there is evidence for a position angle rotation of $\sim 30^{\circ}$ and the rotation is present in all three wavebands. The infrared flux during the December burst was 2×10^{48} ergs s^{-1}, which is one of the highest luminosities observed in any extragalactic object. Simultaneous optical polarimetry during this period was obtained by S. Tapia at Steward Observatory and the results from 0.4μm to 2.2μm are contained

in the paper ('A Polarization Burst in the BL Lac AO 0235+164' by C.D. Impey, P.W.J.L. Brand and S. Tapia - paper submitted to M.N.R.A.S.). One significant result concerning the calibration is the continuity of flux, degree of polarization and position angle between observations at different Observatories using different instruments. By July 1980, the 2.2μm flux had fallen by more than a factor of two from its peak in December and the polarization was at ∿17%. One month later, the polarization was still quiescent at ∿15%, but the flux had risen up to December levels. Throughout the observations, the position angle spanned a range of ∿80°. The data show wavelength dependence of polarization with the degree of polarization increasing towards shorter wavelengths, a trend verified by the optical data. The relevance of these observations to conventional synchrotron explanations for these sources is discussed in Chapter Four.

3.3.2 0306 + 103

0306+103 was found to be an optical variable with a featureless spectrum by Leacock et al. (1976). Subsequently it has been shown to have an archival variability of $\Delta m_B > 5.0$ magnitudes, making it one of the most variable BL Lac candidates known (Miller, 1977). The single infrared measurement shows it to have no detectable polarization, but polarization in BL Lac objects is often episodic, so repeated measurements are needed. Given the general correlation between variability and polarization (Stein et al., 1976), it would be surprising if no degree of polarization was detected in this source.

3.3.3 0735 + 178

This object was shown to have an absorption redshift of z= 0.424 and high and variable optical polarization by Carswell et al. (1974). The polarization varied between 10-31% on a timescale of less than a week, with position angle ranging between 0° and 60°. Other optical polarimetry is presented by Angel et al. (1978), Nordsieck (1976) and Puschell and Stein (1980) and the monitoring of Angel et al. shows moderate stability around p ∿ 22% compared with

the wild fluctuations of previous data. The only infrared measurement was by Rieke et al. (1977) who obtained p(2.2μm) = 18.5% @ 164°. The data in Figure 3.3b show that 0735+178 was remarkably stable in polarization and position angle during December, though there were significant changes in flux. Such a high level of quiescent polarization is considered unusual behaviour in a BL Lac object. In April 1980, however, the polarization was higher and varied by ∿5% between successive nights. 0735+178 also shows infrared polarization which increases towards shorter wavelengths, and this effect is discussed in terms of Nordsieck's (1976) synchrotron model for BL Lac objects in Chapter Four.

3.3.4 0754 + 101

Optical polarimetry for this source shows a range of 3-26%, including a change from 25% to 12% on successive nights (Tapia et al., 1977; Craine et al., 1978). The rapid, variable polarization was confirmed by Angel et al. (1978), who observed a change from 5% to 10% in only 4 hours. This is the most rapid change to be reliably observed in any BL Lac objects and sets stringent limits on the source emitting volume. Large and variable (4-14%) infrared polarization has also been published for OI090.4 (Puschell & Stein, 1980; Rieke et al., 1977), including evidence for a position angle rotation between the visible and the infrared. This was the first such rotation to be discovered, and clearly OI090.4 is an unusual and important object. The infrared data presented here shows a smooth increase over four nights from 2.3% to 8.8%. Apart from the first point which is noisy, the position angle is steady. However, as the polarization increases, the total flux decreases by ∿30%. There are two night observations at H (1.65μm) and the effect is repeated there. The changes may indicate dilution between a polarized and an unpolarized component in the source. The relationship between polarization and flux changes in BL Lac objects is important, and will be discussed later in Chapter Three. There is no indication of strong wavelength dependent polarization in this source.

3.3.5 0851 + 202

OJ287 is one of the most rapidly variable BL Lac objects known. With a tentative emission line redshift of z = 0.306 (Miller et al., 1978b), this source has shown evidence of large amplitude ($\Delta B > 4.0$mag) and rapid ($\Delta t < 1$ hour) variability at radio, infrared and optical wavelengths. There have been four large outbursts with timescales of several months (Visvanathan & Elliot, 1973), and observations of variability of a few tenths of a magnitude per day (Veron & Veron, 1975). An unconfirmed observation cites large amplitude ($\Delta m \sim 0.5$) infrared variability on a timescale of minutes (Wolstencroft et al., 1980), but there are quiescent periods when the flux density is steady (Kiplinger, 1974). Many observers have made polarimetric measurements of OJ287. The radio polarization at 8GHz has been up to ~15%, the highest observed in the integrated radio radiation of an extragalactic object (Aller & Ledden, 1978). The optical polarization has varied between 1% and 29% (Hagen-Thorn, 1972; Kikuchi et al., 1976; Kinman et al., 1974; Kinman, 1976, 1978; Strittmatter et al., 1972; Nordsieck, 1972; Williams et al., 1972). The monitoring of Angel et al., (1978) shows smooth variations from night to night with occasional abrupt changes in position angle. The position angle is generally stable at $\sim 80^{\circ}$, but during an outburst in 1971-2 it varied wildly (Visvanathan, 1974). Before 1973, OJ287 showed no signs of correlated radio, infrared and optical emission (Rieke & Kinman, 1974; Epstein et al., 1972), but the nature of the radio source changed in 1973-4 and since then there is good evidence for correlated radio/optical radiation (Ledden et al., 1976; Pomphrey et al., 1976). The only infrared measurements are by Rudnick et al. (1978) and Puschell and Stein (1980) who obtained values at 2.2μm of 17% and 11% respectively, both with errors of ~5%.

OJ287 was monitored for 5 nights in December in the J, H and K bands. The polarimetry shows a smooth increase at 2.2μm from ~5% to ~10%. The flux is depressed on the 4th night but shows no large changes. For the first four nights the mean position angle agrees well ($90-95^{\circ}$) with previous measurements, but on the fifth night there is a rotation of $\sim 25^{\circ}$ similar to the sudden changes seen by Angel et

al. (1978). The rotation occurs with similar sense and amplitude in all three wavebands. This is the largest position angle rotation between nights to be confirmed in more than one waveband. Four months later, the infrared flux changed by ∿50% between successive nights with no appreciable change in the degree of polarization. Both p and θ were near the December levels. OJ287 is characterized by sudden changes superimposed on smoothly varying flux and polarization (Fig. 3.3c).

3.3.6 0912 + 297

This source was identified by Wills and Wills (1976), and was found to have a range of polarization from 0-13% by Kinman (1976). The maximum radio polarization of 14.7% is one of the highest seen in any BL Lac object (Wardle, 1978). When observed in April the object was too faint (K ∿ 12.7) for a reliable measure of polarization; but from signal-to-noise considerations it is clear that the object was not in a phase of high (p > 5%) infrared polarization.

3.3.7 1147 + 245

1147+245 was also first identified by Wills and Wills (1976) and has no published redshift. Polarimetry by Kinman (1976), Serkowski and Tapia (1975) and Angel et al. (1978) shows it to have a range of 1.5-13% with wide variations in position angle. Two measurements in April give a polarization of 10-15% at a position angle ∿110°. Over a three night period, the 2.2μm flux increased by 15%.

3.3.8 1308 + 326

The Bologna radio source B21308+326 has absorption line redshifts at z = 0.996 and z = 0.879 (Miller et al., 1978) and is a compact, flat spectrum radio source with strong bursts of radio and optical emission. At its brightest, 1308+326 was one of the most optically luminous objects in the universe (Liller, 1976). Puschell et al. (1979) report optical polarimetry with variations on a timescale of ∿15 minutes. They also present two observations at 2.2μm of 19 ± 8% and 18 ± 5%, but in the latter case this is a four day

average. Moore et al. (1980) also give polarimetry obtained during the outburst in the spring of 1978, but do not find variation from hour to hour. They find the optical and infrared polarizations to be correlated; the optical points range from 0-25% and the three infrared points go from <4% to 17%.

Observations in December confirm the rapid variability found by other investigators. The 2.2μm polarization fell by 12% in two nights, then rose again by 6% in the next 24 hours. During the first change the flux fell by 40% but during the subsequent polarization rise the flux was nearly constant. Highly variable polarization is typical behaviour for this object. By April the 2.2μm flux had fallen by nearly two magnitudes from its December peak and the source had dipped below the polarization detection limit of the instrument. However, in July there was another rapid optical flare (Wisneiwski et al., 1980) with a peak near July 4th and changes of $\Delta B \sim 0.9^m$ in 24 hours. On July 10th, the flux in the infrared was ~6mJy and the polarization was ~8%. The position angle had rotated by fully 90° since the December measures. This is obviously an extremely interesting object to monitor on all timescales (Fig. 3.3d).

3.3.9 1400 + 162

1400+162 is one of only two BL Lac objects known to have classic double lobe radio structure (the other is 3C390.3). There is a weak emission line redshift of z = 0.245 and the properties have been discussed by Baldwin et al. (1977). Optical polarimetry in the same paper shows a polarization of 10-14% at 80-100°, which is about 15° away from the position angle of the double lobe structure. In April, 1980 the source was too faint for infrared polarimetry, having a K magnitude of ~14.1 which is 0.6 magnitudes fainter than the flux given in the Baldwin paper.

3.3.10 1418 + 546

OQ530 was confirmed as a BL Lac object by Craine et al. (1978) who found high polarization in a photographic survey, and subsequently obtained photoelectric measures in the range 5-19%. Puschell and

Stein (1980) measured weaker optical polarization of 2-8%. Miller (1978) found that the object, a flat spectrum Ohio radio source, has an archival variability of $\Delta B \sim 4.8^{m}$ on photographic plates with variability on timescales from days to years. In April, the polarizations at K and H were both found to be ∿9%, with no evidence for wavelength dependence. Three months later the source was 20% fainter and the H polarization was undetectable, with an upper limit of ∿1%.

3.3.11 1514 - 241

AP Librae is a BL Lac object located in the centre of an elliptical galaxy (Disney et al., 1974), having an emission line redshift of z = 0.049 (Miller et al., 1978). The range in optical polarization is 2-7%, and the position angle in the collected measurements is stable at $\theta \sim 6 \pm 16^{\circ}$ (Angel et al., 1978; Strittmatter et al., 1972; Kinman, 1976). Capps and Knacke (1978) found 2.2μm polarization in the range 3-6%, but with a position angle $\sim 90^{\circ}$ different from the optical measurements. In April, K and H polarizations of ∿7% were measured, at a position angle ($\sim 175^{\circ}$) which confirms the long-term stability found in the optical data. These observations were obtained with a 15" aperture, and varying amounts of dilution from the surrounding galaxy caused by guiding errors may have lead to systematic errors in the polarization.

3.3.12 1641 + 399

3C 345 is a violently variable, strong-lined source with an emission redshift of z = 0.595 (Burbidge et al., 1977). VLBI measurements show it to be expanding superluminally at a rate of ∿5c, and it is a good candidate for relativistic beaming (Kellerman, 1978). Kinman (1977) has studied eight years of polarization data for this object, and finds that there is a preferred position angle (80°-110°) when the source is bright. This is roughly aligned to the VLBI expansion axis ($\sim 105^{\circ}$), and there may be a "memory" in the emission process. The range of optical polarization is 2-16%

(references in Kinman, 1977; Stockman & Angel, 1978; Moore & Stockman, 1980). Knacke et al. (1979) have made optical and infrared measurements of 3C 345, and the 2.2μm polarization was very large and variable with an increase from 22% to 32% in one night. On the latter occasion the optical limit was $p < 6\%$, and strong wavelength dependence of polarization increasing into the infrared is unique among BL Lac objects.

The single observation presented here is a K polarization $\sim$13% confirming the existence of high IR polarization in this object. The position angle of $\sim 100^{\circ}$ is well aligned with the superluminal expansion axis.

3.3.13 1652 + 398

Mk501 is an extended object, and Ulrich et al. (1975) have published a redshift of $z = 0.034$ based on emission lines in the galaxy component. Optical polarizations are low (2-4%), and the wavelength dependence of optical polarization has been used to separate the galaxy and non-thermal components of this source (Maza et al., 1978; Puschell & Stein, 1979; Ulrich et al., 1975; Angel et al., 1978). Although the source is bright in the infrared, the polarization is too low to be detected above the level of instrumental polarization. Over a 3 day period, however, the infrared flux rose by $\sim$35% at J, H and K which represents a considerable brightening of the non-thermal component.

3.3.14 1727 + 503

The compact galaxy I Zw 186 is another object with a galaxian component and a compact non-thermal core. Oke (1978) has derived an emission line redshift for the surrounding galaxy of $z = 0.055$. Kinman (1976) found the optical polarization to be low (4-6%), while the radio (3.7cm) polarization is surprisingly high for an extended BL Lac object, at 11.3% (Wardle, 1978). The source was too faint for polarimetry, and the photometry over three observing sessions shows moderate ($\sim$25%) variability of the compact component.

3.3.15 1921 - 293

The radio source OV-236 was found to be a variable in a 90GHz survey of sources with flat spectra between 5GHz and 90GHz (Landau et al., 1980). Dent and Balonek (1980) have followed the source during a radio outburst in 1979, and the high frequency flux rose more rapidly than the delayed and self-absorbed lower frequency radiation. By mid-1978, OV-236 was the strongest quasar in the sky at 30GHz. There is evidence for correlated radio/optical activity during the period 1977-9 (Gilmore, 1980a). In April, this object was confirmed as a BL Lac object by a 2.2μm polarization measurement of ∿14 ± 4%. Subsequent to this measurement, the 2.2μm flux decreased by ∿35%, so the source displays another BL Lac-type property of infrared variability. There is no published redshift for this source.

3.3.16 2155 - 304

H2155-304 is a HEAO 1 X-ray source, with an optical identification that has a very tentative redshift of z = 0.17 (Schwartz et al., 1979; Charles et al., 1979). It is a rapidly variable object with 6 hour variations of a factor of 2 in the 0.5-20keV flux (Snyder et al., 1980). Simultaneous X-ray observations did not support the claim for a 1 second flare (Agrawal & Reigler, 1979). Optical variability and optical polarization of ∿5% has been established by Griffiths et al. (1980), and the identification as a BL Lac object seems very likely. In July, the infrared polarization was observed on three nights and found in all cases to be <3%, at a position angle of 120-130° (Fig. 3.3e). The infrared flux was observed on six occasions, but there were no examples of large or abrupt changes between nights or over a baseline of one month. The source has a J-K colour of ∿1, which is less than usual for a violently variable quasar or BL Lac object.

3.3.17 2223 - 052

3C446 has strong emission lines and a redshift of z = 1.404 (Burbidge et al., 1977). Optical variability was observed by Visvanathan (1973) and Miller (1978) noted that at maximum light the

spectrum had much weaker lines characteristic of a BL Lac object. Optical polarization of 4-17% has been monitored by Kinman et al. (1966), Visvanathan (1973), Miller and French (1978) and Moore and Angel (1980). Stockman and Angel (1980) noticed a position angle rotation of $\sim 10^{\circ}$ in a few hours. The polarization position angle in 3C446 takes a wide range of values, 10°-160°. In December, 3C466 was found to be highly polarized at 2.2μm, $p \sim 16\%$ and a position angle of $\sim 137^{\circ}$. In July, measurements were made at K and H, and the polarization was down to ~10%, with a large swing in position angle. There was no substantial flux change between December and July. 3C466 had a very strong infrared excess, with a K-H colour of $\sim 0.9^{m}$. This source is evidently a transitional case between quasars and BL Lac objects.

3.4 Properties of the Sample

Of the 17 BL Lac objects in the sample, 11 have published redshifts. The original definition of BL Lacs as having featureless spectra has been relaxed since high resolution, good signal-to-noise spectra have shown the presence of weak emission lines in many objects. Some of the redshifts must still be regarded as tentative. There are also several objects with absorption-line redshifts and no detectable emission lines. As shown in Table 3.2, three objects are demonstrably within elliptical galaxies at low ($z < 0.05$) redshift, and the others are highly luminous and at large redshift. The maximum values of radio, optical and infrared polarization are not easily related since the highest polarizations come from the most frequently observed objects. However, in general the high frequency polarizations are considerably higher than the radio polarizations. Almost all the objects have maximum values >10% in the optical and infrared. The infrared properties of the sample can be summarized as follows.

3.4.1 Flux and Polarization Variability

Even with the modest data-base presented here, the diversity of behaviour in BL Lac objects is apparent. Of the 5 objects with a timescale coverage of days and months (0235+164, 0851+202, 0735+178, 1308+326, 2223-052), the most luminous objects show the greatest variability. 0235+164 has a 2.2μm polarization range of 15-29%, and the flux varies by more than a factor of two. 1308+326 has a range of 8-20%, with the 2.2μm flux varying by nearly a factor of six. The most rapid changes also occur in these two sources. The 2.2μm polarization of 0235+164 varied by ∿12% between successive nights, and in 1308+326 a similar change in polarization occurred over 48 hours. On one occasion, the 2.2μm flux of OJ287 increased by 50% between nights. The instrumental sensitivity did not allow reliable tests for variations on a timescale of hours.

In contrast to these erratic fluctuations and flares, 0735+178 had stable polarization and position angle over five consecutive nights, and over a similar period OJ287 and 0754+101 had polarizations which smoothly and monotonically increased. There appear to be two types of behaviour in BL Lacs: periods of quiescent flux and polarization and periods of wildly fluctuating Stokes parameters. Often both type of behaviour are present in the same object; all the monitoring programmes in the past have noted active and quiet phases. The data is not extensive enough to say whether the active polarization periods correspond to epochs of high flux, and quite frequently during a low phase the object drops below the detection limit. The amplitude of changes between nights is generally as large as the changes which take place over longer periods between runs; there is no preferred variability timescale.

Figure 3.7 shows the distribution of inter-night changes in polarization and position angle for all the observation in all three wavebands. About 80% of the points refer to 2.2μm measurements. The distribution of errors in p and θ is also illustrated. Most changes in polarization on a timescale of 24 hours are <6% and the distribution falls off at higher levels than this. There is a tail

of large rapid changes of >10% and this is dominated by the extreme example of AO 0235+164. The mean error is 2-3% and apart from the individual cases, there is strong statistical evidence for widespread inter-night changes in BL Lac objects. Unfortunately, the limited sensitivity of the detector system did not allow the investigation of timescales ∿1 hour. The position angle changes also show a distribution weighted well beyond the mean error (2^{o}-4^{o}), with rotations of $>12^{o}$ not being unusual. It should again be emphasized that these plots are weighted in the wings by a few well-studied and extreme objects.

A more visually appealing way of presenting the polarization changes is a Q-U diagram, where the normalized Stokes parameters Q/I and U/I form the y and x axes. The degree of linear polarization is measured by the length of the vector from the data point to the origin, and the position angle is measured by the angle the vector makes with the Q axis (Figs. 3.8 and 3.9). In Figure 3.8 the observations of AO 0235+164 at 2.2μm are plotted in the Q-U plane. Although there are relatively few data points, several interesting features of the variability emerge, which are not obvious from the tabulated data. First, the observations cover three observing runs, and the baseline of polarization is always ∿16% even though the position angle varies widely. The December 1979 flare rises and falls to about the same level of polarization and the position angle has systematically rotated. Even more interestingly, it appears that the polarization changes take place along lines of constant position angle and the position angle rotations take place along lines of constant polarization. To follow this up, the other three objects with monitoring runs in December 1979 are shown in Figure 3.9. The trajectories for these three BL Lac objects agree qualitatively with the data for 0235+164. Both 0735+178 and 0851+202 follow lines of roughly constant polarization, while 0754+101 flares along a line of nearly constant position angle. With such a paucity of continuous monitoring data, it is not possible to do more than note the possible significance of these trajectories. However, if paths of constant polarization and position angle do dominate the

variations of BL Lac objects there will be important implications for the magnetic field geometry of the emitting regions.

3.4.2 Position Angle Rotations

For most of the objects, the position angle behaviour is very erratic; there are small but significant changes between successive nights, and changes of much larger amplitude on a timescale of months. There is not usually a preferred position angle. Ironically, the object with the most stable position angle also shows the largest rotation. For 4 nights the 2.2μm position angle of OJ287 was $94^{\circ} \pm 4^{\circ}$; on the fifth night it rotated to $\sim 62^{\circ}$. A single observation might not be compelling, but a similar rotation can be seen at J and H, and none of the other position angles measured on that night are peculiar. A more gradual rotation is seen in the December 1979 data for AO 0235+164; this time an amplitude of $\sim 30^{\circ}$ over five nights. Once again, the trend is supported by the J and H measures. There is further rotation between later observations and the sense of rotation is the same as the large systematic rotation at radio frequencies found by Ledden and Allen (1979). From the variations in F, p and θ it is possible to note three maximum observed rates of change:

$$\left(\frac{dF}{dt}\right)_{MAX} = 0.50 \text{ day}^{-1} , \left(\frac{dp}{dt}\right)_{MAX} = 12\% \text{ day}^{-1}, \left(\frac{d\theta}{dt}\right)_{MAX} = 30^{\circ} \text{ day}^{-1} \quad (3.5)$$

3.4.3 Wavelength-Dependent Polarization

Only two of the BL Lac objects show any sign of wavelength-dependent polarization, 0235+164 and 0735+178 (Fig. 3.4). The effect is not at a 3σ level in either case, but it is systematic with wavelength and persists during the night-to-night polarization variations. In the case of AO 0235+164, the shape of the $p(\lambda)$ vs. λ curve is constant during the large changes in degree of polarization that occurred during the December burst. The polarization increases with decreasing wavelength in both cases. The slope of the $p(\lambda) - \lambda$ curve is also roughly the same in both cases.

$$\left(\frac{dp}{d\ln\nu}\right)_{0235+164} \simeq 3.0 \ , \quad \left(\frac{dp}{d\ln\nu}\right)_{0735+178} \simeq 2.7 \qquad (3.6)$$

3.4.4 Spectral Flux Distribution

BL Lac objects are characterized by a non-thermal flux distribution rising into the infrared, and approximated by a power law of slope α, where $\alpha = -d\ln F/d\ln\nu$. BL Lac objects are considerably redder than QSOs, which have a mean spectral index of $\sim$1.2 (Neugebauer et al., 1979). The range for BL Lacs is $0.8 < \alpha < 2.2$ (Tapia et al., 1976; O'Dell et al., 1977). Although the wavelength baseline is small, mean spectral indices can be calculated for the sample:

	$\bar{\alpha}_{IR}$		$\bar{\alpha}_{IR}$
0235+164	2.1	1418+546	0.98
0735+164	1.1	1514+241	0.85
0754+101	0.95	1652+398	0.45
0851+202	0.89	1727+503	-0.12
0912+297	1.8	1921-293	1.4
1147+245	1.3	2155-304	0.63
1308+326	1.3	2223-052	1.4

For the objects observed in several colours and several occasions, the α_{JK} parameter can be tabulated night by night,

	Date	α_{JK}		Date	α_{JK}
0235+164	20-12-79	1.51	0851+202	19-12-79	0.95
	22-12-79	1.64		22-12-79	1.22
	10-08-80	1.74		20-04-80	0.90
	11-08-80	1.91		21-04-80	0.98
0735+178	19-12-79	1.14	1652+398	18-04-80	0.48
	22-12-79	1.01		21-04-80	0.17
	20-04-80	0.99			
	21-04-80	0.94	2155-304	09-07-80	0.14
				09-08-80	0.31
				11-08-80	0.24

In 0235+164 and 0735+178 there are systematic changes in α_{JK} with time which are explained in terms of the source energetics and emission mechanism in Chapter Four .

It is recognized that broad band colours over a baseline of 1-2μm are not a perfect tool for defining a continuum slope and hence a power law spectral index. The baseline from J to K is not very long and the filters are broad enough that spectral features passing through the bands will significantly affect the J-K colours. For example it has been known for a long time that the infrared colours of low redshift elliptical galaxies are very susceptible to the strong and complex absorption features of their constituent stars (Frogel et al., 1978). Also it has been demonstrated by Hyland and Schwartz (1977) that the near-infrared colours of quasars are strongly affected by the appearance of redshifted emission lines (especially Hα) through the filters. The case for defining a power law for BL Lac objects rests on the fact that the non-thermal flux swamps the thermal component, and the defining property that BL Lacs have no strong emission lines. BL Lac objects have flux distributions which are generally steeper and closer to power laws than quasars. The continuity of flux between optical and infrared regions is a key result in the assumption of a power law and has been measured for 1652+398 (Ulrich et al., 1975), OJ287 (Kinman et al., 1974), AO 0235+164 (Rieke et al., 1976), 0735+178 (O'Dell et al. 1977a) and others (Strittmatter et al., 1972). Other infrared/optical flux distributions have been published by O'Dell et al., 1977b, Puschell and Stein, 1977 and Tapia et al., 1976. The result is that a power law is a good approximation for the near-infrared spectral flux of BL Lac objects.

3.4.5 Polarization-Flux Relationship

One of the most important clues to the energy-producing mechanism in BL Lac objects is the relationship between total and polarized flux. The distribution of total vs. polarized flux for all the observations is shown in Figure 3.6, where it can be seen that the

graph is not uniformly distributed from high polarizations to the detection limit. This is confirmation of the selection effect against sources of low polarization, since the highly polarized BL Lac objects are most frequently monitored. More than half the observations have p > 10%. In Chapter Four, the polarization-flux relationship will be discussed in terms of models for the polarized emission.

TABLE 3.1 BL Lac Objects

Object	Name	Run No.	R.A. (1950.0)			Dec.			V
0235+164	AO	1,3,4	02^h	35^m	52.6^s	$+16^o$	$24'$	$04''$	14.3-19.5
0306+103	OE 110	1	03	06	21.0	10	17	52	17.5-19.5
0735+178	PKS	1,2	07	35	14.1	17	49	09	16.0-16.5
0754+101	OI 090.4	1	07	54	22.6	10	04	39	14.0-16.5
0851+202	OJ 287	1,2	08	51	57.2	20	17	59	12.7-15.6
0912+297	OK 222	2	09	12	53.5	29	45	56	16.3
1147+245	OM 280	2	11	47	44.0	24	34	35	16.1-17.5
1308-326	B2	1,2,3	13	08	07.6	32	36	41	17.0-19.0
1400+162	OQ 100	2	14	00	20.5	16	14	22	17.0-17.5
1418+546	OQ 530	2,3	14	18	06.2	54	36	57	12.0-15.0
1514-241	AP Lib	2	15	14	45.3	-24	11	22	14.5-16.4
1641+399	3C 345	3	16	41	17.6	39	54	11	15.0-17.0
1652+398	Mk 501	2	16	52	11.7	39	50	26	13.5-14.0
1727+503	I Zw186	2,3,4	17	27	04.3	50	15	31	16.0-16.5
1921-293	OV-236	2,3	19	21	41.4	-29	20	25	15.0-17.5
2155-304	PKS	3,4	21	55	57.9	-30	27	54	14.5
2223-052	3C 446	1,3	22	23	11.1	-05	12	17	16.0-18.4

TABLE 3.2 Properties of BL Lac Objects

Object	Z_{em}/abs*)	α_{OPT}	p^{MAX}_{RAD} (4)	p^{MAX}_{OPT}	$p^{MAX}_{I_R}$	VLBI	Galaxy
0235+164	0.524*,0.852*	4.0	3.8	44	34.6 (1)	0.5×10^{-3}"	-
0306+103	-	-	-	-	2.2	0.5	-
0735+178	0.424*	1.3	4.7	31	29.9	0.9	-
0754+101	-	-	-	26	11.7	0.6	-
0851+202	0.306(?)	1.4	16.6	32	14.3	0.9	-
0912+297	-	1.3	14.7	13	-	0.9	-
1147+245	-	1.9	2.5	13	14.8	0.9	-
1308+226	0.996	1.6	4.0	25	19.6	0.5 (2)	-
1400+162	0.244	1.5	-	14	-	1.4	(3)
1418+546	-	-	-	19	9.7	-	-
1514-241	0.049	2.7	4.4	7	7.4	-	Y
1641+399	0.595	1.1	-	16	12.8	-	-
1652+398	0.034	2.5	-	4	-	1.1	Y
1727+502	0.055	1.9	11.3	6	-	>1.2	Y
1921-293	-	-	-	-	13.9	-	-
2155-304	0.17(?)	1.0	-	7	3.0	-	-
2223-052	1.404	1.8	-	17	16.3	-	-

(1) - Infrared data from this work

(2) - Structure elongated at $\sim10^{o}$ position angle

(3) - Object in a cluster of galaxies at z = 0.24

(4) - Radio measurements made at 3.7cms.

Data from: Miller et al. (1978), Wardle (1978), Angel and Stockman (1978), Weiler and Johnson (1980), Craine (1977).

TABLE 3.3 Polarimetry and Photometry

Object	Run	Date (U.T.)	Wave-band	P ± σ(P)	θ ± σ(θ)	m ± σ(m)
0235+164	1	18-12-79	K	17.5 ± 2.9	137 ± 4.8	11.65 ± 0.02
			H	22.8 ± 1.8	129 ± 2.3	12.86 ± 0.03
		19-12-79	K	18.7 ± 3.1	120 ± 4.8	11.87 ± 0.03
			H	22.3 ± 1.6	114 ± 2.1	12.61 ± 0.03
		20-12-79	K	28.7 ± 3.1	125 ± 3.1	11.71 ± 0.02
			H	34.6 ± 2.9	128 ± 2.4	12.74 ± 0.03
			J	36.2 ± 8.6	137 ± 6.8	14.00 ± 0.06
		21-12-79	K	26.7 ± 3.6	110 ± 3.8	11.81 ± 0.02
		22-12-79	K	14.9 ± 1.9	108 ± 3.0	11.66 ± 0.02
			H	19.4 ± 1.2	109 ± 1.8	12.41 ± 0.03
			J	22.1 ± 2.0	119 ± 2.6	13.65 ± 0.06
0306+103	1	22-12-79	K	2.2 ± 1.9	∿102	12.06 ± 0.02
0735+178	1	18-12-79	K	19.7 ± 1.6	2.6 ± 2.3	11.52 ± 0.02
			H	23.2 ± 1.3	5.7 ± 1.6	12.23 ± 0.03
		19-12-79	K	19.8 ± 2.5	8.6 ± 3.6	11.62 ± 0.03
			H	24.4 ± 2.0	8.5 ± 2.4	12.34 ± 0.03
			J	27.5 ± 5.0	11.3 ± 5.2	13.29 ± 0.06
		20-12-79	K	21.5 ± 2.2	9.7 ± 2.9	11.49 ± 0.02
			H	21.4 ± 2.4	6.4 ± 3.2	12.18 ± 0.03
		21-12-79	K	21.0 ± 1.3	0.7 ± 1.8	11.66 ± 0.02
			H	22.8 ± 1.7	178 ± 2.1	12.56 ± 0.03
		22-12-79	K	19.7 ± 1.8	11.2 ± 2.6	11.50 ± 0.02
			H	23.6 ± 1.5	8.2 ± 1.8	12.20 ± 0.03
			J	22.7 ± 2.0	9.5 ± 2.5	13.09 ± 0.06

TABLE 3.3 (Continued....2)

Object	Run	Date (U.T.)	Wave-band	P ± σ(P)	θ ± σ(θ)	m ± σ(m)
0754+101	1	18-12-79	K	2.3 ± 0.7	49 ± 8.6	10.70 ± 0.02
		19-12-79	K	5.1 ± 0.5	31 ± 2.8	10.69 ± 0.03
			H	5.2 ± 1.3	39 ± 7.2	11.48 ± 0.03
		20-12-79	K	8.0 ± 0.7	36 ± 2.5	10.81 ± 0.02
		21-12-79	K	8.8 ± 2.6	41 ± 8.4	10.98 ± 0.02
			H	11.7 ± 1.2	39 ± 3.0	11.67 ± 0.03
0851+202	1	18-12-79	K	5.6 ± 2.9	89 ± 15	11.02 ± 0.02
			H	10.5 ± 1.6	93 ± 4.4	11.77 ± 0.03
		19-12-79	K	8.4 ± 0.8	98 ± 6.7	10.91 ± 0.02
			H	10.3 ± 1.4	98 ± 3.9	11.73 ± 0.03
			J	10.1 ± 1.1	91 ± 3.1	12.53 ± 0.06
		20-12-79	K	8.9 ± 2.1	98 ± 6.7	10.91 ± 0.02
			H	8.3 ± 1.7	99 ± 5.9	11.74 ± 0.03
		21-12-79	K	9.1 ± 2.5	97 ± 7.8	11.09 ± 0.02
			H	8.8 ± 1.0	85 ± 3.3	11.83 ± 0.03
		22-12-79	K	10.3 ± 2.6	62 ± 7.3	10.93 ± 0.02
			H	8.6 ± 0.8	64 ± 2.6	11.66 ± 0.03
			J	9.7 ± 1.9	60 ± 5.6	12.64 ± 0.06
1308+326	1	19-12-79	K	19.6 ± 1.1	150 ± 1.6	11.8 ± 0.03
		21-12-79	K	7.6 ± 3.7	145 ± 14	12.28 ± 0.02
		22-12-79	K	13.7 ± 4.9	132 ± 10	12.27 ± 0.02
2223-052	1	21-12-79	K	16.3 ± 3.8	137 ± 6.6	12.06 ± 0.02

TABLE 3.3 (Continued....3)

Object	Run	Date (U.T.)	Wave band	P ± σ(P)	θ ± σ(θ)	m ± σ(m)
0735+178	2	20-04-80	K	27.9 ± 2.9	160 ± 3.0	11.56 ± 0.01
			H	29.9 ± 2.5	153 ± 2.4	12.44 ± 0.02
		21-04-80	K	22.5 ± 2.9	149 ± 3.7	11.35 ± 0.02
			H	24.5 ± 3.7	156 ± 4.3	12.05 ± 0.03
			J	27.4 ± 4.2	158 ± 4.4	12.90 ± 0.05
0851+202	2	20-04-80	K	9.2 ± 1.4	82 ± 4.4	11.52 ± 0.01
			H	10.4 ± 1.3	78 ± 3.6	12.35 ± 0.02
			J	11.1 ± 6.7	77 ± 17	13.05 ± 0.05
	2	21-04-80	K	10.5 ± 1.2	79 ± 3.3	11.06 ± 0.02
			H	14.2 ± 5.2	82 ± 10	11.69 ± 0.03
			J	14.3 ± 4.8	71 ± 9.7	12.64 ± 0.05
1147+245	2	18-04-80	K	10.1 ± 3.3	115 ± 9.4	12.30 ± 0.02
		20-04-80	K	14.8 ± 6.3	109 ± 12	12.20 ± 0.01
1418+546	2	20-04-80	K	9.2 ± 3.4	89 ± 18	11.94 ± 0.01
			H	9.7 ± 6.1	76 ± 18	12.61 ± 0.02
1514-241	2	18-04-80	K	7.0 ± 1.4	177 ± 5.7	11.00 ± 0.02
			H	7.4 ± 2.4	175 ± 9.4	11.65 ± 0.02
1921-293	2	20-04-80	K	13.9 ± 4.0	165 ± 8.3	12.57 ± 0.02
0235+164	3	11-07-80	K	17.1 ± 5.0	15 ± 8.4	12.52 ± 0.02
			H	10.0 ± 2.1	16 ± 6.1	13.41 ± 0.08

TABLE 3.3 (Continued....4)

Object	Run	Date (U.T.)	Wave band	P ± σ(P)	θ ± σ(θ)	m ± σ(m)
1308+326	3	10-07-80	K	8.3 ± 0.5	50 ± 1.7	12.46 ± 0.02
			H	7.2 ± 3.2	76 ± 13	13.32 ± 0.08
1418+546	3	10-07-80	K	<0.9	~113	12.15 ± 0.02
1641+399	3	10-07-80	K	12.8 ± 3.9	100 ± 8.9	12.48 ± 0.02
2155-304	3	09-07-80	K	3.0 ± 1.4	124 ± 13	10.64 ± 0.01
			H	1.6 ± 0.4	135 ± 7.2	11.00 ± 0.08
			J	<1.3	~119	11.70 ± 0.02
		10-07-80	K	1.7 ± 1.0	113 ± 17	10.63 ± 0.01
		11-07-80	K	2.9 ± 0.3	130 ± 2.8	10.54 ± 0.02
2223-052	3	09-07-80	K	10.9 ± 2.4	27 ± 6.4	11.95 ± 0.01
		10-07-80	K	8.5 ± 0.8	42 ± 2.8	12.15 ± 0.01
			H	8.4 ± 5.0	41 ± 17	12.97 ± 0.08
		11-07-80	K	11.1 ± 3.8	34 ± 9.7	12.16 ± 0.02
			H	5.5 ± 2.7	29 ± 14	13.09 ± 0.08
0235+164	4	11-08-80	K	15.1 ± 3.4	156 ± 6.4	11.81 ± 0.03

TABLE 3.4 Photometry

Object	Run	Date (U.T.)	Flux (mJ) K	H	J
0235+164	1	18-12-79	14.6 ± 0.3	6.7 ± 0.2	-
		19-12-79	12.2 ± 0.3	8.6 ± 0.3	-
		20-12-79	13.4 ± 0.4	7.6 ± 0.3	4.0 ± 0.2
		21-12-79	13.3 ± 0.2	-	-
		22-12-79	14.3 ± 0.2	10.2 ± 0.4	5.6 ± 0.3
	3	10-07-80	9.2 ± 0.1	-	-
		11-07-80	6.5 ± 0.1	4.0 ± 0.3	-
	4	09-08-80	11.8 ± 0.3	6.3 ± 0.5	-
		10-08-80	12.6 ± 0.4	7.1 ± 0.6	4.6 ± 0.4
		11-08-80	12.6 ± 0.4	6.4 ± 0.4	4.2 ± 0.3
0306+103	1	22-12-80	10.0 ± 0.1	-	-
0735+178	1	18-12-79	16.4 ± 0.2	12.0 ± 0.4	-
		19-12-89	14.9 ± 0.4	11.0 ± 0.4	7.7 ± 0.4
		20-12-79	17.1 ± 0.2	12.5 ± 0.4	-
		21-12-79	13.6 ± 0.2	9.0 ± 0.3	-
		22-12-79	16.7 ± 0.2	12.4 ± 0.4	9.2 ± 0.5
	2	20-04-80	15.7 ± 0.1	10.0 ± 0.2	8.8 ± 0.4
		21-04-80	19.2 ± 0.4	14.2 ± 0.4	11.0 ± 0.3
0754+101	1	18-12-79	34.8 ± 0.6	-	-
		19-12-78	35.1 ± 0.9	24.1 ± 0.9	-
		20-12-79	32.0 ± 0.4	-	-
		21-12-79	25.5 ± 0.5	20.6 ± 0.7	-

TABLE 3.4 (Continued....2)

Object	Run	Date (U.T.)	Flux (mJ) K	H	J
0851+202	1	18-12-79	25.9 ± 0.3	18.5 ± 0.7	-
		19-12-79	27.2 ± 0.7	19.1 ± 0.7	15.5 ± 0.9
		20-12-79	29.2 ± 0.4	19.0 ± 0.7	-
		21-12-79	23.0 ± 0.3	17.8 ± 0.6	-
		22-12-79	28.1 ± 0.4	20.4 ± 0.7	13.8 ± 0.8
	2	20-04-80	16.4 ± 0.2	10.9 ± 0.2	9.6 ± 0.5
		21-04-80	25.0 ± 0.5	19.9 ± 0.6	14.0 ± 0.7
0912+297	2	21-04-80	5.4 ± 0.1	2.9 ± 0.1	-
1147+245	2	18-04-80	8.0 ± 0.1	-	-
		20-04-80	8.8 ± 0.2	6.1 ± 0.1	-
		21-04-80	9.1 ± 0.2	5.7 ± 0.2	-
1308+326	1	19-12-79	11.8 ± 0.3	-	-
		21-12-79	7.7 ± 0.1	-	-
		22-12-79	8.2 ± 0.1	-	-
	2	20-04-80	2.6 ± 0.2	-	-
		21-04-80	2.0 ± 0.2	-	-
	3	10-07-80	6.8 ± 0.1	4.4 ± 0.4	-
1400+162	2	20-04-80	1.5 ± 0.1	-	-
1418+546	2	20-04-80	11.1 ± 0.2	8.6 ± 0.2	6.2 ± 0.3
		21-04-80	12.9 ± 0.2	10.1 ± 0.3	-
	3	10-07-80	9.2 ± 0.2	-	-

TABLE 3.4 (Continued....3)

Object	Run	Date (U.T.)	Flux (mJ) K	H	J
1514-241	2	18-04-80	26.4 ± 0.5	20.6 ± 0.4	15.5 ± 0.7
1641+399	3	10-07-80	6.7 ± 0.2	-	-
1652+398	2	18-04-80	32.6 ± 0.6	29.8 ± 0.6	24.3 ± 1.2
		21-04-80	41.8 ± 0.8	45.5 ± 1.4	37.2 ± 1.8
1727+503	2	20-04-80	4.6 ± 0.3	4.5 ± 0.4	-
		21-04-80	3.7 ± 0.4	-	-
	3	09-07-80	4.2 ± 0.4	-	-
		10-07-80	3.4 ± 0.2	-	-
	4	09-08-80	3.3 ± 0.2	3.8 ± 0.2	-
		10-08-80	3.3 ± 0.2	3.6 ± 0.2	-
1921-293	2	20-04-80	6.2 ± 0.1	3.8 ± 0.1	-
		21-04-80	5.5 ± 0.2	-	-
	3	09-07-80	4.6 ± 0.1	3.9 ± 0.2	-
2155-304	3	09-07-80	36.8 ± 0.3	37.5 ± 3.1	33.3 ± 0.6
		10-07-80	37.1 ± 0.3	-	-
		11-07-80	40.3 ± 0.4	-	-
	4	09-08-80	34.8 ± 1.0	29.0 ± 1.8	28.5 ± 2.2
		10-08-80	37.9 ± 1.1	31.7 ± 2.0	-
		11-08-80	40.0 ± 1.1	28.5 ± 1.8	34.2 ± 2.6

TABLE 3.4 (Continued....4)

Object	Run	Date (U.T.)	Flux (mJ) K	H	J
2223-052	1	21-12-79	9.4 ± 0.2	-	-
	3	09-07-80	11.0 ± 0.2	-	-
		10-07-80	9.2 ± 0.2	6.2 ± 0.5	-
		11-07-80	9.1 ± 0.2	5.5 ± 0.5	-

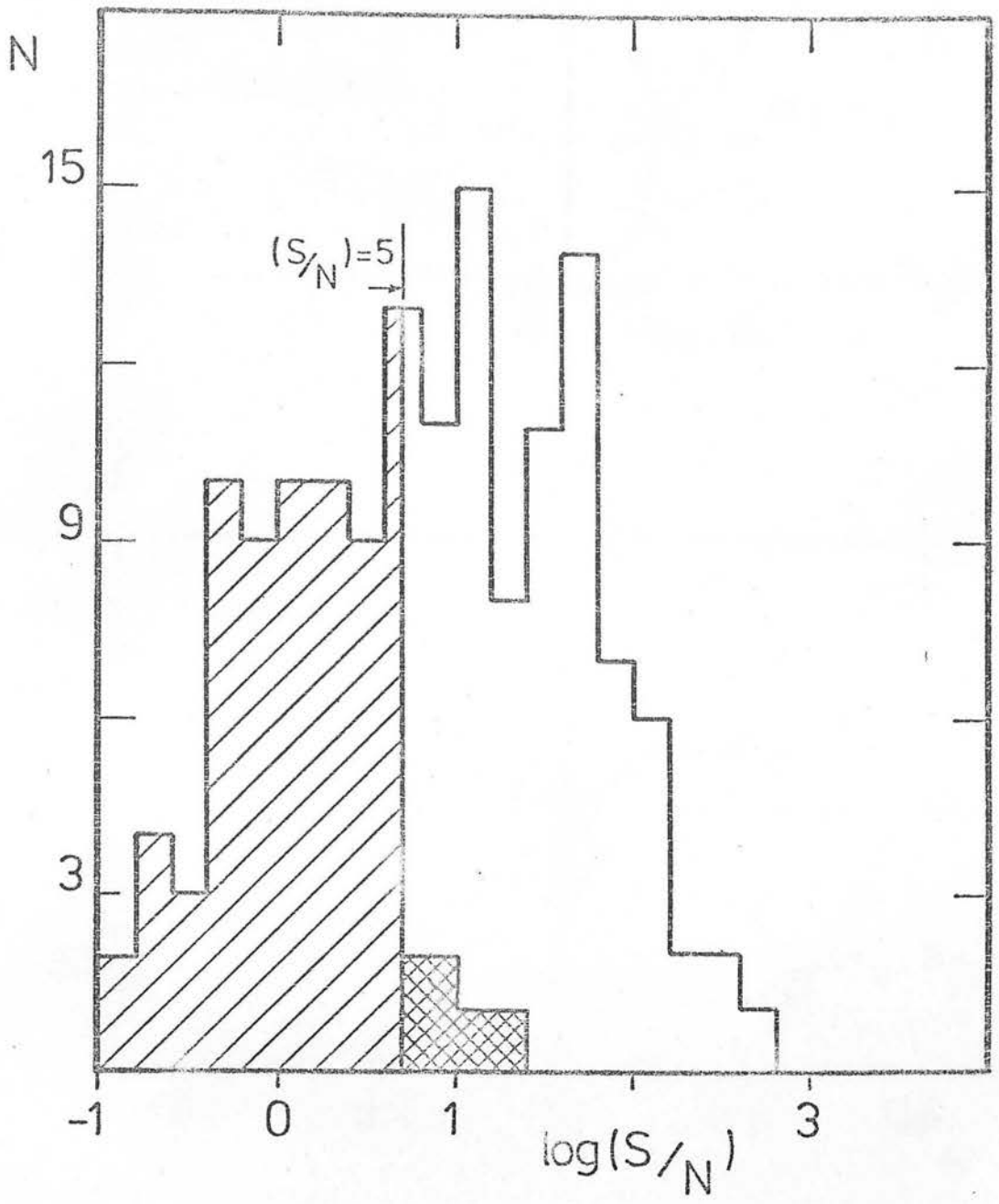

Figure 3.1 Histogram of signal-to-noise for polarization observations. Only those with (S/N)>5 are considered. Crosshatching shows additional observations for which $(A_3^2+B_3^2)^{\frac{1}{2}} > (A_1^2+B_1^2)^{\frac{1}{2}}$.

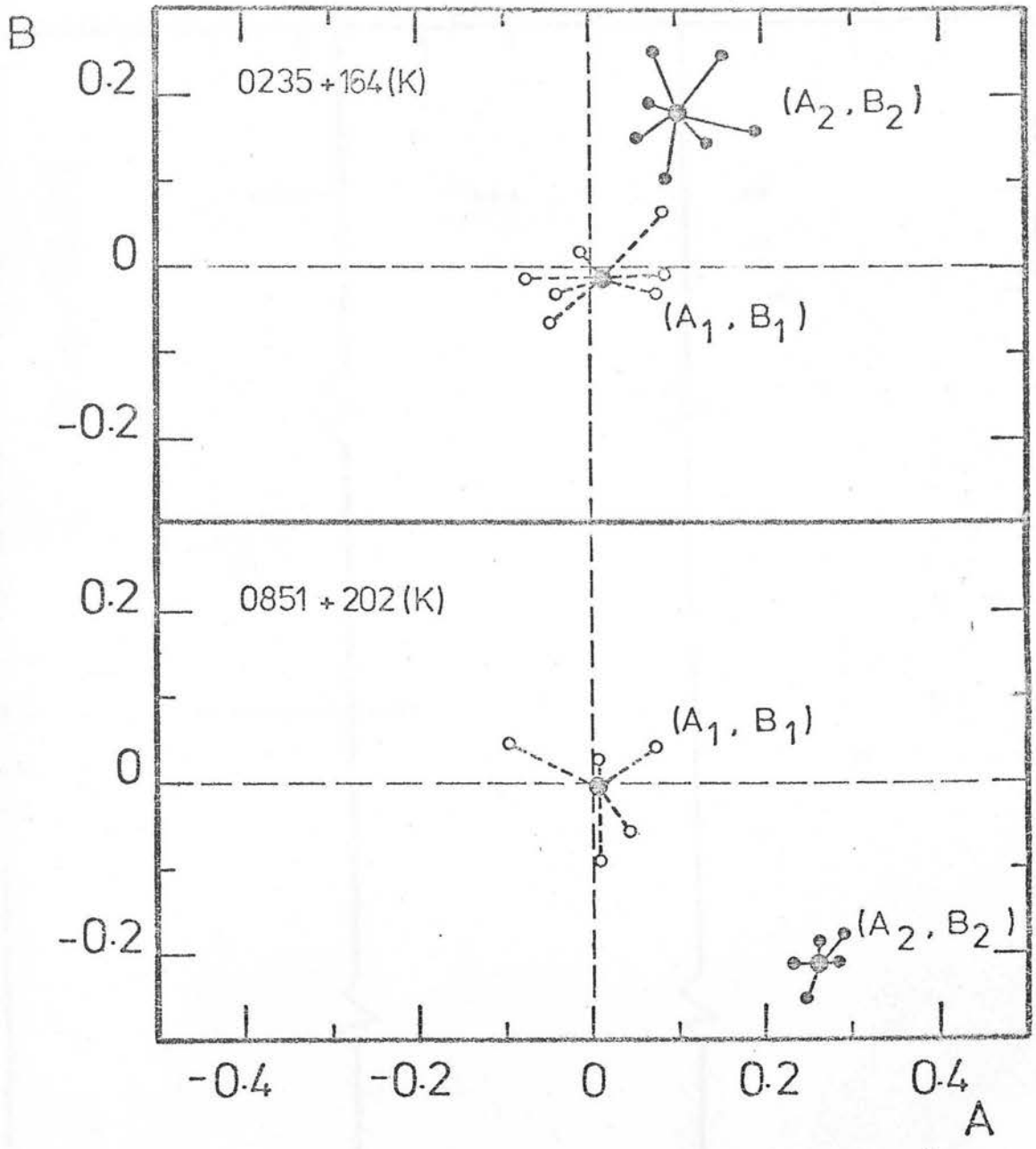

Figure 3.2 Graph showing fitted coefficients A_1, B_1, A_2, B_2 of the individual scans and of the coadded scans. Upper and lower graphs represent moderate and good (S/N) respectively

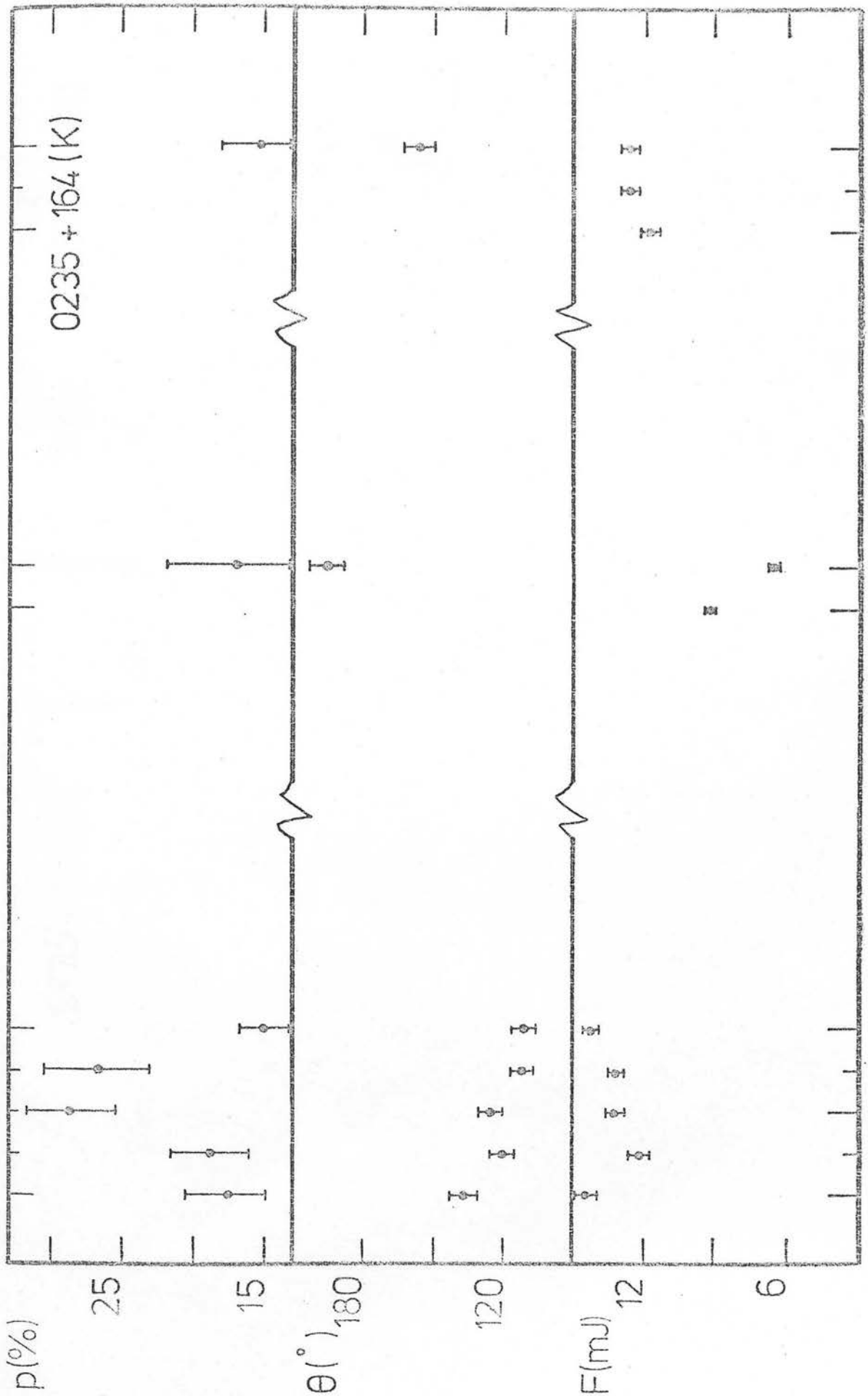
0235 + 164 (K)
p(%)
25
15
θ(°)
180
120
F(mJ)
12
6
18
20
22
Dec '79
10
11
Jul '80
9
11
Aug '80

Figure 3.3a

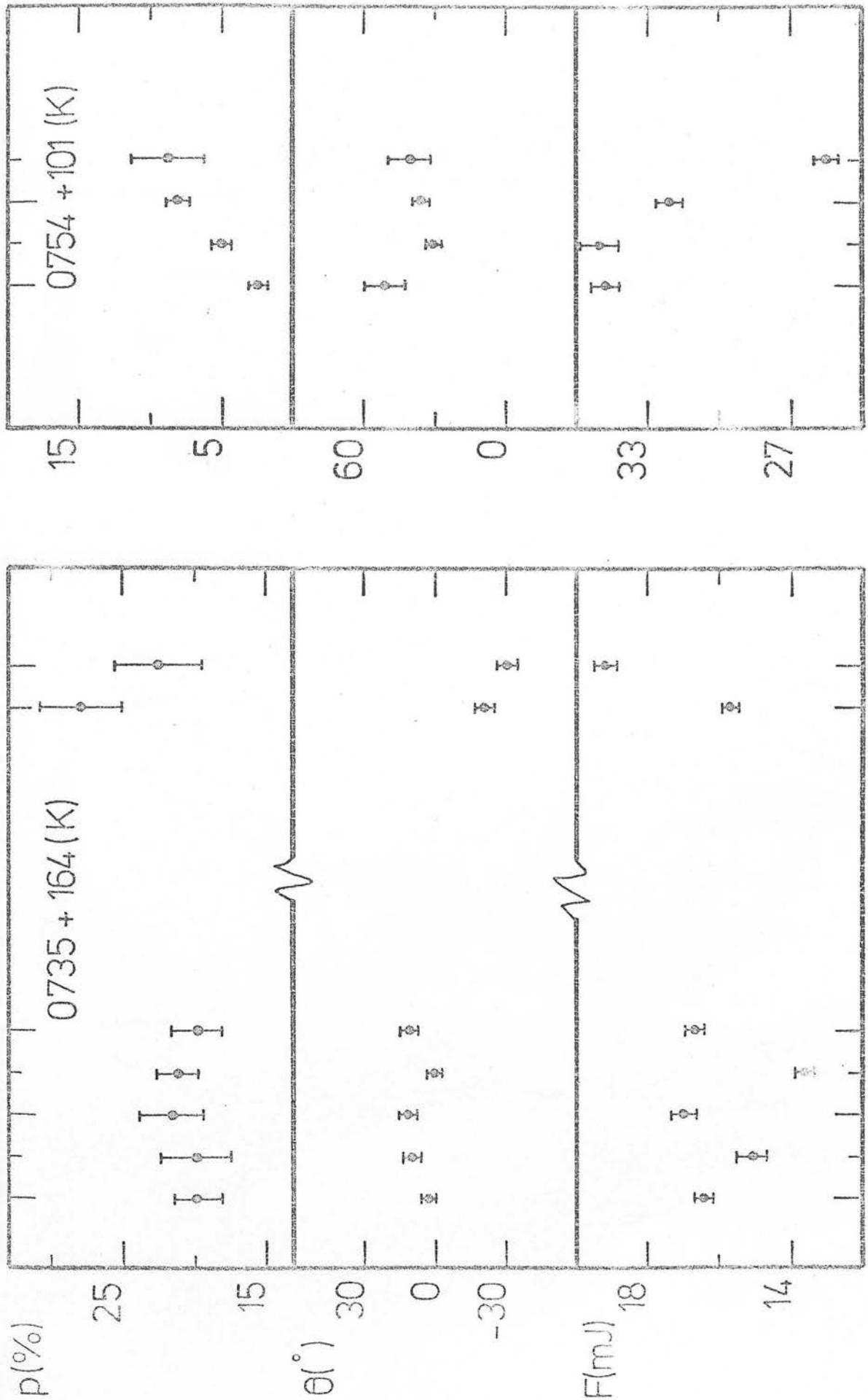
0735 + 164 (K)
0754 + 101 (K)
p(%)
θ(°)
F(mJ)
25
15
30
0
-30
18
14
15
5
60
0
33
27
18
20
22
Dec'79
20
21
Apr'80
18
20
Apr'80

Figure 3.3b

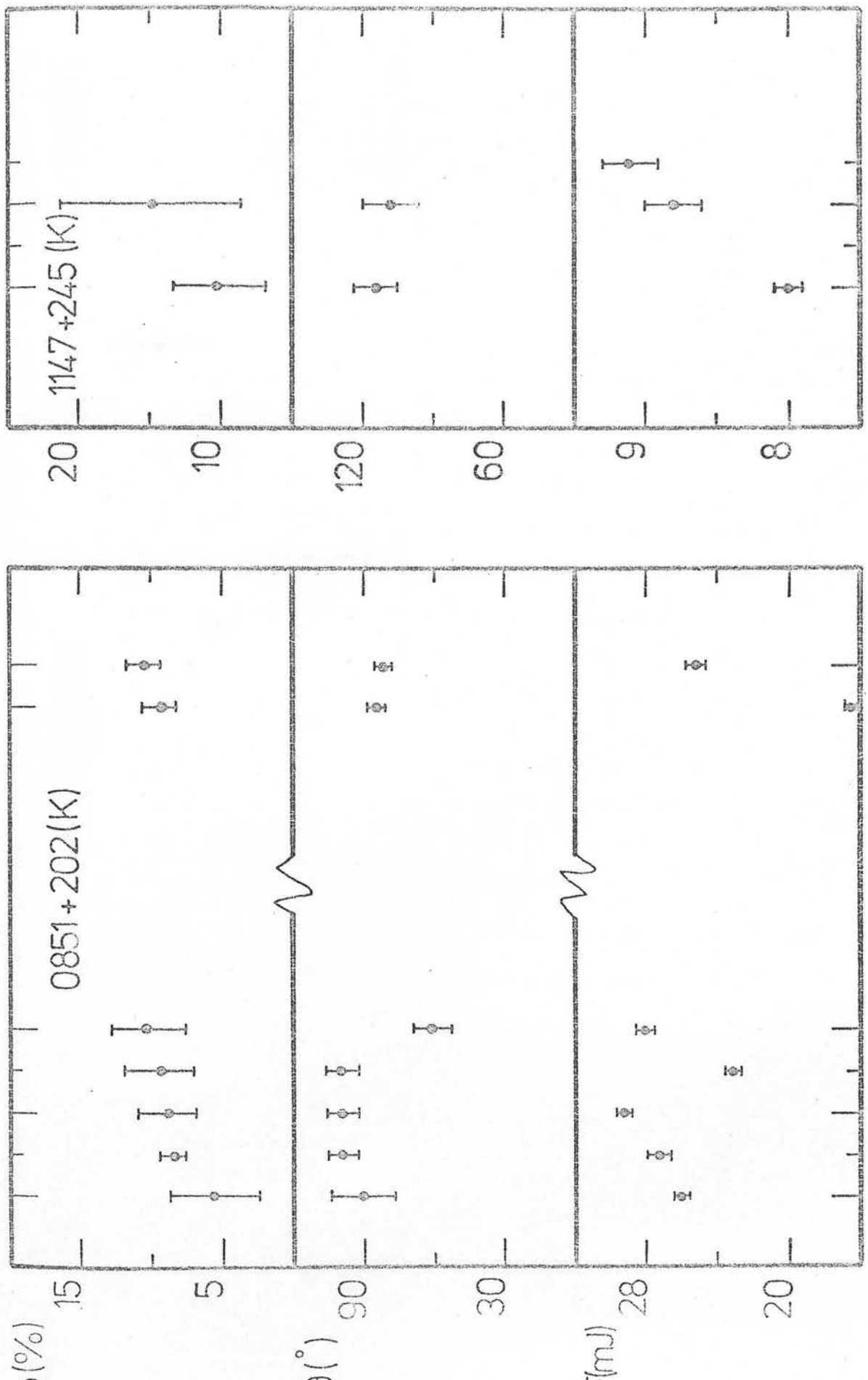

Figure 3.3c

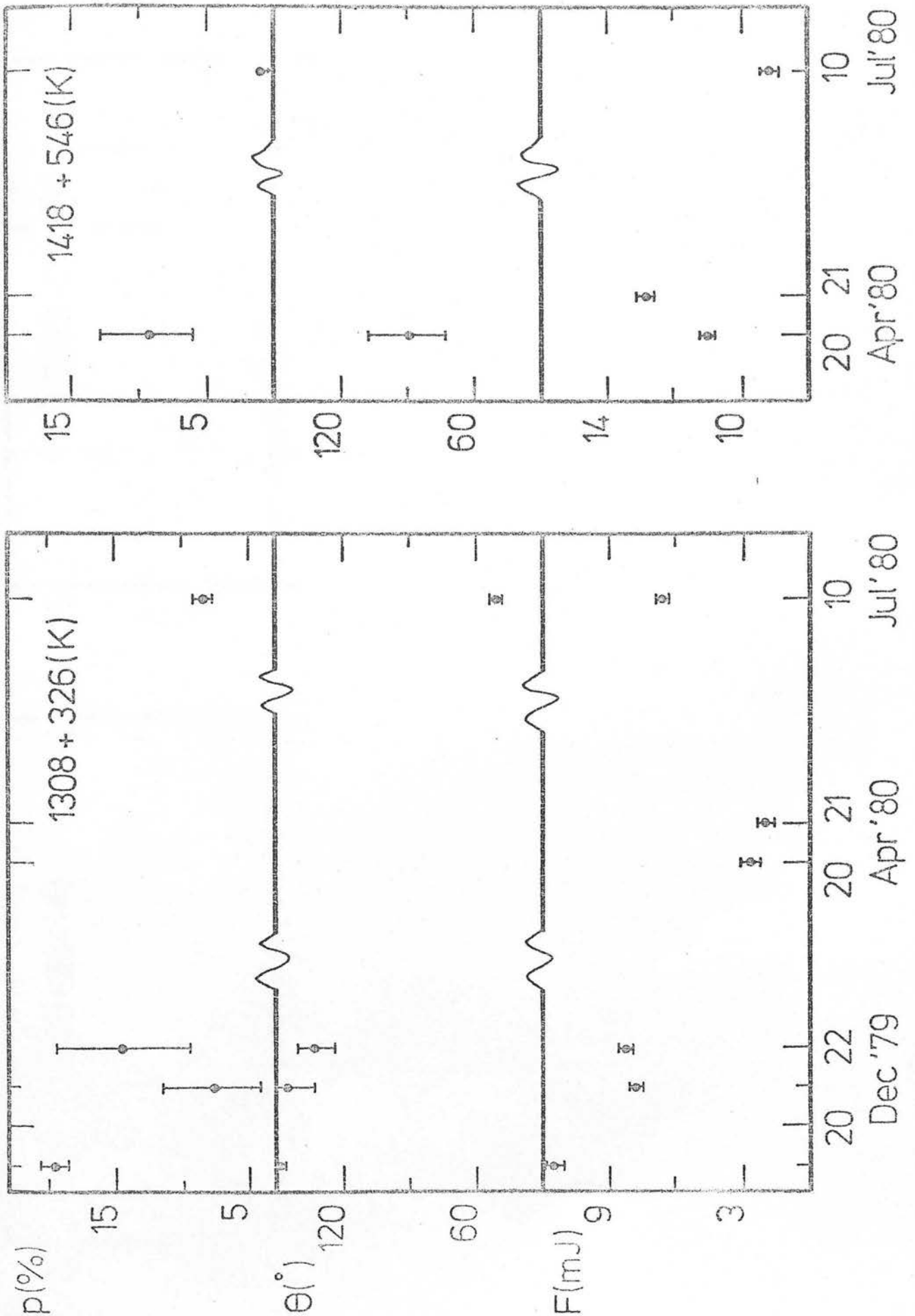
1308+326(K)
1418+546(K)
p(%)
θ(°)
F(mJ)
15
5
120
60
9
3
14
10
20
22
Dec '79
20
21
Apr '80
10
Jul '80

Figure 3.3d

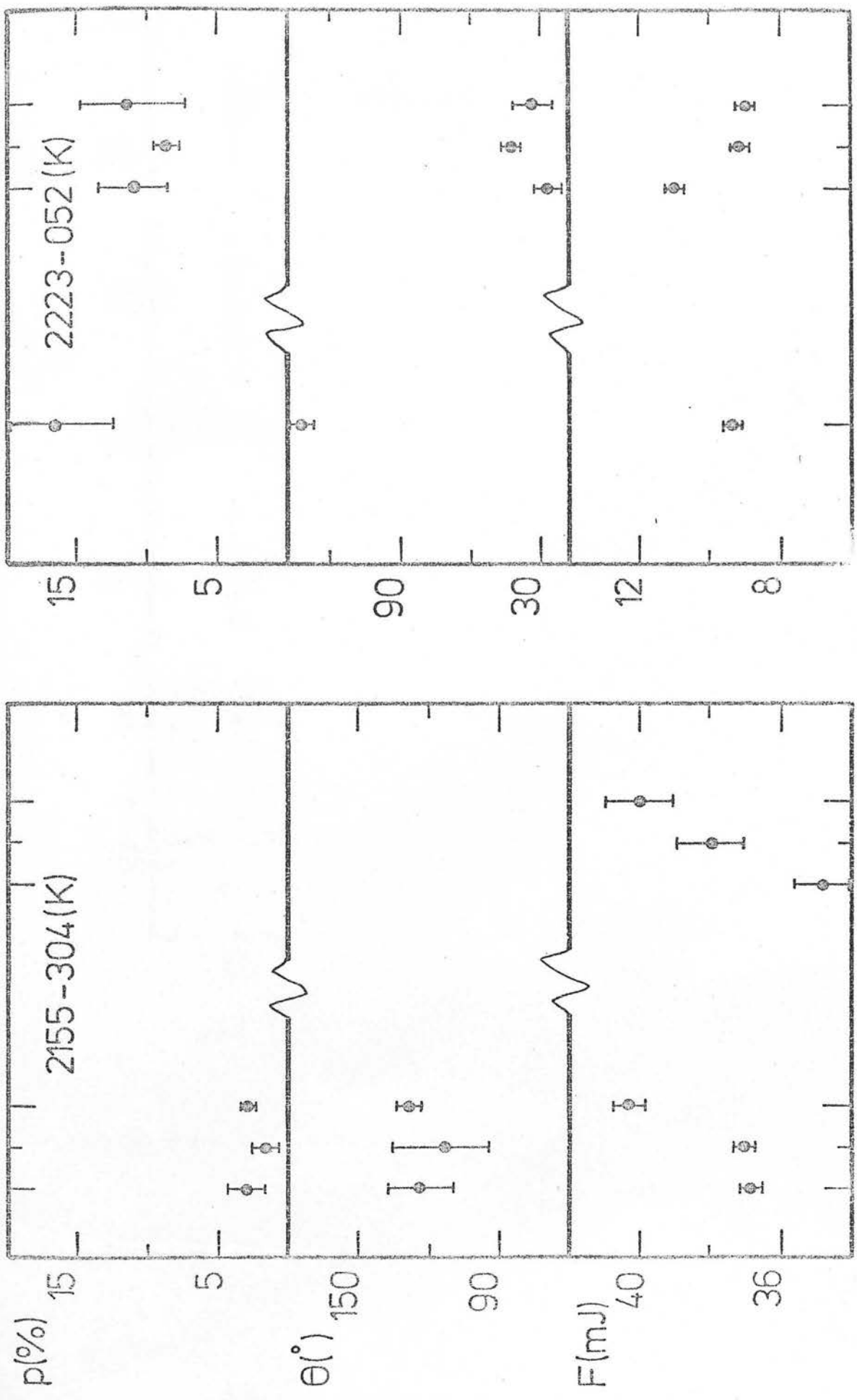
2155-304(K)
2223-052(K)
p(%)
θ(°)
F(mJ)
15
5
150
90
40
36
30
12
8
9
11
21
Jul'80
Aug'80
Dec'79
Jul'80

Figure 3.3e

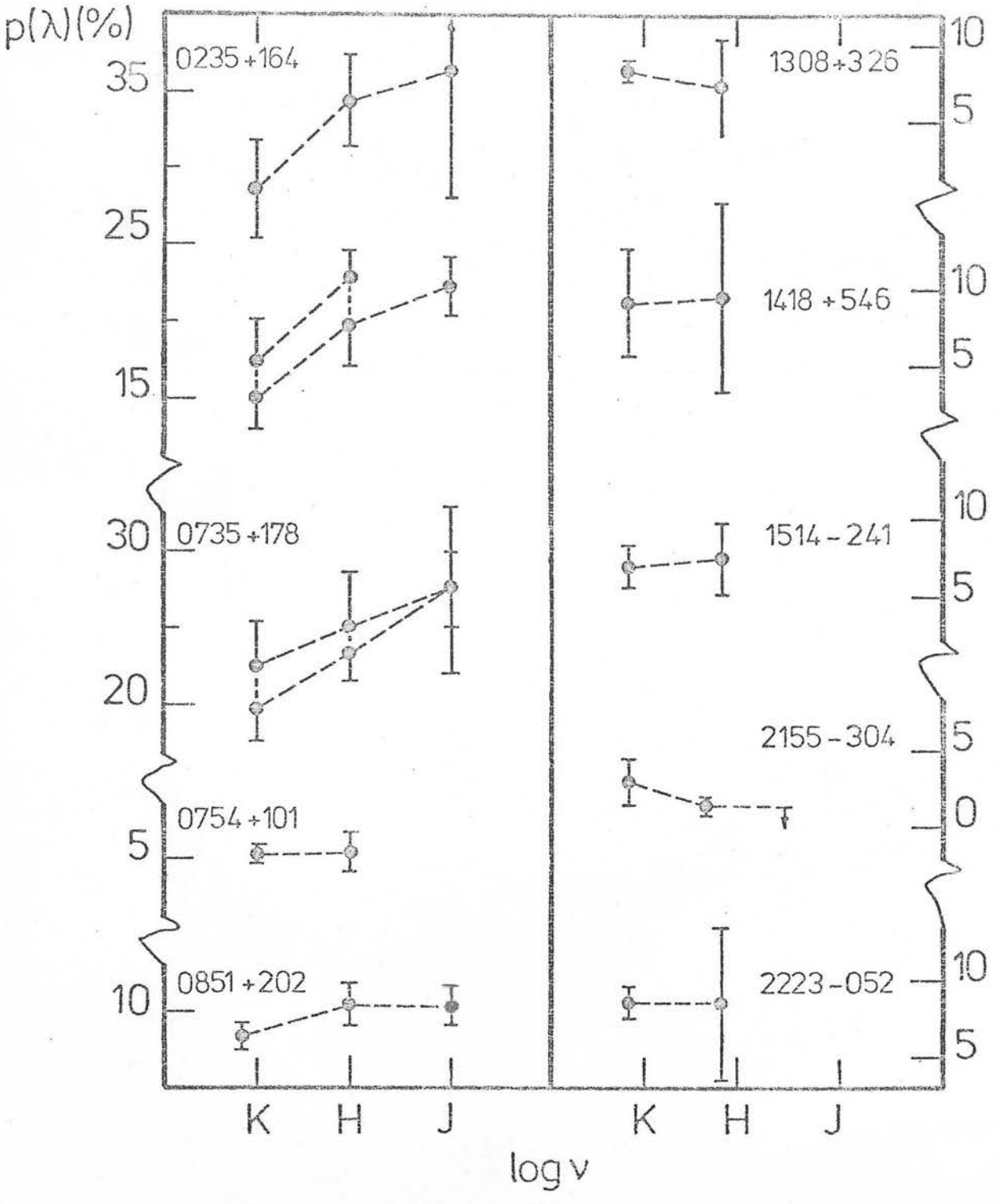

Figure 3.4 Wavelength dependence of polarization for 9 BL Lac objects.

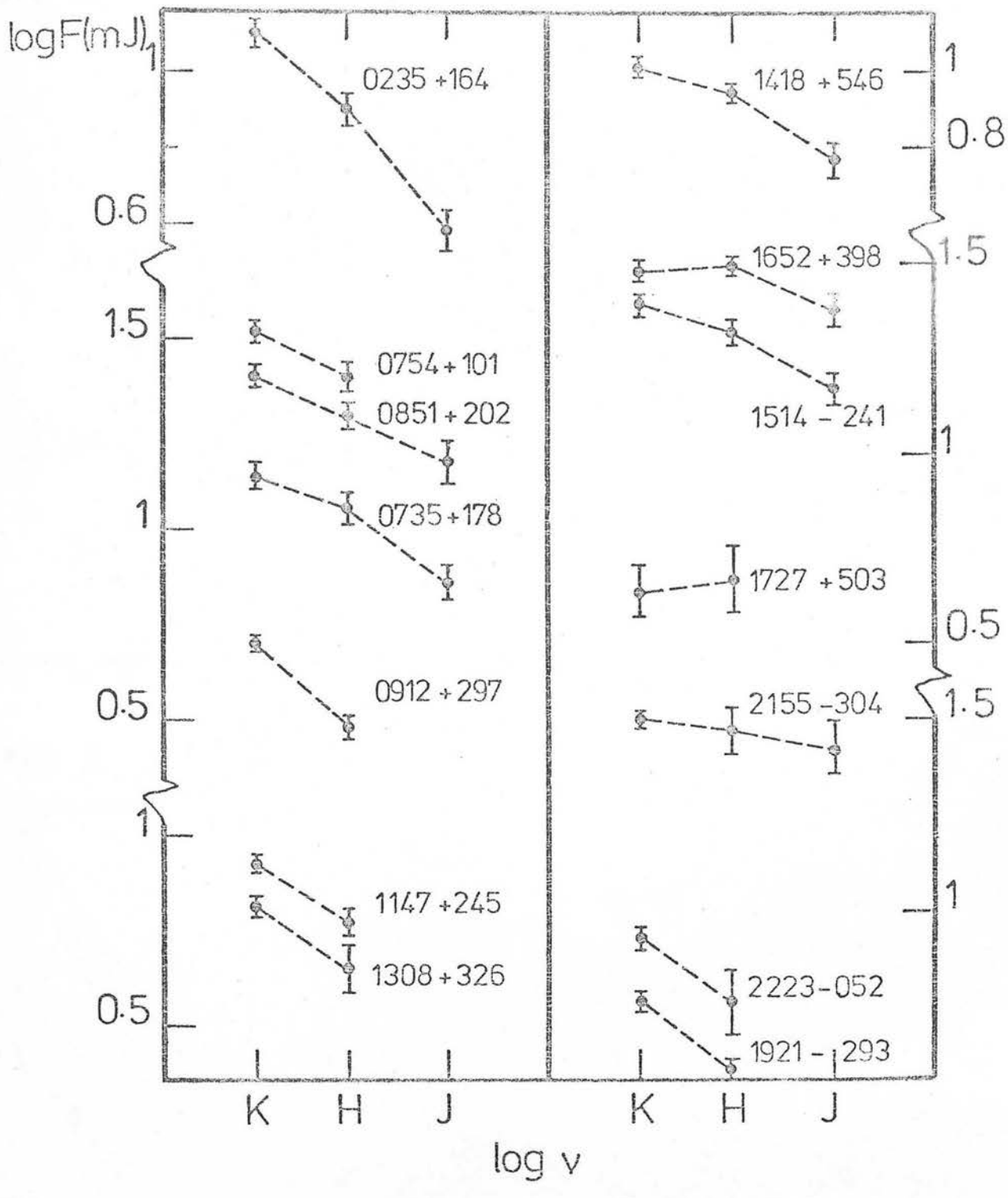

Figure 3.5 Spectral flux distribution from 1-2μm for 14 BL Lac objects.

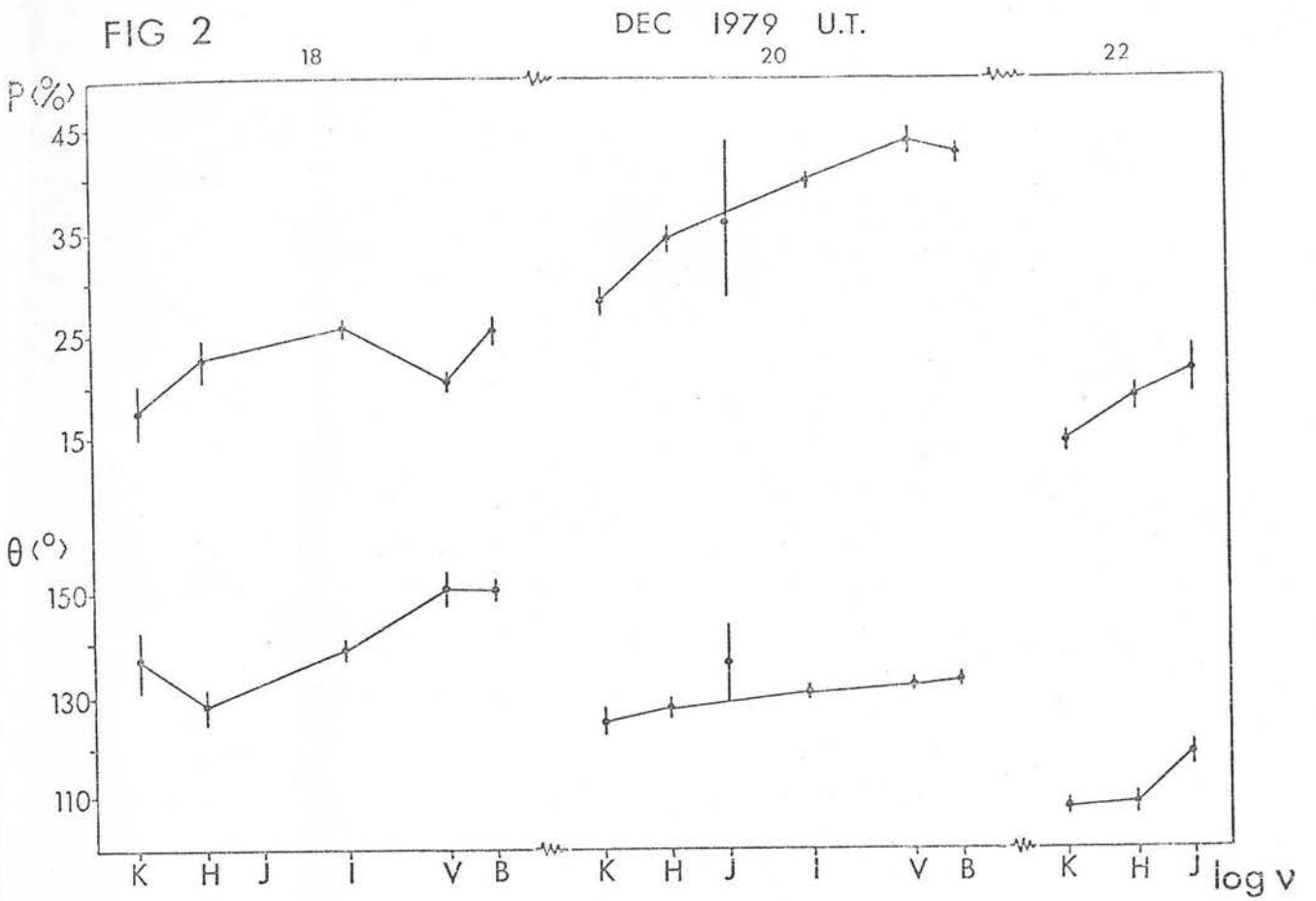

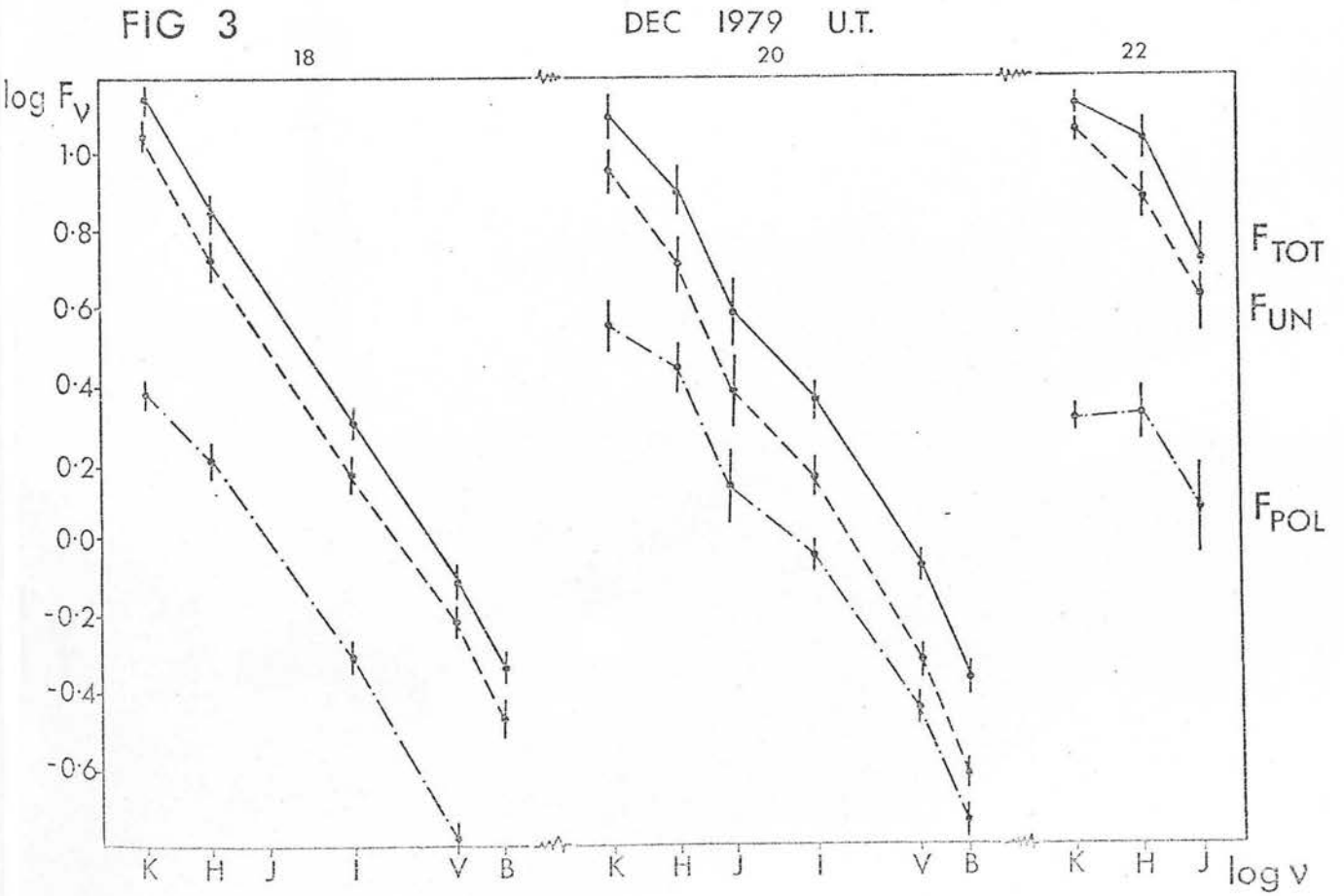

Figure 3.5b Data on AO 0235+164, taken from paper by Impey, Brand & Tapia

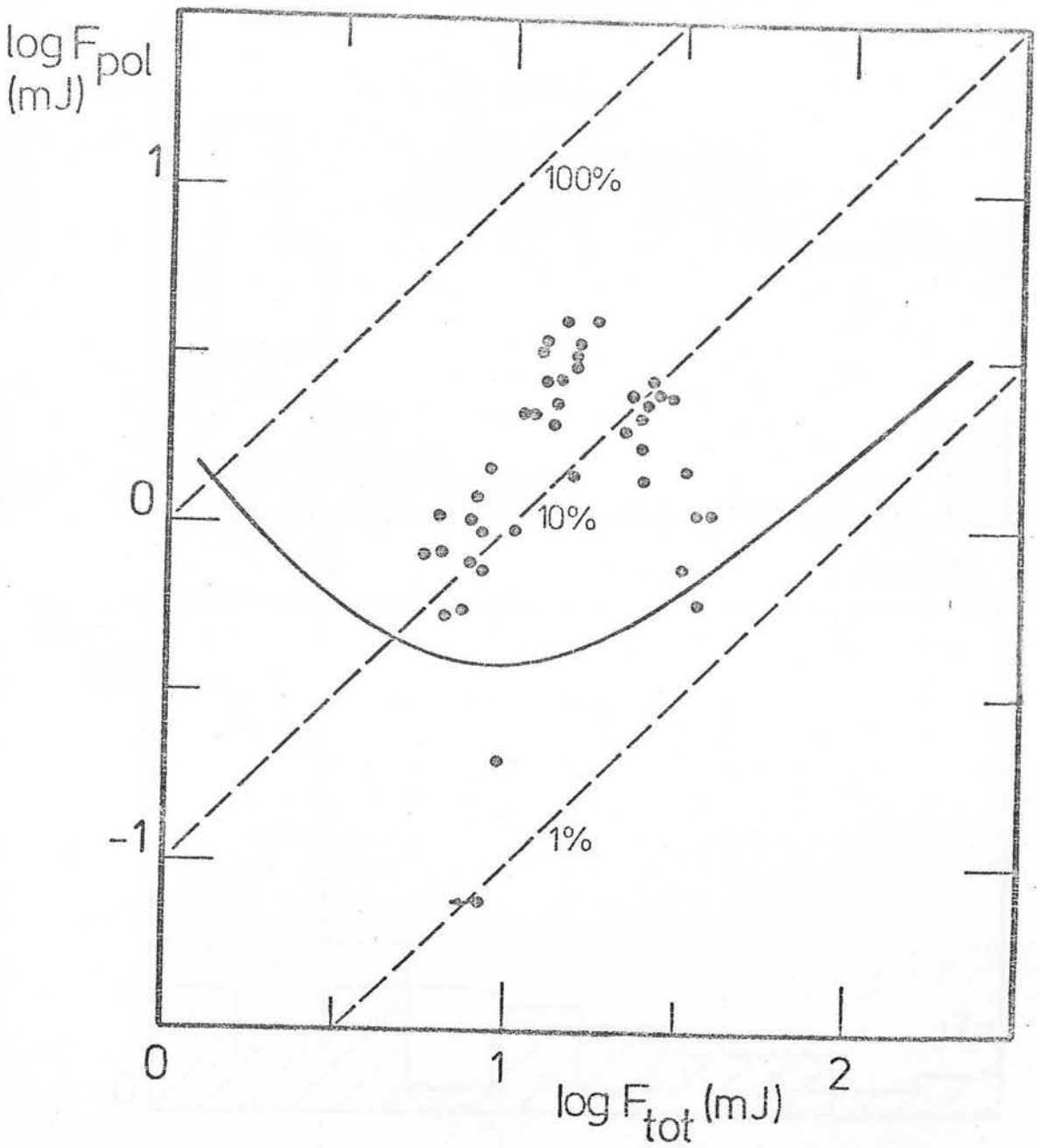

Figure 3.6 Polarized flux plotted against total flux for 40 observations in the K band. The solid line represents the detection limit as a function of magnitude and polarization of the source.

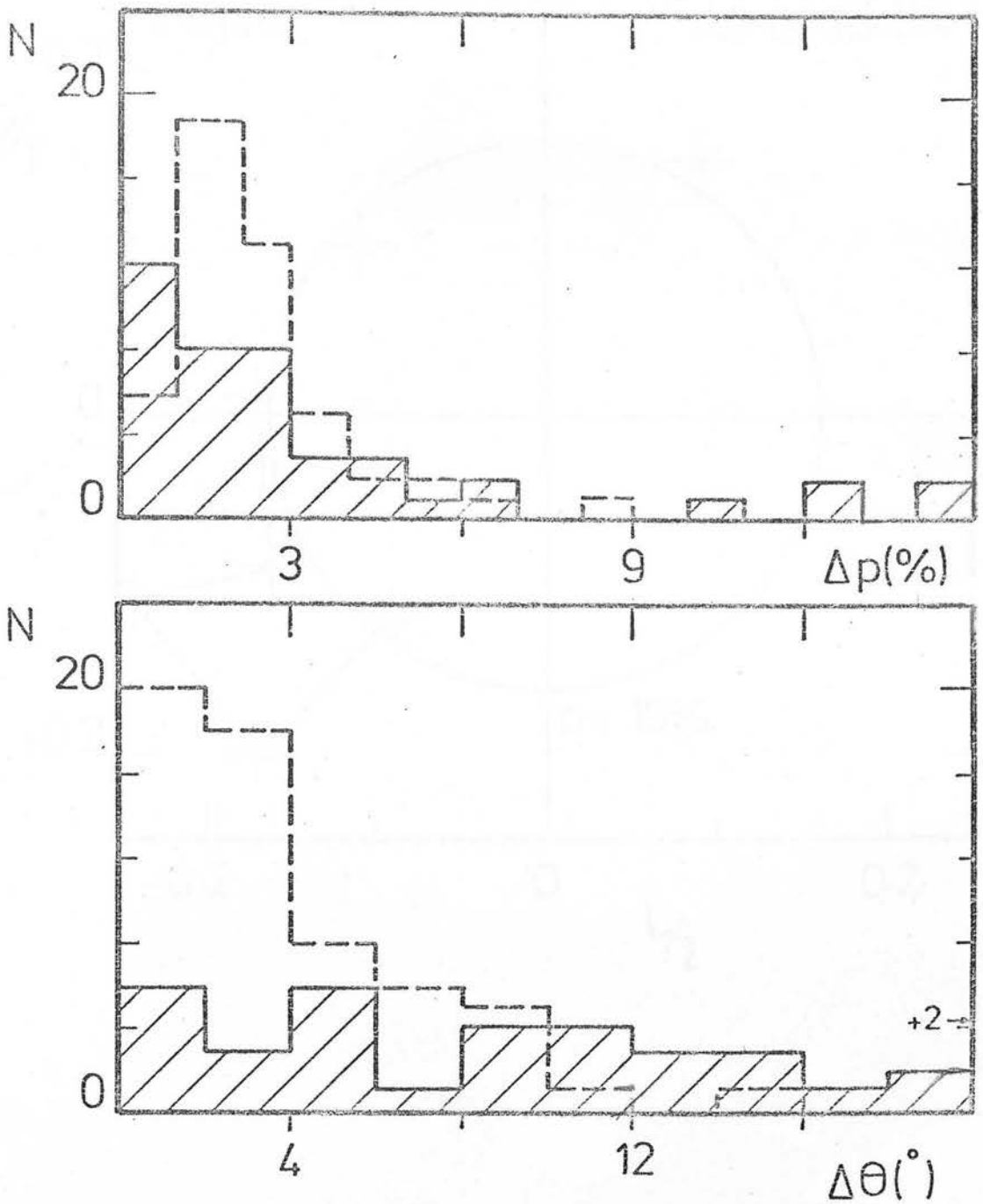

Figure 3.7 Inter-night changes in the degree of polarization and position angle for all observations. Crosshatched area represents measured differences; dashed area represents distribution of errors on individual measurements.

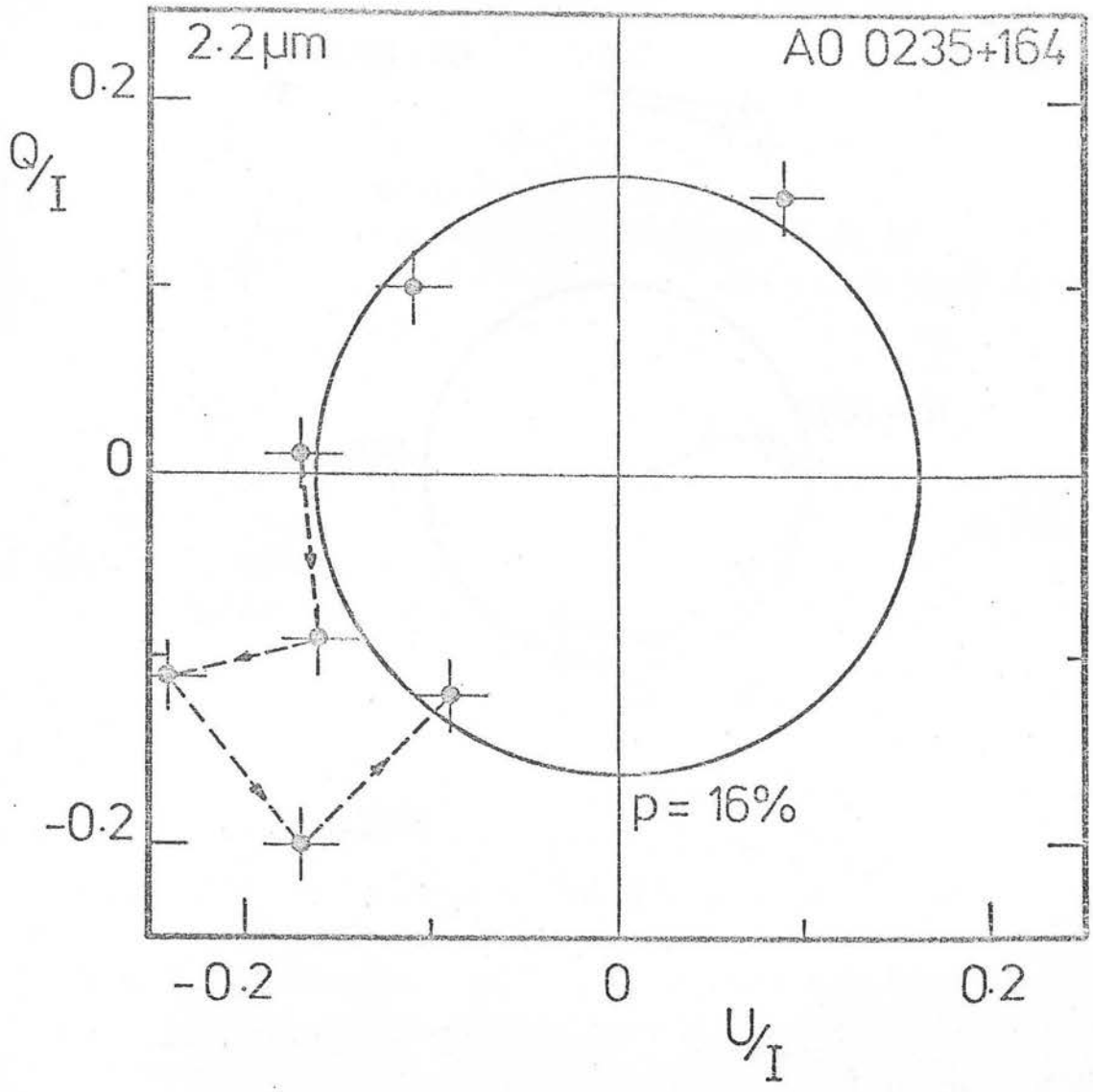

Figure 3.8 Normalized Stokes parameters for AO 0235+164. Error bars for Q/I and U/I are approximated by $\sigma(p)/\sqrt{2}$. Trajectories of constant polarization are circles in the Q-U plane; trajectories of constant position angle are radii in the Q-U plane. The dashed line shows the burst in polarization over five consecutive nights in December, 1979.

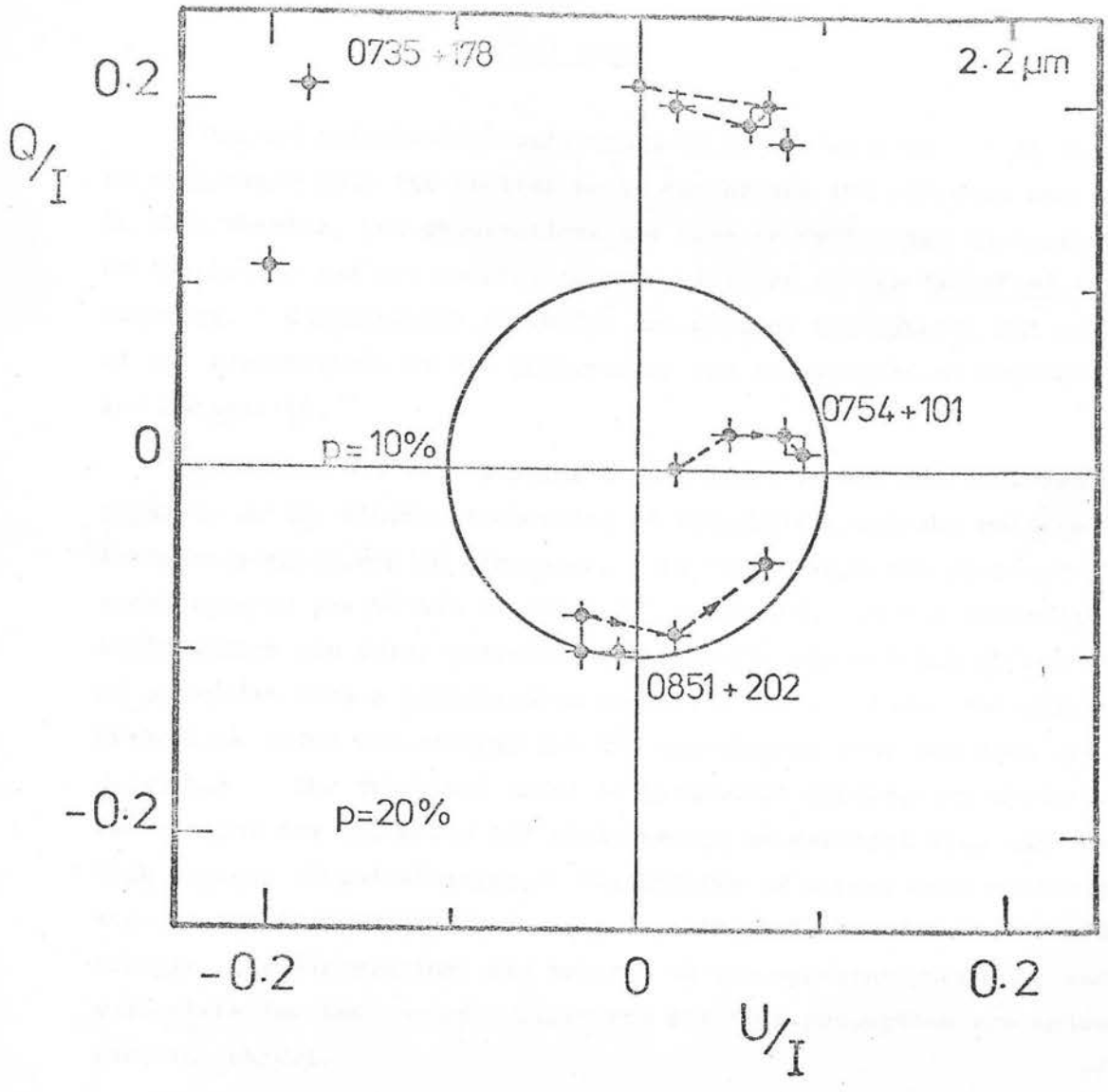

Figure 3.9 Normalized Stokes parameters for 0735+178, 0754+101 and 0851+202. The dashed lines connect observations made on consecutive days.

CHAPTER FOUR

Flux and polarization variations in BL Lac objects can be used to understand both the central power source and the emission mechanism. In this chapter, the observations are used to define the energetics of the source and are related to current ideas on the 'seat' of the activity. Cosmological redshifts are assumed throughout, but many of the implications of the polarimetry are independent of distance and luminosity.

In Section 4.1 the theories of the power source are reviewed with emphasis on the minimum timescales of variability and the maximum luminosity which can be generated. In Section 4.2 the observed energetics of the BL Lac objects are summarized, and the infrared luminosities and total energies of the sample are related to the model of accretion onto a supermassive compact object. Next, the emission mechanisms which can account for the non-thermal infrared flux are described. The canonical model of incoherent synchrotron emission can account for the power law distribution of spectral flux and the high degrees of polarization. The effects of energy loss mechanisms and propagation effects on the spectrum and polarization are considered. Finally, the observations are related to the synchrotron model, and parameters for the magnetic field and electron properties are calculated for each object.

4.1 Theories of the Power Source

In this section it will be assumed that the redshift is of cosmological origin and that BL Lac objects and quasars are closely related in terms of their nuclear properties. These assumptions were justified observationally in Chapter One. The requirements of a model for nuclear activity are to explain systems which radiate up to 10^{49} erg/sec and contain as much as 10^{64} ergs in non-thermal forms, e.g. relativistic particles and magnetic fields. The energy is generated in a very small volume (10^{39} - 10^{45} cm^3) as indicated by timescales of variability. Since galactic nuclei ($M < 10^9 M_\odot$) must give rise to large non-thermal fluxes, the energy production must be extremely efficient ($E > E/M_c^2 \sim 0.1$ - 1%). It should be stressed that some current theories are highly speculative, having little direct confirmation

or refutation by observation. However, the most successful ones do explain the bulk properties of the quasar phenomenon.

4.1.1 Dense Star Clusters

Spitzer (1971) argued that if the core of a galaxy contains a dense cluster of stars (10^{11} pc^{-3}) moving at an average of $\sim 10^{4}$ km sec^{-1}, then each stellar collision could release $\sim 10^{51}$ erg. However, the efficiency of relativistic particle acceleration would be low, and the process would terminate after only 10^{2}-10^{3} years. This is inconsistent with the surface density of quasars. Saslaw (1973) has reviewed the dynamics of dense clusters of stars, and the evolutionary possibilities are considered by Begelman and Rees (1978), Colgate (1967), Colgate *et al.* (1970, 1975) and Petschek *et al.* (1976). For a sufficient stellar density, collisions will lead to gaseous debris being lost and possibly massive coalesced stars. The gas will infall to the centre of the cluster and form new stars, while the stellar population forms an unstable cold disc. As the rate of collisions increases and more energy is released, radiation pressure will eventually prevent further star formation. The dynamical evolution is poorly understood but the system may coalesce into a single massive object, collapse into a black hole, or fragment. Bailey (1979) has shown for galaxies in general that gaseous infall and viscous evolution of the resulting cold disc can lead to the formation of a compact massive object in the centre of the galaxy.

4.1.2 Multiple Supernovae

The energy efficiency of star clusters is improved if inelastic collisions lead to stars of $50M_{\odot}$, which can evolve into supernovae with a total energy release of $\sim 10^{52}$ ergs each. The formation and evolution of star clusters has been studied by Colgate (1967) and others. $\sim 10^{3}$ supernovae per year are needed to account for the strongest sources, and again this leads to a short time for the active phase of galactic nuclei. The specific predictions of the supernova model have not been borne out. One prediction is that the ejecta from the supernovae will be thermalized and plasma oscillations will scatter low frequency photons to higher frequencies. Therefore there will be a scattering time delay between the low energy variations and

the higher energy variations. Also, the rate of flux increase during a burst (which is governed by scattering in the source) will be faster than the rate of decrease (which depends on the energy loss rate). Analysis of the light curve of 3C 273 (Fahlman & Ulrich, 1975) shows that it can be decomposed into a superposition of supernova-like light curves, but the energy release required per explosion is 10^3 times too high. Extensive monitoring of southern quasars by Gilmore (1980) reveals that the rates of flux variation are inconsistent with simple multiple supernova models.

4.1.3 Supermassive Stars

Hoyle and Fowler (1963) suggested that the gravitational contraction of 10^8-$10^9 M_\odot$ would lead to copious energy production. A single massive star could form in the potential well at the centre of a star cluster either by repeated coalescence of smaller stars or by condensation of gas lost in the evolution of normal stars and collisions between those stars (Matthews, 1972; von Hoerner & Saslaw, 1976). The entire topic is reviewed by Wagoner (1969). Objects up to $10^7 M_\odot$ can form provided the stellar mass density exceeds the gas density and bar-mode instabilities are avoided (Saltpeter, 1971). In this case, angular momentum can be lost and masses up to $10^9 M_\odot$ can be stabilized by differential rotation. The characteristic timescales are the rotation period,

$$t_R \sim 1.5 \times 10^{-9} \left(\frac{2GM}{Rc^2}\right)^{-3/2} \left(\frac{M}{M_\odot}\right) \text{ days} \qquad (4.1)$$

and the period of fundamental pulsation,

$$t_p \sim 10^{-7} \left(\frac{M}{M_\odot}\right) \text{ days} \qquad (4.2)$$

for radius R and mass M. The minimum radius is $R_{MIN} \sim 10 R_{SCH}$, where R_{SCH} is the Schwartzchild radius. A rotating massive star is a huge entropy source, with a large amount of energy concentrated in one degree of freedom: rotation. However, the energy release during stable evolution only has the efficiency of thermonuclear burning.

Only during unstable collapse does the energy production rise. This fundamental inefficiency argues against supermassive star models.

4.1.4 Spinars

By analogy with pulsars, Ozernoi (1966) and Morrison (1969) proposed the source of activity in galactic nuclei to be a giant (10^8 - $10^{10} M_\odot$), rotating, magnetized superstar formed by the collapse of a magnetized gas cloud. If the large body is centrifugally-supported, then conservation of angular momentum and magnetic flux increase the rotational energy W according to $1/R^2$ until the rotational frequency Ω becomes $1/\sqrt{G\rho}$, where $\rho \simeq M/R^3$. Subsequently, energy and angular momentum are radiated away by the presence of magnetic fields, and an enormous amount of energy can be liberated in this fashion. Considering a dipole field spinning at a rate Ω - the field lines can no longer co-rotate with the dipole and they are sheared off and radiate with a luminosity,

$$L_{mag} = \frac{2}{3c^3} H^2 \Omega^4 R^6 \sin^2\chi \quad \text{erg/sec} \tag{4.3}$$

compared to the thermal luminosity,

$$L_{ther} = 10^{38} \frac{M}{M_\odot} \quad \text{erg/sec} \tag{4.4}$$

where H is the magnetic pole field strength, and the magnetic axis is inclined by an angle χ to the rotation axis (Morrison, 1969). To produce 10^{48} erg/sec requires $M = 10^9 M_\odot$, $H = 10^5$G, $R = 10^{17}$cm and $T = 2\pi/\Omega \simeq 1$ year. A spinar with these parameters will store energy for 10^6 years and radiate very efficiently; it is a giant machine for converting gravitational binding energy into electromagnetic radiation by means of rotation.

The evolution of a spinar is uncertain. As described by Ginzburg and Ozernoy (1977), the spinar begins its quasi-static contraction at radius,

$$R_1 \sim 3 \times 10^{16} \phi^{\frac{1}{2}} \mathrm{Sin}^{\frac{1}{2}}\chi \left[\frac{M}{10^8 M_\odot}\right]^{\frac{3}{2}} \text{ cm} \qquad (4.5)$$

and contracts towards its Schwartzchild radius,

$$R_{SCH} = \frac{2GM}{c^2} \simeq 3 \times 10^5 \left(\frac{M}{M_\odot}\right) \text{ cm} \qquad (4.6)$$

During this time there are three observational timescales of interest; the rotation period

$$t_R = \frac{2\pi}{\Omega} \simeq 800 \left(\frac{M}{10^8 M_\odot}\right)^{-1} \left(\frac{R}{10^{16}\text{cm}}\right)^{3/2} \text{ days} \qquad (4.7)$$

the pulsation period

$$t_p = \sqrt{3/2}\ t_R \qquad (4.8)$$

and the mass-loss timescale (which is quasi-regular)

$$t_M \simeq 100 \left(\frac{M}{10^8 M_\odot}\right)^{-3/2} \left(\frac{R}{10^{16}\text{cm}}\right)^{5/2} \text{ years} \qquad (4.9)$$

Ozernoy and Usov (1977) have investigated quasar and Seyfert light curves for evidence of t_R and t_M, but the evidence is inconclusive. Because a spinar is a coherent rotating object, a crucial observational test is the detection of periodicity in variable quasars. The existence of a true periodicity is a matter of contention, but no periodicity has been established without doubt (Fahlman and Ulrich, 1975; Chertoprud et al., 1973; Ozernoy et al., 1977; Fahlman, 1977). In fact the interpretation of the features of a quasar light curve as "signal" may be unrealistic (Press, 1978). In common with supermassive stars, the spinar model predicts more rapid increases than decreases in flux, and this is not supported by studies by Angione and Smith (1972) and Gilmore (1979).

As the spinar contracts and spins up, several fates are possible.

It may undergo fragmentation and nuclear explosion (Wagoner, 1971), or it may collapse until the period shortens to a Schwartzchild period of $6^{3/2}\ 2\pi GM/c^3$ and a black hole is formed.

4.1.5 Black Holes

The efficiency of energy production, ε, for a supermassive, accreting black hole can be much higher than the efficiencies of ($\varepsilon < 0.01$) or of thermonuclear burning ($\varepsilon < 0.01$). The variation is from $\varepsilon \sim 0.06$ for a Schwartzchild black hole to $\varepsilon \sim 0.42$ for a disc co-rotating with an extreme Kerr black hole. Another attraction is the fact that a black hole is a natural evolutionary end-point for supermassive stars, spinars and other compact objects. The precursor objects might be able to explain less active phases in galaxies (i.e. Seyfertism), but it seems more profitable to attribute the quasar phenomenon to accreting black holes. Reviews of black hole accretion are given by Rees (1977, 1978b), Lynden-Bell (1978) and Carter (1979), and references to the original literature can be found in these articles (Rees et al., 1974).

Quasar energetics require a mass of 10^7-$10^9 M_\odot$ in a small volume (10^{39}-10^{45} cm^3) and to produce a luminosity L, the accretion rate onto the black hole must be,

$$\frac{dM}{dt} \simeq 0.1\varepsilon^{-1}\left[\frac{L}{10^{46}\ \text{erg/sec}}\right] M_\odot\ \text{year}^{-1} \qquad (4.10)$$

The black hole reaches this mass by accreting general mass loss from stars in the galaxy ($\sim 10^{-11} M_\odot$ year^{-1} per solar mass star), by disrupting stars in the dense core around the black hole, or by swallowing stars whole. Even if general infall from the galaxy cannot supply the required mass, the central black hole is an effective sink for stars approaching too close to it and stellar disruption will occur. When the black hole has existed for a time longer than the relaxation time in the stellar core, a steady inflow of stars is established. Stars are disrupted out to a radius GM/V_c^2 were V_c is the characteristic velocity dispersion dictated by the virial theorem

and given by $(Gm_* n_c r_c^2)^{\frac{1}{2}}$, where n_c and r_c are the typical 'core' density and radius. Peebles (1972) showed that a cusp will form in the stellar density with a power law of the form $n(r) \alpha r^{-7/4}$, the cusp being preferentially populated by stars of higher mass. Stars will be disrupted and their debris accreted if they approach closer than the tidal (Roche) radius,

$$r_T \sim 4 \times 10^{13} \left(\frac{M}{10^7 M_\odot}\right)^{1/3} \left(\frac{m_*}{M_\odot}\right)^{-1/3} \left(\frac{r_*}{R_\odot}\right) \quad \text{cm} \qquad (4.11)$$

Near r_T, some stars may be distorted rather than completely disrupted, and stars with extensive atmospheres may have them removed. At a smaller radius from the black hole, stars will collide,

$$r_c \sim 7 \times 10^{17} \left(\frac{M}{10^7 M_\odot}\right) \left(\frac{m_*}{M_\odot}\right)^{-1} \left(\frac{r_*}{R_\odot}\right) \quad \text{cm} \qquad (4.12)$$

The black hole will grow at a rate $\dot{M}$ somewhat less than the rate of production of tidal debris until at a mass of $10^{\varepsilon} - 10^9 M_\odot$ solar-type stars can be swallowed whole. One of the observational problems of the black hole model is the presence of large extinct black holes in the centre of many galaxies. Recently, Sargent *et al.* (1978) and Young *et al.* (1978) have postulated the central mass of $\sim 5 \times 10^9 M_\odot$ in M87 as a dead quasar. But Dressler *et al.* (1980) have emphasized that the observations do not exclusively indicate a black hole, merely a high concentration of stars.

Much recent theoretical work has concentrated on accretion schemes which allow efficient energy transport and radiation from the central regions. The two favoured geometries are disc accretion and dissipative quasi-spherical accretion; both are well summarized by Rees (1978a). In these models, the maximum rate of energy release dictated by $\dot{M}$ in (4.10) is called the Eddington limit,

$$L_{EDD} = \frac{4\pi GMc}{\sigma_r} \simeq 1.3 \times 10^{38} \left(\frac{M}{M_\odot}\right) \quad \text{erg/sec.} \qquad (4.13)$$

The accretion disc provides a natural explanation for the rapid and erratic variability seen in quasars and BL Lac objects. For a

system radiating at near the Eddington limit, the inner regions of the disc are subject to instability (Lynden-Bell, 1969; Kardashev, 1965) which may result in the explosive release of energy. An example is if the disc plasma becomes magnetically dominated and Rayleigh-Taylor unstable (Pringle et al., 1973), and another is if the magnetic field lines in the disc shear through differential rotation. However, the amplitude of the flare can be no larger than the energy stored in the disc at a given radius or replenished in one dynamical time (Shields & Wheeler, 1976). Elliot and Shapiro (1974) have calculated the minimum timescale of variability (in the quasar rest frame) for a luminosity L,

$$t_{MIN} > 7.8 \times 10^{-44} L \text{ seconds} \qquad (4.14)$$

A difficulty of the simple disc models is that a majority of the radiation will be thermal emission from the viscous-heated disc, and the radiation peak will be in the optical/ultraviolet part of the spectrum. This is at odds with the known peak in most quasars in the infrared (> 20μm), and re-radiation by dust cannot supply the necessary energy. However, if the radiative cooling limit at 10^4K is exceeded, the temperature can rise to $\sim 10^{10}$K when non-thermal cooling becomes significant.

With certain provisos, the efficiency for irregular quasi-spherical accretion can be just as high as for a disc (Fabian et al., 1976). If the cooling is very efficient, the gas will stay at about 10^4K. For a typical quasar luminosity, the temperature cannot stay that low in the central regions because the mass inflow is so quick that radiation does not have time to diffuse out. Therefore, if bremmstrahlung and line cooling are inefficient, the gas will heat adiabatically up to $\sim 10^{10}$K when more efficient cooling mechanisms (synchroton, Compton, etc.) take over. The efficiency of dissipative accretion is high even for low $\dot{M}$, and non-thermal radiation will come from regions near the Schwartzchild radius.

4.1.6 Current Ideas

The model receiving most support at the present is of a massive black hole at the centre of a galaxy, feeding on stars and gas in its environs. Its advantage over its rivals is that the efficiency is high enough to account for most quasar luminosities, and most other compact objects would be expected to evolve into a black hole eventually. Its disadvantage, in common with its rivals, is that the physics of stars, gas and radiation interacting near a massive collapsed object is extremely complex. The available models all tread the line between being simplistic and having many free parameters; but advances are being made very rapidly. It is worth noting that no observation has done more than establish the presence of a deep gravitational well in the centre of a galaxy. Direct evidence for supermassive black holes does not yet exist.

Recent developments in black hole theories have broadened to encompass the morphology of radio galaxies, objects with jets, BL Lac objects and the whole spectrum of active nuclei. The most profitable new directions include:

(a) Supercritical accretion. Accretion-driven sources will tend to stabilize at the Eddington limit - governed by the balance between radiation pressure and gravitational infall. The Eddington luminosity L_{EDD} can be exceeded in certain non-spherical accretion models (e.g. Icke, 1977), or if the gas is supplied by stellar disruption (Rees, 1978a). Since radiation pressure has little effect on the bulk motion of a star, the stellar density can become high enough for a large source of tidally disrupted gas to exist. If $L > L_{EDD}$, some of the material would be blown off as a wind, with the gravitational energy released by inflow of the rest providing the power. For such a radiation driven wind, L_{EDD} can be exceeded and some of the K.E. of the wind can be converted into yet more luminosity at large distances from the hole.

(b) Beam models. One of the most interesting lines of research is the possibility that accretion models can naturally explain the linear structure and superluminal velocities seen in many radio sources. In the presence of a massive, rotating body it seems natural to

associate the aligned radio components with the stable rotation axis. In a classic paper, Blandford and Rees (1974) showed how the relativistic plasma generated in an active nucleus can be channelled into 'twin exhausts'. If there is sufficient dense gas surrounding the nucleus, an equilibrium flow is established where the plasma escapes in oppositely directed channels perpendicular to the accretion plane. The formation of a De Laval nozzle leads to supersonic flow into the intergalactic medium. Some properties of vortices around Kerr and Schwartzchild black holes have been described by Lynden-Bell (1978). For the disc accretion model, the luminosities generated from the collimated relativistic wind and the spin energy of the black hole are,

$$L_{DISC} \simeq 10^{45} \left(\frac{B}{1T}\right)^2 \left(\frac{M}{10^8 M_\odot}\right)^2 \quad \text{erg/sec} \qquad (4.15)$$

and

$$L_{SPIN} \simeq 2 \times 10^{43} \left(\frac{a}{m}\right)^2 \left(\frac{B}{1T}\right)^2 \left(\frac{M}{10^8 M_\odot}\right) \quad \text{erg/sec} \qquad (4.16)$$

where a is the angular momentum per unit mass which can range from 0 up to GM/c^2 (Blandford, 1979). The bulk kinetic energy of the beam is finally converted into relativistic particles and hence into the observed power-law spectrum at an interface with the swept-up intergalactic material. VLBI studies have recently revealed a wealth of radio morphologies such as jets, symmetric double-lobed structure, 'hot spots' in the beams and multiple compact components (Readhead et al., 1978). In the extreme cases, this type of model must be able to explain the giant double sources such as 3C236 (Willis & Strom, 1978) where beams must have remained collimated for 10^8 years with a mean power of $> 10^{45}$ erg/sec.

There are many aspects of beam models that require further work. For instance, the confinement of the beam is not understood, and turbulence and instabilities are bound to complicate the smooth flow. It is also unclear as to what mechanism converts the bulk kinetic energy in the beam into relativistic electrons. Despite these problems, it is evident that energy can be extracted from the throat

of a black hole in preferred colinear directions. A further consequence of beaming is that there will be some lines of sight where the relativistic plasma is viewed 'end-on'. Bulk motion of the emitting region towards the observer will reduce the power consurption in the source. For a bulk lorentz factor Γ, and an observer essentially on-axis ($\theta \sim \Gamma^{-1}$), the mass-energy in the co-moving frame will be reduced by $\sim\Gamma^{4}$. Thus the energy requirement for some of the most luminous objects can be reduced kinematically by a large factor.

(c) Models for BL Lac Objects. Unlike the radio galaxies, there is no direct evidence for beams in BL Lac objects. However the energy budget for BL Lacs is particularly severe because of their large luminosities and rapid variability, and it has been proposed that relativistic beaming is responsible for their radio and optical properties (Blandford & Königl, 1978; Blandford & Rees, 1978). The consequence of looking down the beam will be that special relativistic effects increase the luminosity and decrease the variability timescale. In terms of the accretion model, if the cooling is inefficient at a gas temperature of $\sim 10^{4}$K, the gas will heat up and become relativistic, escaping along the rotation axis. If there is no surrounding gas to reabsorb it, the high polarization which reflects the magnetic field geometry in the central regions will emerge unaltered. The spectrum and polarization depend on the details of the emission mechanism, but the existence of beaming can reduce the brightness temperature and luminosity constraints on BL Lac objects.

4.2 Energetics

4.2.1 Infrared Luminosity

There are 11 objects in the sample with measured redshifts, and assuming the cosmological interpretation of their redshifts, the infrared luminosity in the rest frame of the BL Lac object is given by,

$$L(\nu) = 4\pi\left(\frac{cz}{H_o}\right)^2 (1+z)^3 F(\nu/(1+z)) \qquad (4.15)$$

A Friedman model with cosmological constant $\Lambda = 0$ is assumed, and luminosities have been calculated with $H_o = 75 kms^{-1} Mpc^{-1}$ and q_o

= 1. Choosing $q_o = 0$ would produce a factor of approximately $(1+z/2)^2$ increase in the luminosity (Mattig, 1958). Infrared luminosities using the brightest K measurement for each object are given in Table 4.1 The observed 2.2μm fluxes are converted into 2.2μm fluxes in the BL Lac rest frame by

$$F(\nu/(1+z)) = F(\nu)(1+z)^{\alpha} \qquad (4.16)$$

where α is the near-infrared spectral index ($\bar{\alpha}$) taken from Chapter Three. For BL Lac-type spectra, the flux distribution-dependent part of the K-correction is expected to be small. The term $(1+z)^3$ in equation (4.15) represents the cosmological 'tired light' term, and the technical effect of the decreased bandwidth of the filter in the BL Lac object rest frame. The term $(1+z)^{\alpha}$ corrects for the fact that the K band samples a different part of the energy distribution of a redshifted object. Table 4.1 contains the redshift distance (d_L), the maximum 1-2μm luminosity observed, the range of luminosity and the number of separate observations of each object. The most striking feature is the enormous range of infrared luminosities in the 11 objects studied: a factor of 70,000. At the low end there are objects like 1727+503 with $L_{IR} = 7.9 \times 10^{43}$erg/sec ($2 \times 10^{10} L_{\odot}$), which is a normal infrared flux for an elliptical galaxy. By contrast, 3C446 has a peak luminosity of $L_{IR} = 5.5 \times 10^{48}$erg/sec, making it one of the most luminous objects in the universe. Figure 4.1 shows the distribution of redshift against luminosity, and the selection effect in favour of more luminous, distant sources is apparent. The luminosity spread is vastly greater than the amplitude of variability in a given object; the most extreme archival variability is ∿6.7mag for 3C279 (a factor of ∿500) observed by Eachus and Liller (1975). It is therefore reasonable to question whether the objects like Mk501, AP Lib, 1727+503 (and BL Lac itself) are the same as the three ultra-luminous objects 0235+164, 1308+326 and 3C446. The 11 sources <u>all</u> have the common properties of variability, polarization, infrared excess and power law spectra; these are the features which indicate a non-thermal emission process, and which lead to a BL Lac classification. Line features vary considerably. Sources like AO 0235+164

have strong absorption features but no emission lines, those like 1400+164 and 2155-304 have very weak emission features which are only tentatively identified, and 3C446 has strong emission lines with similar exitations and abundances to normal QSO's. However, emission and absorption lines are considered of secondary importance in the classification of BL Lac objects, because they are created in regions well away from the continuum source. The estimates of continuum luminosity are conservative for several reasons. First, a cosmology with $q_o = 0$ will increase the energy, by a factor of $\sim$3 for 3C446. Second, only a limited infrared bandwidth has been used. For a spectral index of $\alpha = 2$, the power per fractional bandwidth at 2.2μm is $\sim$10 times greater than the power per unit bandwidth in the optical regime. If, as has been shown by Elias et al. (1978), the strong radio and millimeter fluxes for BL Lac-type objects form a smooth extrapolation of the near-infrared data, then most of the energy is emitted in the wavelength range 1-100μm (in the absence of a strong hard X-ray component). The total luminosity may be increased by several orders of magnitude. Photometry and variability studies beyond 10μm will be extremely important in fixing the bolometric luminosity of these sources. Another conservative parameter in the discussion of energetics is the minimum timescale of variability, which in this study was fixed observationally at 1 day. At least 5 of the 11 BL Lacs show evidence for variability on a timescale of hours in the optical (0851+202: Wolstencroft et al., 1980; 1308+326: Puschell et al., 1979; 1514-241: Miller et al., 1974; 2155-304: Snyder et al., 1980; 2223-052: Stockman & Angel, 1978). Therefore, the adopted value of t_{MIN} is likely to be an overestimate. The energetics of the sample are now discussed in terms of the theories outlined in Section 4.1.

4.2.2 Energy Supply

It is clear that the total energy in an outburst of a high redshift BL Lac object generates much more energy than a supernova. The supermassive star hypothesis also fails, because the radius of a stable configuration is >100 times the Schwartzschild radius (Wagoner, 1969). The variability timescale should be greater than observed,

and the star should shine at well above the Eddington limit. The only tenable models involve compact, coherent objects with special accretion geometrics. Stellar collisions can contribute a negligible fraction of the necessary energy. For a virial situation with $2E_{KIN}+E_{GRAV} = 0$ and an average velocity $v = \sqrt{GM/R}$, the number of collisions in the cluster is

$$n_{coll} = n\sigma VN \qquad (4.17)$$

when n is the stellar density, σ is the geometrical cross section, and N is the total number of stars. For $N = 10^7$, $r = 10^{15}$cm and $v = 50 kms^{-1}$, there are $<10^{-10}$ collisions per year. Considering 3C446, and moving on to energy generation from accretion onto compact objects, the dimension of the source corresponding to the minimum variability timescale is given by

$$ct_{MIN} = ct_{VAR}/(1+z) \simeq 1.1 \times 10^{15} cm \qquad (4.18)$$

which corresponds to the Schwartzschild radius of a $3.6 \times 10^9 M_\odot$ black hole. The Eddington luminosity for this mass is 5×10^{47}erg/sec which is exceeded by a factor of ten by the observed IR luminosity. The Eddington limits are also exceeded by A0 0235+164 and B2 1308+326. Figure 4.2 shows a graph taken from Elliot and Shapiro (1974), with the minimum timescale of variability shown as a diagonal line. The three highest redshift objects fall below this line, and the only other objects which fall near are BL Lac, 3C454.3 and 0537-441 (see Equation 4.14). These luminosities correspond to a fuelling rate of

$$\frac{dM}{dt} \simeq 550 M_\odot/year \qquad (4.19)$$

for an efficiency $\varepsilon \sim 0.1$. Since swallowing stars whole is an inefficient way of getting energy out of the black hole, this fuelling rate represents an enormous amount of gas being accreted. Ordinary stellar mass loss processes in a galaxy are insufficient, the gas

must be supplied by stellar disruption in the dense core of the gravitational well. Given that $\sim\frac{1}{3}M_{\odot}$ can be torn from each star, $\sim 10^{3}$ stars/year must be pulled to within the Roche tidal radius given by equation (4.11),

$$r_T \sim 2.8 \times 10^{14}\left(\frac{M}{M_{\odot}}\right) \text{ cm.} \qquad (4.20)$$

This important result means that the total disruption radius lies well inside the Schwartzschild radius. Therefore, a star is swallowed whole before it can have its atmosphere removed and swallowed, and there is no efficient way of generating the gas to fuel the black hole unless a large proportion of the stars are giants with $M > 10M_{\odot}$. This verifies a suggestion by Frank (1979) who argued that the mass supply for the most powerful quasars cannot come from stellar disruption or collisions in the dense core. This dilemma is only eased by relaxing the assumption of the Eddington limit, and adopting super-critical accretion. Although the limit is based on a spherically symmetrical geometry, its use is supported by the upper bound on the luminosity of binary X-ray sources (Gursky, 1973; Margon and Ostriker, 1973). Shakura and Sunyaev (1973) have also argued theoretically that the accretion rate will automatically regulate at the value appropriate to the Eddington Limit. Various accretion schemes have been proposed which exceed L_{edd}. Using the 'cosmic whirlpool' mechanism of Lynden-Bell (1978), Jaroszynski et al. (1980) have modelled a thick disc (thickness large compared to radius from the hole) rather than the usual geometrically thin disc. The gas flows from this disc, which is in hydrostatic equilibrium, along a thin supersonic stream onto the black hole. Most of the radiation is emitted through the walls of two funnels close to the rotation axis, and for a stable configuration the luminosity is given by,

$$L/L_{edd} \simeq 2\ln\left[\frac{r_{OUT}}{r_{IN}}\right] - 2.44 \qquad (4.21)$$

from Abramowicz et al. (1980), where r_{OUT} and r_{IN} are the outer and inner radii of the thick part of the disc. It is possible for L_{edd} to be exceeded by several orders of magnitude. However, this and all other super-critical accretion models are vulnerable to instabilities.

If $L/L_{edd} \sim 100$, then a vast majority of the energy is channelled along the rotation axis; and a 1% instability would be sufficient to disrupt the hydrostatic equilibrium and blow the disc away. In addition, stability must be maintained for $>10^6$ years. It is clear that all accretion models have difficulty accounting for the three most luminous BL Lac objects.

An alternative way of reducing the energy budget is for the emitting region to have a bulk relativistic motion towards the observer. This effect was proposed by Rees (1978) to explain the burst of AO 0235+164 in 1975, when it reached a peak luminosity of $>2 \times 10^{48}$ erg/sec. A bulk Lorentz factor of Γ will reduce the luminosity in the comoving frame by Γ^2, if the observer is in the emission cone. The idea of relativistic beams was first postulated by Blandford and Rees (1974) to explain the apparent continuous supply of energy from the nucleus of a radio galaxy to its outer lobes. Beyond the accelerating "nozzle", the relativistic particle energy in the beam of width r is converted into bulk kinetic energy with a Lorentz factor $\Gamma \propto r$. One of the implications of the "beam" model of BL Lac objects is that they represent a preferred orientation of the observer, looking down the rotation axis of the central power source. This is essentially a kinematic effect.

4.2.3 Total Energy

It is possible to estimate the total energy requirement for a luminous source such as 3C446 during the cumulative duration of its active phase. From 14 observations at 2.2μm covering 12 years, Neugebauer *et al.* (1979) found a range of magnitudes from 11.30 to >14.1 for 3C446. The mean value is 12.92, which accounts to first order for the duty cycle of high and low flux levels. Assuming a similar spectral index to that found in this work, the appropriate IR luminosity is 2.2×10^{48} erg/sec. In Figure 4.3 the available X-ray, optical, infrared and radio fluxes are plotted over a range of 10 decades in frequency and nearly 10 decades in flux. The well-studied quasars now have an enormous observational baseline. By interpolating a smooth continuum between the measured points it is possible to estimate a bolometric luminosity, though it can only be

an order of magnitude estimate because of the interpolation, and known variability from radio to optical wavelengths. The integrated flux is,

$$L_{BOL} \sim 4 \times 10^{49} \text{erg/sec} \qquad (4.22)$$

The majority of this energy is produced from 1-100μm, and the radio and X-ray fluxes make only a small contribution. Therefore the wavelength range of interest is tantalizingly inaccessible to ground-based observations at present. A wide range of active galactic nuclei have their maximum energy output in the far infrared region (Rieke & Lebofsky, 1979).

To estimate the total energy output it is necessary to know the fraction of its lifetime a quasar spends undergoing violent activity. This can be done by assuming that quasars reside in the nuclei of galaxies, and comparing the relative numbers of active and non-active galaxies in a given class. de Vaucouleurs and de Vaucouleurs (1968) found that about 1% of spiral galaxies showed Seyfert characteristics, implying a timescale for Seyfert activity of $\sim 10^8$ years. For radio galaxies, it has been shown that ~10-20% of elliptical galaxies have radio emission, and that both the proportion and the radio luminosity increase with the elliptical's absolute magnitude (Colla et al., 1975). Radio galaxy emission therefore lasts $\sim 10^9$ years. It should be noted that these arguments cannot distinguish between one period of activity in the lifetime of a galaxy and recurrent activity. Inevitably, the nature of the galactic component of quasars is uncertain, but where spectroscopy of the nebulosity surrounding low redshift BL Lac objects is possible, the evidence is always consistent with an elliptical galaxy. Since growing continuity arguments point to the similarity between the Seyfert and quasar phenomena (Weedman, 1976), the active cycle can be scaled by the ratio of average Seyfert/quasar luminosities giving a quasar lifetime of $\sim 10^6$ years. The total energy output during the lifetime of 3C446 is therefore

$$E_{TOT} \sim 1 \times 10^{63} \text{ergs} \qquad (4.23)$$

Even as an order of magnitude estimate, this is a phenomenal amount of energy, equal to the amount of energy entrained in the particles and magnetic fields of the most luminous and extended radio galaxies. It is equivalent to $\sim 10^{14} L_\odot$ for 10^6 years or $\sim 10^9 M_\odot c^2$. Given $\epsilon \sim 0.1$, it is clear that only the most extreme kind of energy source can process 10^{10} stars and emit the prodigious power seen in 3C446.

4.2.4 Range of Properties

For the 8 low-redshift sources studied, accretion onto a massive, compact object can account for the observed infrared luminosity. Only the three high-redshift sources pose any problem, which can be eased by invoking a bulk motion of the emitting volume. The range of IR luminosities is large; it is important to see whether the three extreme sources have any other distinguishing properties. The discussion is brief, because the sample is very incomplete. 3C446, 1308+326 and 0235+164 are extreme in many of their other properties too. They are among the intrinsically brightest sources known at 2700 MHz ($\sim 10^{35}$ erg/sec/Hz), which verifies the non-thermal nature of the continua. From plate archives, they all have large amplitudes of variability (3C446: $\Delta B > 6.0$, 1308+326: $\Delta B > 4.5$, 0235+164: $\Delta B > 5.2$): these are among the largest known. From the data presented here, they are all highly polarized. Of the 17 objects studied, they form three out of the four with the largest polarization fluctuations. There is no evidence for a preferred position angle, large swings occur on a timescale of months. Part of the range of parameters is undoubtedly because they are well-observed, but in all respects they represent the most extreme BL Lac objects.

The Scott effect biasses any BL Lac sample with objects like the three above; they are likely to be exceptionally rare. At high redshifts, the steep optical continuum is redshifted through the visual band, and such objects will be difficult to identify optically. In fact, almost all BL Lac objects have been discovered by their radio emission. Although there are strong effects against optically selecting BL Lacs (the most commonly used techniques of ultra-violet excess and objective prism spectroscopy are not appropriate), the

presence of radio emission is not entirely due to selection effects. The fact that all BL Lac objects have non-thermal radio emission supports the premise that non-thermal processes are also responsible for the polarization.

In summary, the properties of variability, high polarization and extreme redness are common to the whole sample, indicating that the emission process is the same in all BL Lac objects. The three luminous sources only differ in the degree of variability, etc. The span of luminosities is enormous and it is uncertain whether a single compact object in different accreting environments can account for the range, without reducing the intrinsic luminosity by "beaming" effects. The three luminous sources provide the most stringent test of the available theories.

4.3 Emission Mechanisms

Emission mechanisms for the infrared flux in BL Lac objects are discussed, with special emphasis on those which can explain rapid variability and high polarization. The small volumes around the compact centres of BL Lac objects contain relativistic particles, highly ionized matter, magnetic fields and electromagnetic radiation. The interaction of these constituents can produce electromagnetic radiation in a variety of ways: synchroton emission (electrons in magnetic fields), inverse Compton effect (scattering of photons by electrons), bremmsthahlung or free-free emission (collisions of electrons with ions or atoms), γ rays through π-production and decay (collisions of protons with nuclei). In addition, the radiation will be modified due to propagation effects of plasma, dust and particles along the line-of-sight.

4.3.1 Incoherent Synchroton Emission

The canonical theory for the emission in extragalactic sources has become the incoherent synchroton process, ever since the light from the Crab Nebula was proposed to be radiation from high-energy electrons gyrating in a magnetic field (Shklovsky, 1953). The discovery of strong polarization in the optical emission by Vashakidze (1954) and Dombrovsky (1954) confirmed the hypothesis. Since then

the synchroton theory has been extended with success to explain the power-law spectra of extragalactic radio sources (Shklovsky, 1961), and the flat spectra of compact sources which are believed to be a superposition of many components of varying optical depth (Kellerman & Pauliny-Toth, 1968). Synchroton emission has been adopted for all quasars, though this interpretation is not compelling. For instance, most optically selected quasars show no clear evidence of synchroton radiation at any frequency (only ~10% are detectable as radio sources (Murdoch & Crawford, 1977)). Ar in most quasars, radio-quiet or radio-loud, the IR/optical continuum is not highly polarized (Stockman & Angel, 1978), not highly variable (Bonoli et al., 1979), and not a simple power law (Neugebauer et al., 1979). The interpretation is most secure for the BL Lac objects. Synchroton emission has been discussed extensively in many review articles and textbooks, notably Westfold (1959), Jackson (1962), Ginzburg and Syrovat-skii (1964, 1965), Blumenthal and Gould (1970) and Tucker (1975). In this section the spectrum and polarization properties of incoherent synchroton radiation are summarized.

A relativistic electron ($E = \gamma m c^2$) being accelerated and radiating in a uniform magnetic field $\underline{B}$ will describe a helix with pitch angle α between the velocity and magnetic field vectors. The frequency of gyration ω_L is

$$\omega_L = \frac{eB}{\gamma mc} \tag{4.24}$$

The velocity vector therefore describes a cone about the direction of the field, and observers on the surface of this cone far from the emitting particle would record radiation pulses at intervals $T \sim 2\pi/\omega_L$ and of duration $\Delta t \sim 1/\gamma$. The radiation spectrum therefore consists of harmonics of the gyration frequency ω_L, and since $T \gg \Delta t$ the spectrum is continuous and the maximum corresponds to the frequency

$$\omega_c \sim \frac{1}{\Delta t} \sim \frac{3}{2}\gamma^3 \omega_L \sin\alpha \sim \frac{3eB}{2mc}\left[\frac{E}{mc^2}\right]^2 \tag{4.25}$$

For the highly relativistic case ($\gamma >> 1$), the power per unit frequency range emitted by each electron is given by (Rybicki & Lightman, 1979),

$$P(\omega) = \frac{\sqrt{3}}{2\pi} \frac{e B \sin\alpha}{mc^2} F(\frac{\omega}{\omega_c}) \qquad (4.26)$$

and the total power over all frequencies is equal to (Landau & Lifshitz, 1975),

$$P_{tot} = \frac{2e^4 B_\perp^2 \gamma^2}{3m^2 c^3} = \frac{2e^4 B_\perp^2}{3m^2 c^3} \left(\frac{E}{mc^2}\right)^2 \qquad (4.27)$$

From Figure 4.4 it can be seen that the E-vector of the radiated wave describes an ellipse in the plane perpendicular to the plane of the observer. The synchroton radiation from individual electrons is generally elliptically polarized. When $\Psi = 0$, the polarization becomes linear because the wave vector lies on the surface of the velocity cone. For large Ψ, the radiation approaches circular polarization but the intensity diminishes rapidly when $\Psi >> \xi$. The polarization of the spectrum of an individual relativistic electron has been calculated by Westfold (1959), and the total and polarized fluxes as a function of frequency are plotted in Figure 4.5,

$$F(X) = x \int_x^\infty K_{5/3}(\eta)\, d\eta \qquad (4.28)$$

$$F_p(X) = x K_{2/3}(X) \qquad (4.29)$$

where $x = \omega/\omega_c$, and $K_{5/3}$ and $K_{2/3}$ are the modified Bessel functions defined by Abramowitz and Stegun (1965), Chapter Ten. The polarization, which by convention is labelled Π is given by $F_p(x)/F(x)$. These expressions can be generalized into the power emitted parallel and perpendicular to the component of the magnetic field in plane K (directions ℓ_1 and ℓ_2 in Figure 4.4),

$$\frac{dW_\perp}{d\omega} = \frac{\sqrt{3}e^2\gamma\sin\alpha}{2c} \left[F(x)+F_p(x)\right] \qquad (4.30)$$

$$\frac{dW_\parallel}{d\omega} = \frac{\sqrt{3}e^2\gamma\sin\alpha}{2c} \left[F(x)-F_p(x)\right] \qquad (4.31)$$

with the total power per frequency interval given by the sum of the above (Figure 4.5),

$$P(\omega) = \frac{\sqrt{3}e^3 B \sin\alpha}{2\pi mc^2} F(x) \qquad (4.32)$$

The radiation from an ensemble of particles can be considered, and since the emission is incoherent, the Stokes parameters are additive giving,

$$I(\omega, \underline{k}) = \frac{\sqrt{3}e^3}{2\pi mc^2} \int B \sin\alpha F(x) N(E,r,\underline{k}) dE\, dr \qquad (4.33)$$

$$Q(\omega, \underline{k}) = \frac{\sqrt{3}e^3}{2\pi mc^2} \int B \sin\alpha \cos 2\chi\, F_p(x) N(E,r,\underline{k}) dE\, dr \qquad (4.34)$$

$$U(\omega, \underline{k}) = \frac{\sqrt{3}e^3}{2\pi mc^2} \int B \sin\alpha \sin 2\chi F_p(x) N(E,r,\underline{k}) dE\, dr \qquad (4.35)$$

where α is the angle between $\underline{k}$ and B, χ defines the position angle reference frame, and the distribution of particles $N(E,r,\underline{k})$ will in general depend on the distance r. Korchak and Syrovat-skii (1961) have shown that in the ultra-relativistic case, $V(\omega,\underline{k}) = 0$ to order $\gamma(= E/mc^2)$. The absence of elliptical polarization is intuitively obvious since the total emission does not depend on the sign of Ψ, and for any distribution of particles the positive and negative values of Ψ will cancel out. Thus the polarization will be linear. Only in the unlikely case of extremely anisotropic velocity distribution would there be a component of elliptical polarization.

The most important example of electron energy distributions is the power law defined within the limits $E_1 < E < E_2$

$$N(E,\underline{k}) dE = K(\underline{k}) E^{-p} dE \qquad (4.36)$$

where $N(E,\underline{k})$ is the number of electrons along the line-of-sight per unit solid angle. For the power law approximation to be valid, the limits E_1 and E_2 must be such that $E < E_1$ and $E > E_2$, i.e. energy outside these limits is negligible. In cosmic radio sources this approximation is true over a large energy range, and in BL Lac objects

it is almost always true in the region 1-100μm. To evaluate equations (4.33) - (4.35), the integrals over $F(x)$ and $F_p(x)$ are used as given by Westfold (1959). First, it is noted that for an isotropic and homogeneous electron distribution,

$$N(E,r,\underline{k}) = \frac{1}{4\pi} N(E) \tag{4.37}$$

where $N(E) = KE^{-p}dE$, which gives

$$K(\underline{k}) = \frac{L}{4\pi} K \tag{4.38}$$

where L is the dimension of the emitting region along the line-of-sight. The Stokes parameters of the ensemble average are,

$$I(\omega,\underline{k}) = \frac{p+7/3}{p+1} \overline{\phi}(\nu,p) \int_{\nu} (B \sin\alpha)^{(p+1)/2} d\nu \tag{4.39}$$

$$Q(\omega,\underline{k}) = \overline{\phi}(\nu,p) \int_{\nu} (B \sin\alpha)^{(p+1)/2} \cos 2\chi d\nu \tag{4.40}$$

$$U(\omega,\underline{k}) = \overline{\phi}(\nu,p) \int_{\nu} (B \sin\alpha)^{(p+1)/2} \sin 2\chi d\nu \tag{4.41}$$

where

$$\overline{\phi}(\nu,p) = \frac{\sqrt{3}\, 2^{(p-1)/2}}{16\pi} \Gamma\left(\frac{3p-1}{12}\right) \Gamma\left(\frac{3p+7}{12}\right) \left(\frac{K}{r^2}\right)\left(\frac{e^3}{mc^2}\right)\left(\frac{3e}{4\pi\nu m^3 c^5}\right)^{(p-1)/2} \tag{4.42}$$

and $\Gamma(x)$ is the Euler gamma function of argument x. These relations are only fulfilled under the condition $p > 1/3$. The function $\overline{\phi}(\nu,p)$ is not generally easily expanded, but Westfold has tabulated the case $p = 5/3$ (Figure 4.6). The degree of polarization in a homogeneous field is given by equations (4.39) - (4.41) and the relation $p = \sqrt{Q^2+U^2}/I$,

$$\Pi = \frac{p+1}{p+7/3} \tag{4.43}$$

This important result means that for a power law distribution of electrons in a homogeneous magnetic field, the degree of polarization

only depends on the exponent of the energy spectrum. Finally, from (4.32) and the relations defined by Rybicki and Lightman (1979), the total power per unit volume per unit frequency is

$$P_{tot}(\omega) = \frac{\sqrt{3}\, e^3 KB\sin\alpha}{2\pi mc^2(p+1)} \Gamma\left(\frac{3p+19}{12}\right) \Gamma\left(\frac{3p-1}{12}\right) \left(\frac{mc}{3eB\sin\alpha}\right)^{-(p-1)/2} \qquad (4.44)$$

Therefore, a power-law energy spectrum of radiating electrons corresponds to a power-law frequency spectrum of the radiation, with the important relation

$$I(\nu) \sim \nu^{-\alpha}, \quad \alpha = \frac{p-1}{2} \qquad (4.45)$$

All these results apply to incoherent synchrotron radiation in a uniform homogenous field and a vacuum. However, any magnetic field distribution can be used in equations (4.39) - (4.41). The assumption of a power law energy interval of $E_1 \rightarrow E_2$ allows the limits of integration to be zero and infinity, and for a power law spectrum the energy interval with the most radiative power depends strongly on p. As $p \rightarrow 1/3$, this interval becomes infinite. For most BL Lac objects in the infrared $3 < p < 5$, so the relaxing of the limits on the integral is a very good approximation. In summary, incoherent synchrotron emission predicts two of the important properties of the BL Lac objects: power law spectra and high degrees of polarization.

4.3.2 Energy Loss Mechanisms

Synchrotron radiation has been used to explain the emission in extragalactic sources over an enormous frequency range: up to 10 orders of magnitude (Figure 4.3). Inevitably, one idealized electron distribution will not account for the spectral shape; in particular, the flat radio spectrum is believed to be the sum of several separate components. Two features are common to almost all spectra of quasars and BL Lac objects. At low frequencies (10^7 - 10^8 Hz) there is a steepening which is due to self-absorption, when the surface

brightness temperature of the source is comparable to the kinetic temperature of the radiating electrons. This becomes important at the frequency

$$\nu_{abs} \sim 10(1+z)(F^2\theta^2 B)^{1/5} \qquad (4.46)$$

where F is the observed flux density at ν_{abs}, θ is the angular size of the source and B is the magnetic field strength (Pacholczyk, 1970). There is thus a low frequency cutoff to the spectrum. The optically thick emission is proportional to the source function $\alpha\nu^{5/2}$ and is independent of the spectral index p (the index differs from the Rayliegh-Jeans value of -2 because the radiation is non-thermal). As already shown, the optically thin emission is proportional to the emission function, i.e. $\alpha\nu^{-(p-1)/2}$.

At high frequencies (optical/IR : 10^{14} - 10^{15} Hz), the relativistic electrons which emit synchrotron radiation may lose energy in a variety of ways: bremsstrahlung, inverse Compton scattering and synchrotron radiation itself. All these mechanisms are energy-dependent, so they will affect the energy spectrum of the radiating electrons. The shape of the optical/IR continuum will depend on the balance between the rate of synchrotron and inverse Compton losses and the rate of replenishment of electrons into the radiating region. Blumenthal and Gould (1970) have calculated the losses on the particle spectrum from synchrotron radiation. The energy loss rate is given by equation (4.27). There are two interesting special cases with relevance to energetic sources. First, the energy distribution for a steady injection of electrons is given by

$$n(E) = \frac{3}{4}\frac{(mc^2)^2}{c\sigma_T U}\quad\frac{\Psi}{(\gamma-1)}\,\gamma^{-(\gamma-1)} \qquad (4.47)$$

where σ_T is the Thomson scattering cross section, and U is the total energy in the radiation and magnetic fields of the medium $U = U_{ph} + B^2/8\pi$. If the electrons have a lifetime longer than the age of the source, the density increases with time as in Figure 4.7a (Fyter, 1979). For a burst of particles, the energy evolves as

$$n(E) = E_o / \left[1 + \frac{4}{3} E_o \frac{c\sigma_T U}{mc^2} t \right] \qquad (4.48)$$

where $E_o = \gamma_o mc^2$ is the initial energy. The time development is shown in Figure 4.7b. It should be noted that synchrotron loss rates depend on the pitch angle Ψ. For an ultrarelativistic electron, equation (4.48) becomes,

$$\gamma = \gamma_o \left[1 + \frac{2e^4 B_\perp^2}{3m^3 c^5} \gamma_o t \right]^{-1} \qquad (4.49)$$

and the time for an electron to lose half its energy is

$$t_{\frac{1}{2}} = \frac{3m^3 c^5}{2e^4 B_\perp^2 \gamma_o} \qquad (4.50)$$

The change of γ with time appears to disagree with the electron's equation of motion $e\underline{v}\cdot\underline{E} = \frac{d}{dt}(\gamma mc^2) = 0$ because the correction term for self-radiation has not been taken into account, but the term is small.

At high electron energies, inverse Compton scattering becomes an effective way for the particles to lose energy by scattering off photons. At high photon energies ($mc^2 << h\nu$) relativistic corrections are important and the Kein-Nishina formula replaces the classical elastic derivation (Heitler, 1954). The cross section is reduced to

$$\sigma = \frac{3}{8}\sigma_T \left[\frac{h\nu}{mc^2} \right]^{-1} \left\{ \ln\left(\frac{2h\nu}{mc^2} \right) + \frac{1}{2} \right\} \qquad (4.51)$$

However, at optical and infrared wavelengths $\lambda >> \lambda_c$ and the assumption of elastic scattering is normally valid. For relativistic electrons, the energy of the photon in the rest frame of the electron is $\gamma\varepsilon$ and the condition

$$\gamma\varepsilon << mc^2 \qquad (4.52)$$

must be met. The scattered photon energy is $\gamma^2\varepsilon$, so photons of enormous energy can be produced. The power lost per electron is given by Blumenthal and Gould (1970),

$$P_c = \frac{4}{3}\sigma_T c\gamma^2\beta^2 U_{ph} \tag{4.53}$$

For the synchrotron case use equation (4.24) and the formula for the power emitted by a relativistic particle $P = 2e^2/3c^3(\gamma^4(a_\perp^2 + \gamma^2 a_{||}^2))$ where $a_\perp$ and $a_{||}$ are the components of the four-force,

$$P_s = \frac{4}{3}\sigma_T c\gamma^2\beta^2 U_B \tag{4.54}$$

giving the simple result

$$\frac{P_c}{P_s} = \frac{U_{ph}}{U_B} \tag{4.55}$$

From a single scattering, the radiation is concentrated in a cone of angle $1/\gamma^2$ in the direction of the electrons motion and has an energy in the range (Figure 4.8),

$$(\gamma^2/4)\varepsilon < \varepsilon' < (4\gamma^2)\varepsilon \tag{4.56}$$

with a mean value $\bar{\varepsilon}' = (4\gamma^2/3)\varepsilon$ (4.57)

For a power law electron distribution $N(\gamma) = K\gamma^{-p}$, the power rate per electron (4.53) can be integrated over γ and the energy spectrum giving

$$\frac{dN_{TOT}}{dtd\varepsilon_1} = \frac{3\sigma_T}{8} cK2^{p+3} \frac{p^2+4p+11}{(p+3)^2(p+1)(p+5)} \varepsilon_1^{-(p+1)/2} \int \varepsilon^{(p-1)/2} n(\varepsilon) d\varepsilon \tag{4.58}$$

The function for a single scattered photon is shown in Figure 4.9, showing a distribution which is broad, peaked at $\hat{\varepsilon}_1 = 0$ and has a centroid $f(\hat{\varepsilon}_1)d\hat{\varepsilon}_1 = 1/3$. The general result (4.58) contains the same assumptions as the synchrotron case about the limits of the power law spectrum. Jones et al. (1974) have calculated the effect of anisotropy where the Compton scattered flux will be reduced if the angle between the electrons pitch angle and the direction of B was small. The correction term in terms of this angle ϕ multiplies the

RHS of equation (4.58),

$$(\text{corr}) = 2^{-(p+1)/2}(1-\cos\phi)^{(p+1)/2} \tag{4.59}$$

In a cosmic source, the medium is pervaded by both magnetic fields and radiation fields, so the contributions of both the Synchrotron and Compton mechanisms are important. Most of the published analyses refer to the radio frequencies; at infrared frequencies the balance of loss mechanisms is critical. To produce synchrotron radiation in the optical and infrared, the electron energies must be considerably higher than those needed to produce the radio emission. Alternatively, if the electron energies are unchanged the magnetic field must be increased substantially. From equation (4.25),

$$\frac{\omega_2}{\omega_2} = \frac{B_{\perp,2}}{B_{\perp,1}}\left[\frac{E_2^2}{E_1^2}\right] \tag{4.60}$$

Synchrotron losses are $\propto B_\perp E^2$, so particles at very high energies and in strong fields are quickly decelerated in a half-life $t_{\frac{1}{2}}$(4.50). In the Thomson limit, the ratio of inverse Compton flux to synchrotron flux is

$$\frac{F_c}{F_s} \simeq 1.1\left(\frac{7.5\times10^3 T}{B}\right)^{(p-3)/2}\frac{U_{ph}}{U_B}\left(\frac{\omega_c}{\omega_s}\right)^{-(p-1)/2} \tag{4.61}$$

where ω_s is the typical radio synchrotron frequency, and ω_c is the upscattered Compton frequency, and the numerical factor has been calculated for p = 3. It is clear that the Compton power will dominate if $U_{ph} >> U_B$, where $U_B = \int_V B^2/8\pi dV$ over the emitting volume. This ratio can alternatively be expressed in terms of the brightness temperature, T_B

$$\frac{F_c}{F_s} \simeq \frac{\nu_c}{2}\left(\frac{T_B}{10^{12}}\right)^5\left\{1+\frac{\nu_c}{2}\left(\frac{T_B}{10^{12}}\right)^5\right\} \tag{4.62}$$

where ν_c is the high frequency cutoff for a maximum energy electron

(Kellerman & Pauliny-Toth, 1969). The brightness temperature T_B is defined as the temperature of the black body which would generate the same flux,

$$T_B = 4.4 \times 10^{11} \frac{F(\nu)}{\theta^2 \nu^2} \quad {}^{o}K \tag{4.63}$$

The significance of the brightness temperature of 10^{12}K is that above this value, Compton losses are proportional to $(T_B/10^{12})^{10}$ and by increasing the frequency of the scattered photon by $\sim\gamma^2$, a large amount of energy is quickly lost.

It is also possible that the magnetic field will vary within different emitting volumes of the source. If radiation at ω_1 comes from a volume V_1 of field strength B_1, and radiation at ω_2 comes from V_2 with field strength B_2, and the radiation comes from electrons with $E_1 = E_2$; then the frequencies are related by equation (4.60) and the fluxes are related by

$$\frac{F_2(\omega_2)}{F_1(\omega_1)} = \frac{V_2}{V_1} \left(\frac{B_2}{B_1}\right)^{(p+1)/2} \left(\frac{\omega_1}{\omega_2}\right)^{(p-1)/2} \tag{4.63}$$

which becomes,

$$\frac{F_2(\omega_2)}{F_1(\omega_1)} = \frac{V_2}{V_1} \frac{B_2}{B_1} \tag{4.64}$$

These relations apply if a small volume V_2 within V_1 has a field $B_2 >> B_1$ and high energy cutoff which prevents the electrons in V_1 radiating near ω_2.

Finally, in very compact sources where U_{ph} and U_B are both large, the electrons may Compton scatter the radiation they have just produced by the synchrotron mechanism. This is called synchrotron self-Compton radiation, and it increases the photon energy to $h_\omega \sim \gamma^4 h_L$ (ω_L given by equation (4.24)). It has been considered for several simple source geometrics by Jones et al. (1974).

4.3.3 Propagation Effects

So far, the medium in the source and along the line-of-sight has been treated as a vacuum. More precisely, the medium is a tenuous neutral ionized gas or plasma. The plasma frequency and index of refraction are given by,

$$\omega_p^2 = \frac{4\pi ne^2}{m_e} = (5.6 \times 10^4 n^{\frac{1}{2}})^2 \text{Hz} \qquad (4.65)$$

$$n_r = (1-\omega_p^2/\omega^2)^{\frac{1}{2}} \qquad (4.66)$$

where n is the electron density (cm^{-3}). In the optical/infrared region $\omega_p << \omega$ and $n_r \approx 1$, so the complex propagation effects which must be taken into account at radio frequencies can be neglected. In particular, since $n_r = 1$ no Cerenkov radiation is possible. Also, the Razin effect which suppresses beaming in a plasma of $n_r < 1$ is negligible because the beaming angle in a medium $\theta_B \sim \sqrt{1-n_r\beta^2}$ reduces to the vacuum case $\theta_B \sim \sqrt{1-\beta^2} \sim 1/\gamma$. However, in an inhomogeneous source, there may be propagation effects within the emitting volume. If the component of the magnetic field along the line-of-sight changes with depth in the source, then the plane of polarization can rotate by an amount

$$\Delta\theta = \frac{2\pi e^3}{m^2 c^2 \omega^2} \int_o^d nB_{||}\, ds = \left(\frac{2\pi e^3}{m^2 c^2 \omega^2}\right) n_c H \text{Cos}\theta\, \ell \qquad (4.67)$$

where n_c is the number density of cold electrons, and ℓ is the thickness along the line-of-sight. Since $\Delta\theta \propto \omega^{-2}$, there is negligible Faraday rotation of infrared frequencies in the intervening medium. However, if the direction of B changes within the source such that $\Delta\theta \sim 1$ radian, the radiation will be depolarized. The existence of high polarizations in BL Lac objects means that $\Delta\theta$ must be small, both within the source and along the line-of-sight. The subtle effects which can alter the polarization of radio sources have been treated by Jones and O'Dell (1977a,b) and Wilson (1980), but they are negligible for $\omega >> \omega_p$. The only other alteration to the plane of

polarization would be if there was a significant optical depth of an absorbing material such as dust.

4.3.4 Source Evolution

The previous formulae apply only to quasi-static synchrotron theory, which is valid when the source parameters (j_e, B, γ, $n(\varepsilon)$, etc.) vary very slowly over the period of observation. However, there is direct evidence for violent activity and bulk motion of the emitting region in many sources similar to BL Lacs. The dynamics of an expanding source will be complex, but simple relations can be derived for the case of spherical symmetry and isotropy. If a volume of dimension R containing magnetic fields and relativistic particles expands, the flux is 'frozen' and is conserved as

$$B \sim R^{-2} \tag{4.68}$$

The particles cool adiabatically (if the expansion is slow) according to $dU + pdV = 0$, where $p = U/3V$ for a relativistic gas. This leads to

$$U \sim V^{-1/3} \sim E^{-1} \tag{4.69}$$

If $N(E) = KE^{-p}$, then $K \sim R^{-(p+2)}$. Using equation (4.39), which gives $I(\omega) \propto B^{(p+1)/2}$ and the relations above,

$$I(\omega) \sim R^{-2p} \tag{4.70}$$

Therefore adiabatic losses are very important, and a large energy reservoir is needed to supply an expanding source. Conversely, if an emitting volume is compressed (e.g. by a shock) the emission is also changed substantially. For relativistic particles $U \propto \gamma$, so from (4.69) $\gamma \propto R^{-1}$. From equation (4.27), $P_{tot} \propto B^2\gamma^2$ therefore

$$P_{tot} \propto R^{-6} \tag{4.71}$$

From equations (4.25) and (4.50), the critical frequency and synchrotron loss times go as $\omega_c \propto R^{-4}$ and $t_{\frac{1}{2}} \propto R^5$. In addition the synchrotron and Compton loss rates vary as $F_s \propto R^4$ and $F_c \propto R^8$ so a large amount of energy can in principal be liberated from a shocked region in the source.

Recently, models for reducing the energetics problems of variable quasars and explaining the variable radio structure have centred on relativistic jets and bulk motion of the emitting region produced by relativistic blast waves. As mentioned before, a Lorentz factor Γ of the emitting region towards the observer will lower the luminosity in the comoving frame by Γ^2, the brightness temperature by Γ^3 and the total mass-energy required by Γ^4. Ways of realizing this kinematic effect dynamically have been studied by Blandford and Rees (1978), Blandford and McKee (1977), Blandford and Königl (1979), Christiansen et al. (1978) and others. Many of the processes involve non-linear systems and there are many free parameters. More work is needed to extend geometrically simple models to the complicated radio structures seen by VLBI. However, several lines of evidence indicate that BL Lac objects can be explained by incoherent sychrotron radiation from relativistic electrons with a moderate ($\gamma\beta \sim 1$) relativistic expansion of the compact components.

First, and independent of the emission mechanism, relativistic separation velocities are present in some sources. The observations are well summarized by Cohen et al. (1977) and Kellerman (1979), and the various interpretations are presented by Blandford et al. (1977). Second, the low frequency (< 1GHz) variability timescales for some radio sources are so short that the radio brightness temperature, based on the source size, ct_{VAR}, exceeds the "inverse Compton" limit of $\sim 10^{12}$K. The highest value of T_B is $>10^{17}$ (McAdam, 1979) and $\sim$10% of compact radio sources show this behaviour (Condon et al., 1979). Screen models have been proposed to explain the variations, but they are at odds with the high percentage of sources with $T_B > 10^{12}$K. Relativistic motion with moderate Γ(= 5-10) can bring the inferred values of T_B in line with synchrotron theory. In the cases studied by Burbidge et al. (1974), the magnetic field inferred from isotropic synchrotron emission is less than would be inferred from equipartition

between magnetic and electron energies. The dynamics appear to be particle dominated, and in the absence of external pressure or a confining medium, relativistic expansion would result. These observations are critically dependent on a large power of the inferred angular size of the source. Finally, the lack of Faraday depolarization places limits on the number of non-relativistic electrons in compact sources (Jones & O'Dell, 1977c). From a lack of differential rotation at two radio frequencies

$$\frac{n_{rel}}{n_c} \geq 6.5 \times 10^{-10} \left(\frac{T_B}{\Delta\chi \tan\theta} \right) \qquad (p = 3.0) \qquad (4.72)$$

where θ is the angle between B and the line-of-sight and $\Delta\chi$ is the differential Faraday rotation, observed to be <0.5 radians (Wardle, 1977). From this analysis, $n_{rel}/n_c > 10^4$, which is indirect evidence (independent of B) for a shock propagating through a thermal plasma. The electron spectrum which is more applicable to this result than a power law is a relativistic Maxwellian,

$$N(E) = N_o E^2 e^{-E/KT} \qquad (4.73)$$

Plasma temperatures of $\sim 10^{12}$K are needed to produce this distribution (Pacholczyk, 1970). It should be remembered also that relativistic motions of the emitting region towards the observer reduce the energetics problems discussed in Section 4.2.

4.3.5 Other Emission Mechanisms

Several alternatives to incoherent synchrotron radiation have been explored, mostly to avoid the inferred problems of variability timescales, brightness temperature and the associated Compton problem. They have not yet been as fully developed as the canonical model, but can reproduce the basic properties of power-law spectra. They will only be considered here in as far as they predict the polarization properties of BL Lac objects. A coherent emission mechanism based on plasma oscillations has been proposed by Colgate *et al.* (1975) and Petschek *et al.* (1976). Coherent radiation at $\omega = 2\omega_p$ is generated

and scattered in frequency by non-thermal plasma oscillations in a hot thermal gas ($kT \sim \frac{1}{2}m_e c^2$). The spectrum above a critical frequency ($\nu_c \sim 10^{11}$Hz) is normal Compton scattered from the hot plasma. Producing high polarization is a problem for this model, because each optical/infrared photon is multiply Compton scattered. The lack of observed Faraday rotation sets a severe limit of $B < 10^{-7}$G on the magnetic field, and it has not been demonstrated whether photons scattering off the plasma oscillation can become polarized. In any case, high polarizations would require the plasma K-vectors to be highly anisotropic. The non-relativistic Compton scattering model of Katz (1976) may produce linear polarization, but the amount is geometry dependent and will be high (>20%) only in cases of extreme anisotropy. Thermal dust emission can be ruled out for BL Lac objects because the dimensions implied by the variability timescale rule out all dust models. The example of the Seyfert NGC1068 was considered by Burbidge and Stein (1970); the limitations for BL Lac objects are orders of magnitude more severe. A general critique of thermal models is given by Jones and Kellogg (1972).

4.4. Details of the Observations

In this section the characteristics of infrared flux, variability and polarization are extracted from the data. Initially, they are interpreted in terms of the canonical model of isotropic incoherent synchrotron emission. In most cases the data does not require any more sophisticated model, but in a later section the ideas of relativistic 'beaming' are included and the infrared observations are merged with the other data which indicates 'beaming'.

4.4.1 Luminosity and Variability Timescale

For the case of isotropic emission, some parameters can be defined which are independent of the exact emission process. As in Cavaliere and Morrison (1980) define

$$L/R = (1+z)L_{IR}/ct_{VAR} \qquad (4.74)$$

L/R defines the optical depth for photon-electron collisions in a region of energy density W; the number of collisions expected will be

$$(\tau_e)_N = \sigma_T(\frac{W}{h\nu})R = 3 \times 10^5 L_{45}/R_{15}\nu_{15} \qquad (4.75)$$

$L_{45}=L/10^{45}$ergs s^{-1}
$R_{15}=R/10^{15}$cm.
$\nu_{15}=\nu/10^{15}$Hz.

where the photon density is $W/h\nu$. In the extreme relativistic case, the optical depth is reduced by the fractional energy loss per electron, but is still in general much greater than unity

$$(\tau_e)_{Rel} \simeq (\tau_e)_N \quad \gamma^2 \frac{h\nu}{\gamma mc^2} = \gamma L_{45}/R_{15} \qquad (4.76)$$

This interaction rate applies both to inverse Compton losses and synchrotron losses. The transition from inverse Compton to synchroton occurs when $U_B > L/4\pi R^2 c$ or

$$B^2 > \frac{L}{2R^2 c} \qquad (4.77)$$

The synchrotron cooling time for the electrons is given by (4.50), and this can be compared to the electron crossing time of the source ($v \sim c$). These five parameters are listed in the first five columns of Table 4.3. The parameter L/R indicates that in all cases the optical depth τ_e to radiation transfer is large. The compactness of BL Lac objects leads to efficient energy loss from the high energy electrons, and is the basis of the 'inverse Compton catastrophe' as described by Hoyle *et al.* (1966). In Table 4.3, the magnetic field necessary to make $U_B > U_{ph}$ is listed in which case synchrotron losses dominate. For the most luminous sources, $B \sim 10^4$G is necessary to prevent excessive Compton losses. The inevitable result, independent of emission mechanism, is that the radiative lifetime of an electron $t_{\frac{1}{2}}$ is far less than the travel time across the source R/v ($V \sim c$). As pointed out by Blandford and Rees (1978), 'spent' electrons will rapidly accumulate and cut-off photon emission by drastically increasing the Thomson optical depth.

Since the energy during t_{VAR} is Lt_{VAR}, the number of electrons

contributing to this energy is $Lt_{VAR}/\gamma mc^2 N$, where N is the number of reaccelerations. Given a Thomson optical depth $\tau_T = n_e \sigma_T / R^2$, the condition on N for $\tau_T < 1$ is

$$N > \frac{\sigma_T L}{\gamma mc^4 t_{VAR}} \qquad (4.78)$$

Typically, this leads to $N > 100$ for $\gamma \sim 50$ (which is low enough to ensure the predominance of synchrotron over Compton losses). The luminous sources can only remain optically thin if the electrons are re-cycled many times. Another constraint is that the density of 'cold' electrons should not be sufficient to Faraday depolarize the continuum flux. For a number density of $Lt_{VAR}/\gamma mc^2 R^2$, the Faraday rotation is given by equation (4.67) and the condition on t_{VAR} becomes

$$t_{VAR} > \frac{\gamma m^3 c^4 \omega^2 R^2}{2\pi e^3 B_{||}} \qquad (4.79)$$

This limit is not severe at infrared wavelengths, but in the radio regime ($\omega \sim 10^8$ Hz), the variability timescale must be days or the condition $\Delta\theta \sim 1$ radian is not satisfied. The result of these simple arguments is that the eight BL Lac objects with redshifts and infrared variability timescales split into two groups. The luminous group (0235+164, 0735+178, OJ287, 1308+326 and 3C446) require magnetic fields >1000G, have very short synchrotron cooling times and require reacceleration of the electrons if the variable, polarized flux is to emerge. The other three sources are explicable in the isotropic model for smaller magnetic fields; and although $t_{\frac{1}{2}} \ll R/v$ in all cases, the energy density is smaller and reacceleration is not required to keep the opacity to Thomson scattering low. The problems of the luminous sources have been tackled in two ways. Blandford and Rees (1978) have proposed relativistic bulk motion in a beam of opening angle Γ^{-2} (where Γ is the bulk Lorentz factor). A moderate factor of $\Gamma = 10$ would reduce timescales and luminosities in the proper frame to values in agreement with brightness temperature and Compton-scattered X-ray limits. The problems are then transferred onto finding an efficient electron acceleration mechanism. Cavelière

and Morrison (1980) have avoided collimated beaming at small pitch angles ($\Psi < 1$) and propose continuous reacceleration in the emitting region itself. The rate of reacceleration balances the rate of radiative loss in the extreme equilibrium situation they describe. The acceleration mechanism must be very efficient.

It is central to the previous discussion that synchrotron losses dominate Compton losses in luminous BL Lac objects at infrared wavelengths. Since the high magnetic fields and short radiative lifetimes of Table 4.3 are a direct result of this condition, it is worth studying the role of Compton scattering in more detail. The synchrotron interpretation of the optical/IR continuum in BL Lac objects is quite secure. It is based on the high polarizations observed and the fact that the spectra are well fitted by a power law which extends smoothly through the infrared and sub-millimetre points to the high frequency radio data. BL Lacs are the only extragalactic class to show simultaneous outbursts in the optical and radio regions, where the synchrotron interpretation has been confirmed.

At radio wavelengths, the maximum brightness temperature of a source emitting incoherent synchrotron radiation is 10^{12}K (equation 4.63). Above that level, the source will rapidly lose energy by Compton losses and radio photons will be up-scattered by a typical factor of γ^2 into the X-ray region. The ratio of Compton to synchrotron flux is a sensitive function of the brightness temperature (equation 4.62), which is itself a function of the observed angular diameter θ. Therefore the expressions for the magnetic field and electron Lorentz factors are poorly determined unless the angular diameter is accurately known. Consequently, the procedure is often reversed and limits on the X-ray flux are used to put limits on the equipartition field.

At infrared wavelengths, the energy density of some BL Lac objects will also lead to excessive Compton X and γ-ray fluxes unless the magnetic field is appropriately strong. Consider the most luminous source in the sample, 3C446. From Figure 4.3 and the 2.2μm fluxes in Table 3.4, the infrared/optical spectrum of

3C446 is well represented by a power law of slope -1 and a spectrum of $1.5 \times 10^{-13} \nu^{-1} Wm^{-2}$. The luminosity distance is 5620Mpc and the variability timescale defines a source dimension of 1.1×10^{25}cm. Taking the limits of the spectrum to be 0.3 - 20μm and using the approximations of Rieke and Weekes (1969) to calculate the high energy spectral flux gives $1.2 \times 10^{-28} Wm^{-2} Hz^{-1}$ at 10^{18}Hz (∿4KeV). This corresponds to almost 600 times the 2-6KeV sensitivity of the UHURU catalogue, where 3C446 was not detected (Giacconi et al., 1974). Therefore the source is constrained to have no Compton-scattered X-ray flux, leading to the requirement that $U_B > U_{ph}$ and the magnetic field is large (equation 4.77). 3C446 is among the extragalactic sources which have been detected by the sensitive Einstein X-ray telescope. Tanambaum et al. (1979) quote a measurement in the 0.23-1.8keV band of $1.5 \times 10^{-33} Wm^{-2} Hz^{-1}$. Similarly severe X-ray limits have been set for the rest of the sample, except 2155-304, which was originally detected as an X-ray source (Schwartz et al., 1979; Mushotzky et al., 1978; Agrawal & Riegler, 1979). The origin of the X-ray flux in BL Lac objects is uncertain. Soft X-ray luminosities are comparable to optical luminosities for most quasars and BL Lac objects. The small range of Lx/Lo and the smooth spectral energy distribution from optical to higher frequencies implies that the soft X-rays come from the high frequency tail of the optical and infrared synchrotron emission. For some BL Lacs both the high and low energy X-ray components join up to the optical data in a single power law (Ledden et al., 1980). The X-ray measurements support the contention that the infrared flux is dominated by synchrotron losses.

The difficulties caused by high infrared energy densities can be illustrated for 3C446. For pure synchrotron losses, the equation for synchrotron power (4.27) can be integrated over a power law energy distribution $\int N_o E^{-p} P(E) dE \rightarrow N_o B_\perp \int E^{-p+1} \delta(\nu - \nu_c) d\nu_c$ where ν_c is the critical frequency ($\nu_c \propto B_\perp E^2$). For p = 2, this reduces to an electron lifetime of $\tau = 10^{12} \nu^{-\frac{1}{2}} H^{-3/2}$ seconds. If

the dimension of the source is $r = \tau c$, then the field energy can be given as $B^2/8\pi = 5 \times 10^{28} \nu^{-2/3} r^{-4/3}$. Secondly, the radiation energy is given simply in terms of the luminosity Uph $= 4R^2 F_\nu (1+z)/r^2 c$ where R is the distance of the source. The ratio is

$$\frac{\text{Uph}}{(B^2/8\pi)} = \frac{4R^2 F_\nu (1+z)}{5 \times 10^{28} c} \left(\frac{\nu}{r}\right)^{2/3} \qquad (4.80)$$

Taking values for 3C446 of $R = 1.7 \times 10^{28}$ cm, $r = 1.1 \times 10^{15}$ cm, $\nu = 1.4 \times 10^{14}$ Hz and $F_\nu = 10^{-11}$ ergs cm^{-2} s^{-1} gives Uph/$(B^2/8\pi) = 4.7 \times 10^6$. The problem with this result is clear: Uph was calculated only for synchrotron losses but for the synchrotron process Uph/$(B^2/8\pi)$ must not exceed unity. Therefore the energy density from the Compton process must be $>10^6$ times greater than the synchrotron energy density, which not only leads to a catastrophic X and γ-ray flux but makes a synchrotron self-Compton flux inevitable. In the synchrotron self-Compton process a photon is inverse Compton scattered by the electron which has just emitted it by the synchrotron mechanism. The photon energy gain of γ^4 leads to an even greater divergence with observations.

For an isotropic source with uniform pitch angle distribution the only three ways to ease this dilemma are to adopt non-cosmological redshifts, reduce the energies by invoking a relativistic motion of the emitting region towards the observer and reduce the 'coherence' length of the source r. Given the energy densities (at cosmological redshifts), it is inevitable that the electrons must be reaccelerated within the emitting volume. If they are reaccelerated N times, the conflict is reduced by $\sim(N)^{2/3}$. It is also likely that relativistic motion of the emitting volume plays a part in reducing Uph/$(B^2/8\pi)$.

4.4.2 High Degree of Polarization

High and variable linear polarization was observed in 13 out of the 17 objects. In eight BL Lacs, p_{MAX} was >12% and in two it was >25%. In many cases both the maximum value and range of polarization are a function of how frequently the object has been observed, but there is a definite relationship between the published range of optical variability and maximum degree of polarization. In a variability study by Usher (1975), 11 of his 13 objects with $\Delta B > 2$ magnitudes were highly polarized; and in a similar study by Grandi and Tifft (1974) 6 out of 8 objects with $\Delta B > 2$ were BL Lac objects. A second strong correlation is between infrared spectral index and maximum degree of polarization. The redder sources tend to be more highly polarized. This has been recognized in terms of optical spectral index for some time (Kinman, 1976; Stein et al., 1976). The two distributions are shown in Figure 4.10. There is no obvious correlation between ΔB and P_{IR}^{MAX}, but the average ΔB and P_{IR}^{MAX} for a complete radio sample is shown and all the BL Lac objects have both greater variability and higher polarization than the means for a quasar. Extreme variability and polarization are therefore related. In Figure 4.10b, there is a surprisingly good correlation between redness and maximum polarization. Only 0735+178 lies appreciably off the best-fit line through the points. Interestingly, 0735+178 is farthest removed from the other points in Figure 4.10a as well. Infrared excess, variability and polarization are all related in this sample.

The emitting regions must be optically thin to produce high polarizations. Faraday rotation along the line-of-sight is negligible, because $\Delta\theta > 1$ radian would wash out the polarization. The implication

of the synchrotron mechanism is that the polarization directly reflects the magnetic field geometry in the emitting region. Any changes in polarization and position angle represent changes in the structure of the field rather than propagation effects. The great value of infrared (and optical) polarimetry is that the flux and variability define a small emitting volume, and the high polarization defines a well-ordered field. In no other part of the spectrum are these restraints as severe.

The limit on thermal plasma within the source comes from equation (4.67),

$$n_e B \cos\theta < 1.9 \times 10^9 \qquad (4.81)$$

where θ is the angle between B and the line of sight. This relation is satisfied for the large magnetic fields derived in Table 4.3 for any reasonable plasma density. In fact a far more severe restriction on the amount of thermal gas in BL Lac objects comes from the lack of strong emission lines. In quasars the emitting gas is distributed in small clouds and filaments with a small filling factor, each cloud being optically thick to Lyman continuum flux. Shields has shown that to create broad emission lines around a continuum source of optical luminosity 10^{46} erg/sec requires only a mass $M \sim 2.0 \times 10^6 M_\odot / n_e$ of gas (Shields, 1978). For a typical broad-line region of $n_e \sim 10^9 cm^{-3}$ a small fraction of a solar mass of gas is present. Yet, as seen in Section 4.1.5, large masses of gas are accreted in the lifetime of an active BL Lac object. The accretion geometry presumably explains the differences in the emission-line properties of quasars and BL Lacs.

The degree of polarization in a homogeneous field is given by (4.43). The maximum value depends only on the local spectral index. A homogeneity parameters can be defined as the ratio of the maximum measured value to the maximum allowed value

$$h = \Pi / p_{IR}^{MAX} \qquad (4.82)$$

It is also possible to define the average shear angle on the field to produce a given value of h. Assuming that the line-of-sight contains components of B uniformly distributed at shear angles of θ_1, θ_2, $\theta_3 \ldots \theta_{MAX}$, then the intergrated shear component is

$$nhB = 2(B\,\mathrm{Cos}\theta_1 + B\,\mathrm{Cos}\theta_2 + \ldots B\,\mathrm{Cos}\theta_n) = 2Bn\int_0^{\theta_{MAX}} \mathrm{Cos}\theta d\theta \qquad (4.83a)$$

$$\bar{\theta} = \tfrac{1}{2}(90^\circ - \arcsin(h)) \qquad (4.83b)$$

The values of $\bar{\theta}$ are given in Table 4.4, where $\bar{\theta} = 45^\circ$ corresponds to a range of θ of 90° and a completely turbulent field. The range of shear is small ($\sim 22^\circ$) between all the objects. In these simple terms the amount of alignment needed to change the 2.2μm polarization of AO 0235+164 from 29% to 15%.(Table 3.3) is only 10°. However, this represents a net alignment over the whole emitting volume in an environment which is magnetically dominated ($U_B > U_{ph}$). Therefore a large amount of energy in shock fronts or relativistic particles is needed to compress the field.

As seen in Table 4.4, h ranges up to 0.42 which represents nearly half the maximum polarization for the uniform field case. Since a completely uniform field is unphysical in a cosmic source, an impressive degree of alignment is involved. The highest value of h occurred in AO 0235+164 during a polarization burst, when the optical polarization rose to 44%. The range of polarization in this source is enormous: at optical wavelengths from 6-44%. In general, high polarizations are temporary and occur during flares in the source. The only BL Lac objects with stable polarizations are the ones with low levels (e.g. 2155-304, AP Lib), indicating that the emission and field alignment mechanisms are closely related. As always with BL Lacs, there is an exception to this behaviour. 0735+178 maintained a level of 2.2μm polarization of $\sim$20% for five nights (see Section 3.3.3) which is uncommon. An alignment mechanism must feature in any model of these sources.

4.4.3 Wavelength-dependent Polarization

There are two objects with evidence of wavelength dependence of polarization (Figure 3.4). In both cases the degree of polarization increases towards shorter wavelengths. The amount is small but was confirmed by successive observations and in the case of 0235+164, optical polarimetry on a baseline out to 0.4μm continues the trend (figure 3.5b) Making the assumption that these two sources lie at the cosmological distances indicated by their redshifts, and that the

compact source lies at the centre of a normal galaxy, it is possible to discover whether the wavelength dependence is intrinsic to the BL Lac object or the effect of thermal dilution from the galaxy. Most BL Lac objects show constant polarization over the optical part of the spectrum (Moore et al., 1980), and the few observations over the longer baseline of the near infrared generally support this. The exceptions include OJ287 (Kikuchi et al., 1976), 0735+178 (Nordsieck, 1976) and BL Lac (Puschell & Stein, 1980). The polarization increase towards the blue in BL Lac is too large to be caused by dilution from a galactic component. For the low redshift objects Mk 421 and Mk 501, Maza et al. (1978) explained a slight wavelength dependence in the optical with a two-component model. 0235+164 and 0735+178 have redshifts of 0.852 (absorption) and 0.424 and there is no sign of surrounding nebulosity in either case.

To determine the visual luminosity, the infrared spectral index is used to extrapolate the spectral flux down to the appropriately redshifted optical windows. $H_o = 75 kms^{-1} Mpc^{-2}$ and $q_o = 0$ are assumed throughout. The rest frame luminosities per unit frequency for the two objects are

$$\begin{aligned} L(0.55\mu m) &= 8 \times 10^{32} ergs\ s^{-1} Hz^{-1} \quad \text{AO 0235+164} \\ L(0.55\mu m) &= 3 \times 10^{30} ergs\ s^{-1} Hz^{-1} \quad \text{0735+178} \end{aligned} \qquad (4.84)$$

First ranked cluster galaxies (usually giant ellipticals) have a magnitude range $-23.4 < M_V < -21.4$ (Burbidge, 1974; Frogel et al., 1978) for $H_o = 75 kms^{-1} Mpc^{-1}$. The corresponding magnitudes for 0235+164 and 0735+178 are $M_V = -32.1$ and -26.0 respectively. It is straightforward to show that dilution from a galactive component has a negligible effect on the polarization of the non-thermal sources. The visual luminosity of 0235+164 is more than 100 times that of a first-ranked giant elliptical, therefore none of the observed parameters are contaminated. 0735+178 is less luminous, but it is still possible to calculate that the wavelength-dependent polarization must be intrinsic to the non-therral source. In the worst case, assume that the surrounding galaxy is at the top of the range for elliptical galaxies (-23.4) and that the BL Lac object is at its faintest measured

flux level. The only uncertainty in the other direction is if the spectral index decreases at optical wavelengths, hence the optical luminosity inferred by extrapolating the IR flux would be an overestimate. Figure 4.11 shows the appropriately redshifted energy distribution for a giant elliptical (from Whitford, 1971 and Grasdalen 1980) and the measured power law for the BL Lac object. It is clear that from 1-2μm the relative contribution of the elliptical is decreasing sharply, because the BL Lac flux is rising rapidly and the galaxy flux is beginning to decrease. Therefore the galaxian dilution will decrease with increasing wavelength, in the opposite sense to the observed wavelength dependence. Not only must $p(\lambda)$ be intrinsic to the BL Lac object, but if the galaxy contributes a sizeable fraction (10-20%) of the infrared flux then the intrinsic $p(\lambda)$ is even steeper than observed. The optical appearance of 0735+178 gives no indication of extended image structure on the Polomar Sky Survey plates, so it is very reasonable to attribute the wavelength dependent polarization to the compact BL Lac object.

The degree of polarization of synchrotron radiation in a uniform field depends only on the spectral index of the flux distribution. For simple power law spectra, the linear polarization will be wavelength independent (equation 4.4.3). If the spectral index changes with wavelength, so will the maximum degree of polarization. Assuming that the observed polarization is always a fixed percentage of the maximum allowed value,

$$dp = d\Pi = \frac{6\alpha}{(3\alpha+5)^2}\, d\alpha \qquad (4.85)$$

where α is the spectral flux power law slope. In many BL Lac objects the power law steepens in the optical, and in the objects where wavelength dependence is seen it is always increasing towards the blue as predicted by equation (4.85). However, this statistical correlation is weak and in the only object with reasonable wavelength coverage, the prediction is not borne out. Over the duration of the burst in December 1979, of AO 0235+164, the IR spectral index changed from $\alpha = 2.4$ to $\alpha = 1.1$ which is highly significant with respect to the 5% photometric errors. The polarization would therefore be expected

to change by ∿15% of its value, when in fact the polarization flare was far more spectacular, and unrelated in any obvious way to α. Also the wavelength dependence stayed constant (Figure 3.4) during the time that the spectral flux developed from a power law to a curved spectrum. The stability of p(λ) for 0235+164 is intriguing; a more detailed model will be considered in the next Chapter.

4.4.4 Polarization-Flux Relationship

As mentioned in Chapter Three, the relationship between changing total and polarized flux in BL Lac objects is particularly interesting. It represents the interplay between the aligned magnetic field which produces the high degree of polarization and the emission mechanism, which (if it is synchrotron radiation) hinges on the strength of the magnetic field. It is difficult to perceive trends by looking at the nightly variations in an individual object. Sometimes the polarization increases as the flux increases, and sometimes it decreases. Every combination seems to occur, and few of the night-to-night changes are large enough to dominate the errors by a large factor. The first stage is to look for any statistical correlations. The changes in total and polarized flux were calculated between every pair of adjacent nights of observation for every object. These data points can be compared with a simple two-component model: one component with a steady flux and arbitrary polarization, and a second, variable component of fixed polarization p. The realization of this situation might be a variable beam pointed at the observer imbedded in a disc region of low polarization. The initial flux is,

$$I^{A}_{tot} = I_u + I_p \qquad (4.86)$$

where I_u and I_p are unpolarized and polarized fluxes. The change is entirely due to the second component,

$$I^{B}_{tot} = I_u + I_p + I'_u + pI'_{tot} \qquad (4.87)$$

Therefore the change in polarized flux is

$$\Delta I_p = I_p^B - I_p^A = pI'_{tot} \qquad (4.88)$$

But I'_{tot} is just the change in total flux, therefore

$$\Delta I_p = p\Delta I_{tot} \qquad (4.89)$$

This simple result means that the slope of the ΔI_p vs. ΔI_{tot} plot gives the polarization of the variable component. The test of whether nature is so simple is shown in Figure 4.12. The area between the x-axis and the long dashed line corresponds to $p < 100\%$ and positive, and the unshaded area corresponds to the more physically realizable $p < 75\%$. Out of the 47 data points, 37 lie within the allowed region for a two component model. However, points are scattered in all four quadrants and the relationship is not clear. A more interesting result emerges if two BL Lacs, 0735+178 and OJ 287, are plotted separately. There are 22 points for these objects, and 20 lie within the unshaded zone. These objects are represented by crosses in Figure 4.12. Figure 4.13 shows that the two-component model is tolerably good for 0735+178 and OJ 287. The inferred polarizations, p, for each data point have a small dispersion and the mean is centred at small, positive p. Considering that the observations are collated from 3 runs separated by 9 months, the scatter is surprisingly small. The calculated polarizations for the variable components are,

$$\begin{aligned} &0735{+}178 : \quad p = 0.14 \pm 0.12 \\ &0851{+}202 : \quad p = 0.15 \pm 0.17 \end{aligned} \qquad (4.90)$$

p and $\sigma(p)$ for 4 other objects are shown in Table 4.4; in these cases there is no well-defined stable value. Therefore a definite difference in the polarization behaviour of BL Lac objects has been detected. For two well-studied objects, the variations in flux and polarization are interpreted as the effect of a variable source of polarization of order 15% on a stable background source. There is no requirement that the variable component should always have $p \sim 15\%$ since the maximum optical polarizations for both objects are

considerably higher than that (31% for 0735+178, 32% for OJ 287). For the other sources there is no correlation between changes in total and polarized flux, and this is not simply an effect of fewer data points. Whether the two kinds of behaviour can be seen at different times in the same object is not known.

The formal coefficient of determination (r^2) is noted in Figure 4.12. r^2 is about 5 x higher for the two noted BL Lac objects and the difference between these two objects and the rest is significant at the 2.5σ level. r^2 is defined by,

$$r^2 = \frac{\left[\Sigma x_i y_i - \frac{\Sigma x_i \, \Sigma y_i}{n}\right]^2}{\left[\Sigma x_i^2 - \frac{(\Sigma x_i)^2}{n}\right]\left[\Sigma y_i^2 - \frac{(\Sigma y_i)^2}{n}\right]} \qquad (4.91)$$

where $x_i = \Delta I_{TOT}$ and $y_i = \Delta I_{POL}$. In this two-component model it should be noted that the steady component of low (or zero) polarization does not represent an underlying galaxy. For the dilution to apply the two components must have roughly equal intensity. It was shown in Section 4.4.3 that the non-thermal mechanism in 0735+178 must dominate, so the non-varying component in this model must be non-thermal in addition to the varying polarized component. A natural site for the non-varying component might be the hot, magnetically turbulent accretion zone around the central power source. For OJ 287 the argument is not as strong, because the BL Lac is nearer and fainter and a luminous giant elliptical could conceivably match the output of the compact source. However, there is no sign of an underlying galaxy on deep direct plates so the galactic dilution argument is weak. A more likely interpretation is that the static component in OJ 287 is non-thermal also.

A synchroton explanation of BL Lac objects can account for several important features. Unless beaming is invoked, an enormous range of luminosities must be explained. The large and rapid changes in polarization and position angle can be explained in terms of partially aligned magnetic fields, since Faraday effects do not dominate. The intrinsic wavelength dependent polarization in at least a couple of sources must be explained. Finally, the different behaviour for flux and polarization changes can be brought into the same framework, with simple geometries considered in the next Chapter.

TABLE 4.1 Infrared Luminosity

Object	z	d_L(M)	L_{IR}^{MAX} (erg/sec)	$\frac{L_{MAX}}{L_{MIN}}$	No. Obsn.
0235+164	0.852	3410	1.3×10^{48}	2.2	10
0735+178	0.424	1700	7.9×10^{46}	1.4	7
0851+202	0.306*	1220	4.1×10^{46}	1.9	7
1308+326	0.996	3980	1.2×10^{48}	5.8	6
1400+162	0.244*	970	1.3×10^{45}+	-	1
1514-241	0.049	200	4.1×10^{44}	-	1
1641+399	0.595	2380	8.7×10^{46}+	-	1
1652+398	0.034	140	2.9×10^{44}	1.3	2
1727+503	0.055	220	7.9×10^{43}	1.4	6
2155-304	0.17*	680	1.1×10^{46}	1.2	6
2223-052	1.404	5620	5.5×10^{48}	1.2	4

+ Optical spectral index used

* Redshift uncertain.

TABLE 4.2 Parameters of Black Hole Models

Object	t_{MIN} (10^4 s)	M_H ($10^9 M_\odot$)	L_{IR}/L_{edd}	dM/dt ($M_\odot yr^{-1}$)	ct_{MIN} (10^{15} cm)
0235+164	4.7	4.7	2.10	130	1.4
0735+178	6.1	6.0	0.10	8	1.8
0851+202	6.6	6.7	0.05	4	2.0
1308+326	4.3	4.3	2.15	120	1.3
1400+162	-	-	2×10^{-3} +	0.1 +	-
1514-241	-	-	6×10^{-4} +	0.04 +	-
1641+399	-	-	0.13 +	9 +	-
1652+398	>8.4	8.3	3×10^{-4}	0.03	>2.5
1727+503	24.6	24.7	2×10^{-5}	0.008	7.4
2155-304	16.1	16.0	0.01	1	4.8
2223-052	3.5	3.7	11.43	550	1.1

+ Assume $M_H \sim 5\times10^9 M_\odot$

TABLE 4.3 Parameters of Synchroton Models

Object	L/R ($ergs^{-1}\,cm^{-1}$)	$(T_e)_N$	$(T_e)_{Rel}$	B (gauss)	$t_{\frac{1}{2}}$ (sec)	N
0235+164	9.3×10^{32}	1.4×10^{9}	930γ	5700	0.1	500
0735+178	4.4×10^{31}	6.6×10^{7}	40γ	1100	0.7	25
0851+202	2.1×10^{31}	3.1×10^{7}	20γ	720	1.3	15
1308+326	9.2×10^{32}	1.4×10^{9}	920γ	6000	0.1	∿1
1652+398	1.2×10^{29}	1.8×10^{5}	0.1γ	48	80	<1
1727+503	1.1×10^{28}	1.7×10^{4}	0.01γ	9	1000	<1
2155-304	2.3×10^{30}	3.5×10^{6}	2γ	160	420	∿1
2223-052	5.0×10^{33}	7.5×10^{9}	5000γ	15100	0.01	1400

TABLE 4.4

	Alignment		2-Component		Features			
Object	h	$\bar{\theta}$ (deg)	p	σ(p)	p(λ)	θ(t)	p_2 +	$>L_{edd}$ *
0235+164	0.42	33	0.33	1.25	√	√	-	√
0735+178	0.39	34	0.14	0.12	√	-	√	-
0754+101	0.16	40	0.64	1.62	-	-	-	-
0851+202	0.19	40	0.15	0.17	-	√	√	-
1147+245	0.19	40	-	-	-	-	-	-
1308+326	0.25	38	0.61	0.34	-	-	-	√
1418+546	0.13	41	-	-	-	-	-	-
1514-241	0.10	42	-	-	-	-	-	-
1921-293	0.18	40	-	-	-	-	-	-
2223-052	0.21	39	-0.44	1.13	-	-	-	√

+ Fits 2-Component polarization model

* Maximum IR luminosity exceeds Eddington limit.

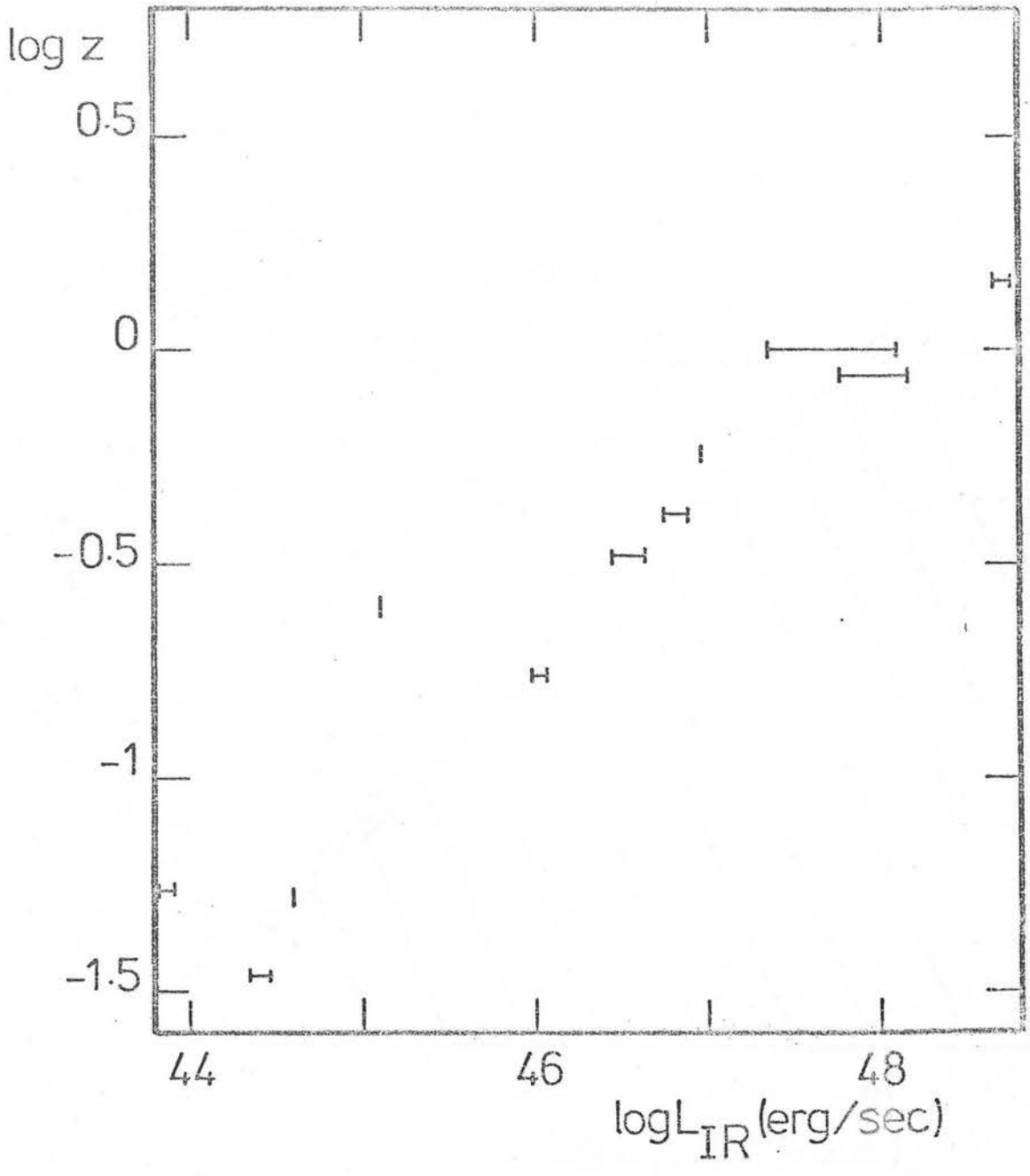

Figure 4.1 Redshift against infrared luminosity for 11 BL Lac objects. Range of luminosity (data in Chapter 3) is shown as error bar.

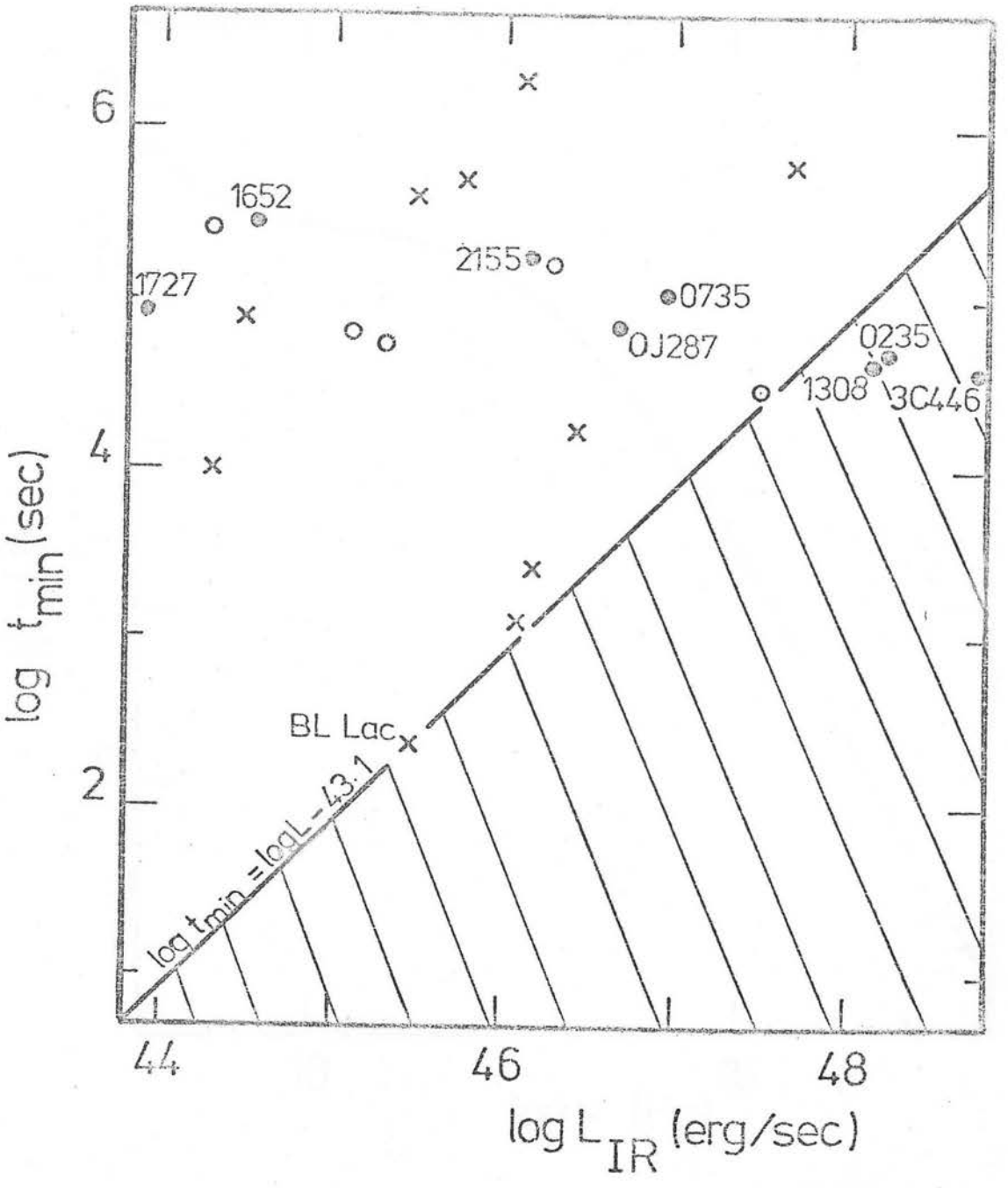

Figure 4.2 Minimum timescale of variability against infrared luminosity (from Elliot & Shapiro 1974).

x Optical quasar data from Elliot & Shapiro (1974)

• Infrared observations from this work

o Optical quasar data from Gilmore (1978)

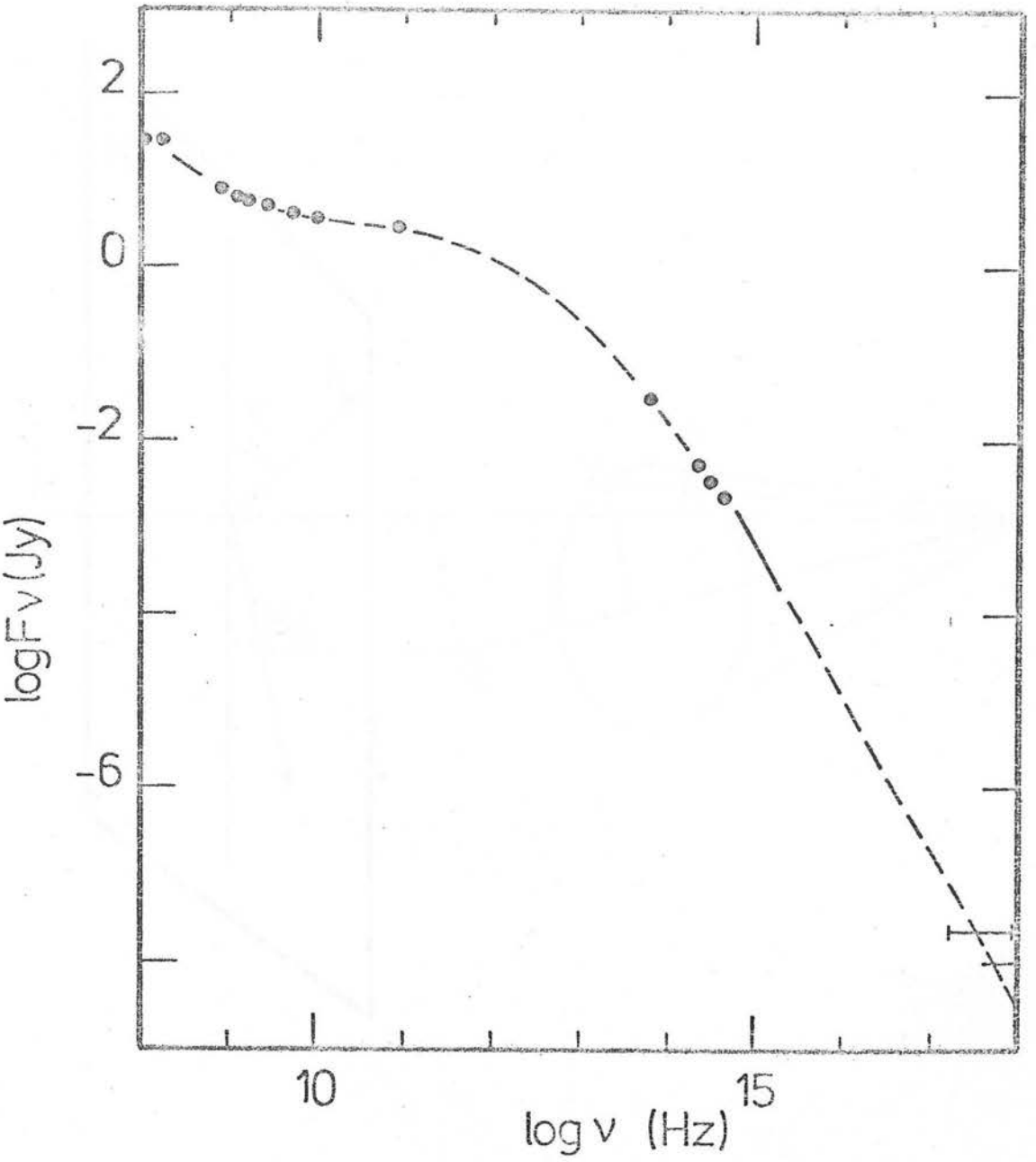

Figure 4.3 Spectral flux distribution of 3C 446.
X-ray data from Tananbaum et al. (1979)
Optical data from Oke (1966)
IR data from this work and Neugebauer et al. (1979)
Radio data from Landau et al. (1980), Wall et al. (1976), Gardner et al. (1975) and Pauliny-Toth et al. (1966).

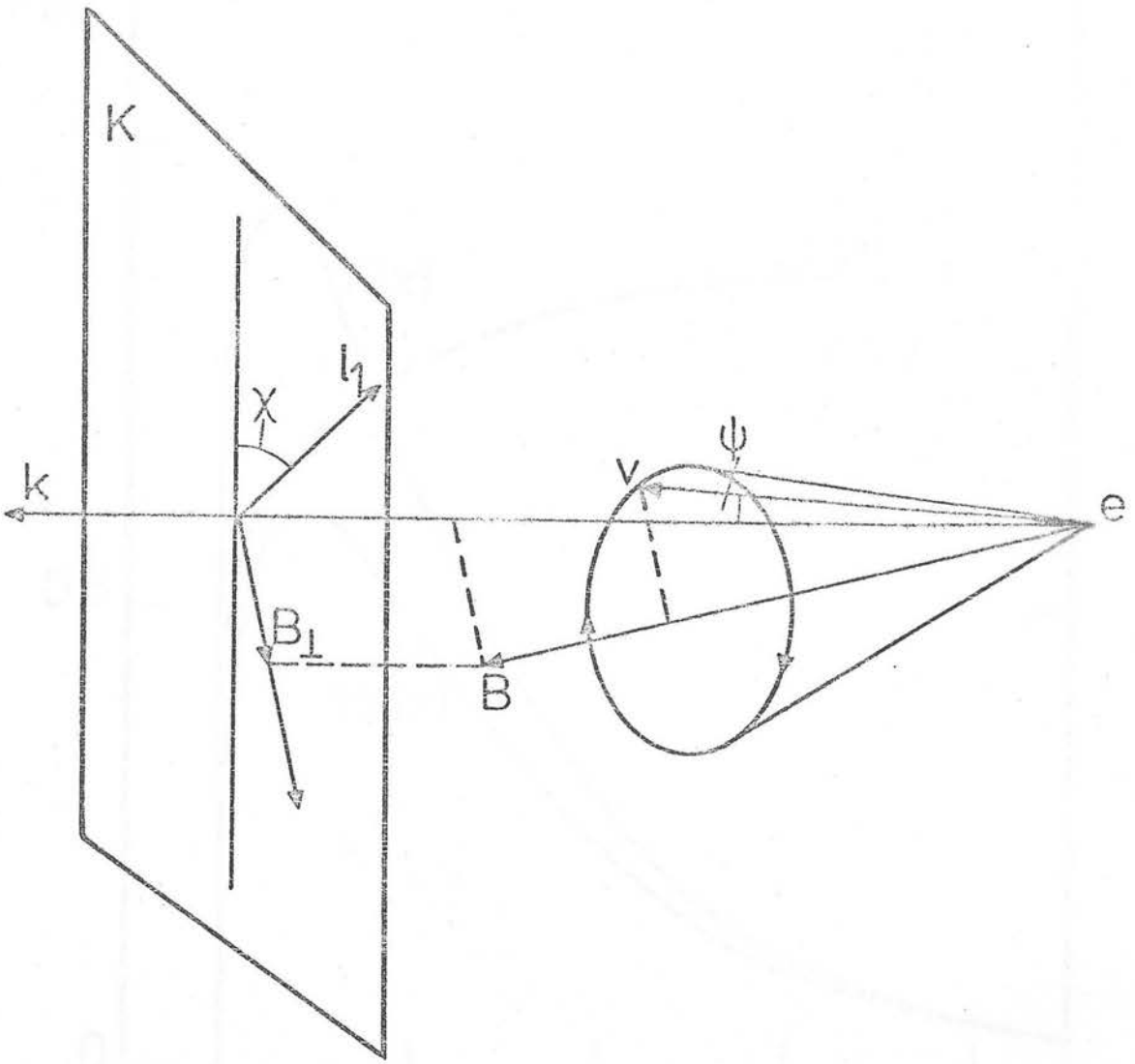

Figure 4.4 Orientation of the polarization ellipse of synchrotron radiation of an electron (taken as a positive charge). Plane K is the plane perpendicular to the direction to the observer. l_1 and l_2 are orthogonal unit vectors, one of which defines the projection of $\underline{B}$ onto the plane K.

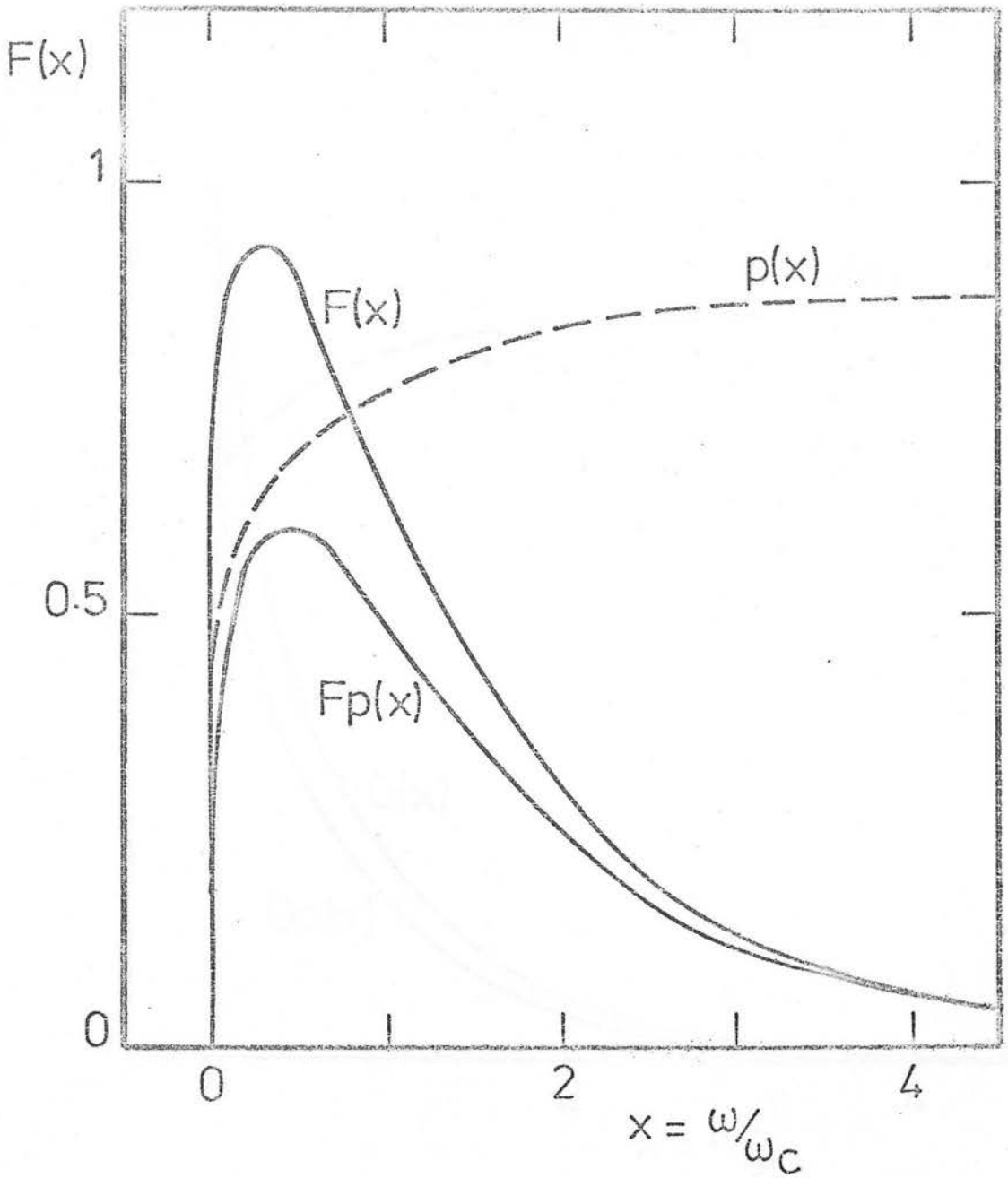

Figure 4.5 Frequency spectrum of polarization and polarized and unpolarized flux for a single relativistic electron. The maximun in the spectrum occurs at $\omega=0.29\omega_c$ (adapted from Westfold 1959).

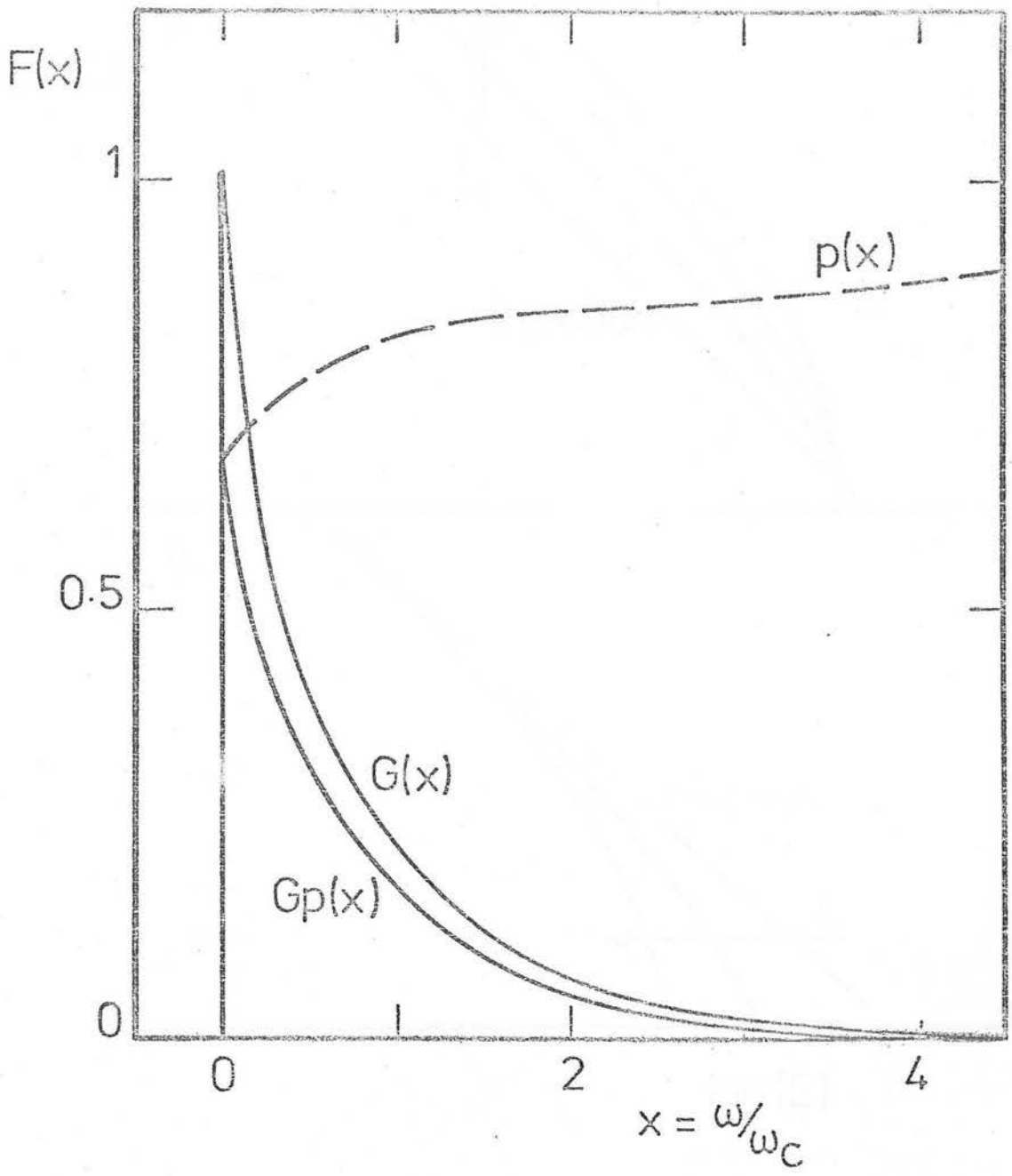

Figure 4.6 Frequency spectrum of polarized and unpolarized flux for an ensemble of electrons with $\gamma=5/2$. Polarization is shown as a dashed line. In this diagram, $G(x)=I(\omega,\underline{k})$ and $G_p(x)=\sqrt{Q(\omega,\underline{k})^2+U(\omega,\underline{k})^2}$ / $G(x)$ (adapted from Westfold 1959).

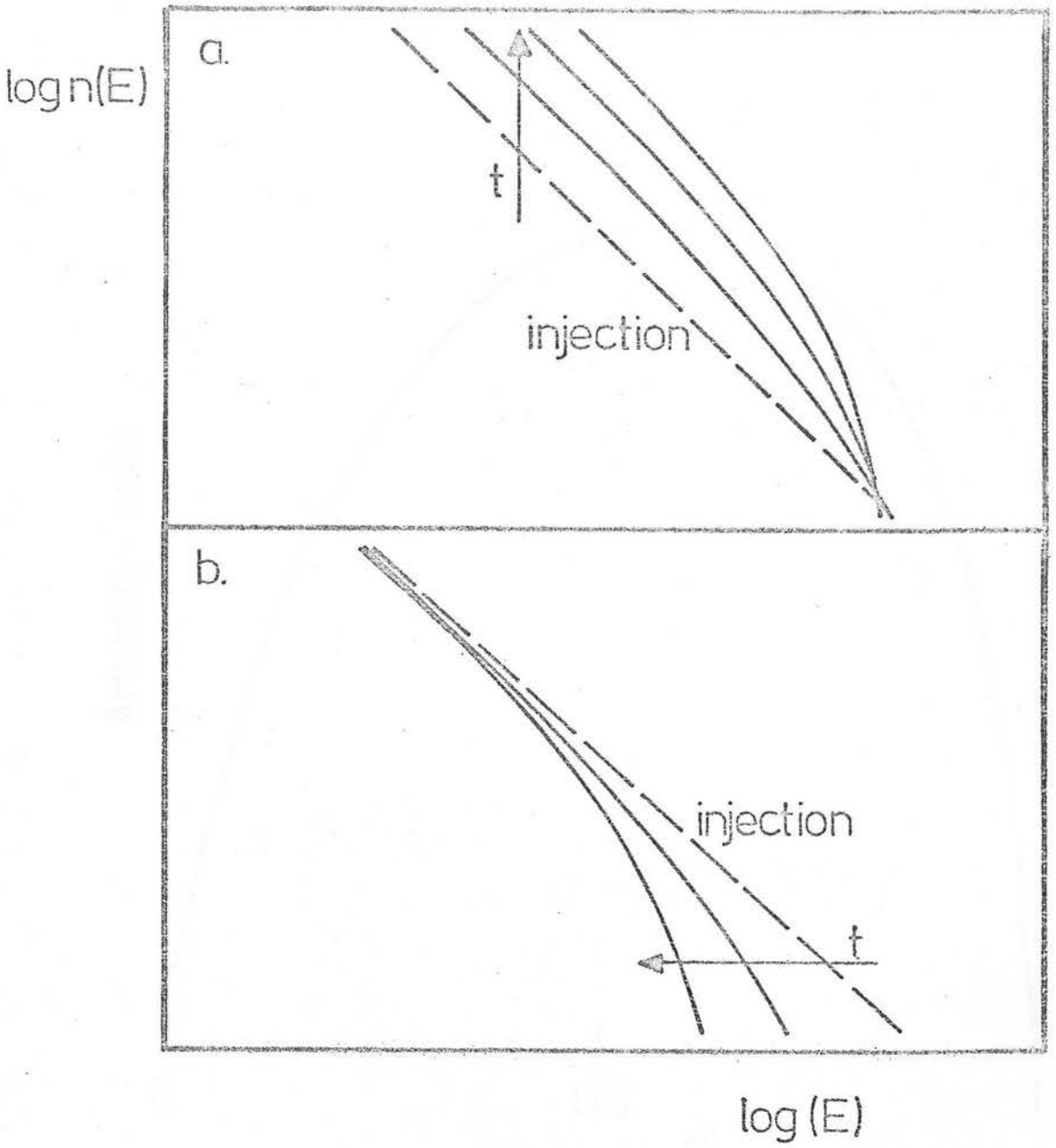

Figure 4.7 Time evolution of electrons with a power law energy spectrum:
a) with steady injection
b) with burst injection
(from Ryter 1979).

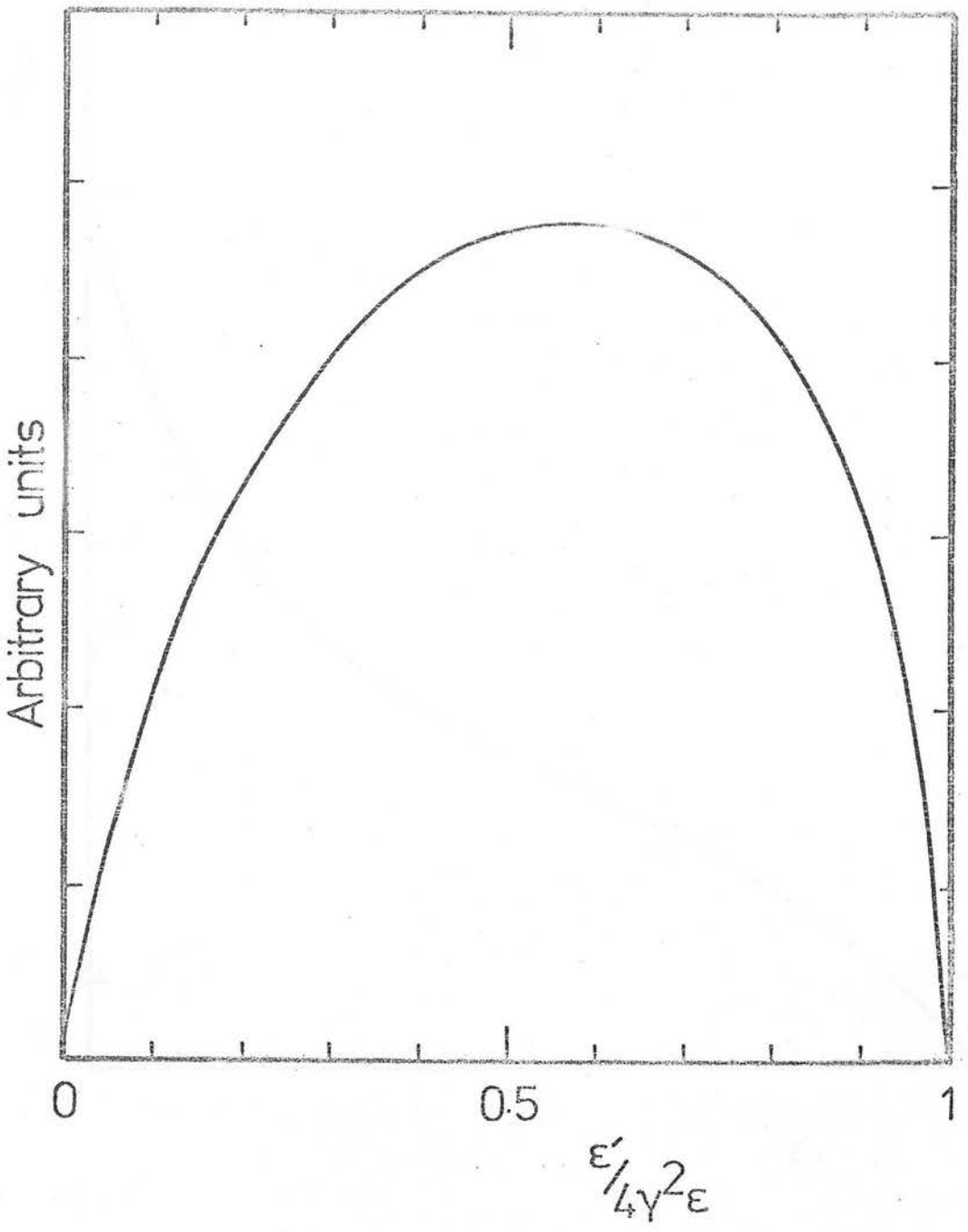

Figure 4.8 Energy distribution of photons with initial energy ε after scattering with electrons of energy γmc^2.

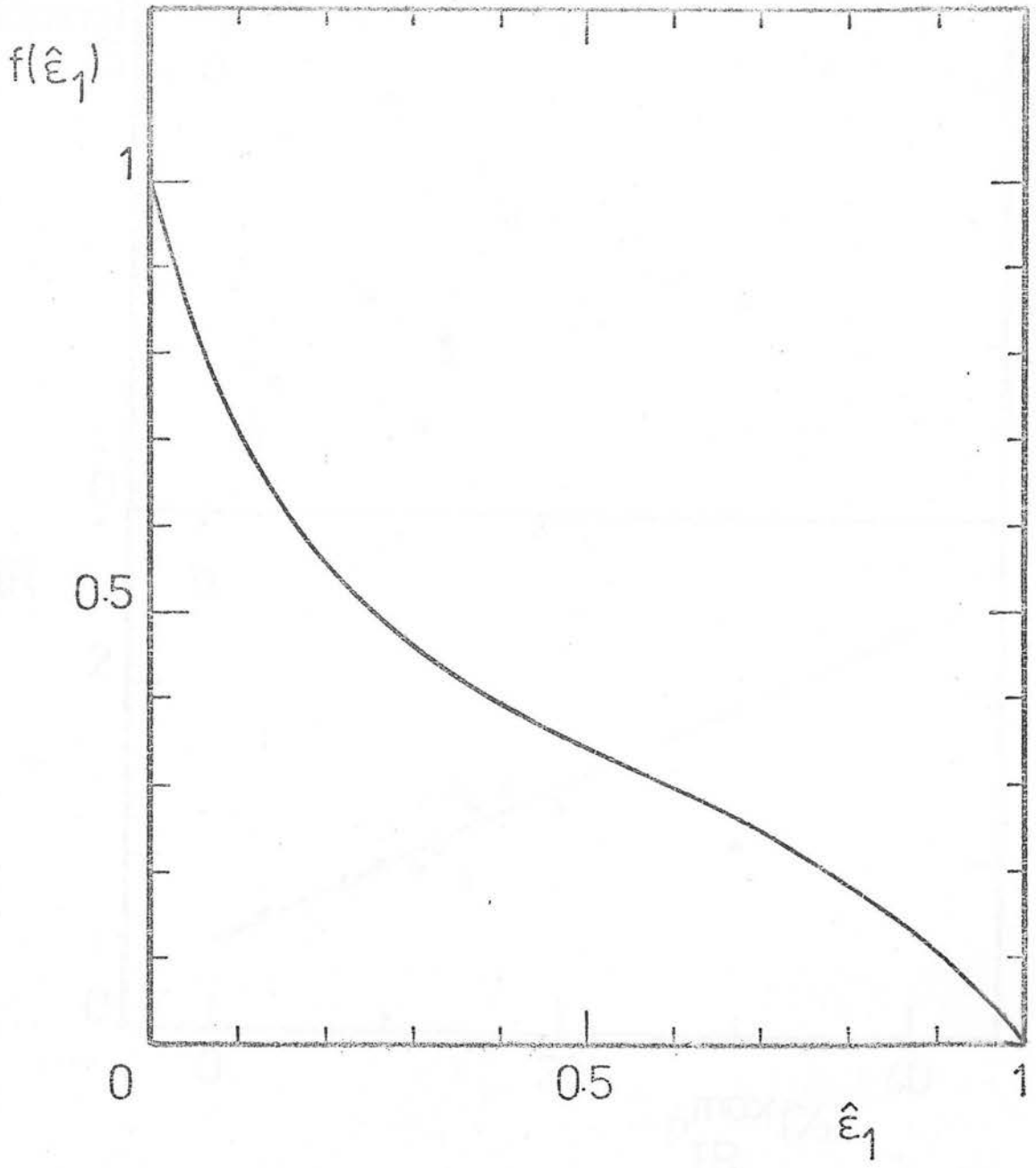

Figure 4.9 Integrated energy distribution of scattered photons in terms of the maximum energy $\varepsilon_1=4\varepsilon\gamma^2\hat{\varepsilon}_1$.

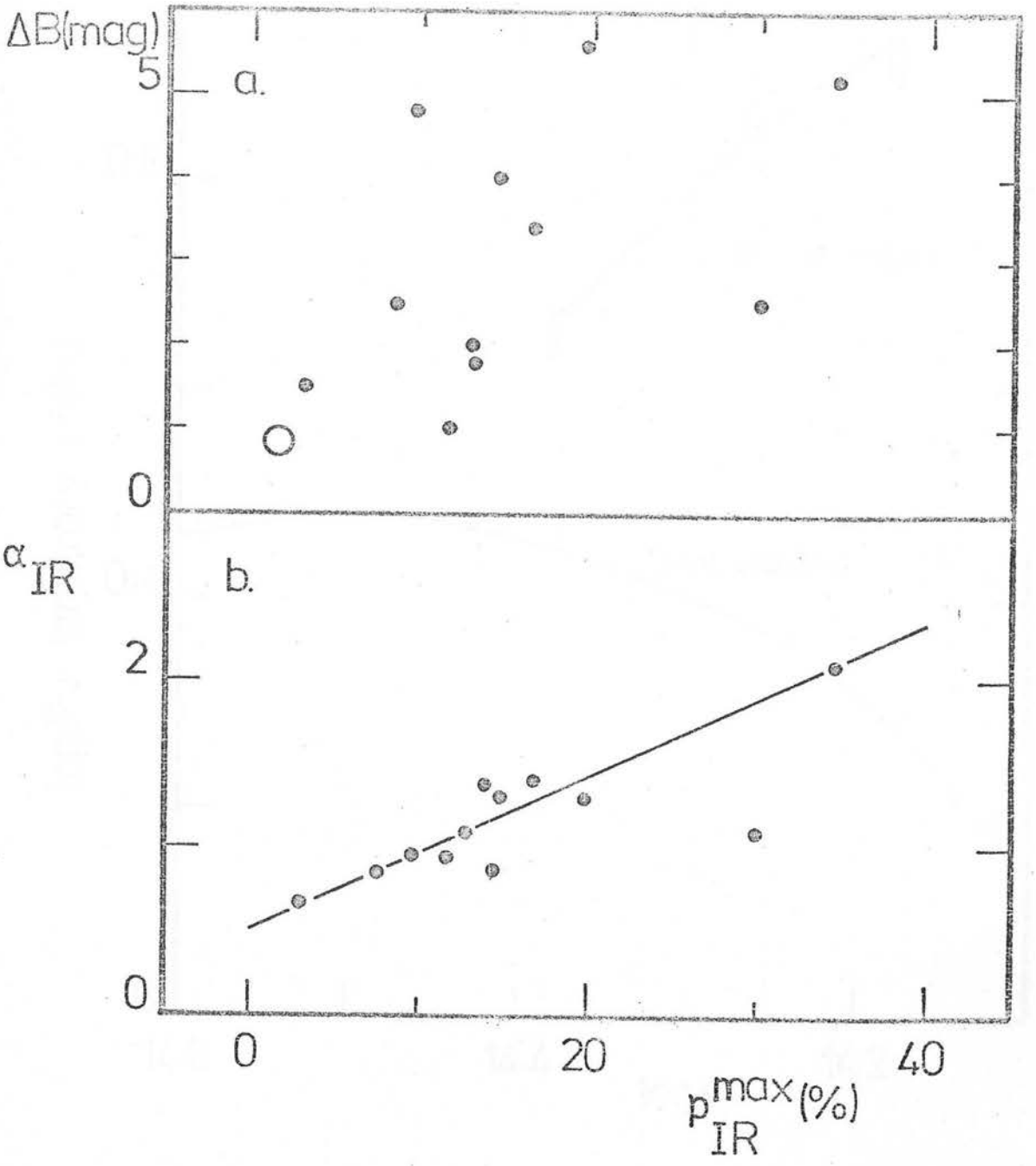

Figure 4.10 a) Optical variability against maximum polarization. Open circle is average of complete radio sample of Grandi & Tifft (1974) for ΔB and Stockman & Angel (1978) for p_{max}. Other values of ΔB are from Angel & Stockman (1980). b) IR spectral index against maximum IR polarization. All data from this work. The correlation coefficient is $r^2=0.78$ with $\sigma(p)=9.0$ and $\sigma(\alpha)=0.38$.

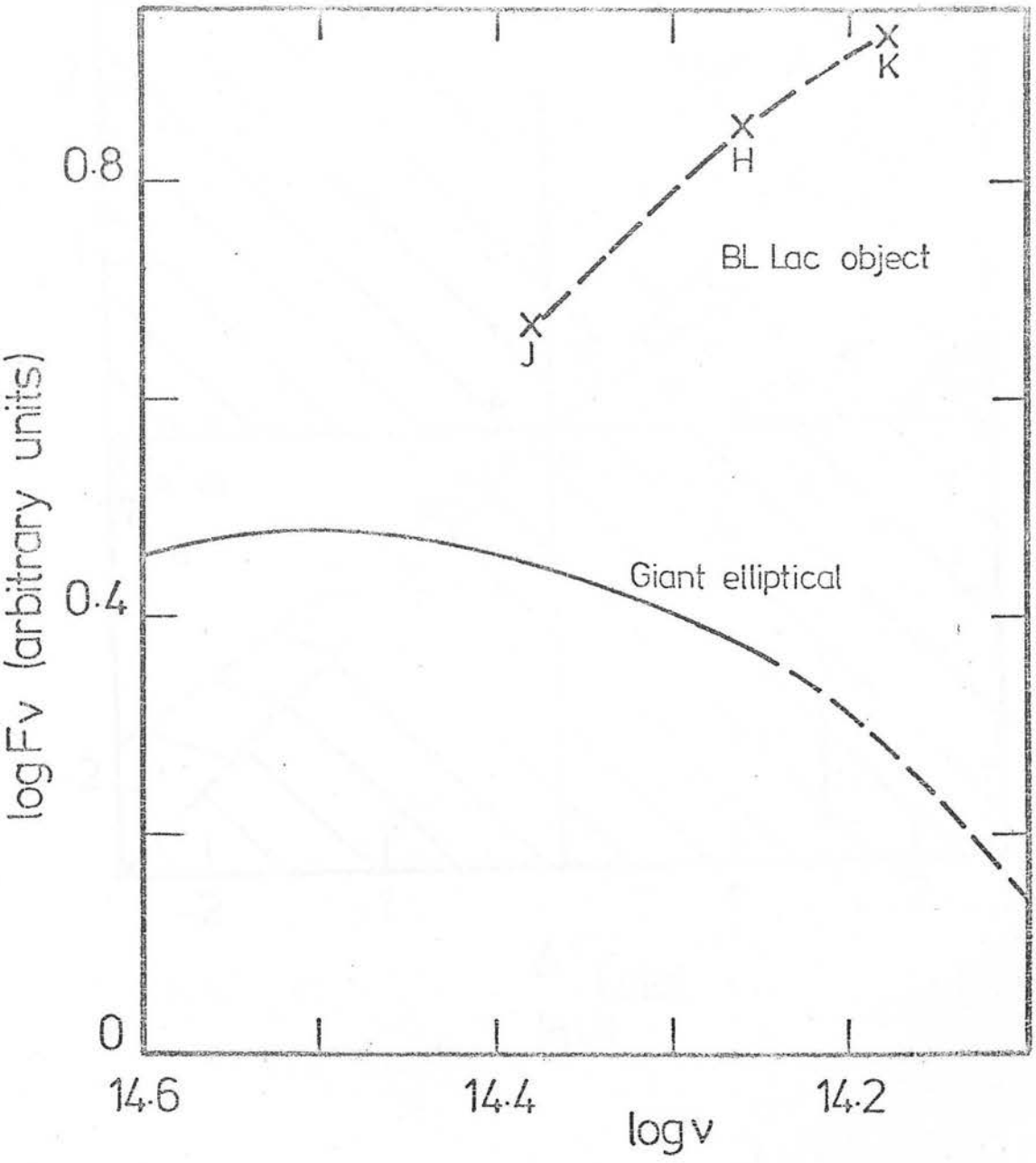

Figure 4.11 Energy distribution of giant elliptical from Whitford (1971) redshifted to z=0.424, and measured broad band fluxes for 0735+178.

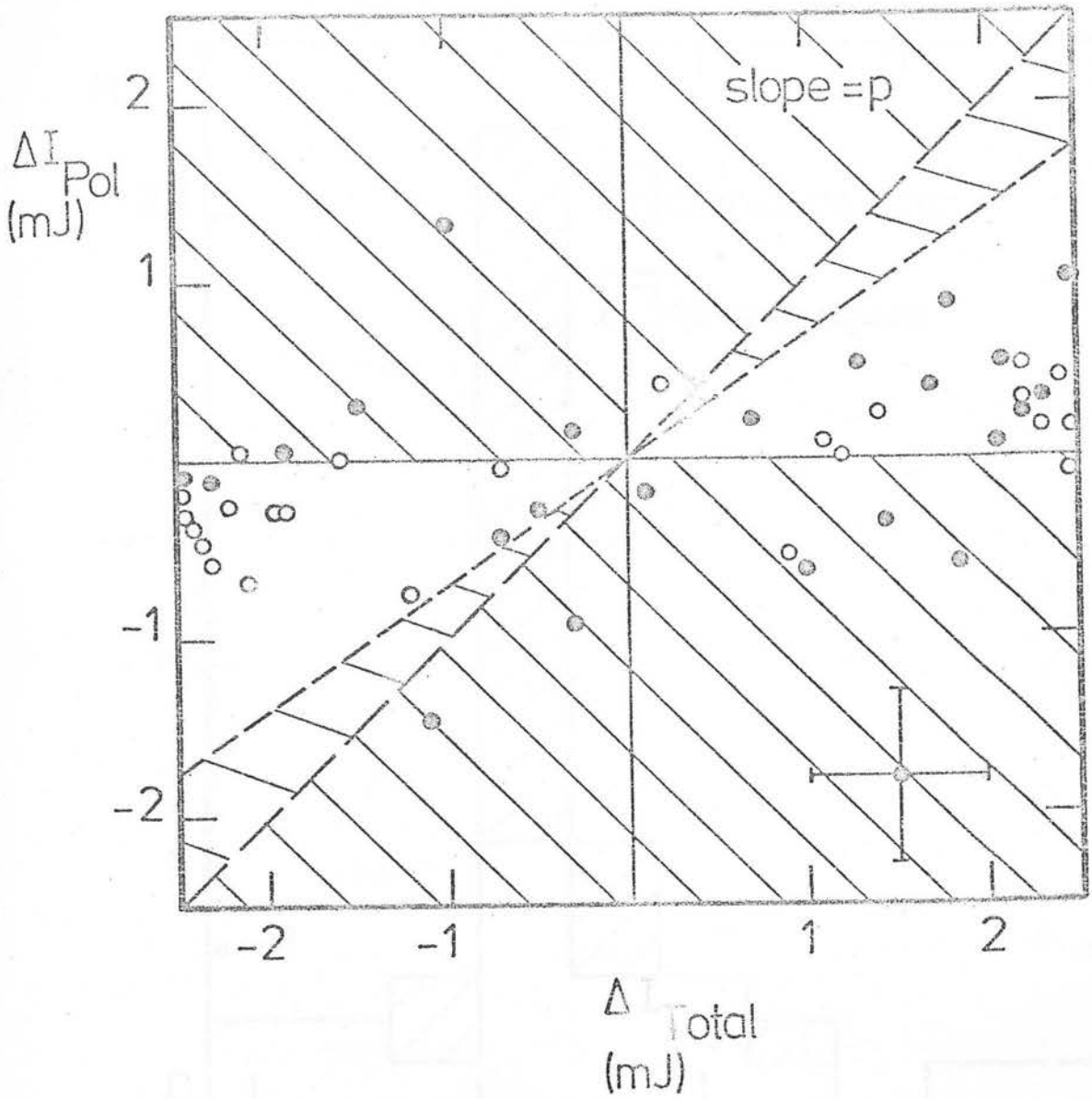

Figure 4.12 Inter-night changes in polarized against total flux. In a two-component model for polarization variability, the shaded area corresponds to the variable component having p>100% or p negative. Physically realizable region is unshaded (p<75%).

- o 0735+178/0851+202 (r^2=0.49)
- o All other objects (r^2=0.09)

Maximum error bars are shown in the bottom right corner. The two named objects (x) and the rest come from different populations at the 95% confidence level. The inter-night changes in total and polarized flux for 0735+178 and 0851+202 are correlated at the 99% confidence level.

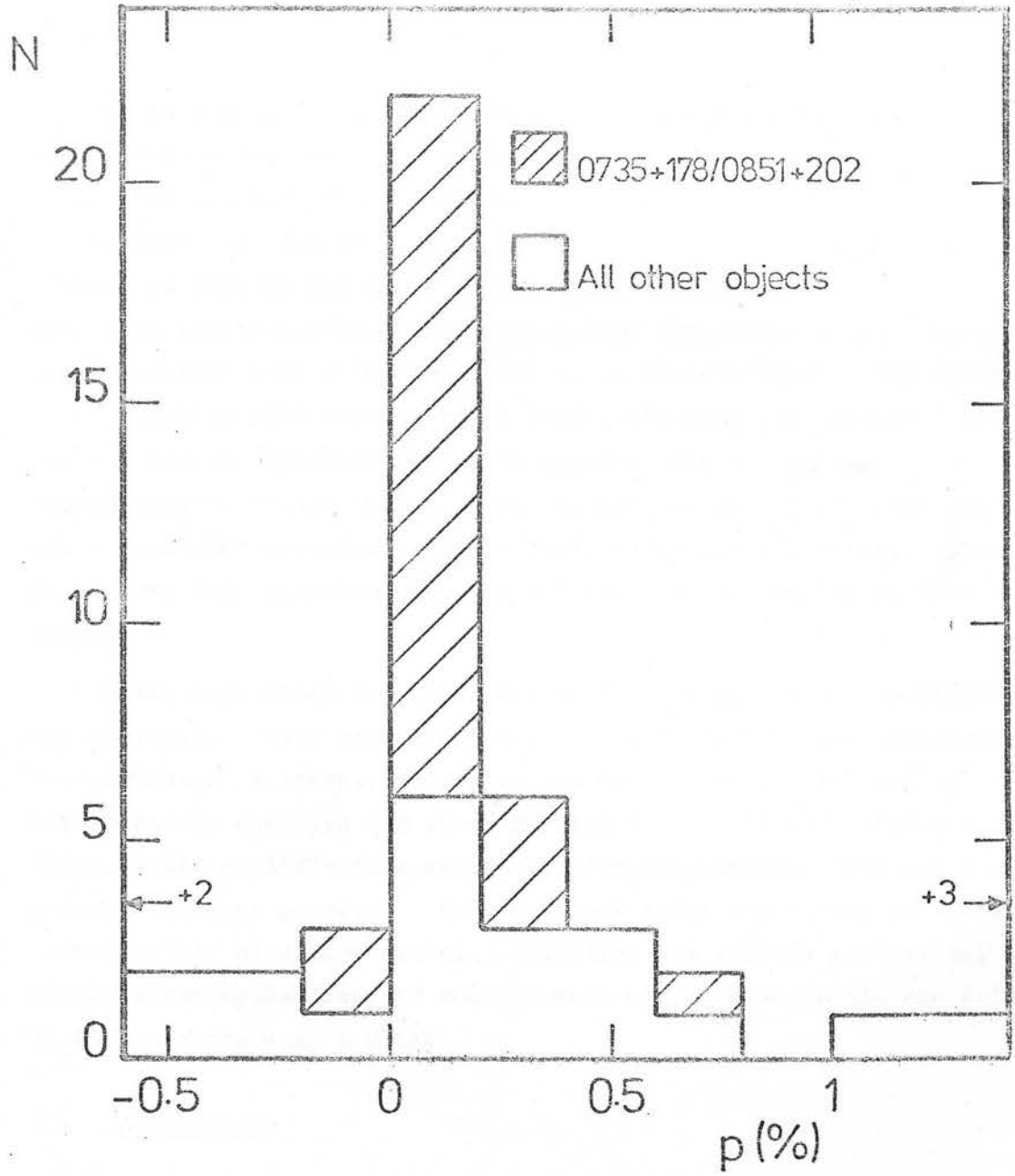

Figure 4.13 Histogram of the polarization of the varying component in the two-component model. The range $0<p<0.75$ is the range of synchrotron polarizations. Five observations lie off the graph.

CHAPTER FIVE

In this Chapter the observations are interpreted in terms of simple models for the emitting regions of BL Lac objects. Two classes of magnetic field geometry are considered. The first consists of the superposition of uniform an isotropic fields, with the polarizations of most BL Lac objects indicating nearly equal mixtures of the two. In particular the polarization/flux variations of two objects are consistent with a two-component model of this kind. The second model consists of a non-isotropic field with spherical symmetry and various radial dependencies of the magnetic field strength. A common feature of all these models is that the resulting polarization has a quadratic dependence on the field alignment parameter. These models are then compared with the polarization properties of the sample.

Next, mechanisms for accelerating electrons in magnetic fields are reviewed. This can take place most plausibly in the turbulent region behind a strong, collisionless shock front. Because of the high electron energies and short cooling times, the particle acceleration, field amplification and generation of polarized flux are all part of the same process. Many of these ideas are incorporated in 'beam' models of active nuclei. Finally, the various geometries, acceleration mechanisms and consequences of the beam models are related to BL Lac objects as a class.

5.1 Assumptions

5.1.1 Emission Mechanism

The optical/infrared flux is presumed to be generated by incoherent synchrotron radiation; the main results for a uniform magnetic field are contained in equations (4.24) - (4.45). The electron energy distribution is taken to be a power law, resulting in a power law flux distribution. The top range of electron energies is ultrarelativistic ($\gamma > 100$), and a discussion of how the particles are efficiently accelerated is postponed until later in the chapter. In the emitting volume synchrotron losses dominate inverse Compton losses ($U_B > U_{ph}$). It is not necessary to assume any relationship between the radio and infrared fluxes, which probably come from different emitting volumes.

5.1.2 Pitch Angle Distribution

Conventional synchrotron theory deals with situations where the pitch angle between the particle velocity and the magnetic field is large ($\Psi \sim 1$), and the emission is confined to a small angle $\theta < 1/\gamma$ around the velocity vector (Figure 5.1b). The pitch angle distribution is assumed to be isotropic (although that is not critical). It was pointed out by Epstein and Feldman (1967) that when $\Psi \neq 90^{o}$, the power emitted by an electron does not equal the power received, the proper relationship being $P_{rec} = P_{em} \sin^{2}\Psi$. This is a Doppler effect due to the continually changing distance between the electron and the observer. However, if a distribution of electrons is confined to a specific volume, the average distance of each electron is unaltered and the observed and emitted powers are equal.

Several studies have modelled the behaviour of active nuclei by synchrotron emission at very small pitch angles (O'Dell & Sartori, 1970; Cavaliere et al., 1970), i.e. the case where $\Psi < \gamma^{-1}$ (Figure 5.1a). Epstein has calculated the emission from sources where most of the particles have small pitch angles (Epstein, 1973). If the magnetic field is not uniform, then the net emission is critically dependent on the relative sizes of θ_B (the typical misalignment angle of the field throughout the source), and the emission cone angle θ. It has been seen in Table 4.4 that θ_B can vary by $\sim 10^{o}$ between BL Lac objects, and for a single variable object it can vary by $>5^{o}$ (0235+164). Therefore, in the general case of $\Psi << 1$ considered by Epstein, $\theta_B >> \Psi$ will always be satisfied. The simple result derived from integrating over the source volume is a maximum linear polarization of $p_{MAX} < \theta/\theta_B \sim 1/\gamma\theta_B << 1$, though the exact value depends on the detailed particle distribution and source structure. The small pitch angle case does not therefore account for high (10 - 20%) degrees of polarization, and the assumption of a distribution out to $\Psi \sim 1$ is justified.

5.1.3 Dynamics

Without any knowledge of the geometry of the source, changing magnetic fields are not a unique explanation of the polarization behaviour of BL Lac objects. If different sectors of field are traversed

and illuminated by the electrons, then no physical reordering of the field is necessary. However, field alignment is desirable to explain the variations. Quasi-static synchrotron theory does not encompass the changes in physical conditions occurring in the source. All the available electron acceleration mechanisms entrain and alter the magnetic field to some degree, so field alignment should be a parameter in the model.

5.2 Magnetic Field Geometry

The synchrotron formulae in Chapter Four were presented for the case of a uniform magnetic field, with the Stokes parameters given by equations (4.39) - (4.41). The maximum degree of polarization is $(\alpha+1)/(\alpha+5/3)$, where α is the spectral flux power law index. If the field is instead isotropic, averaging equations (4.40) and (4.41) over χ gives $Q = U = 0$ and the polarization is zero. In a true physical situation, the maximum polarization is somewhere between the uniform and isotropic cases,

$$(\alpha+1)/(\alpha+5/3) > p_{MAX} > 0 \qquad (5.1)$$

Korchak and Syrovatskii (1962) considered two intermediate cases: a uniform field superimposed on a homogenous field, and a non-isotropic field of constant magnitude. For the first case with a strong homogenous field, the polarization is

$$p = \left(\frac{\alpha+1}{\alpha+5/3}\right)\left(1 - \frac{2}{3\beta^2}\right) \qquad (5.2)$$

where β is on the ratio of homogeneous to isotropic fields. The second case dealt with a near isotropic field, and the functional form of p critically depends on the geometry. Nordsieck (1976) also considered small degrees of alignment of an isotropic field and obtained maximum polarizations which were proportional to the square of the alignment parameter and the spectral index α. In general, the simplest approaches to this problem are to either consider alignments

of an isotropic field or perturbations of a uniform field. The coordinate system is set up as in Figure 5.2, with angle α between field $\underline{B}$ and the line of sight ($\underline{k}$), and $\chi = 0$ being the x axis. The sense of polarization is such that Q = I for polarization in the y direction.

First, as in Nordsieck (1976), define a probability function $P(\underline{B}, \chi)$ that a particular volume element has an electron radiating in a magnetic field $\underline{B}$ and angle χ to the line of sight. The total radiation is then given by the incoherent sum of the radiation from all the volume elements in the source. For the uniform and isotropic cases, $P(\underline{B}, \chi)$ is separable in $\underline{B}$ and χ.

5.2.1 Uniform and Isotropic Fields

Consider an isotropic field of magnitude $\underline{B}_1$ superimposed on a uniform field $\underline{B}_0$ giving a resultant $\underline{B} = \underline{B}_0 + \underline{B}_1$. Integrated over the volume of the source both $\underline{B}_0$ and $\underline{B}_1$ contribute to the intensity of the source, but only $\underline{B}_0$ contributes to the degree of polarization. This geometry is a realization of the two-component model discussed in section 4.4.4, with $I_p = 0$. The uniformity of the resultant field is characterised by $h = B_0/B_1$ integrated over the emitting volume. Figure 5.2 shows the geometry of the source. Use equations (4.39) - (4.41),

$$I(\omega,\underline{k}) = \frac{p+7/3}{p+1}\ \bar{\emptyset}(\nu,p)\int_V (B\sin\alpha)^{(p+1)/2}\ dv \qquad (4.39)$$

$$Q(\omega,\underline{k}) = \bar{\emptyset}(\nu,p)\int_V (B\sin\alpha)^{(p+1)/2}\ \cos 2\chi\, dv \qquad (4.40)$$

$$U(\omega,\underline{k}) = \bar{\emptyset}(\nu,p)\int_V (B\sin\alpha)^{(p+1)/2}\ \sin 2\chi\, dv \qquad (4.41)$$

where $V(\omega,\underline{k}) = 0$ to order mc^2/E (Korchak & Syrovatskii, 1961). The volume integral can be replaced by a polar coordinate integral where $dv = d\Omega/4\pi = v\sin^K dK d\emptyset/4\pi$. The integration is performed with respect to the isotropic field, so α and χ are expressed in terms of polar

angles κ and ϕ. The conversion is performed by taking projections of the fields in the image plane and using the Cosine rule on triangle OLM in Figure 5.2,

$$B^2\sin^2\alpha = B_1^2\sin^2\kappa + h^2B_1^2\sin^2\varepsilon + 2hB_1^2\sin\varepsilon\sin\kappa\sin\phi \tag{5.3}$$

where $LM = B_o\sin\varepsilon = hB_1\sin\varepsilon$. If a coordinate system is chosen such that the uniforms field $\underline{B}_o$ always lies parallel to the y-axis, then

$$B\sin\alpha\sin\chi = B_1\sin\phi\sin\kappa \tag{5.4}$$

Therefore, converting to double angles,

$$\cos2\chi = \frac{B^2\sin^2\alpha - 2B_1\cos^2\phi\sin^2\kappa}{B^2\sin^2\alpha} \tag{5.5}$$

$$\cos2\chi = \frac{B_1^2}{B^2\sin^2\alpha}\left(h^2\sin^2\varepsilon + 2h\sin\nu\sin\ \sin\phi - \sin^2\kappa\cos2\phi\right) \tag{5.6}$$

In the coordinate system with B_o parallel to the y-axis, $\bar{U}(\omega,\underline{k}) = 0$. Substituting (5.3) and (5.6) into (4.39) and (4.40) gives,

$$I(\omega,\underline{k}) = \frac{p+7/3}{p+1}\bar{\phi}(\nu,p)\int_0^{2\pi}\int_0^{\pi}\frac{\nu B_1}{4\pi}^{(p+1)/2}\left(\sin^2\kappa + h^2\sin^2\varepsilon + 2h\sin\varepsilon\sin\kappa\sin\phi\right)^{(p+1)/4}$$

$$\times \sin\kappa d\kappa d\phi \qquad \{X\} \tag{5.7}$$

$$Q(\omega,\underline{k}) = \bar{\phi}(\nu,p)\int_0^{2\pi}\int_0^{\pi}\frac{\nu B_1}{4\pi}^{(p+1)/2}\left(\sin^2\kappa + h^2\sin^2\varepsilon + 2h\sin\varepsilon\sin\kappa\sin\phi\right)^{(p-3)/4} \tag{5.8}$$

$$\times \left(h^2\sin^2\varepsilon + 2h\sin\varepsilon\sin\kappa\sin\phi - \sin^2\kappa\cos2\phi\right)\sin\kappa\, d\kappa d\phi$$

$$\{Y\}$$

There are two limiting cases to consider. When the field is highly isotropic then $h^2 = (B_o/B_1)^2 << 1$ and the integrands of equations (5.7) and (5.8) can be expanded in a series of terms in h^2.

$$\{X\} = (\sin\kappa)^{(p+1)/2}\left[1+\frac{p+1}{4}\left(\frac{h^2\sin^2\varepsilon X}{\sin^2\kappa}\right)+\frac{(p+1)(p-3)}{32}\left(\frac{h^2\sin^2\varepsilon X}{\sin^2\kappa}\right)^2\right] \tag{5.9}$$

where $X = (1+2\sin\kappa\sin\phi/h\sin\varepsilon)$, and any $\int_o^2 \sin\phi d\phi = 0$ so $X = 1$. Taking only the first two terms,

$$I(\omega,\underline{k}) = \frac{p+7/3}{p+1}\bar{\phi}(\nu,p)\int_o^{2\pi}\int_o^{\pi}\frac{vB_1}{4\pi}^{(p+1)/2}(\sin\kappa)^{(p+3)/2}\left[1+\frac{p+1}{4}\left(\frac{h^2\sin\varepsilon}{\sin^2}\right)\right]d\kappa d\phi \tag{5.10}$$

$$Q(\omega,\underline{k}) = \bar{\phi}(\nu,p)\int_o^{2\pi}\int_o^{\pi}\frac{vB_1}{4\pi}^{(p+1)/2}(\sin\kappa)^{(p-1)/2}\left[1+\frac{p-3}{4}\left(\frac{h^2\sin^2\varepsilon}{\sin^2}\right)\right]\{Y\}d\kappa d\phi \tag{5.11}$$

Now use the fact that (Dwight, 1961),

$$\int_o^{\pi/2}(\sin\kappa)^p d\kappa = \frac{\sqrt{\pi}}{2}\frac{\Gamma(\frac{p+1}{2})}{\Gamma(\frac{p+2}{2})} \tag{5.12}$$

Let,

$$\{I_p\} = \frac{V}{4\pi}\int_o^{2\pi}\int_o^{\pi}(B\sin\ )^{(p+1)/2}\sin\kappa\, d\kappa\, d\phi$$

$$\therefore \{I_p\} = vB_1^{(p+1)/2} \frac{\sqrt{\pi}}{2} \frac{\Gamma(\frac{p+5}{4})}{\Gamma(\frac{p+7}{4})} \tag{5.13}$$

Substituting in equation (5.10),

$$I(\omega,\underline{k}) = 2\pi \frac{p+7/3}{p+1} \bar{\emptyset}(\nu,p) \{I_p\} \left[1+ \frac{(p+7)}{(p+5)} \frac{p+1}{4} h^2 \sin^2\varepsilon\right] \tag{5.14}$$

Using the recurrence relation $\Gamma(z+1) = z\Gamma(z)$, and substituting in equation (5.11),

$$Q(\omega,\underline{k}) = 2\pi\bar{\emptyset}(\nu,p) \{I_p\} h^2 \sin^2\varepsilon(\frac{p+7}{p+5}) \left[1+(\frac{p+3}{p+1}) \frac{(p-3)}{4} h^2 \sin^2\varepsilon\right] \tag{5.15}$$

Giving the polarization,

$$(p_i) = \frac{(p+1)h^2 \sin^2\varepsilon(\frac{p+7}{p+5})\left\{1+ (\frac{p+3}{p+1}) \frac{(p-3)}{4} h^2 \sin^2\varepsilon\right\}}{(p+7/3)\left\{1+(\frac{p+7}{p+5}) \frac{(p+1)}{4} h^2 \sin^2\varepsilon\right\}} \tag{5.16}$$

In the second case, the field is highly uniform and $h^2 = (B_o/B_1)^2 >> 1$. The integrands of equations (5.7) and (5.8) can be expanded in powers of h^{-2}.

$$\{X\} = (h\sin\varepsilon)^{(p+1)/2}\left[1+ \frac{p+1}{4} \frac{\sin^2\kappa}{h^2\sin^2\varepsilon} + \frac{(p+1)(p-3)}{32} \left(\frac{\sin^2\kappa}{h^2\sin^2\varepsilon}\right)^2\right] \tag{5.17}$$

Taking only the first two terms,

$$I(\omega,\underline{k}) = \frac{p+7/3}{p+1} (h\sin\varepsilon)^{(p+1)/2} \bar{\emptyset}(\nu,p) \int_0^{2\pi}\int_0^{\pi} \frac{vB_1}{4\pi}^{(p+1)/2} \left[1 + \frac{(p+1)}{4} \left(\frac{\sin^2\kappa}{h^2\sin^2\varepsilon}\right)\right] \sin\kappa d\kappa d\emptyset \tag{5.18}$$

$$Q(\omega,\underline{k}) = \bar{\emptyset}(\nu,p)(h\sin\varepsilon)^{(p+1)/2} \int_0^{2\pi}\int_0^{\pi} \frac{vB_\perp}{4\pi}^{(p+1)/2} \left[1 + \frac{(p-3)}{4} \frac{\sin^2\kappa}{h^2\sin^2\varepsilon}\right] \sin\kappa d\kappa d\emptyset \qquad (5.19)$$

Using $\sin^3\kappa d\kappa = (\frac{\cos^3\kappa}{3} - \cos\kappa)$, and integrating over κ and $\emptyset$,

$$I(\omega,\underline{k}) = 4\pi \frac{p+7/3}{p+1} (h\sin\varepsilon)^{(p+1)/2}\{I_o\}\left[1 + \frac{(p+1)}{6} \frac{1}{h^2\sin^2\varepsilon}\right]\emptyset(\nu,p) \qquad (5.20)$$

where $\{I_o\} = vB_\perp^{(p+1)/2}/4\pi$, and

$$Q(\omega,\underline{k}) = 4\pi\emptyset(\nu,p)(h\sin\varepsilon)^{(p+1)/2}\{I_o\}\left[1 + \frac{(p-3)}{6} \frac{1}{h^2\sin^2\varepsilon}\right] \qquad (5.21)$$

The polarization is,

$$(p_u) = \frac{p+1}{p+7/3} \frac{\left\{1 + \frac{(p-3)}{6} \frac{1}{h^2\sin^2\varepsilon}\right\}}{\left\{1 + \frac{(p-1)}{6} \frac{1}{h^2\sin^2\varepsilon}\right\}} \qquad (5.22)$$

It can be seen that in the appropriate limits, $p_i \to 0$ and $p_u \to (p+7/3)/(p+1)$. Now $h\sin\varepsilon = B_o\sin\varepsilon/B_\perp = B_\perp/B_\perp$, where $B_\perp$ is the projection of the uniform field on the image plane. So the appropriate parameter for field anisotropy is $(B_\perp/B_\perp)^2$ and this quantity can be determined knowing only the degree of polarization and the spectral index of the source. If $p_{MAX} = (p+1)/(p+7/3)$, the form of the results (5.16) and (5.22) is

$$\{p_i\} \propto p_{MAX} \frac{B_\perp}{B_\perp}^2 \quad , \{p_u\} \propto p_{MAX}(1+k \frac{B_\perp}{B_\perp}^2) \qquad (5.23)$$

These expressions show the behaviour in near-isotropic and near-uniform geometries for any spectral index. However, many BL

Lac objects spend time at polarizations between zero and p_{MAX}, where the above approximations are not valid. The integrations can be carried out fully for the simple (and useful) case of p = 3, corresponding to $\alpha = 1$,

$$I(\omega,\underline{k}) = \frac{2}{3}\,\frac{p+7/3}{p+1}\;\bar{\emptyset}(\nu,p)\;\nu B_1^2\left(1+\frac{3}{2}\left(\frac{B_\perp}{B_1}\right)^2\right) \tag{5.24}$$

$$Q(\omega,\underline{k}) = \bar{\emptyset}(\nu,p)\;\nu B_1^2\left(\frac{B_\perp}{B}\right)^2 \tag{5.25}$$

$$(p_{\alpha=1}) = \frac{3}{2^p}p_{MAX}\;\frac{\left(\frac{B_\perp}{B_1}\right)^2}{\left[1+\frac{3}{2}\left(\frac{B_\perp}{B_1}\right)^2\right]} \tag{5.26}$$

As would be expected, the value of (p) for $\alpha = 1$ and any degree of anisotropy is just a simple combination of the algebraic forms for the uniform and isotropic cases. The other easily calculable case is $\alpha = 3$, and <u>all</u> observed BL Lac objects have spectral indices in the range $1 < \alpha < 3$. From equations (5.7) and (5.8),

$$I(\omega,\underline{k}) = \frac{p+7/3}{p+1}\;\bar{\emptyset}(\nu,\,p)\int_0^{2\pi}\int_0^{\pi}\frac{\nu B_1^4}{4\pi}\{X\}^2\sin\kappa d\kappa d\emptyset \tag{5.27}$$

$$Q(\omega,\underline{k}) = \bar{\emptyset}(\nu,p)\int_0^{2\pi}\int_0^{\pi}\frac{\nu B_1^4}{4\pi}\{X\}\{Y\}\sin\kappa d\kappa d\emptyset \tag{5.28}$$

using $\sin^5\kappa d\kappa = \left(\frac{-5\cos\kappa}{8}+\frac{5\cos 3\kappa}{48}-\frac{\cos 5\kappa}{80}\right)$, this gives

$$I(\omega,\underline{k}) = \frac{8}{15}\;\frac{p+7/3}{p+1}\;\bar{\emptyset}(\nu,p)\;\nu B_1^4\left[1+\frac{5}{2}\left(\frac{B_\perp}{B_1}\right)^2+\frac{15}{8}\left(\frac{B_\perp}{B_1}\right)^4\right] \tag{5.29}$$

$$Q(\omega,\underline{k}) = \frac{2}{3}\bar{\varphi}(\nu,p)\ \nu B_1^4 \left[1 + \frac{3}{2}\left(\frac{B_\perp}{B_1}\right)^2\right]\left(\frac{B_\perp}{B_1}\right)^2 \tag{5.30}$$

$$(p_{\alpha=3}) = \frac{5}{4}\, p_{MAX}\ \frac{\left[\left\{1 + \frac{3}{2}\left(\frac{B_\perp}{B_1}\right)^2\right\}\left(\frac{B_\perp}{B_1}\right)^2\right]}{\left[1 + \frac{5}{2}\left(\frac{B_\perp}{B_1}\right)^2 + \frac{15}{8}\left(\frac{B_\perp}{B_1}\right)^4\right]} \tag{5.31}$$

where in this case $p_{MAX} = 6/7$ (for $\alpha = 1$, $p_{MAX} = 3/4$). The polarization for the isotropic field and uniform field limits is plotted in figures 5.3 and 5.4. Near the isotropic limit the polarization is quadratic in the anisotropy parameter $B_\perp/B_\parallel$, but is at levels of only a few percent. The polarization is asymptotic on p_{MAX} near the uniform limit. The region of observed polarizations (1-35%) corresponds to a near balance of the random and uniform fields or $B_\perp/B_\parallel < 1$ (Figure 5.5). $B_\perp/B_\parallel$ must vary by a factor of $\sim$5 to account for the observed range. Unfortunately, the realistic geometry differs from simple perturbations of the two limiting cases. Higher order asymmetries are involved and the equations are not soluble analytically.

The changing polarization in a given object may be explained by a variation in $B_\perp/B_\parallel$, and this does not necessarily involve restructuring the magnetic field. If the electrons radiate in volumes with different values of B, the polarization will depend on which portion of the source is illuminated. Further progress requires a distribution of field strengths throughout the source, rather than the constant strength fields assumed so far. A general comment about the previous analysis is that the redness-polarization correlation seen in the data is a feature of all the equations (independent of the value of $B_\perp/B_\parallel$).

5.2.2 Non-isotropic Fields

Consider a non-isotropic magnetic field distributed over the source volume. It is assumed that the bivariate probability function $P(\underline{B},\chi) = F(B)F(\Omega)$, where Ω is the solid angle. Taking the general case of spherical symmetry, the function $F(\Omega)$ can be expanded into a series of orthogonal Legendre functions,

$$F(\Omega) = \sum_{n=0}^{\infty} \sum_{m=-n}^{n} A_{nm} P_n^{|m|}(\cos\theta) e^{in\phi} \qquad (5.32)$$

and the appropriate Spherical harmonics (m = 0),

$$F(\Omega) = \sum_{\ell=0}^{\infty} Y_{\ell}(\Omega) = \sum_{\ell=0}^{\infty} \sqrt{\frac{2\ell+1}{4\pi}} P_{\ell}(\cos\theta) \qquad (5.33)$$

see, for example, Morse and Feshbach (1953). For the axial symmetry being considered here, these harmonics describe 'zones' on the surface of a sphere since nodal lines are lines of constant θ. The first three terms of the series are,

$$F(\Omega) = \frac{1}{\sqrt{4\pi}} \left\{ 1 + \sqrt{3}\cos\theta + \frac{\sqrt{5}}{2}(3\cos^2\theta - 1) \right\} \qquad (5.34)$$

The geometry is illustrated in Figure 5.6, where B_o is the axis of symmetry of the field at an angle ε to the line-of-sight. Now define an anisotropy parameter

$$h^2 = \frac{\bar{B}_{\parallel}^2 - \bar{B}_{\perp}^2}{B^2} = 2\cos^2\theta - 1 \qquad (5.35)$$

$$\therefore F(\Omega) = \frac{1}{\sqrt{4\pi}} \left\{ 1 + \sqrt{3}\cos\theta + \frac{\sqrt{5}}{2} h^2(3\cos^2\theta - 1) \right\} \qquad (5.36)$$

where $\int h\,d\theta = 0$ over all possible angles w.r.t. the symmetry axis, by definition. When h = 0, the field is isotropic and it can be seen that $\int F(\Omega)\,d\theta = 1/\sqrt{4\pi}$. h^2 is the anisotropy parameter w.r.t. $\underline{b}_o$, the symmetry vector of the field.

The Stokes parameters are calculated, as before, from equations (4.39) and (4.40). First, the integration with respect to the field symmetry axis (solid angle $d\Omega = \sin\theta d\theta d\phi$) is transformed to an integration along the line-of-sight z axis (solid angle $d\Omega = \sin\chi d\chi d\chi$). The expansion in terms of spherical harmonics is still valid because of the properties of the harmonics under an arbitrary rotation of polar coordinate system. For polar systems Ω and Ω',

$$\sum_{\ell m} Y^*_{\ell m}(\Omega') Y_{\ell m}(\Omega) = \delta(\Omega - \Omega') \qquad (5.37)$$

where $\delta(\Omega-\Omega') = 0$ for $\Omega \neq \Omega'$, and $\int d\Omega d(\Omega) = 1$. $d(\Omega-\Omega')$ only depends on the angle between the two systems θ. From spherical trigonometry,

$$\cos\theta = \cos\alpha\cos\varepsilon + \sin\alpha\sin\varepsilon\cos\chi \tag{5.38}$$

The general result which can be obtained is (Jeffries & Jeffries, 1956),

$$Y_{\ell m}(\Omega') = \sum_{m=-\ell}^{\ell} C^{\ell}_{mm'} Y_{\ell m'}(\Omega) \tag{5.39}$$

Therefore, if the corodinate system of an arbitrary spherical harmonic is rotated, the result is a linear combination of spherical harmonics in the new polar coordinates, with the same value of ℓ, so the functional form of (5.34) is unaltered. The results can be calculated for various radial dependences of the strength of the magnetic field. Korchakov and Syrovatskii (1962) considered only the case of uniform strength, and their analysis differs somewhat from that derived here.

(a) $B_1(\underline{r}) \propto B_o$

$$I(\omega,\underline{k}) = \frac{p+7/3}{p+1}\,\bar{\phi}(\nu,p)\int_o^{2\pi}\int_o^{\pi}\frac{V}{(4\pi)^{3/2}}(B_o\sin\alpha)^{(p+1)/2}\left[1+\sqrt{3}\cos\theta + \frac{\sqrt{5}}{2}\,h^2(3\cos^2\theta-1)\right]\sin\alpha\,d\alpha\,d\chi \tag{5.40}$$

$$Q(\omega,\underline{k}) = \bar{\phi}(\nu,p)\int_o^{2\pi}\int_o^{\pi}\frac{V}{(4\pi)^{3/2}}(B_o\sin\alpha)^{(p+1)/2}\left[1+\sqrt{3}\cos\theta + \frac{\sqrt{5}}{2}\,h^2(3\cos^2\theta-1)\right]\sin\alpha\cos 2\chi\,d\alpha\,d\chi \tag{5.41}$$

Using the identity (5.38), and integrating over the aximuthal angle χ,

$$I(\omega,\underline{k}) = \frac{p+7/3}{p+1}\,\bar{\phi}(\nu,p)\int_o^{\pi}\frac{V}{4\sqrt{\pi}}\,B_o^{(p+1)/2}\sin\alpha^{(p+3)/2}\left[(1-\frac{\sqrt{5}}{2}h^2)\right.$$

$$\left.+\sqrt{3}\cos\alpha\cos\varepsilon+\frac{3\sqrt{5}}{2}h^2(1-\tfrac{1}{2}\sin^2\alpha\sin^2\varepsilon)\right]d\alpha \qquad (5.42)$$

Now, using equation (5.12) and the recurrence relation,

$$I(\omega,\underline{k}) = \frac{p+7/3}{p+3}\,\bar{\phi}(\nu,p)(\pi)^{3/2}\{I_p\}\left[(1+\sqrt{5}h^2)-3h^2(\frac{p+5}{p+7})\sin^2\varepsilon\,\frac{\sqrt{5}}{4}\right] \qquad (5.43)$$

where $\{I_p\}$ is given by equation (5.13). $\cos 2\chi$ is expressed in single angles to calculate $Q(\omega,\underline{k})$, and the integration over χ uses $\int_o^{2\pi}\cos^{2,3,4}\chi d\chi = 2\pi,\ 0,\ \frac{3\pi}{4}$

$$Q(\omega,\underline{k}) = \bar{\phi}(\nu,p)(\pi)^{3/2}\{I_p\}\left[(1+\sqrt{5}h^2)+\frac{3\sqrt{5}h^2}{4}(\frac{p+5}{p+7})\sin^2\varepsilon-(1+\sqrt{5}h^2\right.$$

$$\left.-\frac{3\sqrt{5}h^2}{8}(\frac{p+5}{p+7})\sin^2\varepsilon\right] \qquad (5.44)$$

$$Q(\omega,\underline{k}) = \bar{\phi}(\nu,p)(\pi)^{3/2}\{I_p\}\,\frac{3\sqrt{5}h^2}{8}(\frac{p+5}{p+7})\sin^2\varepsilon \qquad (5.45)$$

$$(p) = \frac{p+1}{p+7/3}\,\frac{\frac{3\sqrt{5}}{8}(\frac{p+5}{p+7})h^2\sin^2\varepsilon}{1+\sqrt{5}h^2-\frac{3\sqrt{5}}{4}(\frac{p+5}{p+7})h^2\sin^2\varepsilon} \qquad (5.46)$$

Since h^2 represents the field anisotropy about the symmetry axis, $h^2\sin^2\varepsilon$ is the anisotropy in the image plane (as before). For very small h^2 (nearly isotropic field), $(p) \to p_{MAX}\,\frac{3\sqrt{5}}{8}(\frac{p+5}{p+7})h\sin^2\varepsilon$.

(b) $B_1(\underline{r}) \propto B_o/r$

The radial dependence of the magnetic field is taken to be centred near the line of sight in this treatment, which has relevance to 'beam' models which will be discussed later. The transverse

component in the image plane is therefore proportional to $1/\mathrm{Sin}\theta$. For small ε, $\cos\theta \simeq \cos\alpha\cos\varepsilon$ and $\sin\theta \simeq \mathrm{Sin}\alpha - \mathrm{Sin}\varepsilon$, so $\sin\theta$ can be expanded as a series in $\sin\varepsilon/\sin\alpha$.

$$\frac{1}{\mathrm{Sin}\theta} \simeq \frac{1}{\mathrm{Sin}\alpha}\left\{1 + \frac{\mathrm{Sin}\varepsilon}{\mathrm{Sin}\alpha} - \tfrac{1}{2}\left(\frac{\mathrm{Sin}\varepsilon}{\mathrm{Sin}\alpha}\right)^2 + \ldots\ldots\right\} \qquad (5.47)$$

Using equation (5.42),

$$I(\omega,\underline{k}) = \frac{p+7/3}{p+1}\,\bar{\emptyset}(\nu,p)\int_o^{\pi}\frac{V}{4\sqrt{\pi}}\;B_o^{(p+1)/2}\sin\alpha^{(p+1)/2}\left[(1+\sqrt{5}h^2) - \frac{3\sqrt{5}}{4}\,h^2\sin^2\alpha\sin^2\varepsilon\right]$$

$$\left[1 + \frac{\mathrm{Sin}\varepsilon}{\mathrm{Sin}\alpha} - \tfrac{1}{2}\frac{\sin^2\varepsilon}{\sin^2\alpha}\right]\,d\alpha \qquad (5.48)$$

Omitting terms in $\sin^3\varepsilon$ and $\sin^4\varepsilon$ leads to,

$$I(\omega,\underline{k}) = \frac{p+7/3}{p+1}\,\bar{\emptyset}(\nu,p)(\pi)^{3/2}\left[\{I_p'\}\left\{\frac{1+\sqrt{5h^2}}{2}\sin^2\varepsilon + (1+\sqrt{5h^2}\,(\frac{p-1}{p+1})\right.\right.$$

$$\left.\left. - \frac{3\sqrt{5h^2}}{4}\sin^2\varepsilon(\frac{p+3}{p+5})(\frac{p-1}{p+1})\right\} + \{I_p''\}\,(1+\sqrt{5h^2})\sin\varepsilon)\right] \qquad (5.49)$$

where,

$$\{I_p'\} = vB_o^{(p+1)/2}\,\frac{\sqrt{\pi}}{2}\,\frac{\Gamma(\frac{p-1}{4})}{\Gamma(\frac{p+1}{4})}\;,\quad \{I_p''\} = vB_o^{(p+1)/2}\,\frac{\sqrt{\pi}}{2}\,\frac{\Gamma(\frac{p+1}{4})}{\Gamma(\frac{p+3}{4})} \qquad (5.50)$$

$$\therefore\ \{I_p''\} = \frac{v^2B_o^{(p+1)}}{\{I_p'\}\,(p-1)} \qquad \text{valid for } p > 3 \qquad (5.51)$$

To calculate $Q(\omega,\underline{k})$ and integrate over the azimuthal angle χ the relationship (5.38) must be used. However (5.47) is still a good

approximation as a radial factor. The result is very similar in form to the uniform strength case, because the same terms in $\cos^2\chi$ drop out of equation (5.49),

$$Q(\omega,\underline{k}) = \bar{\emptyset}(\nu,p)(\pi)^{3/2}\{I_p'\}\left(\frac{3\sqrt{5}}{4}h^2\sin^2\varepsilon\left(\frac{p+3}{p+5}\right)\left(\frac{p-1}{p+1}\right)\right) \qquad (5.52)$$

$$(p) =$$

$$\frac{p+1}{p+7/3}\;\frac{\frac{3\sqrt{5}}{4}h^2\sin^2\varepsilon\left(\frac{p+3}{p+5}\right)\left(\frac{p-1}{p+1}\right)}{\left[\frac{1+\sqrt{5}h^2}{2}\sin^2\varepsilon+(1+\sqrt{5}h^2)\left(\frac{p-1}{p+1}\right)-\frac{3\sqrt{5}}{4}h^2\sin^2\varepsilon\left(\frac{p+3}{p+5}\right)\left(\frac{p-1}{p+1}\right)+\frac{\pi\nu B_o^{(p+1)}(1\sqrt{5}h^2)}{\{1\beta\}^2(p-1)}-\sin\varepsilon\right)\right]}$$

(5.53)

The factor $\{I_p\}$ cannot be eliminated from the denominator, so the solution is only rigorous when B and ν are known. However, in the limit $\varepsilon \to 0$ when the line of sight corresponds to the symmetry axis, $(p) \to p_{MAX}\frac{3\sqrt{5}}{4}\left(\frac{p+9}{p+7}\right)h^2\sin^2\varepsilon$. Also, in the situation of a uniform field we can verify that the terms in $h^2\sin^2\varepsilon$ may dominate. The minus sign of $h^2\sin^2\varepsilon$ is due to the definition of h^2 (5.35), which gives it a range $-1 < h^2 < 1$, but the polarization will not be negative.

(c) $B_1(r) \propto B_o/r^2$

Once again, the axis of symmetry of the field is assumed to be centred near the line-of-sight. The transverse component in the image plane is proportional to $1/\mathrm{Sin}^2\theta$, and for small ε,

$$\frac{1}{\mathrm{Sin}^2\theta} \simeq \frac{1}{1-\mathrm{Cos}^2\alpha\mathrm{Cos}^2\varepsilon} \simeq \frac{1}{\mathrm{Sin}^2\alpha} \qquad (5.54)$$

Using equation (5.42),

$$I(\omega,\underline{k}) = \frac{p+7/3}{p+1}\,\bar{\varphi}(\nu,p)\int_0^{\pi}\frac{}{4\sqrt{\pi}}\,B_o^{(p+1)/2}\sin\alpha^{(p-1)/2}\left[\left(1-\frac{\sqrt{5}h^2}{2}\right)\right.$$

$$\left.+\sqrt{3}\cos\alpha\cos\varepsilon+\frac{3\sqrt{5}h^2}{2}\left(1-\tfrac{1}{2}\sin^2\alpha\sin^2\varepsilon\right)\right]d\alpha \qquad (5.55)$$

$$I(\omega,\underline{k}) = \frac{p+7/3}{p+1}\,\bar{\varphi}(\nu,p)(\pi)^{3/2}\{I_p\}\left[(1+\sqrt{5}h^2)\left(\frac{p+3}{p+1}\right)-3h^2\left(\frac{p+5}{p+7}\right)\sin^2\varepsilon\frac{\sqrt{5}}{4}\right] \qquad (5.56)$$

and

$$Q(\omega,\underline{k}) = \bar{\varphi}(\nu,p)(\pi)^{3/2}\{I_p\}\,\frac{3\sqrt{5}h^2}{8}\left(\frac{p+5}{p+7}\right)\sin^2\varepsilon \qquad (5.57)$$

$$\therefore\ \{p\} = \frac{p+1}{p+7/3}\;\frac{\frac{3\sqrt{5}}{8}\left(\frac{p+5}{p+7}\right)h^2\sin^2\varepsilon}{\left[(1+\sqrt{5}h^2)\left(\frac{p+3}{p+1}\right)-3h^2\left(\frac{p+5}{p+7}\right)\sin^2\varepsilon\,\frac{\sqrt{5}}{4}\right]} \qquad (5.58)$$

This differs from the uniform strength case by a factor in terms of p in the denominator, which reduces the polarization for a given p_{MAX} and h^2. The limit as $h^2 \to 0$ is the same as the uniform case. In three cases considered, $h^2\sin^2\varepsilon$ is a measure of the field anisotropy in the image plane

$$h^2\sin^2\varepsilon = \frac{(\overline{B_{\parallel}^2}-\overline{B_{\perp}^2})}{B^2}\sin^2\varepsilon = \frac{\overline{B_y^2}-\overline{B_x^2}}{B^2} \simeq \left(\frac{\Delta B}{B}\right)^2 \qquad (5.59)$$

The degrees of polarization as a function of source anisotropy are illustrated in Figure 5.7. The radial dependence $\alpha 1/R$ is much closer to the constant field situation than the $1/R^2$ dependence. In general, the polarization is quadratic in the anisotropy parameter. This is an important result which holds for any spectral index and can be shown to be valid for any radial dependence of the magnetic field strength. The assumptions in this calculations must be emphasized. The constant strength case holds for all angles ε, but the radially dependent cases hold only for the magnetic

field symmetry axis near the line-of-sight. Since ε is small in the latter two examples, the integration over the emitting volume is performed zonally, i.e. with respect to α but not χ.

The polarization is lower for the $1/R^2$ geometry than the $1/R$ field strength case. The reason can be seen from equation (5.59). For constant anisotropy across the volume, the polarization is roughly proportional to $(\Delta B/B(\underline{r}))^2$. When $B(\underline{r}) \alpha 1/R$, the polarization scales as $1/R^2$, but is weighted by the zonal area, so is independent of radius. However, when $B(\underline{r}) \alpha 1/R^2$ the polarization scales as $1/R^4$ but is weighted as $1/R^2$ giving relatively lower values. The polarization is always a weak function of the spectral index, increasing for redder sources. For $\alpha = 3$, the maximum polarization at $(\Delta B/B) = 1$ is $\sim$34%. Integrating over a sphere considerably reduces the maximum polarization from the uniform field value $(p+1)/(p+7/3)$. The most highly polarized objects can exceed this predicted limit, which implies that spherical symmetry does not apply to cosmic sources. Models with higher order asymmetries can probably reproduce any polarization behaviour, but the simple examples of two component fields (5.1.1) and non-isotropic fields (5.1.2) show much behaviour which is independent of specific geometry. Features from both models can be used to explain much of the polarization properties described in Chapter Three.

5.3 Polarization Properties

The observed polarization properties of BL Lac objects are interpreted in terms of the simple geometries derived in Section 5.2. The variability of polarization which is a common feature in all BL Lacs can be interpreted in terms of the interplay between a varying flux of relativistic particles and the magnetic field entrained in the source. In the optically thin regime, the degree of polarization directly reflects the field geometry.

5.3.1 High and Variable Polarization

A model must be able to easily explain polarizations of up to 45%, corresponding to the highest value yet observed. Therefore

$\int B\cos\theta d\ell$ is small, which can represent either a large-scale nearly uniform field or local 'hot spots' of regular magnetic field. The first case is harder to envisage, because of the isotropizing force needed to wash out the high polarization and produce the large range of observed values. The alternative is to employ two components whose emitting strengths are of the same order, but one of which is variable and polarized and the other of which is static and may be weakly polarized ($\sim$1-3%). The polarization-flux relationship of two objects in the sample agrees with the two-component model reasonably well (Section 4.4.4). Figure 5.5 is applicable, with a D.C. polarization shift if the static component is weakly polarized. The graph shows the change in polarization as the strength of the uniform field is increased with respect to the isotropic field. From the observed range of polarizations for the two objects, the range of $B_\perp$ is a factor of 1.6 for OJ287 and 1.3 for 0735+178 (These factors rise to 3.2 and 4.5 respectively if the full range of optical polarization in the literature is adopted). Rather than invoke an increased field strength, the same effect occurs if the flux in the polarized component changes. From equation (5.7), $I(\omega,\underline{k}) \propto B^{(p+1)/2}$ and using the spectral indices listed in Section 3.4.4 the flux factors are 2.68 and 1.64. So the variability of the polarized component need only be $\sim$1 magnitude on a timescale of weeks, and the full archival range of polarization is covered by $\sim$4 magnitudes. For both objects, the infrared data fits a variable component with $p \sim 15\%$, albeit with large errors. The data is not good enough to say whether the static component is non-variable or polarized. The important fact is that because of the dilution scheme the static component must be emitting a sizeable fraction of the high luminosities found for these two BL Lac objects. One possibility is that these objects consist of a small luminous core in the hot accretion disc surrounding the power source. The tangled magnetic field in the turbulent inner regions of the disc would not produce polarization, but could generate a large synchrotron flux. The polarized component could either be due to a transient event (e.g. magnetic flare) or relativistically beamed emission (which would

circumvent some of the energy density and luminosity constraints).

There are no correlations between flux and polarization changes in the other BL Lac objects, and the alternative interpretation is emission from 'hot spots' in the source. Evidence that the polarized flux comes from localized regions can be inferred from Figure 5.7. The maximum polarization generated in a spherically symmetrical source with $B(r) = B_o$ and $\alpha = 2$ is $\sim$31%. To produce levels >35% requires a fraction of the volume even when there is no anisotropy of the field. However, if the bulk of the emission comes from a small solid angle directed along the line of sight, small regions of nearly uniform magnetic field will change the polarization by substantial amounts. The lack of a polarization-flux correlation indicates that both a restructuring of $B_\perp$ and changes in particle flux contribute. The monolithic nature of the changes in 0J287 and 0735+178 is unusual. Only one other object has shown strong evidence for having several components. Kinman et al. (1968) found that the polarized flux of 3C345 can be explained by the super-position of three components: one non-varying and unpolarized, and the other two variable and polarized (only one component, p = 17%, could be specified from the data). However, few published papers consider the polarization-flux relationship.

To generalize the two-component behaviour of 0J287 and 0735+178, a BL Lac object may consist of a number of highly polarized regions, each with nearly uniform magnetic field and with different polarization position angles. With n regions each radiating L/n the polarization will be $\sim 75\%/\sqrt{n}$ for random orientations. For a small number of regions, polarizations can be >30% and changes in p of 10 - 15% can be caused by switching on or off a sub-unit. However, even with an arbitrary number and distribution of emitting regions, this scheme predicts a correlation between polarization and flux which is not observed. In Figure 4.12, except for the two objects discussed above, the data points show no correlation. The data is only explained if amplification of the magnetic field is possible; mechanisms will be discussed in the next section. Then the net polarization will be the sum from the individual regions, and the

polarization of the individual regions will vary with the transverse component of the magnetic field (along trajectories shown in Figure 5.5). Another consequence of uncorrelated polarization and flux and many emitting regions is that polarization variability may underestimate the size of the emitting region, as pointed out by Blandford and Rees (1978b). For small numbers of sub-units, observations will selectively choose just those regions where large changes in polarization are occurring. The total emitting volume may be much larger. This does not ease the energy density problem. Transitions in polarized flux in a highly polarized region still involve the majority of the output of the source within a small volume; the energetics are still severe. In addition, the variability timescales based on the infrared data are known to be conservative (Table 4.2).

5.3.2 Wavelength-dependent Polarization

Inspection of equations (4.39) - (4.41) shows that the polarization for an isotropic distribution of electrons in a uniform magnetic field is independent of wavelength because the only term containing ν, $\overline{\phi}(\nu,p)$, drops out. The electron energy spectrum must be described by a power law over the energy range producing the synchrotron emission. The simple result of Section 5.1 is that the polarization is only a function of the spectral index and a magnetic alignment parameter. Over the range of constant power law index, the polarization should be constant. However, many BL Lac objects show curved spectra when a broad wavelength baseline is taken. Nordsieck (1976) calculated the polarization from a power law distribution of electrons with a high energy cut-off, using the formulae derived by Westfold (1959). This distribution results in a spectrum that steepens at high frequencies as the synchrotron losses degrade the high energy population (see Figure 4.7). Nordsieck derived the important result that the polarization due to a curved spectrum is given by the local power-law slope. Therefore for a source with a steeper optical than infrared power law, the polarization should rise towards shorter wavelengths. The magnitude of the effect can be calculated from the equations in Section 5.1.

From equation (5.16) for the isotropic limit,

$$\frac{\Delta p_i}{\Delta\alpha} = \frac{1}{2}\frac{(\alpha+4)\ (\alpha+1)}{(\alpha+3)(\alpha+5/3)}\left[\frac{1}{(\alpha+1)} + \frac{1}{(\alpha+4)} - \frac{1}{(\alpha+5/3)} - \frac{1}{(\alpha+3)}\right]h^2\sin^2\varepsilon \quad (5.60)$$

$$\frac{\Delta p_i}{p_i} = \frac{\Delta\alpha}{2}\left[\frac{1}{(\alpha+1)} + \frac{1}{(\alpha+4)} - \frac{1}{(\alpha+5/3)} - \frac{1}{(\alpha+3)}\right] \quad (5.61)$$

From equation (5.22) for the uniform limit,

$$\frac{\Delta p_u}{p_u} = \frac{\Delta\alpha}{2}\left[\frac{1}{(\alpha+1)} - \frac{1}{(\alpha+5/3)} + \frac{1}{(\alpha-1)} + \frac{1}{\alpha}\right] \quad (5.62)$$

Figures (5.3) and (5.4) can apply either to different objects or to different spectral regions in the same object. The polarization in the isotropic limit is very insensitive to changes in α. For nearly uniform field, $\Delta p_u \quad p_{MAX}(\alpha+\Delta\alpha) - p_{MAX}(\alpha)$ where p_{MAX} takes the asymptotic value in Figure 5.4. Two objects show wavelength-dependent polarization, increasing towards shorter wavelengths in both 0235+164 and 0735+178 (Figure 3.4). Both objects also have slightly curved spectra in the expected sense (Figure 3.5). The wavelength dependence is $\Delta p_{JK} \sim 7.5\%$ for 0235+164 and 0735+178, and the change of spectral index across the near infrared needed to produce that change is $\Delta\alpha_{JK} \simeq 0.52$ for 0235+164 and $\Delta\alpha_{JK} \simeq 0.63$ for 0735+178. The values from the data are $\Delta\alpha_{JK} = 0.40\pm0.2$ and 0.44 ± 0.2 respectively. The agreement seems adequate; the curvature of the spectra predicts within the errors the observed degree of polarization. Note that this calculation has assumed the artificial situation of a uniform field. Any more realistic geometry increases the discrepancy in the sense that the observed wavelength dependence will be too steep to be explained by spectral curvature alone.

The wavelength-dependent polarization of AO 0235+164 warrants a more sophisticated explanation. The data is more convincing because the optical points obtained by S. Tapia extend the baseline substantially (Impey et al-see Figure 3.5b). On the 18th of December,

the spectral flux from 0.44 - 2.25μm was well-fitted by a power law of slope $\alpha = 1.99 \pm 0.05$. The upper limit on the polarization slope is $\Delta p/p < 0.04$, and the polarization is predicted to increase by no more than 2-3% across the infrared/optical bands. In fact there is an increase of 8% between K(2.2μm) and I(0.85μm). Furthermore, since the infrared flux increases its curvature over the burst, $p(\lambda)$ is expected to increase with time. Figure 3.5b shows that the shape of $p(\lambda)$ was steady within 1% while $\Delta\alpha_{HK}$ was decreasing from 1.21 to 1.03 to 0.75. This result conflicts with equations (5.61) and (5.62). If Nordsieck's model is relevant then as high energy losses steepen the spectrum, $p(\lambda)$ should become stronger. Alternative explanations are hard to find. The polarization is also a function of $h^2 \sin^2 \varepsilon$, but it is unlikely that the field anisotropy parameter will vary with wavelength. It is also unlikely that the infrared and optical fluxes come from different parts of the source. More observations are required to be certain, but one speculative possibility is that two populations of electrons with similar power laws but different high energy cut-offs are involved. After injection the combined energy spectrum would develop according to equation (4.49) and would look very similar to the 'kinked' spectral flux distribution in Figure 3.5b -data for 20th December . The spectrum can easily be envisaged as the superposition of two curved components. $p(\lambda)$ is then explained as the fact that the high energy tail of the electrons that dominate at high frequencies is depolarized by the low energy tail of the lower frequency electrons. This would suppress the increased slope of $p(\lambda)$ at higher frequencies. Clearly, AO 0235+164 is an unusual object and an injudicious amount of speculation is needed to approximate its behaviour.

5.3.3 Position Angle Rotation

The analysis in Section 5.1 is not very informative about polarization position angle. To ease the calculations, symmetry about the y-axis was assumed which ensured that $U(\omega,\underline{k}) = 0$ and the position angle was indeterminate. However some interpretations can be made remembering that the optically thin regime represents the

projected magnetic field in the image plane. BL Lac objects split into those with a preferred position angle and those with erratic variations covering all possible angles. Highly polarized objects are almost always the latter type.

The BL Lac objects fitted by a two-component model both have a history of scattered position angles. If only one polarized component is present, the position angle swings are likely to be due to rotation of the symmetry plane of the field. This is more evidence for the dynamics that must be aligning and rotating field lines in a magnetically dominated volume on short timescales. For the sources where the 'hot spot' interpretation is preferred, position angle changes are a natural result of randomly oriented sub-units fading in and out. If one out of n regions changes, the position angle swing is typically $p_{MAX}/p \sim \sqrt{n}$ radians. The sources with fewer composite regions will in general have the highest polarization and the largest changes in polarization and position angle. No restructuring of the magnetic field is necessary. Large changes in position angle are also expected in the beam models. If the emitting volume is moving at a small angle θ to the line-of-sight then projection effects become important. The maximum rotation rate described in Section 3.4.2 is $\sim 30^{o}$ day^{-1} for OJ287, which is one of the 'two component' BL Lac objects. Rotations of the same order were observed in 0235+164 and 0735+178 over a five day period. Between observing sessions ($\sim$ months) the position angle can change by $\sim 60\text{-}70^{o}$. It has already been demonstrated that these rotations occur internally since the Faraday rotation limit (equation 4.80) rules out a large amount of thermal plasma surrounding the source. The Faraday effect occurs because a plasma is an anisotropic medium to the passage of left and right-hand polarized waves. The dispersion relation between the orthogonal components leads to a rotation of the plane of polarization during propagation, which is proportional to ν^{-2} (equation 4.67).

The data for OJ287 can be probed further with differential Faraday rotation. If observations are made at two or more frequencies, changes in Faraday rotation can be separated from intrinsic

changes in position angle. If variable Faraday rotation was acting the position angle rotation at K(2.25μm) should be ∿4 times larger than the rotation at J(1.25μm). From Table 3.3 it can be seen that between 19 - 22 December, 1979 the position angle of OJ287 rotated by

$$\Delta\theta_K = 36 \pm 5^o \quad , \qquad \Delta\theta_J = 31 \pm 3^o \tag{5.63}$$

The upper limit on the variable Faraday component is defined by the errors to be $\sim 5^o$ or 0.1 radians. Using the approach of Wardle (1977), which is independent of B, and equations (4.63) for T_B and (4.72) for n_{rel}/n_c gives,

$$n_{rel}/n_c \sim 10 \qquad (\theta \sim 45^o) \tag{5.64}$$

There is a larger density of ultra-relativistic than cold electrons, but the limit is not nearly as severe as the radio limit of Wardle's. The reason is that the brightness temperature constraint is weaker. At infrared wavelengths the brightness temperature is orders of magnitude below the limit for incoherent synchrotron radiation, even for the most compact sources. Nevertheless, this limit confirms that propagation effects are small for the polarized flux.

5.4 Acceleration Mechanisms

The discussion so far has encompassed the energetics of the power source and the properties of incoherent synchroton radiation that account for the observed spectrum. A very important black box between these two is the process by which the power law electron energy spectrum is created. There are several reasons why the acceleration mechanism is important in understanding the polarization data. Strong arguments based on radiative life-times indicate that *in situ* acceleration of electrons must occur well away from the central power source. Constant replenishment of electrons for the life-time of the source is an unattractive

possibility. Therefore the re-acceleration of electrons and generation of polarized continuum are happening in the same volume. Also it has been demonstrated that restructuring of the magnetic field is important in some BL Lac objects. Therefore, the dynamics of the magnetic structure and the polarization spectrum are strongly linked.

Unfortunately, the cosmic acceleration of particles is one of the most difficult areas in astrophysics. In addition to generating a power law energy spectrum, the process must be very efficient. The key role played by turbulence in most theoretical mechanisms may rule out any quantitative solution to the problem. In this section a few simple mechanisms will be discussed, with emphasis on those where magnetic fields are important.

5.4.1 Acceleration by Shocks

A general phenomenon in plasmas is the tendency for compression waves to steepen and form shock waves. As the wave progresses the balance between convective (non-linear) and dissipative effects determines the dimension of the transition region between undisturbed and shocked fluid. The presence of magnetic fields in the hydrodynamic fluid adds complications by permitting two extra modes of wave propagation, which have longitudinal components and can form shock waves also.

Figure 5.8 shows a simple geometry for a stationary magnetic discontinuity (shock). The perpendicular corponent of the magnetic field is continuous across the boundary, and the shock strength is defined as the ratio of the field strengths on the two sides,

$$s = \frac{B_2}{B_1} = \frac{\cos\theta_1}{\cos\theta_2} \qquad (5.64)$$

and the density increases by the compression ratio

$$r = \frac{U_1}{U_2} = \frac{\tan\theta_2}{\tan\theta_1} \qquad (5.65)$$

where U is the fluid velocity. From the propagation of waves in the plasma, two useful velocities can be defined (e.g. Kantrowitz & Petschek, 1966),

$$a^2 = \frac{\gamma p}{\rho} \quad , \quad b^2 = \frac{B^2}{4\pi\rho} \tag{5.66}$$

where γ is the ratio of the specific heats C_p/C_v, p is the plasma pressure, ρ is the density and B is the magnetic field strength. The geometry in Figure 5.8 shows a 'fast' shock, where the tangential component of B increases across the discontinuity and the entropy is higher on the high density side (Ericson & Bazer, 1959). The ratio a/b represents the ratio of gas to magnetic pressure in front of the shock, and Figure 5.9 shows s and t plotted against the shock Mach number for a/b = 0 (i.e. magnetic pressure dominating) and arbitrary directions of propagation with respect to the magnetic field. It can be seen that in the limit of very strong shocks the tangential field and density increase by the same amount.

The energy gained by a particle crossing (or being reflected by) the front at oblique incidence is given by Toptyghin (1980). The approximate energy increase for arbitrary energy density and angle of incidence is,

$$\Delta\varepsilon \approx \frac{pu_1}{(\pi/2-\theta_1)} << \varepsilon - mc^2 \tag{5.67}$$

and the maximum energy gains for passages through, and reflections from the shock are,

$$\Delta\varepsilon^T_{MAX} = \varepsilon(\frac{V}{c})^2\left\{\frac{B_2}{B_1} - 1\right\}, \qquad \Delta\varepsilon^R_{MAX} = 2\varepsilon(\frac{V}{c})^2\left\{\frac{B_2}{B_1} - 1\right\} \tag{5.68}$$

where ε is the initial kinetic energy, and p the particle momentum. Although energy is gained by any crossing of the front by the particle, the average energy increase is less than the initial kinetic energy.

In the astrophysical situation relevant to active nuclei, several assumptions can be made. It can be assumed that the central source is generating a stream of plasma which represents a supersonic energy flow. The outflow need not be relativistic and no assumption is made about its geometry. A strong shock will be set up for a wide range of plasma conditions, because the

presence of magnetic fields ensures that waves will be excited in more than one mode. There are several important scale lengths. One is the shock thickness δ, another is the Larmor radius of the electron given by equation 4.24 ($\omega_L = eB/\gamma_{mc}$), and the third is the scale length in the shocked fluid L. For mildly relativistic electrons, $\delta << r_L << L$ and the shock appears as a discontinuity to the gyrating particle. Also, the electron density in the flowing plasma, n_e, will be such that the mean free path for collisions $\lambda >> \delta$. This justifies the neglect of the plasma pressure ($a << b$). The implication of a strong, collisionless shock is that viscosity and collisions are ineffective for dissipating the energy in the shock transition region. The mode of dissipating energy is theoretically uncertain, but it is likely that the flow energy is first turned into turbulent energy, and subsequently damped into random (thermal) motions. The basic properties of plasma shocks are reviewed in Zel'dovitch and Raizer (1966) and Boyd and Sanderson (1969).

5.4.2 Turbulence and Fermi Acceleration

As a mechanism for accelerating electrons up to ultra-relativistic energies, simple shocks are very inefficient. The energy gain across the front is a fraction of the kinetic energy, and since $\delta << r_L$ there is usually only one crossing before the particle escapes. Large accelerations require multiple interactions with the wavefront, which can occur either through multiple shock fronts of the action of a shock front in a turbulent medium. The existence and form of turbulence near a strong shock is an uncertain theoretical area. However the wealth of instabilities which a magnetized plasma can support are a strong reason for expecting turbulence to occur. Most theories predict a microstructure on the order of the ion gyroradius (r_L^i), and turbulence will accelerate the particles by stochastic crossings of the shock front. Multiple shocks may also play a part in the acceleration. Therefore the action of turbulence can transform the plasma flow energy into a reservoir of turbulent magnetic energy.

Subsequently, the turbulent energy is damped into particle energy in a volume which depends on the damping mechanism. The density behind the shock is increased (equation 5.65) but collisions can still be neglected. There are several modes by which the damping energy accelerates particles. All derive their energy from the entropy generated by the shock front, and all can be calculated by assuming a diffusive solution for the energy transport. Fermi (1954) considered an important process where particles were accelerated by colliding with moving magnetic inhomogeneities. Considering the simplified one dimensional case, with magnetic inhomogeneities moving at velocity V, particles at velocity v, and a mean free path L_F between collisions; the rates of collision from both directions are (v+V)/L and (v-V)/L. In the frame of the inhomogeneity, the gains in kinetic energy are 2MV(v+V) and 2MV(v-V), and the mean rate of change of kinetic energy is,

$$\frac{dE}{dt} = \frac{4MV^2 v}{L} \tag{5.69}$$

giving a fractional change of K.E. per collision of

$$\frac{1}{E}\ \frac{dE}{dt}\ = 8\frac{v}{L}\ (\frac{V}{v})^2 \tag{5.70}$$

where v/L is the collision rate. Assume a steady state situation of particles being injected at E_o and being accelerated until they are too energetic to be contained in the magnetic field, then $N(E) = A/\frac{dE}{dt} = A/kE$ in the relativistic case where $v \approx c$ and the mean free path L is independent of E (i.e. dE/dt = kE). k and A are constants. Since the acceleration does not depend on the particle mass, protons are accelerated to the same energy (in equipartion) as electrons. The injection at E_o is $N_o = N(E_o)(dE/dt)_o = N(E_o)kE_o$. Now $A = N_o$, therefore

$$N(E) = \frac{N_o}{kT_o}\ \frac{T_o}{T} \tag{5.71}$$

The energy spectrum has a slope of -1. To make this more realistic, it is known that the particles will leak away with a lifetime τ (independent of E). Given the particle conservation

equation,

$$\frac{\delta N}{\delta t} + \frac{\delta}{\delta E}\left(\frac{dE}{dt} N\right) = 0 \qquad (5.71)$$

the additional loss term leads to

$$\frac{\delta N}{\delta E} + \frac{\delta}{\delta E}(kEN) + \frac{N}{\tau} = 0 \qquad (5.72)$$

and the steady state solution is

$$N(E) = \frac{N_o}{kT_o}\left\{\frac{T_o}{T}\right\}^{1+1/k\tau} \qquad (5.73)$$

Therefore the spectrum is steepened by an amount which increases the more quickly the particles leak away, in a similar effect to radiative losses.

Many authors have considered the formation of a power law electron spectrum via the Fermi process (Burn, 1975; Axford et al. 1977, Bell, 1977; Blandford & Ostriker, 1978). The initial problem was that the original Fermi model predicts a spectral index of $1+\tau/T$ where τ is the acceleration timescale and T was the escape time, and it was not obvious that these two should be related and hence lead to the observed narrow range of α observed. Kulsrud and Ferrari (1971) have demonstrated that the rate of acceleration is a direct function of the turbulent energy density, and Burn (1975) has shown how this will lead to a self-regulating regime of a power law spectrum with a stable slope. Unfortunately, the treatment is only valid in the adiabatic limit for a small gyroradius. The ideas of Blandford and Ostriker (1978) are more applicable. They postulate that high energy particles can be scattered from Alfvèn waves behind a strong shock and lead to Fermi acceleration in which $\tau \approx T$ and a power law is produced. In fact, a power law spectrum is a natural result of a stochastic acceleration process such as acceleration by transfer of turbulent energy. These ideas have been extensively developed to explain

the acceleration of cosmic rays (Davis, 1956; Fisk, 1971 and many others) and the processes occurring in expanding supernova shells (Chevalier, 1977; Shklovsky, 1976). Direct evidence of shock acceleration comes from the bow shock of the Earth's magnetosphere (Ness et al., 1964).

The particular choice of Fermi acceleration is not crucial. Many modes of oscillation can be set up in a cold, magnetized plasma, but the physics can be quite complicated and the power spectrum of accelerated particles is not always well determined. Most of these modes have wavelengths much shorter than the scale lengths of turbulence relevant to Fermi acceleration, but can accelerate electrons efficiently by a variety of mechanisms which are not mentioned here. The simple model of a power law electron distribution can be summarized as follows. Bulk motion of a magnetized plasma is converted to turbulent energy at the site of a strong, collisionless shock. The shock itself may be thought of as a discontinuity, but the region of dissipation into turbulent energy is larger and should be as large as the gyroradius for the pre-shock electrons. The turbulent energy is then converted by some stochastic collision process into random particle motions, which in the steady state will have a power law spectrum. This is shown schematically in Figure 5.10.

5.4.3 Magnetic Field Reconnection

Hoyle (1949) and Dungey (1953) originally suggested that particles in solar flares could be accelerated between regions of oppositely directed magnetic field (neutral sheets). Magnetic lines of force will rapidly reconnect if two regions of opposite field are compressed with insufficient fluid pressure between to keep them apart. The basic physics has been described by Parker (1973). If there is a crossover region where the magnetic field changes sign, and hydrostatic equilibrium demands that the sum of magnetic and gas pressures is constant,

$$p + B^2/8\pi = k \qquad (5.74)$$

then the fluid pressure will be highest (above ambient) in the crossover region and the fluid will flow away along lines of force. Therefore the regions come closer, and since (5.74) is always satisfied, the field gradient continues to increase. If the thin layer has a characteristic thickness , then Maxwell's equations in a conducting fluid $\nabla \wedge \underline{B} = 4\pi \underline{j}/c$ and $\underline{E} = -(\underline{v} \wedge \underline{B})/c + \underline{j}/\sigma$ lead to,

$$E = \frac{c}{4\pi\sigma} \frac{dB}{dX} + \frac{v(x)B(x)}{c} \qquad (5.75)$$

where x is the direction across the reconnection zone. The electric field generated is transverse to the x direction since under steady conditions $\delta \underline{B}/\delta t = 0$ and from the induction equation $\nabla \wedge \underline{E} = 0$. The limitations on the rate of reconnection are the conductivity of the fluid and the timescale needed to dissipate the fluid from between field lines. Petschek (1964) and others have argued that the large electric fields generated in zones of reconnection can accelerate particles to high energies.

A situation where this mechanism is relevant was encountered in the last section. At the shock discontinuity, a transverse component of strong electric field is induced. However, it is only significant for particles travelling along the shock front. The most important oscillations in a magnetically stressed fluid are Alfvèn waves. A magnetic fluid has a tension $B^2/4\pi$ along the lines of force, and transverse waves can be excited in direct analogy with elastic strings. When field lines reconnect, the characteristic speed for the fluid to be ejected from the region between is the Alfven speed $V_A = B/\sqrt{4\pi\rho}$. Therefore the electric field induced is related to V_A by,

$$E = nBV_A/c \qquad (5.76)$$

where n is a number of order 0.1 (Yeh and Axford, 1970). It can also be noted that compressional Alfven waves may be excited, and they will act to locally compress the field lines. Although this

mechanism has the potential for accelerating particles. If the region of reconnection is small the process will be very inefficient because most of the available energy will go into acceleration of the streaming fluid. If oppositely directed fields meet over a long front, the proportion of magnetic energy turned into relativistic particles can be higher. However in its simplest form, field reconnection does not seem a promising acceleration mechanism.

The situation improves if the idea of topological dissipation is included (Parker, 1972). If a magnetic field with a large scale value B_o has complicated field structure on a smaller scale (e.g. twisting, braiding of field lines), then rapid reconnection of the field lines will limit the small scale fields to equipartion value $\frac{1}{2}\rho u^2$, where u is the characteristic velocity of the fluid in the small scale disturbances. A complicated topology is always a non-equilibrium state, and field lines merging will always act to reduce the structure to the simple form B_o. In a turbulent plasma, very efficient particle acceleration may be possible by this mechanism. For turbulent eddies of scale length ℓ, field B, life-time τ and velocity u, Parker (1972) has shown that the topological dissipation rate is $\sim\alpha\ell/V_A$, where α is a number near unity. The scale ℓ decreases and B increases, and then reconnection dissipates the field when $\ell = \tau V_A/\alpha$ and $B = B_o \alpha u/V_A$. Topological dissipation limits the growth of small scale fields

$$\frac{B}{B_o} \simeq \alpha^{\frac{1}{2}} \left(\frac{\frac{1}{2}\rho u^2}{B_o^2/8\pi} \right)^{\frac{3}{4}} \qquad (5.77)$$

Therefore if turbulent energy is created such that $\frac{1}{2}\rho u^2 > B_o^2/8\pi$ then the small scale fields can be stronger than B_o, but weaker than the equiparition value. In other words, a large amount of turbulent energy can be concentrated in small scale magnetic fields which will dissipate through field reconnection and hence accelerate particles. The process will be more efficient than the 'tearing mode' instability because reconnection occurs throughout the turbulent volume. The particle energy spectrum

is difficult to predict, but since the energy reservoir is in the form of stochastic eddies, a power law might be expected.

5.4.4 Beam Models

Rees (1971) originally proposed the beam model to explain the transport of energy into the extended components of double-lobed radio sources. Since then, it has been expanded ambitiously to encompass the luminous jets and bridges seen linking 'hot spots' to the compact sources in the nuclei of radio galaxies, and even the difference between quasars and BL Lac objects. The principles of the model are presented in a classic paper by Blandford and Rees (1974), and can be succinctly stated. Relativistic plasma is generated near the active nucleus and escapes along oppositely directed exhausts which are collimated in a manner similar to a de Laval nozzle. The relativistic beam travels until it interacts with the external (intergalactic) medium in a series of strong shocks, and the bulk motion is converted into particle energy at a 'working surface'. Many of the principles discussed in this Chapter are relevant to particle acceleration at the ends of the beams. Blandford and Rees (1974) invoked a strong shock, and extensions of this idea have explained the energetics by relativistic blast waves (Blandford & McKee, 1976, 1977; Jones and Tobin, 1977). The problems of setting up a beam which will remain stable for up to 10^8 years are mostly unsolved, and involve the stability of the nozzle flow and the protection and confinement of the beam when Kelvin-Helmholtz and Rayleigh-Taylor stabilities may arise (Sheuer, 1974). A common feature of beam models is the relativistic bulk motion of the emitting volume (Γ). For certain lines of sight the energetics of the source are eased, as described in Section 4.2.1. With a jet as an underlying structure, some authors explain the differences between BL Lac objects, OVV quasars and quasars, and extended and compact radio structure as being projection effects (Blandford & Rees, 1978; Blandford & Königl, 1979; Marscher, 1980). BL Lac objects represent lines

of sight very near the beaming axis where the continuum radiation is boosted in the observer's frame. Emission line clouds may exist around the central source, but the emission lines in BL Lac objects are weak because the continuum is strongly beamed. The beam model has strong statistical consequences for BL Lac properties. The probability of an orientation down the jet is $1/\Gamma^2 4$, and observed jets in radio sources indicate $\theta \sim 5\text{-}10^{\circ}$ and about 1% of the population of active nuclei have beams towards the observer. Because of the enhanced continuum, BL Lac objects should be the brightest among quasars in a given redshift range, and they may not be rare w.r.t. other quasars because of the obvious selection effect in favour of the beamed sources. BL Lac objects are expected to be anti-correlated with double-lobed radio structure. These effects are borne out in general, though the sample used in this study is too small to add to these arguments. The polarization properties of beamed emission are predictably very dependent on the beam geometry. Simple predictions are that the polarization of the 'jet' will depend on the transverse component of B which goes as r^{-1} where r is the distance from the nozzle. $B_{||} \propto r^{-2}$ and a small shear can isotropize the field and wash out the polarization. The polarization position angle will depend on projection effects if θ is small, and may vary drastically. However, specific predictions become very model-dependent.

5.4.5 Applications to BL Lac Objects

There are many ingeneous schemes which can accelerate electrons to ultrarelativistic energies, and few solid physical reasons for choosing between them. In the environment of BL Lac objects several acceleration mechanisms may contribute, and the principle requirements are high efficiency and a power law energy spectrum. The dissipation of turbulent energy behind a shock front can naturally lead to a power law spectrum. However there is a contradiction which results from the acceleration and synchroton emission occuring in the same volume (which is demanded by $t_{sync} \ll t_{VAR}$). Turbulent acceleration implies $\rho_e > B^2/8\pi$, the energy in stochastic motions

dominates the magnetic energy. Yet the highly polarized synchroton emission implies $B^2/8\pi > \rho_e$, the aligned magnetic field dominates particle motions. Some way must be found of injecting the accelerated spectrum of electrons into a region of uniform magnetic field in a time $< t_{sync}$. The extremely short radiative life-time of the electrons is a powerful constraint on all theories. For the most luminous objects, even a bulk Lorentz factor of the emitting region $\Gamma = 5$-10 does not help. The radiative life-time (Table 4.3) remains much smaller than the source crossing time and re-acceleration cannot be avoided.

There are two modes of acceleration which avoid the paradox of the last paragraph. If the acceleration is impulsive and the electrons are accelerated to a high energy $\gamma_{acc} m_e c^2$ in a time $t_{acc} < t_{sync}$, radiative cooling will take over and reduce the energy $\alpha\gamma^2$. The appropriate mechanism would be either a relativistic blast wave or rapid magnetic reconnection. Sudden acceleration could account for the short timescale flares in BL Lac objects. Alternatively, a steady state situation can be envisaged based on the stochastic acceleration mechanisms such as turbulence and ion collisions which gradually accelerate the electrons to large γ's. The situation depicted in Figure 5.10 is modified as follows. As before, a fixed efficiency of bulk outflow energy from the nucleus is turned into turbulent energy across the shock. The electrons are accelerated in this turbulent region to an energy where the rate of energy gain is balanced by the synchrotron cooling rate. The turbulent zone acts as an energy reservoir, and in an equilibrium situation accelerated electrons will stream away from the turbulent zone into regions where magnetic stresses dominate (a strong shock increases $B^2/8\pi$ by x16). Equating synchrotron lifetime to the acceleration time,

$$\frac{3m^3c^5}{2e^4B_\perp^2\gamma} = \frac{K}{U_1^2} = \frac{vL}{U_1^2} \qquad (5.78)$$

where K is the diffusion rate across the shock, L is the concentration scale length in the shocked fluid and U_1 is the flow velocity

of the unshocked fluid. For the luminous sources in Table 4.3, $B \sim 10^4$ Gauss., $\tau_{\frac{1}{2}} < 1$ second and the diffusion length is given by the gyroradius of the most energetic electrons $L > 3 \times 10^6$cm. If the electrons are injected into the shock at near-relativistic speeds, then the fluid flow required is $U_1 > 1000 kms^{-1}$. Therefore the most energetic electrons have a diffusion time $L/c < \tau_{\frac{1}{2}}$ and can emit most of their synchrotron power in a region of aligned magnetic field beyond the turbulent zone. The maximum energy is < 1GeV and the electrons radiate behind the shock at a frequency of $\sim 2 \times 10^{12}$Hz ($\sim 100 \mu$m) which corresponds to the peak spectral energy of observed quasars and BL Lac objects.

This picture of extreme non-thermal radiation where the acceleration and radiation rates reach an equilibrium implies a very high energy density in the thin acceleration zone.

$$U_{acc} > \frac{2e^4 B_\perp^2 \gamma^2 n_c}{3m^2 c^3} \qquad (5.79)$$

which gives $U_{acc} > 2 \times 10^{10}$erg cm^{-3} for BL Lac objects like AO 0235+164 and 3C446. To illustrate this energy density, if the region contained interstellar ionized gas ($\rho \sim 10^{-28}$gcm^{-3}) rather than turbulent energy, the protons would reach a kinetic cosmic ray temperature of 2×10^{30}eV (this is 10^{22} times higher than the cosmic ray energy density in ambient interstellar space, Kulsrud and Pearce, 1969). As far as the energetics are concerned, the observed levels of $L \sim 5 \times 10^{48}$ergs s^{-1} in a volume $R^3 \sim 10^{45}$cm^3 can be achieved in this picture. The most energetic electrons, radiating on a timescale <1 second can be accelerated in a fraction of the emitting volume,

$$\eta = \frac{U_{acc} R^3}{L t_{\frac{1}{2}}} \simeq 2 \times 10^{-5} \qquad (5.80)$$

If a spherical geometry is assumed, the shock acceleration zone represents a shell of thickness dR ($\equiv$L),

$$4\pi R^2 dR = 2 \times 10^{-6} \frac{4\pi}{3} R^3 \qquad (5.81)$$

giving $L \sim 6 \times 10^7$ cm which is in order-of-magnitude agreement with the thickness given by the gyroradius of the most energetic electrons. As mentioned with the beam models, spherical symmetry may not be applicable. In that case, any preferred frame for the observer will reduce the energy requirements.

The polarization properties are also comprehensible in terms of this description. The interpretation of the models in Section 5.2 is that the highest observed polarizations must come from localized regions in the emitting volume, which is more indirect evidence of a 'shell' structure of emitting zones. The 'hot spots' described in Section 5.3 can now be identified with shock fronts behind which the electrons are accelerated directly into the amplified magnetic field. It is likely that many shock fronts will form and in converging and diverging streams they can reheat the electrons from previous bursts. The high (>20%) polarizations of some BL Lacs indicate that very few events are involved, and the magnetically stressed region behind the shock has a high degree of alignment. There is a final argument suggestive of this picture based on the non-isotropic models in Section 5.1.2. It is shown in Figure 5.9 that a strong shock can increase the ambient magnetic field by up to a factor of four. It is easily seen that this is directly equivalent to changing the anisotropy factor $\Delta B/B$ in the model (see equation 5.59). Moreover, Figure 5.7 shows the polarization as a function of $\Delta B/B$, and comparing it with the data a factor of 4 change in $\Delta B/B$ can explain the ranges of polarization for <u>each</u> object. This agreement, even for the artificial model with spherical symmetry, indicates that this mechanism is a useful approach to explaining the polarization properties of BL Lac objects.

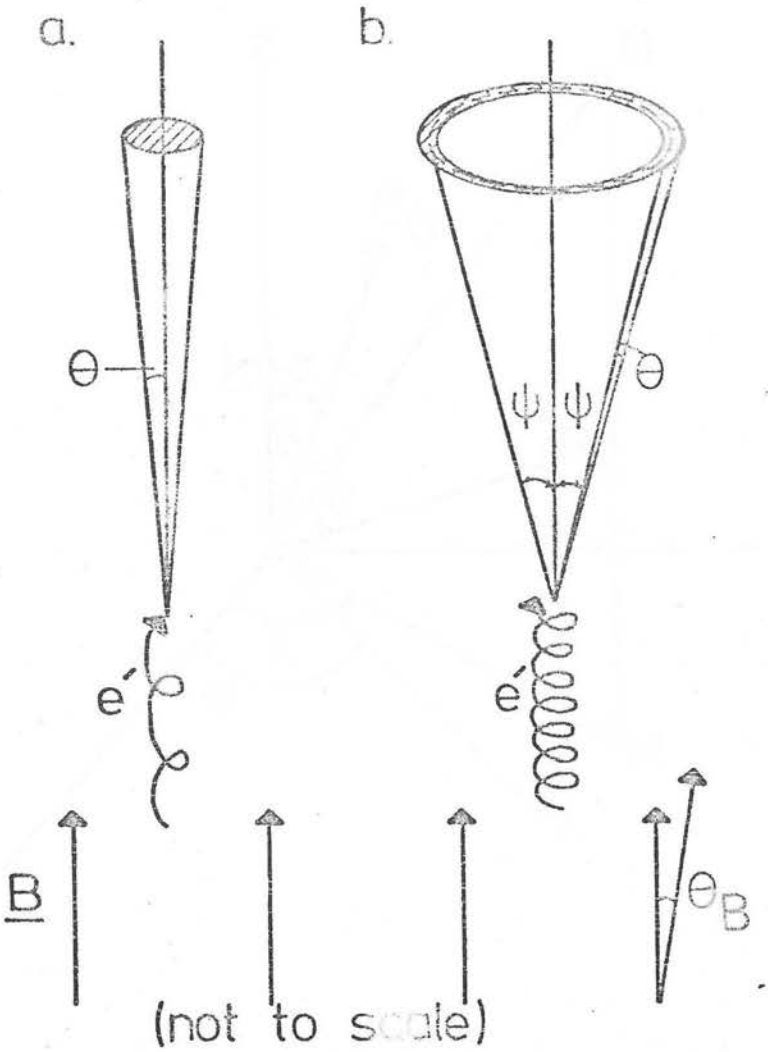

Figure 5.1 a) $\Psi < \gamma^{-1}$ b) $\Psi \simeq 1$

Synchrotron emission from an electron in a magnetic field $\underline{B}$ with a pitch angle Ψ. Emission is within the shaded area, and θ_B represents typical anisotropy in $\underline{B}$.

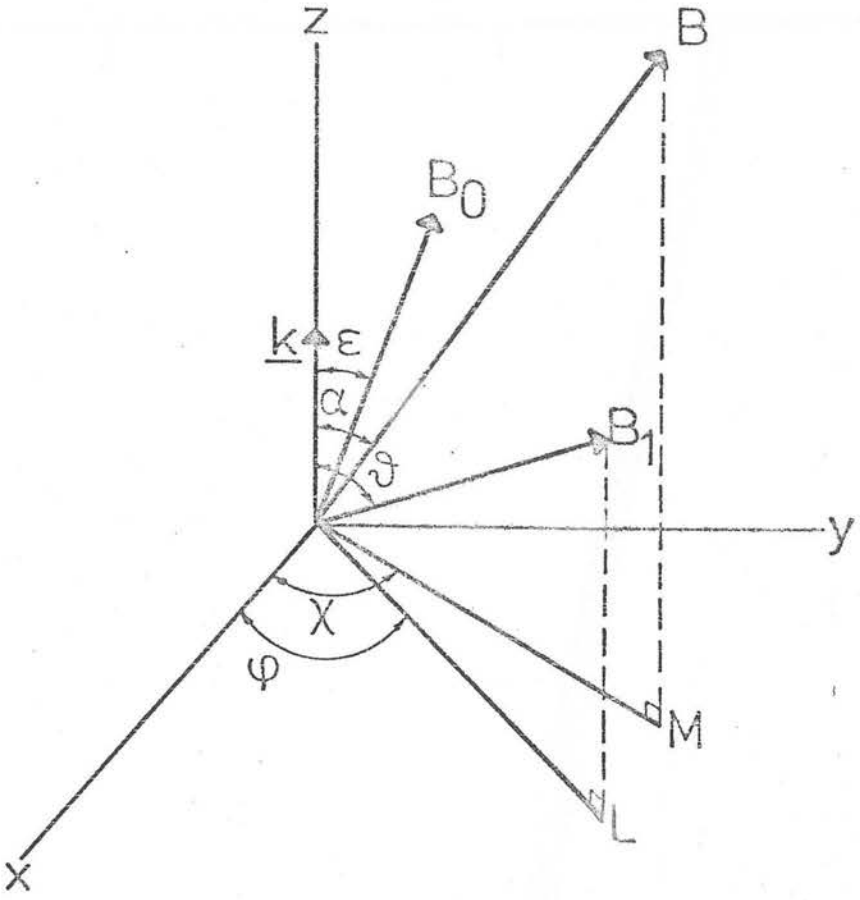

Figure 5.2 Uniform and isotropic magnetic fields.
Uniform field (B_o) is superimposed on an isotropic field (B_1) in a polar coordinate system.

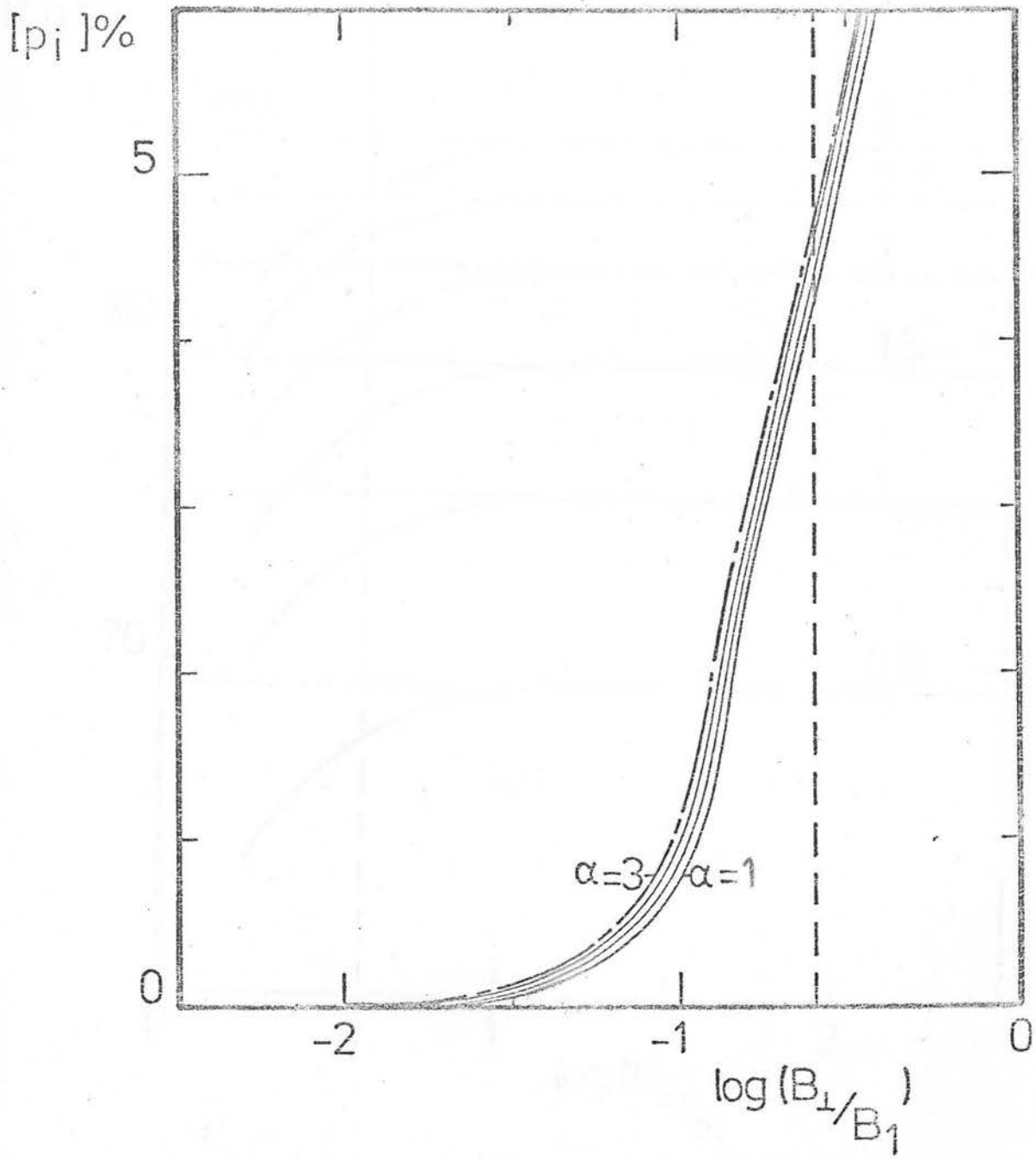

Figure 5.3 Degree of polarization against ratio of uniform to isotropic fields for the isotropic limit $(B_\perp/B_1)^2 \ll 1$.

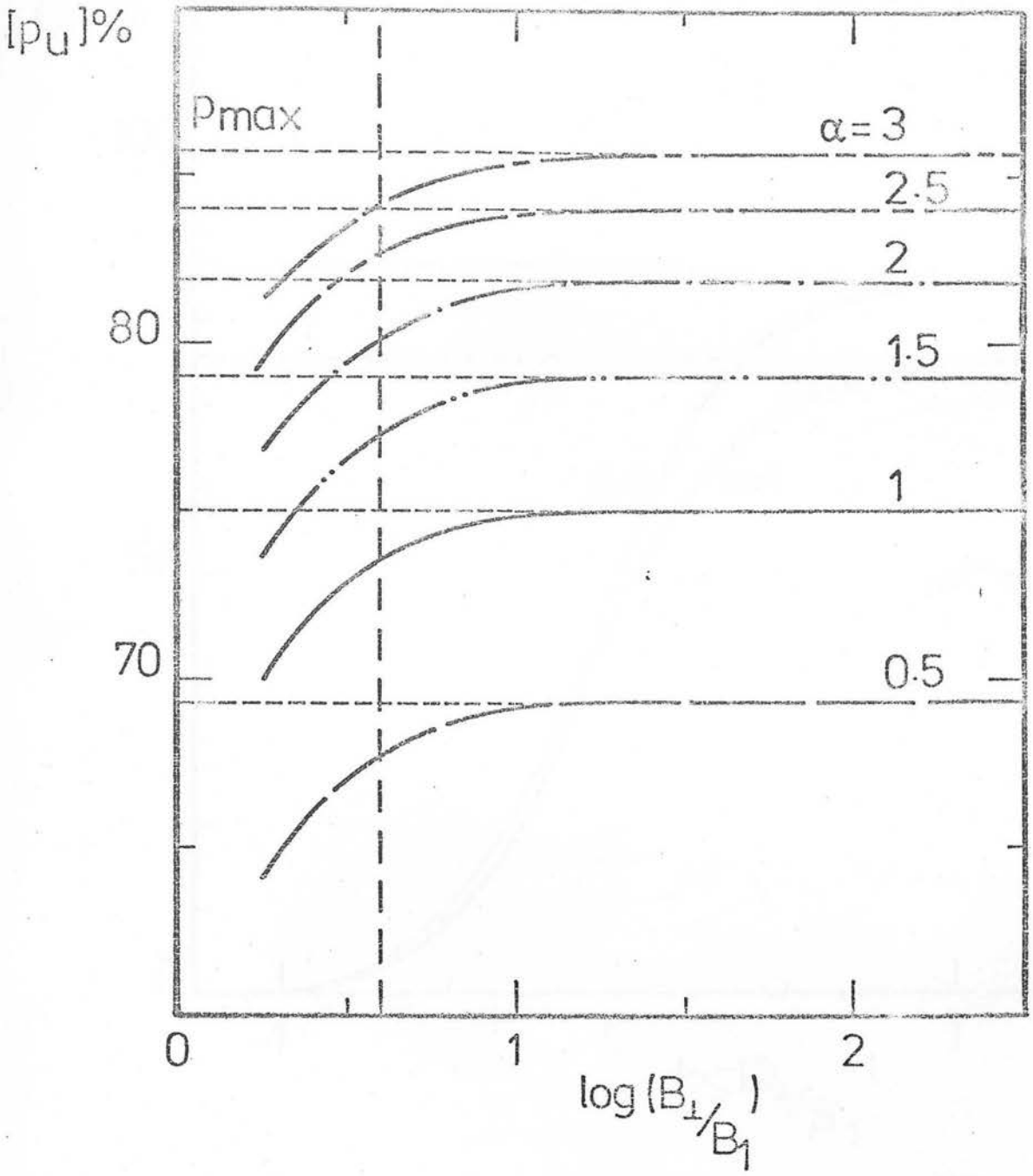

Figure 5.4 Degree of polarization against ratio of uniform to isotropic fields for the uniform limit $(B_{\perp}/B_1) \ll 1$.

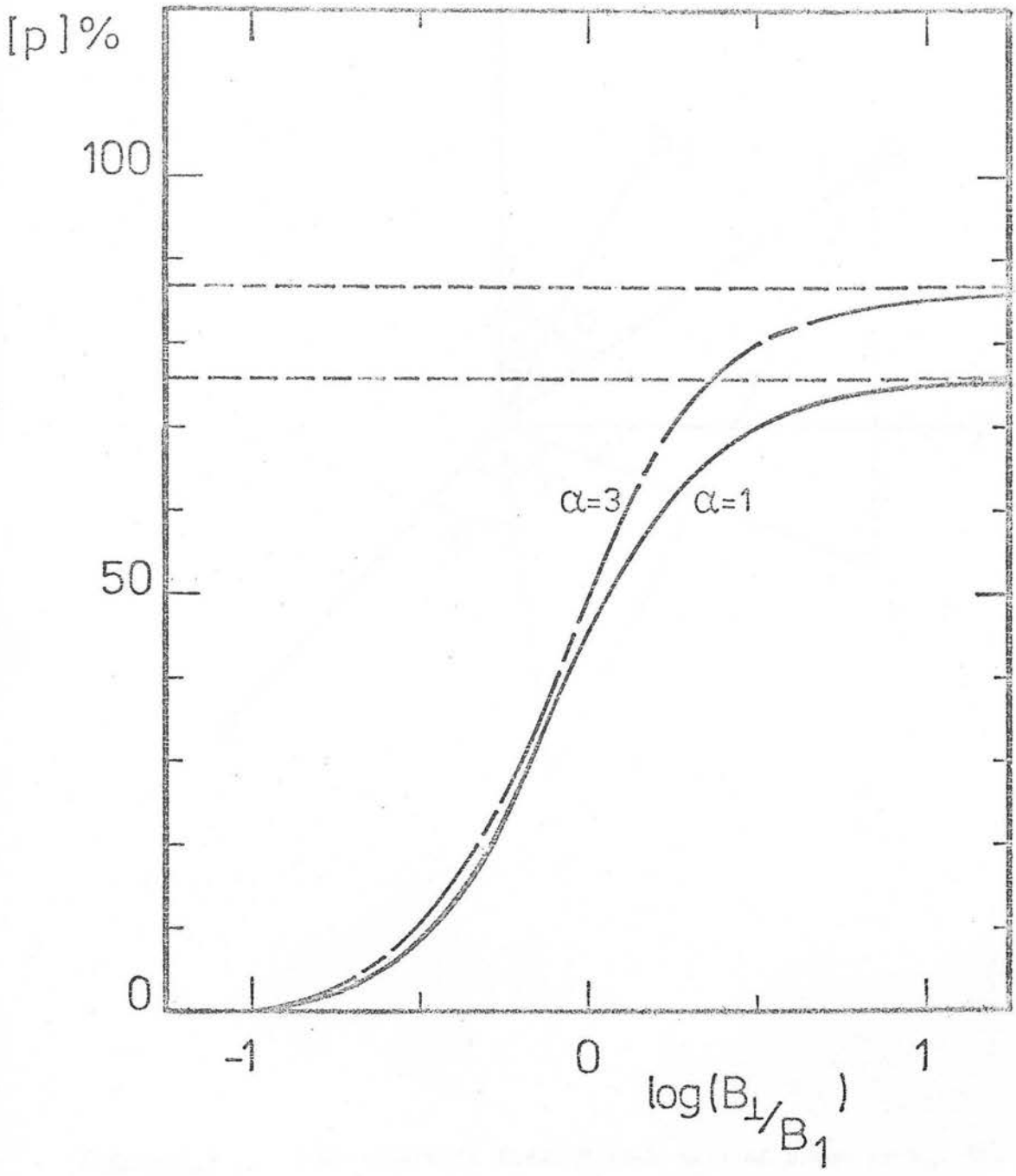

Figure 5.5 Degree of polarization against ratio of uniform to isotropic fields for spectra with power law slopes of $\alpha=1$ and $\alpha=3$.

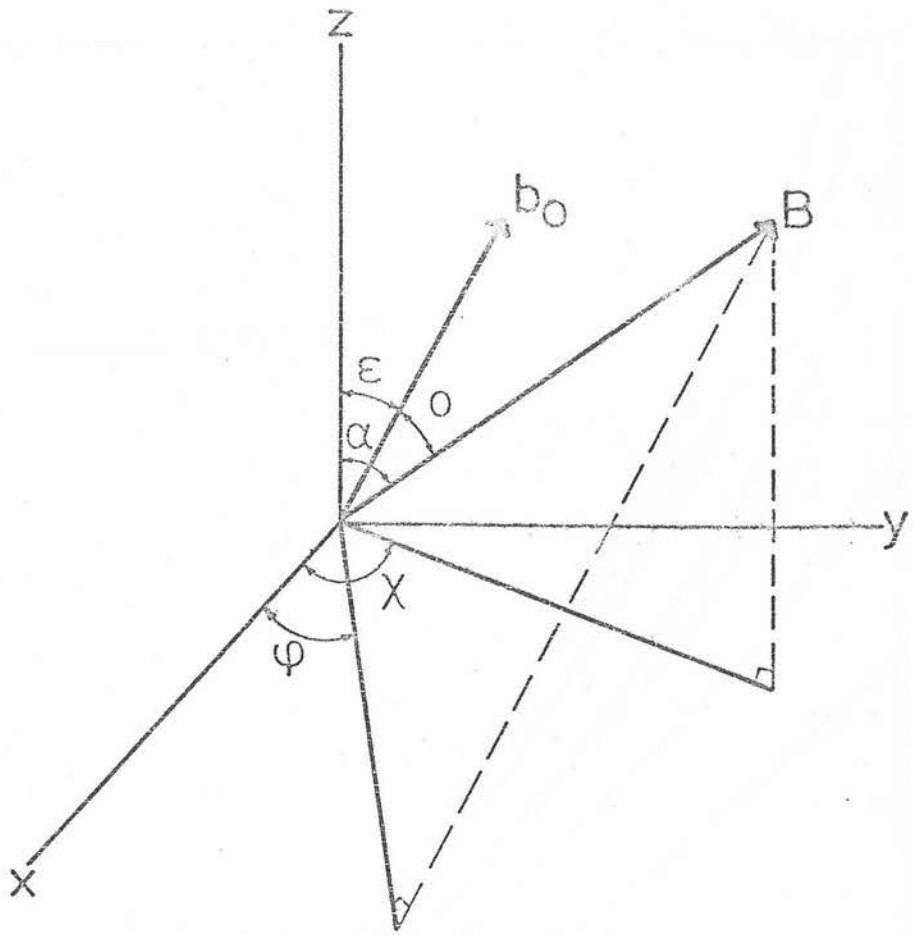

Figure 5.6 Non-isotropic field B with axis of symmetry b_o. The case of axial symmetry can be expanded in terms of $\cos\theta$.

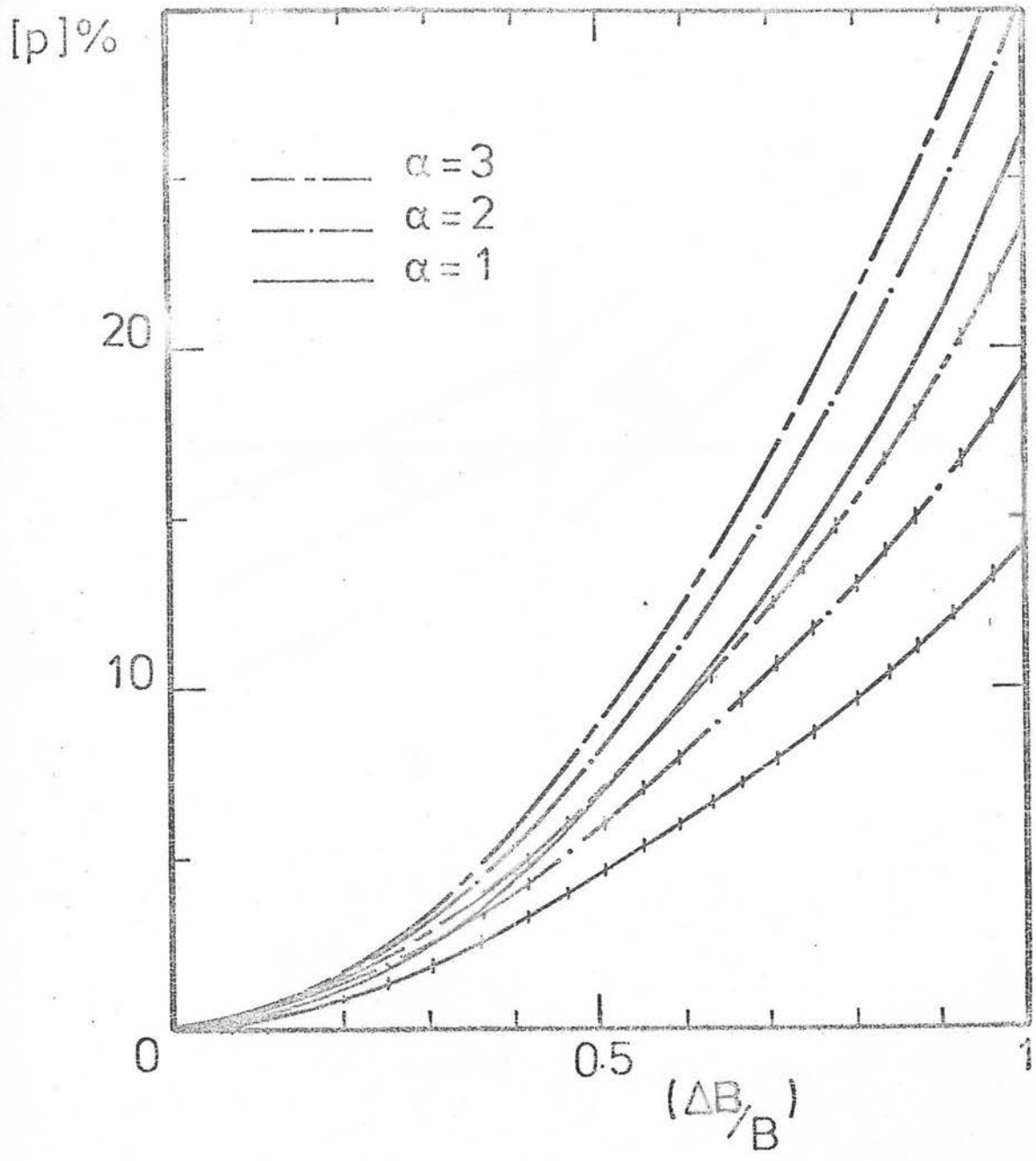

Figure 5.7 Degree of polarizaion against anisotropy parameter for a non-isotropic, spherically symmetric source. Magnetic field strength uniform (untagged curves) and proportional to $1/R^2$ (tagged curves).

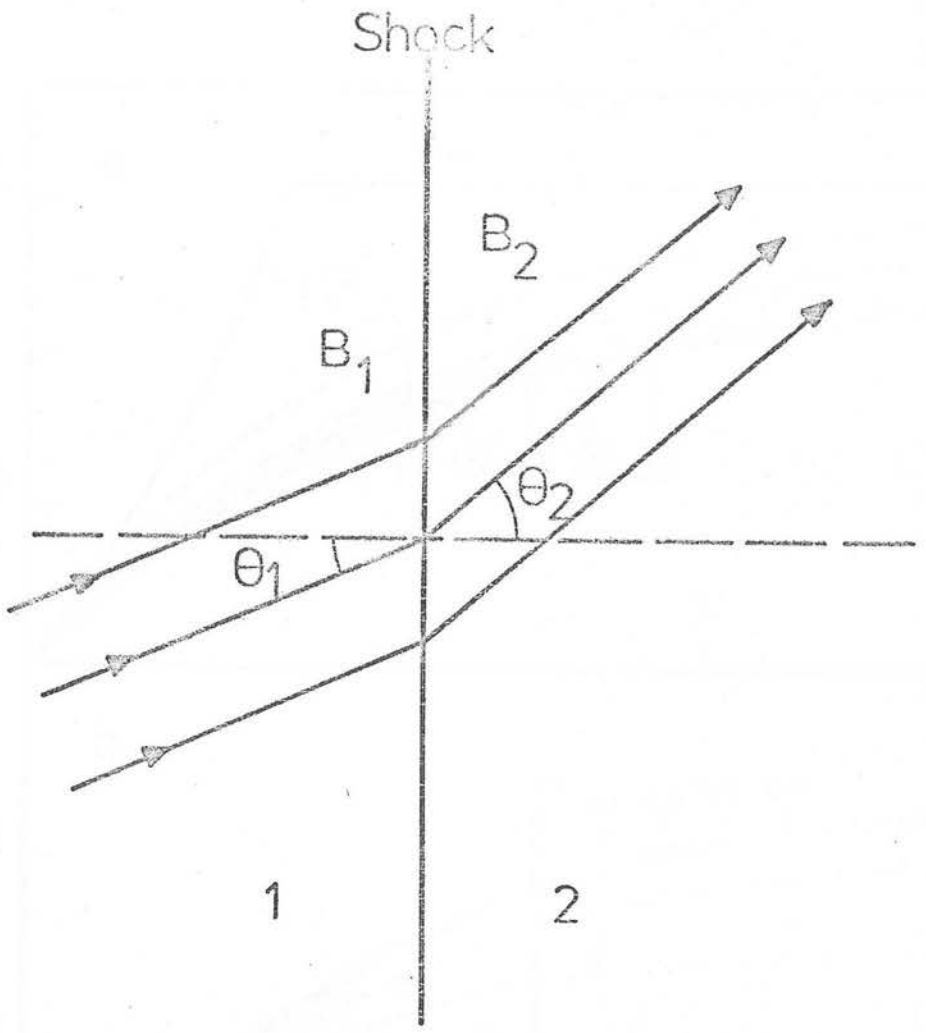

Figure 5.8 Geometry of the magnetic field across a shock front. 1 is the pre-shocked medium, 2 is the post-shocked medium.

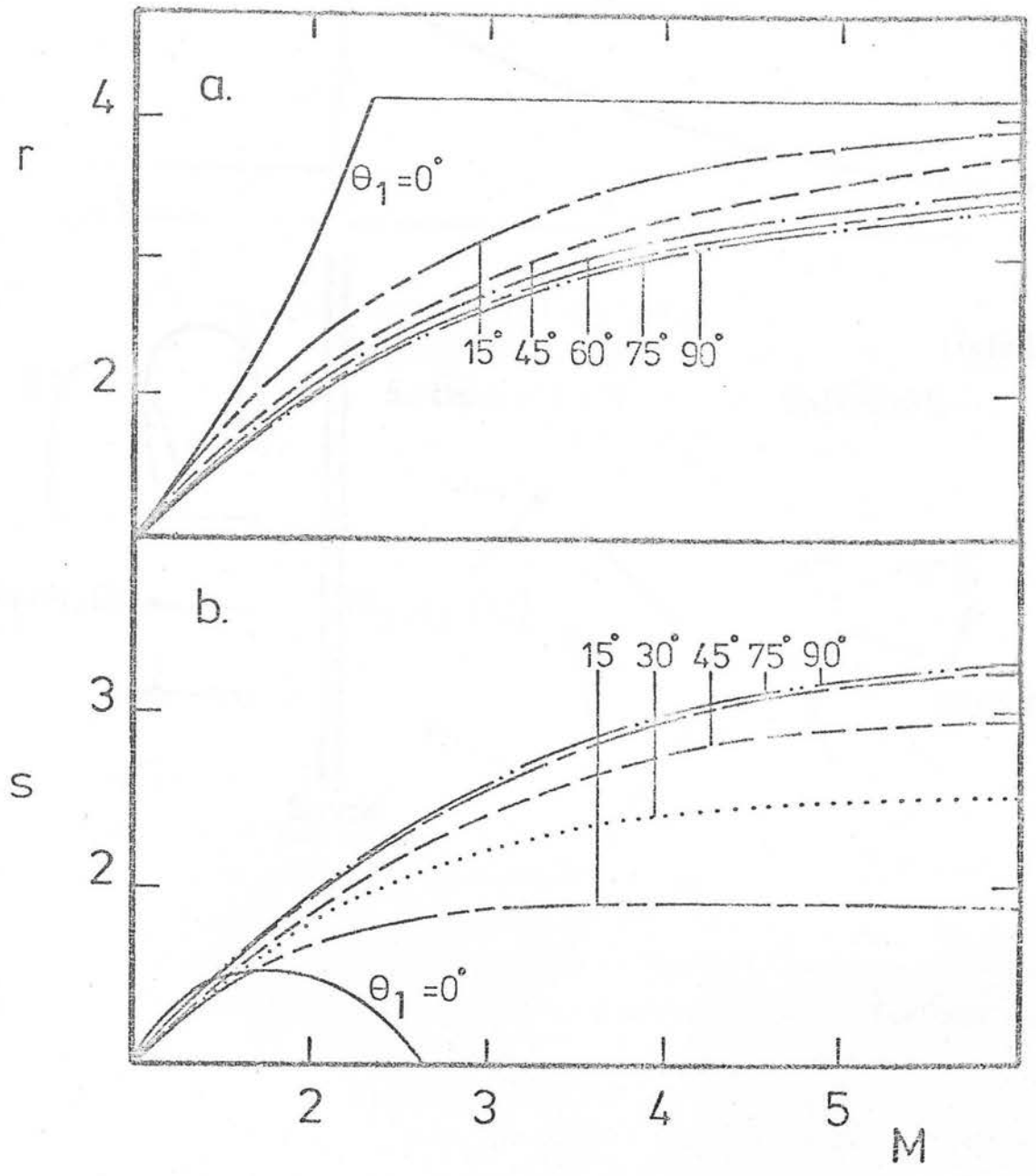

Figure 5.9 Fast, collisionless shock in a cold gas (a/b=0). θ_1 is the propagation angle w.r.t. the magnetic field. a) Density ratio and b) Magnetic field ratio are plotted against shock Mach number (from Kunkel 1966).

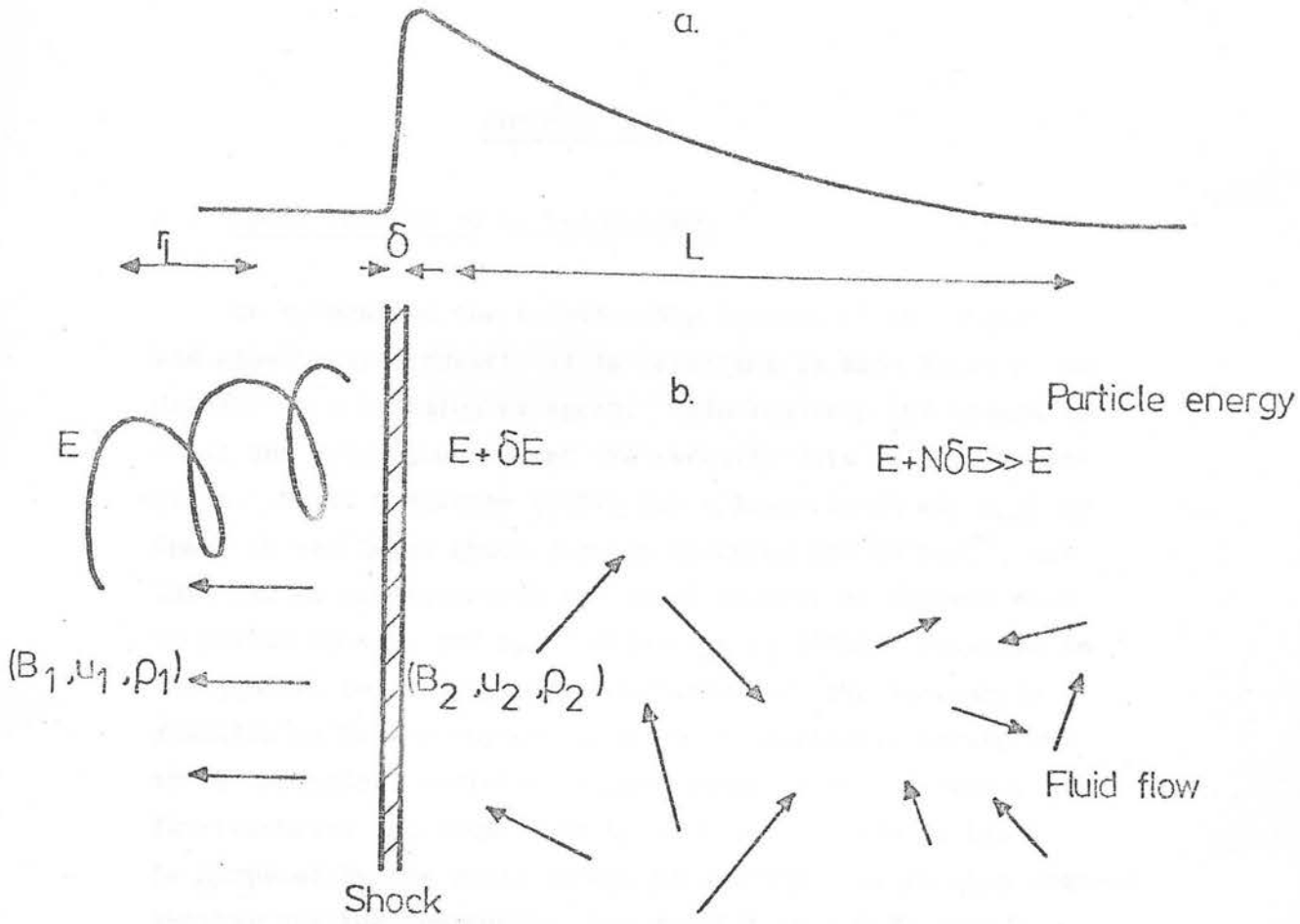

Figure 5.10 Schematic diagram of particle acceleration behind a strong, collisionless shock.

a) represents the scale length L on which major changes in $\underline{B}$, $\underline{u}$ and ρ take place where $L >> r_L >> \delta$.

b) represents the conversion of flow energy into turbulent energy in the shocked region, and subsequent dissipation of the turbulent energy into particle acceleration by successive interactions.

CHAPTER SIX

6.1 Space Density of BL Lac Objects

To understand the relationship between BL Lac objects and other active nuclei, it is important to know their space density as a function of epoch. Unfortunately the sample is small and heterogenous, and the redshift data is very incomplete. Setti & Woltjer (1977) put a lower limit of $n_{BL} > 30$ Gpc^{-3} on the local space density assuming $Ho = 50$ kms^{-1}, and this can be compared with the local density of quasars down to $Mv < -23$ of $n_q \sim 100$ Gpc^{-3} (Fanti et al 1973). Relative to the quasars, Setti & Woltjer concluded that the luminosity function of BL Lac objects must be comparatively strong and the cosmological evolution comparatively weak. However, at low redshifts the comparison between quasars and BL Lacs is hampered by the small number of quasars. It is also unclear whether the low luminosity, low redhift ($z < 0.7$) objects like AP Lib and Mk 421 are part of the same population as the ultra-luminous sources like 3C 446. There are few high redshift BL Lac objects and their selection is probably dominated by the Scott effect which favours distant, luminous sources.

More recently, Setti (1978) has put an upper limit on the surface density of BL Lac objects using the Braccesi field which is complete down to $B = 19.3$ (Braccesi et al 1970), and has Westerbork 1415MHz flux levels down to 15 mJy. The limit for $B < 19.3$ and radio flux densities > 15 mJy is $< 7 \times 10^{-2}$ $(sq.deg.)^{-1}$. However, this estimate suffers from several biasses. First, the optical candidates were chosen to have an ultraviolet excess $U-B < -0.35$ and it is now clear that the optical colours of BL Lacs vary considerably and ultraviolet excess is generally not a good selection criterion (Stein et al 1976). Also, the selection of candidates was

based on radio emission which excludes radio quiet (or weak) BL Lac objects. The radio properties of the class were summarized in Chapter One, and it was argued that despite almost all BL Lac objects being found in radio surveys, the presence of strong radio emission was not simply a selection effect. On the other hand, the composition of the current sample of BL Lacs is very dependent on the method of radio measurement and identification.

The strongest effect on the composition of the sample comes from the radio detection frequency. The original low frequency surveys such as the 3CR survey at 178 MHz selected sources with steep spectra i.e. a slope in the log S - logν plane of -0.7. Only a small fraction had unusual spectra in the sense of a high frequency excess or a low frequency cut-off, and the sources were contained in a small region of the radio "two-colour" diagram (Brandie and Bridle 1974, Wall 1975). Quasars and radio galaxies are virtually indistinguishable in a low frequency sample. Surveys conducted at a higher search frequency (2·7 GHz, 5GHz) pick up a new population of sources with flat or inverted spectra. The proportion of these "flat" spectrum sources increases with finding frequency because of the greater sensitivity to sources with an excess of high frequency flux. Approximately 40% of the Parkes 2.7 GHz sources have flat spectra ($\alpha < 0.5$) and they are well-dispersed on the radio "two-colour" diagram and can be easily distinguished from the type of radio galaxy which predominates in low frequency surveys. A great majority of flat spectrum sources in the GHz range are identified with quasars and BL Lac objects (Condon et al 1977). The proportion of quasar identifications rises from 15-20% for 3CR sources (Smith et al 1976) to 50% for strong 5 GHz sources. Of these quasars, 5-10% are BL Lac objects in a typical 5 GHz survey of sources > 0.6 Jy (Shaffer 1978b). BL Lac objects have almost universal centimetre-excess spectra and are often opaque out to 90 GHz, so it is not surprising that the proportion of sources identified with BL Lacs

increases with radio frequency (Pacht 1976). In a 90 GHz survey by Owen & Mufson (1977), 5 out of the 10 strongest sources were BL Lac objects. BL Lac objects may well predominate in a millimetre-wavelength survey, and it is clear that ratio of identified BL Lacs to quasars and radio galaxies is very dependent on the radio search frequency.

The method of identification of radio sources also has an effect on the proportion of BL Lac objects discovered. If accurate radio positions are available, identifications can be made solely on the basis of positional coincidence with an optical image, without regard to morphology or colour. As already noted, the criteria of UV excess and strong emission lines which work well for quasar identifications, are not always appropriate for BL Lac objects. Condon et al (1978) identified a complete sample of 99 2.7 GHz sources stronger than 0.35 Jy using only positional coincidence, and the fraction of identifications achieved was 78%. The nature of the remaining blank fields is of considerable interest, and two separate approaches have indicated that the counterparts to these sources may be BL Lac objects. First, Peterson et al (1973) succeeded in identifying $\sim$95% of a sample of 2.7 GHz flat spectrum sources. They used double exposure plates to look for UV excess, but the greater completeness resulted from taking second epoch plates in the cases where no identification had originally been made. Since 20% of the sources identified in their search correspond to blank fields on the Palomar Survey prints (which has the same magnitude limit as the double exposure plates), variability is an important parameter in achieving completeness. Several of the sources in the blank fields turned out to be BL Lac objects, including two of the most extreme variables known (0537-441 and 2315-404). A different approach was taken by Ricke et al (1979) who investigated the blank fields of a similar radio sample by looking for 2.2μm flux at the radio position. They detected infrared sources at half the radio positions, and in common with BL Lac objects these sources have the properties of strong infrared

excess and rapid variability (Soifer & Neugebauer 1980). Rieke & Lebofsky (1979) have claimed that with a combination of infrared and optical techniques ~95% of a sample of flat spectrum sources can be identified. The implication of this work is that past identification procedures have tended to underestimate the proportion of BL Lac objects among flat spectrum radio sources. Their representation is more complete when the identification is based not only on the presence of UV excess and emission lines, but also on infrared excess, variability and polarization.

The final influence on the current sample of BL Lac objects is the radio flux limit of the survey. Since BL Lac objects are mostly flat spectrum sources, it is the constitution of this population with decreasing flux density which is of interest. The cosmic evolution of flat spectrum radio sources with redshift information has been estimated in two ways. Schmidt (1977) and Peterson et al (1976) both found $\langle V/V_{MAX} \rangle = 0.52$ for samples of flat spectrum sources selected in the GHz range. This value is consistent with a uniform space distribution, and differs substantially from the values of $\langle V/V_{MAX} \rangle$ for steep spectrum quasars and optically selected quasars which both indicate strong evolution. Differential source counts at 2.7 GHz support this conclusion, the shape of the flat spectrum counts indicating no evolution and a "Euclidean" space density. (Condon and Jauncey 1974, Wall et al 1980). It is noted that the difference in evolution between flat and steep spectrum sources depends on the redshift distributions of the two samples being identical. Because of the high luminosity of most flat spectrum sources, their numbers are expected to fall off at lower flux densities (Fanaraff & Longair 1973). Yet there is a considerable excess of flat and inverted spectrum sources at faint levels (< 20 mJy), the observations being discussed by Wall (1978) and Davis (1977). It may be significant that these excess sources have exactly the radio spectra and luminosities of the majority of low redshift($z < 0.1$) BL Lac objects.

It is clear that the properties of BL Lac objects are dominated by the manner of their radio selection and identification.

Therefore a radio-independent search is very desirable, and it can be undertaken most efficiently in the optical band. In a homogenous sample of radio sources these identified with BL Lac objects tend to be 1-2 magnitudes brighter than those identified with quasars (Usher 1975). In terms of their radio selection, BL Lac objects are very bright optically. For example, the list of 56 BL Lacs in Angel & Stockman (1980) contains 13 at $M_V < 15.0$ and only 8 at $M_V > 18.0$. This can be compared with the magnitude distribution of radio-selected quasars which peaks near $M_V = 18.5$, and the magnitude distribution of optically-selected QSO's which is still rising beyond $M_V = 20$ (Hewitt & Burbidge, 1980). The corollory of this view is that when selected optically, BL Lac objects differ from quasars in having a lower radio flux. Certainly if each of the known BL Lac objects was placed at the redshift distance corresponding to the flux limit of the original radio survey almost all of them could easily be detected in a faint optical search. An optical search down to $M_V = 19$ will probe the known properties of BL Lac objects down to very low radio flux levels i.e. it will test whether there are any radio quiet BL Lacs.

The two optical properties which distinguish BL Lac objects from other active nuclei are high linear polarization and rapid variability. Photographic polarimetry using a Schmidt telescope is the most effective optical search technique because of the large fields which can be covered ($\sim$10sq. degrees) and the faint limiting magnitude which can be reached ($m_B \simeq 20$). In addition, the plate material can be analyzed for flux variability as well as polarization. The sensitivity of the survey relies on the fact that most BL Lac objects have maximum polarizations greater than 10%. Since the polarization is known to vary, the completeness of the survey must be estimated from the known polarization properties of BL Lac objects. A polarization search detects BL Lac objects by their most physically interesting property. A high degree of polarization in the optically thin regime indicates an ordered magnetic field, if the emission mechanism is synchrotron radiation. It was shown in Chapter One that there is a 1:1 correspondence between the occurence

of high polarization, variability and strong radio emission. So the polarization search defines the radio properties of an optically selected sample, and puts an important new upper limit on the surface density of BL Lac objects.

6.2 Photographic Polarimetry

The first use of photographic polarimetry was by Öhman (1941) who used a twin image polarimeter to detect polarization in extended objects such as the moon and M31. He used a spectrograph where the prism or grating was replaced by a Wollaston prism, and eventually extended the technique to deduce polarization in two colours (Öhman 1947). Since then, the effort has divided between work done with a beam-splitting polarimeter on a single exposure and multiple exposures taken through a Polaroid filter. The first apprach requires a birefringent crystal to split the light into perpendicularly polarized beams. Serkowski (1960) used pairs of calcite prisms with their axes perpendicular, and by comparing photographic and photoelectric measures for the same stars found an r.m.s. deviation of 0.02 magnitudes for stars brighter than $M_{pg}=10$. Brand (1971) has shown that in the fast beam of a Schmidt telescope, the photometric accuracy of the double calcite plate method is probably limited to 2%.

The alternative method involving sheet Polaroid was used by Tripp (1956) and Baade (1956a) to produce relative measures of the polarization of extended objects like the Crab Nebula. Zwicky (1956) generated composite photographs from exposures at different position angles of the Polaroid, and suggested that the entire pattern of linear polarization of a nebulous object could be revealed. Gieseking (1977) confirmed this by taking prints from Baades' original plates of the Crab and forming composite photographs. By comparing the composites with photelectric polarization measurements, he concluded that the polarization detection limit was about 10%. Unfortunately the nonlinearity of the emulsion makes it very difficult to calibrate the photographic method directly. Baade (1965b) also took

Palomar 5 m.plates of the jet in the giant E galaxy M87, and showed the knots of the jet to be polarized. Twenty two years later, Sulentic et al (1979) carefully repeated the original set of 5m plates under conditionswhich were as identical as possible. With PDS measurements and extensive image processing they showed that the intensity and polarization of at least one of the knots had changed in the 22 year interval. An ingenious method for detecting the polarization of large numbers of stars was developed by Treanor (1967). A slightly inclined plane-parallel glass plate and sheet of Polaroid were rotated at 1-2Hz during the exposure, and the deviation introduced by the plate converted each image into a ring. Polarization was detected by looking for modulation in the intensity of the ring, and microphotometer tracings of stars in Cygnus II association showed a prominent modulation. The first accurate photographic study of polarization was carried out by Pratt (1968) using a Polaroid filter on the Edinburgh Schmidt telescope to observe 527 stars down to $M_v = 13$ in a one degree diameter field. Images through different position angles of the Polaroid were multiply exposed on each plate and sixteen plates were used. Comparison between photoelectric and photographic measures for 54 stars gave an r.m.s. deviation of 0.029 magnitudes.

The first photographic search for highly polarized BL Lac objects was carried out by Craine et al (1978) using a double calcite plate. They used the plates of fields 6.5 arc minutes in diameter to look for BL Lac objects at relatively inaccurate radio positions. In a search of 60 flat spectrum radio source fields, 8 BL Lac objects were discovered with a detection limit of about 12%. Despite the magnitude limit of $m_B = 19$, all the objects found were brighter than $m_B = 17.5$. The technique was not applied to blank (or randomly selected) fields because of the small field size, so all the detections were dependent on the presence of radio emission. The advantage of a search carried out on a Schmidt telescope is that large numbers of stars ($\sim$ 50,000) down to faint limiting magnitudes can be measured at one time. The greater inaccuracy caused by using separate exposures through Polaroid rather than multiple

exposures through a calcite prism can be alleviated by averaging more than one set of plates. This work constitutes the first radio-independent search for BL Lac objects over a large area of sky.

The properties of the Polaroid filter used in the survey are discussed in Chapter Seven, as well as the measurement procedures and reduction algorithm. In Chapter Eight, the photometric calibration of the plate material is covered, and in Chapter Nine the results of the machine measurement of the polarization plates are presented.

CHAPTER SEVEN

This chapter describes polarization filter designed for the U.K. Schmidt Telescope, and the instrumental tests carried out at the telescope and in the lab. All plates discussed here were taken with the rotating linear polarization filter, and the emulsion in each case was hypersensitized IIIa-J. Secondly, the COSMOS measuring machine is described and the way in which it measures stellar images is analyzed. The majority of the reductions use COSMOS data. Finally, the sources of error in photographic polarimetry are considered, and the reduction procedure is outlined.

7.1 Linear Polarizing Filter

7.1.1 Description

The filter consists of two pieces of HN 32 Polaroid vacuum-laminated between 1/8" high quality float glass (Figure 7.1). The program region is defined by a circular piece of diameter 25.4cm which gives a clear field of 560cm^2 (19.4 square degrees). It rotates on a friction bearing between positions 45° apart, located by ball bearings pressed into the rim and locating slots. The second piece is fixed and defines a control region. The remainder of the plate is occluded by the filter holder, and the Schmidt calibration spots are not visible. In Figure 7.1, the unvignetted region is shown as a dotted line of diameter 30.5cm. The unvignetted region encompasses the entire program area and ~60cm^2 of the control area. Note that the program area is centred 2.5cm from the centre of the unvignetted region.

7.1.2 Laboratory Tests

Several tests were carried out before the filter was used, to determine the properties of the Polaroid-glass sandwich. Polaroid material is manufactured by the Polaroid Corportion, U.S.A. and HN 32 is one of several types of visible polarizers which they make. H-sheet consists of a stretched sheet of polyvinyl alcohol which is bonded to clear cellulose aceto-butylrate to keep its shape. The

long molecules align themselves along the direction of stretch. Iodine is diffused into the polyvinyl alcohol where it forms a complex within the long molecular chains. These iodine complexes absorb light polarized parallel to the length of the molecules and transmit visible light polarized perpendicular to the molecules. There are many industrial applications for this elegant form of dichroism. The N in the designation refers to 'neutral' and the number 32 indicates the approximate transmittance of unpolarized visible light. Polaroid has a very wide acceptance angle and can be used in convergent beams of light such as a fast Schmidt beam.

The figure of merit for Polaroid material is characterized by the transmission coefficients for light polarized parallel and perpendicular to the axis of alignment, k_1 and k_2 respectively. The intensity transmission coefficient at an arbitrary angle θ to the axis of alignment is,

$$T(\theta) = k_1 \cos^2\theta + k_2 \sin^2\theta \tag{7.1}$$

As stated in Appendix E, two other important parameters are the polarizance $P = (k_1-k_2)/(k_1+k_2)$ and the extinction ratio k_1/k_2. HN 32 is the best compromise between good transmission and high crossed-polaroid extinction. When two identical polarizers are placed in an unpolarized beam with an angle θ between their principal axes the transmission is,

$$T(\theta) = \tfrac{1}{2}(k_1^2+k_2^2)\cos^2\theta + k_1 k_2 \sin^2\theta \tag{7.2}$$

which has maximum and minimum values,

$$T_{\parallel} = \tfrac{1}{2}(k_1^2+k_2^2) \quad , \quad T_{\perp} = k_1 k_2 \tag{7.3}$$

Figure 7.2 shows data provided by the Polaroid Corporation with the transmittance to unpolarized light $(k_1+k_2)/2$ and the cross-polaroid values $T_{\parallel}$ and $T_{\perp}$ plotted against wavelength. The manufacturer's data show that over the wavelength range of interest, $p > 99\%$ and $\rho > 10000$ making HN 32 an excellent polarizer for the job

required. Lab tests were needed to check the uniformity of the filter. HN-sheet is cut from 19" wide rolls and there may be transmission variations due to uneven iodine concentrations across the sheet. Also, the polaroid film is very thin (50-100μm) and when it is sandwiched under vacuum between glass plates it is known that corrugations can develop. These corrugations are caused by the polaroid film undulating in the glue layer between the glass sheets and can lead to transmission variations also. Finally, the process of sandwiching and cutting the glass can cause stress patterns and non-planarity of the filter surface. Image focus across a Schmidt plate is critical and it is essential that the filter does not act like a weak lens.

The optical train for the three lab tests is shown in Figure 7.3. The corrugations in the filter are visible by eye in reflected light and were mapped both along and perpendicular to their axis by scanning a light beam across the filter. The mapping resolution was 0.5mm and the intensity resolution was 0.2%. The corrugations are perpendicular to the maximum transmission (fast) axis of the polaroid. Figure 7.4 presents the transmission scans. The top scan clearly shows the ripples in the polaroid with a characteristic wavelength of 3-4cm and a peak-to-peak amplitude of ∿2.5% in transmission. The scan <u>along</u> the corrugations also shows a systematic change in transmission which is presumably due to inhomogenous iodine dyeing of the polaroid polymer. The range of transmission is ∿4% with a localized dark patch near the centre of the filter which shows up as a dip in transmission at d ∿ 20mm. Other scans at position angles 30°, 60°, 120°, 150° (0° and 90° are in Figure 7.4) show that the dip is the only major blemish in the filter and apart from it the peak-to-peak transmission variations are ∿3%. The transmission variations crucially affect the precision of this method of polarimetry because a set of exposures at different position angles will have the variable filter transmission mapped into the true intensity. If uncorrected, a polarization 'noise' level of ∿3% due to the filter will result, and no detections below 3% or precisions better than 3% will be possible. This test was done with a converging f/3 beam, which is quite close to the f ratio of the Schmidt.

The second test was to measure axis wander across the filter. Axis wander occurs when the average orientation of the dichroic molecules rotates or varies, and it was tested using two identical polaroid filters in the beam. The minimum transmission for crossed polaroids gave a polarizance (in white light) of 99.993%. With one piece of polaroid set at the minimum transmission position, the other piece was moved across the light beam and its angle carefully adjusted to get the minimum back again. This readjustment indicated the amount the fast axis of the filter was rotating over its width. Because it is a null method, this technique is very sensitive to tiny rotations of the fast axis. The measurement was made with a light beam covering $\sim$0.25mm^2 on the surface of the filter; resolution greater than this was not possible. The result in Figure 7.5B is that the axis wander is $<0.05^{\circ}$ across the entire filter. Therefore the filter is very uniform in its polarizing properties. The ellipticity due to residual birefringence in the polaroid substrate or glass support was not measured, but Bennett and Bennett (1978) found a range of $0.01\text{-}0.5^{\circ}$ for HN 32. An ellipticity of 0.5° contaminates the linear polarization by <1% (i.e. $\cos\delta = 1$, $\sin\delta = 0.009$ in matrix (P1) in Appendix F).

Finally, it is important to check the planarity of the glass-polaroid sandwich. The float glass was specified to a thickness of $\pm$160μm, but the stresses induced by cutting glass can change its profile. To sensitively map the contour of the top surface, a laser lever arm of $\sim$24 meters was set up (Figure 7.5C). The second reflection used an optical flat figured to $\lambda/8$. By moving the filter in its own plane the deviations of the laser spot were recorded. In this way a very sensitive map of the shape of the top filter surface is obtained. The centre of the filter is bowed out by $\sim$20μm with respect to the circumference. There is also evidence that the rim is slightly raised. This profile has the circular symmetry of the filter; scans at other position angles showed the same shape. From this test alone it is not possible to test for changes in optical thickness, but the glass layer of the sandwich is shown to be regular to a high degree.

The crossed-polaroid experiment was used to accurately position the rotating filter in its support at a known position angle. The filter was lined up so that the axis of maximum transmission located in the ball-and-slot retaining mechanism when it was North-South in the filter-holder. This zero point location was defined on the optical bench to $\pm 0.2^{\circ}$. On the telescope exposures were taken in the celestial reference frame of polarization position angle, i.e. North-South equals zero, and angles increasing measured North through East.

7.1.3 Telescope Tests

Further tests were carried out at the U.K. Schmidt Telescope Unit at Siding Spring, Australia. Several flat fielded plates were taken through the filter to map the transmission variations again. A series of different exposures was taken in the light tunnel which is constructed from a diffused light source and a long ($\sim$5m) tunnel which has a matt reflecting surface and a cross-section the size of a Schmidt plate. A IIIa-J plate was illuminated with a uniform diffuse field of light. A second set of plates was taken with a flat field on the telescope. A sheet was taped across the top of the telescope tube to act as a diffuser and the telescope was left at 'access/park', i.e. a zenith distance of $\sim 90^{\circ}$ pointing at the base of the dome. Strong lights were shone at the opposite side of the dome so that the light was reflected several times before entering the telescope. These plates can test the combination of the filter and the telescope optics. A grid of transmission values was measured with a MacBeth spot sensitometer on the developed plate and the range of transmissions was the same as the range found in the lab test. No new transmission effects were found on the plates taken on the telescope through a diffuser.

To determine the optimum focus with the Polaroid filter in the plateholder, a focus plate was analyzed. A multiple exposure plate is taken with each star represented by 15 images side by side, each image at a focus position differing from the adjacent image by 50μm. As the best focus is passed the 'doughnut' images shrink to a point

and expand again. It is possible to interpolate an optimum focus to 1/10 of the difference between adjacent images, i.e. 5μm. By definition this technique can be used to analyze thickness variations in the filter with a resolution of ∿5μm. The maximum amplitude of thickness variation across the filter is ∿55μm, and this can be converted by simple geometrical optics into a defocussing across the plate (Figure 7.6),

$$dx = dt \tan\theta' \sin(90-\theta+\theta') \qquad (7.4)$$

where θ = arctan f/2, $\sin\theta'/\sin\theta = 1.5$, f is the f-ratio of the Schmidt, and dt is the thickness change. The maximum defocussing from this formula is ∿3.3μm across an image, which is less than a tenth of the average image diameter in 1½-2 arc second seeing. Therefore images through different parts of the filter will be defocussed by a tenth of the seeing disc. Since the measuring machine used for the plate integrates the pixels of an image, a smudging out of the intensity distribution should not significantly affect the calculated magnitude. It is noted that the thickness of the Polaroid filter is very nearly as uniform as the standard Schott colour filters used by the Schmidt. For a summary, see Table 7.1.

7.1.4 Single vs. Multiple Exposures

A complete set of polarization plates is obtained by making four consecutive exposures, each through a different position angle of the filter. Four orientations is the minimum number needed to completely sample the polarization information on the plate. The four angles used are 0°, 45°, 90° and 135° measured from North-South through East. Early on it was decided to take separate exposures at each angle rather than multiple exposures on the same plate. The reason was that 4 consecutive exposures down to $m_B \sim 21$ would give an unreasonable number of overlapping images. To demonstrate this assume that all stellar images have radius r and that there are N stars above $m_B \sim 21$ per square millimetre on the plate. The Gaussian probability that a given stellar image does not overlap another star is,

$$p_* = \exp(-4\pi r^2 N) \qquad (7.5)$$

The probability of a multiple overlap of n stars is

$$p_*^n = p_*(1-p_*)^{n-1} \tag{7.6}$$

and the total number of multiple overlaps is given by the series

$$n_o = \sum \frac{Np_*^n}{n} = Np_*\left\{1 + \frac{(1-p_*)}{2} + \frac{(1-p_*)^2}{3} + \ldots\right\} = \frac{Np_* \log_e p_*}{(p_*-1)} \tag{7.7}$$

In this situation $(1-p_*) \ll 1$, so only overlaps of two stars are significant (i.e. the first two terms). If the area of the circular filter is A mm^2,

$$n_o = \frac{A}{2}(1-p_*) \tag{7.8}$$

From Allen (1973), the mean number of stars per square degree down to $m_{pg} \sim 21$ at medium galactic latitude is $\sim 10^4$. Therefore N $\simeq$ 3.5 and a seeing disc of 2" gives r $\simeq$ 0.015. Assuming that successive exposures place images randomly with respect to the first set (true if the mean distance between images is much greater than the displacement for subsequent exposures), the number of overlaps for multiple exposures to different limiting magnitudes is given below:

No. of Exposures	No. of overlaps/limiting magnitude (m_{pg}) 21	20	19	18	17	
2	3070	1230	490	387	310	
3	4590	1840	740	580	470	Total no. of images
4	6090	2450	980	770	620	194,000

For four exposures down to 21st magnitude there are $\sim$3% of the images which are double. However, in practice the situation is much worse than this because of the development of latent images, the explanation of which requires a brief discussion of the theory of the photographic process. The absorption of a photon by a silver halide crystal (which lies in the emulsion/gelatin matrix) raises an electron

from the valence to the conduction band of the crystal. Each absorption releases an electron-hole pair which is mobile and will diffuse through the crystal lattice. If recombination occurs a photon is emitted and no permanent chemical action takes place. But photoelectrons are usually trapped in regions of chemical impurity or lattice defects, and there they can neutralize an interstitial silver ion. A single silver atom formed at one of these sensitivity centres is not stable, but further neutralizations lead to a speck of silver of increasing size and stability. For a fine-grain, high-speed emulsion such as IIIa-J between three and six atom of silver are sufficient to form a developable image. The holes, which could act as a detrimental oxidizing agent on the latent images, are generally absorbed in the gelatin matrix.

Latent image formation is a probabilistic concept because of its dependence on microscopic parameters such as the mobility of ions, holes and electrons. A latent image is generally defined as a grain which as a result of exposure has a chance of 0.5 or better of being developed (Mees & James, 1966). Not every developable grain will end up being developed. The relevance to multiply exposed plates is clear. The first exposure will produce developable images down to (say) $m_B \sim 21$, but there will also be a continuum of grains which represent fainter objects and have a development probability low enough that they are not latent images. The second exposure will allow photons onto some images which were not developable and make them developable; it is entirely possible that undevelopable grains created by two exposures will together create a developed image. The relevant surface density in equation (7.6) will be larger than the nominal magnitude limit of each exposure implies. At a level fainter than $m_B \sim 21$ stars are outnumbered by galaxies and the number counts indicate $\sim 10^4$ per square degree down to $m_B \sim 23.5$ (Kron, 1978; Tyson & Jarvis, 1979; Karachentsev, 1980). The number of extra overlaps depends on the form of the probability function for grain development, but it will obviously become a substantial fraction of the total number of images. Moreover, the approximation $(1-p_*) << 1$ will not hold and multiple overlaps must be taken account of in equation (7.7).

The latent image problem necessitated taking separate exposures, and two advantages of multiple exposures were lost. First, with the set of four images in a very small area of the plate, emulsion sensitivity variations and plate-to-plate variations are minimized. Second, the matching of images is relatively easy because they are all in close proximity and in a fixed orientation with respect to each other. The use of the COSMOS measuring machine and software can bypass the second problem.

7.1.5 Operation

The principle of the filter is that intensities (or magnitudes) through four position angles can yield a degree of polarization and position angle for each stellar image. Measurements through the control region of the filter are used to define differences in exposure time, emulsion sensitivity, atmospheric transmission and other effects between successive exposures. Use of the filter does not distinguish between polarization and variability; a change in the magnitude of an image could be due to either effect. The time for a set of sky-limited exposures is ~5 hours, so an object must vary by >0.2 magnitudes on that timescale to register falsely as a polarization candidate. BL Lacs are not only polarized but also highly variable, though there is little evidence for significant variability on a timescale of hours. An important aspect of the method is using more than one set of plates to search for the polarized objects. Several sets of plates can be used both to reduce the photometric errors for the bulk of unpolarized objects and to confirm the polarization and/or variability of the candidate BL Lac objects.

When partially linearly polarized light of intensity I is incident on the filter the transmitted intensity is,

$$T_{\phi}I = I\left\{\frac{(k_1+k_2)}{2} + p\,\frac{(k_1-k_2)}{2}\,\cos 2(\phi-\theta)\right\} \qquad (7.9)$$

where ϕ is the position angle of the filter and p and θ are the degree of polarization and position angle of the incident radiation. The intensity at angle ϕ is also written in terms of a control factor C_{ϕ}

which is taken from the control region and accommodates changes in observing conditions and sensitivity between plates,

$$I_{\phi} = C_{\phi} T_{\phi} I \tag{7.10}$$

From measured values of I_{ϕ} and C_{ϕ}, $T_{\phi} I = I_{\phi}/C_{\phi}$ can be calculated, hence the normalized Stokes parameters,

$$\frac{U}{I} = p \sin 2\theta = R\{\frac{T_{45}-T_{135}}{T_{45}+T_{135}}\} \tag{7.11a}$$

$$\frac{Q}{I} = p \cos 2\theta = R\{\frac{T_{0}-T_{90}}{T_{0}+T_{90}}\} \tag{7.11b}$$

Q, U and I are the Stokes parameters of the incident light, and R is essentially unity ($R - 1 < 0.006$ from instrumental tests). There are two levels of complexity in the analysis of the data.

(a) Differential Detection. If no calibration existed at all, it would still be possible to detect high degrees of polarization with the rotating filter. The overwhelming majority of stars will have no intrinsic linear polarization beyond a couple of percent and the differences of the transmitted intensities from the mean $(I_{\phi}-\bar{I}_{\phi})$ will be determined by noise, instrumental and measuring errors and other stochastic errors. The differences between T_0, T_{45}, T_{90} and T_{135} will be determined by the same errors, which by definition means that $(T_{45}-T_{135})$ and $(T_0-T_{90}0$ averaged over all stars will be zero. Most stars therefore define a transformation between values of T_{ϕ}, and highly polarized objects will stand away from this distribution. The significant transformations are between T_{45} and T_{135} and between T_0 and T_{90} because these correspond to the Stoke's parameters Q and U. The differential technique is useful for a quick-look for any highly polarized objects, since polarization represents a modulation of intensity and no zero point is required.

(b) Calibrated Detection. Evaluating the polarizations and magnitudes of all the objects on the plate requires knowledge of I, the total intensity. A photoelectric sequence defines the relationship between I_ϕ and I and p and θ can then be calculated from equations (7.11). The standard stars must be unpolarized otherwise they do not define a relationship where $\bar{I}_\phi$ corresponds to p = 0. It is inevitable that calibration introduces a host of new problems and uncertainties, including zero points, colour corrections, etc. In this case two techniques were used for the calibration, since obtaining a photoelectric sequence was only feasible down to $m_B \sim 16$. The sequence was extended down to $m_B \sim 19.3$ using sub-beam prism plates taken both at the U.K. Schmidt and the Anglo-Australian telescopes. The calibration of the photometry and polarimetry is discussed in Chapter Eight.

7.2 COSMOS

7.2.1 Description

The COSMOS machine at ROE, Edinburgh is a high-speed automatic microdensitometer. The scanning system digitises areas up to $\sim 700 cm^2$ with a flying spot scanner mapping the x-direction and the plate carriage being drifted in the y-direction. The plate is therefore scanned in lanes ∿1mm wide. The resolution of the machine is adjustable between 8, 16 and 32 micron spot sizes, and the position of the spot in a scan is controlled by a velocity control loop. A photomultiplier digitizes the transmitted intensity into 256 values, and a second photomultiplier provides a feedback loop to control the intensity of the spot. In practice the bandwidth of the feedback loop is sufficient to maintain the spot uniformity to better than 1%, which is compatible with the transmission digitisation error. 128 transmission levels corresponds to a dynamic range in photographic density of over two. Autofocus is a feature to correct for the sag of up to 250μm in a Schmidt plate held in the COSMOS plate carriage. Focus is maintained to $\pm$ 10μm. The mechanical aspects of the machine are controlled by a mini-computer.

The power and flexibility of COSMOS result from the use of a microprocessor for on-line image analysis. With Threshold Mapping (TM) data, the sky background level is followed across the plate and images a fixed percentage above the sky level in transmission are stored on magnetic tape. This compressed mapping saves a large amount of data storage for an entire Schmidt plate. Background following is done using a digital filter and is described by Martin and Lutz (1979). The threshold mapped data is passed through a software pattern analyser which connects up the separate pixels of an image into a coherent whole, and joins up split images which fall across a lane boundary. Parameters for up to 300,000 images can be stored on one magnetic tape, and there is flexibility in the choice of parameters that are retained. The design, construction and use of COSMOS is described by Pratt (1977). See also Stobie et al. (1979) and Dodd et al. (1979).

7.2.2 Image Parameters

The COSMOS parameters retained for each image are summarized below. Two sets of positions are available, with X and Y centroids intensity weighted and unweighted. The centroids can in practice be determined to ±1-2μm (or 0.1 arcseconds on the Schmidt plate). Second is the pixel area of the image above the threshold cut, and the minimum transmission level of the image which corresponds to the peak intensity. The maximum and minimum X and Y extents of each image are recorded in units of 0.1μm, along with the value of the sky intensity determined locally to the image. Finally, the pixel integrated intensity of the image is stored as calculated by,

$$I^* = \sum_{i=1}^{n} (I_i - I_{sky}) \qquad (7.12)$$

where n is the number of pixels contained in the image. It is the properties of I* that are of most interest in this work. The conversion from machine transmission level to intensity requires knowledge of the characteristic curve of the emulsion used. Normally, a calibration is established from the uniformly illuminated step wedges at the North and East fringes of each plate. The seven-step wedge

has fixed intensity ratios between successive steps and can be used to define a slope (γ) for the linear portion of the characteristic curve. Transmission scans across the wedges show that the profiles are very poor and the projection wedges have recently been replaced by calibration projectors based on the Kitt Peak design (Schoening, 1976). The calibration wedges are occluded on plates taken through the Polaroid filter, so a γ appropriate to IIIa-J emulsion was assumed (usually $\gamma = 4$). From this value a look-up table of conversions between transmission and intensity is calculated. It is recognized that the COSMOS intensities do not have a 1:1 relation with real intensities for several reasons. The assumed value of γ may not be correct. The COSMOS calibration is only valid for the linear part of the characteristic curve, and no account is taken of transmissions on the toe of the curve where the slope is changing. Photoelectric calibration is needed for a relationship between I* and true intensity.

For all the plates measured in this study, a 7% threshold cut was used. Only pixels with intensities 7% higher than the sky background were summed into I*. As will be shown in section 7.4 this leads to a systematic underestimating of the brightness of an image. The effect becomes worse at faint levels because a larger percentage of the image volume lies in the wings of the profile which are not included in the $\Sigma(I_i - I_{sky})$ parameter. COSMOS parameters for a typical unsaturated, stellar image are shown in Figure 7.7. A resolution of 8μm and a step size of 16μm were used for all the measurements, since a step size of twice the resolution optimizes the signal-to-noise, from information theory (Lynn, 1973). For each plate, the largest inscribed square in regions A and B (Figure 7.1) was mapped.

COSMOS software permits images to be reliably matched between plates. The image transformation is accurate to ∿1μm, so mismatches are extremely rare since the image size is ∿30μm. On one set of four 96.94% of the images were common to all four plates and on all sets of polarization plates the pairing completeness was very high.

7.3 Photographic Emulsion

7.3.1 Description

Kodak IIIa-J emulsion was used exclusively for this project. IIIa-J is a fine grain, high sensitivity emulsion which is optimum for long exposures at low light levels. The response curves are contained in Kodak publication P315 "Plates and films for scientific photrography". Prokof'eva (1979) has measured the DQE of a baked plate to be ~0.07%, and the spectral sensitivity extends from the ultraviolet up to 550nm. The slope of the linear part of the characteristic curve is $\gamma \simeq 4$ and is not very sensitive to differences in development time. The Schmidt Unit have evolved a method of hypersensitization which involves both long-term soaking in oxygen-free dry nitrogen gas at N.T.P. and a briefer period soaking in hydrogen gas. An optimum hypersensitizing procedure is determined for each new batch of plates, and the speed gain is normally a factor of ~20. For more details, see Sim (1977), Sim et al. (1976) and Kaye (1977).

Since the uniformity of a set of polarization plates is so important, several precautions were taken to avoid unnecessary variations between the plates. For an ideal set of exposures, the plates were mated throughout the development process. The four plates initially come from the same batch and the same Kodak box (but not the first or last plates in a box which are sometimes slightly spoiled). The plates are then hypersensitized in the same aluminium box. Ideally, the four exposures are taken consecutively on a night of stable conditions in terms of moonlight, seeing, humidity, temperature, etc. Finally, the plates are mated through every phase of the developing procedure: developing, stopping, fixing (twice), rinsing, hypo-clearing, washing and photoflo. While there is no indication as to the degree of improvement in plate-to-plate consistency using these procedures, they should minimize the variability factors which are not accounted for using the control regions.

7.3.2 Filter/Emulsion Combination

IIIa-J emulsion is normally used in conjunction with the Schott UV cut-off filter GG395; the combination defines the non-standard "J" photometric band. The transformation to the standard Johnson system is,

$$(B-J) = (0.32 \pm 0.03)(B-V) \qquad (7.13)$$

from the UK Schmidt Telescope Handbook (1980). There is only room in the Schmidt plateholder for one filter, so the GG395 could not be used in conjunction with the Polaroid filter. The spectral band is defined by the convolution of the spectral response function of IIIa-J emulsion and the transmission curve of the Polaroid-glass sandwich (Figure 7.8). It can be seen that the HN 32/glass transmissivity cuts off nearly as steeply as the GG 395 filter, so there should not be any blue leak. On the other hand, the transmissivity is rising across the B band, so a red leak is expected. By convolving the curves numerically at 100 Å intervals, normalizing, and convolving with the Johnson B and V passbands, the colour term for the Polaroid magnitude J′ was found to be,

$$(B-J') = (0.37 \pm 0.04)(B-V) \qquad (7.14)$$

which is similar to the Schmidt J magnitude. It should be noted that J and J′ have no relation to the Johnson J (1.25μm) band described earlier.

7.4 Sources of Error

There are many sources of error which must be folded into the analysis of photographic photometry, and which fall into three general classes. First, there are effects due directly to the manufacture and treatment of the emulsion; such as sensitivity variations, non-uniform developing, fixing or hypersensitizing, and chemical fog variations. Second, there are effects which change the photon flux

onto the plate; such as differences in exposure, vignetting due to telescope optics, transmission variations across the filter, and sky brightness variations. Finally, there are errors in the machine measurement. Some of these, like digitization noise, are obvious; but some depend subtly on the way COSMOS measures a stellar image and will tend to exaggerate systematically the difference between COSMOS intensity and true intensity for an object.

It is convenient to operate in Baker densities because the background densities on the polarization plates are not much above the chemical fog level. de Vaucouleurs (1968) exhumed the original Baker (1925) formalism as a way of linearizing the toe of the characteristic curve. Diffuse density of a developed image is normally defined as,

$$D = \log_{10}(1/T) \tag{7.15}$$

where T is the transmittance. The relationship between D and log (exposure), or equivalently log (intensity) is given by the familiar characteristic curve (Figure 7.9a). It has been found empirically that a simpler relation results by using,

$$D_B = \log_w = \log(\frac{T_c}{T} - 1) \tag{7.16}$$

where T_c is the background fog level or clear transmission of the plate. Note that transmissions T, T_c measured by COSMOS must have other contributions due to stray light, photomultiplier dark current and zero-point shift of the A-D converter subtracted off. The significant feature of the Baker formalism is that it relates densities to a zero point of T_c and produces a linear slope at low densities ($D_E < 2.5$).

$$I = A(\frac{T_c}{T} - 1)^n = A\omega^{1/\gamma'} \tag{7.17}$$

where A is a constant, and the gradient of the Baker density characteristic curve is $\gamma' = 1/n$. The Schmidt Unit have measured D_B for different batches of IIIa-J emulsion (Figure 7.9b) and the linearity is not as good as for other emulsions such as IIa-O. The

slope at D = 0.2 above chemical fog level for instance is $\gamma' = 2.0$ compared to $\gamma'_{MAX} = 2.8$. The equivalent figures for normal density are $\gamma' = 1.0$ at D = 0.2 above fog and $\gamma'_{MAX} = 4.2$. Therefore COSMOS calibration in terms of Baker density will not produce a 1:1 relationship between COSMOS intensity and true intensity. However the fact that γ for areas of sky and image will be similar allows a simplified treatment of many of the sources of error in COSMOS photometry.

7.4.1 Emulsion Sensitivity and Development Variations

The effect of development time on the characteristic curve is shown in Kodak publication P-315. The shape of the characteristic curve is unchanged and is shifted vertically on the density axis, therefore for small variations in developing the change in image density is proportional to γ' (i.e. the speed). Emulsion sensitivity variations can be considered as the same sort of small displacement, this time along the intensity axis. In other words small changes in development time are equivalent to small changes in density, and small changes in emulsion sensitivity are equivalent to small exposure changes. These assumptions hold for Baker densities, where γ' = constant for dD_B and d(logI)small. For small changes,

$$dD_B = \gamma' d\,\log I \tag{7.18}$$

and

$$\frac{(dD_B)_{sky}}{(dD_B)_{obj}} = \frac{\gamma'_{BG}}{\gamma'_{obj}} = \alpha \tag{7.19}$$

If the Baker density was linear over its entire range with logI then α would equal 1, which from Figure 7.9 is a good assumption. Now move to the transmissions used by COSMOS, from equation (7.19),

$$\frac{\log\left\{T^{(2)}_{sky}/T^{(1)}_{sky}\right\}}{\log\left\{T^{(2)}_{obj}/T^{(1)}_{obj}\right\}} = \frac{\log(1+k_{sky})}{\log(1+k_{obj})} = \alpha \tag{7.20}$$

where k_{sky} and k_{obj} are the fractional changes in transmission for sky and image pixels respectively. If $\alpha = 1$, $k_{sky} = k_{obj} = k$ and the incoming intensity is,

$$I_i = A\left[\frac{T_c}{T_i(1+k)} - 1\right]^n \tag{7.21}$$

for most pixels $T_c/T >> 1$ and for small sensitivity changes $k << 1$, therefore approximately,

$$I_i = A(1+k)^{-n}\left[\frac{T_c}{T_i} - 1\right]^n = A(1+k)^{-n}\omega_i^n \tag{7.22}$$

The variations in the amplitude of k will always be small over the localized region covered by one image, so the summation over pixels will have the same k, and the locally determined sky background will also have the same k value,

$$I_{sky} = A(1+k)^{-n}\left[\frac{T_c}{T_{sky}} - 1\right]^n = A(1+k)^{-n}\omega_{sky}^n \tag{7.23}$$

Thus the sensitivity factor can be scaled out by dividing the image intensity by I_{sky} at each pixel,

$$I^* = \sum_{i=1}^{n} (I_i - I_{sky})/I_{sky} \tag{7.24}$$

This is an important result which can correct for emulsion variations in principle. There is an important exception, which is if there are <u>real</u> variations in sky intensity across the plate (see next section). The effect of assuming $\alpha = 1$ can be calculated. In general, Figure 7.9b is not a straight line and α will be a function of density. The worst case assumes that $\gamma'_{obj} = \gamma'_{MAX} = 2.8, \gamma'_{BG} = 2.0$, therefore $\alpha = 0.71$ and from (7.20),

$$(1+k_{sky}) = (1+k_{obj})^{\alpha} \tag{7.25}$$

Substituting in (7.22) and (7.23) gives,

$$\Delta I^* = \sum_{i=1}^{n} \left[(1-k_{obj})^{-n(1-\alpha)} - 1\right](I_i - I_{sky})/I_{sky} \tag{7.26}$$

For $\alpha = 0.71$ and $n = 0.5$ and a 10% senstivity variation $k_{obj} = 0.1$, the extra factor gives $\Delta I^* \approx 0.01 I^*$ so the use of equation (7.24) is valid even if the true non-linear form of the Baker density curve is used.

7.4.2 Vignetting, Sky Variations and Filter Transmission Variations

These effects are independent of the varying properties of the IIIa-J emulsion and result from modulation of the incident light before it reaches the photographic plate. The vignetted part of the plate is where obstructions in the optical path reduce the photon flux; the periphery of the plate sees a smaller telescope aperture. The transmission variations due to the corrugations in the filter also reduce the photon flux in certain areas. In both cases the fractional loss in the image pixel, I_i, is the same as the fractional loss in sky background, I_{sky}.

$$\frac{\Delta I_i}{I_i} = \frac{\Delta I_{sky}}{I_{sky}} = K \qquad (7.27)$$

$$\text{and} \quad I_i' = (1+K) I_i \,, \quad I_{sky}' = (1+K) I_{sky} \qquad (7.28)$$

$$\text{therefore} \quad I^* = \sum_{i=1}^{n} (I_i - I_{sky})/I_{sky} \qquad (7.24)$$

applies again. The effects of k and K can be shown graphically in terms of COSMOS transmission. Taking values of $T_c = 500$, $n = 0.5$, and various values of T, I_i is plotted against both k and K in Figure 7.10 (a & b). I_i goes as $\sim 1/\sqrt{k}$ and $\sim 1/K$ respectively. Comparing equations (7.21) and (7.22), the approximation is good to <1% for $0 < T < 100$.

Some of the contributors to k and K can be estimated. Tests on the filter show the effect of corrugations to be $K_c < 0.04$. The vignetting function in the UKSTU Handbook indicates that out to the edge of the circular filter $K_v < 0.05$. Sensitivity variations are more difficult to estimate since little systematic work has been published in this area. Tests by the Schmidt Unit on batches of IIIa-J

suggest that variations across a plate are likely to be $k_s < 0.01$. A IIIa-J plate from the same batch as the polarization plates was exposed in a light tunnel at UKSTU in Australia and variations in density measured on a MacBeth spot densitometer confirm that $k_s < 0.01$. The important qualification on the use of equation (7.24) is if the sky variations across the plate are real, or exceed the sensitivity variations. Then scaling by I_{sky} for each image is inappropriate and the original intensity $I^* = \Sigma_n(I_i - I_{sky})$ should be used (equation 7.12). When a calibration is available equations (7.12) and (7.24) can be decided between empirically.

7.4.3 COSMOS Measurement Biases

One of the limitations of COSMOS for faithfully recording the density of a photographic plate is the limited dynamic range, which compares unfavourably with a PDS machine. COSMOS can only handle a density range of ∿2 and transmission levels are digitized into 256 steps. Obviously, for a given pixel the digitization noise is more significant when I_i is not much larger than I_{sky}. Propagating errors in (7.17) with $\sigma(T_c)$ and $\sigma(T_i) = 1$ by definition,

$$\sigma_D^2(I_i) = \left[\frac{An}{T_i}\left(\frac{T_c}{T_i} - 1\right)^{n-1}\right]^2\left[1 - \frac{T_c^2}{T_i^2}\right] \qquad (7.29)$$

giving, $$\frac{\sigma_D(I_i)}{I_i} = \frac{n}{T_i}\left(\frac{T_c+T_i}{T_c-T_i}\right)^{\frac{1}{2}} \qquad (7.30)$$

and, $$\frac{\sigma_D(I_{sky})}{I_{sky}} = \frac{n}{T_{sky}}\left(\frac{T_c+T_{sky}}{T_c-T_{sky}}\right)^{\frac{1}{2}} \qquad (7.31)$$

therefore, $$\sigma_D(I^*) = n\left\{\left(\frac{I_i}{T_i}\right)^2 + \left(\frac{I_{sky}}{T_{sky}}\right)^2\right\}^{\frac{1}{2}} \qquad (7.32)$$

Even more important than the limited dynamic range is the systematic biassing of faint magnitudes by the thresholding procedure. In

Figure 7.7 the volume integrated by COSMOS is indicated by the shaded area, and the unshaded wings are lost. For a given threshold cut, the loss is clearly greater for fainter and fainter images. Empirically, the density profiles of faint stars have a Gaussian shape (Auer & van Altena, 1978), and it is assumed that the intensity profile is Gaussian with half-width a_e and maximum height above sky I_o. a_t is the width at the threshold intensity I_{thr}. Let c be the fractional percentage cut above sky intensity and s be the ratio of peak object to sky intensity,

$$I_o = s\, I_{sky} \tag{7.33}$$

$$I_{thr} = (1+c) I_{sky} \tag{7.34}$$

$$\Delta I = c\, I_{sky} \tag{7.35}$$

The total image intensity can now be expressed in terms of COSMOS parameters I_o, I_{sky}, I_{thr} and a_t without summing over $(I_i - I_{sky})$. The image profile is,

$$I(r) = I_o e^{-r^2/a_e^2} \tag{7.36}$$

Integrating over the volume,

$$I^* = \int_o^\infty I(r) 2\pi r dr \tag{7.37}$$

$$I^* = \pi a_e^2 I_o \tag{7.38}$$

However, note that,

$$\Delta I = I_c e^{-a_t^2/a_e^2} \quad , \quad a_t = \sqrt{\log s/c} \tag{7.39}$$

since $I_o/\Delta I = s/c$. This gives,

$$I^* = \frac{\pi a_t^2 I_o}{\log(s/c)} \tag{7.40}$$

The wings of the image are given by,

$$I^*_w = \int_{\infty}^{a_t} I_o \left\{ e^{-r^2/a_c^2} \right\} 2\pi r dr \tag{7.41}$$

$$I^*_w = \pi a_e^2 I_o \left(\frac{c}{s}\right) = I^* \left(\frac{c}{s}\right) \tag{7.42}$$

$$\therefore I^*_w / I^* = c/s \tag{7.43}$$

This is a very simple relationship between the fraction of image intensity lost by thresholding, the threshold cut c and the signal/sky ratio s. s can be related directly to the magnitude if a calibration is available, and it is clear from (7.43) that as s approaches c the COSMOS summed intensity will heavily underestimate the true intensity (see Figure 7.11). The question is whether in practice the Gaussian intensity indicator is any better than the ΣI parameter. The quantization noise affecting (7.40) can be calculated by propagating errors in,

$$I^* = \frac{AI_o}{\log\left[\frac{I_o}{I_{thr} - I_{sky}}\right]} \tag{7.44}$$

with the result,

$$\left(\frac{\sigma_D(I^*)}{I^*}\right)^2 = \left(\frac{1}{A}\right)^2 + \left(\frac{I^*}{A\Delta I}\right)^2 + \left(\frac{1}{I_o} - \frac{I^* \Delta I}{AI_o^2}\right)^2 \tag{7.45}$$

The largest uncertainty in the use of equation (7.40) is the assumption that all the image profiles are Gaussian. Recent work with IIIa-J plates and COSMOS measurements indicates that there are "field effects" or magnitude offsets across some plates of amplitude up to 0.3-0.4 magnitudes (Gilmore, Ellery: private communications). These field effects can be explained at least in part by image profile variations over the plate. While this does not prove that profile variations dominate the errors, once it is acknowledged that the Gaussian approximation may not be entirely correct then equation (7.40)

becomes a bad brightness indicator. In practice, the ΣI parameter is often a better choice. On a calibrated plate it is possible to invert the procedure and detect the image profile variations by the deviations of the measured intensities from (7.40).

7.4.4 Photon Signal-to-noise

For faint objects the DQE of the photographic plate becomes important. The DQE of 0.0007 for IIIa-J is typical but the value depends on exposure and can be maximized by judicious choice of exposure and film speed. In general,

$$DQE = \frac{(S/N)^2_{OUT}}{(S/N)^2_{IN}} \tag{7.46}$$

and for a high contrast emulsion it can be shown that,

$$DQE \propto \frac{(dD/d\ \log E)^2}{\sigma(D)^2} \tag{7.47}$$

where S, D and E are speed, density and exposure. $\sigma(D)$ is a measure of granularity. It is more important to have fine grain and high contrast than speed, and IIIa-J is optimal in this regard. Experimentally it is found that $\sqrt{DQE}$ increases with increasing exposure, flattens off and falls (Marchant & Millikan, 1965). Meanwhile the $(S/N)_{IN}$ is increasing as $\sqrt{t}$, so the optimum $(S/N)_{OUT}$ occurs when the product of $(S/N)_{IN}$ and $\sqrt{DQE}$ is a maximum as equation (7.46) indicates. Hypersensitization is very helpful for low $(S/N)_{IN}$ because it increases the speed without lowering the DQE or $(S/N)_{IN}$, and minimizes the effect of low intensity reciprocity failure. Kodak quote the optimum exposure level for IIIa-J to correspond to a diffuse density of 0.6 to 1.0 above clear plate, and since most of the polarization plates have D ~ 0.3 to 0.4 the DQE will not be optimized. Most of the exposures are 50-60 minutes, so even longer exposures would, in principal, be advantageous. However the problem of taking four consecutive exposures in constant atmospheric conditions made longer exposures impractical.

The plate limit through Polaroid in ∿50 minutes is $m_B \sim 21$. For $m_V = 0$, use a flux of 10^3 photons $s^{-1} cm^{-2} \text{Å}^{-1}$ which gives an input signal-to-noise of,

$$(S/N)_{IN} = 5.8 \times 10^4 \tag{7.48}$$

and even for a modest DQE of 0.0007, $(S/N)_{OUT} > 10^3$. So the photon statistics only produce 0.1% fluctuations for the images of interest. Photon noise is heavily dominated by the other systematic errors discussed in this section.

7.5 Reduction

7.5.1 Assumptions

The response of the filter to partially polarized light was given by equation (7.9). From the instrumental tests $k_1/k_2 > 2 \times 10^4$ and (7.9) reduces to,

$$T_\phi I = \frac{Ik_1}{2} \left\{ 1 + p \cos(\phi - \theta) \right\} \tag{7.49}$$

which becomes Malus' Law when p = 1. The transmitted intensity at an angle ϕ takes into account the control factor C_ϕ,

$$I_\phi = C_\phi T_\phi I = C_\phi \frac{Ik_1}{2} \left\{ 1 + p \cos(\phi - \theta) \right\} \tag{7.50}$$

To calculate a degree of polarization, it is assumed that neither the degree of polarization nor the total intensity of the object change during the four consecutive exposures (usually a duration of 4-5 hours). The infrared data in Chapter Three and other observations of BL Lac objects discussed in Chapter One indicate that this is true to ∿2-3%. The plates are equally sensitive to rapid variability and to high polarization, but only a very limited number of objects (eclipsing binaries, novae, flare stars) have flux that varies by ∿0.5 magnitudes in several hours. There will be only minor contamination of any BL Lacs by variables (which are liable to be interesting

objects in their own right). A variable and a polarized object are also distinguishable by their light curves. The four position angles sample a complete cycle of polarization modulation while the light changes between the exposures for a variable would be monotonic.

Another assumption is that the four angles $\phi = 0^\circ, 45^\circ, 90^\circ, 135^\circ$ sample a unique polarization curve, with mean (unpolarized) intensity $\bar{I}$. From (7.49),

$$\bar{I} = \tfrac{1}{4} \sum_{\phi} T_{\phi} I = \frac{Ik_1}{2} \tag{7.50}$$

Therefore the mean measured intensity, including the control factors, is

$$\bar{I} = \tfrac{1}{4} \sum_{\phi} I_{\phi} = \left\{ C_0 T_0 + C_{45} T_{45} + C_{90} T_{90} + C_{135} T_{135} \right\} I \tag{7.51}$$

Finally, the analysis is only correct for partially polarized light. Any component of intrinsic circular polarization will be seen as a D.C. level by the analyzer. BL Lac objects show no evidence of significant circular polarization in the optical region (for references see Section 2.3.4). As in Section 2.3.2, the instrumental polarization due to telescope optics is ignored. For the purposes of this survey, the telescope/filter combination is a perfect polarimeter.

7.5.2. Control Factors

The control factors C_ϕ are derived from comparisons between stars in the control regions on different exposures. C_ϕ compensates only for bulk differences between the plates, which can involve exposure time, emulsion sensitivity, atmospheric transmission, zenith distance, seeing and processing effects. $C_\phi(I)$ will generally be a function of magnitude. Unfortunately, the control regions cannot correct for the fact that $C_\phi(I)$ may vary across a given plate, $C_\phi(I) \longrightarrow C_\phi(I,x,y)$. Some of these variations across a plate have already been discussed: they include field effects, filter corrugations, sensitivity variations, vignetting and a range of processing faults. It is the variations in x and y (of C_ϕ) that will limit the photographic technique since C_ϕ can not be a factor for an entire plate. In the

control regions (with no variations in x and y),

$$I^c_\phi = A\, C_\phi\, I \tag{7.52}$$

where A is a constant. Therefore,

$$\frac{C_0}{C_{90}} = \frac{I^c_0}{I^c_{90}} \quad , \quad \frac{C_{45}}{C_{135}} = \frac{I^c_{45}}{I^c_{135}} \tag{7.53}$$

7.5.3 Analysis

For dealing in polarization, it is more convenient to deal with intensities than magnitudes. From equations (7.11a & b),

$$p = \left\{ \left(\frac{1 - T_{90}/T_0}{1 + T_{90}/T_0} \right)^2 + \left(\frac{1 - T_{45}/T_{135}}{1 + T_{45}/T_{135}} \right)^2 \right\}^{\frac{1}{2}} \tag{7.54}$$

$$\theta = \tfrac{1}{2} \arctan \left(\frac{1 - T_{135}/T_{45}}{1 + T_{135}/T_{45}} \right) \Bigg/ \left(\frac{1 - T_{90}/T_0}{1 + T_{90}/T_0} \right) \tag{7.55}$$

From equation (7.10),

$$\frac{T_{90}}{T_0} = \frac{I_{90} C_0}{I_0 C_{90}} \quad , \quad \frac{T_{135}}{T_{45}} = \frac{I_{135} C_{45}}{I_{45} C_{135}} \tag{7.56}$$

and using equation (7.53),

$$\frac{T_{90}}{T_0} = \frac{(I_{90}/I^c_{90})}{(I_0/I^c_0)} \quad , \quad \frac{T_{135}}{T_{45}} = \frac{(I_{135}/I^c_{135})}{(I_{45}/I^c_{45})} \tag{7.57}$$

Since the two terms in (7.54) represent independent Stokes parameters, for conciseness write $T_Q = T_0/T_{90}$ and $T_U = T_{45}/T_{135}$, giving

$$p = \left\{ \left(\frac{T_Q - 1}{T_Q + 1} \right)^2 + \left(\frac{T_U - 1}{T_U + 1} \right)^2 \right\}^{\frac{1}{2}} \tag{7.58}$$

$$\theta = \tfrac{1}{2} \arctan \left\{ \left(\frac{T_U - 1}{T_U + 1} \right) \Big/ \left(\frac{T_Q - 1}{T_Q + 1} \right) \right\} \tag{7.59}$$

Propagating errors through (7.58) and (7.59),

$$\sigma^2(p,\theta) = \left(\frac{\delta(p,\theta)}{\delta T_Q} \right)^2 \sigma^2(T_Q) + \left(\frac{\delta(p,\theta)}{\delta T_U} \right)^2 \sigma^2(T_U) \tag{7.60}$$

therefore,

$$\sigma^2(p) = \frac{4}{p^2} \left\{ \left(\frac{T_Q - 1}{T_Q + 1} \right)^2 \frac{\sigma^2(T_Q)}{(T_Q+1)^4} + \left(\frac{T_U - 1}{T_U + 1} \right)^2 \frac{\sigma^2(T_U)}{(T_U+1)^4} \right\} \tag{7.61}$$

where,

$$\frac{\sigma^2(T_Q)}{T_Q^2} = \sigma^2(T_O) - \frac{\sigma^2(T_{90})}{T_{90}^2} \tag{7.62}$$

and

$$\frac{\sigma^2(T_U)}{T_U^2} = \sigma^2(T_{45}) - \frac{\sigma^2(T_{135})}{T_{135}^2} \tag{7.63}$$

For θ, use the fact that $d(\tan 2\theta) = 2\sec^2\theta d\theta$ and the relation $\sec^2\theta = 1 + \tan^2\theta$. After manipulation,

$$\sigma^2(\theta) = \frac{1}{p^4} \frac{\left\{ (T_Q^2 - 1)^2 + (T_U^2 - 1)^2 \right\}}{(T_Q + 1)^2 (T_U + 1)^2} \tag{7.64}$$

The most important feature of equations (7.54) and (7.55) for p and θ is that they are independent of the incident intensity I. The only parameters required are the ratio of measured intensities between orthogonal filter positions, and the ratio of the two measured

intensities in the control areas. The polarization is a measure of the modulation of the intensity and does not require a zero point. Therefore intensities from any measuring machine such as COSMOS can be used without calibration, as long as COSMOS always measures a given image in the same way (repeatability and consistency).

The reality is very different from this idealized picture. In practice, most of the scatter in a plot of I_{90} vs. I_0 or I_{135} vs. I_{45} will be due to noise and systematic errors already described. For the average star, with very low (1-3%) intrinsic polarization, the polarization signal-to-noise ratio will be very low. Formulae derived in this section will not apply, and the noise scatter can only be quantified with a photoelectric calibration. Therefore, a calibration is needed to derive a rigorous detection limit of polarization even though an individual measure is independent of I.

To understand the effect of noise on polarization detectability, consider the simple case where $T_U = 1$, i.e. all polarized flux lies in the Q Stokes' parameter. From equations (7.58) and (7.61),

$$\frac{p}{\sigma(p)} = \frac{2\sigma(T_Q)}{(T_Q^2-1)} \qquad (7.65)$$

$\sigma(T_Q)$ represents the photometric scatter in a plot of I_{90} vs. I_0. The signal-to-noise $p/\sigma(p)$ as a function of p and $\sigma(T_Q)$ is plotted in Figure 7.12a. For example, a polarization of 10% is impossible to detect at a level of 5 times the noise unless the r.m.s. scatter on I_{90} vs. I_0 is less than 5%. This graph can be used as a rough guide to the detectability of different levels of polarization in the presence of all other kinds of random noise. Another factor that affects the detection is the position angle of the polarization. In theory, if Q = 0 then $I_0 = I_{90}$ and if U = 0 then $I_{45} = I_{135}$. Each orthogonal pairing defines a Stokes' parameter, and Q and U are independent. To consider detectability and position angle, rearrange (7.11a & b),

$$T_Q = \frac{1+p\sin 2\theta}{1-p\sin 2\theta} \qquad (7.66a)$$

$$T_U = \frac{1+p\cos 2\theta}{1-p\cos 2\theta} \tag{7.66b}$$

Rewriting (7.61) in terms of p and θ, with $\sigma(T_Q) = \sigma(T_U)$,

$$\sigma^2(p) = \frac{\sigma^2(T_{Q,U})}{4}\left\{\cos^2 2\theta(1-p\cos 2\theta)^4 + \sin^2 2\theta(1-p\sin 2\theta)^4\right\} \tag{7.67}$$

$$\text{For small p,}\quad \sigma(p) \simeq \frac{\sigma(T_{Q,U})}{2} \tag{7.68}$$

When p is larger, $\sigma(p)$ is a complicated function of θ which is plotted in Figure 7.12b. For large polarizations, the signal-to-noise can be quite sensitive to the intrinsic position angle. In principle, a degree of polarization can be calculated from measures on any three out of the four plates. However, one of the Stokes' parameters would then only be represented by one measurement and the error on that ill-determined Stokes' parameter would dominate the final error in p. For this reason, the reductions from three plates are of limited value and are not considered here.

It is much more convenient to deal with intensities than magnitudes when calculating degrees of polarization. However, it is conventional in photographic photometry to work in terms of magnitude. The detection of polarization calls for detecting a certain magnitude difference between images on plates taken through orthogonal positions of the filter. For a polarization p, the magnitude difference between I_{90} and I_0, I_{135} and I_{45} is,

$$-\frac{\sqrt{2}}{2}\ 2.5\log\left(\frac{1+p}{1-p}\right) < \Delta m < -\ 2.5\log\left(\frac{1+p}{1-p}\right) \tag{7.69}$$

The lower limit corresponds to $\theta = 22.5^\circ$ and equal contributions from both Stokes' parameters since the position angle is midway between sampling angles. The top limit occur for a position angle at one of the sampling angles and all the modulation in one Stokes' parameter. The 0°-90° and 45°-135° magnitude differences can be tabulated,

p(%)	Δm(max)	Δm(min)
5	0.11	0.08
10	0.22	0.15
15	0.33	0.23
20	0.44	0.31
25	0.55	0.39
30	0.67	0.48
35	0.79	0.56

TABLE 7.1

Details of the Polaroid Filter

Program area = 560cm^2 Control area (unvignetted) = 62cm^2

Glass:
- Nominal thickness = 0.686cm
- Thickness variations $\lesssim$ 55μm
- Radius of curvature of top surface 8x10^{4}cm

Polaroid:
- Type = HN32
- Polarizance, R = 0.99993
- Extinction Ratio, ρ = 28,570
- Transmission variations < 4%
- Transmission variations, $\lambda \simeq$ 3-4cm
- Position angle, absolute = $\pm$0.2^o
- Position angle, wander < 0.05^o

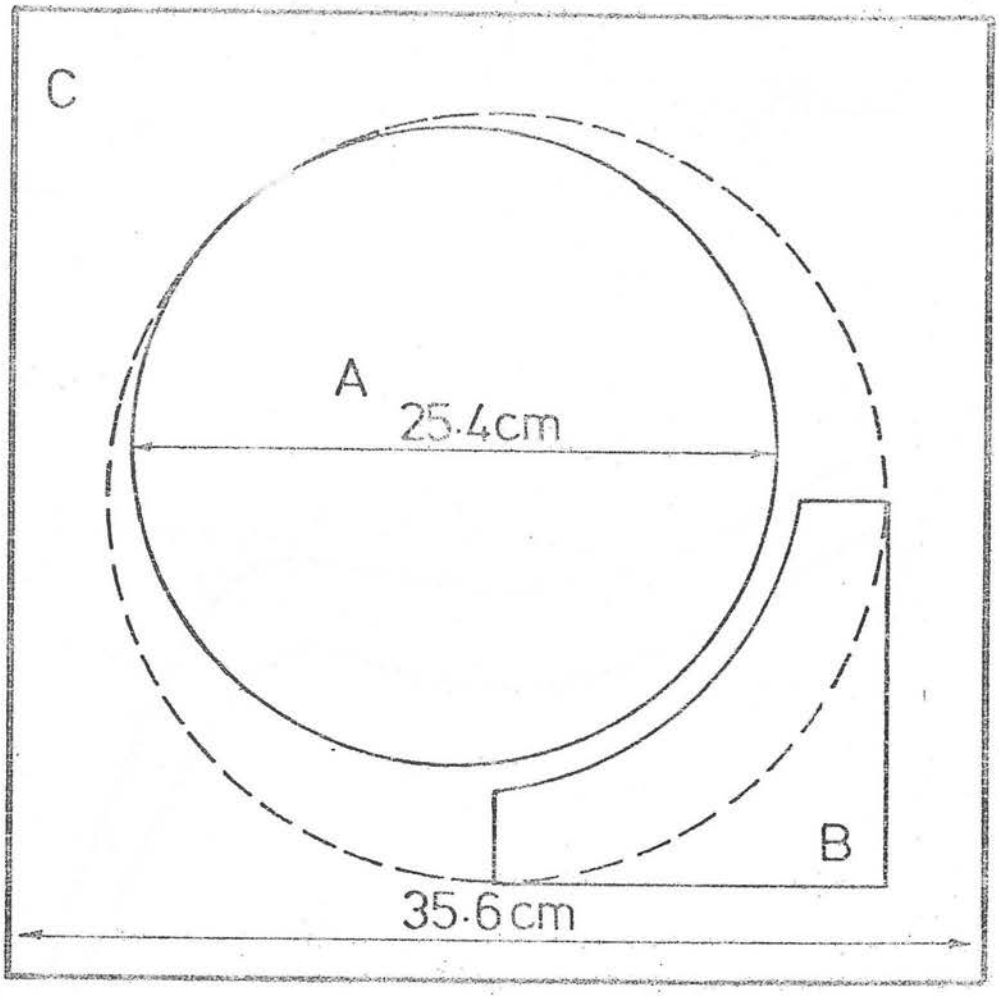

Figure 7.1 Linear polarizing filter.
(A) is a rotatable program area (diameter 25.4cm) of HN-32 Polaroid, and (B) is a static piece of HN-32 to act as the control area. The rest of the plate is occluded by the filter-holder, and the dotted line is the unvignetted region of the plate.

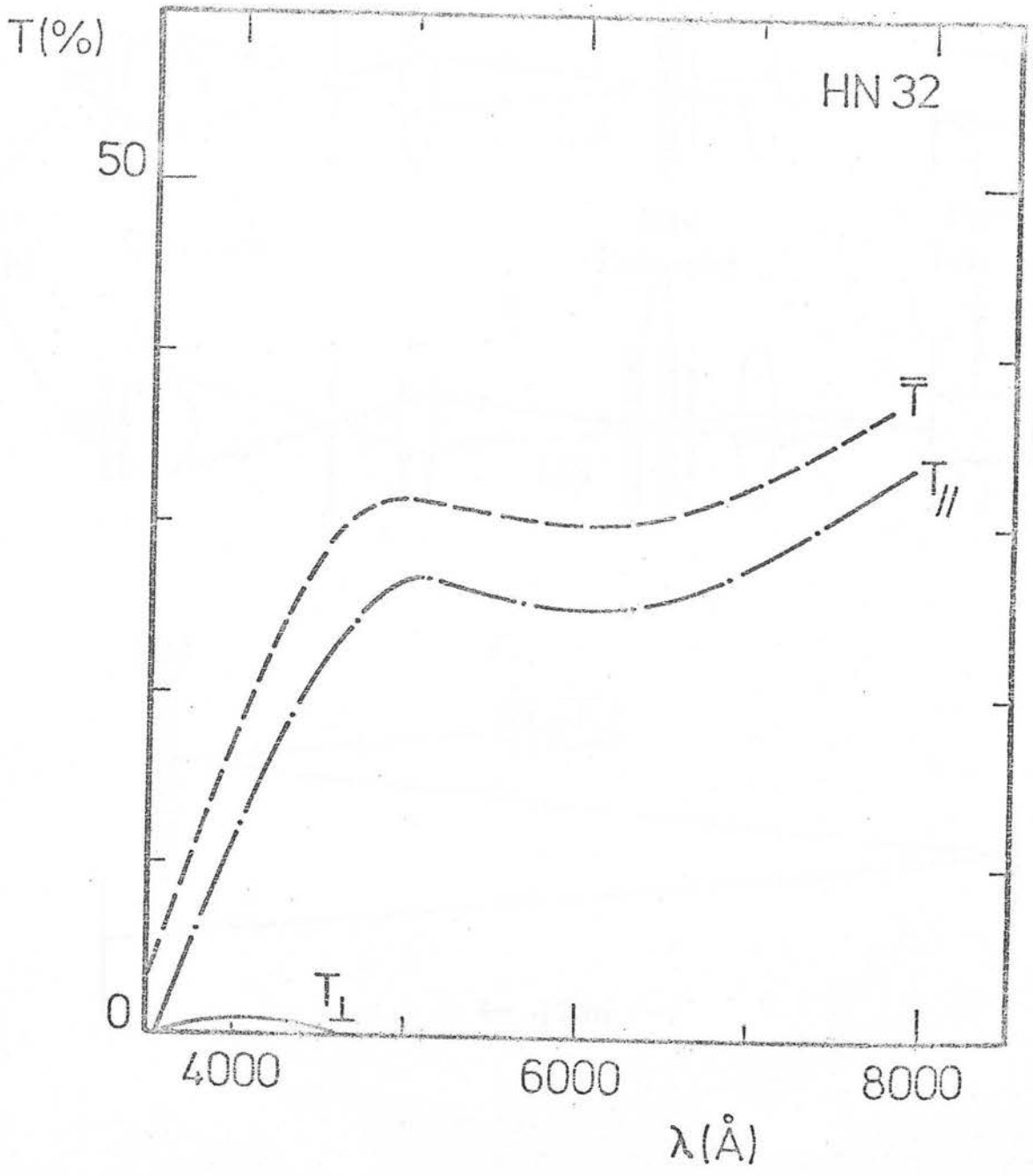

Figure 7.2 Spectral transmission of HN-32 with respect to:
$\bar{T}$ - unpolarized light, single polarizer
T - two polarizers, axes parallel
T - two polarizers, axes crossed
Vertical scale is magnified 1000 times for T
(data from Polaroid Corporation Ltd.).

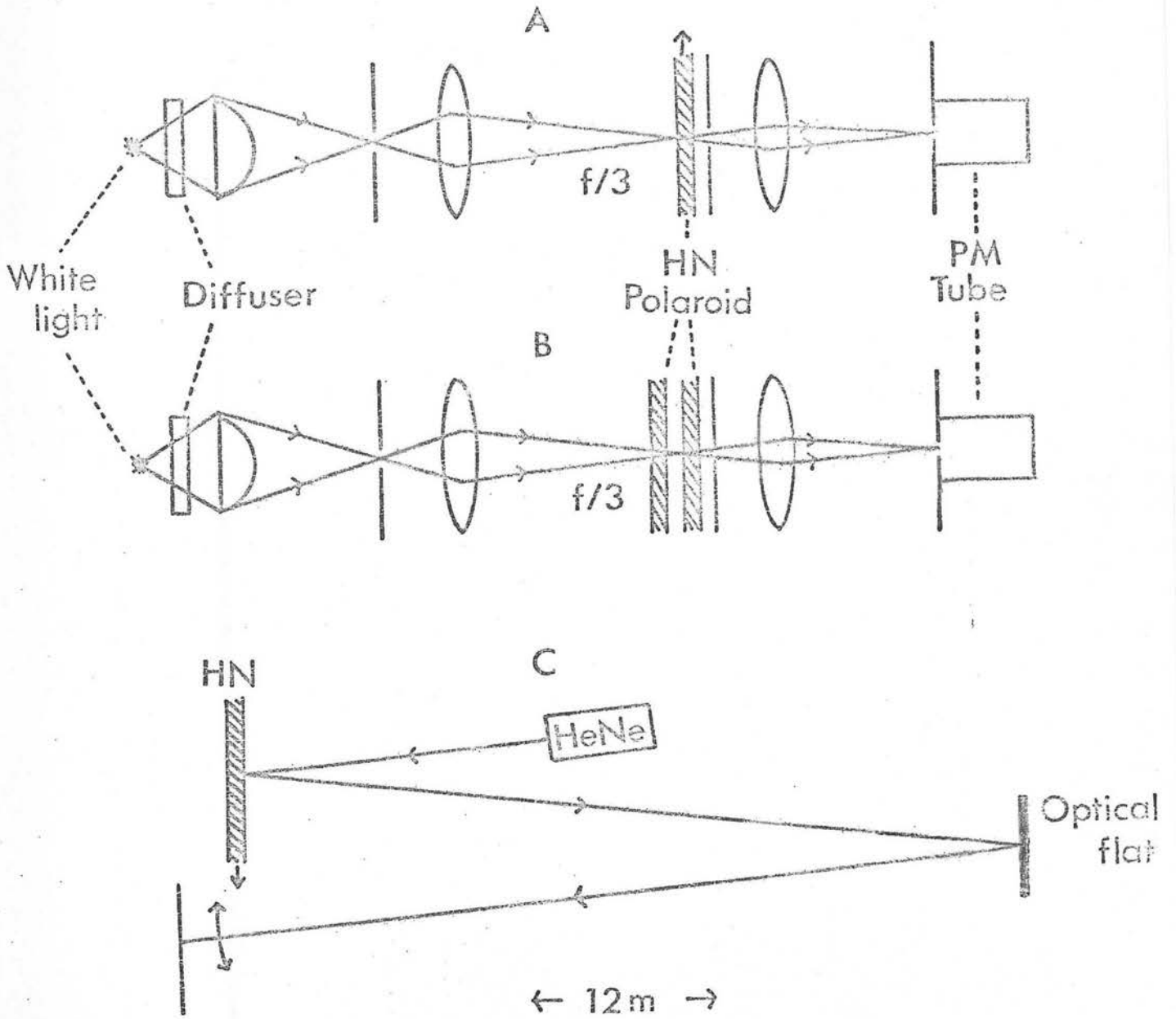

Figure 7.3 Optical train for laboratory filter tests.

a) Transmission test.

b) Crossed Polaroid extinction and optical axis test.

c) Planarity test.

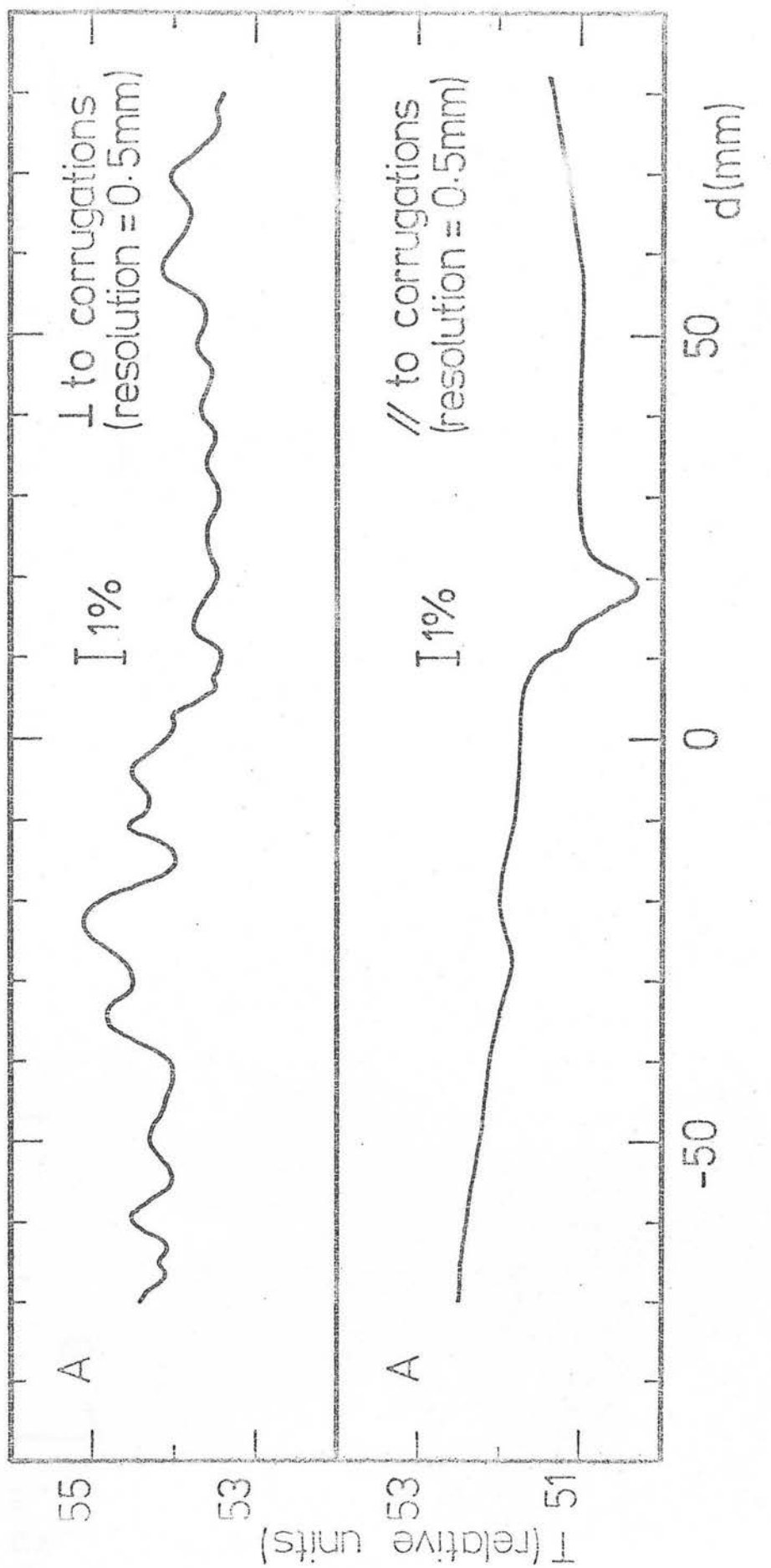

Figure 7.4 Transmission scans across the filter perpendicular and parallel to the axis of corrugation. ΔT of 1% is shown as error bar. d=0 is centre of the filter.

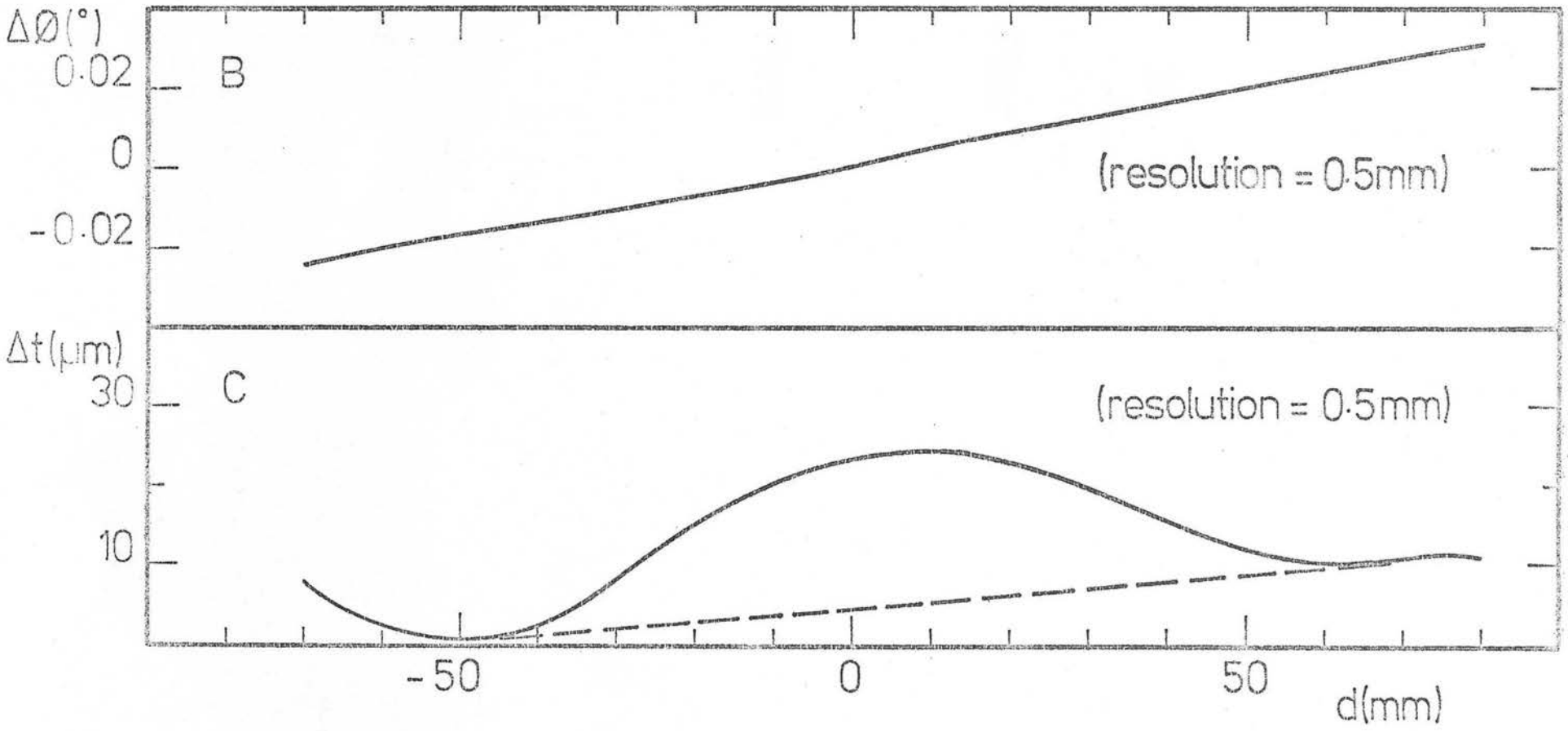

Figure 7.5 B) Angle of maximum transmission axis as a function of position across the filter.
C) Deviation of top surface from planarity as a function of position across the filter.

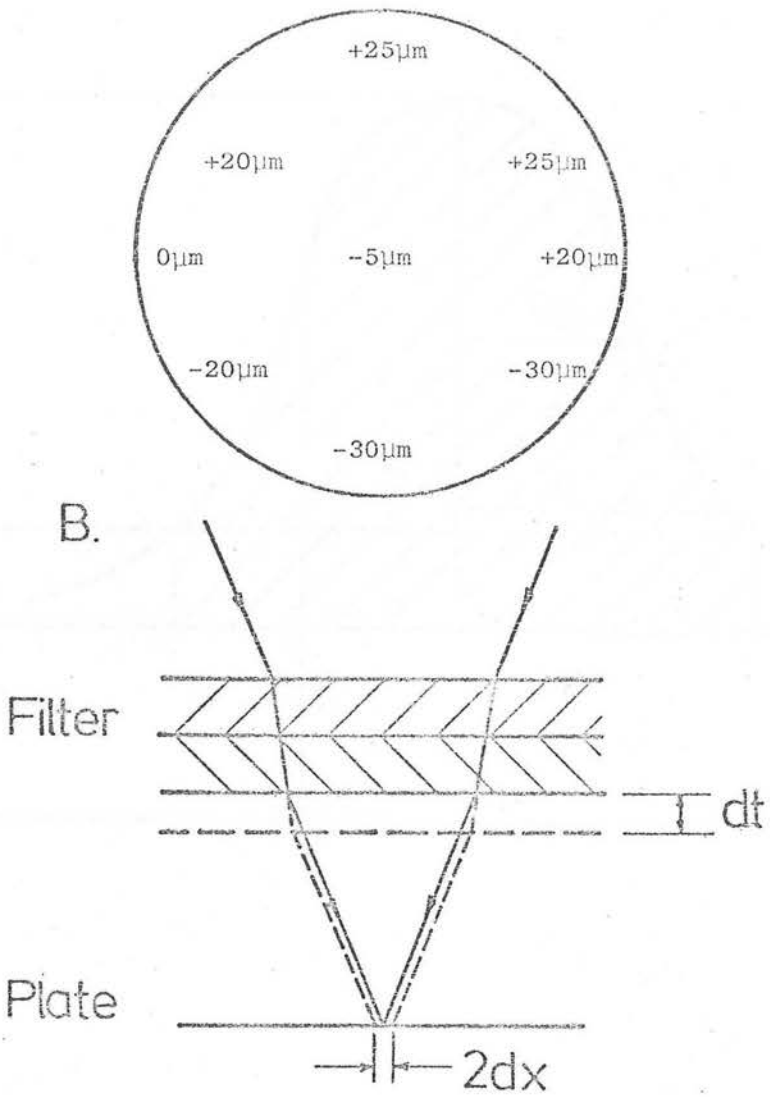

Figure 7.6 A) Map of thickness variations across circular filter (resolution = 5μm).
B) Change in image size due to thickness variation dt in filter (scale exaggerated).

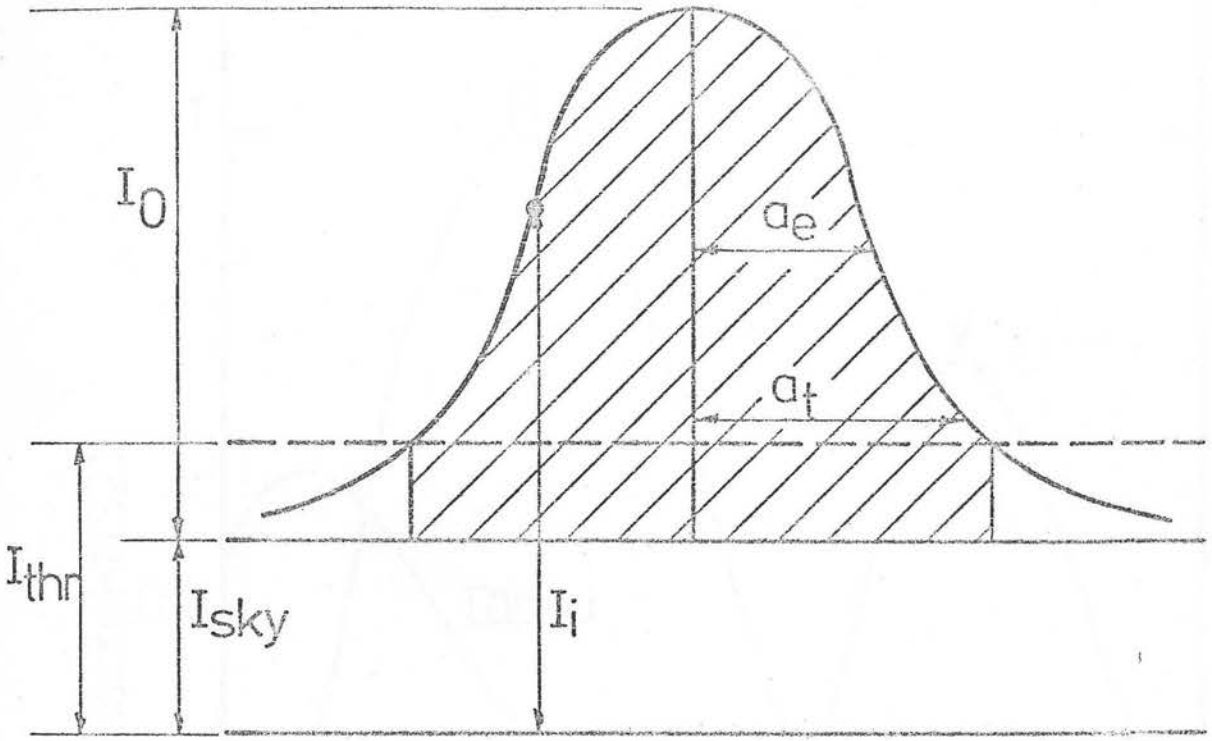

Figure 7.7 COSMOS parameters for an unsaturated stellar image. I_i is the intensity at a given pixel (i). I_{sky}, I_{thr} and $(I_{sky}+I_o)$ are the sky, threshold and peak intensities respectively. The integrated intensity $I^*=\sum_{i=1}^{n}(I_i-I_{sky})$ is given by the shaded area. a_t is the radius of the thresholded image and a_e is the radius where $I_i-I_{sky} = I_o/e$ (schematic diagram only).

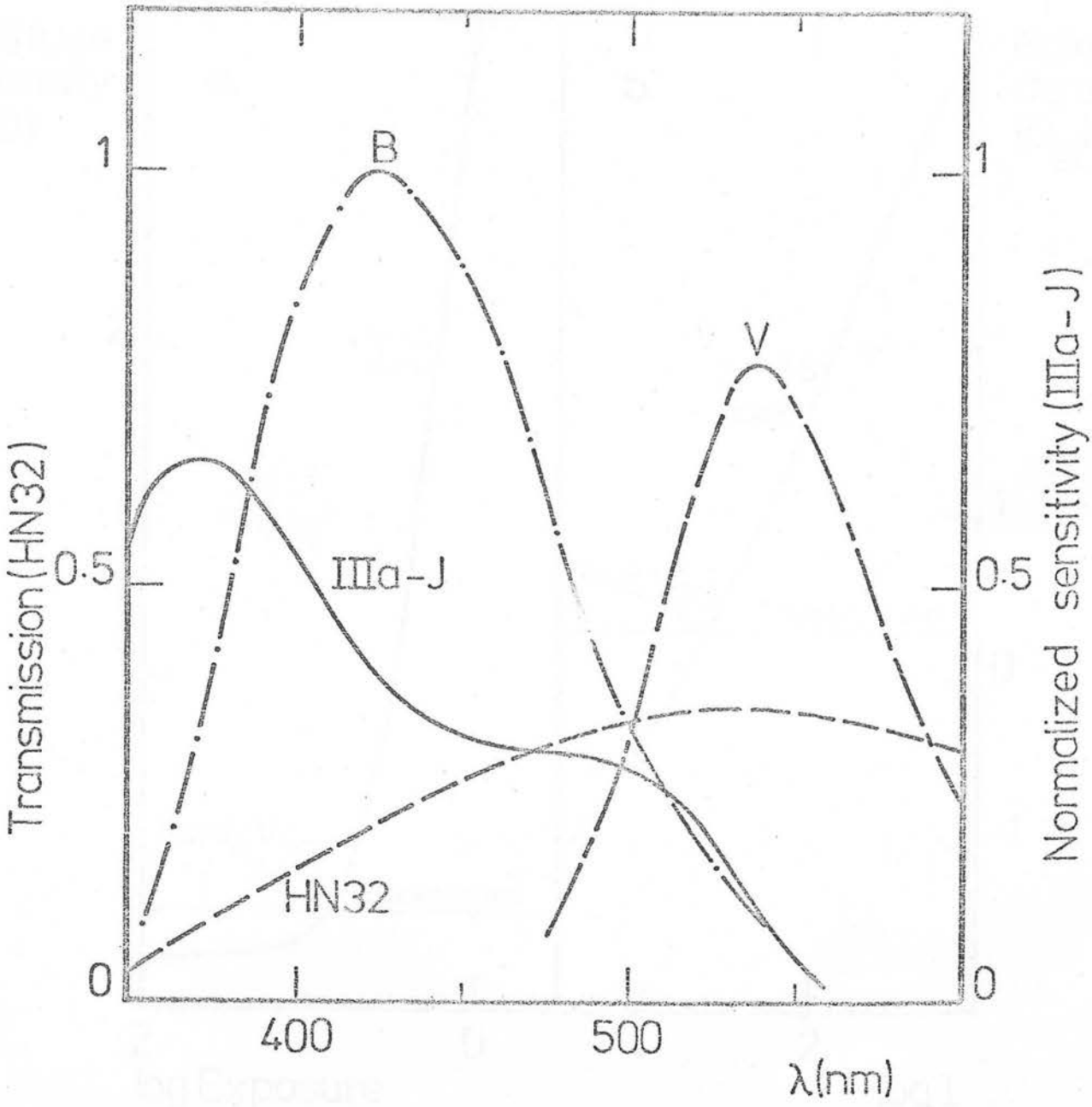

Figure 7.8 Passband of filter/emulsion combination.
The normalized sensitivity of IIIa-J emulsion is shown, in units of reciprocal exposure (1/ergs cm^{-2}), along with the HN-32 transmission to unpolarized light (data from Kodak Company and Polaroid Corporation). The spectral transmission of the Johnson B and V filters is also plotted (Weaver 1962).

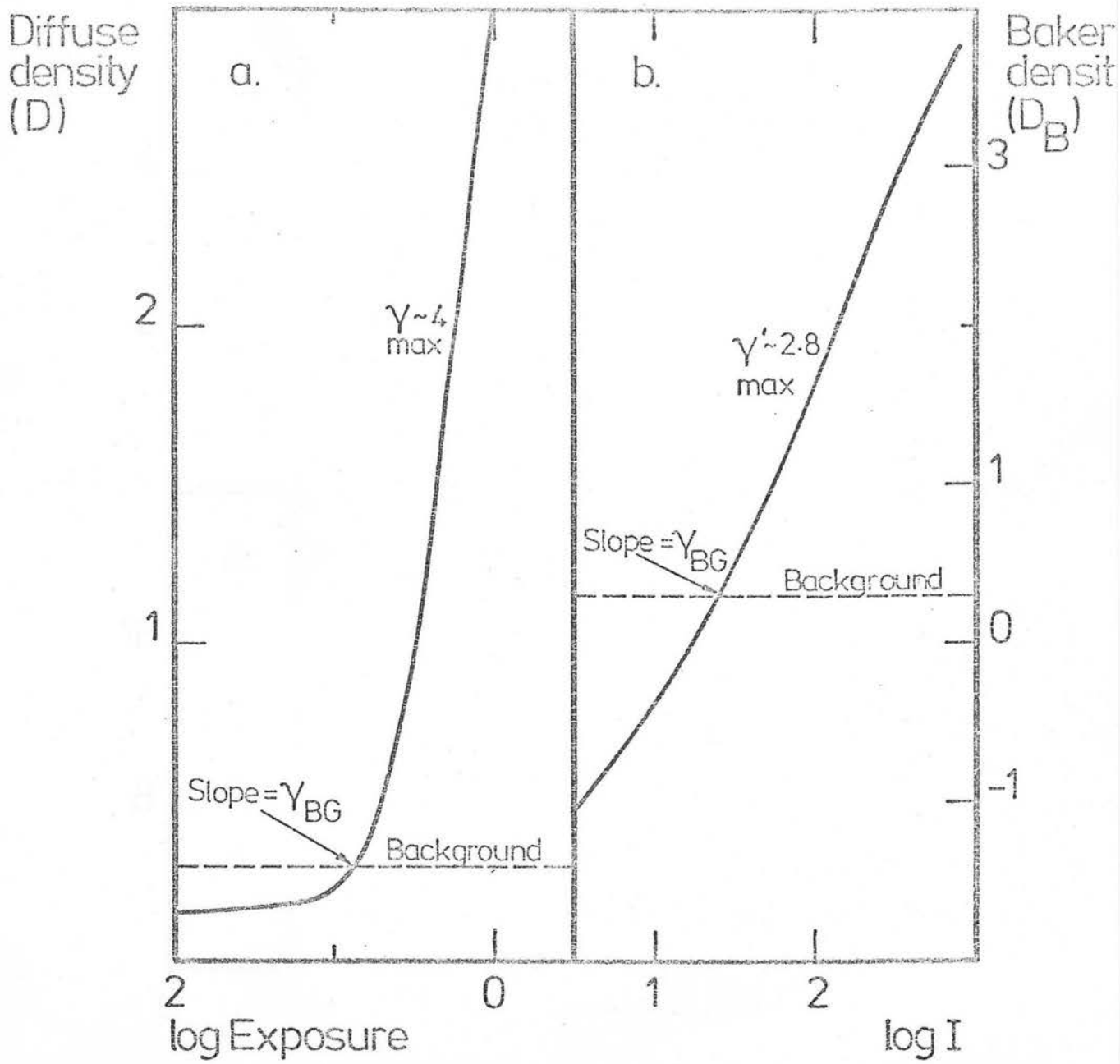

Figure 7.9 Characteristic curves of IIIa-J emulsion for normal, diffuse density and Baker density. Typical sky background level for the Schmidt polarization plates is indicated (data from Kodak Company and UKSTU).

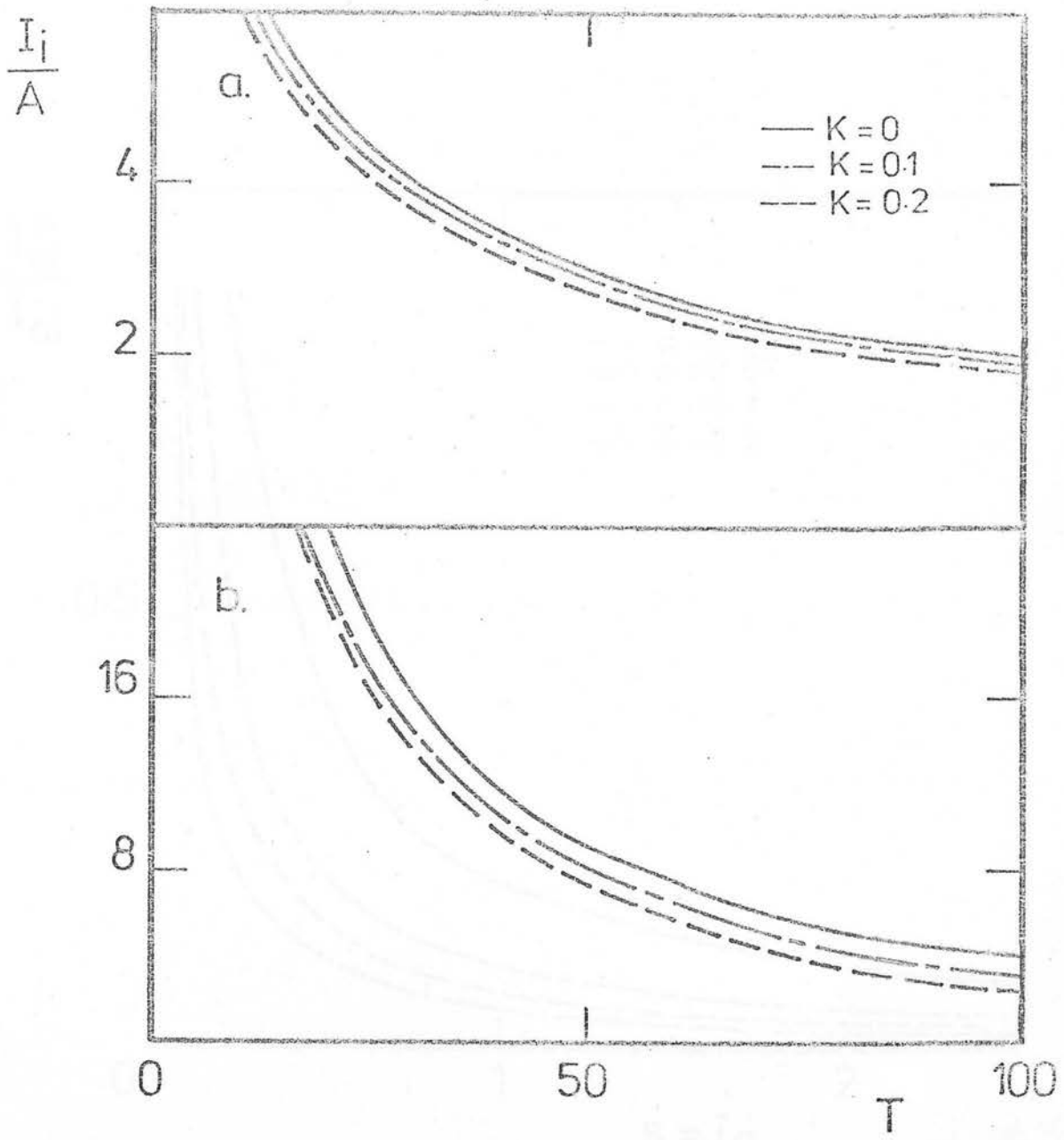

Figure 7.10 Graph of pixel intensity against COSMOS transmission.
a) Variations in emulsion sensitivity by a fractional amount k ; I_i is changed by $\sim 1/\sqrt{k}$ %.
b) Variations in transmission by a fractional amount K ; I_i is changed by $\sim 1/K$%.

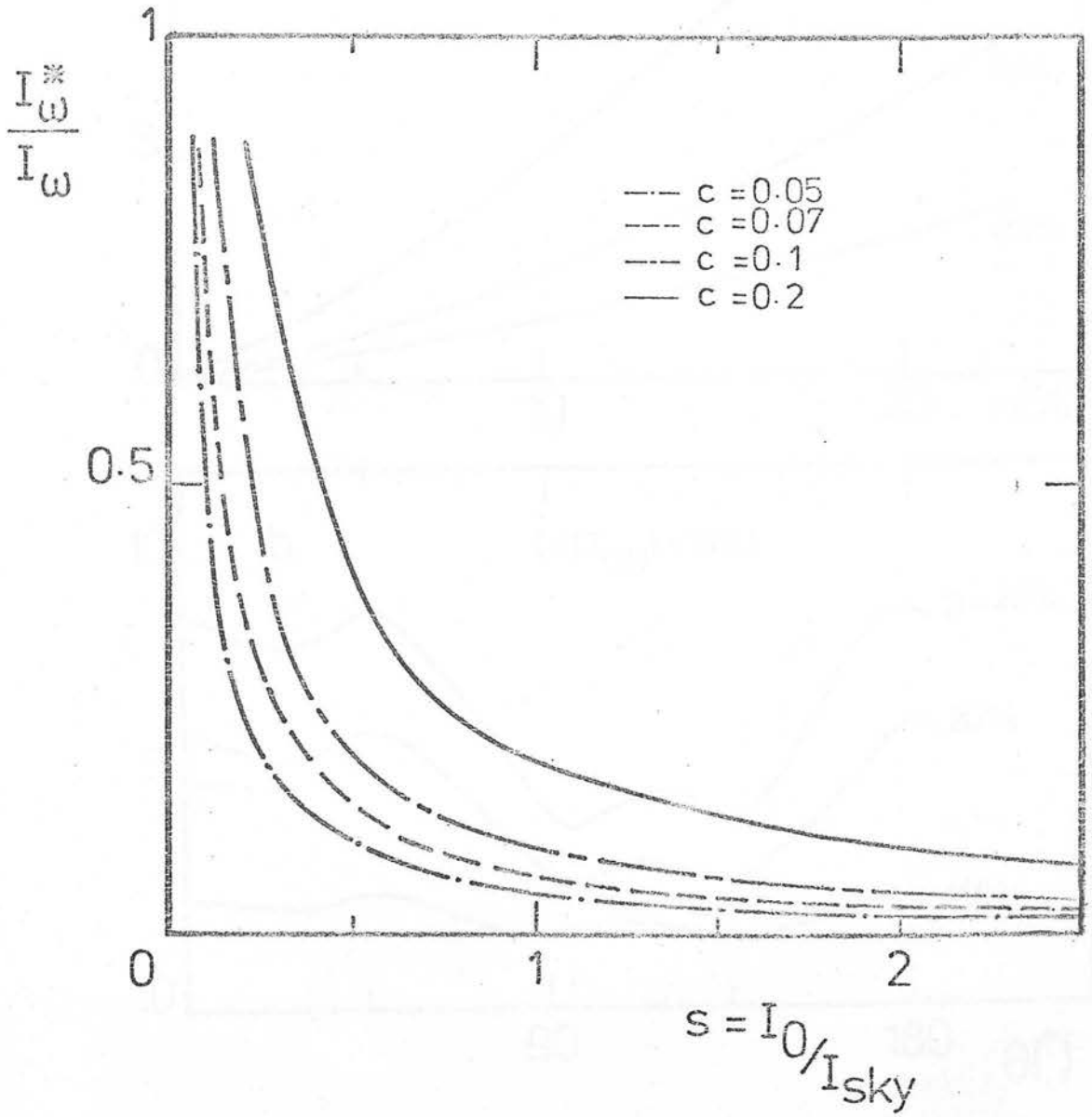

Figure 7.11 Fraction of the image lost by COSMOS thresholding ($I_\omega^*/I\omega$) plotted against ratio of signal-to-sky level. Lines of different threshold cut c are shown, where $I_{thr} = (1+c)I_{sky}$. Dashed line corresponds to c=7%, the value used for all plates used in this work.

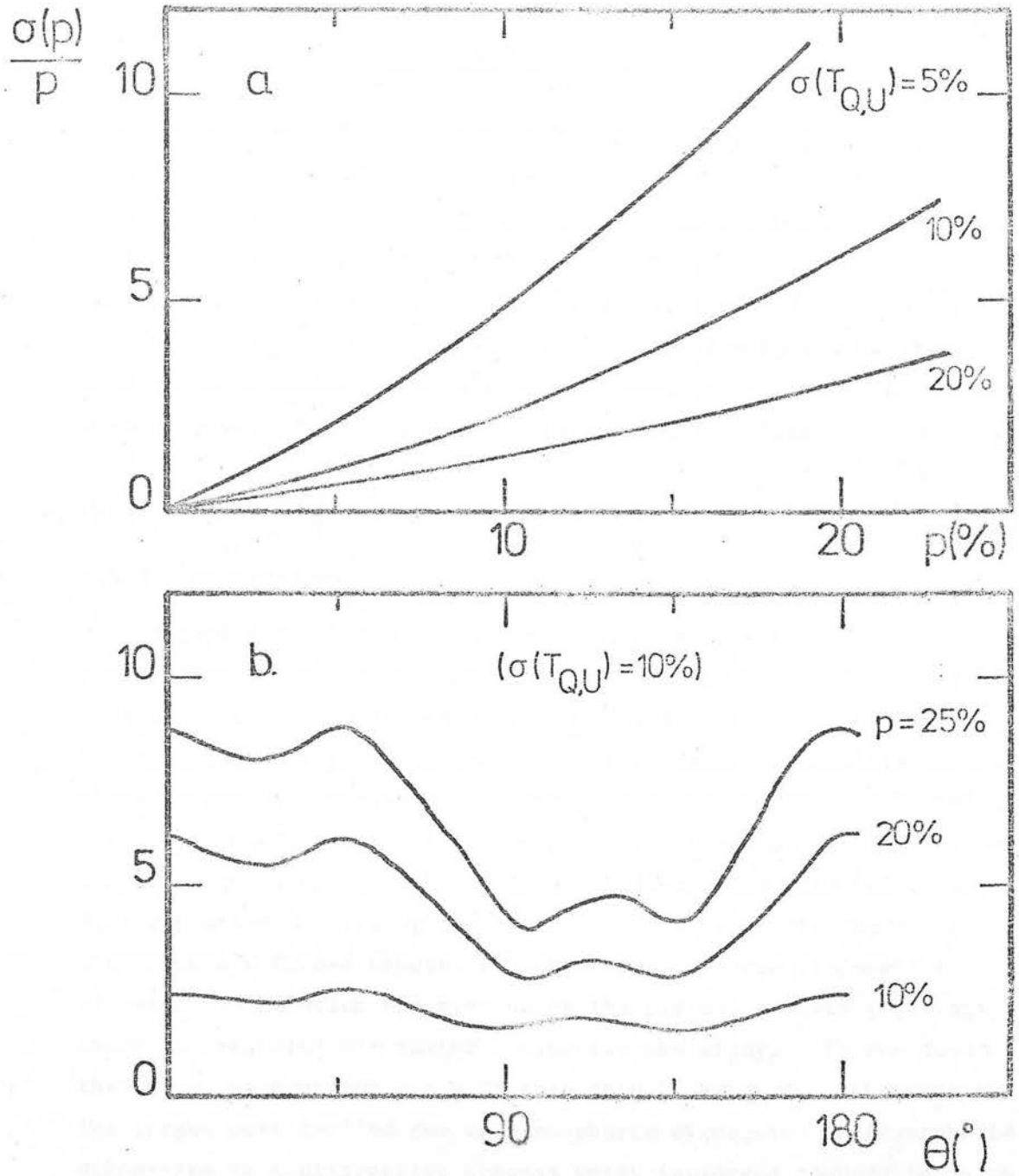

Figure 7.12 a) Polarization signal-to-noise against degree of polarization. Plotted for different values of $\sigma(T_{Q,U})$, the rms noise due to calibration errors.

b) Polarization signal-to-noise against polarization position angle. Plotted for different polarizations, p. $\sigma(p)/p$ is also proportional to $\sigma(T_{Q,U})$.

CHAPTER EIGHT

In this chapter the calibration of the Schmidt plate material is described. A photoelectric sequence was set up in a one degree square area at the centre of one of the program areas. Sub-beam prism plates were taken both at the UK Schmidt Unit and at the Anglo-Australian Telescope to extend the photoelectric calibration down to the plate limit of the Schmidt plates. A polarimetric calibration is covered in Appendix G, and alternative methods to COSMOS for selecting highly polarized objects are considered and appraised.

8.1 Plate Material

8.1.1 Description

A full set of plates for detecting polarization consists of four consecutive exposures at angles 0°, 45°, 90° and 135° of the polaroid filter. To be able to set meaningful limits on the space density of BL Lac objects it is important to probe as faint as possible with the plate material. Therefore exposures of 50-60 minutes per position angle were needed to get down to $m_B \sim 20$. Since only one filter can be accommodated by the Schmidt filter holder, using the Polaroid filter precluded mounting the GG395 Schott filter which normally accompanies a IIIa-J exposure. Therefore an extra component of ultraviolet radiation was present on the plates, and was important enough to restrict the target fields for the study. It was found that if an observation was made more than $2\frac{1}{2}$ hours from the zenith the images were trailed due to atmospheric dispersion. Atmospheric dispersion is a diffractive process which increases towards the blue; the presence of an extra UV component will naturally lead to elongated images on plates taken at large zenith distances. It was noted that the sense and degree of elongation on the trailed plates was consistent with atmospheric dispersion. Unfortunately this ruled out Northern fields where there might have been a calibration polarized object. The field chosen for the polarization plates was at: $12^{h}\ 58^{m}$, -20° 09' which is a region of medium galactic latitude, low obscuration and generally low interstellar polarization (Mathewson & Ford, 1974). The field is observable from the North, but is far enough South that

a set of 60 minute exposures can be taken without trailed images. The major disadvantage is that there is no known BL Lac object in the field, which is not surprising since <15% of the BL Lacs in the literature are in the South.

8.1.2 Polarization Plates

In March, 1979 a set of four 60 minute exposures was taken with the last ($\theta = 135^{o}$) plate unfortunately being heavily trailed. Otherwise the observing conditions during these consecutive exposures were very stable. Also in March, a set of four 10 minute exposures of the calibration BL Lac object OJ287 were taken (see Appendix G). It was not possible to get another set of plates on 12^{h} program field that season. In August, 1979 plates were taken of the second priority field at $21^{h}\ 15^{m}$ and $-39^{o}\ 52'$. A complete set was obtained but they were split between two nights and the transparency and seeing were not stable during any of the sequence. In March, 1980 two further complete sets of the 12^{h} field were taken: one of 50 minutes per exposure and the other of 30 minutes per exposure. This is the material used in this study; details of the individual plates are given in Table 8.1. Seven of these plates were measured on COSMOS and will be discussed extensively.

8.2 Photoelectric Sequence

8.2.1 Equipment

The photoelectric observations were obtained during 6 - 12 May, 1980 at the South African Astronomical Observatory, Sutherland. Photometry in the Johnson B and V bands was carried out on the 1m telescope at Sutherland using the St Andrews Photometer. The photomultiplier was a water-cooled RCA C31034A tube, and a 14" aperture was used throughout. Standard colour equations and extinction corrections were applied to the data. Standard stars from the Cousins "E" regions were observed (Menzies *et al.*, 1980). A detailed description of the equipment used can be found in the SAAO Facilities Manual (1979).

8.2.2 Observations

34 stars in a one degree square were observed in the two colours B and V. The centre of this 1^{o} field corresponds to the centre of the region defined by the circular filter on the 12^{h} plates. The nine brightest stars in the sequence are listed in the SAC catalogue and the 34 stars cover a range of $7.7 < B < 15.9$ and a range of $0.4 < B-V < 1.7$. 22 of the stars were observed on two separate nights, and the faintest star was observed on three separate nights. Cousirs' standard stars E502, E527, E550, E604, E633, E688, E745 and E782 were used to calibrate the zero point. The residuals during a night were always <0.01 magnitudes and the consistency of a repeated measurement was always <0.02 magnitudes. Two wavebands were considered sufficient to determine the colour term for the Schmidt plate material.

The photoelectric measurements are listed in Table 8.2 and a finding chart for the sequence stars is shown in Figure 8.1. Unless otherwise stated, the error on an individual measurement is ±0.01mag. All of the stars are within a 1^{o} square box, and most of the 15 faintest stars are in a 24' square area in the centre of the 1^{o} box. The SAAO reduction system corrects for atmospheric extinction, colour terms and photomultiplier dead time.

8.2.3 COSMOS Calibration

The photoelectric calibration for each plate was different, which is expected from the different conditions the plates were taken in, and the plate-to-plate emulsion variations. For the purposes of deriving a colour correction and understanding the form of the calibration curve, it is convenient to take the 'best' set of plates. In terms of uniformity of observing conditions and uniformity of image parameters, the best-matched set is the sequence X4902-3-4-5. The last (135^{o}) was trailed, but the pair (0^{o} - 90^{o}) defining the Stokes parameter Q are of very high quality. The colour correction is found by plotting (B-J′) against (B-V) where J′ is the filter magnitude. Using the mean intensity $(I_{o}+I_{90})/2$ for J′ gave,

$$(B-J') = (0.32\pm0.03)(B-V) \qquad (8.1)$$

The relationship for all 24 stars in the sequence has a linear regression correlation coefficient of 0.938, and is plotted in Figure 8.2. Note that in all the graphs in this section, the photoelectric error bars on each point are too small to be plotted. The errors are always dominated by that of the machine measurement. Relation (8.1) is in excellent agreement with the colour correction calculated numerically in Chapter Seven. The calibration curve can be plotted for each plate separately and for the average of the pair. When dealing with calibrations it is the convention to deal in magnitudes, rather than intensities which are more convenient for calculating polarizations. To make the treatment of magnitude and intensity analogous, assume

$$\bar{m} = \frac{1}{4}\sum_{\phi} m_{\phi} = \frac{(m_0+m_{90})}{2} = \frac{(m_{45}+m_{135})}{2} \qquad (8.2)$$

in direct analogy to $\bar{I} = \frac{1}{4}\sum_{\phi} T_{\phi} I$. The mean of the magnitudes at four angles is to be contrasted with the magnitude corresponding to the mean intensity, $\tilde{m}_{\phi}$. Since the magnitude scale is logarithmic, in general $\bar{m} \neq \tilde{m}_{\phi}$. Therefore the correction factor is given by,

$$C = \frac{1}{4}\sum_{\phi} (m_{\phi}-\bar{m}) \qquad (8.3)$$

The right hand side can be rewritten using equation (7.9),

$$C = \frac{1}{4}\left\{-2.5\log(1+p\sin 2\theta)(1-p\sin 2\theta)(1+p\cos 2\theta)(1-p\cos 2\theta)\right\} \qquad (8.4)$$

$$C = -0.1\ \log(1-p^2+\frac{p^4}{4}) \qquad (8.5)$$

at maximum, which is when $\theta = 0^{\circ}, 45^{\circ}, 90^{\circ}, 135^{\circ}$. From (8.5) it is seen that $C < 0.01$ magnitudes for polarizations up to 50%, therefore the assumption (8.2) is justified and magnitudes can be manipulated in a similar way to intensities. Returning to the calibration curves, linear and polynomial least-squares fits are made to m_0, m_{90} and $(m_0+m_{90})/2$ which have just been shown to be equivalent to I_0, I_{90} and $(I_0+I_{90})/2$.

In the plots, $y = J' = B-0.38(B-V)$ and $x = m_{\phi}$ (Figure 8.3):

	$y = mx + c$			$y = a + bx + cx^2 + dx^3$				
	m	c	r.m.s. (mag.)	a	b	c	d	r.m.s. (mag.)
m_o	1.91	-9.00	0.111	44.9	-13.7	1.50	-0.05	0.057
m_{90}	2.00	-9.52	0.075	39.0	-12.1	1.35	-0.04	0.042
$(m_o+m_{90})/2$	1.97	-9.40	0.083	33.9	-10.7	1.23	-0.04	0.035

The COSMOS magnitude is calculated according to the formula,

$$m_{\phi} = -250 \log\Sigma(I_i - I_{sky}) + 25 \qquad (8.6)$$

where the added term simply scales COSMOS magnitudes into the same range as the photoelectric magnitudes. There are several points to be made about the calibration:

(i) The calibration curves do not depart substantially from a straight line over the magnitude range $7.5 < B < 16$, and a cubic polynomial fit is the highest order needed to match the data: the residuals do not reduce for orders higher than 3. The r.m.s. errors are low over the whole 8.5 magnitude range, with all the sequence stars included. The slope between COSMOS and photoelectric magnitudes is ~ 2, so there is no 1:1 relationship between COSMOS ΣI and true intensity. γ of 4.0 was assumed for the machine measurement.

(ii) It is significant that the scatter on $\Sigma(I_i - I_{sky})/I_{sky}$ is no smaller than the scatter on $\Sigma(I_i - I_{sky})$. From the discussion in Section 7.4 there are alternative explanations for this. The variations which scaling by I_{sky} corrects for may be very small: vignetting, filter transmission variations and non-uniformity in emulsion sensitivity and development. Alternatively, these variations may be dominated by real variations in sky background which scaling each pixel by I_{sky} will not improve. In either case the r.m.s. error in the calibration is an upper limit to the sum of all these effects. The contribution due to filter transmission variations has been measured, and contributes ~ 0.03 mag. (= 4% peak-to-peak) to the r.m.s. error in the table

above. Therefore the combined influence of all the other possible effects must be only a few hundredths. This statement naturally only holds over the 1^{o} square covered by the sequence.

The other reason scaling by I_{sky} gives no improvement is digitization noise. The mean sky level on the plates is $I_{sky} = 332$ and the variation about that is only ± 4 units which corresponds to a change of only ± 2 transmission levels. Therefore real changes in sky brightness at that level are contaminated by digitization noise. For this set of plates, the $\Sigma(I_i - I_{sky})$ parameter is the most suitable.

(iii) The effect of COSMOS thresholding can be estimated. The peak intensity of the faintest of the sequence stars is $\sim$1800 (see Section 7.4.3). Therefore signal-to-sky $s \approx 5.4$ and $c = 0.07$ and the fraction of the image lost in the wings of the Gaussian is $s/c \approx 1\%$. Thresholding only becomes significant for images much nearer the plate limit.

(iv) There is an assumption which underpins the whole calibration procedure, which is that the photoelectric sequence stars are either unpolarized or are polarized but with randomly orientated position angles. In either case the mean relationship formed by all the stars will define zero polarization. If the field stars have significant interstellar polarization with a preferred position angle, polarizations could only be detected with respect to that mean interstellar value. In other words, the differential technique for detecting BL Lac objects would have an unknown polarization offset. The only reliable way to test the assumption is with photoelectric polarimetry of some of the standard stars. Although that was not possible during this project, there are several reasons for believing the intrinsic polarizations of the field stars to be low (< 1-2%). In the compilation of data by Mathewson and Ford (1974) the stars in the vicinity do not show a local high level of interstellar polarization. Unfortunately, there are no measurements in the Schmidt field itself. The second argument is from the reduction in the r.m.s. calibration error which results when the mean magnitude of the 0^{o} and

90^{o} plates is used. If the scatter on each of the two plates separately is due to noise, then the error on the mean magnitude would be: $\sigma^2_{0,90} = (\sigma^2_0 + \sigma^2_{90})/2$, $\sigma_{0,90} = \{(0.057)^2 + (0.043)^2\}^{\frac{1}{2}}/2$ = 0.035. The measured error on the mean calibration is identical to this. However the mean magnitude also removes polarization modulation to first order, so the fact that the r.m.s. error is not less than 0.035 means that the scatter is dominated by noise rather than polarization. The limit on the randomly directed polarization is therefore <1%. In principle this limit does not preclude a high, totally aligned component of polarization. In practice, however, the random component of interstellar polarizaton is not much less than the uniform component (i.e. the position angles are not highly aligned). So the limit of <1% infers a similarly strict limit on the total intrinsic polarization. Down at the level of a few percent, noise will dominate intrinsic polarization.

Plotting the two COSMOS magnitudes m_o vs. m_{90} gives an indication of the way the differential detection technique will work (Figure 8.4). A straight line fit by linear regression results in y = 1.03 x -0.18 in units of COSMOS magnitude. These are magnitudes uncorrected for observing conditions and the slope implies that the difference in control factors between the two plates will not be more than ~3% (i.e. $C_{90}/C_0 \simeq 1.03$). A quadratic fit gives $y = 3.22 + 0.4x + 0.029x^2$ with an r.m.s. of 0.023 COSMOS magnitudes, which from the calibration curve corresponds to ~0.04 photoelectric magnitudes. Therefore the null (zero polarization) relationship can be defined accurately over the whole range of calibration. Unfortunately, the one certainty is that the r.m.s. deviation of all the stars in 1^{o} square will be more than 4 hundredths of a magnitude, and that the 3σ detection limit will be more than 0.12mag. and its equivalent polarization of ~6%. The photographic process leads to errors which are not normally distributed and which may have a high-σ tail. When detecting discrepant objects from ~30,000 images there are two separate problems. One is the scatter of the bulk of the images from the mean line which defines a polarization detection limit. The other is the problem of sifting polarized objects from the high-σ tail in the presence of noise, plate flaws, mismatches and other spurious effects.

8.3 Sub-beam Prism Plates

8.3.1 Description

The Schmidt plate material extends considerably deeper than the photoelectric sequence, and some form of extra calibration down to the plate limit is needed. It was not possible to obtain photoelectric observations down to B ∿ 20, so plates taken with a sub-beam prism were used. The original idea of a sub-beam prism to calibrate photographic photometry was suggested by Pickering (1891). A small low-dispersion prism is placed in the primary beam of the telescope, producing images that are a fixed factor of intensity fainter than the primary images. The factor is the prism constant Δm (in magnitudes), and a bright photoelectric sequence can be extended down by Δm using the prism. The idea of the prism was exhumed by Racine (1969), but he used a figured sub-beam prism in the converging beam just above the focal plane and not the type of prism discussed here. A "Pickering" prism (in future referred to simply as a sub-beam prism) has been successfully used at the Cerro Tololo Inter-American Observatory by Canterna and Flower(1971) and Carney (1979), and at the Anglo-Australian Observatory by Couch and Newell (1980).

Plates were taken using the sub-beam prisms at both the U.K. Schmidt Telescope and the Anglo-Australian Telescope. The AAT prism is circular with a clear aperture of 145mm and a nominal apex angle of 45 arcseconds. It is used at prime focus (f/3.3) where the plate scale is 16.0 arc second mm^{-1}. Couch and Newell (1980) have derived a prism constant of 7.10 ± 0.09 for IIIa-J emulsion at an effective wavelength of 4385 Å. There is no evidence for wavelength dependence of the prism constant. The UKSTU sub-beam prism has a diameter of 250mm and is fitted just in front of the corrector. The apex angle is ∿50 arc seconds and the Schmidt plate scale is 67.12 arc seconds mm^{-1}. The UKSTU Handbook quotes a prism constant of 3.3 magnitudes.

8.3.2 Properties of the Sub-beam Prisms

The technique of extending a plate calibration with sub-beam prism data is an extrapolation. A calibration curve is formed between photoelectric measures and "machine" measures for the primary images, and an effective prism constant Δm_{eff} is calculated from the magnitude interval of overlapping primary and secondary images. Finally, Δm_{eff} is used to calculate calibrated magnitudes down to the faintest secondary images on the plate. It is only in the overlap region of faint primary and bright secondary images that Δm_{eff} can be verified; at the faint end the constancy of Δm_{eff} must be assumed. Crouch and Newell (1980) have pointed out that the value of the effective prism constant will depend intimately on the measuring machine and data reduction system used for the plates. Therefore different observers may disagree on the precise value of Δm_{eff}.

There is a theoretical prism constant, Δm_{th}, based on the light throughput and diffracting properties of the prism. Many factors are involved in the calculation of Δm_{th}, including the losses due to scattering and absorption in the prism, vignetting of the primary mirror and diffraction and dispersion of the secondary images. The prism constant is given approximately by,

$$\Delta m_{th} = -2.5 \log \left(\frac{vD^2}{td^2}\right) \qquad (8.7)$$

where v is the fraction of the primary mirror which remains after vignetting has been accounted for, t is the percentage transmission of the prism, and d and D are the prism and primary mirror diameters. For fused silica at 4000Å, t = 92%, and using v = 0.90 for the AAT and v = 0.85 for the UKST,

$$(\Delta m_{th})_{UKST} \simeq 3.39, \quad (\Delta m_{th})_{AAT} \simeq 7.10 \qquad (8.8)$$

These expectation values are in good agreement with the empirical values already quoted. The design of a sub-beam prism involves a trade-off between image separation and dispersion. The opening

angle of the prism must be sufficient to well separate the primary and secondary images, but must not be so wide that the dispersion spreads the secondary images out into small spectra. The separation of the images can be accurately measured from COSMOS positions and is given by $S = A/n$ where A is the prism opening angle and n the refractive index. The dispersion is given by,

$$\delta = (n_1 - n_2)A = (n_1 - n_2)nS \qquad (8.9)$$

where n_1 and n_2 are the refractive indices at either end of the spectral passband of the plates, corresponding to $\lambda_1 = 3500\text{Å}$ and $\lambda_2 = 5500\text{Å}$. Using refractive indices from the Handbook of Optics (1978),

$$\delta_{UKST} = 0.75'' \quad , \quad \delta_{AAT} = 0.65'' \qquad (8.10)$$

Since these figures are a sizeable fraction of the seeing disc, the image structure of the secondary images may show the effect of this dispersion. The best results occur when the seeing is poor and the spectral dispersion is small compared to the image diameter. The worst effects will be for red objects where most of the energy is in the part of the spectrum where the dispersion is highest. Another reason for preferring poor seeing is that the diffraction limit of the prism is,

$$\ell_{UKST} = 0.37'' \quad , \ell_{AAT} = 0.64'' \qquad (8.11)$$

a limit which will be significant if the atmospheric seeing is excellent. Finally, poor seeing is preferred to minimize the effect on the image structure of the changed focus for the secondary images (which have a path length through the prism). Whether these potential pitfalls lead to systematic differences between primary and secondary images depends on the measuring machine, and whether the reduction system assumes that all images have the same properties. Much of the previous work with sub-beam prism plates has been done using Iris

Photometers. An Iris Photometer measures the integrated light through a circular aperture, and for certain wedge settings and faint images where the iris diameter is larger than the image diameter, the results should be relatively insensitive to changes in image structure. However, it was shown in Section 7.4.3 that COSMOS measures have a systematic bias due to the thresholding procedure. If the energy in the secondary images is dispersed then the COSMOS bias will be worse for those than for the primary images. For this reason the plates were measured on two different measuring machines: COSMOS at Edinburgh, and the PDS machine at the Royal Greenwich Observatory.

The COSMOS machine, as previously described, pixel-integrates the image volume above a sky threshold cut, and subtracts the local sky intensity from each image pixel. The PDS machine and its associated software fit a 2-dimensional Gaussian profile to each image, and integrate under the curve for a machine magnitude. The sky background is averaged from groups of four pixels at each corner of the image. Details of the machine and the reduction software are given in the RGO PDS User's Manual (Penny, 1978). In sub-beam prism work images with a very large range in intensity are being directly compared, and the limited dynamic range of the measuring machine is a problem. COSMOS digitizes into only 256 transmission levels corresponding to a density range of less than two. The PDS has four times greater resolution in transmission. In both cases images saturate from 3.5 to 4.5 magnitudes above the plate limit and the sub-beam prism calibration covers more than this range. Therefore the calibration curves for the primary and secondary sequences will naturally have non-linear sections, but the important part is the region of overlap. It is important that primary and secondary images of identical machine magnitude have a constant difference in photoelectric magnitude, i.e. that Δm_{eff} is constant with intensity.

8.3.3 UKSTU Plates

Three plates were taken with the UKSTU prism in April, 1980. The exposures were consecutive in seeing of 2-3 arcseconds, and of

duration 20 minutes each. Details of the exposures are given in Table 8.3. The plates were measured on COSMOS with 8μm resolution and a 7% threshold cut (like all the other plates mentioned in this work). The filter/emulsion combination was GG385/IIa-O which approximates the Johnson B passband. A plot of residual (m_c-B) against (B-V) confirmed that no colour correction was necessary.

(a) COSMOS: The calibration curves for the primary images showed that there were differences between the three plates. The next stage was to average measures from the three plates, in the hope of reducing the errors. An alternative school of thought is to discard all but the best plate; i.e. retain only the one which gives the smallest r.m.s. scatter. However if there is no independent reason for suspecting one of the plates to be inferior, it is unwise to choose in this way because the reliability of the measure will be reduced even if the precision is increased. Any measurement from only one photographic plate is unreliable. Unfortunately, the random errors in photographic photometry may be non-normally distributed and the net error may not reduce as $\sqrt{N}$ where N is the number of plates coadded. Only the 23 faintest members of the photoelectric sequence could be used because the brighter stars merged with their own secondaries and were treated as single images by COSMOS. Sequence star No. 23 was suspected of being a variable and was discarded from the analysis. On the sub-beam prism plates the star deviates by ~0.3 magnitudes from the mean curve, and it is also displaced on both the AAT sub-beam prism plates and the polarization plates X4902-X4904. This left 22 stars covering a range of $11.5 < B < 16$.

In Figure 8.5 the mean COSMOS magnitudes for the three UKSTU sub-beam prism plates are plotted against photoelectric B magnitude. The r.m.s. deviation for the primary sequence is 0.073 mag., and the r.m.s. deviations for the individual plates are X5895-0.090 mag., X4896 - 0.084 mag., X4897 - 0.062 mag. By visual inspection, the magnitude offset in the overlap region Δm_{eff} appears to be a function of magnitude, growing larger at fainter magnitudes. This is confirmed by fitting a straight line to the portions of overlap of both the primary

and secondary images and calculating the difference in photoelectric magnitude B,

$$\begin{aligned} &\text{Primary} \quad : \quad B = 1.785m_c - 7.85, \qquad \text{r.m.s.} = 0.059 \text{ mag.} \\ &\text{Secondary} \quad : \quad B = 1.537m_c - 7.75, \qquad \text{r.m.s.} = 0.067 \text{ mag.} \end{aligned}$$

$$\begin{aligned} &\text{At } B = 14.5 \qquad \Delta m_{eff} = 2.97 \\ &\text{At } B = 16.0 \qquad \Delta m_{eff} = 3.22 \end{aligned} \tag{8.12}$$

In the overlap region, covering only 1.5 magnitudes, there is a substantial magnitude-dependent offset and the prism constant is not constant. It is therefore unwise to use the COSMOS sub-beam measures to extend the photoelectric sequence. The reason for the magnitude-dependent offset presumably lies in the machine measurement. Since the problem occurs for images with the same COSMOS magnitude well above the plate limit, the thresholding procedure is not directly responsible. The likely explanation is a change in image structure between the primary and secondary images, possibly due to the dispersion of the secondaries. The ratio of the x and y extents of the two sets shows signs of this, with the ellipticity for the primaries being 1.13±0.06 and the secondaries 1.19±0.07. If the secondary was extended by the dispersion of the prism, then a substantial fraction of the image would slip under the threshold cut. The COSMOS measures are obviously unsatisfactory for this purpose.

(b) PDS: The same three Schmidt plates were measured on the PDS machine at the Royal Greenwich Observatory. The PDS is a raster scanning microdensitometer which converts transmission into diffuse density, and the total density in the image is a machine magnitude estimator. For these measurements a 30 x 30 pixel array was scanned around each image using an aperture of 11μm and a pixel size of 10μm. An optimum scanning speed was set so that the photomultiplier could accurately respond to rapid changes in density across an image. A 2-dimensional Gaussian is fitted to the image profile and the machine magnitude is,

$$m_{PDS} = -2.5 \log_{10}(h\, r_x r_y) \qquad (8.13)$$

where h is the height of the Gaussian above sky background, and r_x and r_y are the e-folding radii in orthogonal directions. The background is determined by looking at 4 x 4 pixel averages in the four corners of the raster box and averaging them for a mean background level. There should be no other faint stars in the raster, or bright stars with centres near the raster. For optimum use of the PDS, the apertures should be small with respect to density changes which in practice means that it should be less than 1/5 of the e-folding radius of a typical star.

In Figure 8.6, the mean PDS magnitudes are plotted against photoelectric B measures for the primary and secondary images of the sequence stars. A comparison with Figure 8.5 shows that the region of overlap is considerably greater for the PDS measurements than for the COSMOS measurements. Maximizing the overlap region is a general problem with the sub-beam prism method. At the bright end the secondaries become contaminated by the wings of the very bright primaries, and at the faint end the secondaries are close to the plate limit. Furthermore, in the intermediate region there is a transition from saturated to unsaturated images, and the calibration curve will normlly bend at this point. The PDS has a larger dynamic range in density than COSMOS ($\Delta d = 4$, compared to $\Delta d = 2$ for COSMOS), and the calibration is linear over a larger range in intensity. As before straight lines are fitted to the primary and secondary images in the overlap region. The four faintest points in the primary sequence are not included because they unfortunatley correspond to a gap in the secondary sequence. Calculating the prism constant,

$$\begin{aligned}
&\text{Primary} \quad : \quad B = 2.078 m_{PDS} - 22.27, \quad \text{r.m.s.} = 0.044 \text{ mag.} \\
&\text{Secondary} \quad : \quad B = 2.099 m_{PDS} - 25.90, \quad \text{r.m.s.} = 0.065 \text{ mag.} \\
&\text{At } B = 12.4 \qquad \Delta m_{eff} = 3.25 \\
&\text{At } B = 15.0 \qquad \Delta m_{eff} = 3.28
\end{aligned} \qquad (8.14)$$

The improvement over the COSMOS measures is obvious. The r.m.s. deviations of the fits to the two sets of images are smaller and the prism constant differs by only 3 hundredths of a magnitude over 2.5 magnitudesof photoelectric overlap. In other words, the two calibration curves are parallel within the errors. There are no obvious differences in image profile between primary and secondary image of the same machine magnitude. The profiles of images at the boundaries of the overlap region are illustrated in Figure 8.7, the labels A, B, C and D being indicated on Figure 8.6 (the software to generate these diagrams was written by A.J. Penny at RGO). The primary-secondary pairs A-B and C-D are similar, verifying that the magnitude step will be constant over this range. Note that in the region ABCD the PDS machine measurements do not substantially saturate because of the large dynamic range $\Delta d \sim 4$. By contrast, the COSMOS measurements are becoming unsaturated towards the faint end of the overlap region and the calibration is expected to bend. In addition the COSMOS magnitude parameter does not account for saturation because the central pixels of a bright image are given the saturation (minimum) transmission value and their information content is lost, whereas the PDS fits a Gaussian to the unsaturated wings of the image and calculates a volume underneath the Gaussian (see Figure 8.8).

However, it may not be valid to assume that since the prism constant does not vary in the overlap region that it can be extrapolated down to the limit of the secondaries. The reason is that the secondary calibration curve clearly bends just at the end of the overlap region when the primaries run out. Rather than an effect of the measuring machine this is caused by the images becoming unsaturated on the plate (for a 20 minute exposure on unfiltered IIIa J, the images become unsaturated approximately 5 magnitudes from the plate limit, i.e. at $J \simeq 16$). This problem is essentially unavoidable, because a very extensive photoelectric sequence is needed to give an overlap that covers both saturated and unsaturated ranges on the plate. Since the PDS measures magnitudes in a way which is reasonably insensitive to the degree of image saturation, it will be assumed that the calibration can be

extended down to the limit of the secondaries. The extended calibration is shown in Figure 8.9. A reliable error for the extended calibration is difficult to determine since it is an extrapolation. A reasonable error would be 0.1 mag, which is bigger than r.m.s. errors on either of the individual calibrations or the difference between values of Δm_{eff} in the overlap region. The calibration is carried back to the original plate material by measuring field stars of similar magnitude to the faintest secondaries of the sequence and defining a calibration curve for those field stars which can be applied. This transfer sequence is shown in Figure 8.10 for the mean of the polarization plates X4902 and X4904, the r.m.s. error of the extended calibration is 0.08 mag and over the entire sequence is 0.052 mag in a 6th order polynomial fit:

$$\text{Extended calibration: } J' = a + bm_c + cm_c^2 + \ldots$$

	a = 119.8	d = 0.0844	
(X4904)	b = -37.50	e = -0.0279	r.m.s. = 0.052mag
	c = 3.340	f = 0.00147	

This is the only stage of the whole calibration procedure where the residuals are decreased by going beyond a cubic fit, an indication that the functions involved are reasonably well-behaved. The final transfer of the extended sequence from the sub-beam prism plates to the polarization plates increases the r.m.s. error slightly due to a colour term when going from B (sub-beam prism) to J' (polarization). Thus instead of using just <u>one</u> field star of similar magnitude to the sequence secondary, five were averaged in order to take out most of the colour term. A typical error bar on each of these points (shown as open circles in Figure 8.10) is 0.1mag. The least-squares fit to the extension has a smaller r.m.s. than this (0.08mag) but 0.1mag is a good error estimate for the extended calibration. The final transfer has only been illustrated for one polarization plate (X4904), but the procedure can be applied to any plate. Since X4904 is a particularly good plate,

the final r.m.s. error at the faint end will normally be greater than 0.1mag.

The calibration from UKSTU sub-beam prism plates can be summarized:

(i) Identify primary and secondary images of photoelectric sequence stars on sub-beam prism plate(s).

(ii) Fit calibration curves to primary and secondary images in overlap region and calculate Δm_{eff} over range of overlap.

(iii) Displace secondary image sequence to define extended calibration on sub-beam prism plates.

(iv) Take several field stars at the same machine magnitude as each displaced secondary image, and identify them on the original polarization plates.

(v) Average the machine magnitudes of the field stars on the polarization plates to define the extended calibration on the polarization plates.

8.3.4 AAT Plates

Four plates were taken with the AAT prism in March, 1980. The plates were exposed at the prime focus with the triplet corrector and the exposures were consecutive in seeing of 2-3 arc seconds. One exposure was 60 minutes, one was 20 minutes, and two others were 5 minutes each. Details of the plates are given in Table 8.3. Three of the plates (one of each exposure) were measured on COSMOS, and two (a 60 minute and a 5 minute exposure) were measured on the PDS. The filter/emulsion passband was GG385/IIIa-J which defines the photographic J band. A plot of residual $(m_c - J')$ against (B-V) showed no colour correction; therefore the AAT sub-beam prism plates are in the same colour system as the polarization Schmidt plates.

The AAT plates have some obvious advantages and disadvantages with respect to the UKSTU plates. The much larger magnitude step of the AAT prism (7.1mag) allows a calibration down to $B \sim 23$, and the improved plate scale gives better pixel resolution on the

measuring machines. Working always in one colour system removes one of the causes of uncertainty in the last section. However the disadvantages are also important. Foremost is the fact that the large magnitude step rules out a large range of overlap to check the constancy of Δm_{eff}. The photoelectric sequence covers only 8.2 magnitudes, so the overlap is at best only defined by a few points. In practice there may be no suitable overlap stars at all because at one end of the overlap zone the bright secondaries are swamped by very bright primaries, and at the other end the faint primaries have secondaries which fall below the plate limit. The region where the photoelectric sequence runs out is B $\sim$ 16 which corresponds to the secondary image of an SAO star (B $\sim$ 9). The large plate scale and partial vignetting by struts in the beam leave a clear field of only 0.5 square degrees, and there are few SAO stars in such a small field. Therefore the overlap region corresponds to just the point at which bright stars are running out and the prism constant Δm_{eff} cannot be checked. Since it has already been shown how the measuring machine can affect the results from sub-beam prism data, the lack of a verification for Δm_{eff} on the AAT plates is a severe problem.

(a) COSMOS: COSMOS measures of the 60 minute exposure show that there is no overlap between faint primary and bright secondary images. Δm_{eff} cannot be determined directly. The slopes of the two calibration curves are considerably different, and neither of the curves are very smooth. To proceed further would involve assuming the canonical prism constant $\Delta m_{eff} = 7.10$ is correct, which is unwise between different measuring machines.

(b) PDS: As shown in Figure 8.12, the extra dynamic range of the PDS creates an overlap, but it hinges totally on the brightest secondary image, which may possibly be contaminated by the diffraction spikes of the primary (see Figure 8.13 showing maps of stars A and B in Figure 8.12). The large Δm_{eff} sub-beam prism requires sophisticated measuring procedures to smooth the background in the presence of bright images or in crowded fields. With the relative merits of

the UKSTU and AAT sub-beam prism plates and the comparison of measurements by COSMOS and the PDS in mind, the extended calibration will be carried out using UKSTU plates and PDS measurements.

The conclusions of these experiments in extending photoelectric calibration using photographic techniques are:

(i) As pointed out by Crouch and Newell (1980) the results on identical plates depend on the measuring machine used.

(ii) COSMOS measurements of UKSTU plates yield a magnitude-dependent offset, which may be attributable to the effect of COSMOS thresholding on secondary images with different image structure to the primary images.

(iii) PDS measurements of UKSTU plates yield a satisfactory Δm_{eff} which is constant in the overlap region (machine saturation is not important there). However, the characteristic curve bends after this point, and the extension is inevitably an extrapolation and must be treated with caution.

(iv) On an excellent plate, a photoelectric sequence down to $B \sim 16$ can be extended down to $B \sim 19.3$ with an r.m.s. error of 0.1mag. This should be regarded as optimal.

(v) There is no satisfactory overlap region or check on Δm_{eff} from PDS or COSMOS measurements of AAT sub-beam prism plates. Use of these plates is limited by the number of bright stars in the field, and the dynamic range and sophistication of the measuring machine and its associated software.

8.4 Measuring Techniques

8.4.1 Polarimetric Calibration

The disadvantage of the primary program region at $12^h\ 58^m$ and $-20^\circ\ 09'$ is that there is no calibration object, i.e. a BL Lac object with known linear polarization. To estimate a polarization detection limit, a set of short exposure plates was taken of the BL Lac object

OJ287. Since the polarization of BL Lacs can change on short timescales a contemporaneous photoelectric measure of the polarization was obtained. The plates were measured on the Iris Photometer at ROE and the results are included in Appendix G. The detection limit ($p = 12\%$ at 4σ) is not directly applicable to the program region plates because of the smaller numbers of stars involved and the different measuring machine used. However it is a guide to the eventual sensitivity of the photographic technique.

8.4.2 Zeiss 'Blink'

Several experiments were carried out to see whether polarized objects could be detected 'by eye' over an entire Schmidt plate. If successful, this would allow a quick look for extreme objects without the complexities of machine measurement or reduction. Experience with 'blink' techniques to look for variable stars, blue objects, supernovae, etc. has shown that it is difficult to reliably spot differences of less than 0.5 magnitudes. Reference to the end of Chapter Seven shows that this corresponds to polarizations of 23-32% depending on the intrinsic position angle. The technique of positive-negative superposition of images was thought to be potentially more sensitive to small magnitude differences than a simple blink of two negatives. Therefore a positive contact copy of plate X4902 (0^{o}) was made and superimposed in the ROE Zeiss T.V. Comparator with the original negative of X4904 (90^{o}). The T.V. Comparator has the facility for mounting two plates and imaging small areas through a mixing prism onto a T.V. camera where the focus, contrast and position of each image can be altered to achieve the best cancellation. Successful cancellation naturally presumes that the plates were taken in very similar observing conditions. In principle, polarized objects should appear as 'doughnuts' with respect to the well-cancelled field stars. However, because a difference in field curvature between the two plates, images could only be exactly superimposed in a very small region (1 arc minute square) near the optical axis.

At any given time few field stars were in registration against which a BL Lac object might show up. An entire Schmidt plate would have taken >40 hours to scan this way. For these reasons the technique was not used on any other plates.

8.4.3 Photographic Cancellation

An attractive alternative to the Zeiss 'blink' technique was to photographically cancel a positive and a negative and cover the whole area at once. To perform this test the positive (90^{o}) and the negative (0^{o}) were placed emulsion to emulsion and shifted until registration was obtained over a large area. Immediately below the two plates a film emulsion was placed to record the transmitted light. Unfortunately it proved impossible to get registration of the positive and negative images over more than a few square centimetres of the plate. The radial displacement of negative with respect to positive images indicated that the negative may have 'shrunk' with respect to the positive, which is possible since the negative was film and the positive was glass. The shift need only be $\sim$0.01% to lose registration, since the image sizes are $\sim$30μm and the comparison is over 300mm. The obvious alternative of using a glass-glass sandwich with more rigidity was not possible since the throughput must image directly onto the recording film. With two glass plates faced emulsion to emulsion, the transmitted light would be diffused by 1mm of glass and would not be properly imaged on the film. The size of the transmitted 'doughnut' is very small (5-10μm) and corresponds only to the width of a few IIIa-J grains, so direct imaging is essential. In conclusion, the stringencies of cancelling whole Schmidt plates photographically precluded using the technique for a quick look for highly polarized objects.

TABLE 8.1

Details of the Schmidt Plates

Number	Field Centre				Position Angle	Exposure	Seeing	Min. Image Size	Machine	Grade
X 4875	08^h	52^m	$+20^\circ$	03′	0°	10 min.	2"	20μm	Iris	α
X 4876					45°	10	2	25	Iris	α
X 4877					90°	10	2	25	Iris	α
X 4878					135°	10	2	25	Iris	α
X 4902	12	58	-20	09	0	60	2	35	COSMOS	α
X 4903					45	60	2	40	COSMOS	α
X 4904					90	60	2	35	COSMOS	α
X 4905					135	60	2	40x55	-	β
X 5297	21	15	-39	52	0	50	2	55	-	α
X 5298					45	50	2	60	-	β
X 5299					90	50	2	45	-	β
X 5302					0*	50	2	60	-	α
X 5303					135*	50	2	35	-	α
X 5742	12	58	-20	09	0	50	1-2	30	COSMOS	α
X 5743					45	50	1-2	30	COSMOS	α
X 5744					90	50	1-2	35	COSMOS	α
X 5745					135	50	1-2	35	COSMOS	α
X 5751	12	58	-20	09	0	30	1-2	30	-	α
X 5752					45	30	1-3	25	-	α
X 5753					90	30	1-3	25	-	α
X 5754					135	30	1-2	25	-	α

All plates use unfiltered IIIa-J emulsion taken through HN32 Polaroid. The grading system is the one used by the UK Schmidt Telescope Unit (for details, see UKSTU Handbook). Plates marked with an asterisk are the only ones taken on a separate night; plates in all other sets were taken consecutively.

TABLE 8.2

Photoelectric Sequence

No.	V	B	B-V	Comments
2	6.92	8.23	1.31	SAO 157679
1	7.23	7.73	0.50	SAO 181342
3	8.65	9.17	0.52	SAO 157666
4	9.21	10.29	1.08	SAO 181330
6	9.37	10.31	0.94	SAO 181311
5	9.73	10.22	0.49	SAO 181319
8	9.98	10.52	0.54	SAO 157645
10	10.01	11.67	1.66	
7	10.03	10.45	0.42	SAO 181297
9	10.31	10.84	0.53	
13	10.31	11.84	1.53	
17	10.71	11.92	1.21	
16	10.91	11.63	0.72	
20	11.24	11.89	0.65	
18	11.28	12.05	0.77	
23	11.55	12.18	0.63	Possible Variable
39	11.64	12.72	1.08	
42	11.71	12.70	0.99	
28	11.83	12.39	0.56	
49	12.23	12.88	0.65	
54	12.34	12.99	0.65	
59	12.55	13.29	0.74	
80	12.94	13.58	0.65	
87	13.15	13.70	0.55	
106	13.18	14.18	1.00	
118	13.45	14.40	0.95	
127	13.67	14.52	0.85	
132	13.90	14.77	0.87	
156	14.10	14.61	0.51	
169	14.17	14.93	0.76	
192	14.54	15.26	0.72	
243	14.72	15.68	0.96	
223	14.86	15.48	0.62	$\pm$ 0.02
285	15.28	15.95	0.67	$\pm$ 0.02

TABLE 8.3

Details of the Sub-beam Prism Plates

Number	Telescope	Field Centre	Exposure	Seeing	Emulsion	Filter	Machine
B 5895	UKST	$12^h\ 58^m\ -20^o\ 09'$	20 min.	2"	II aO	GG385	COSMOS/PDS
B 5896	UKST		20	3	II aO	GG385	COSMOS/PDS
B 5897	UKST		20	3	II aO	GG385	COSMOS/PDS
1819	AAT	12 58 -20 09	60	1.5	III a-J	GG385	COSMOS/PDS
1820	AAT		20	2	III a-J	GG385	COSMOS/PDS
1821	AAT		5	2	III a-J	GG385	COSMOS/PDS
1822	AAT		5	2	III a-J	GG385	COSMOS/PDS

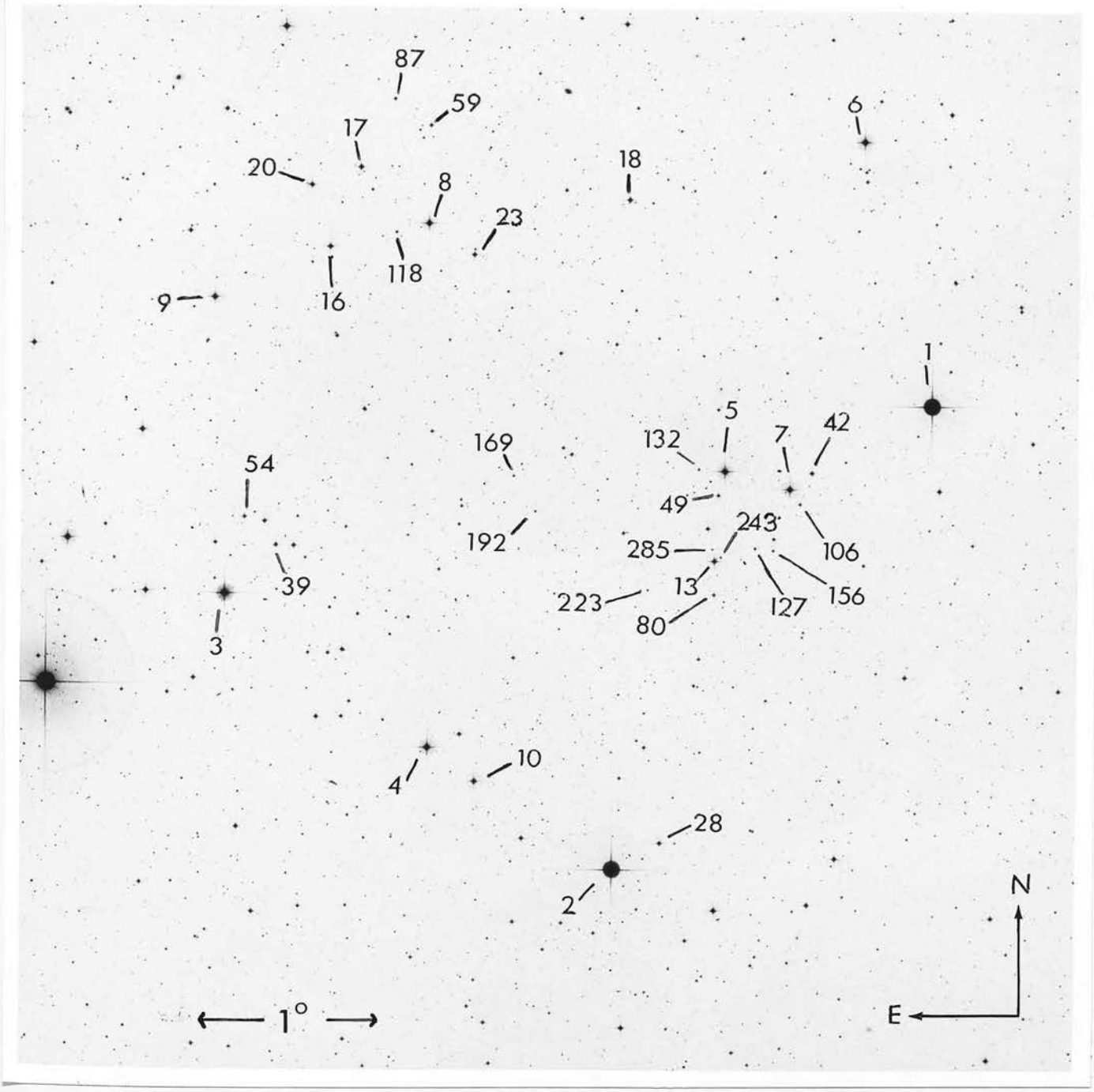

Figure 8.1 Finding chart for the photoelectric sequence in the field centred on $12^h\ 57^m$, $-20^o\ 09'$. Johnson B and V magnitudes are listed in Table 8.2.

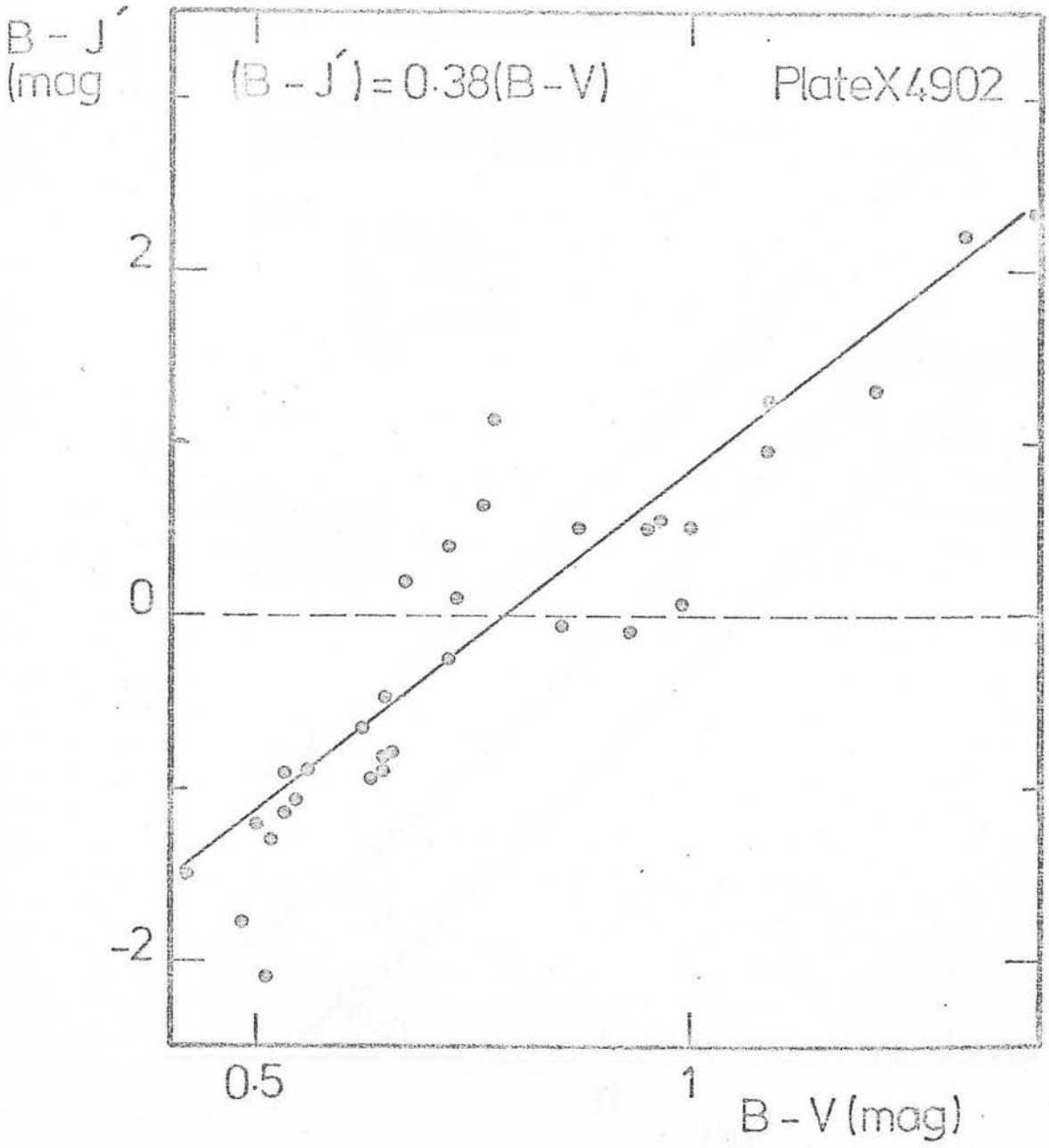

Figure 8.2 The colour correction between the Polaroid/emulsion bandpass J' and the Johnson B,V system. Solid line is the best least-squares fit for the photoelectric sequence stars, with J' magnitudes taken from COSMOS measures of plate X4902.

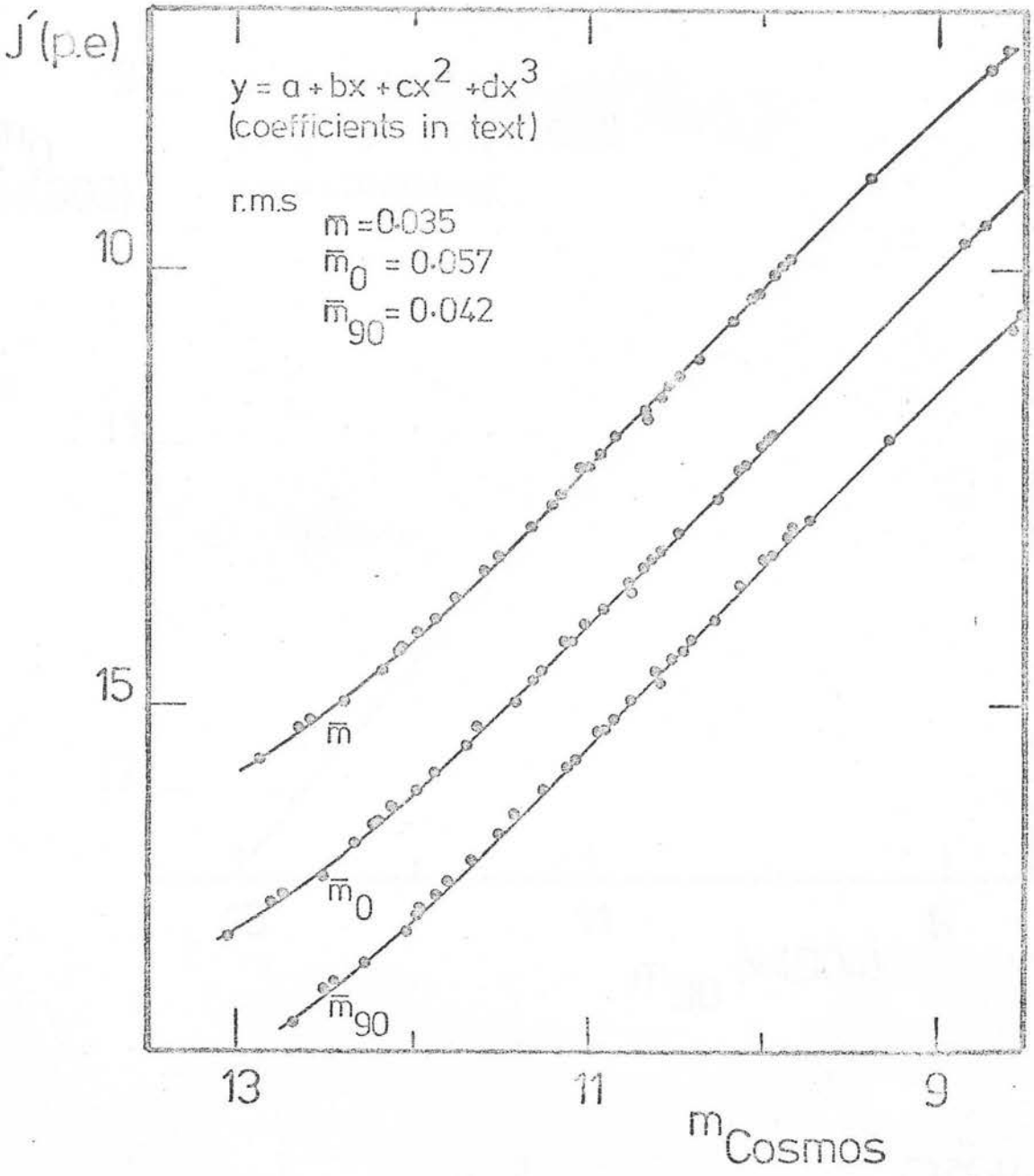

Figure 8.3 Photoelectric calibration. Colour-corrected photoelectric magnitude J'=B-0.38(B-V) is plotted against COSMOS magnitude for $0^{o}(m_{o})$, $90^{o}(m_{90})$ and the mean $\bar{m} = (m_{o}+m_{90})/2$. (Plate X4902=$m_{o}$ and plate X4904=m_{90} curves are displaced downwards by 1 and 2 magnitudes respectively).

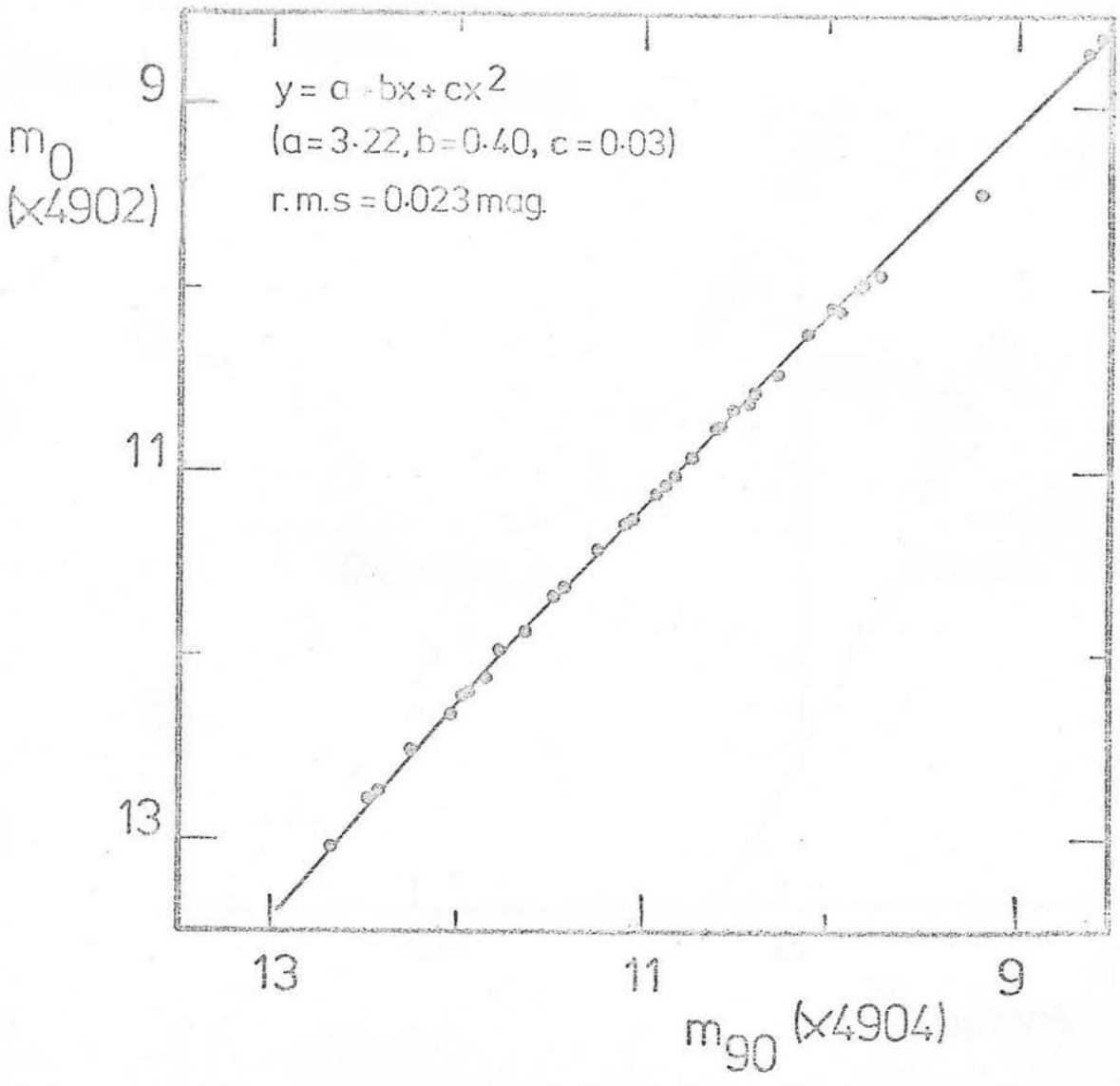

Figure 8.4 COSMOS magnitudes: 0° vs. 90°.
The coefficients of the least-squares quadratic fit are shown. All 34 stars in the photoelectric sequence are plotted.

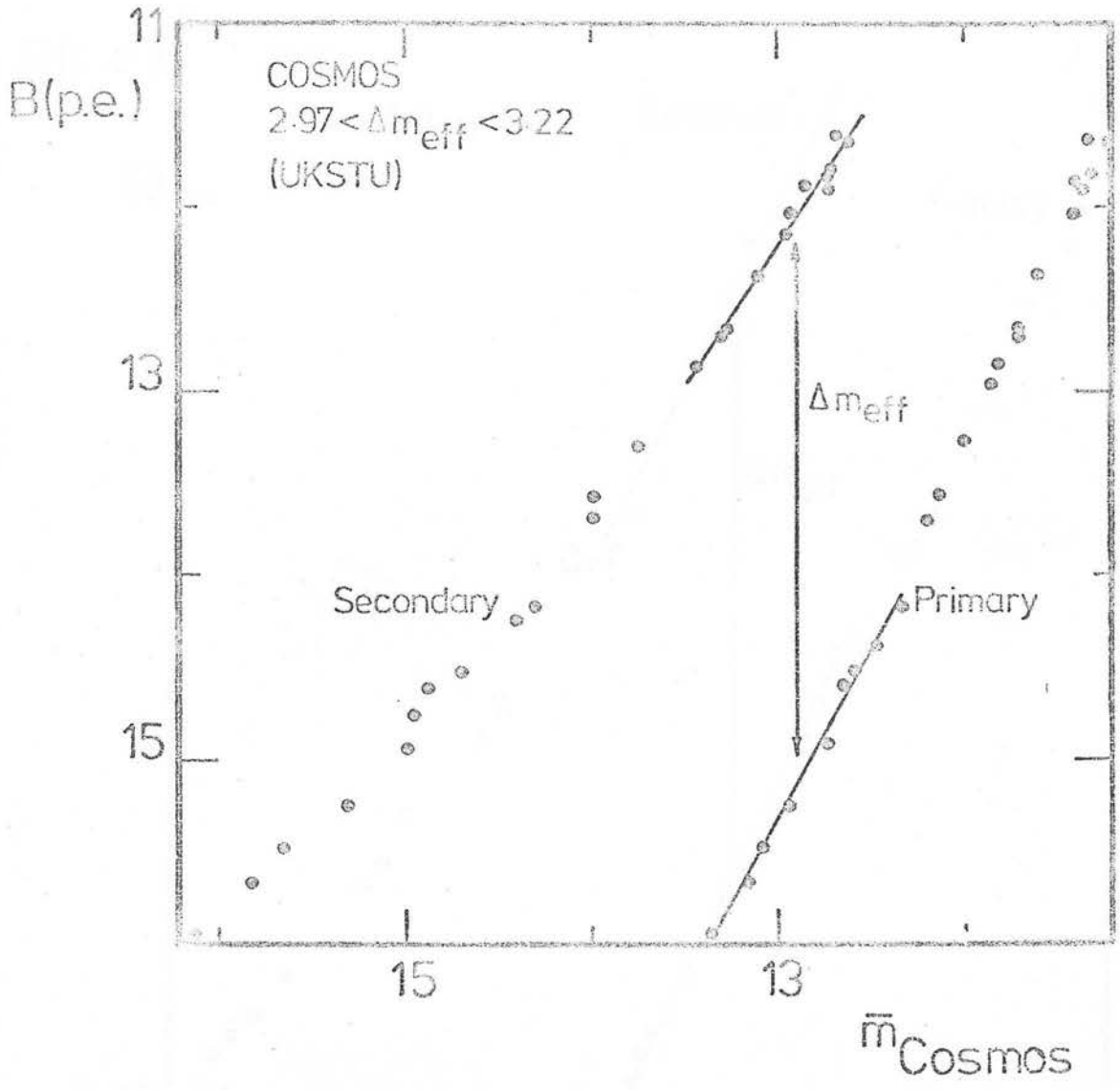

Figure 8.5 Sub-beam prism calibration (COSMOS).
Johnson B magnitude plotted against mean COSMOS magnitude for three plates. Primary and secondary images are plotted, with a linear regression straight line fit to the stars in the overlap region.

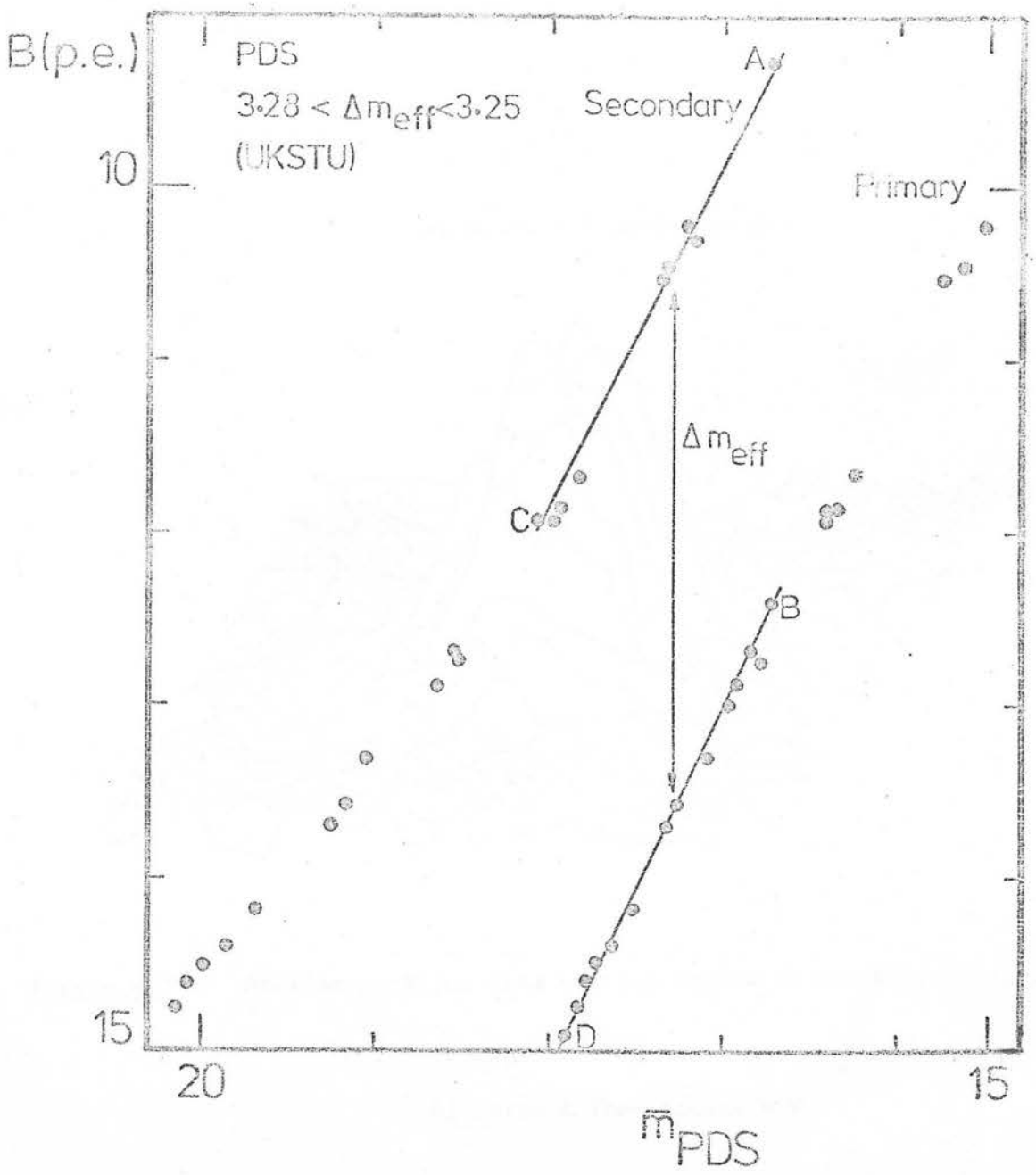

Figure 8.6 Sub-beam prism calibration (PDS).
Johnson B magnitude plotted against PDS magnitude for three plates. Primary and secondary images are plotted, with a linear regression straight line fit to the stars in the overlap region.

a) Image A from figure 8.6

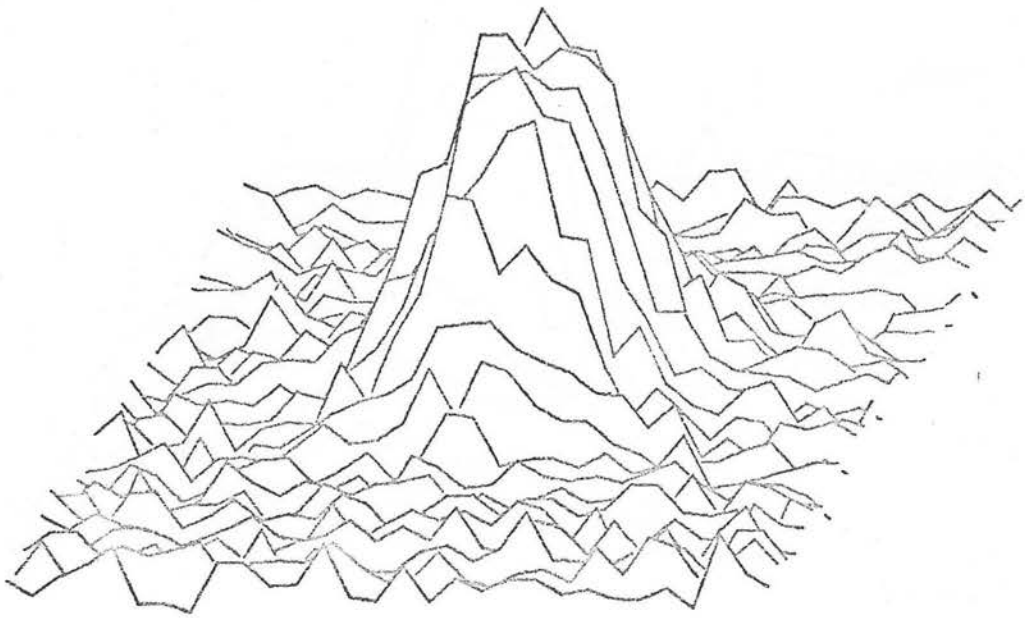

Figure 8.7 Stellar profiles from overlap region of sub-beam prism plates.

b) Image B from figure 8.6

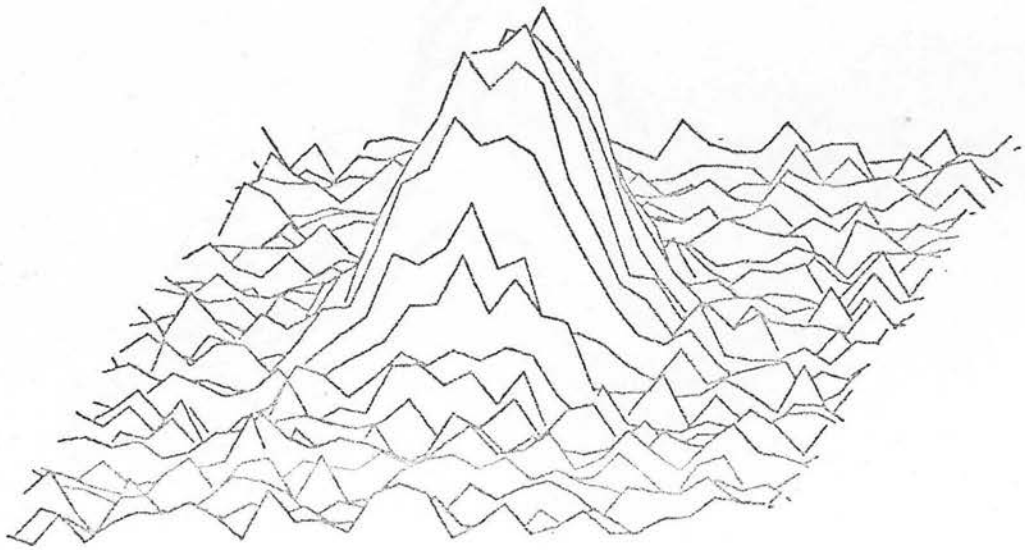

c) Image C from figure 8.6

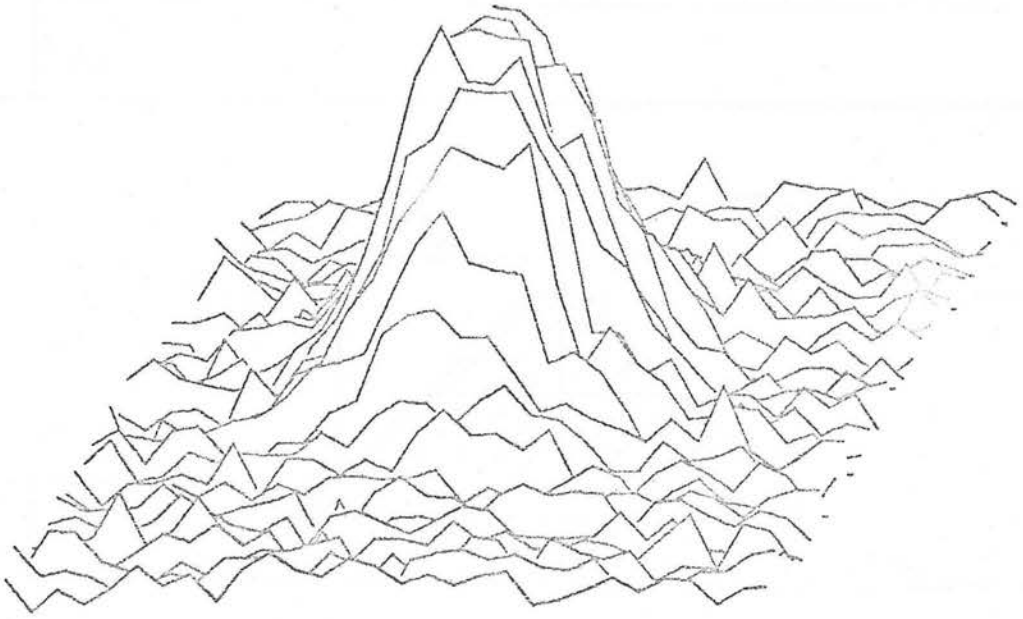

Figure 8.7 Stellar profiles from overlap region of sub-beam prism plates.

d) Image D from figure 8.6

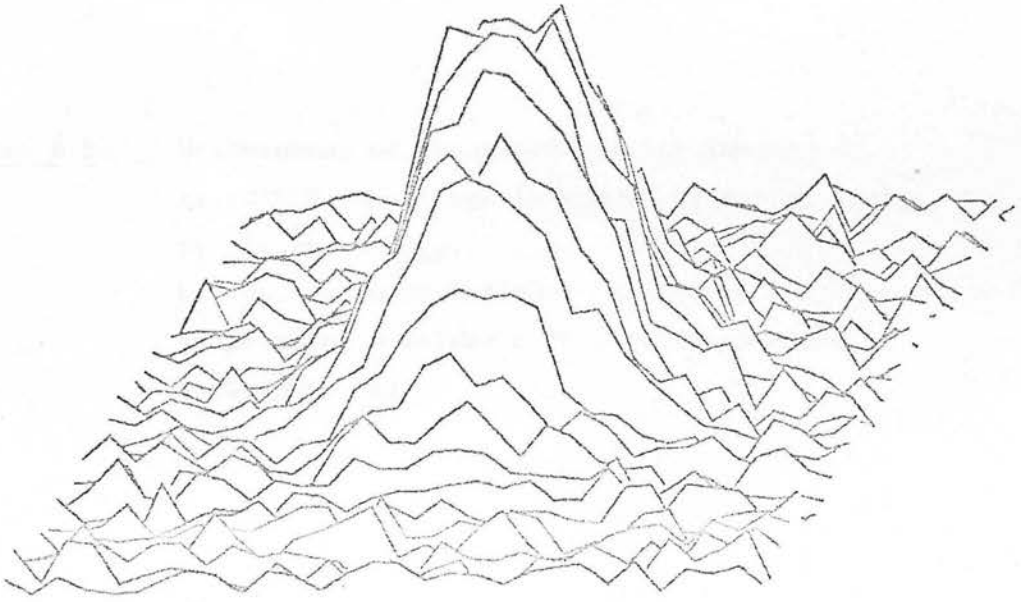

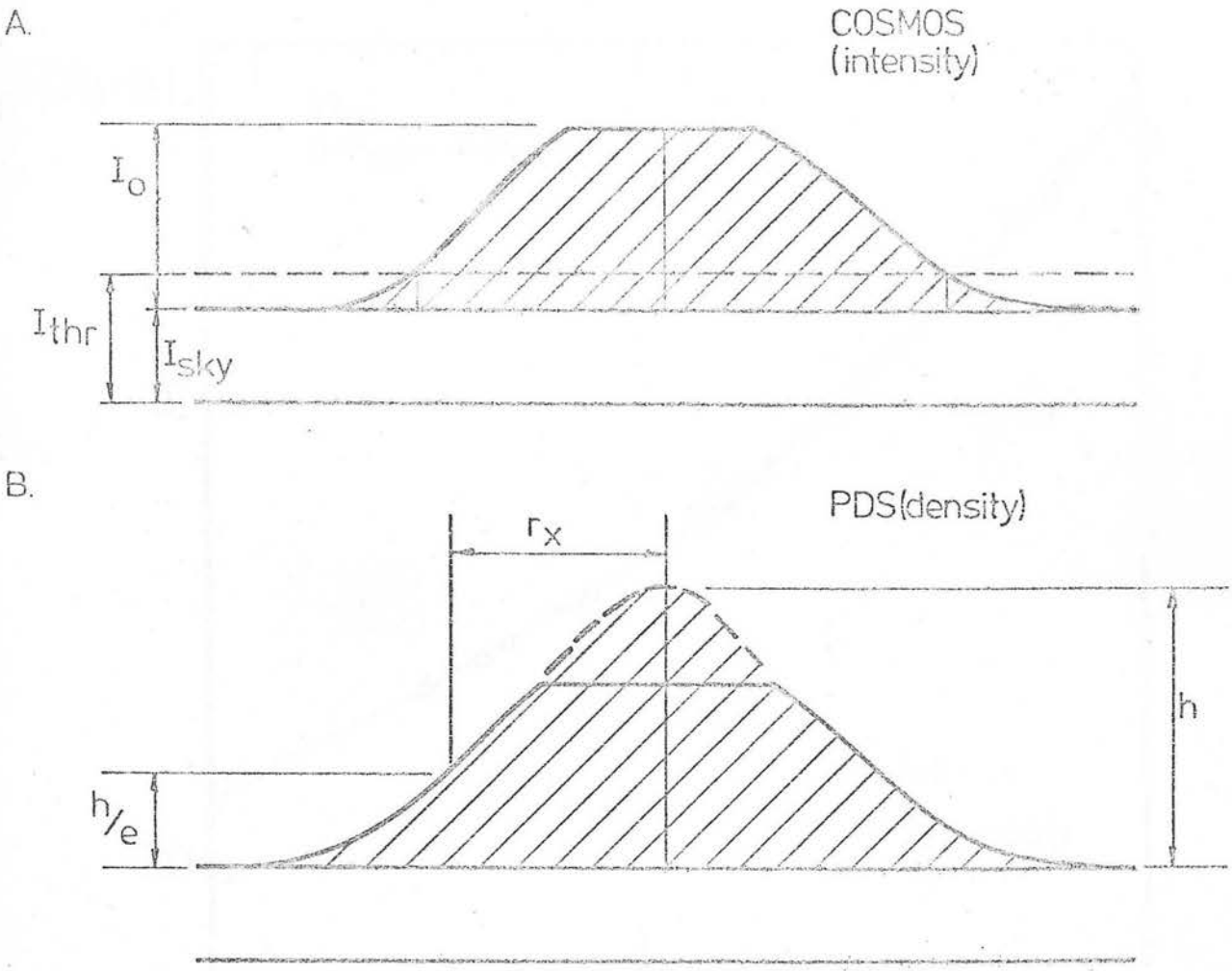

Figure 8.8 Measurement of saturated stellar images.
a) COSMOS. The image is summed by taking $I_o - I_{sky}$ for all pixels above I_{thr}.
b) PDS. A two dimensional Gaussian fit to the wings of the image gives a volume $r_x^2 h$ in density space.
(schematic only).

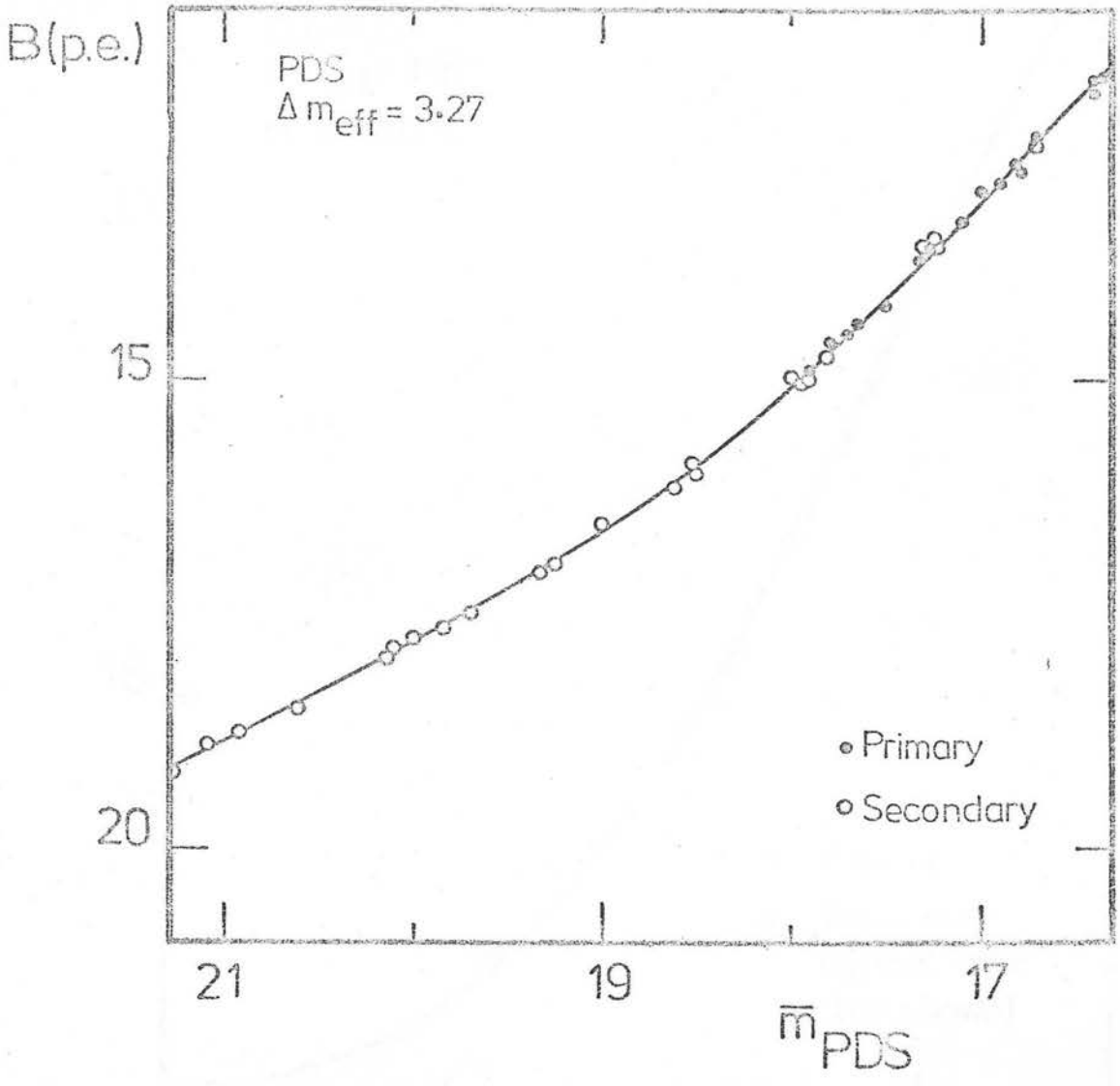

Figure 8.9 Sub-beam prism calibration (PDS).
Johnson B magnitude plotted against mean PDS magnitude for three plates. As in figure 8.6, but here the secondary images have been mapped onto the primary images assuming $\Delta m_{eff}=3.27$.

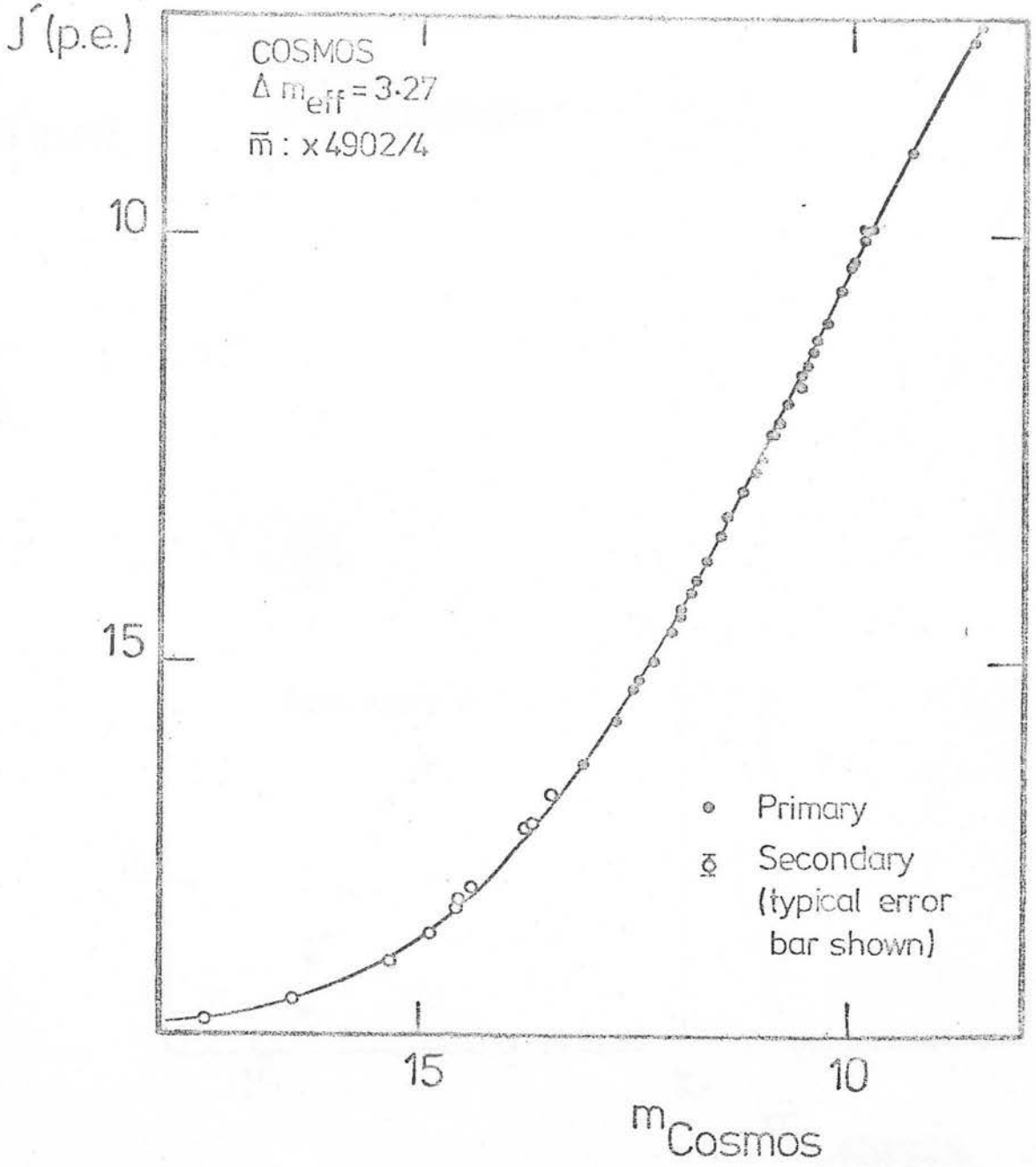

Figure 8.10 Extended photoelectric calibration (COSMOS). Colour-corrected J' magnitude is plotted against COSMOS magnitude for plates X4904 & X4902. Solid points are the photoelectric sequence data from figure 8.3; open points are the sub-beam prism extension sequence transferred from plates B5895-6-7. 6th order polynomial fit is shown with rms $\sigma(J') = 0.052$ mag.

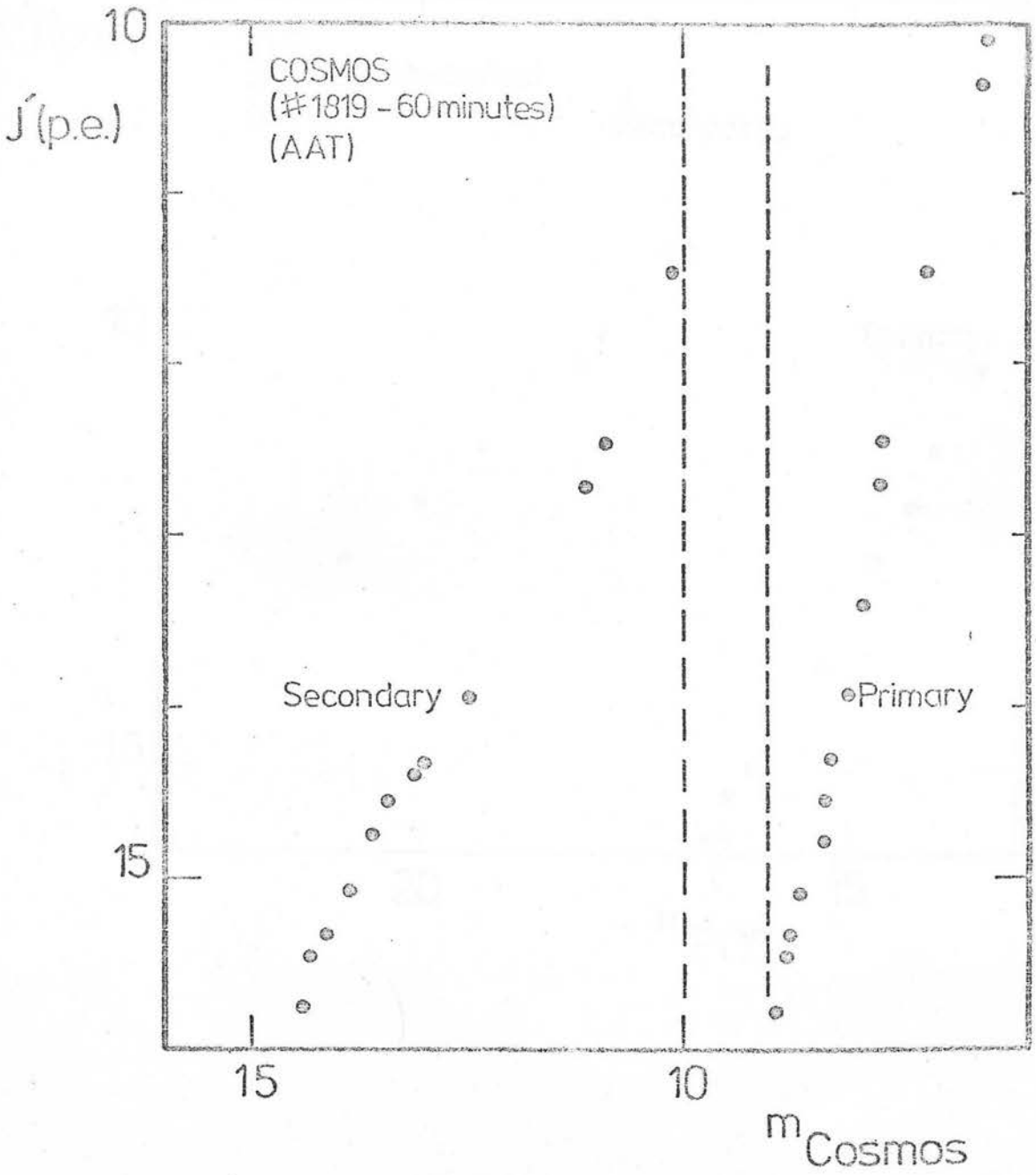

Figure 8.11 Sub-beam prism calibration (COSMOS).
Photographic J' magnitude plotted against COSMOS magnitude. There is no region of overlap between primary and secondary images.

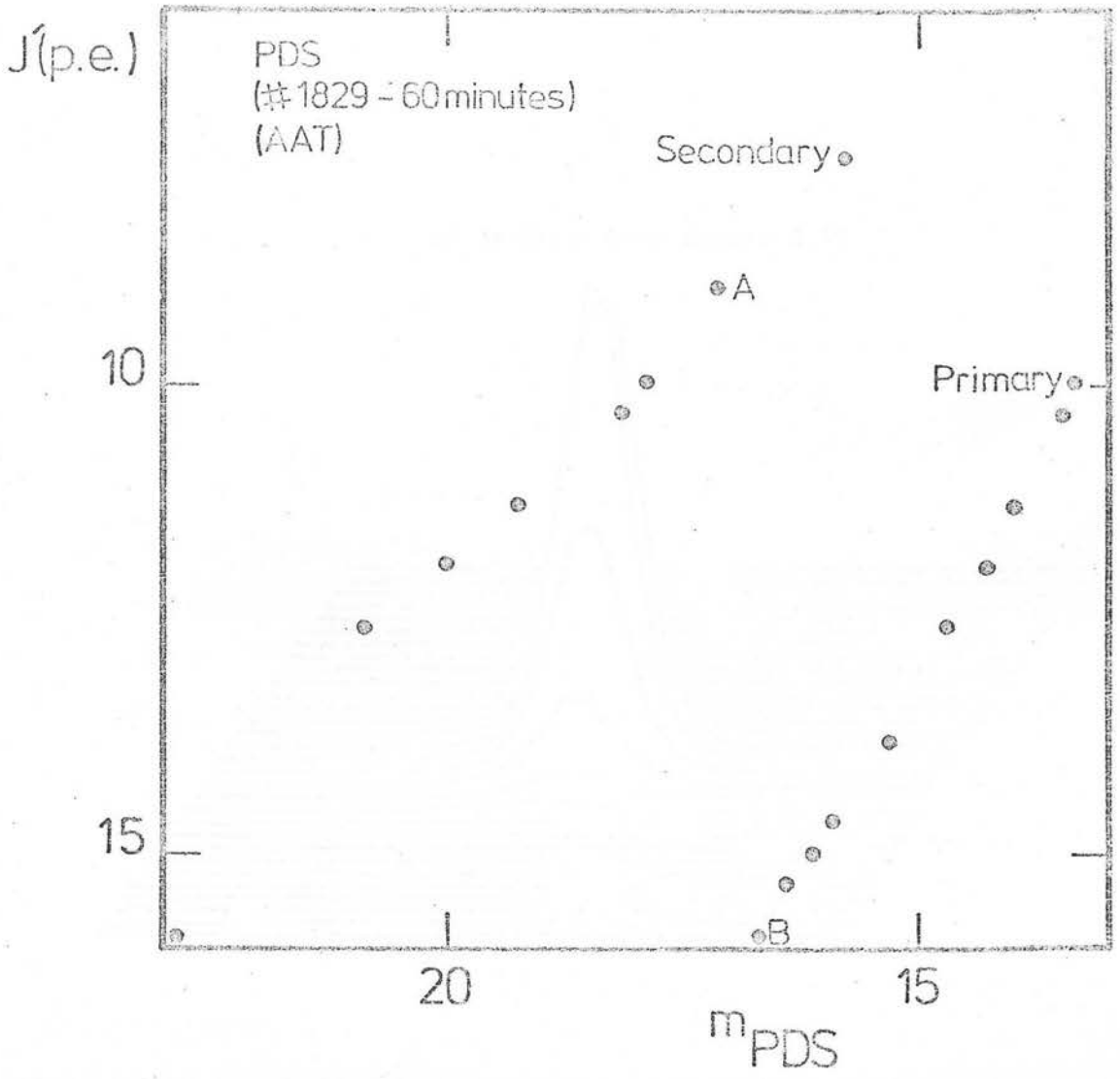

Figure 8.12 Sub-beam prism calibration (PDS).
Photographic J' magnitude plotted against PDS magnitude.
The region of overlap is defined by only one observation.

a) Image A from figure 8.12

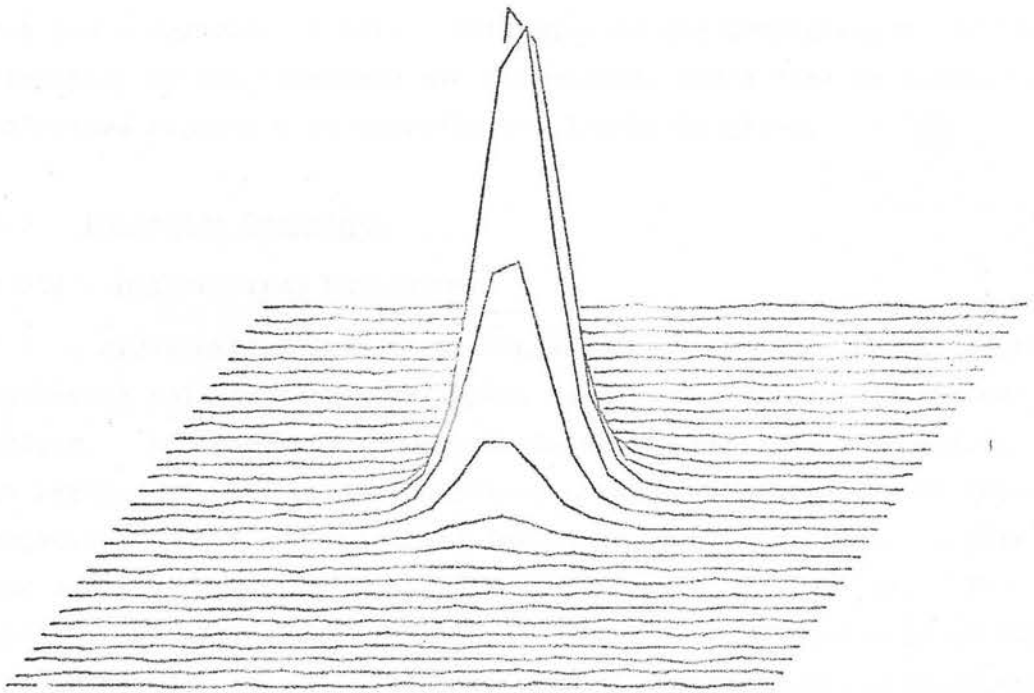

Figure 8.13 Stellar image profiles from overlap region of sub-beam prism plates.

b) Image B from figure 8.12

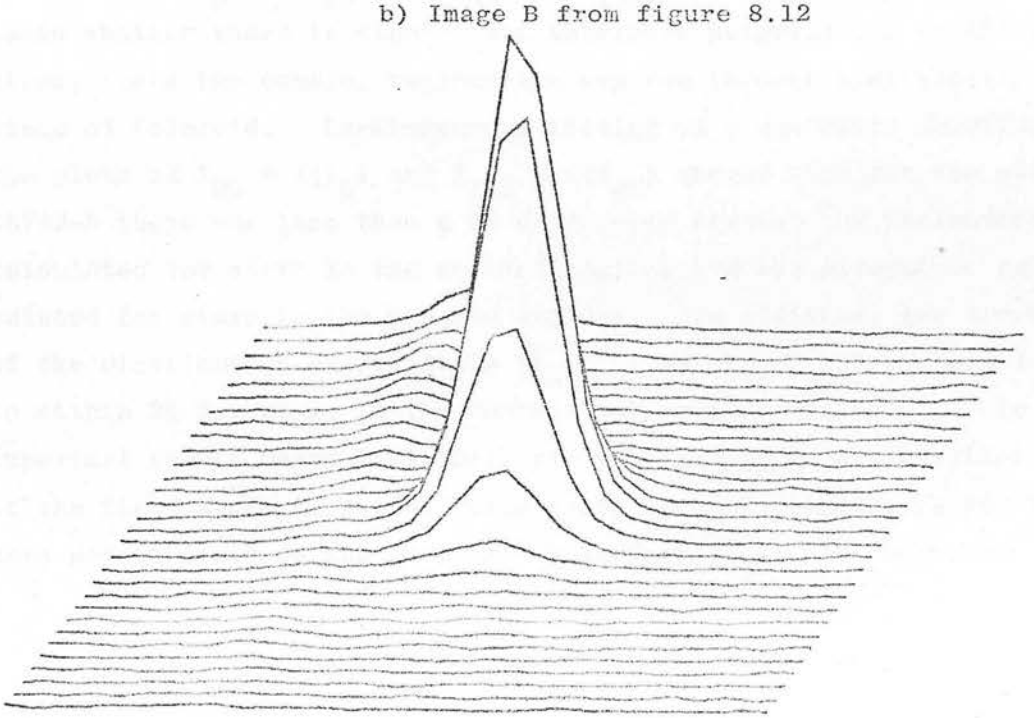

CHAPTER NINE

The technique for selecting polarization candidates is described in this chapter. Selection is made from one complete set of polarization plates, with corroboration from a single Stokes parameter set and a variability set. Estimates of the completeness and reliability of the technique are calculated, and a list of candidate polarized objects with significance levels is given.

9.1 Detection Technique

9.1.1 Differential Measurement

A differential detection technique has important benefits for selecting polarized objects, apart from the simplicity of the calculations. As described in Chapter Seven, no photoelectric calibration is required. The degree of polarization is a dimensionless quantity representing the modulation of intensity through different angles of the analyzer, and the intensity can be in arbitrary units. The photographically extended calibration sequence is used only to tag the magnitudes of images down to near the plate limit, with an error of ±0.1 magnitude; polarizations are calculated directly from COSMOS machine magnitudes. The control factors (C_ϕ) are intended to compensate for differences in observing conditions and emulsion sensitivity between the four plates comprising a polarization set. The relationship between I_0 and I_{90}, and I_{45} and I_{135} in the control regions also tests whether there is significant intrinsic polarization in the field stars, since the control regions are exposed through a stationary piece of Polaroid. Least-squares fitting of a quadratic function to the plots of $I_{90} = f(I_0)$ and $I_{135} = f(I_{45})$ showed that for the plates X5742-5 there was less than a 3% difference between the parameters calculated for stars in the control regions and the parameters calculated for stars in the program regions. In addition, the r.m.s. of the distribution of residuals (I_0-I_{90}) and $I_{45}-I_{135})$ was similar to within 3% for stars in the control and program regions. This important result means that there are no systematic polarizations of the field stars at a level of greater than 3%, confirming an even more severe limit on the intrinsic polarization of <1% which came from

the photoelectric sequence in Section 8.2.3. Therefore, the control factors C_{ϕ} were applied to correct the shape of the functions $I_{90} = f(I_0)$ and $I_{135} = f(I_{45})$, and it was assumed that the corrected functions $I_{90} = f'(I_0)$ and $I_{135} = f'(I_{45})$ defined zero polarization for the field stars. This method is an internal polarimetric calibration. In any magnitude interval, the fitted functions are of the form,

$$I_{90} = f'(I_0) = a_0 + a_1 I_0 + a_2 I_0^2 + a_3 I_0^3 + \ldots \tag{9.1}$$

$$I_{135} = f'(I_{45}) = b_0 + b_1 I_{45} + b_2 I_{45}^2 + b_3 I_{45}^3 + \ldots \tag{9.2}$$

or in this case as a function of COSMOS magnitude,

$$m_{90} = f'(m_0) = a_0 + a_1 m_0 + a_2 m_0^2 + a_3 m_0^3 + \ldots \tag{9.3}$$

$$m_{135} = f'(m_{45}) = b_0 + b_1 m_{45} + b_2 m_{45}^2 + b_3 m_{45}^3 + \ldots \tag{9.4}$$

In this chapter, except where specifically referred to as J magnitudes, all magnitudes are COSMOS machine magnitudes. The internal polarimetric calibration makes an assumption that the mean residuals averaged over many stars will be zero

$$\sum_1^i (m_{90} - f'(m_0)) = \sum_1^i (m_{135} - f'(m_{45})) = 0 \tag{9.5}$$

However, the residual of an individual star will not in general be zero, and will be related to the Stokes parameters in the following way,

$$\left\{m_{90} - f'(m_0)\right\}_i = \varepsilon_i^Q \,, \quad \left\{m_{135} - f'(m_{45})\right\}_i = \varepsilon_i^U \tag{9.6}$$

and therefore using equations (7.56) and (7.58),

$$\frac{Q}{I} = \frac{10^{-(\varepsilon_i^Q/2.5)} - 1}{10^{-(\varepsilon_i^Q/2.5)} + 1} = p \sin 2\theta \tag{9.7a}$$

$$\frac{U}{I} = \frac{10^{-(\varepsilon_j^U/2.5)}-1}{10^{-(\varepsilon_i^U/2.5)}+1} = p \cos 2\theta \qquad (9.7b)$$

where Q/I and U/I are normalized Stokes parameters and I is the mean intensity of the four position angles. As demonstrated in Section 8.2.3, there is a direct correspondence between dealing in magnitudes and intensities, so equations (9.7a) and (9.7b) are equivalent to (7.11a) and (7.11b).

It is evident that the polarization referred to above is a pseudo-polarization. The distribution of residuals ε_i^Q and ε_i^U when two plates are compared simply indicates the distribution of random photometric errors involved in faint stellar photometry. The control regions show just the same residual distributions from areas exposed through the same angle of the Polaroid filter. Although not implying that there is any substantial intrinsic polarization associated with the vast majority of stars on the plate, it is nevertheless useful to deal in terms of polarization. Rather than being thought of as polarization signal, Q/I and U/I represent polarization noise. The width of the residual distribution can be converted into a polarization detection level, and the width of the distribution also gives the probability that an individual residual will occur due to random errors rather than intrinsic polarization. A pseudo-polarization is also convenient because it incorporates measurements from four plates in one parameter.

Inevitably, coping with poor signal-to-noise is the dominant problem in the differential technique. The search involves ~30,000 stars down to $m_B \sim 19.5$, and the objects of interest will be buried in the wings of a broad distribution of photometric noise. Large numbers of objects and large areas of sky must be searched to have any expectation of finding polarized objects, but large numbers will also contaminate the wings of any random distribution. Without confirmation by photoelectric observations or measurements from a large number of plates, each polarization candidate will be tentative. The technique is only of importance if the error distribution can be modelled, and each candidate assigned a statistical weight. Three

relevant concepts which can be identified are the completeness, significance and reliability of the polarization search. The completeness relates the detection limit of the search to the known polarization properties of BL Lac objects. The significance of a polarization candidate assumes a model for the distribution of photometric errors and indicates the probability that a given polarization could occur by chance. The reliability is complementary to the significance, since it takes into account errors not modelled in the significance estimate. For example, if the errors are non-normally distributed (due to the presence of galaxies, merged images, mis-matches, etc.) then the reliability is a confidence level that the candidate is not in one of these spurious categories.

9.1.2 Procedures

The polarization search was centred on $12^h\ 57^m$ and $-20^\circ\ 09'$ (UK Schmidt survey field No. 575), and the machine measurements covered an area of $3.2^\circ \times 3.2^\circ$. The program area of 10.2 square degrees is entirely within the unvignetted part of the Schmidt plates. In addition, an area of 1.27 square degrees was measured in the control region of each of the plates. Six plates were used in the search: the complete polarization set X5742 (0°), X5743 (45°), X5744 (90°) and X5745 (135°) taken in March, 1979, and the partial polarization set X4902 (0°) and X4904 (90°) taken in March, 1980. The data from each of these plates was held on a separate magnetic tape, and the first step was to pair images between plates. The COSMOS pairing program treats one plate as the 'master' and uses 5 - 10 stars to define a coordinate transformation between the 'secondary' and 'master' plates. The images on the 'secondary' plate are paired using a 25μm search box from the transformed position. The pairing success rate is very high; only near the plate limit do mis-matches and non-matches become more likely. By repeating the procedure, more than one 'secondary' plate can be paired to the same 'master'. Three paired tapes were produced from these six plates. First, the four plates X5742-5 were matched with X5742 as the master. The pairing was ~96.94% complete for all images with COSMOS areas greater than 50 square

pixels. This image area was used as a limit in all the work discussed here; as a general rule it corresponds to a level ∿1 magnitude above the plate limit. Second, the plates X4902 and X4904 were paired with X4904 as the master. This pairing defines the Stokes parameter Q and was 99.86% complete for images of area >50. Finally, the plates X5744 and X4904 were paired with X4904 as the master. The comparison between plates taken through the same Polaroid angle (90°) but one year apart gives a check on variability. For this pair the success rate was 98.9% for image areas >50. The full pairing statistics are given in Table 9.1, and the three sets will in future be referred to as P, Q and V respectively. Due to the different plate limit for the pairing X4904/X4902, there are considerably fewer images on the Q and V sets than the P set. Therefore the completeness of the Q and V sets (>99% of images paired) extends down to a magnitude ∿0.6 mag. brighter than the limit of the P set. Candidates chosen from P alone are complete down to J = 19.5, but candidates chosen from P and either Q or V are only complete down to J = 18.9.

Four selection parameters can be derived from these six plates, corresponding to residual deviations from the four pairings X5743/X5744, X5743/X5745, X4904/X4902 and X4904/X5744. The first two define Stokes parameters Q' and U', the third defines the Stokes parameter Q and the fourth describes a degree of variability. These four parameters are combined to give the significance level of a polarization candidate. The selection procedure can be summarized as follows:

(i) Control factors C_ϕ were derived by least-squares fitting a relationship to data from the control regions of three of the four pairings and comparing it to the relationship for data from the program regions (see Section 7.5.2). There were no control factors for the fourth variability pairing because the plates were taken through the same Polaroid angle. About 1000 stars in the magnitude range 14 < J < 19.3 were used to define C_ϕ.

(ii) For the subsequent analysis, the program area was broken down into nine sub-units each ∿1° x 1°. This was done partly to alleviate the field effects which were found on all the plate pairs

by using a relatively 'local' internal calibration. Also the smaller areas were needed to keep the number of stars in the least-squares fitting routine tractable. In a 1^{o} square on the paired plates X5742-5 there were found to be ~2800 stars in the range $14 < J < 19.3$.

(iii) For each sub-area, and for each of the four plate pairs of interest, several tests were carried out. First, residuals were plotted against position on the plate to check for field effects. Then the residuals were histogrammed and fitted by a Gaussian distribution. A minimum χ^2 search was carried out for a Gaussian of variable amplitude and width, and the parameters of the best fit Gaussian were noted. Finally a list of discrepant objects was compiled using cuts on the selection parameters and the image eccentricity (to exclude double images and obvious galaxies). One list was produced for each of the P, Q and V plate sets.

(iv) The three selection lists in each area were paired and images common to more than one list were tagged as polarization candidates. The prime list consisted of objects which appeared on all three lists, and using the combined selection parameters a significance level could be assigned to each candidate.

(v) The reliability of the candidates was assessed with a star/galaxy separation algorithm, and also by visual inspection of the plates. Each prime candidate was examined on direct, polarization and objective prism plates.

9.2 Data

9.2.1 Field Effects.

One of the most striking features of all the plate pairs analyzed was the existence of large amplitude, systematic field effects. Field effects are magnitude offsets which vary across a photographic plate, and can be caused by defects in the plate such as emulsion sensitivity gradients or by errors in the machine measurement. It is difficult to disentangle these two contributions. If there are photometric standards well distributed

across a Schmidt plate, then the field effects can be defined absolutely. However very few fields have sufficient calibrators to map the variations sensitively, and only relative field effects are discussed here. Comparison of relative field effects on the polarization plates with absolute field effects on COSMOS measures of ∿1500 standards in the SGP field show that both types have the same characteristics (Gilmore, Reid: private communication). On some plates the amplitude of the offsets can be >0.4 COSMOS magnitudes (>0.7 photoelectric magnitudes) and it is possible that they may have been caused by the lack of autofocus on the COSMOS machine at the time of the measurement. Autofocus is a closed-loop system which compensates for the sag of the photographic plate in determining the optimum focus of the scanning light beam. Slight defocussing of the beam will degrade the effective resultion, increase the amount of scattered light and alter the machine magnitude. However, since field effects have also been observed on plates measured with an iris photometer, the problem cannot be due to COSMOS in all cases.

To investigate the field effects, the brightest 3500 stars in the 10 square degree program area were considered. First a polynomial was fitted by least squares to each of the four plate pairs and a histogram of the residuals was plotted. The distribution of residuals is characterised by an r.m.s. deviation and is often asymmetric with substantial wings. To correct the raw data, a 20 x 20 grid was formed from the 10 square degree area, and residuals from all the stars in a bin were summed and averaged. This created a 20 x 20 array of mean residuals. With 3500 stars in the field, there were often less than 10 stars in each bin and the second stage was to smooth the elements of the 20 x 20 array in 3 x 3 bin areas. A Gaussian function with a half-width of one bin was used for the smoothing. The resulting 20 x 20 array of smoothed residuals was then applied to correct the raw data. The raw data was recalled from magnetic tape, each star within a given bin being corrected by the appropriate array element to give the corrected data point. The improvement was tested by once again least squares fitting a polynomial to the paired data and calculating an r.m.s.error.

Finally, the effectiveness of the procedure can be checked by binning the residuals of the corrected data and contour plotting the field effects again. In theory this process can be repeated until the residuals are negligibly small, but in practice after one iteration the level of residuals was buried in the photometric noise and further iterations did not improve the error.

The improvements which result from correcting for field effects are shown in Table 9.2 and Figures 9.1 - 9.4. Table 9.2 contains the polyfit coefficients and r.m.s. errors for the raw and corrected data. The reduction in the r.m.s. error is substantial: between 25% and 35%. Figure 9.1b shows the residual distribution for the pairing X5742/X5744, and Figure 9.1a is a contour plot of the field effects across the program region. The contours are at intervals of 0.02 magnitudes and the systematic variations are clearly seen. Figure 9.1d shows the residual distribution corrected for field effects and plotted on the same x-axis scale as 9.1b. Not only is the distribution much narrower but it is more symmetrical and looks more like a normal error distribution. The high-σ wing of images appears to form a different component from the smooth curve of the majority. Figure 9.1c demonstrates that the correction has successfully removed the field effects and the residual contours are well within the calculated r.m.s. Figures 9.2 - 9.4 contain the same four plots for the other three pairings: X5743/X5745, X4904/X4902 and X4904/X5744. The features are qualitatively the same and it should be noted that the strongly concentric residual contours on X4904/X4902 are the most direct evidence for COSMOS focussing contributing to field effects. The centre of the contour plot corresponds exactly to the geometrical centre of the Schmidt plates. Even for these very severe gradients, a dramatic improvement in the r.m.s. error is possible.

The implication of field effects on Schmidt plates is very serious for many types of project. Galaxy counts of photographic photometry down to faint levels will be severely affected by apparent sensitivity changes, especially since the amplitude is so large. A high density of standards is needed to calibrate them out directly.

In this study, the polarization detection limit depends directly on the width of the residual distribution; and any smearing out of that distribution will be very deleterious. A differential technique will show up field effects, and by taking a 'local' transformation between plates over a very small area (in this case 10 arc minutes ≡ 9mm) the gradients can be almost entirely removed. To optimize the detection level the residuals must be photometric-noise limited. It has been shown that this can be successfully achieved for the bright images, but the results cannot be safely used to correct the faint images since there may be field effects on a scale finer than can be probed by the bright images. Therefore the procedures described above were carried out for the 1 degree square sub-areas as well.

9.2.2 "P" Set

The four plates X5742-5 define a complete polarization set, and the pairings X5742/X5744 and X5743/X5745 represent the Stokes parameters Q and U respectively. In each sub-area there were 2900-3100 stars, and the best fit to the functions $m_{90} = f'(m_0)$ and $m_{135} = f'(m_{45})$ was a linear function with no improvement in r.m.s. by going to a higher order polynomial. Contour plots of residuals against position within the sub-area showed that there were systematic field effects even across this small area, with a peak-to-peak amplitude of 0.24 mag. for the 0°-90° pair and 0.14 mag. for the 45°-135° pair. This time a 10 x 10 element array was used for the correction, because a 20 x 20 array would have left an average of less than eight stars in each bin and the average residual from so few and faint stars would have been dominated by photometric errors rather than field effects. Applying these corrections had a negligible effect, the r.m.s. for 0°-90° decreasing from 0.259 → 0.251 mag. and the r.m.s. for 45°-135° going from 0.199 → 0.198 mag. When the corrected residuals were plotted against position, the contour plots showed that the field effects had been largely removed. The very small reduction in the r.m.s. error showed that the errors for the faint stars on these plates are dominated by random noise rather than systematic gradients. Therefore corrections were not applied to

residuals in any of the sub-areas. In the rest of this chapter, one of the sub-areas (denoted Sub 1) will be taken as being typical and graphs will only be shown for this one region. The tables will display the full data for all nine sub-areas.

In order to derive an objective level of significance for each of the polarization candidates, the residuals were modelled by a Gaussian distribution

$$p(X_i, \mu, \sigma_G) = \frac{A}{\sigma_G\sqrt{2\pi}} \exp\left\{ -\tfrac{1}{2}\left(\frac{X_i - \mu}{\sigma_G} \right)^2 \right\} \qquad (9.8)$$

where $X_i - \mu = \varepsilon_i$, the residual for the ith data point, and σ_G is the standard deviation (Wall, 1979). Empirically, the Gaussian or normal distribution is a good description of random errors in most experiments. The parent distribution of the residual distribution is assumed to be a symmetric Gaussian, and even though there is definitely a non-normal high-σ tail to the residuals it is important to see how well the bulk of the observations are described by a distribution with well-understood properties. The standard deviation of the least-squares fit is σ_F, and the residuals are binned at intervals of $0.1\sigma_F$. If the total number of data points is N, the parent distribution is given by

$$\sum_{\mu - \frac{\varepsilon_i}{\sigma_G}}^{\mu + \frac{\varepsilon_i}{\sigma_G}} p(X_i, \mu, \sigma_G)\,dx = 1 \qquad (9.9)$$

where $\varepsilon_i = n(0.1\sigma_F)$. The fit is performed by minimizing χ^2, defined as

$$\chi^2 = \sum_{j=1}^{n} \frac{\left\{ f(X_j) - Np(X_j, \mu, \sigma_G) \right\}^2}{\sigma_j (f)^2} \qquad (9.10)$$

where n is the number of bins and $f(X_j)$ is the observed bin population. The measurements X_i are distributed according to the parent population, and for each bin value X_j a sample of the parent population is chosen. The fluctuations in $f(X_j)$ are described by the Poisson distribution where the variance equals the mean (i.e. $\sigma_j^2(f) = f(X_j) = Np(X_j,\mu,\sigma_G)$) and equation (9.10) becomes

$$\chi^2 = \sum_{j=1}^{n} \frac{\left\{ f(X_j) - Np(X_j,\mu,\sigma_G) \right\}^2}{Np(X_j,\mu,\sigma_G)} \qquad (9.11)$$

To carry out the test the data was truncated at $\pm 3\sigma_F$, and a two parameter χ^2 search was performed to calculate the optimum mean and standard deviation of the parent distribution. The residual histograms and best-fit Gaussians are displayed in Figure 9.5, along with the contours of χ^2 for the parameter search. The values of σ_F (from a least-squares fit to all the data), χ^2_{MIN} and σ_G (from a Gaussian fit to the truncated data) are given in Table 9.3 for all the sub-areas. The value of χ^2_{MIN} has been divided by the number of degrees of freedom $\nu = n-2$, and the reduced values indicate a tolerably good fit of the Gaussian to the observed distribution. σ_G is less than σ_F because the highly deviant images have been removed, and σ_G will be the basis for the significance test for the candidates. A single value of σ_G for all the images in each sub-area is not strictly valid, since a 3.5 magnitude range is covered and the dispersion will increase with magnitude. However the majority of the points are at the faint end and σ_G will be a good estimator there, despite being an over-estimate for the brighter stars. The magnitude range also explains why the values of χ^2_{MIN} are not closer to 0.5.

Figure 9.6 shows the magnitude plots of the two pairs X5742/X5744 and X5743/X5745, along with the calibrated number-magnitude distribution and the number-eccentricity distribution. The eccentricity is a COSMOS image parameter defined as the ratio of the semi-minor to semi-major axes. By discarding highly non-circular images it is possible to filter out double images (artificially joined by COSMOS into a single image) and some galaxies. The important diagrams of pseudo-polarization are shown in Figure 9.7. The histogram

of polarization noise shows that ∿12% of the images lie beyond values of 20%. Even with a relatively high detection cut, the number of candidates to sift through is enormous. Extended objects will contaminate the tail of the n(p) histogram because the COSMOS thresholding procedure can readily produce 10 - 20% deviations in the summed intensity of an image with a galaxian profile. The number-magnitude plot shows that the high polarization images increase sharply beyond J = 18.8, and it is not clear from the diagram whether the spread is caused by an increase in the random noise at the faint end, or an increase in the number of galaxies in the sample. If it is the first, then the polarization detection limit cannot be improved; if the second, then an appropriate star/galaxy separation algorithm will increase the sensitivity of the search. Perhaps the most information is contained in the Q-U plot, which is a two-dimensional plot of n(p) with contours of polarization noise being concentric circles of radius p in the Q-U plane. The distribution does not quite have circular symmetry, which represents the fact that σ_G = 0.254 for the Q pairing (X5742/X5744) and σ_G = 0.183 for the U pairing (X5743/X5745). A skewness in the Q-U plane is important because the plates are not then equally sensitive to all position angles of polarization. The weighting of the high-σ points causes the zero-points of Q and U to pass a few percent from the centre of the condensed part of the distribution. Therefore an error of 2-3% is involved in the zero point of the internal calibration. The contamination of images with high polarization noise is equal at all position angles.

9.2.3 "Q" Set

The two plates X4904 and X4902 define the Stokes parameter Q and there are about 1800 stars in each of the 9 sub-areas on these plates. The field effects for this pair were particularly severe for the bright images across the entire program region, and the same tests reveal that they are still severe over 1 square degree.

Using a method exactly analogous to that for the "P" set in Section 9.2.3, the plates were corrected using a 10 x 10 smoothed array of mean residuals. The reduction in the r.m.s. error of the residual histogram is ~21%, and the residual histograms and Gaussian-fit χ^2 contours both before and after correction are similar to those for the P set, and the value of σ_F was not improved by going beyond a linear fit. Values of σ_F, χ^2_{MIN} and σ_G are listed in Table 9.4.

9.2.4 "V" Set

The plates X4904 and X5744 are used to look for variability over an interval of one year. Both are 90^o plates, so each stellar image passes through the same piece of Polaroid. The 90^o plates of each set were chosen because the calibration photoelectric sequence had a smaller scatter on these than on the 0^o plates. Different limiting magnitudes mean that the completeness limit of the paired data is constrained by X5744. The field effects on a scale of 1 degree are doubtless introduced by X4904, and as before were removed by a 10 x 10 array. The field effect contours before and after correction are similar to those for the P set, and residual histograms and Gaussian-fit χ^2 contours also have the same form. The reduction in σ_F is typically ~10%. Values of σ_F, χ^2_{MIN} and σ_G are listed in Table 9.5.

9.2.5 Star/Galaxy Separation

A simple method of star/galaxy separation and double-image rejection was needed to compress the n(p) distribution and allow a lower polarization cut while reducing the number of polarization candidates to reasonable proportions. It was decided to use an image eccentricity cut of 1.5 to achieve this. An eccentricity cut must be used with care because the eccentricities of ordinary stellar images increase with fainter magnitudes. As the number of pixels in an image gets smaller, small variations in background intensity and the addition or subtraction of single pixels can make substantial differences to the ratio of semi-major to semi-minor axes. For an N pixel image, the eccentricity could be typically $100(\sqrt{N}/N)\%$, which is ~15% for the smallest images in this study. The eccentricity cut

must not be so crude that it compromises the completeness of the stellar images. A cut of 50% was used on all the plates, meaning that if any one of the images in a paired set had an eccentricity >1.5 the image was rejected. To test the cut, a sample of 100 images with eccentricities greater than 1.5 were studied by eye on plate X5742. The sample covered the entire magnitude range. By visual inspection, each of the 100 images were galaxies, putting an upper limit of 1% on the stellar rejection rate caused by such an eccentricity cut. From the eccentricity distribution in Figure 9.6, ∿26% of all images in the range $16 < J < 19.5$ are rejected; and the effect on the n(p) distribution is very significant. Figure 9.7d shows n(p) for all images (solid curve), and for images with eccentricities less than 1.5 (dashed curve) with the selected images normalized to the node of the total population. For the unselected images, ∿37% have p > 15%; whereas for the selected images, only 15% have p > 15%. Therefore the total number of images N has been reduced to $(0.75)(0.15)\ N \approx 0.11N$. Compact galaxies and face-on ellipticals will not be removed at this stage, but this crude cut has reduced by an order of magnitude the number of stars to be searched and allowed a polarization detection limit of ∿15%.

9.3 Candidate Selection

9.3.1 Composite Lists

Three data files were created for each sub-area. The first held images from the "P" set of plates selected by eccentricity less than 1.5 and p > 15%. The second held images from the "Q" pairing selected by eccentricity less than 1.5 and a residual $\epsilon_i^Q > 2.0\sigma_G$. The third held images from the "V" pairing also selected by eccentricity less than 1.5 and a residual $\epsilon_i^V > 2.0\sigma_G$. The images on these lists were paired, and objects appearing on more than one list were put into a separate file. It is an important part of the selection procedure that a candidate appears on more than one list; the reliability increases according to the number of independent measurements which have revealed it as potentially polarized.

Several lists were made, in order of importance:

(i)	PQV :	p > 15%	$\varepsilon_i^Q > 2.0\sigma_G$	$\varepsilon_i^V > 2.0\sigma_G$	ecc < 1.5
(ii)	PV :	p > 15%	-	$\varepsilon_i^V > 4.0\sigma_G$	ecc < 1.5
(iii)	PQ :	p > 15%	$\varepsilon_i^Q > 4.0\sigma_G$	-	ecc < 1.5
(iv)	V :	(J > 18)		$\varepsilon_i^V > 6.0\sigma_G$	ecc < 1.5
	V :	(J < 18)		$\varepsilon_i^V > 3.0\sigma_G$	ecc < 1.5

The reduction in the number of candidates under these conditions is charted in Table 9.6; the number of objects in the prime PQV list is 33.

To reduce these lists a final time, the compact galaxies and extended objects which escaped the eccentricity cut must be culled out. If the logarithm of the COSMOS image area is plotted against COSMOS magnitude then the stellar images form a closely-defined relationship while the galaxies have a larger area for a given machine magnitude and scatter on one side of the stellar band (Figure 9.8). The logA-m relationship determines the compactness of an image, although at fainter magnitudes the distinction between stars and galaxies becomes blurred. It is also impossible to distinguish stars and very compact galaxies, but if the image properties are so similar then the COSMOS parameters for a compact galaxy will be just as reliable as for a star. Figure 9.8 shows the logA-m plots for all the stars in a sub-area, with the candidates superimposed in larger symbols. For the PQV objects, only 9 out of 33 images are found to be stellar in appearance on the original plate, another 3 are 'soft' or marginally non-stellar, and the remainder are obvious galaxies. The eye is highly sensitive to contrast, and is a much better star/galaxy discriminator than COSMOS; so visual classifications must be used to test the effectiveness of the logA-m diagram. Figure 9.8a demonstrates that there is a clear demarcation between

stellar and galactic images and a line can be drawn which uniquely separates them. The PQV candidates divide into bright galaxies and fainter stars, though even the candidates identified as stars have a range of compactness on the logA-m plot.

The composition of the other three lists is somewhat different. To counter the fact that the candidate is selected from fewer independent measurements, the selection cuts on all parameters (except polarization) have been raised. The PV list has only 9 out of 91 candidates as stellar, with a majority of bright galaxies showing up as extended (Figure 9.8b). The PQ list contains more than 60% stars, dominated by a clutch of faint objects which fall on the compact side of the star/galaxy separation line. As with the PQV list, a single line completely separates stars and galaxies and there is only one moderately bright stellar candidate (Figure 9.8c). The selection criteria for the V list divide into objects brighter than and fainter than J = 18 with variability cuts of $\varepsilon_i^V > 3\sigma_G$ and $\varepsilon_i^V > 6\sigma_G$ respectively. 11 out of the 36 candidates appear stellar on the original plates, a similar proportion to the PQV list. The star/galaxy separation is clear-cut, but the increasing confusion between stars and galaxies can be seen on the logA-m plot (Figure 9.8d) as the completeness limit is approached. There are to candidates which fall well below the compactness curve for stars, though inspection of the plate shows them to be stellar in appearance. 35% of the objects on these four lists can be classified unambiguously as stellar.

9.3.2 Confidence Limits

For each of the final 46 candidates, two statistical quantities are derived which define the likelihood that the object is polarized and/or variable. The first is called the <u>significance</u> of the observation, and uses statistics based on the assumption that the errors from any two intensity measurements are normally distributed. For the PQV candidates there are four residuals which combine to give this parameter,

$$\langle S \rangle = \left\{ \left(\frac{\varepsilon_i}{\sigma_G} \right)^2_{Q'} + \left(\frac{\varepsilon_i}{\sigma_G} \right)^2_{V'} + \left(\frac{\varepsilon_i}{\sigma_G} \right)^2_{Q} + \left(\frac{\varepsilon_i}{\sigma_G} \right)^2_{V} \right\}^{\frac{1}{2}} \qquad (9.12)$$

where the subscripts Q´ and U´ refer to the plate pairs X5742/X5744 and X5743/X5745, Q refers to X4904/X4902 and V refers to X4904/X5744. For PQ candidates the last term is zero, and for PV candidates the third term is zero. <S> is a dimensionless quantity which treats the four residuals as independent. Each quantity (ε_i/σ_G) represents the integral probability that a random measurement X_i will have a deviation less than ε_i,

$$p_i = \frac{1}{\sqrt{2\pi}} \int_{-\frac{\varepsilon_i}{\sigma_G}}^{\frac{\varepsilon_i}{\sigma_G}} e^{-X^2/2} \, dX \qquad (9.13)$$

and if the measurements are independent, then

$$\langle p \rangle = (1-p_i)_{Q'}(1-p_i)_{U'}(1-p_i)_{Q}(1-p_i)_{V} \qquad (9.14)$$

i.e. for each residual having $(\varepsilon_i/\sigma_G) = 2$, $\langle S \rangle = 6$ and $\langle p \rangle = 4 \times 10^{-6}$. Unfortunately it is not completely true that the measurements are independent. For example, an image may appear to be polarized because a faint image becomes appended to it in the COSMOS measurement (the eccentricity limit need not be violated). Whether the image appears as a polarization candidate would depend on the background level on each plate and the effect of COSMOS thresholding. In addition, the plate pairings are not independent. If an image is peculiar on plate X5744 it will show up on both the Q´ and V pairings. Therefore <S> should only be regarded as a 'figure of merit' rather than representing a probability. Higher values of <S> indicate the more significant polarization candidates. Note that this statistic differs from the one used by Penston and Cannon (1970) and others to look for variability in quasars from photographic plates. The χ^2 test that they have described can only be used for a larger number ($N > 10$) of independent measurements.

The second statistic is the reliability of an observation, which takes into account as far as possible the component of non-normally distributed residuals. The reliability is the product of three factors,

$$\langle R \rangle = \left(\frac{4}{n_p}\right)^2 \times \left(\frac{1}{n_{S/G}}\right) f(m) \qquad (9.15)$$

n_p is the number of plate pairs involved in the candidate's selection, and $(4/n_p)^2 = 1$ for a PQV candidate. $n_{S/G}$ is the percentage of the candidates in a list which are borderline between stars and galaxies. f(m) is a signal-to-noise factor to account for the range of brightness of the candidates and the fact that the demarcation between stars and galaxies dissolves at faint magnitudes. f(m) is normalized to the magnitude range of the sample and is defined by,

$$f(m) = 10^{-\left\{\frac{m_i - m_{MIN}}{5.0}\right\}} \qquad (9.16)$$

where m_{MIN} is the bright magnitude limit of the sample (J magnitudes are used). $\langle R \rangle$ is only equal to 1 for a PQV candidate at the bright end of a sample where the star/galaxy separation is unambiguous; otherwise $\langle R \rangle$ is less than 1. The product $\langle R \rangle \langle S \rangle$ is a comprehensive statistic for each candidate. Tables 9.7 - 9.10 list the four sets of candidates numbered according to their sub-area of the plate. PQV candidates which appear on other lists as well have only been shown on the PQV list. As defined by the $\langle R \rangle\langle S \rangle$ statistic, the PQV candidates are nearly all more significant than any of the others. Therefore, the 9 objects in the PQV list are regarded as potentially polarized sources.

The finding charts for the objects are shown in Figure 9.9a and the spectra from the UKSTU objective prism plate of the field are presented in Figure 9.9b 1950 positions are listed in Table 9.11. The positions were obtained by using a coordinate transformation fitted to 12 SAO stars across the field, and interpolating the positions of the objects. Each position has an accuracy of σ(R.A.)

= 1.1 arc seconds and σ(Dec) = 0.3 arc seconds. None of the candidates is a radio source down to the limits of the Parkes 2700MHz survey (revised August 1978). Photoelectric polarimetry, comprehensive variability studies, and spectroscopy are needed to confirm any of the candidates as a BL Lac object. This work puts an upper limit on the space density of BL Lac objects according to the following limits:

$$\left.\begin{array}{l} p > 15\% \\ \Delta V > 0.3 \text{ mag.} \\ J < 18.9 \ (B < 19) \end{array}\right\} \quad n_{BL} < 1 \ (\text{sq.deg.})^{-1} \qquad (9.17)$$

9.3.3 Completeness

The sensitivity limits of the survey can be interpreted in terms of the properties of the current sample of BL Lac objects, using the review by Angel and Stockman (1980) as a source of data. All 57 polarized objects listed by Angel and Stockman have mean visual magnitudes brighter than the limit of the survey and accounting for variability they spend ~90% of the time above the brightness limit (Pollock et al., 1979; Pica et al., 1980). 24 (42%) have maximum optical polarizations greater than 15%. The variable polarization means that each object with p_{MAX} >15 will have a duty cycle of time when the polarization is less than 15%. The most comprehensive optical monitoring is that by Angel et al. (1978). Of the 241 observations of objects with p_{MAX} > 15%, 90 (37%) individual measurements had p > 15%. A substantial duty cycle at high polarizations is also seen in the infrared data from Part I. In 22 observations of objects with $(p_{MAX})_{IR}$ > 15%, 15 (68%) were at levels greater than 15%. The completeness is also affected by the image pairing statistics of the PQV candidates, which introduces a factor of (0.969)(0.999)(0.989) = 0.96. Finally, there is a term due to the proportion of BL Lac objects rejected by only including stellar or very compact objects. This term is 0.86. Combining these factors gives a completeness of ~0.13, which means that roughly 1 in 8 of the known BL Lac objects

could be detected photographically from one set of plates. The number of plates used in this study should be regarded as the bare minimum; increasing the number of plates has two important effects. More complete polarization sets at one epoch would allow the polarization detection limit to be lowered, and sets of plates at several different epochs would increase the completeness of the survey. More observations also increase the reliability of each candidate found.

9.3.4 BL Lac Objects and QSOs

The surface density of QSOs has been estimated from samples selected by ultraviolet excess and by the presence of strong emission lines. Braccesi et al. (1980) have summarized number-magnitude counts of UV-excess quasars and find a steep increase of a factor of 7.3 per magnitude interval. The integrated counts down to B = 19 give a surface density ~ 4 (sq.deg.)$^{-1}$. Searches for UV-excess quasars are biassed towards low-redshift objects. Low dispersion slitless spectroscopy has begun to produce large numbers of QSOs, and recent samples have been compared by Vaucher and Weedman (1980). The differential number counts seem to be less steep than for the UV-excess objects, and the surface density down to B = 19 is in the range 2-4 (sq.deg.)$^{-1}$. Emission-line QSO surveys suffer from their own selection effects, and are biassed towards high redshift QSOs. As previously mentioned, there is only one optically selected quasar with substantial polarization, and the emission mechanism in that source may not be synchroton radiation. The result $n_{BL} \approx 0.25 n_{QSO}$ implies that if only one of the BL Lac candidates is confirmed, there will be evidence for a new class of extragalactic object.

Usher (1978) and Usher and Mitchell (1978) have selected QSOs by criteria of blueness and variability in two fields, using plates with a time coverage of 23 years. Cumulative number counts yield a lower limit on the surface density of variable QSOs down to an average magnitude of B = 19: >1(sq.deg.)$^{-1}$. Given the higher variability detection threshold of the Usher sample $\Delta V > 0.4$ compared to

$\Delta V > 0.3$ in this study), it appears that the surface density of objects selected by polarization is less than the surface density of variable objects. For a χ^2 probability of detecting variability of >97% and a variability signal-to-noise of >3, these studies by Usher achieved a 60% success rate in identifying quasars. In common with the UV-excess and emission line samples, the variable QSOs increase rapidly at a rate of ~6 per magnitude interval. QSOs selected by variability are more likely to be related to BL Lac objects than those selected by colour or emission lines, because of the good correlation between polarization and variability. The radio detection rate for variable QSOs is even lower than the detection rate for emission line QSOs, though the most variable QSOs are more likely to be detectable at radio wavelengths (Condon et al., 1980; Smith & Wright, 1980). Unfortunately, the colour selection $(U-V) < -0.4$ selects against most OVV quasars and BL Lac objects, so the variability sample may not be probing the same population as this polarization sample.

Finally, it is possible to relate the surface density limit to current ideas of the relationship between QSO's and BL Lac objects. Blandford and Rees (1978) have proposed that BL Lac objects are active nuclei where the continuum emission is beamed towards the observer. Whether an object is a QSO, OVV quasar or BL Lac object depends precisely on the line of sight with respect to the 'jet' axis. If the emitting region has a bulk relativistic factor Γ, the apparent luminosity for an observer in the emission cone is increased by Γ^2. It is already clear from the infrared data in Part I that relativistic motion is required to reduce the energy requirements of individual objects. However, the idea of Blandford and Rees has important statistical consequences. In searches to a given flux density, BL Lac objects need not be rare compared to QSOs. If active nuclei have a luminosity function $n(L) \propto L^{-s}$ and the luminosity of BL Lacs is enhanced by Γ^2, then the proportion of BL Lac objects to QSOs in samples to a given flux limit will increase both with s and Γ. This is because the sample probes deeper into the luminosity function of those objects with a special orientation

(i.e. a strong selection effect in favour of seeing BL Lac objects among active nuclei of a given luminosity).

By integrating the luminosity function, it is straightforward to show that the expected ratio of BL Lac objects to QSOs is,

$$\frac{n_{QSO}}{n_{BL}} = \left(\frac{4\pi}{\Omega}\right) \Gamma^{-2(s-1)} \qquad (9.18)$$

Inverting that argument, the observed upper limit on the surface density of BL Lac objects can be used to put an upper limit on Γ. Two parameters must be used. The increase in QSO numbers is a factor of order 6 per magnitude interval which corresponds to $s \simeq 2.5$. $(\Omega/4\pi)$ is the probability of an orientation down the jet axis; from radio source jets the typical observed opening angle is $5^{Q}10^{O}$ giving $(\Omega/4\pi) = 10^{-2}$. From eqn. (9.18),

$$\Gamma < \frac{\Omega}{4\pi}\left(\frac{n_{QSO}}{n_{BL}}\right)^{-1/2(s-1)} \qquad (9.19)$$

Using $n_{QSO} = 5\ (\text{sq.deg.})^{-1}$ and substituting gives $\Gamma < 2.7$. Therefore the BL Lac objects are constrained to be only mildly relativistic, and this does not account for the few sources which require $\Gamma = 5\text{-}10$ to avoid super-Eddington luminosities and enormous synchrotron magnetic fields. Note that if none of the candidate BL Lacs is confirmed, the upper limit on n_{BL} is decreased by an order of magnitude and the bulk motion limit becomes $\Gamma < 1.3$, at which point the orientation model of Blandford and Rees has severe difficulties in accounting for the most luminous BL Lac objects. The major uncertainty in this limit is the relative completeness of the QSO and BL Lac search techniques. The weight of these arguments can be increased by widening the search area substantially beyond 10 square degrees. Since the calibration, reduction and candidate selection are based on automated machine measurement and tested software, there is no reason that the same technique should not be applied to many Schmidt fields. Either way, the polarization survey puts significant limits on the space density of BL Lac objects. If any of the candidate objects is confirmed, there is evidence for a

radio quiet population of polarized objects. If none is confirmed, then limits are put on the models which relate BL Lac objects to QSOs and other active nuclei.

TABLE 9.1

Pairing Statistics for Polarization Plates

Set	Plate	Angle	No.of Images (A > 50)	% Paired	Mag.limit for 99% pairing
P	*X5742	0°	29,350	-	J = 19.3
	X5743	45°	29,203	99.5	
	X5744	90°	28,763	98.0	
	X5745	135°	28,452	96.9	
Q	*X4904	90°	16,410	-	J = 18.6
	X4902	0°	16,399	99.9	
V	*X4904	90°	16,410	-	J = 18.6
	X5744	90°	16,197	98.9	

* indicates 'master' plate

TABLE 9.2

Correction for Field Effects ($8 < J < 16$)

Plates	Before					After			
m_x/m_y	a_0	a_1	a_2	a_3	RMS	a_0	a_1	a_2	RMS
X5742/X5744 (0° vs. 90°)	-3.83	3.28	-0.31	0.01	0.218	16.05	-1.76	0.11	0.179
X5743/X5745 (45°vs.135°)	9.71	-0.77	0.07	-	0.148	-0.61	0.99	-	0.111
X4904/X4902 (90°vs.0°)	-0.50	1.06	-	-	0.0932	-0.78	1.08	-	0.0573
X4904/X5744 (VAR)	-0.65	0.98	-	-	0.144	-0.70	0.99	-	0.106

Data covers entire program region corrected by 20 x 20 smoothed array, a_0, a_1, a_2 and a_3 are the coefficients in the polynomial:

$$m_y = a_0 + a_1 m_x + a_2 m_x^2 + a_3 m_x^3$$

TABLE 9.3

"P" Set - Residual Distributions

	X5742/X5744 (0^{o} vs.90^{o})			X5743/X5745 (45^{o}vs.135^{o})		
	σ_F	χ^2_{MIN}	σ_G	σ_F	χ^2_{MIN}	σ_G
Sub 1	0.259	1.74	0.254	0.199	1.50	0.183
Sub 2	0.260	1.67	0.252	0.199	1.63	0.184
Sub 3	0.259	1.41	0.257	0.190	1.38	0.175
Sub 4	0.264	1.89	0.251	0.213	1.36	0.194
Sub 5	0.261	1.43	0.256	0.195	1.07	0.181
Sub 6	0.254	1.44	0.248	0.204	1.56	0.188
Sub 7	0.267	1.38	0.253	0.205	1.48	0.182
Sub 8	0.245	1.48	0.242	0.203	1.43	0.195
Sub 9	0.244	1.71	0.240	0.212	1.59	0.182

$\bar{\sigma}_G = 0.97\ \bar{\sigma}_F$ $\qquad$ $\bar{\sigma}_G = 0.92\ \bar{\sigma}_F$

TABLE 9.4

"Q" Set - Residual Distributions

	$(\sigma_F)_{Raw}$	$(\sigma_F)_{Corr}$	χ^2_{MIN}	$\sigma_G/(\sigma_F)_{corr}$	σ_G
Sub 1	0.246	0.194	2.07	0.69	0.134
Sub 2	0.201	0.169	3.85	0.82	0.139
Sub 3	0.176	0.159	1.75	0.73	0.116
Sub 4	0.189	0.177	1.68	0.70	0.124
Sub 5	0.193	0.177	2.24	0.74	0.131
Sub 6	0.169	0.160	2.29	0.78	0.125
Sub 7	0.187	0.165	1.29	0.63	0.104
Sub 8	0.188	0.158	1.70	0.74	0.117
Sub 9	0.194	0.155	2.12	0.74	0.115

$$\bar{\sigma}_G = 0.73\ \bar{\sigma}_F$$

TABLE 9.5

"V" Set - Residual Distributions

	$(\sigma_F)_{Raw}$	$(\sigma_F)_{Corr}$	χ^2_{MIN}	$\sigma_G / (\sigma_F)_{Corr}$	σ_G
Sub 1	0.195	0.155	0.75	0.68	0.105
Sub 2	0.181	0.171	1.88	0.71	0.121
Sub 3	0.177	0.159	0.85	0.61	0.097
Sub 4	0.159	0.153	0.98	0.63	0.093
Sub 5	0.149	0.143	1.36	0.79	0.113
Sub 6	0.181	0.169	0.34	0.60	0.101
Sub 7	0.164	0.138	0.53	0.64	0.088
Sub 8	0.151	0.142	1.51	0.53	0.075
Sub 9	0.195	0.144	0.61	0.65	0.094

$$\bar{\sigma}_G = 0.65\ \bar{\sigma}_F$$

TABLE 9.6

Selection of Polarization and Variability Candidates

File	"P"	"Q"	"V"	"P"	"Q"	"V"	PVQ	PV	PQ	V
Selection Cuts	-	-	-	p>15%	$\epsilon_i^Q>2\sigma_G$	$\epsilon_i^V>2\sigma_G$	p>15% $\epsilon_i^Q>2\sigma_G$ $\epsilon_i^V>2\sigma_G$	p>15% - $\epsilon_i^V>4\sigma_G$	p>15% $\epsilon_i^Q>4\sigma_G$ -	- - $\epsilon_i^V>6\sigma_G$
Sub 1	3148	1651	1543	367	189	123	1	4	1	4
Sub 2	3084	1726	1599	328	159	148	4	16	4	3
Sub 3	2911	1583	1681	371	184	140	4	3	4	2
Sub 4	3074	1589	1630	314	172	137	5	12	3	5
Sub 5	3030	1624	1643	352	186	161	5	14	4	4
Sub 6	2917	1679	1673	353	190	171	5	9	3	3
Sub 7	3156	1757	1588	379	163	152	3	8	4	6
Sub 8	3166	1760	1694	327	171	143	3	15	1	4
Sub 9	3108	1685	1617	366	175	149	3	10	2	4
Totals	27594	15054	14668	3157	1589	1324	33	91	26	36
								Star/Galaxy separation		
						Uncertain	3	7	3	6
						Stellar	9	9	17	11

TABLE 9.7

PQV Candidates

Number	J.Mag.	P(%)	Q′	U′	$\lvert(\epsilon_i/\sigma_G)_{Q',U'}\rvert$	Q	$\lvert(\epsilon_i/\sigma_G)_Q\rvert$	V	$\lvert(\epsilon_i/\sigma_G)_V\rvert$	<S>	<R>	<S><R>
Sub 2.1	18.58	17	0.122	0.123	1.80	-0.339	2.43	-0.30	2.48	3.91	0.36	1.39
Sub 2.2	18.60	17	0.165	-0.016	1.44	0.290	2.09	0.33	2.73	3.73	0.35	1.32
Sub 2.4	18.69	63	0.621	-0.087	6.35	0.274	1.97	1.91	15.79	17.13	0.34	5.80
Sub 4.1	16.51	16	0.047	0.155	1.80	-0.665	5.36	-0.33	3.55	6.68	0.92	6.17
Sub 5.1	18.90	[illegible]	0.086	-0.171	2.20	-0.671	5.12	0.41	3.63	6.65	0.31	2.04
Sub 5.4	17.12	19	0.098	0.162	2.13	-0.312	2.38	-0.25	2.21	4.18	0.70	2.91
Sub 7.2	18.55	16	0.132	-0.084	1.52	0.444	4.27	0.36	4.09	6.11	0.36	2.21
Sub 7.3	17.34	17	-0.139	0.098	1.68	-0.571	5.49	0.22	2.50	6.26	0.63	3.95
Sub 9.3	18.74	17	0.093	-0.144	1.87	0.431	3.75	0.28	2.98	5.14	0.33	1.70

TABLE 9.8

PV Candidates

Number	J.Mag.	P(%)	Q'	U'	$(\varepsilon_i/\sigma_G)_{Q',U'}$	V	$(\varepsilon_i/\sigma_G)_V$	<S>	<R>	<S><R>
Sub 2.14	18.93	19	-0.035	-0.189	2.28	0.47	2.73	3.56	0.20	0.72
Sub 3.2	19.05	17	-0.146	-0.069	1.49	0.42	2.67	3.06	0.19	0.58
Sub 4.5	19.04	22	0.197	-0.087	1.98	0.34	2.24	2.99	0.19	0.57
Sub 5.13	18.30	16	0.118	0.109	1.65	-0.46	-3.24	3.64	0.27	0.98
Sub 7.8	17.60	18	-0.171	-0.069	1.70	-0.41	-2.95	3.40	0.37	1.26
Sub 8.1	17.25	20	0.157	0.117	1.93	-0.63	-4.42	4.82	0.44	2.11
Sub 8.9	16.63	23	0.160	0.161	2.32	-0.40	-2.81	3.64	0.58	2.12
Sub 8.10	18.81	18	0.118	-0.138	1.88	0.32	2.26	2.94	0.21	0.63
Sub 9.5	18.65	20	-0.068	-0.166	2.09	0.45	3.10	3.74	0.30	0.86

TABLE 9.9

PQ Candidates

Number	J.Mag	P(%)	Q′	U′	$(\varepsilon_i/\sigma_G)_{Q',U'}$	Q	$(\varepsilon_i/\sigma_G)_Q$	<S>	<R>	<S><R>
Sub 1.1	18.72	17	-0.097	-0.142	1.89	-0.813	-4.19	4.60	0.10	0.68
Sub 2.3	18.88	15	-0.136	-0.062	1.39	-0.519	-3.07	3.37	0.09	0.47
Sub 2.4	18.58	15	-0.140	-0.058	1.39	0.633	3.75	4.00	0.11	0.64
Sub 3.3	18.56	16	-0.153	0.025	1.34	0.497	3.13	3.40	0.11	0.54
Sub 5.1	18.80	22	-0.185	-0.121	2.16	-0.587	-3.31	3.95	0.10	0.56
Sub 5.2	18.71	22	-0.220	-0.033	1.94	-0.617	-3.48	3.98	0.10	0.59
Sub 5.3	18.75	16	-0.154	0.015	1.33	0.583	3.29	3.55	0.10	0.52
Sub 6.1	18.15	15	-0.149	-0.039	1.39	-0.834	-5.21	5.39	0.13	1.05
Sub 6.2	18.16	18	-0.127	-0.133	1.91	0.633	3.96	4.40	0.13	0.84
Sub 7.1	18.42	19	-0.187	-0.029	1.66	0.600	3.64	4.00	0.12	0.68
Sub 7.2	18.62	16	-0.139	0.084	1.55	-0.793	-4.81	5.05	0.11	0.78
Sub 7.4	17.93	18	0.167	0.065	1.63	-1.093	-6.62	6.82	0.15	1.45
Sub 8.2	18.80	17	-0.062	-0.158	1.86	-0.480	-3.04	3.56	0.10	0.51
Sub 9.1	18.69	23	-0.227	-0.011	2.09	0.591	3.81	4.35	0.10	0.65
Sub 9.2	18.78	17	0.035	-0.164	2.00	0.514	3.32	3.88	0.10	0.57

TABLE 9.10

V Candidates

Number	J.Mag.	V	$(\varepsilon_i/\sigma_G)_V$	<S>	<R>	<S><R>	
Sub 1.3	19.07	-0.69	-4.43	4.43	0.01	0.04	
Sub 1.4	18.78	0.51	3.26	3.26	0.01	0.04	
Sub 2.5	19.09	2.29	13.37	13.37	0.01	0.13	
Sub 3.1	18.65	0.43	2.95	2.95	0.01	0.03	
Sub 4.3	19.11	0.64	4.20	4.20	0.01	0.04	J > 18.0
Sub 4.4	19.02	-1.13	-7.37	7.37	0.01	0.07	
Sub 4.5	18.24	0.84	5.46	5.46	0.01	0.08	
Sub 5.4	19.01	-0.80	-5.61	5.61	0.01	0.06	
Sub 7.6	19.03	-0.57	-4.14	4.14	0.01	0.04	
Sub 1.5	17.88	0.32	2.08	2.08	0.02	0.03	
Sub 3.2	17.84	-0.33	-2.07	2.07	0.02	0.04	J < 18.0
Sub 5.2	17.79	0.31	3.14	3.14	0.03	0.05	
Sub 5.3	17.65	0.29	2.04	2.04	0.02	0.04	

TABLE 9.11

Candidate Positions

Number	J.Mag.	R.A. (1950.0)	Dec.(1950.0)
PQV 2.1	18.58	$13^h\ 05^m\ 24.2^s$	$-19^\circ\ 51'\ 38.4''$
PQV 2.2	18.60	13 03 30.8	-20 36 38.8
PQV 2.4	18.69	13 01 06.7	-20 41 23.8
PQV 4.1	16.51	13 00 21.0	-21 13 28.1
PQV 5.1	18.90	12 59 34.1	-20 12 57.8
PQV 5.4	17.12	12 56 56.7	-20 34 53.8
PQV 7.2	18.55	12 55 39.0	-21 18 52.8
PQV 7.3	17.34	12 54 08.8	-21 26 19.6
PQV 9.3	18.74	12 53 01.3	-19 45 01.7

σ(R.A.) = 1.1 arc seconds

σ(Dec.) = 0.3 arc seconds

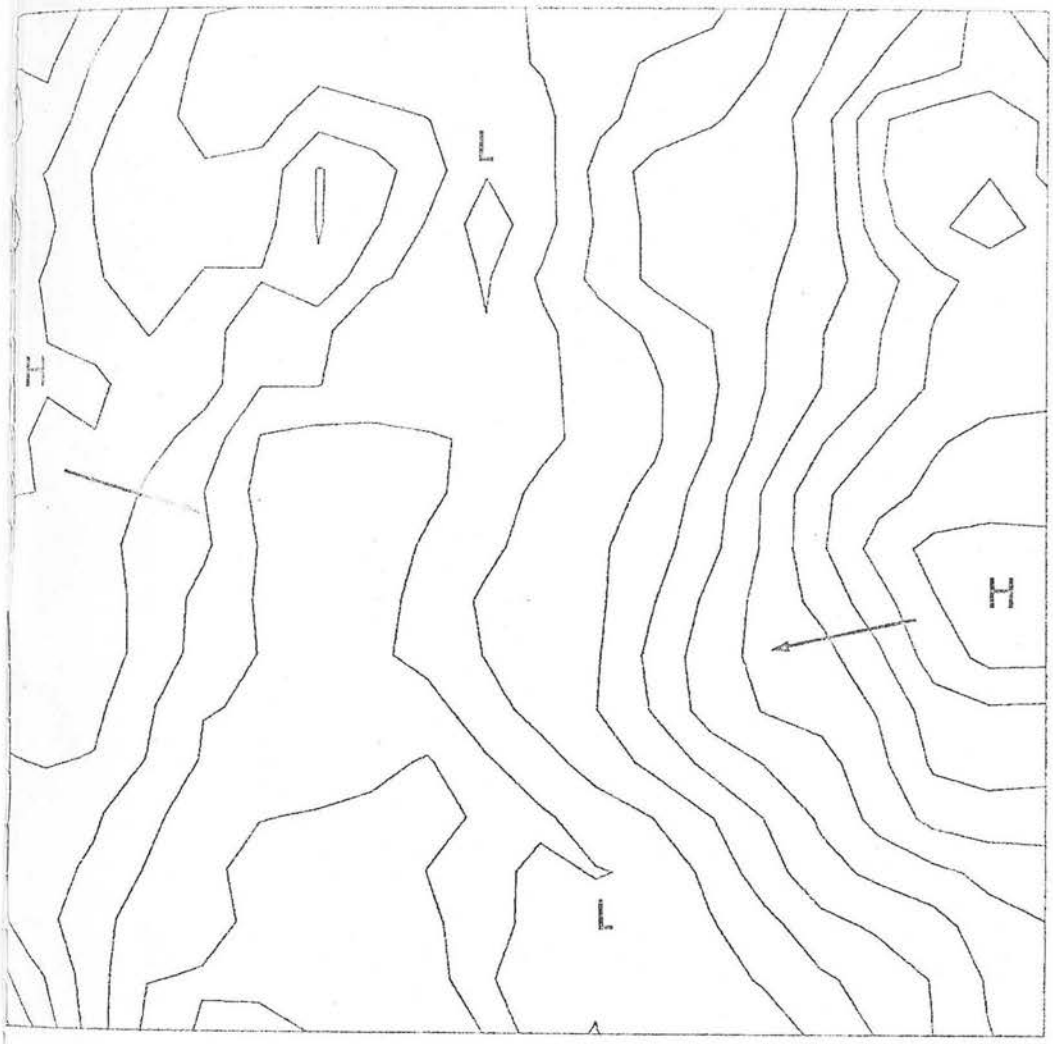

POL1

LOWEST -.40000E 0

INTERVAL .20000E 0

MIN -.83100E 0

MAX .17530E 1

a) Residual contours
(interval=0.02 mag)

H : high, $\varepsilon_i \rightarrow$+ve

L : low , $\varepsilon_i \rightarrow$-ve

Figure 9.1 X5742/X5744 BEFORE correction.

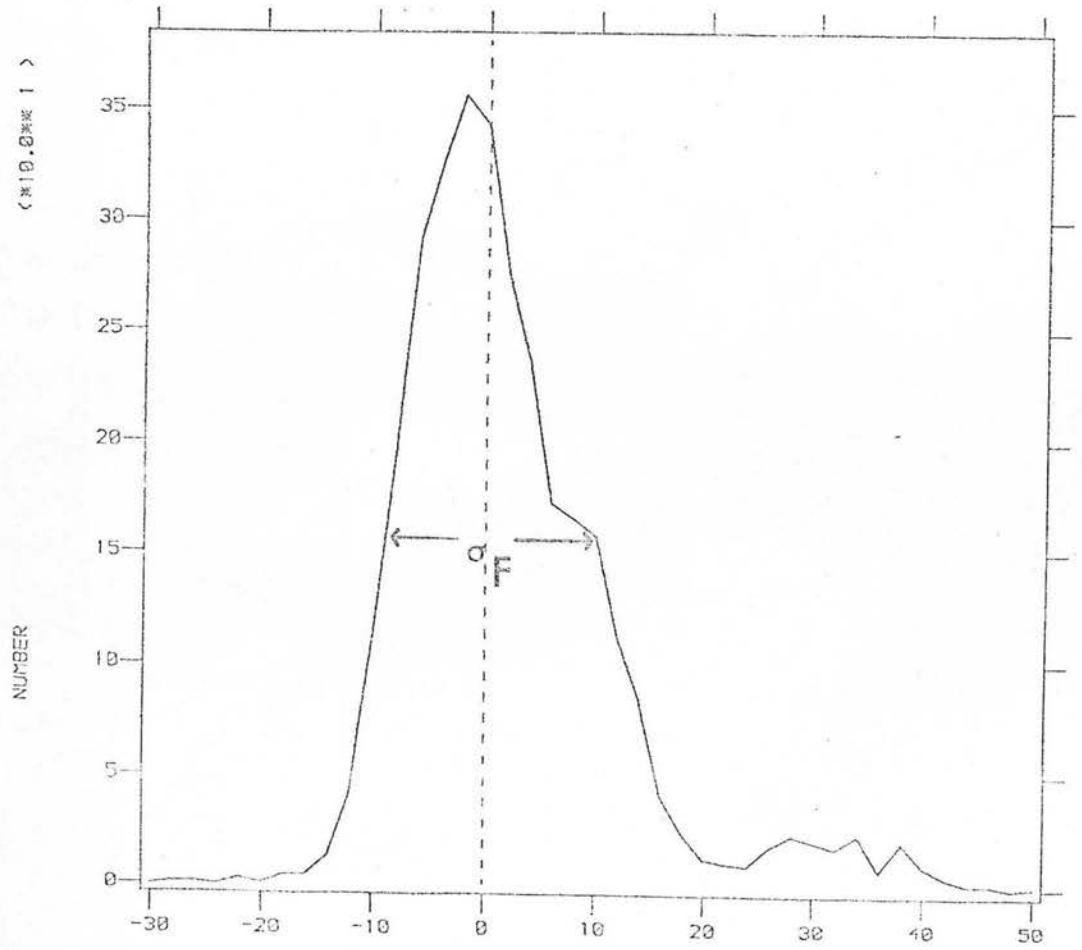

b) Residual Histogra
(σ=0.218 mag)

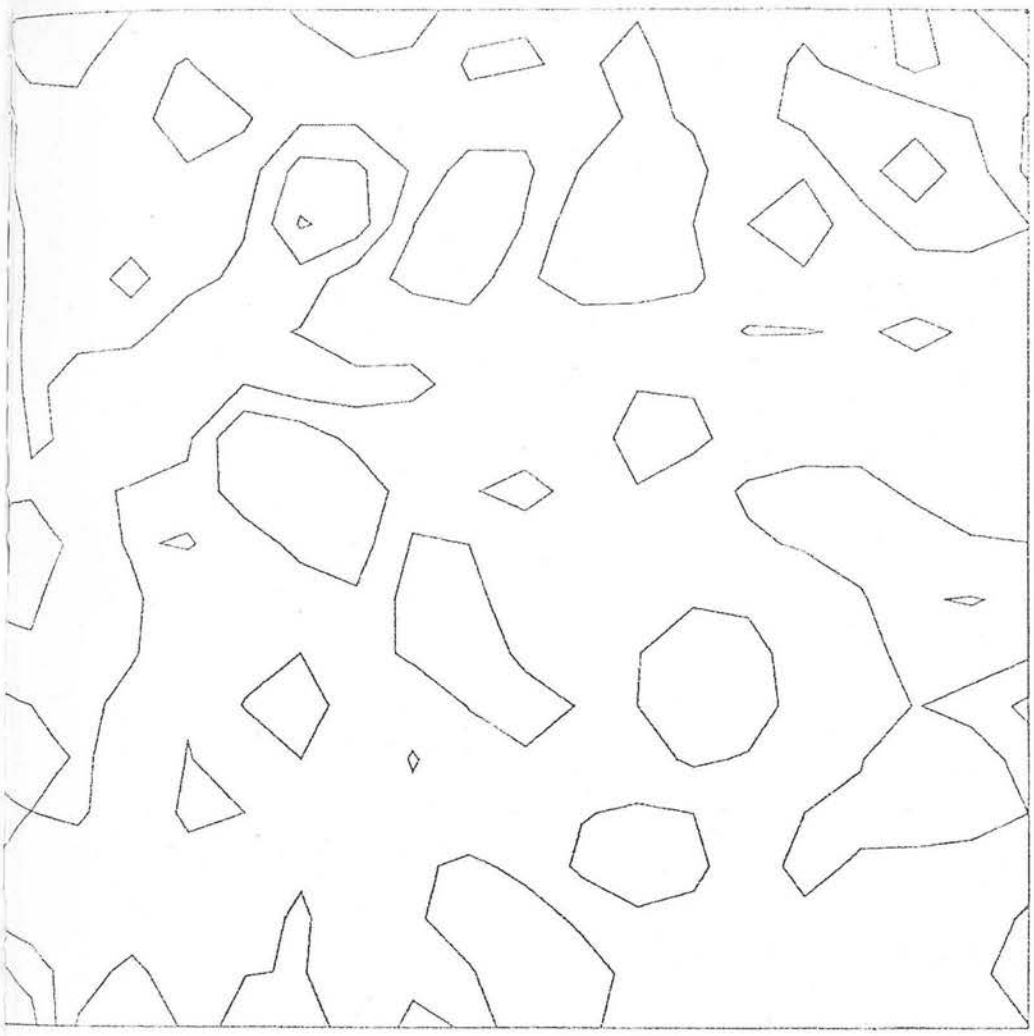

c) Residual Contours
(interval=0.02 mag)

Figure 9.1 X5742/X5744 AFTER correction.

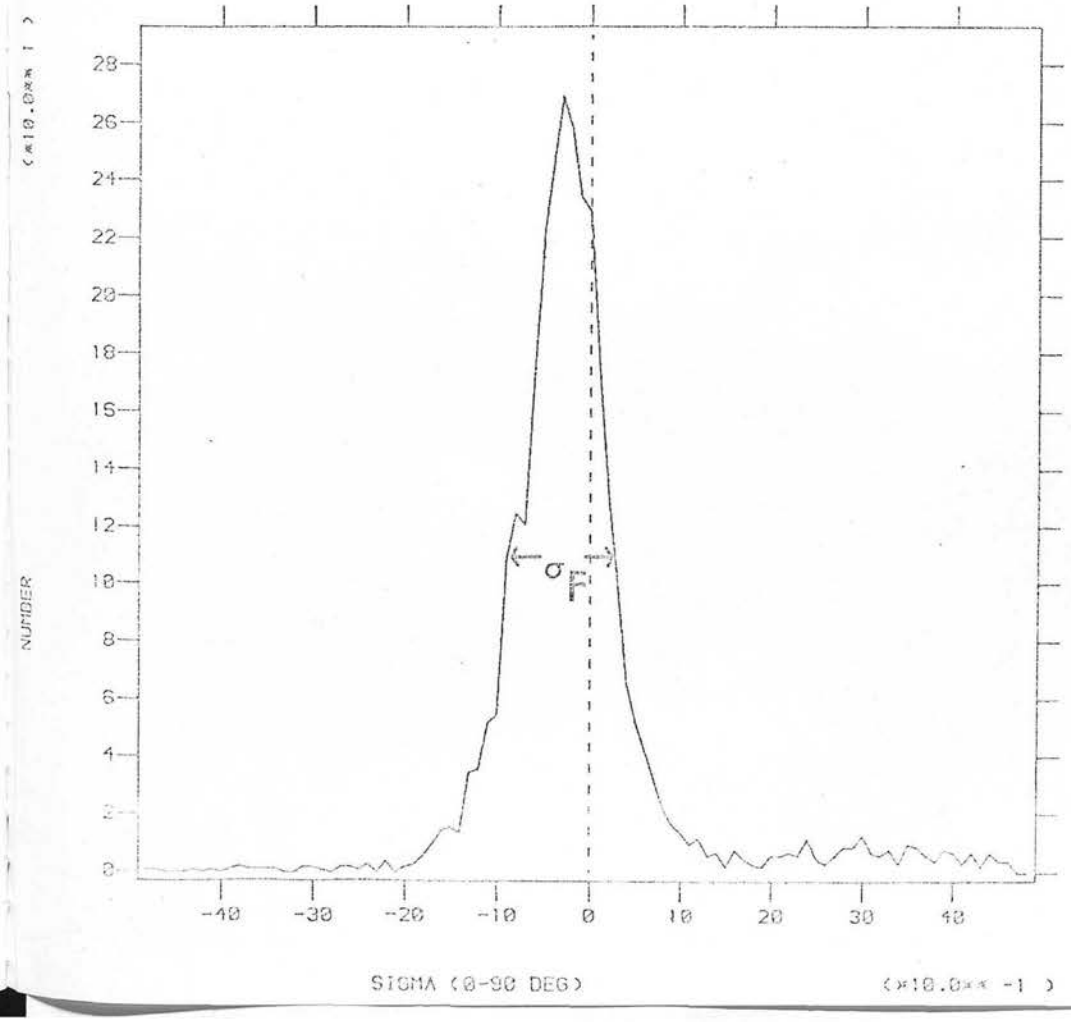

d) Residual Histogram
(σ=0.179 mag)

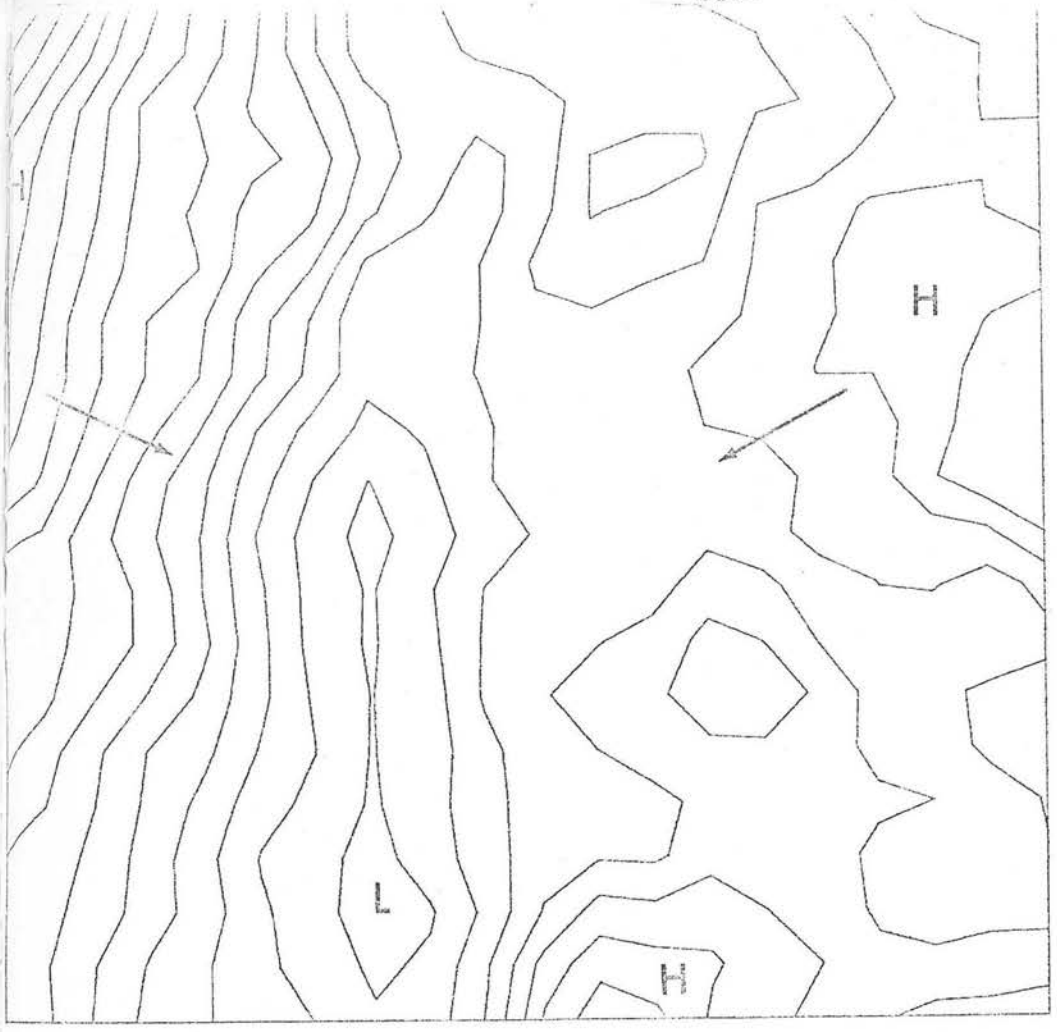

a) Residual Contours
(interval=0.02 mag)

Figure 9.2 X5743/X5745 BEFORE correction.

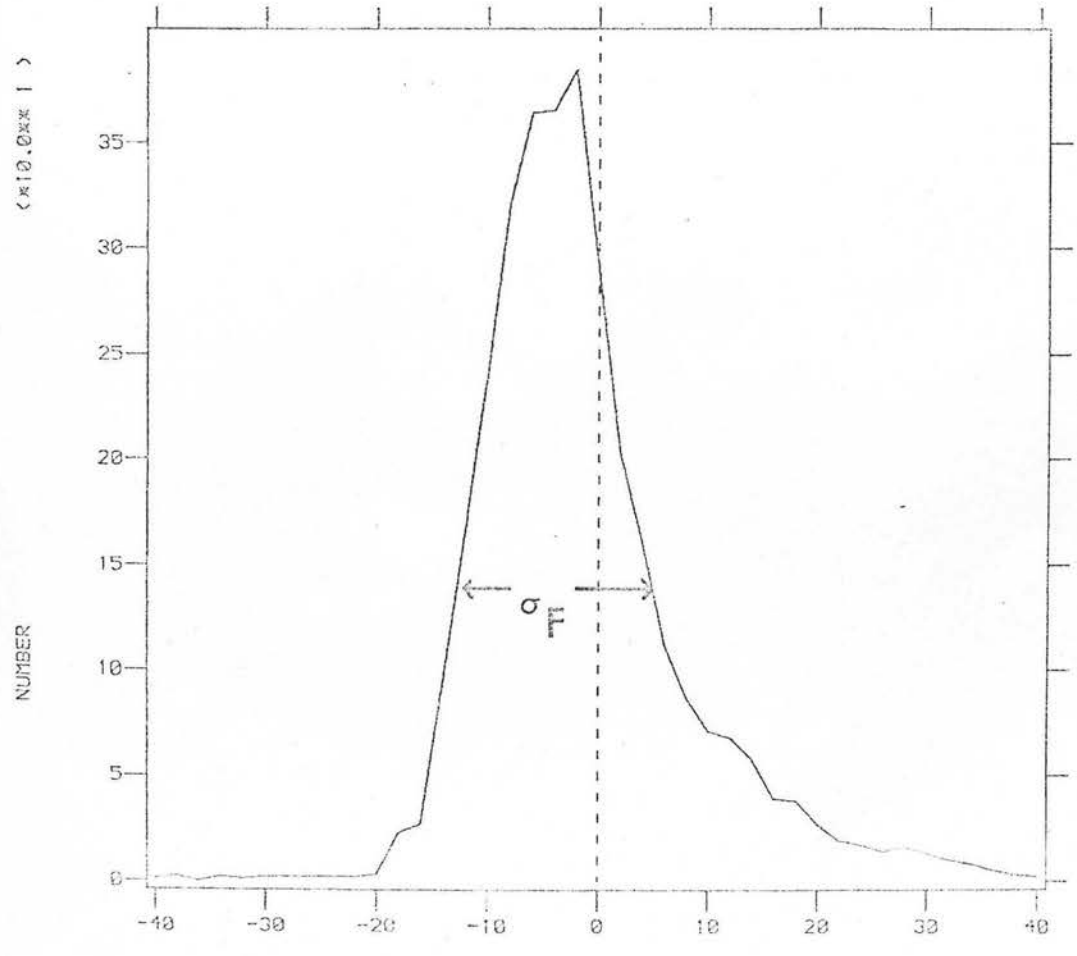

b) Residual Histogra
(σ=0.148 mag)

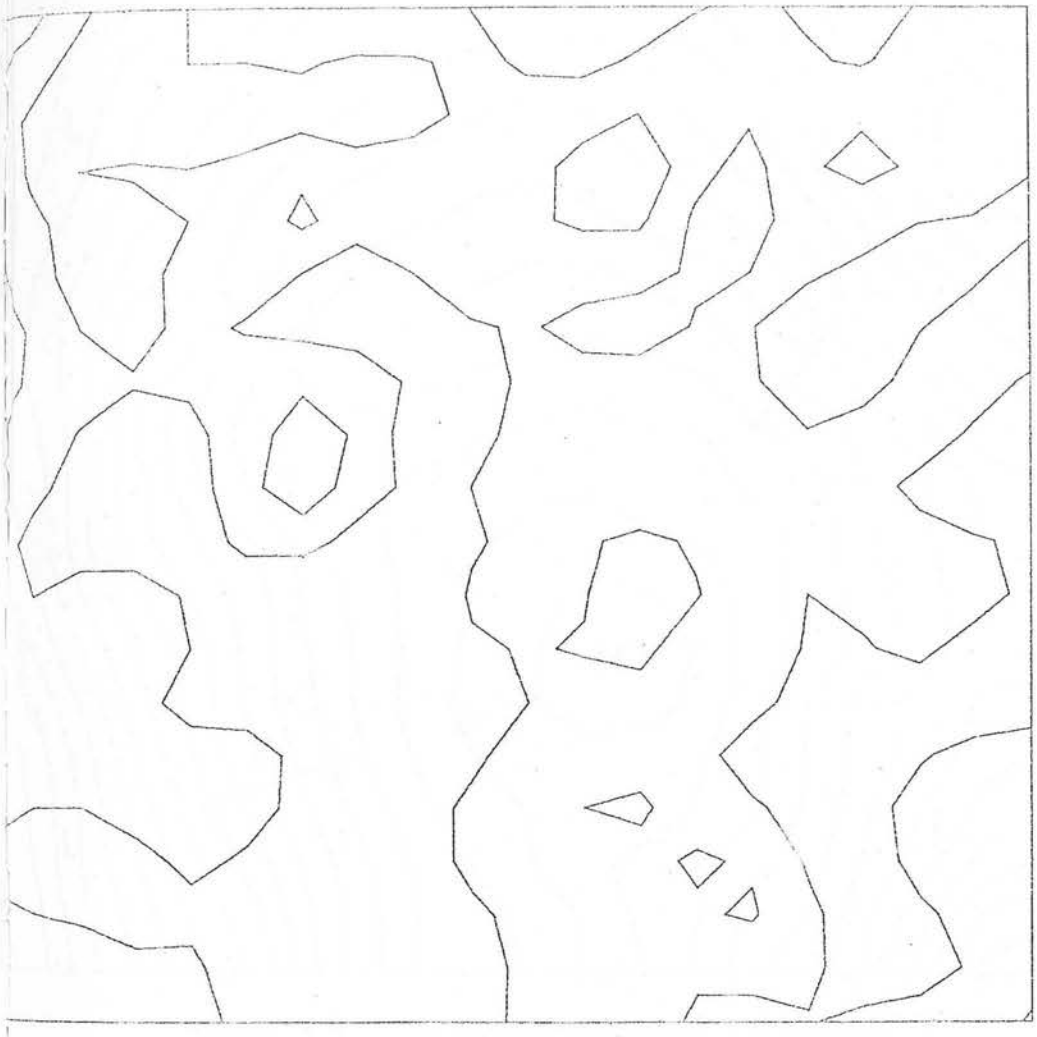

c) Residual Contours
(interval=0.02 mag)

Figure 9.2 X5743/X5745 AFTER correction.

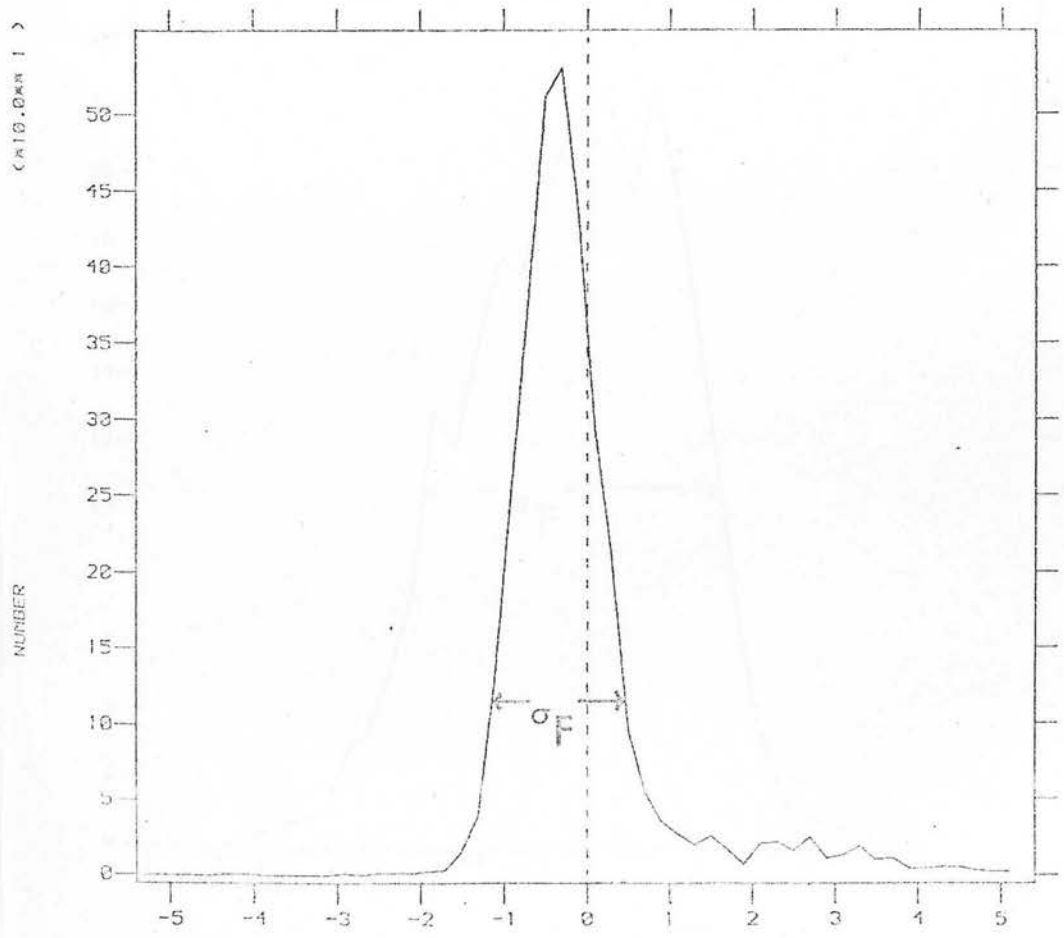

d) Residual Histogram
(σ=0.111 mag)

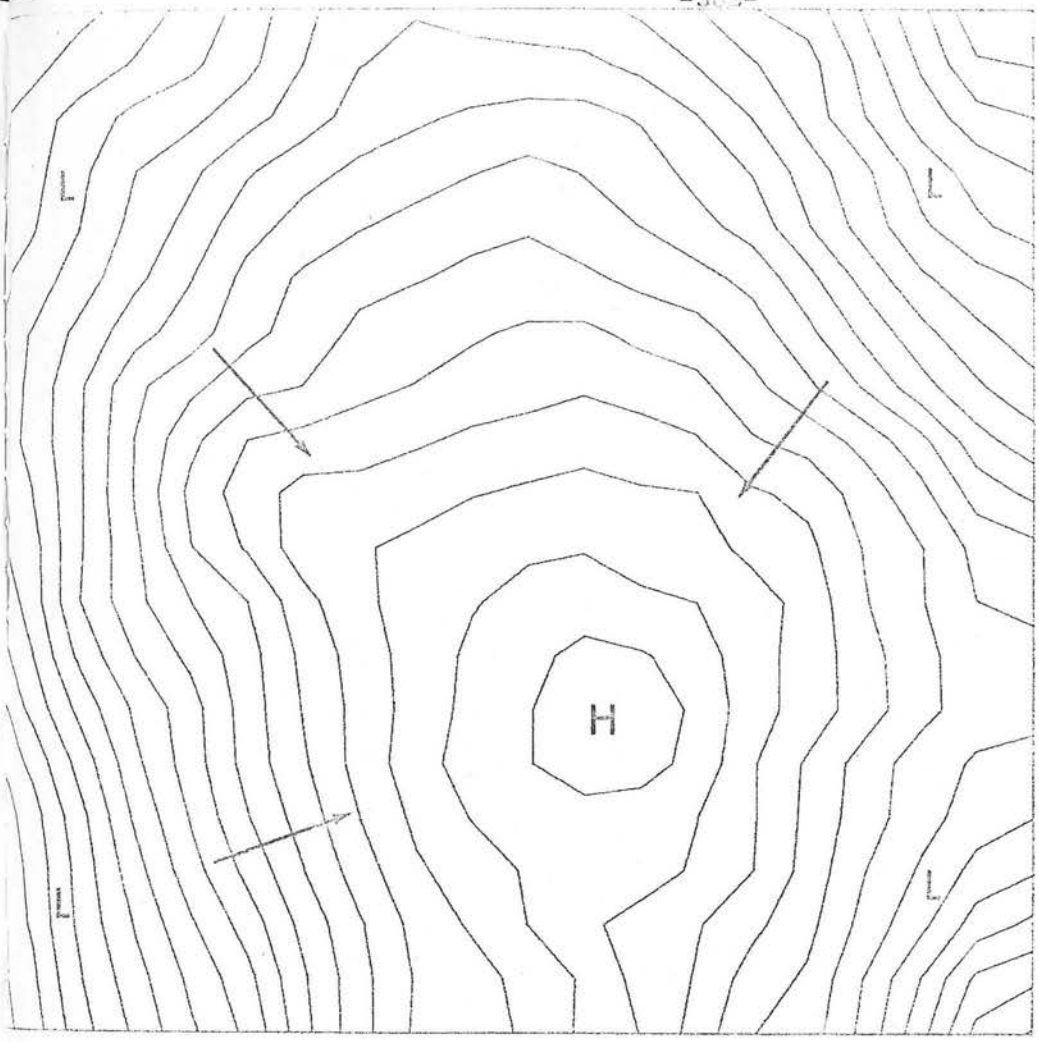

POL1

LOWEST -.18000E 1

INTERVAL .20000E 0

MIN -.20150E 1

MAX .19270E 1

a) Residual Contours
(interval=0.02 mag)

Figure 9.3 X4902/X4904 BEFORE correction.

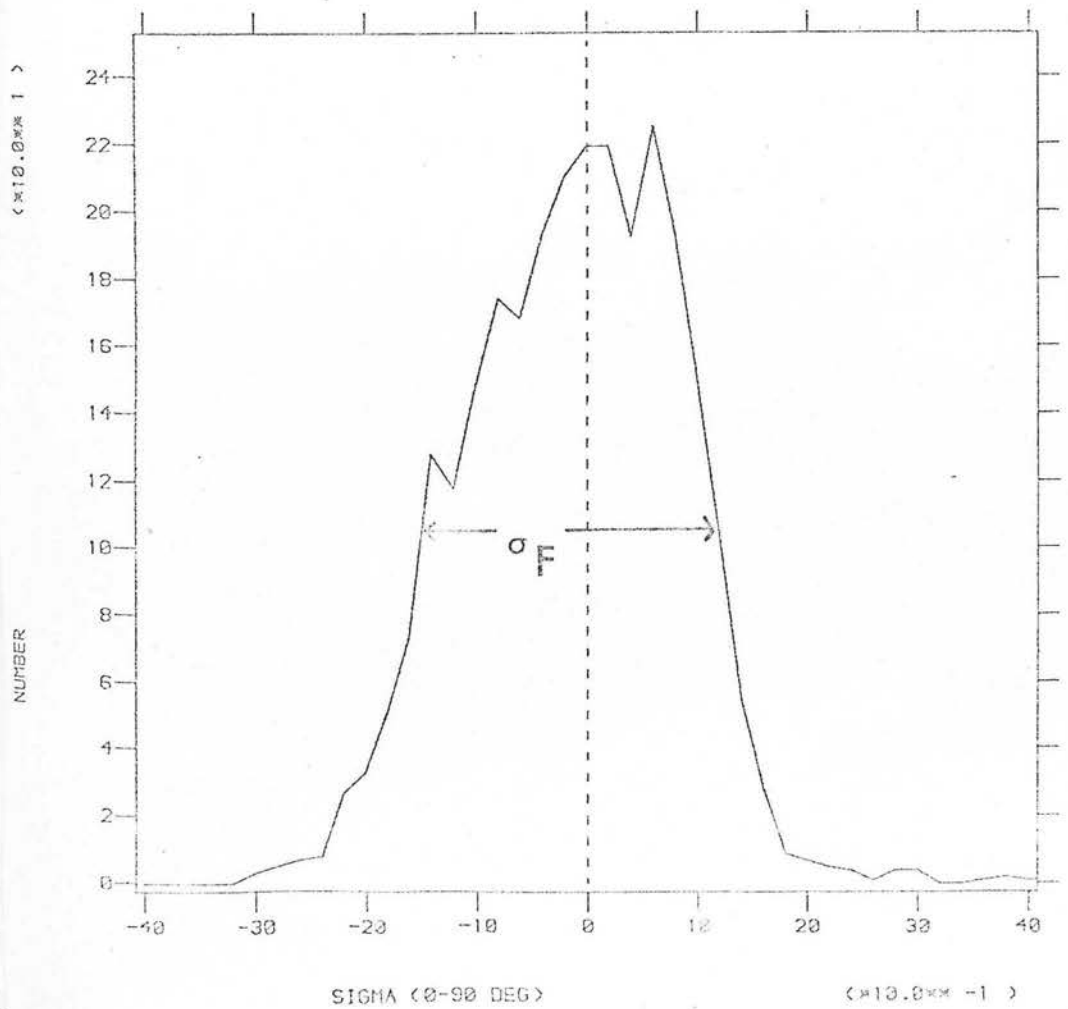

b) Residual Histogram
(σ=0.093 mag)

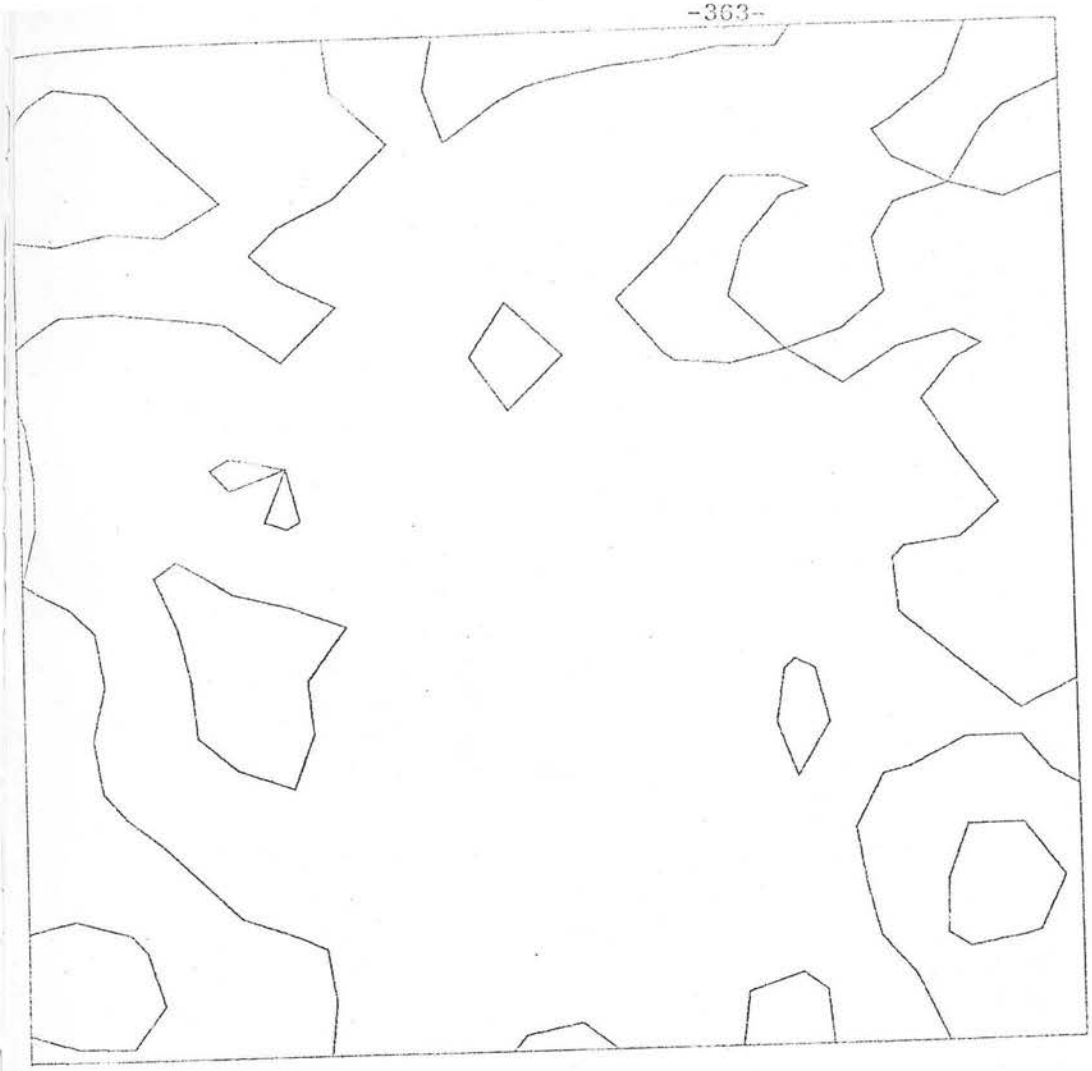

c) Residual Contours
(interval=0.02 mag

Figure 9.3 X4902/X4904 AFTER correction.

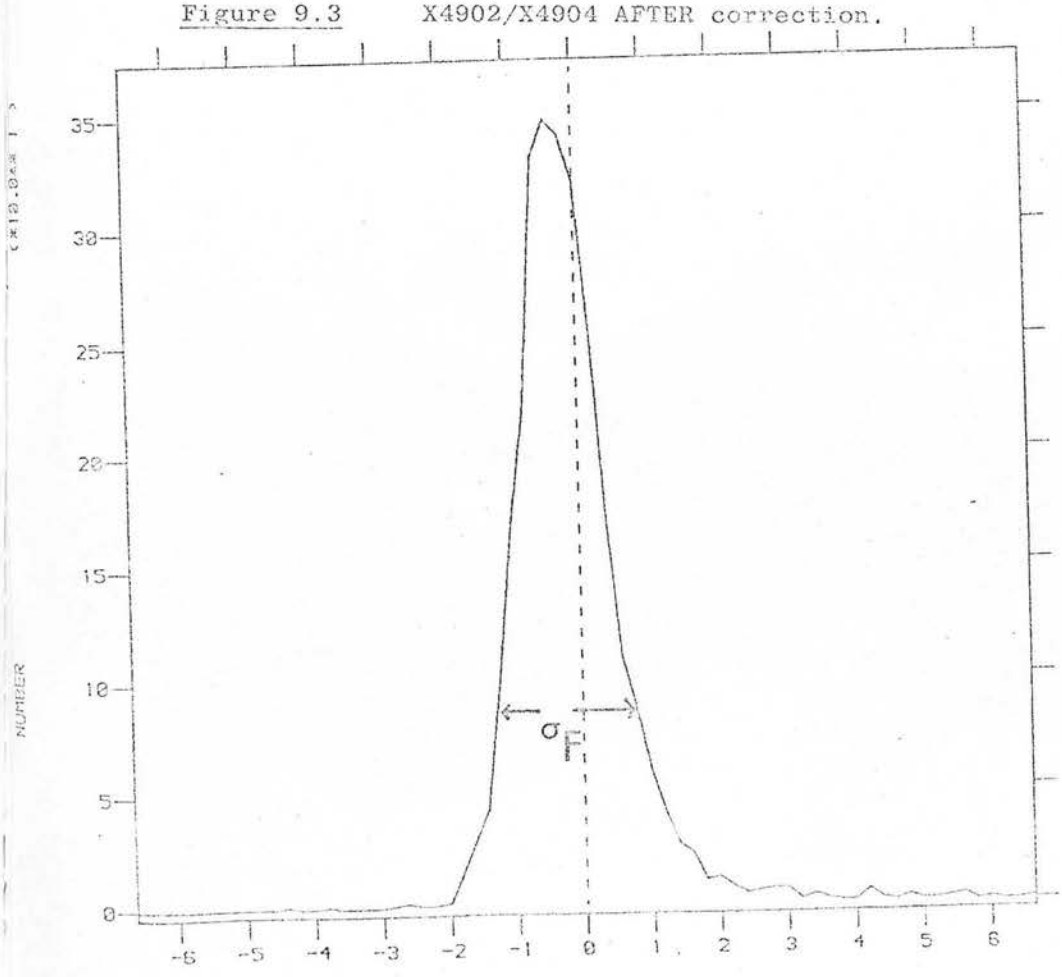

d) Residual Histogram
(σ=0.057 mag)

a) Residual Contou
(interval=0.02 ma

Figure 9.4 X4904/X5744 BEFORE correction.

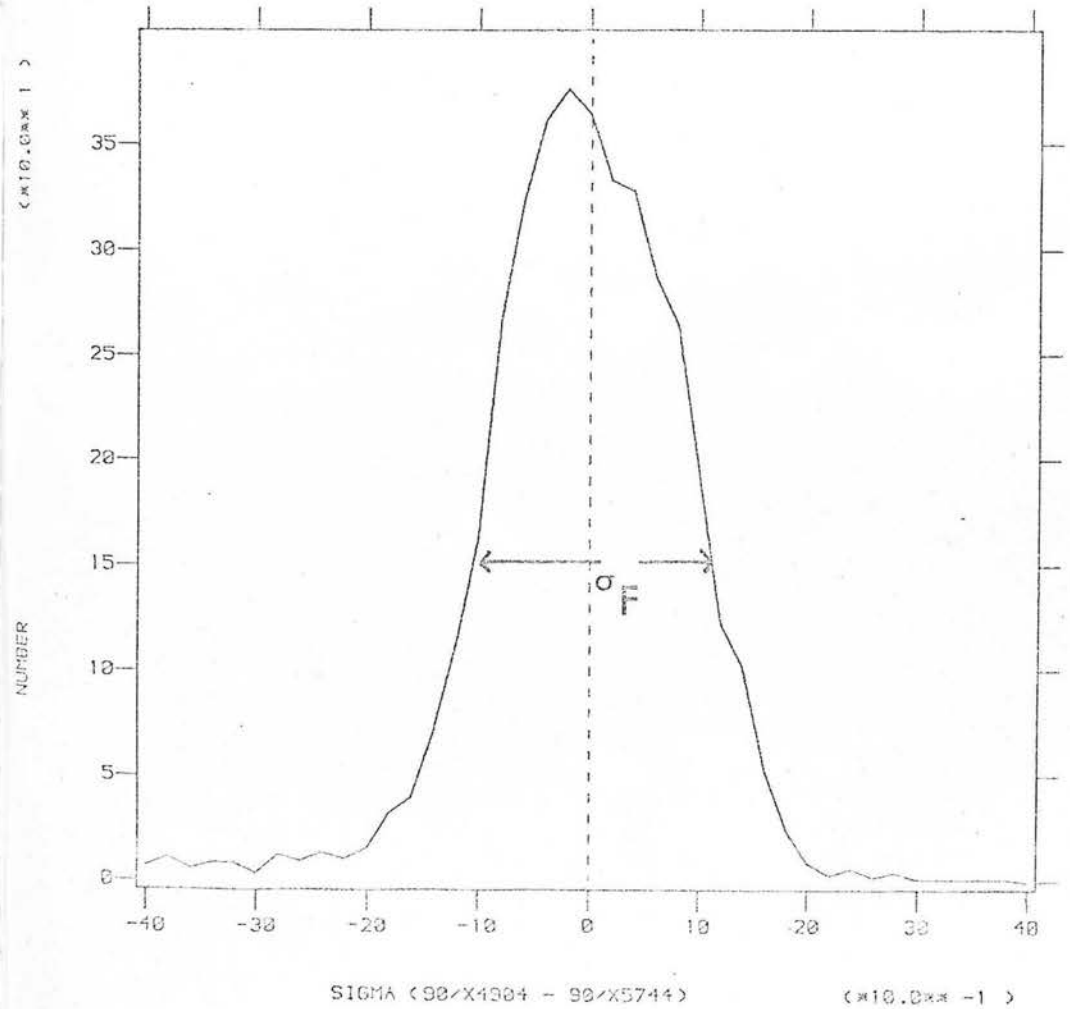

b) Residual Histogram
(σ=0.144 mag)

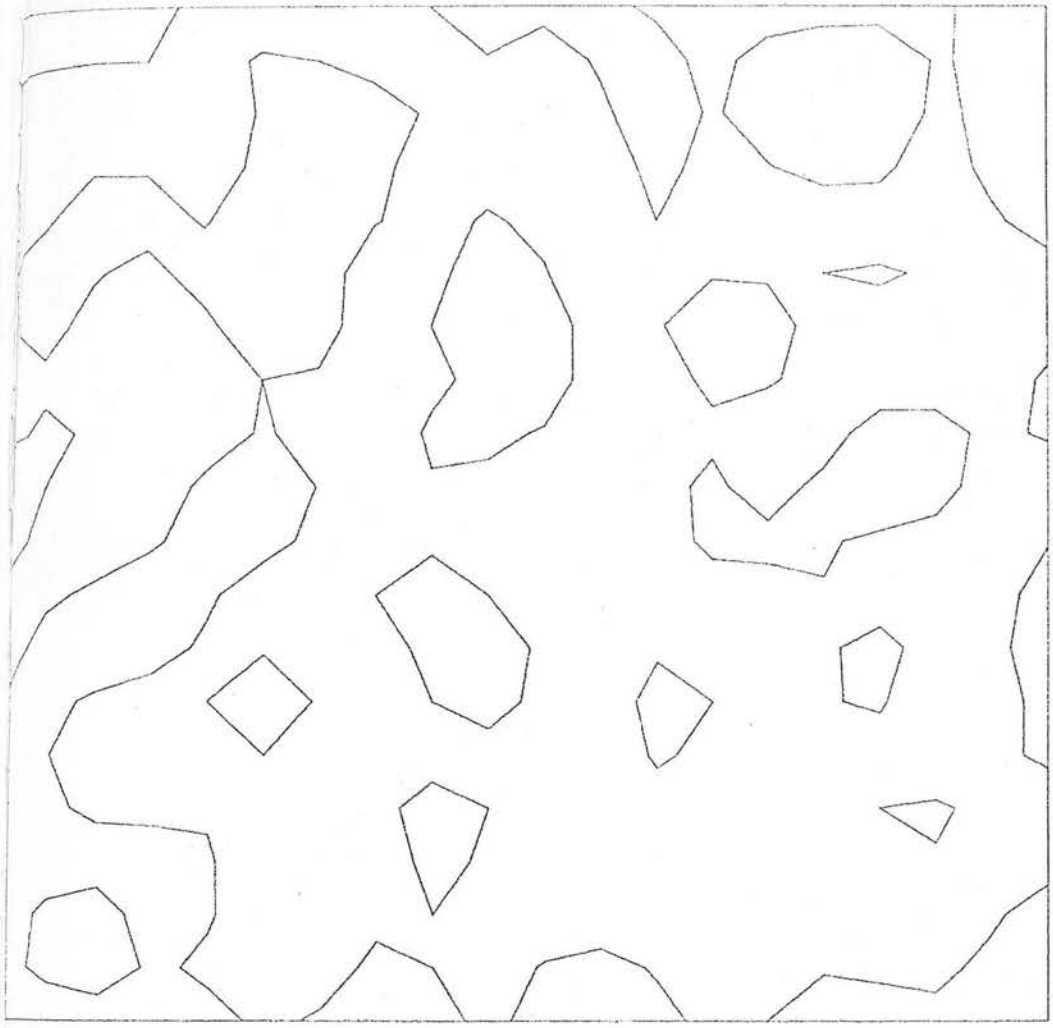

POL1

LOWEST .00000E 0

INTERVAL .20000E -1

MIN -.27000E -1

MAX .15000E -1

c) Residual Contours
(interval=0.02 mag)

Figure 9.4 X4904/X5744 AFTER correction.

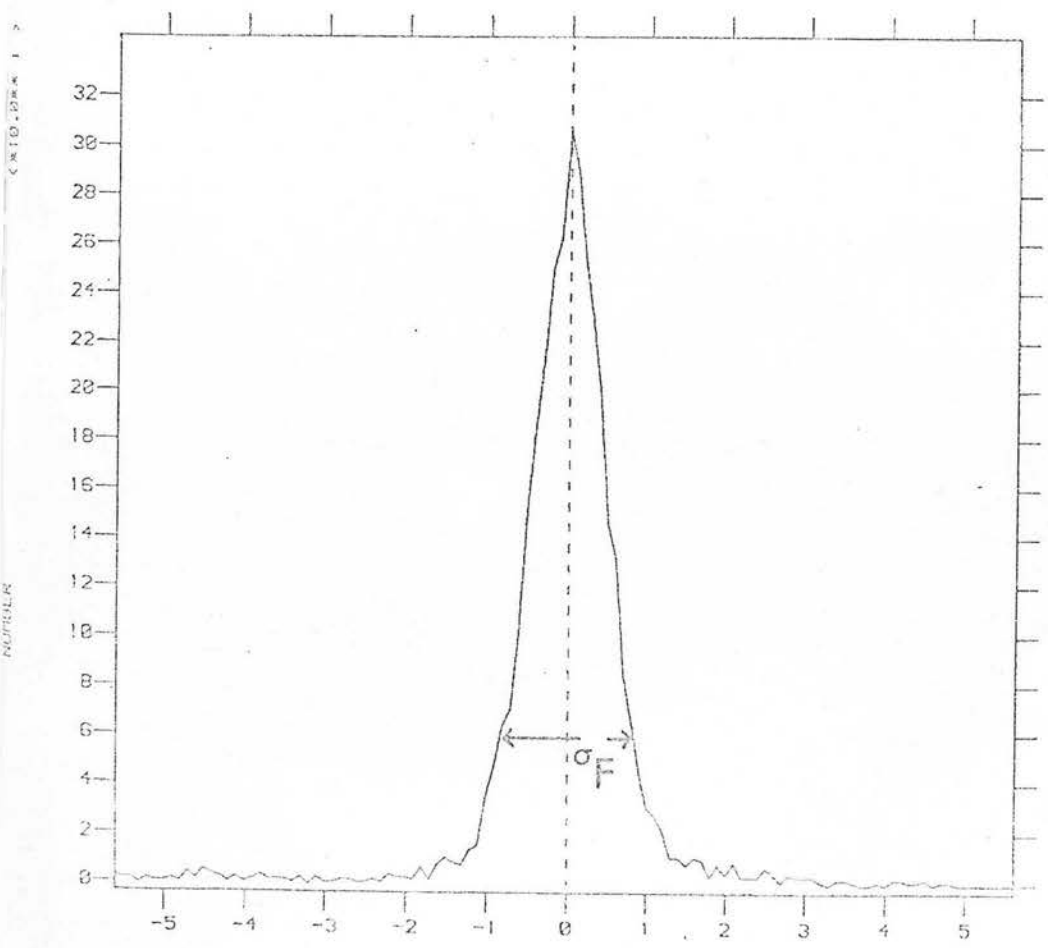

d) Residual Histogram
(σ=0.106 mag)

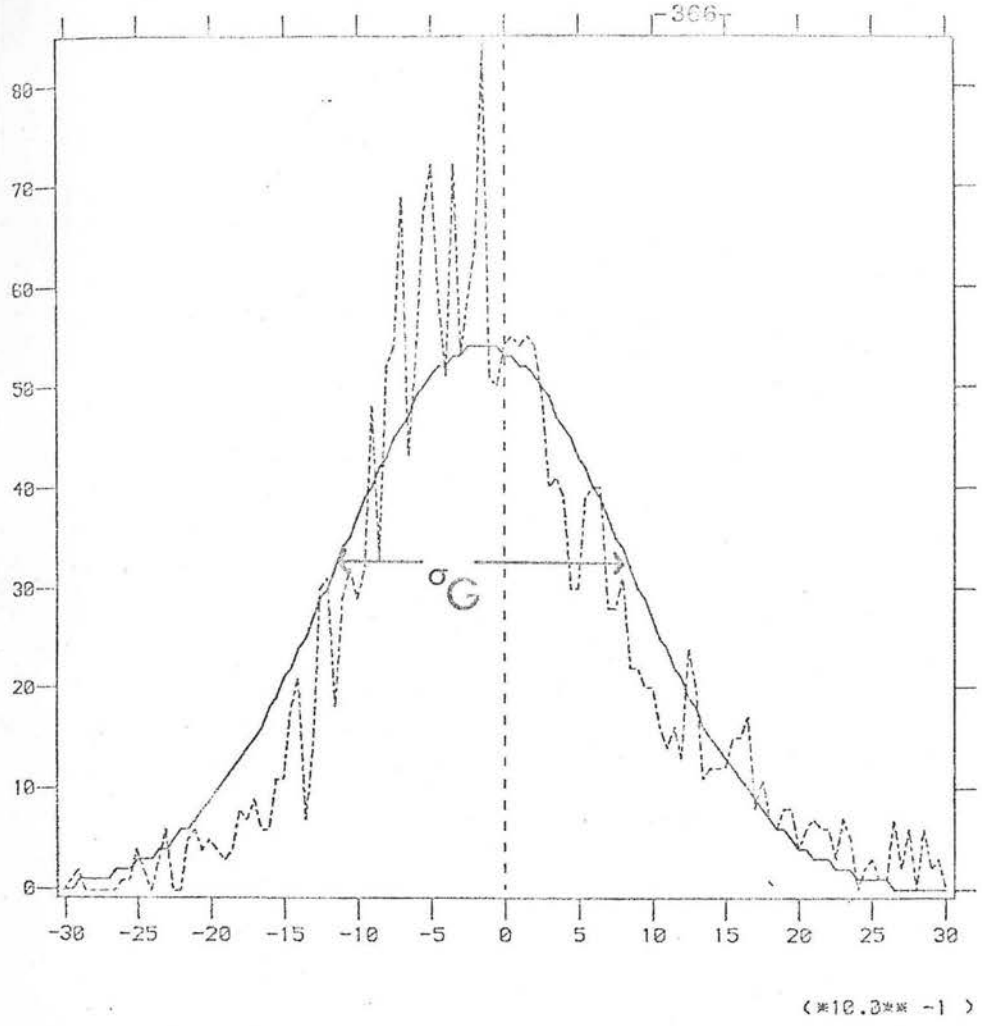

a) Residual Histogram showing data (dashed) and fitted Gaussian (solid).

Figure 9.5 X5742/X5744 AFTER correction (Sub 1).

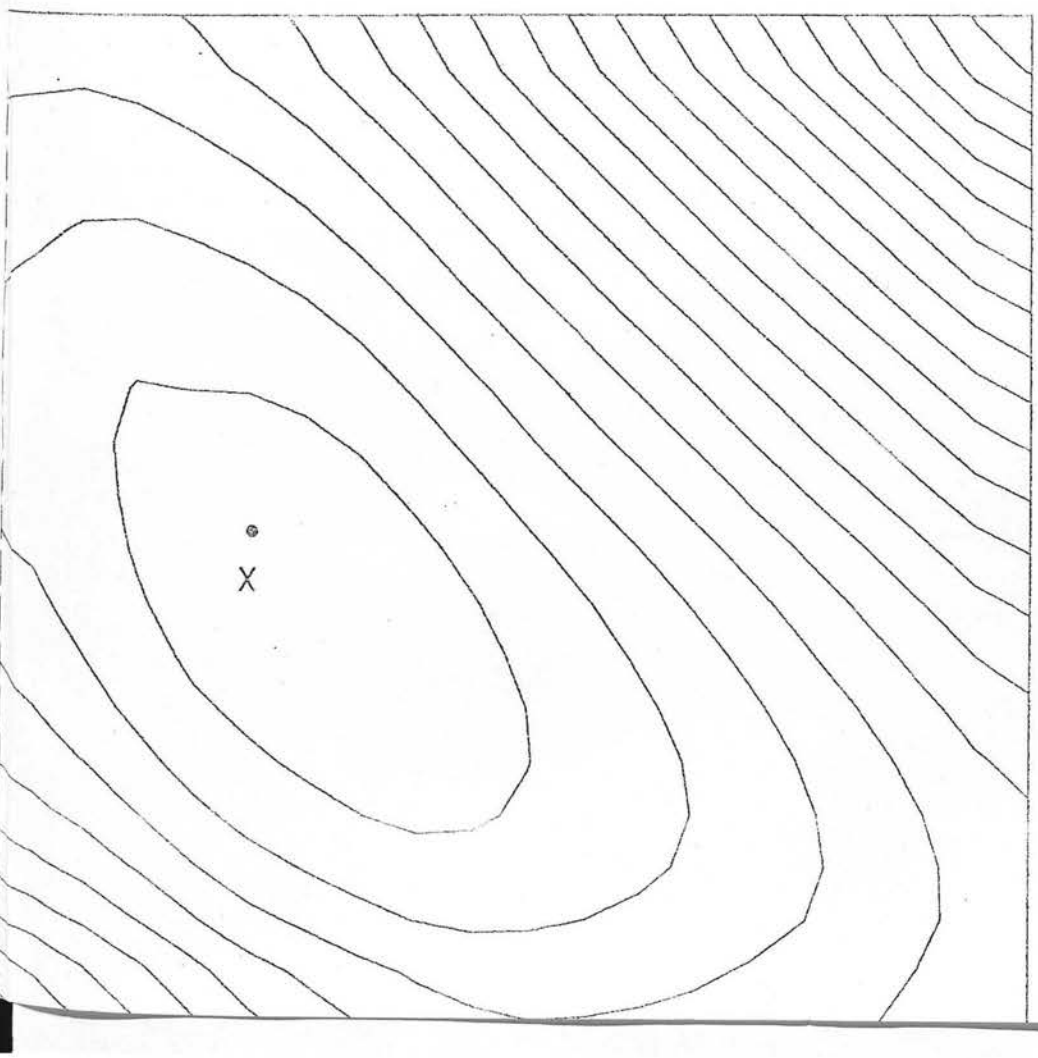

b) Contours of χ^2

χ^2_{min}=1.74 for 60 degrees of freedom at σ_G=0.98σ_F.

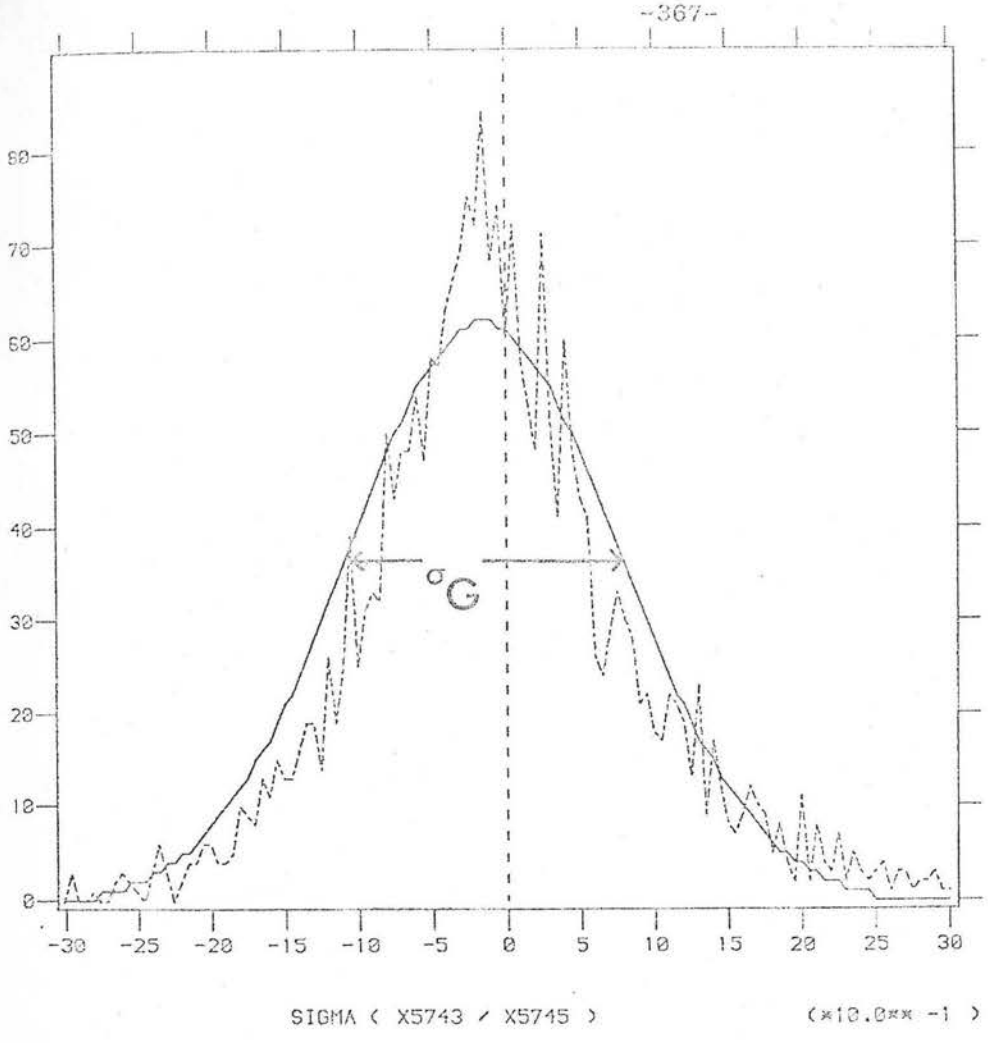

c) Residual Histogram showing data (dashed) and fitted Gausssian (solid).

Figure 9.5 X5743/X5745 AFTER correction (Sub 1).

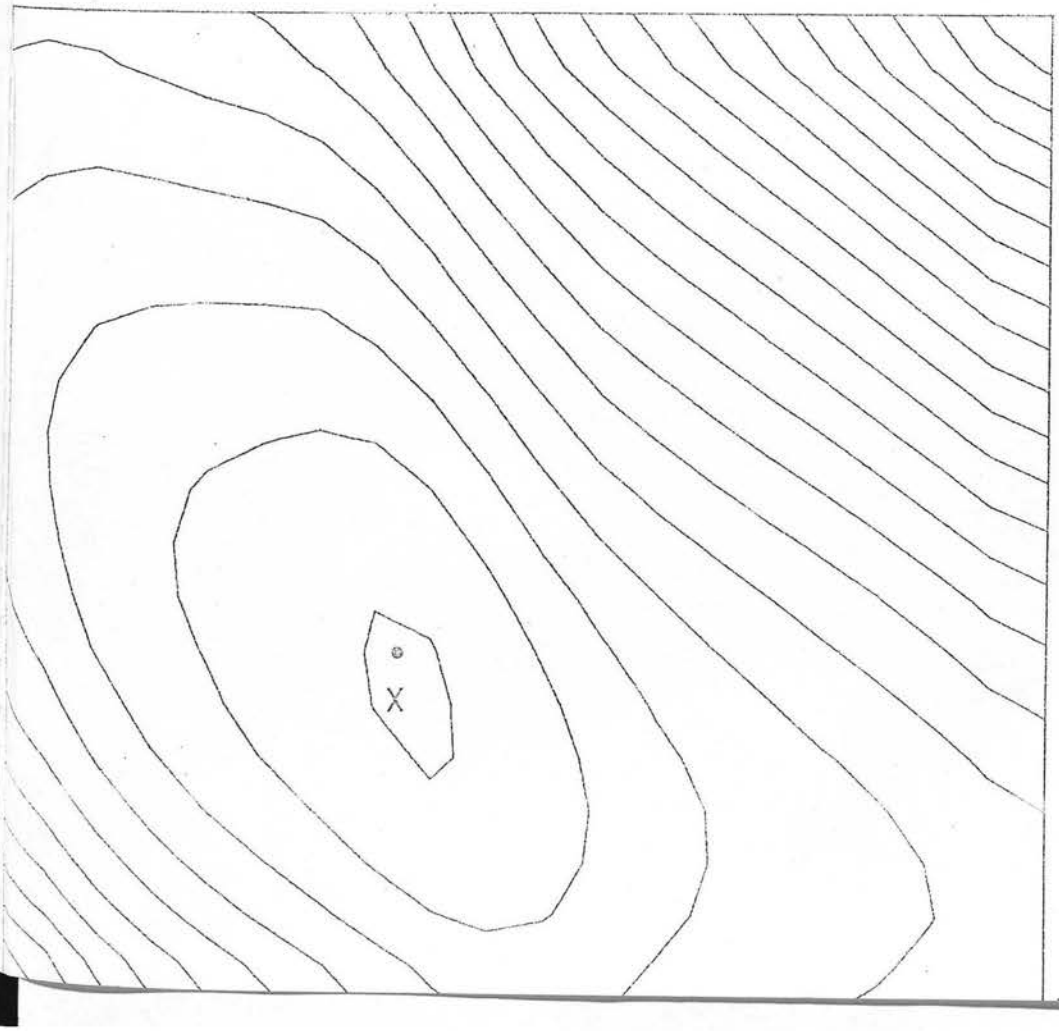

d) Contours of χ^2
χ^2_{min}=1.50 for 60 degrees of freedom at σ_G=0.92σ_F.

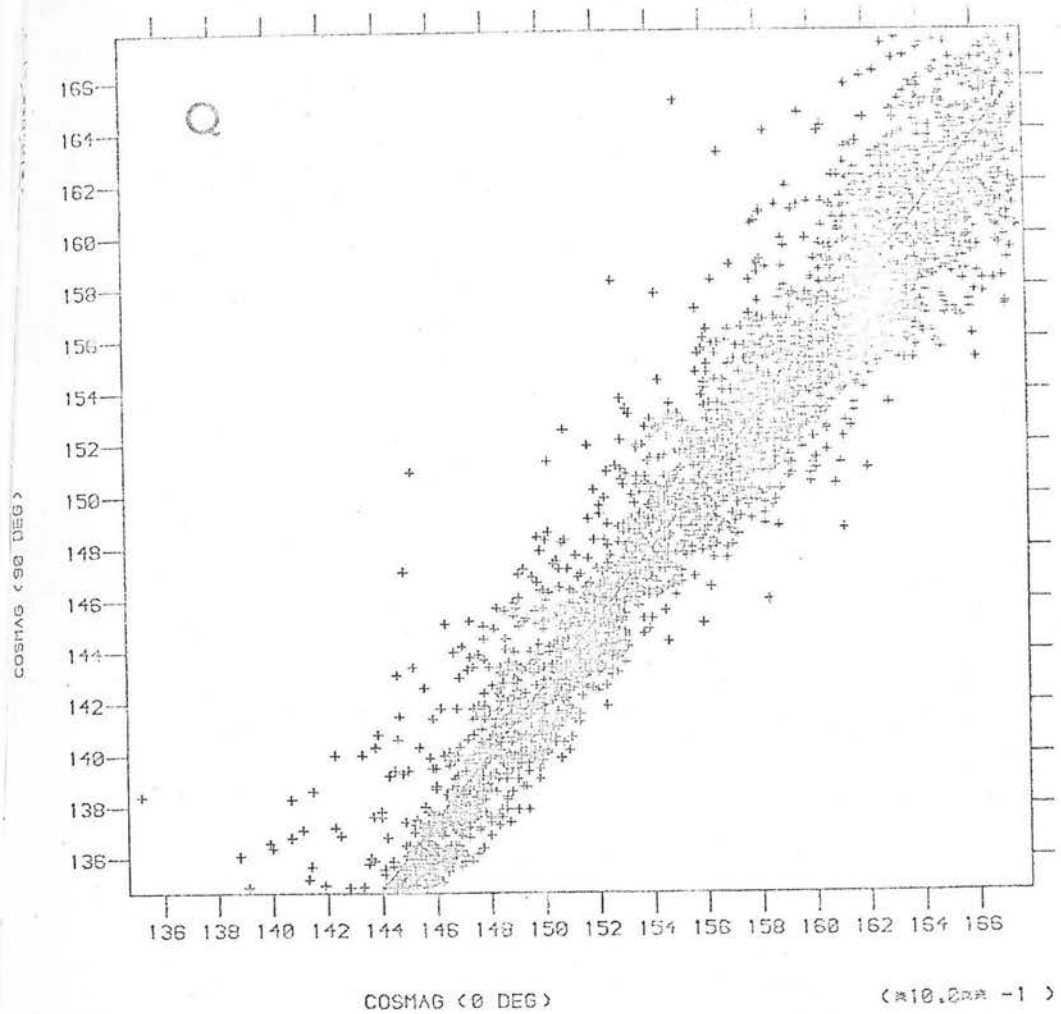

a) X5742/X5744 (Q')
3150 points plotted in
the range 16<J<19.3.

Figure 9.6 COSMOS Magnitudes (Sub 1).

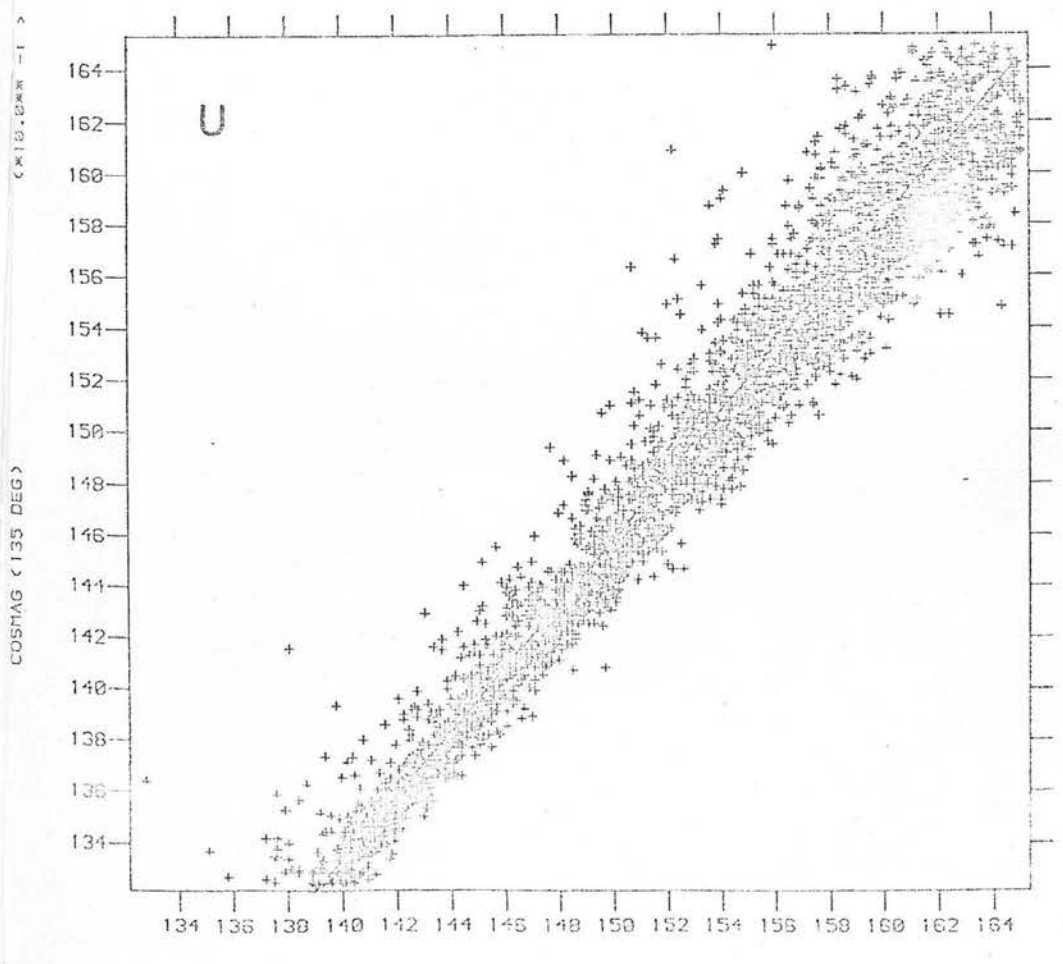

b) X5743/X5745 (U')
3150 points plotted in
the range 16<J<19.3.

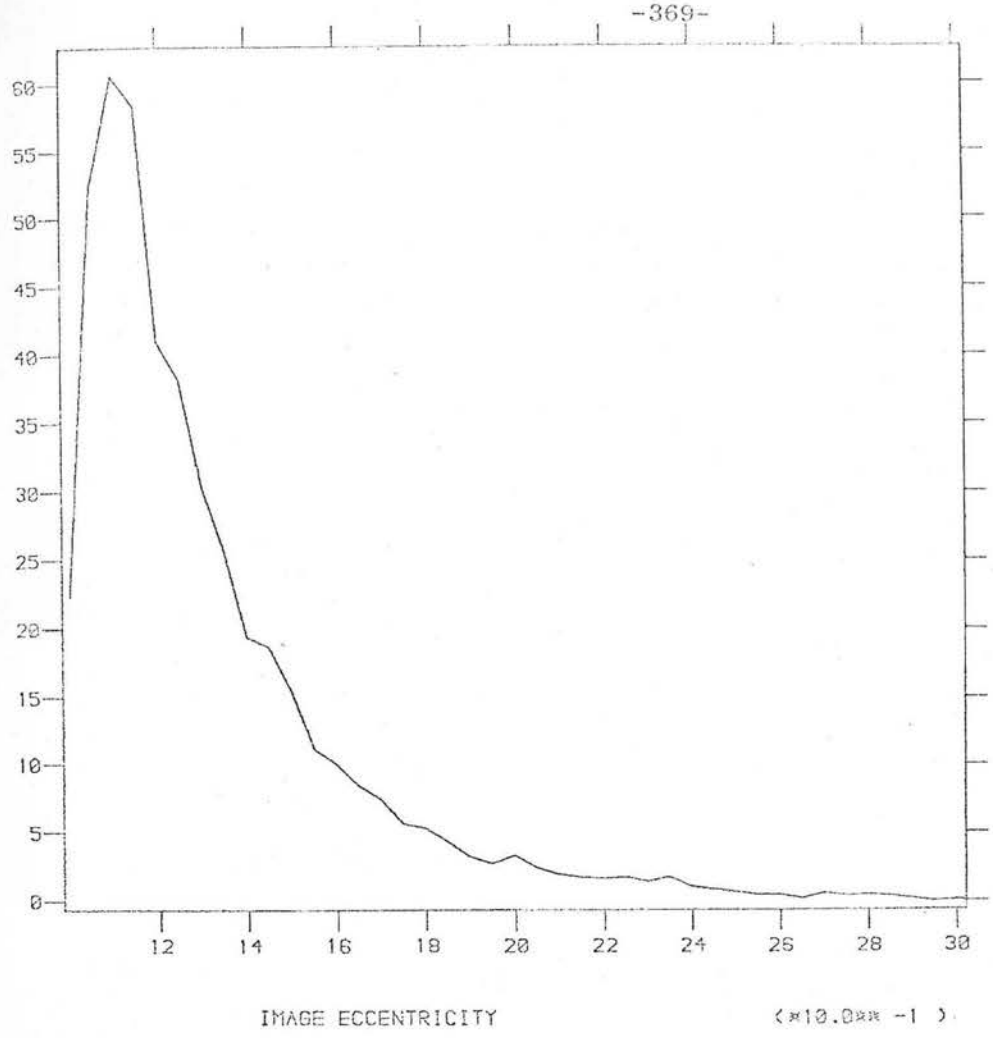

c) Image Eccentricity
Ratio of semi-major to semi-minor axes for 3150 images.

Figure 9.6 Image Eccentricity and J Magnitude X5742-5.

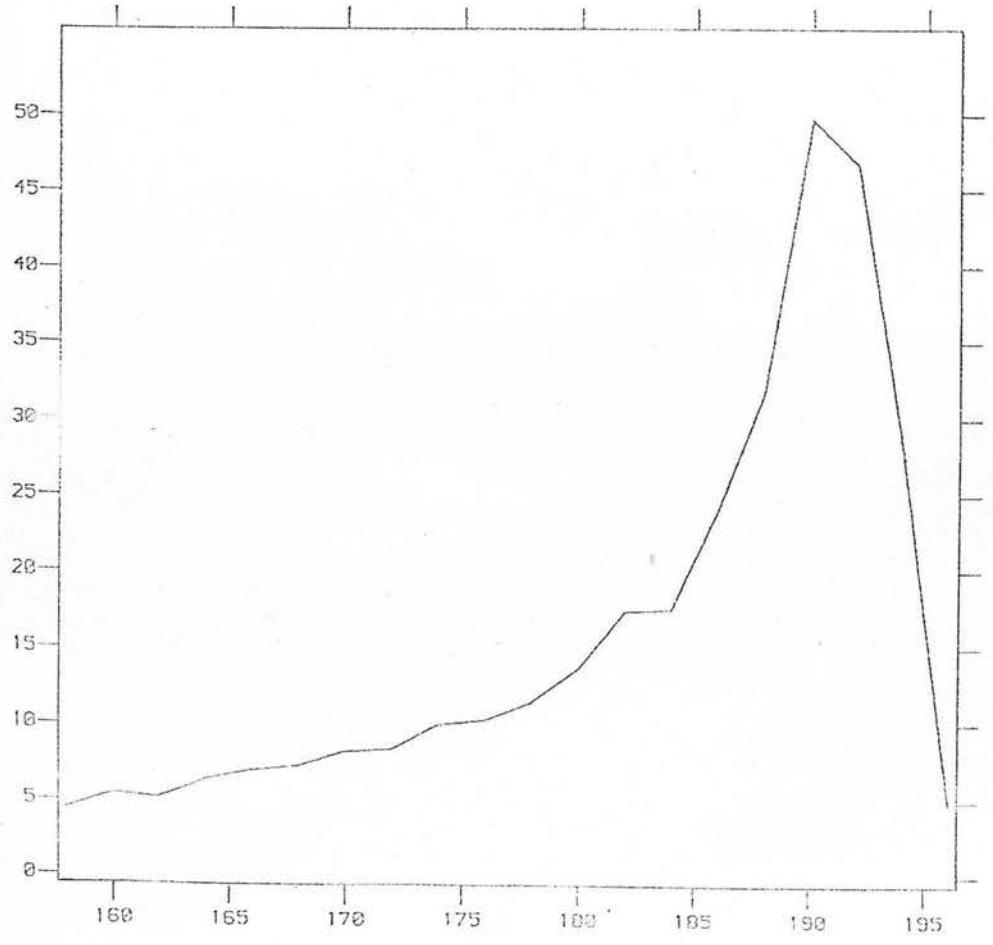

d) Calibrated J Magnitude
Using photoelectric sequence and sub-beam prism extension.

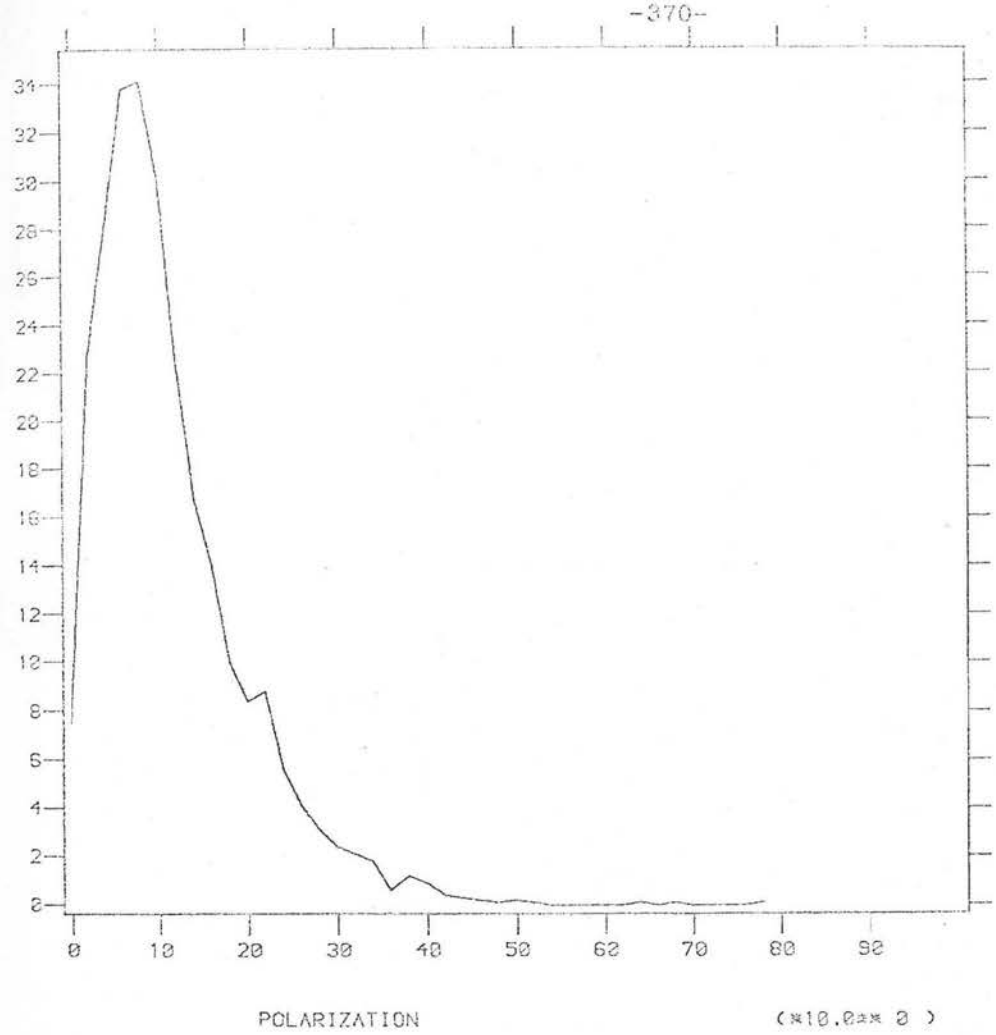

a) Polarization Histogram
$\bar{p}$=16% and 1 in 8 images lie beyond p=20%.

Figure 9.7 Polarization X5742-5 (Sub 1).

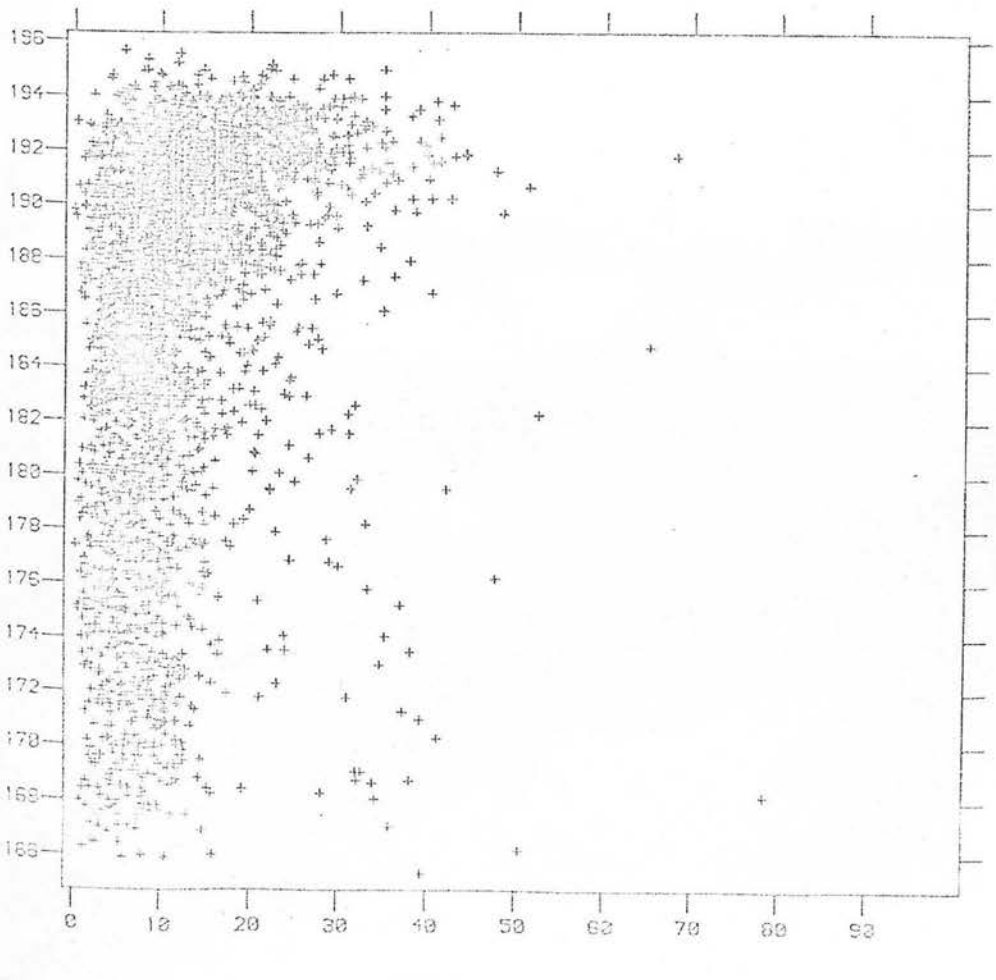

b) Polarization against calibrated J magnitude.

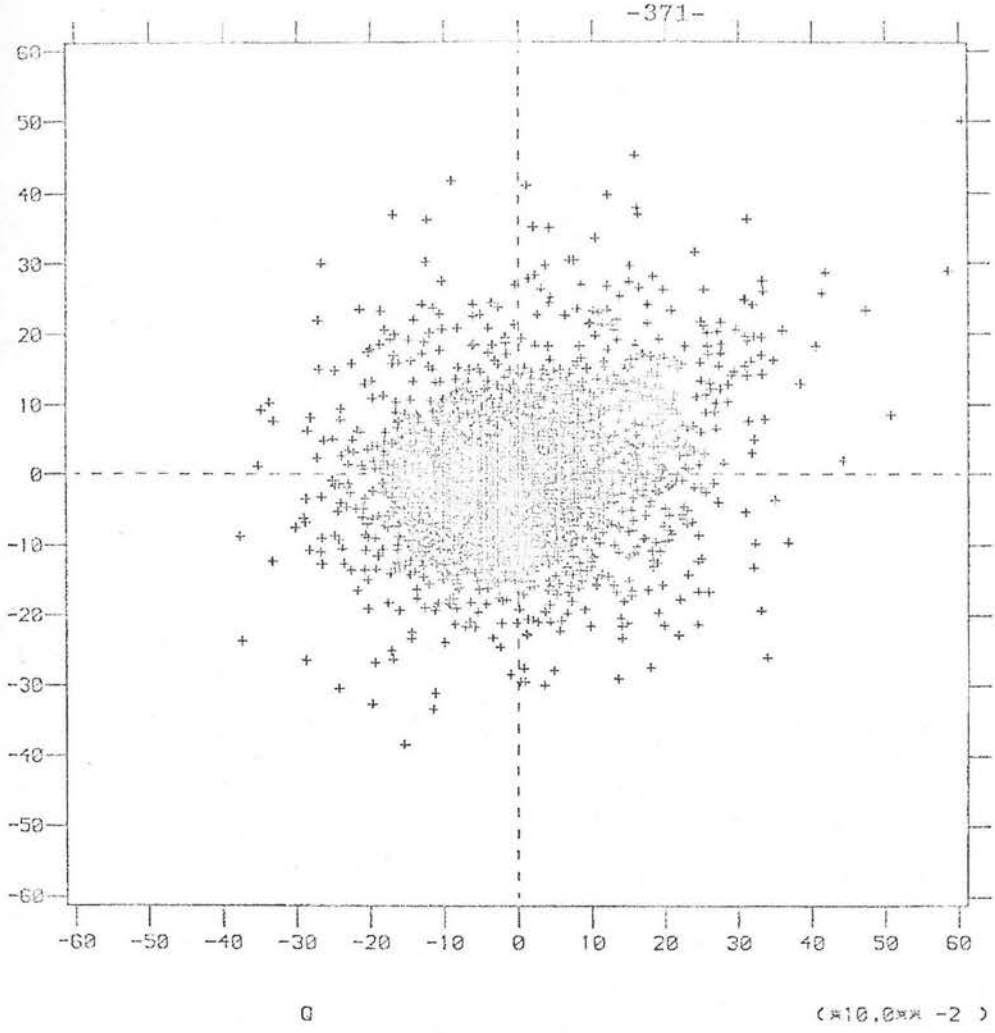

c) Normalized Stokes parameters Q and U. Contours of constant polarization are circles of radius p in the Q-U plane.

Figure 9.7 Polarization X5742-5 (Sub 1).

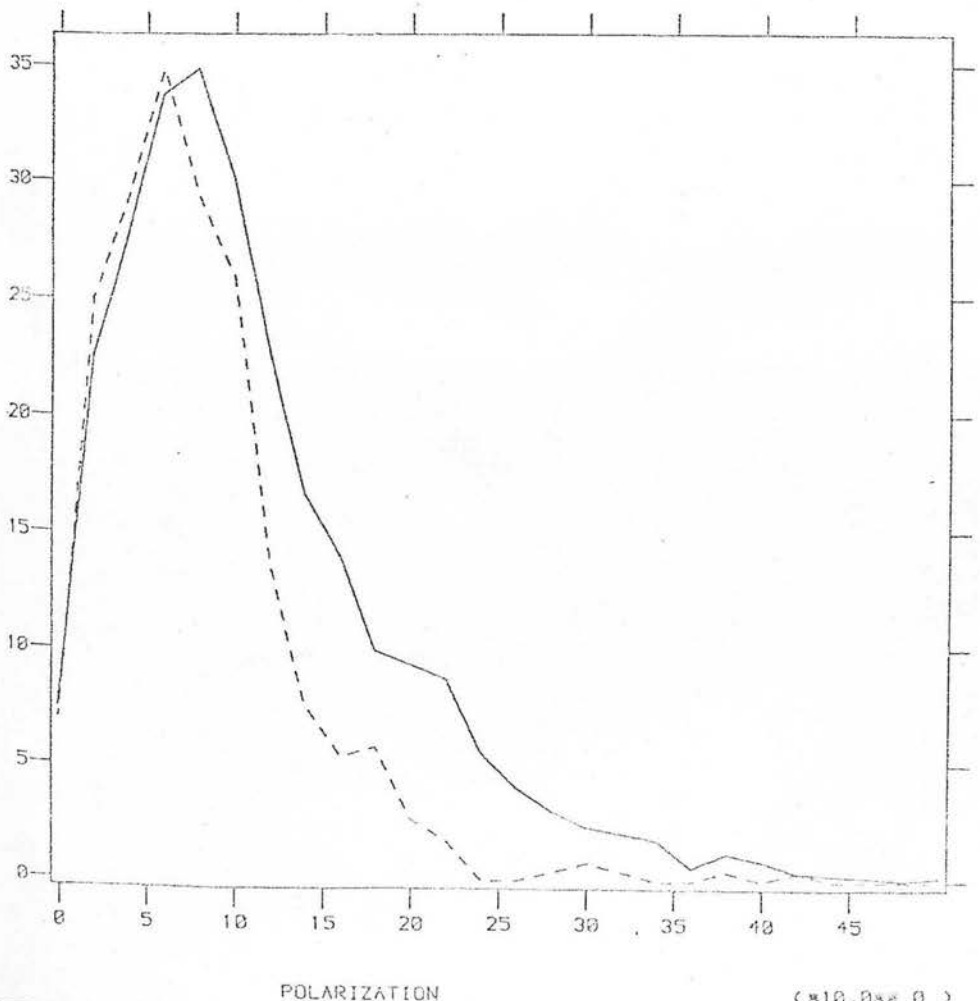

d) Polarization Histogram. Solid curve shows all images dashed curve shows those with eccentricities less than 1.5 (normalized to the mode of the total distribution.

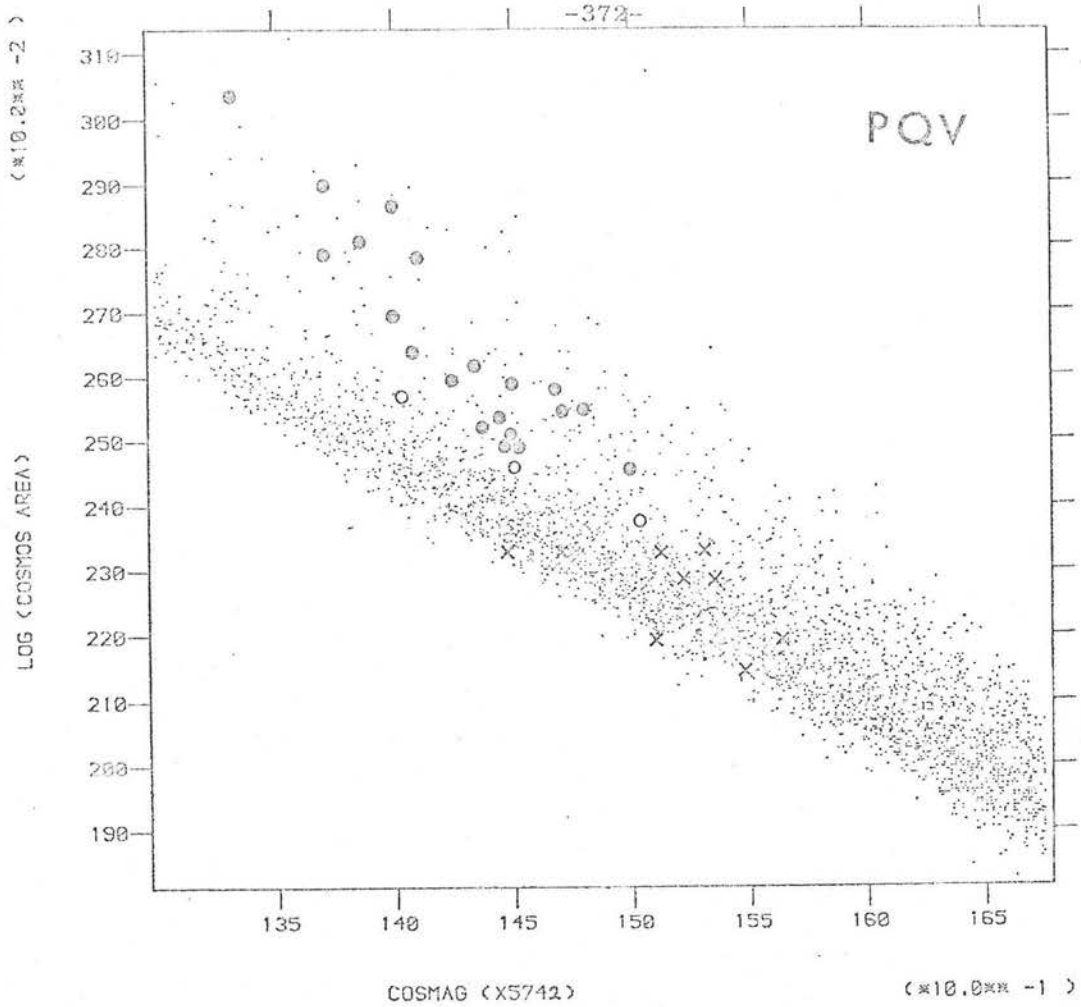

Figure 9.8 Star/Galaxy Separation for polarization candidates.

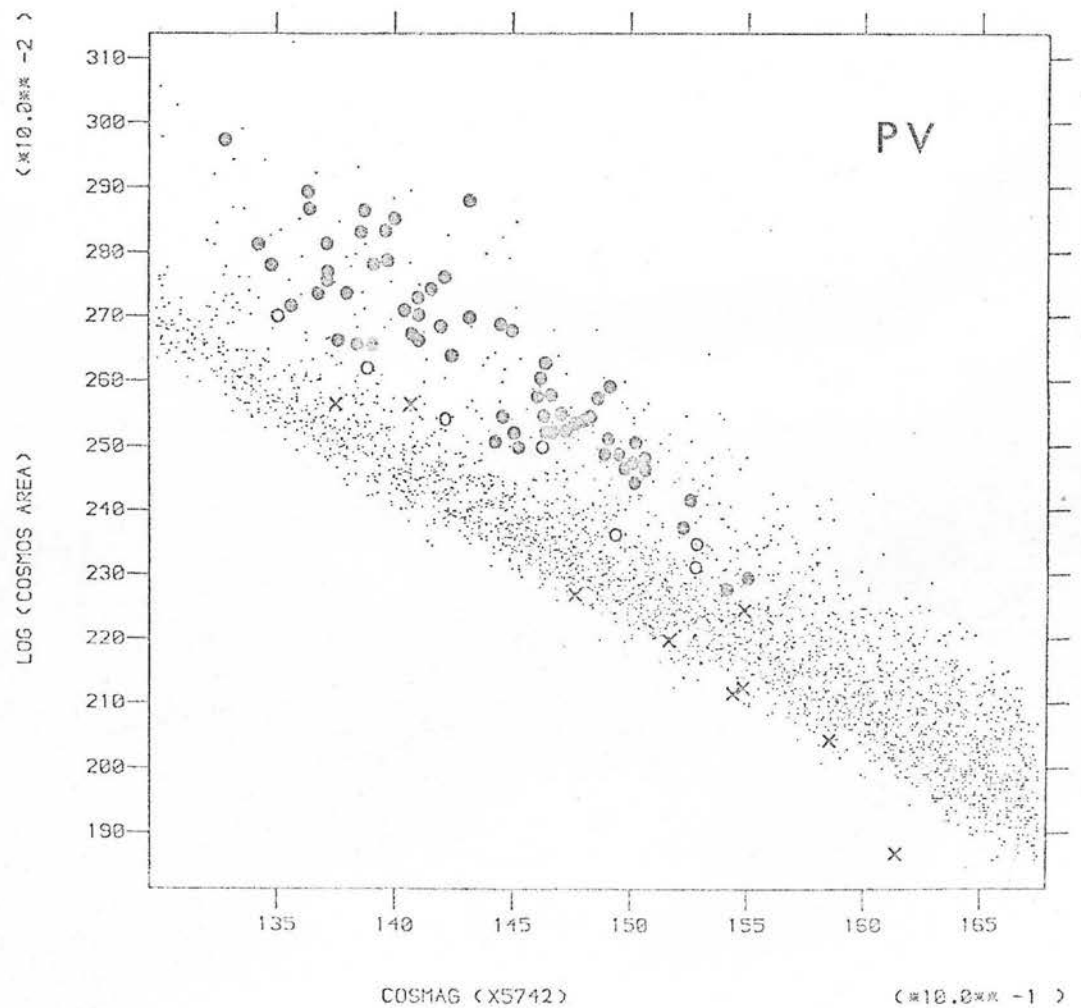

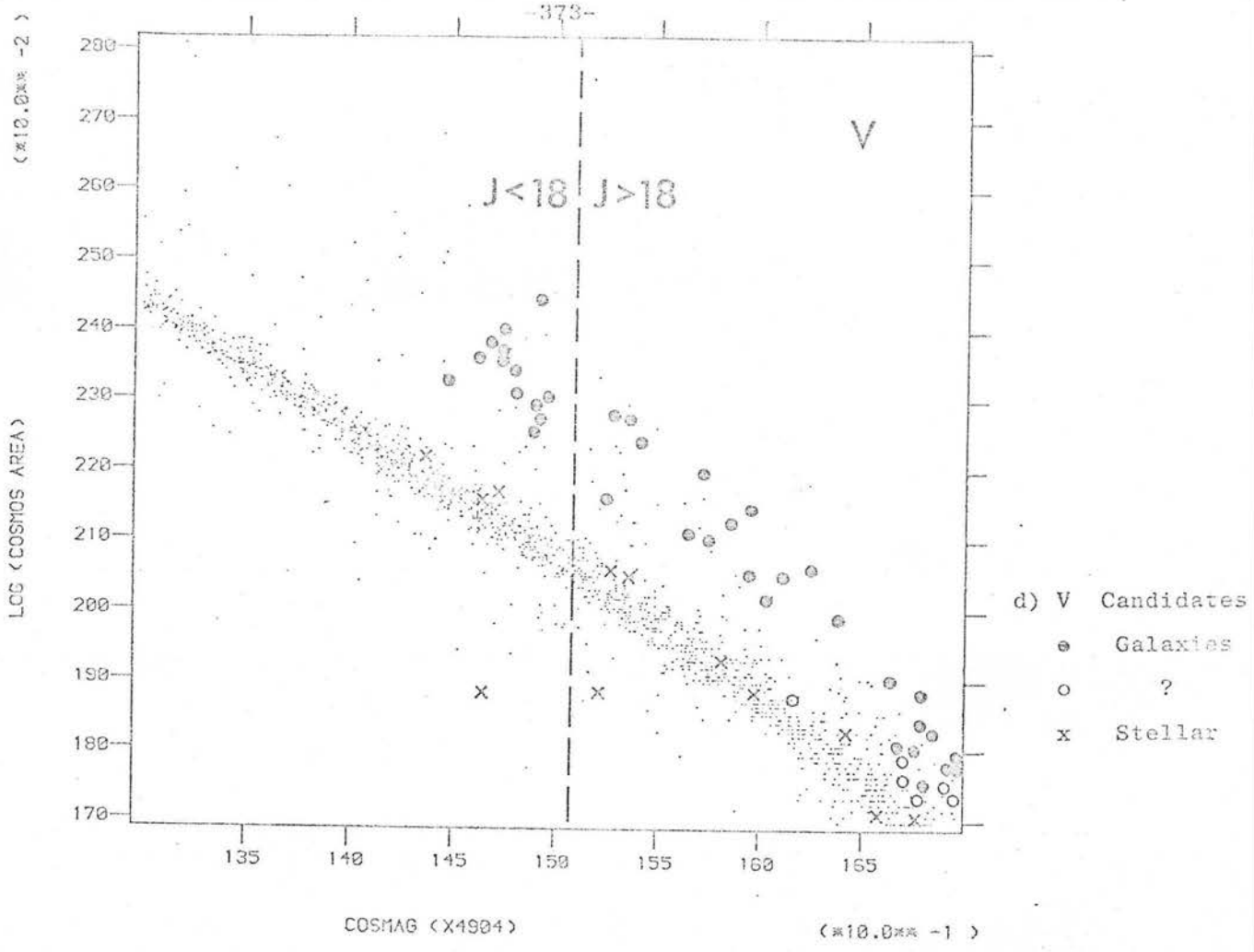

Figure 9.8 Star/Galaxy Separation for polarization candidates.

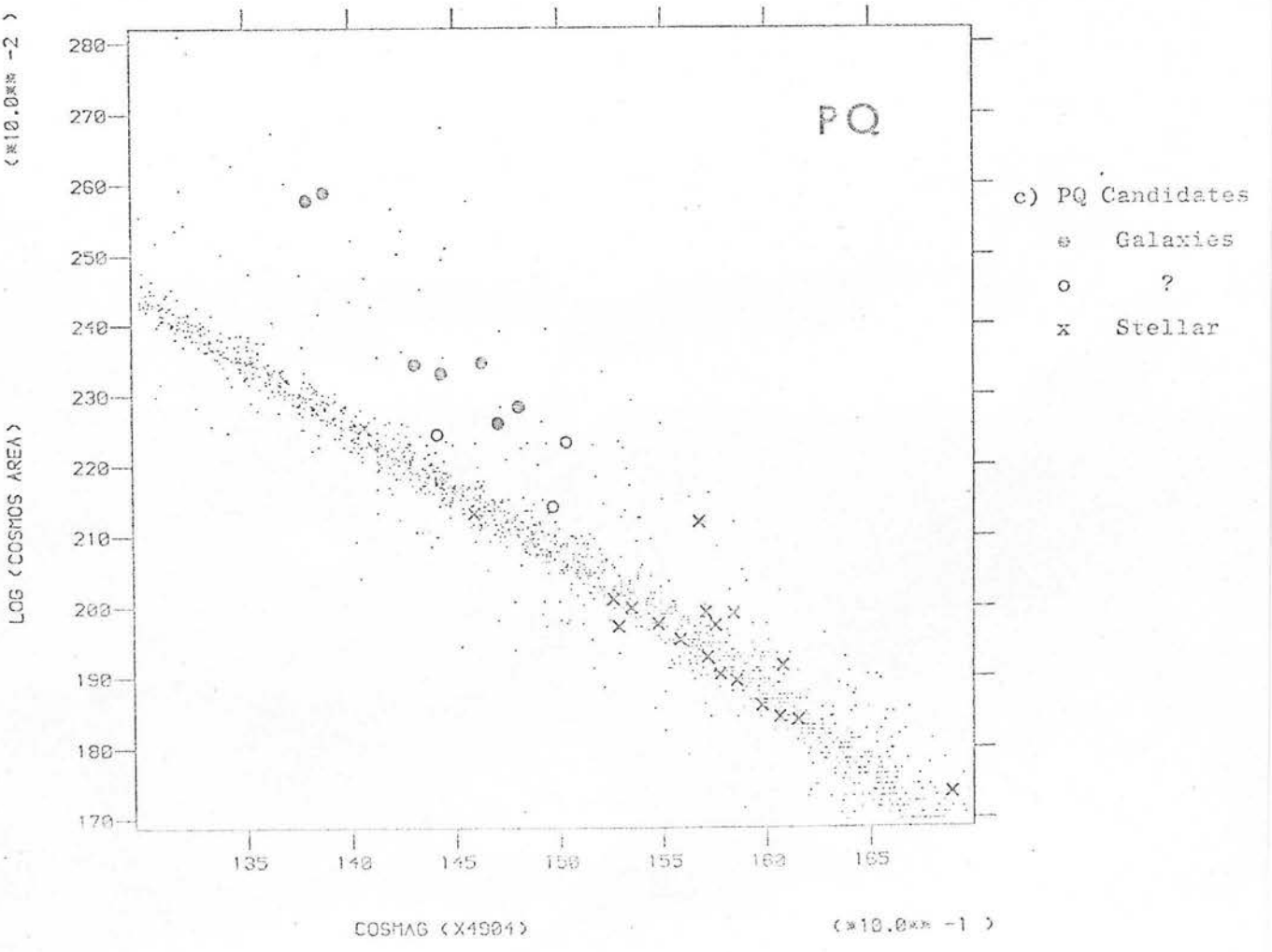

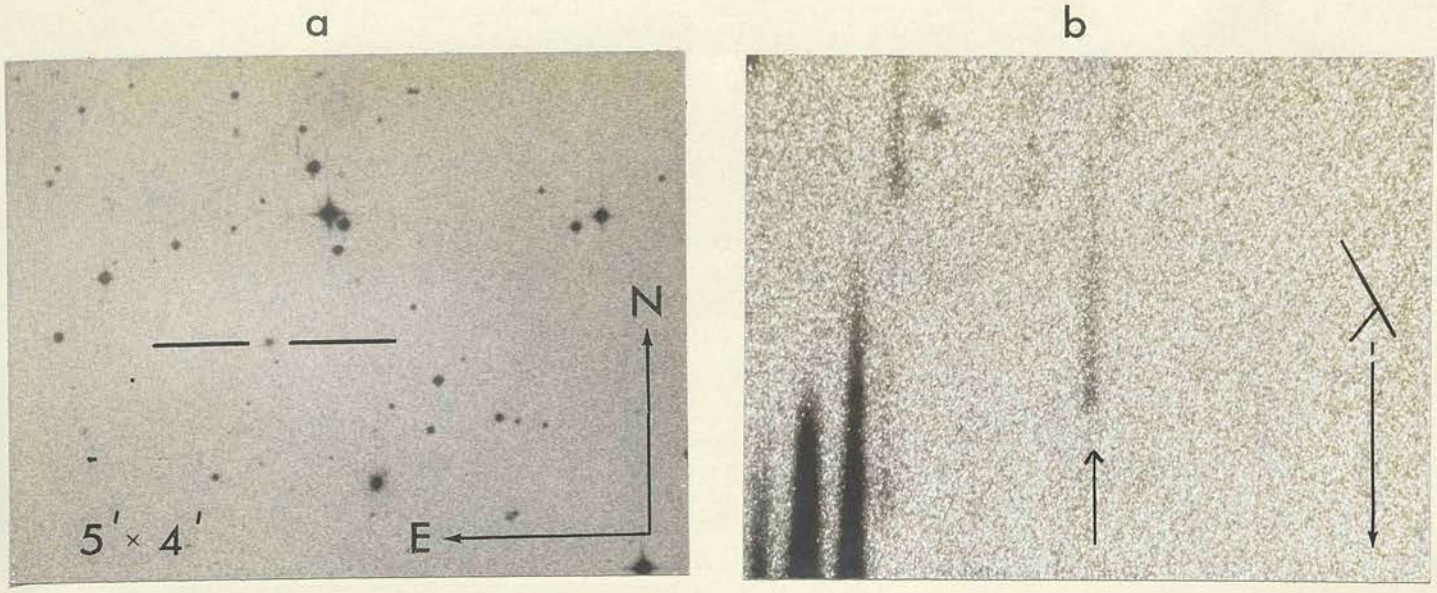

PQV 2.1

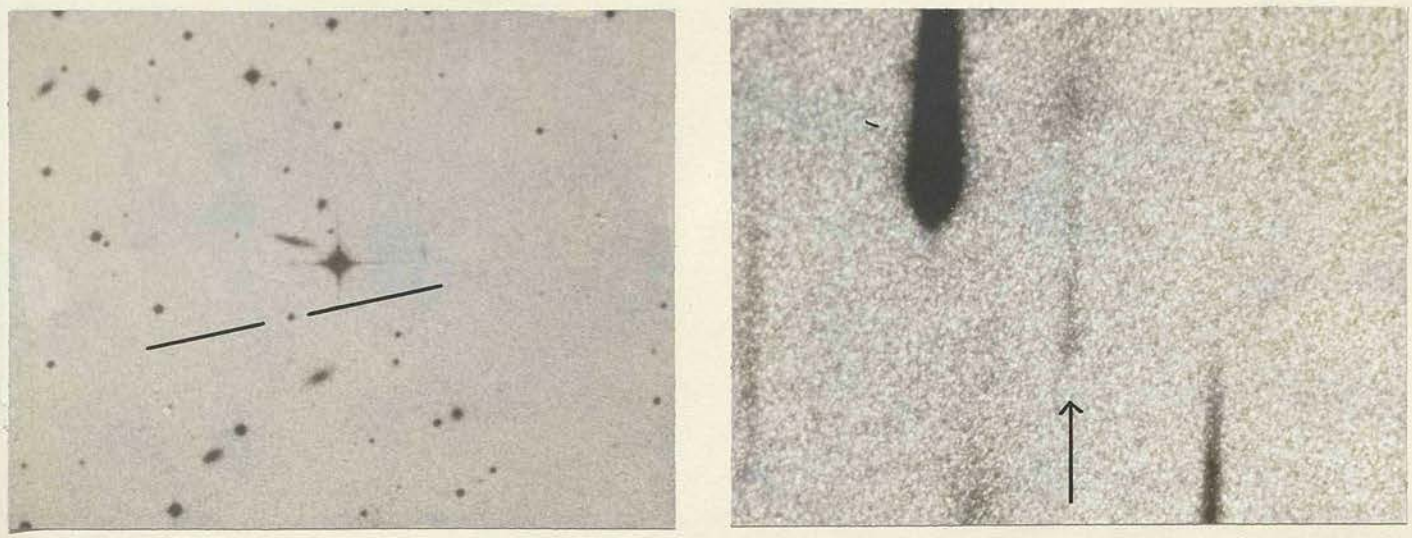

PQV 2.2

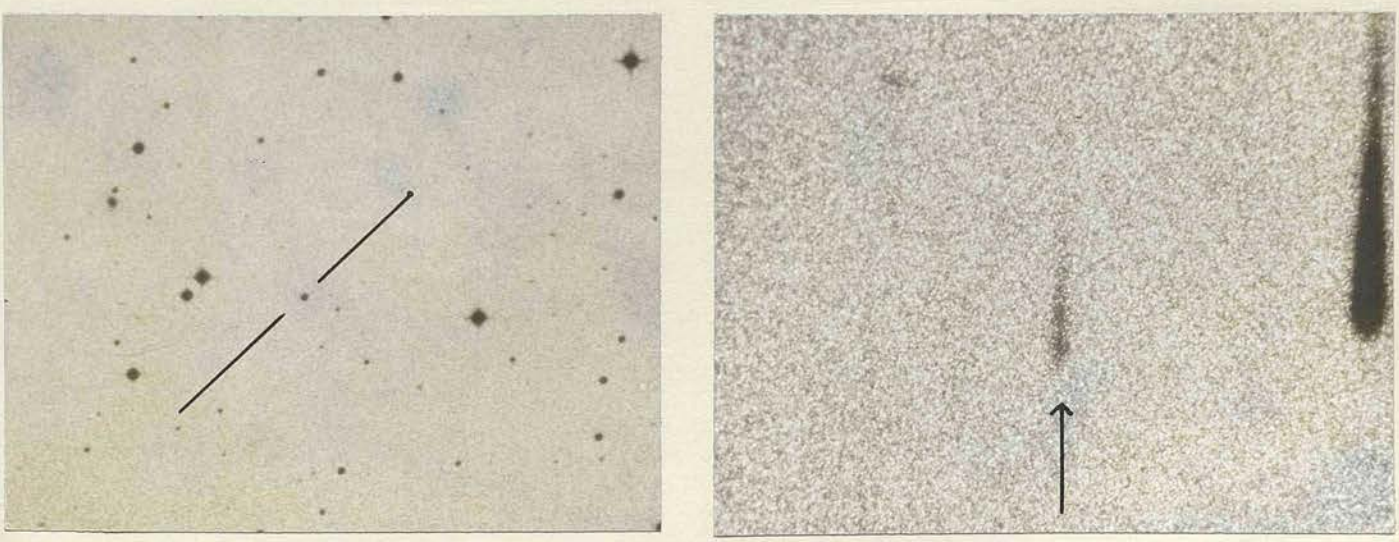

PQV 2.4

Figure 9.9 a) Finding Charts and b) Objective Prism Spectra.

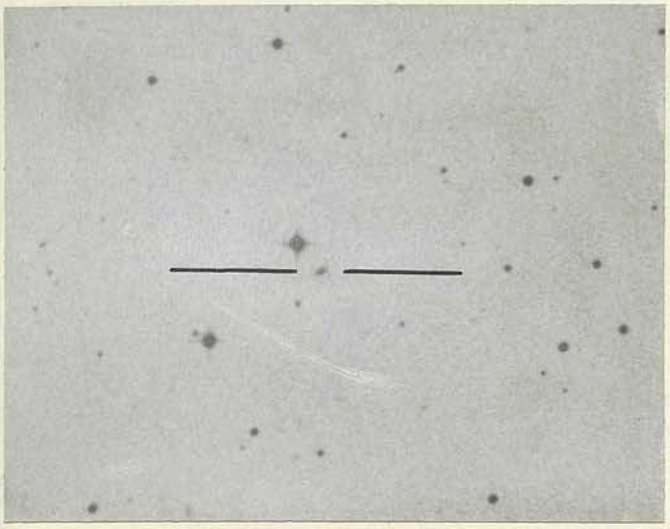

Image non-stellar

PQV 4.1

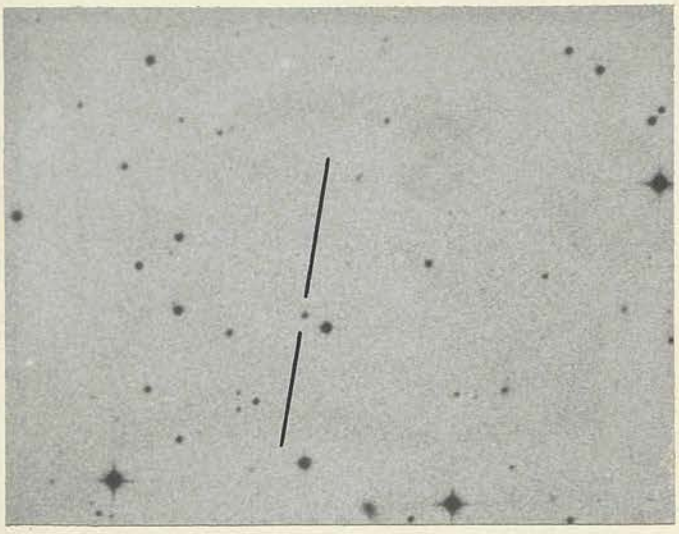

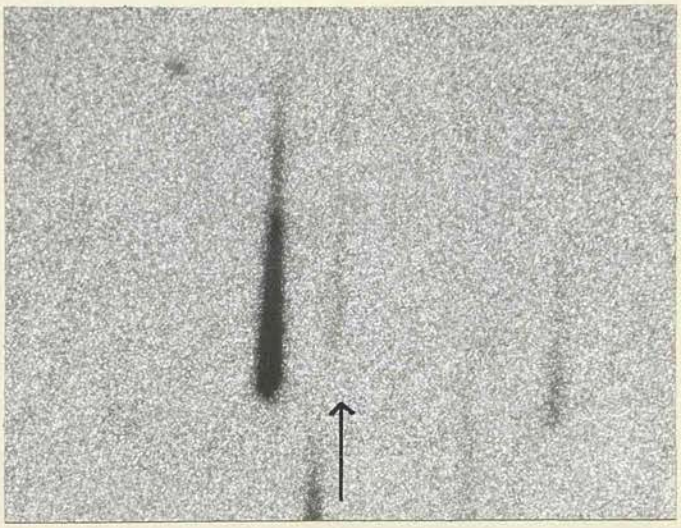

PQV 5.1

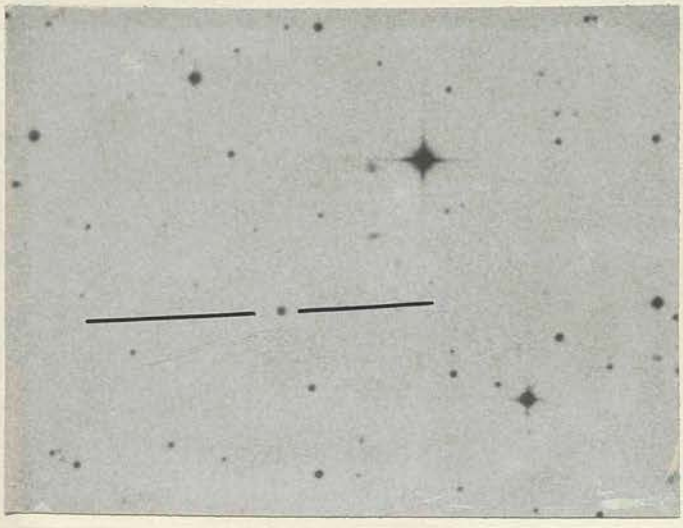

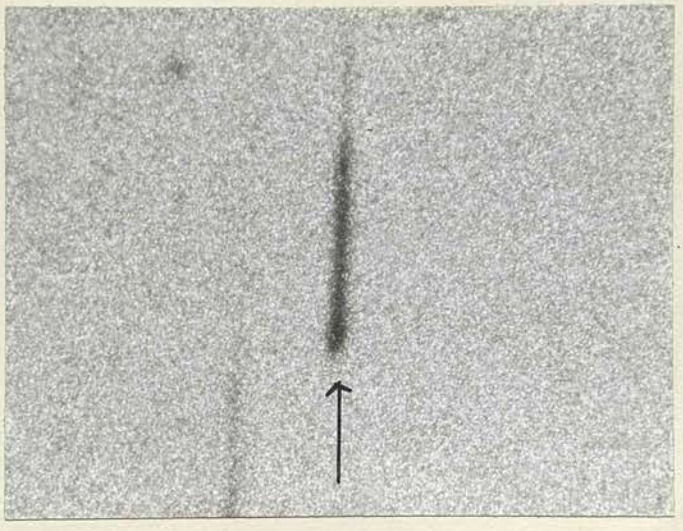

PQV 5.4

Figure 9.9 a) Finding Charts and b) Objective Prism Spectra.

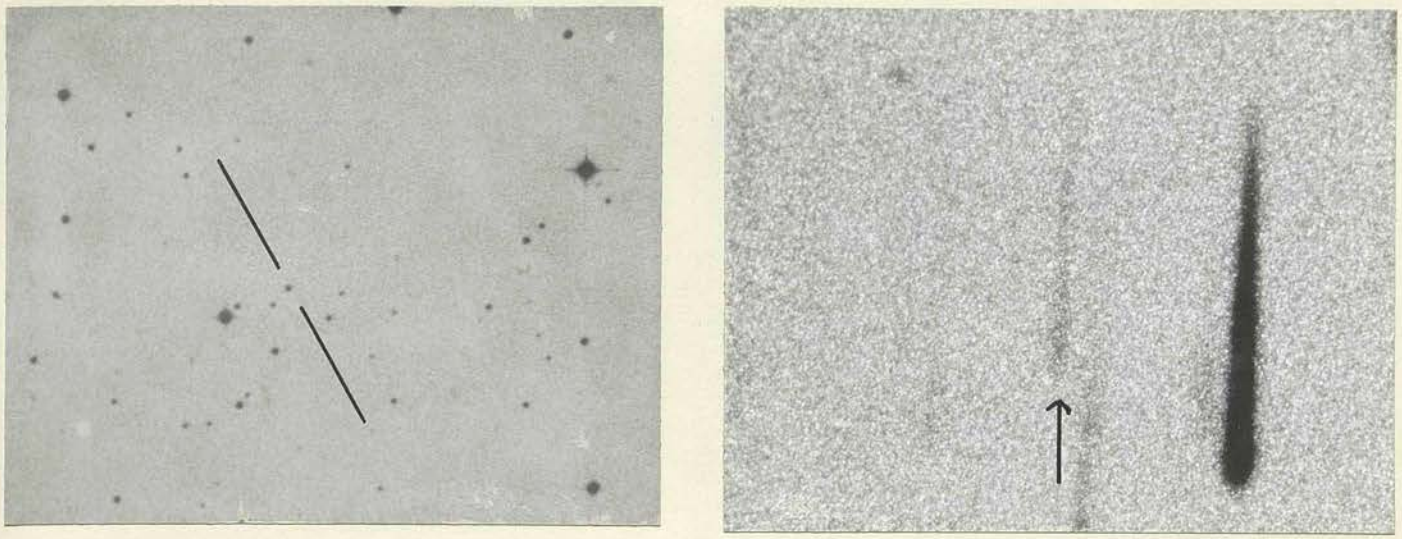

PQV 7.2

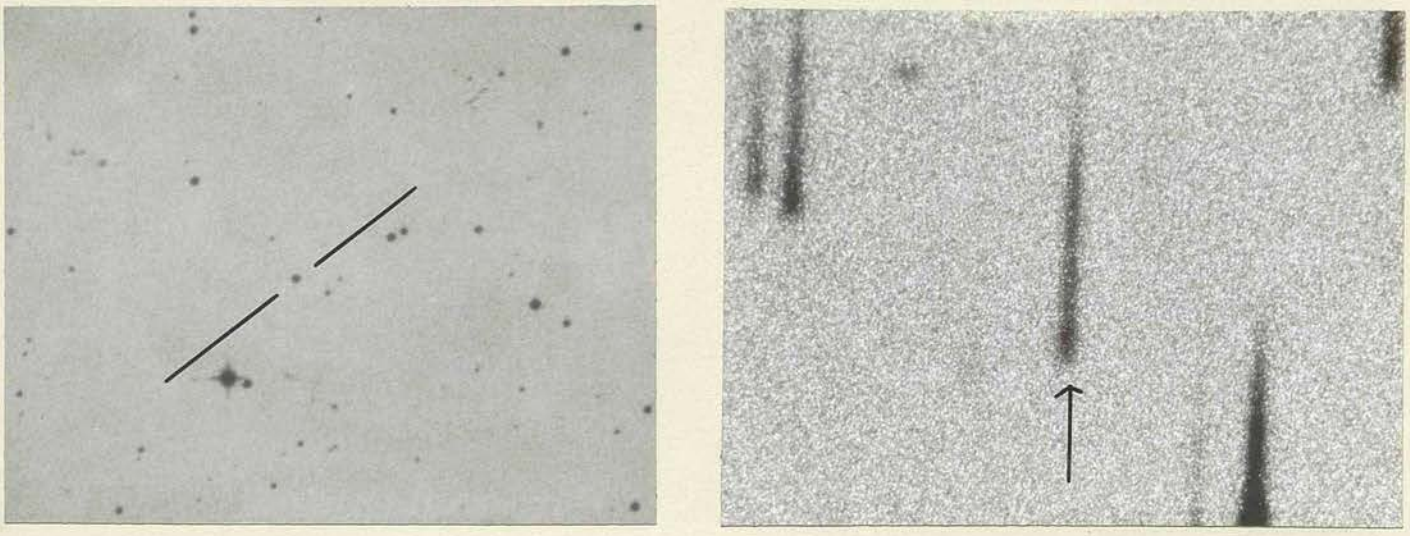

PQV 7.3

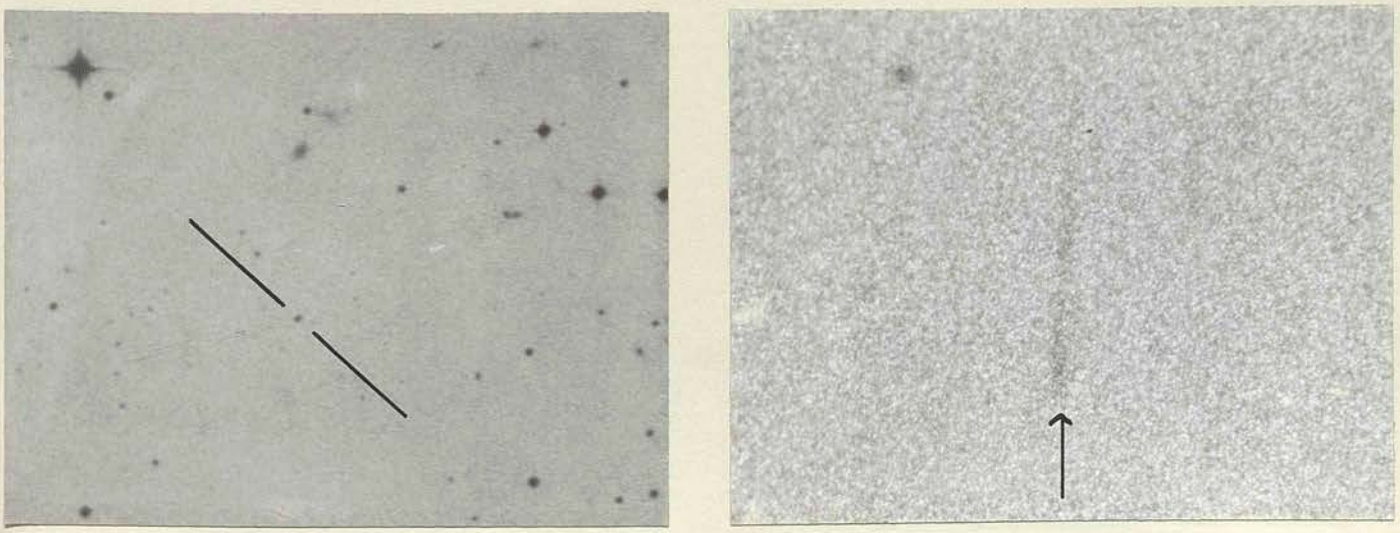

PQV 9.3

Figure 9.9 a) Finding Charts and b) Objective Prism Spectra.

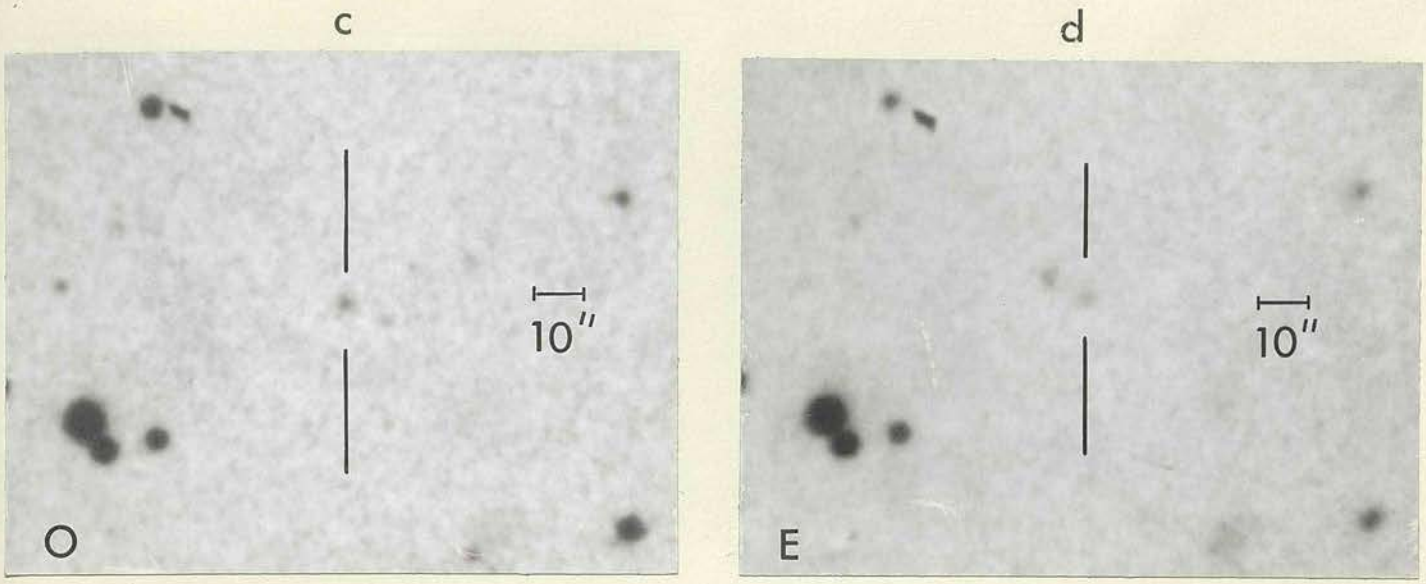

PQV 2.1

PQV 2.4

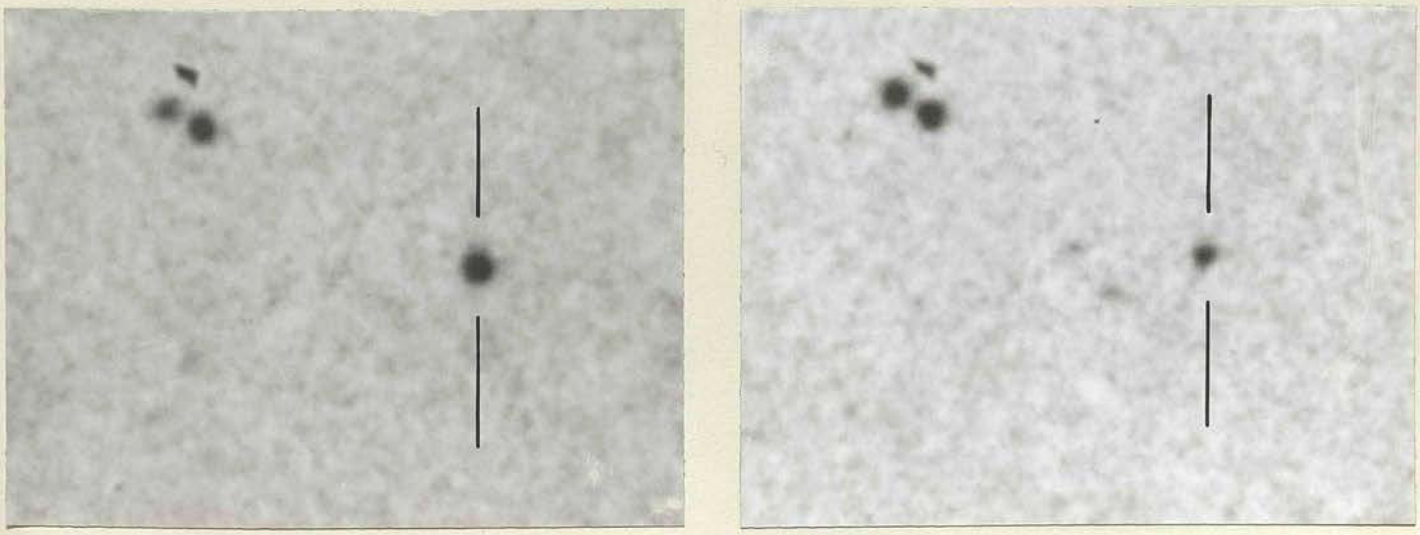

PQV 7.3

Figure 9.9 c) Palomar "O" plates and d) Palomar "E" plates.

CONCLUSIONS

17 BL Lac objects have been observed in the near infrared. Polarimetry was obtained for 13 of the sample, and all the observations were made in the J, H and K wavebands. BL Lac objects have an enormous range of infrared luminosity. Some are similar to normal elliptical galaxies, while the non-thermal flux in others ranks them among the most luminous extragalactic objects known. The typical infrared excess for the sample indicates that most of the energy is emitted at wavelengths longer than 1μm. High and variable linear polarization is a common characteristic, with variations in both flux and degree of polarization occurring on a timescale of one day. 9 of the sample have been monitored over a period of months, and there are many examples of large changes in polarization, position angle and flux on longer timescales. Two BL Lacs (AO 0235+164, 0735+178) show wavelength dependent polarization, with the degree of polarization increasing towards shorter wavelengths. Systematic position angle rotations with time and wavelength are seen in two objects (AO 0235+178, OJ 287). The relationship between flux and polarization changes divides the sample into those where the changes are correlated and those where the changes appear unrelated. There is also evidence for a correlation between infrared excess, degree of polarization and amplitude of variability. In terms of all three properties, BL Lac objects are more extreme than any other active nuclei.

The range of infrared luminosities can be explained by a supermassive rotating magnetoid, possibly a black hole, accreting material with a high efficiency of energy conversion. Even these theories are taxed by the most luminous BL Lac objects, where the variability timescale and infrared flux define a very high energy density. Assuming isotropic emission, three of the sample exceed the Eddington limit. Schemes for generating super-Eddington luminosities exist, but it is likely that there is bulk relativistic motion of the emitting region towards the observer in some BL Lac objects, which reduces the demands on the power source. The severe energy densities derived here are probably underestimates for two reasons. First, the observations were constrained not to probe

variability timescales shorter than one day, and most of the sample have shown evidence for intraday variability. Second, the near infrared spectral indices indicate that the energy output of BL Lac objects is greatest at longer infrared wavelengths.

The infrared flux from BL Lac objects is presumed to be incoherent synchrotron emission because of its high polarization, power law spectral slope and continuity with the radio observations. Appreciable Compton scattering can be ruled out by the low X-ray flux limits. If synchrotron losses dominate, the energy loss time for relativistic electrons is less than the travel time across the source in all objects (where the redshift is known). Reacceleration within the emitting volume is inevitable. For the three most luminous BL Lacs, equipartition fields >1000 Gauss are inferred. Polarization properties can also be used to understand the emitting electrons. The existence of high polarization rules out the presence of a significant amount of thermal plasma in the source or along the line-of-sight. Differential Faraday rotation in OJ 287 is used to put a limit on the ratio of relativistic to non-relativistic electrons in the source. Neither example of wavelength dependent polarization is due to dilution by an underlying galaxy; in both cases $p(\lambda)$ is intrinsic to the non-thermal source. Spectral curvature is not responsible for $p(\lambda)$ in either case, and separate populations of synchrotron-emitting electrons may be combining to produce the effect.

Simple polarization models can be used to mimic the behaviour of BL Lac objects. 0735+178 and OJ 287 have correlated inter-night changes in polarized and unpolarized flux which can be understood as two non-thermal components: one variable and polarized and the other quiescent, but both of roughly equal luminosity. The night-to-night variations depend on the admixture of uniform and isotropic fields in the source. The rest of the objects can be modelled with a non-isotropic geometry and various radial dependences of magnetic field strength. To produce high polarizations ($p > 30\%$), most of the flux must come from a fraction of the emitting

volume (hot spots), and the polarization changes are caused by restructuring the magnetic field. The changing field strength is characterized by a field alignment parameter. Although it cannot account for $p(\lambda)$ over a short wavelength range, changes in the alignment parameter of a factor of ~ 4 are sufficient to explain the observed polarization variability.

It is possible that a strong shock in the environment of the power source can both align the magnetic field and accelerate electrons up to the requisite power law energy spectrum. Once again the high energies and short synchrotron cooling times of the electrons are a problem. The electrons must be accelerated in a turbulence-dominated region and by definition radiate in a magnetically-dominated region to generate a high degree of polarization. The acceleration may either be impulsive up to high energy or it may take place in a thin post-shock shell. It is interesting to make the link between these ideas and the observations (Willis, 1978; Högbom, 1979; Perley et al., 1980; Willis & Strom, 1978; Laing, 1980b) and models (Swinbank, 1980; Laing, 1980a) of jets and 'hot spots' in radio galaxies. Similar structure in BL Lac objects can best be investigated by polarization studies.

In the second part of this work, a radio-independent search for BL Lac objects was carried out using a Polaroid filter on the UK Schmidt telescope. With this technique, large areas of sky ($\sim$10 square degrees) can be searched down to a faint limiting magnitude ($B \sim 19$). The efficacy of the technique depends on reducing the photometric scatter of the majority of the field stars and filtering out plate flaws, mismatches, double images and galaxies from the polarization candidates. The selection of candidates involves eight plates combined into sets for detecting both polarization and variability. The photometric calibration was done with a photoelectric sequence and a photographic extension down to $B \sim 19.3$ using sub-beam prism plates. The mean accuracy at the faint end is 0.1 magnitudes.

By using an internal polarimetric calibration and 'local' transformations between small areas of the plates, a polarization detection limit of 15% is possible. Each candidate object is assigned a significance value by modelling the error distribution between measurements on two plates by a Gaussian. The significance incorporates four separate deviations, and a candidate is selected by appearing simultaneously on two polarization lists and one variability list. A star/galaxy separation algorithm (calculated from the original machine measurement but checked by eye) is used to produce a final list. Further polarimetry, photometry and spectroscopy are needed to confirm any of the candidates as BL Lac objects; but the search gives an upper limit of $n_{BL} < 1$ (sq.deg.)$^{-1}$ at a level $p > 15\%$ down to $B \sim 19.3$. None of the candidates is a strong radio source, so if one is confirmed to be polarized it will be the first known example of a radio quiet BL Lac object. The space density of BL Lac objects can be related to the space density of quasars and other active nuclei.

APPENDIX A

This Appendix derives the matrix elements for all the components used in the light path of the telescope-polarimeter combination.

(i) Analyzer at angle $\emptyset$ with respect to reference frame - perfect polarizer.

$$\{P\} = \tfrac{1}{2}\begin{pmatrix}1&0&0&0\\0&c&-s&0\\0&s&c&0\\0&0&0&1\end{pmatrix}\begin{pmatrix}1&1&0&0\\1&1&0&0\\0&0&0&0\\0&0&0&0\end{pmatrix}\begin{pmatrix}1&0&0&0\\0&c&s&0\\0&-s&c&0\\0&0&0&1\end{pmatrix}$$

$$\{P\} = \tfrac{1}{2}\begin{pmatrix}1&c&s&0\\c&c^2&cs&0\\s&sc&s^2&0\\0&0&0&0\end{pmatrix} \quad \text{where } c = \cos 2\emptyset, \; s = \sin 2\emptyset \tag{A1}$$

(ii) Analyzer at angle $\emptyset$ with respect to reference frame - partial polarizer.

$$\{P'\} = \tfrac{1}{2}\begin{pmatrix}1&0&0&0\\0&c&-s&0\\0&s&c&0\\0&0&0&1\end{pmatrix}\begin{pmatrix}a&b&0&0\\b&a&0&0\\0&0&e&0\\0&0&0&e\end{pmatrix}\begin{pmatrix}1&0&0&0\\0&c&s&0\\0&-s&c&0\\0&0&0&1\end{pmatrix}$$

$$\{P'\} = \tfrac{1}{2}\begin{pmatrix}a&bc&bs&0\\bc&ac^2+es^2&(a-e)sc&0\\bs&(a-e)sc&as^2+ec^2&0\\0&0&0&e\end{pmatrix} \quad \begin{aligned}&\text{where:}\\&a = K_1+K_2\\&b = K_1-K_2\\&e = \sqrt{a^2-b^2}\\&c = \cos 2\emptyset\\&s = \sin 2\emptyset\end{aligned} \tag{A2}$$

(iii) Dichroic at angle α with respect to reference frame - retarder

$$\{R\} = \tfrac{1}{2}\begin{pmatrix}1&0&0&0\\0&c&-s&0\\0&s&c&0\\0&0&0&1\end{pmatrix}\begin{pmatrix}1&0&0&0\\0&1&0&0\\0&0&C&S\\0&0&-S&C\end{pmatrix}\begin{pmatrix}1&0&0&0\\0&c&s&0\\0&-s&c&0\\0&0&0&1\end{pmatrix}$$

$$\{R\} = \tfrac{1}{2}\begin{pmatrix} 1 & 0 & 0 & 0 \\ 0 & c^2+Cs^2 & sc(1-C) & -sS \\ 0 & sc(1-C) & s^2+Cc^2 & cS \\ 0 & sS & -cS & C \end{pmatrix} \qquad \begin{aligned} \text{where } c &= \cos 2\alpha \\ s &= \sin 2\alpha \\ C &= \cos \delta \\ S &= \sin \delta \end{aligned} \qquad \text{(A3)}$$

(iv) Dichroic at angle α with respect to reference frame - partial polarizer and retarder (no angle between principle axes of polarizance and retardance).

From (A2) and (A3),

$$\{R\} = \begin{pmatrix} I & 0 \\ 0 & C \end{pmatrix} \quad , \quad \{P'\} = \tfrac{1}{2}\begin{pmatrix} A & 0 \\ 0 & eI \end{pmatrix}$$

$$\{D\} = \{R\}\{P'\} = \{P'\}\{R\} = \tfrac{1}{2}\begin{pmatrix} A & 0 \\ 0 & eC \end{pmatrix}$$

$$\{D\} = \tfrac{1}{2}\begin{pmatrix} 1 & 0 & 0 & 0 \\ 0 & c & -s & 0 \\ 0 & s & c & 0 \\ 0 & 0 & 0 & 1 \end{pmatrix}\begin{pmatrix} a & b & 0 & 0 \\ b & a & 0 & 0 \\ 0 & 0 & u & v \\ 0 & 0 & -v & u \end{pmatrix}\begin{pmatrix} 1 & 0 & 0 & 0 \\ 0 & c & s & 0 \\ 0 & -s & c & 0 \\ 0 & 0 & 0 & 1 \end{pmatrix}$$

$$\{D\} = \tfrac{1}{2}\begin{pmatrix} a & bc & bs & 0 \\ bc & ac^2+us^2 & (a-u)sc & -vs \\ bs & (a-u)sc & as^2+uc^2 & vc \\ 0 & vs & -vc & u \end{pmatrix} \qquad \begin{aligned} \text{where } c &= \cos 2\alpha \\ s &= \sin 2\alpha \\ u &= e\cos\delta \\ v &= e\sin\delta \end{aligned} \qquad \text{(A4)}$$

(v) Dichroic at angle α with respect to reference frame - partial polarizer and retarder (polarizer and retarder axes separated by angle $\xi-\alpha$).

$\{D\} = \{\xi'\}\{P'\}\{\xi\}\{\alpha'\}\{R\}\{\alpha\}$

$$\{D\} = \tfrac{1}{2}\begin{pmatrix} 1 & 0 & 0 & 0 \\ 0 & c'^2+Cs'^2 & (1-C)s'c' & -sS \\ 0 & (1-C)s'c' & s'^2+Cc'^2 & cS \\ 0 & sS & -cS & C \end{pmatrix}\begin{pmatrix} a & bc & bs & 0 \\ bc & ac^2+es^2 & (a-e)sc & 0 \\ bs & (a-e)sc & as^2+ec^2 & 0 \\ 0 & 0 & 0 & e \end{pmatrix}$$

where $c = \cos 2\alpha$ $\quad C = \cos\delta$

$s = \sin 2\alpha$ $\quad S = \sin\delta$

$c' = \cos 2\xi$ $\quad u = eS$

$s' = \sin 2\xi$ $\quad v = eC$

$$\{D\} = \frac{1}{2}\begin{pmatrix} a & bc & bs & 0 \\ b(c'\underline{C}+Cs'\underline{S}) & (acc'+eCss')\underline{C}-(aCcs'-esc')\underline{S} & (ac's-eCs'c)\underline{C}+(ecc'+aCss')\underline{S} & -vs \\ b(s'\underline{C}+Cc'\underline{S}) & (as'c-eCc's)\underline{C}-(aCcc'+ess')\underline{S} & (ass'+eCcc')\underline{C}+(esc'-aCs'c)\underline{S} & vc \\ 0 & vs & -vc & u \end{pmatrix} \qquad (A5)$$

where $\underline{C} = \cos 2(\alpha-\xi)$

$\underline{S} = \sin 2(\alpha-\xi)$

Note that when $\alpha = \xi$, (A5) reduces to (A4).

(v) Two analyzers - perfect (one at angle α, the other at angle β).

$$\{P\alpha\}\{P\beta\} = \frac{1}{4}\begin{pmatrix} 1 & c & s & 0 \\ c & c^2 & cs & 0 \\ s & sc & s^2 & 0 \\ 0 & 0 & 0 & 0 \end{pmatrix}\begin{pmatrix} 1 & \underline{c} & \underline{s} & 0 \\ \underline{c} & \underline{c}^2 & \underline{cs} & 0 \\ \underline{s} & \underline{sc} & \underline{s}^2 & 0 \\ 0 & 0 & 0 & 0 \end{pmatrix}$$

where $c = \cos 2\alpha$

$s = \sin 2\alpha$

$\underline{c} = \cos 2\beta$

$\underline{s} = \sin 2\beta$

$$\{P\alpha\}\{P\beta\} = \frac{1+\cos 2(\alpha-\beta)}{4}\begin{pmatrix} 1 & \underline{c} & \underline{s} & 0 \\ c & c\underline{c} & c\underline{s} & 0 \\ s & s\underline{c} & s\underline{s} & 0 \\ 0 & 0 & 0 & 0 \end{pmatrix} \qquad (A6)$$

(a) If $\alpha = \beta$ $\quad P\alpha P\beta = P\alpha = P\beta$

(b) If $\alpha = \beta \pm 90^{\circ}$ $\quad P\alpha P\beta = 0$

(vi) Two analyzers - partial polarizers (one at angle α, the other at angle β).

$$\{P\alpha'\}\{P\beta'\} = \frac{1}{2}\begin{pmatrix} a & bc & bs & 0 \\ bc & ac^2+es^2 & (a-e)sc & 0 \\ bs & (a-e)sc & as^2+ec^2 & 0 \\ 0 & 0 & 0 & e \end{pmatrix}\begin{pmatrix} a & b\underline{c} & b\underline{s} & 0 \\ b\underline{c} & a\underline{c}^2+e\underline{s}^2 & (a-e)\underline{sc} & 0 \\ b\underline{s} & (a-e)\underline{sc} & a\underline{s}^2+e\underline{c}^2 & 0 \\ 0 & 0 & 0 & e \end{pmatrix}$$

where $C = \cos 2(\alpha-\beta)$

$S = \sin 2(\alpha-\beta)$

$\{P\alpha'\}\{P\beta'\} =$

$$\tfrac{1}{2}\begin{pmatrix} a^2+b^2C & abc(1+C)-ebsS & abs(1+C)+ebcS & 0 \\ abc(1+C)+ebsS & b^2cc+a^2ccC+e^2ssC+eaS^2 & b^2cs+a^2csC-e^2scC+aeSC & 0 \\ abs(1+C)-ebcS & b^2sc+a^2csC-e^2scC-eaSC & b^2ss+a^2ssC+e^2ccC+aeS^2 & 0 \\ 0 & 0 & 0 & e^2 \end{pmatrix} \quad (A7)$$

(a) If $\alpha = \beta$,

$$\{P\alpha'\}\{P\beta'\} = \tfrac{1}{2}\begin{pmatrix} a^2+b^2 & 2abc & 2abs & 0 \\ 2abc & e^2 & 0 & 0 \\ 2abs & 0 & e^2 & 0 \\ 0 & 0 & 0 & e^2 \end{pmatrix}$$

Check: If $e = 0$, $a = b = 1$ $\rightarrow P\alpha P\beta = P\alpha = P\beta$

(b) If $\alpha = \beta \pm 90^\circ$,

$$\{P\alpha'\}\{P\beta'\} = \frac{e^2}{4}\begin{pmatrix} 1 & 0 & 0 & 0 \\ 0 & -1 & 0 & 0 \\ 0 & 0 & -1 & 0 \\ 0 & 0 & 0 & 1 \end{pmatrix}$$

Check: If $c = 0$, $a = b = 1$ $\rightarrow P\alpha = P\beta = 0$

(vii) Analyzer, followed by dichroic - {P} perfect polarizer

{D} partial polarizer and retarder

$$\{D\}\{P\} = \tfrac{1}{2}\begin{pmatrix} a & bc & bs & 0 \\ bc & ac^2+us^2 & (a-u)sc & -vs \\ bs & (a-u)sc & as^2-uc^2 & vc \\ 0 & vs & -vc & u \end{pmatrix}\begin{pmatrix} 1 & \underline{c} & \underline{s} & 0 \\ \underline{c} & \underline{c}^2 & \underline{cs} & 0 \\ \underline{s} & \underline{sc} & \underline{s}^2 & 0 \\ 0 & 0 & 0 & 0 \end{pmatrix}$$

where $c = \cos 2\alpha$, $s = \sin 2\alpha$, $\underline{c} = \cos 2\phi$, $\underline{s} = \sin 2\phi$

and define $C = \cos 2(\phi - \alpha)$, $S = \sin 2(\phi - \alpha)$

$$\{D\}\{P\} = \tfrac{1}{2}\begin{pmatrix} a+bC & \underline{c}(a+bC) & \underline{s}(a+bC) & 0 \\ bc+acC-usS & \underline{c}(bc+acC-usS) & \underline{s}(bc+acC-usS) & 0 \\ bs+asC+ucS & \underline{c}(bs+asC+ucS) & \underline{s}(bc+asC+ucS) & 0 \\ -vS & \underline{c}(-vS) & \underline{s}(-vS) & 0 \end{pmatrix} \qquad (A8)$$

(viii) Analyzer, followed by dichroic - $\{P'\}$ partial polarizer

$\{D\}$ partial polarizer and retarder

$$\{D\}\{P'\} = \tfrac{1}{2}\begin{pmatrix} a & bc & bs & 0 \\ bc & ac^2+us^2 & (a-u)sc & -vs \\ bs & (a-u)sc & as^2+uc^2 & vc \\ 0 & vs & -vc & u \end{pmatrix}\begin{pmatrix} \underline{a} & \underline{bc} & \underline{bs} & 0 \\ \underline{bc} & \underline{ac}^2+\underline{es}^2 & (\underline{a-e})\underline{sc} & 0 \\ \underline{bs} & (\underline{a-e})\underline{sc} & \underline{as}^2+\underline{ec}^2 & 0 \\ 0 & 0 & 0 & \underline{e} \end{pmatrix}$$

$$\{D\}\{P'\} = \tfrac{1}{2}\begin{pmatrix} \underline{aa}+bbC & \underline{abc}+b(\underline{ac}C+\underline{es}S) & \underline{abs}+b(\underline{as}C-\underline{ec}S) & 0 \\ bc\underline{a}+\underline{b}(acC-usS) & bc\underline{bc}+ac\underline{ac}C+us\underline{es}C-us\underline{ac}S+ac\underline{es}S & bc\underline{bs}+ac\underline{as}C-us\underline{ec}C+us\underline{ns}S-ac\underline{ec}S & -\underline{e}vs \\ bs\underline{a}+\underline{b}(asC+ucS) & bs\underline{bc}+as\underline{ac}C-uc\underline{es}C+uc\underline{ac}S+as\underline{es}S & bs\underline{bs}+as\underline{as}C+uc\underline{ec}C+uc\underline{es}S-as\underline{ec}S & \underline{e}vc \\ -bvS & v(\underline{es}C-\underline{ac}S) & -v(\underline{ec}C+\underline{as}S) & \underline{e}u \end{pmatrix} \qquad (A9)$$

Note that when $\underline{e} = 0$ and $\underline{b} = \underline{a} = 1$, (A9) reduces to (A8).

(ix) Dichroic, followed by analyzer - $\{P\}$ perfect polarizer

$\{D\}$ partial polarizer and retarder

$$\{P\}\{D\} = \tfrac{1}{2}\begin{pmatrix} 1 & \underline{c} & \underline{s} & 0 \\ \underline{c} & \underline{c}^2 & \underline{cs} & 0 \\ \underline{s} & \underline{sc} & \underline{s}^2 & 0 \\ 0 & 0 & 0 & 0 \end{pmatrix}\begin{pmatrix} a & bc & bs & 0 \\ bc & ac^2+us^2 & (a-u)sc & -vs \\ bs & (a-u)sc & as^2+uc^2 & vc \\ 0 & vs & -vc & u \end{pmatrix}$$

where $c = \cos 2\alpha$

$s = \sin 2\alpha$

$\underline{c} = \cos 2\beta$

$\underline{s} = \sin 2\beta$

$$\{P\}\{D\} = \tfrac{1}{2}\begin{pmatrix} a+bC & bc+acC-usS & bs+asC+ucS & vS \\ \underline{c}(a+bC) & \underline{c}(bc+acC-usS) & \underline{c}(bs+asC+ucS) & v\underline{c}S \\ \underline{s}(a+bC) & \underline{s}(bc+acC-usC) & \underline{s}(bs+asC+ucS) & v\underline{s}S \\ 0 & 0 & 0 & 0 \end{pmatrix} \qquad (A10)$$

where $C = \cos 2(\phi-\alpha)$

$S = \sin 2(\phi-\alpha)$

(x) Dichroic, followed by analyzer - $\{P'\}$ partial polarizer

$\{D\}$ partial polarizer and retarder

$$\{P'\}\{D\} = \tfrac{1}{2}\begin{pmatrix} a & \underline{bc} & \underline{bs} & 0 \\ \underline{bc} & \underline{ac}^2+\underline{es}^2 & (\underline{a}-\underline{e})\underline{sc} & 0 \\ \underline{bs} & (\underline{a}-\underline{e})\underline{sc} & \underline{as}^2+\underline{ec}^2 & 0 \\ 0 & 0 & 0 & \underline{e} \end{pmatrix}\begin{pmatrix} a & bc & bs & 0 \\ bc & ac^2+us^2 & (a-u)sc & -vs \\ bs & (a-u)sc & as^2+uc^2 & vc \\ 0 & vs & -vc & u \end{pmatrix}$$

$$\{P'\}\{D\} = \tfrac{1}{2}\begin{pmatrix} \underline{aa}+\underline{bb}C & \underline{ab}c+\underline{b}(acC-usS) & \underline{abs}+\underline{b}(asC+ucS) & \underline{bv}S \\ \underline{bc}a+\underline{b}(\underline{ac}C+\underline{es}S) & \underline{bcbc}+\underline{acac}C+\underline{es}\underline{us}C+\underline{es}\underline{ac}S-\underline{ac}\underline{us}S & \underline{bcbs}+\underline{acas}C-\underline{es}\underline{uc}C+\underline{es}\underline{as}S+\underline{ac}\underline{uc}S & v(\underline{ac}S-\underline{es}C) \\ \underline{bs}a+\underline{b}(\underline{as}C-\underline{ec}S) & \underline{bsbc}+\underline{as}\underline{ac}C-\underline{ec}\underline{us}C-\underline{ec}\underline{ac}S-\underline{as}\underline{us}S & \underline{bsbs}+\underline{as}\underline{as}C+\underline{ec}\underline{uc}C+\underline{es}\underline{as}S+\underline{as}\underline{uc}S & v(\underline{as}S+\underline{ec}C) \\ 0 & \underline{evs} & -\underline{evc} & \underline{eu} \end{pmatrix} \qquad (A11)$$

Note that when $\underline{e} = 0$ and $\underline{b} = \underline{a} = 1$, (A11) reduces to (A10).

References

Clarke, D. & Grainger, J.F. (1971). Polarized Light and Optical Measurement (Pergamon Press).

Serkowski, K. (1974). Planets, Stars and Nebulae Studied with Photopolarimetry. ed. T. Gehrels (University of Arizona), 135.

APPENDIX B

In this Appendix, the intensity output of all the polarimeter configurations is calculated. The derivations cover measurement of unpolarized standards, stars of known polarization and crossed Polaroid tests in two situations: with the rotating analyzer before and after the dichroic. I* and I represent the measured and incident intensities.

(i)

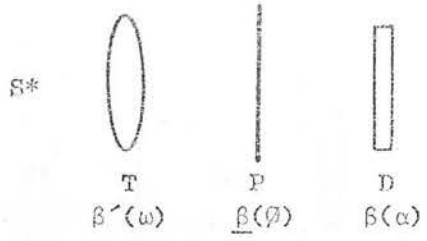

S - unpolarized star

P - perfect polarizer

D - partial polarizer and retarder

$$\begin{pmatrix} I^* \\ Q^* \\ U^* \\ V^* \end{pmatrix} = \{D\}\{P\}\{T\} \begin{pmatrix} I \\ 0 \\ 0 \\ 0 \end{pmatrix}$$

Using (A8) and (A2),

$$\begin{pmatrix} I^* \\ Q^* \\ U^* \\ V^* \end{pmatrix} = \frac{1}{2} \begin{pmatrix} a+bC & \underline{c}(a+bC) & \underline{s}(a+bC) & 0 \\ bc+acC-usS & \underline{c}(bc+acC-usS) & \underline{s}(bc+acC-usS) & 0 \\ bs+asC+ucS & \underline{c}(bs+asC+ucS) & \underline{s}(bs+asC+ucS) & 0 \\ -vS & \underline{c}(-vS) & \underline{s}(-vS) & 0 \end{pmatrix}$$

$$\times \begin{pmatrix} a' & b'c' & b's' & 0 \\ b'c' & a'c'^2+e's'^2 & (a'-e')s'c' & 0 \\ b's' & (a'-e')s'c' & a's'^2+e'c'^2 & 0 \\ 0 & 0 & 0 & e' \end{pmatrix} \begin{pmatrix} I \\ 0 \\ 0 \\ 0 \end{pmatrix}$$

where $c = \cos 2\alpha$ $\quad C = \cos 2(\beta-\alpha)$

$s = \sin 2\alpha$ $\quad S = \sin 2(\beta-\alpha)$

$\underline{c} = \cos 2\beta$ $\quad c' = \cos 2\omega$

$\underline{s} = \sin 2\beta$ $\quad s' = \sin 2\omega$

$$\frac{\partial I^*}{\partial a' I} = (1 + \beta\cos 2(\beta-\alpha))(1 + \beta' \cos 2(\beta-\omega)) \qquad (B1)$$

where $\beta = b/a$ and $\beta' = b'/a'$. The photometer cage is then rotated by 90^{o} and another measurement taken. In this case $\cos 2(\phi-\omega) \rightarrow \cos 2(\phi-\omega)$ giving

$$\frac{\delta I^*}{aa'I} = (1 + \beta \cos 2(\phi-\alpha))(1 - \beta' \cos 2(\phi-\omega)) \qquad (B2)$$

where $\beta = b/a$, $\beta' = b'/a'$, $\underline{\delta} = 1$

(ii)

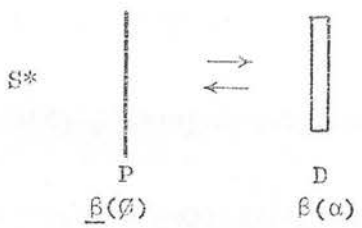

S - unpolarized star
P′ - partial polarizer
D - partial polarizer and retarder

$$\begin{pmatrix} I^* \\ Q^* \\ U^* \\ V^* \end{pmatrix} = \{D\}\{P'\} \begin{pmatrix} I \\ 0 \\ 0 \\ 0 \end{pmatrix} = \{P'\}\{D\} \begin{pmatrix} I \\ 0 \\ 0 \\ 0 \end{pmatrix}$$

Using (A9) and (A11),

$$\frac{4I^*}{aa\underline{I}} = 1 + \beta\underline{\beta} \cos 2(\phi-\alpha) \qquad (B3)$$

where $\beta = b/a$ and $\underline{\beta} = \underline{b}/\underline{a}$. Therefore β and α can be found.

(iii)

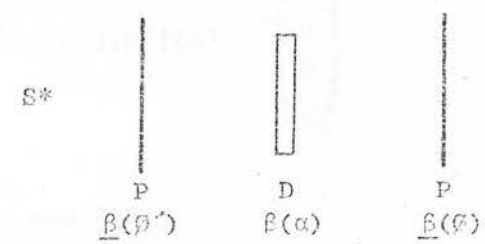

S - unpolarized star
P - partial polarizer
D - partial polarizer and retarder

$$\begin{pmatrix} I^* \\ Q^* \\ U^* \\ V^* \end{pmatrix} = \{P'\}\{D\}\{P'\} \begin{pmatrix} I \\ 0 \\ 0 \\ 0 \end{pmatrix}$$

Using (A9) and (A2),

$$\begin{pmatrix} I^* \\ Q^* \\ U^* \\ V^* \end{pmatrix} = \frac{1}{S} \begin{pmatrix} \underline{a}a+\underline{b}\underline{b}C & \underline{a}bc+\underline{b}(acC-usS) & \underline{a}bs+\underline{b}(asC+ucS) & \underline{b}vS & \underline{a} \\ \cdot & \cdot & \cdot & \cdot & \underline{b}c \\ \cdot & \cdot & \cdot & \cdot & \underline{b}s \\ 0 & \cdot & \cdot & \cdot & 0 \end{pmatrix}$$

where $c = \cos 2\alpha$ $\quad \underline{c} = \cos 2\phi'$

$s = \sin 2\alpha$ $\quad \underline{s} = \sin 2\phi'$

$C = \cos 2(\phi-\alpha)$

$S = \sin 2(\phi-\alpha)$

$$\frac{\partial I^*}{\underline{a}^2 \partial I} = (1+\beta\underline{\beta}C)+\underline{\beta}\left[(\beta c+\underline{\beta}cC-\gamma sS\underline{\beta})\cos 2\phi'+(\beta s+\underline{\beta}sC+\gamma cS\underline{\beta})\sin 2\phi'\right]$$

$$= (1+\beta\underline{\beta}\cos 2(\phi'-\alpha))+\underline{\beta}(\beta+\underline{\beta}\cos 2(\phi'-\alpha))\cos 2(\phi-\alpha)+\gamma\underline{\beta}^2\sin 2(\phi'-\alpha)\sin 2(\phi-\alpha) \qquad (B4)$$

where $\beta = b/a$, $\underline{\beta} = \underline{b}/\underline{a}$

and $\gamma = u/a = \sqrt{1-\beta^2}\cos\delta$

(iv)

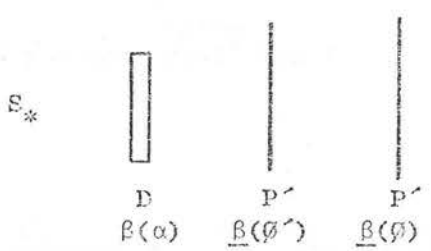

S - unpolarized star

P′ - partial polarizer

D - partial polarizer and retarder

$$\begin{pmatrix} I^* \\ Q^* \\ U^* \\ V^* \end{pmatrix} = \{P'\}\{P'\}\{D\} \begin{pmatrix} I \\ 0 \\ 0 \\ 0 \end{pmatrix}$$

Using (A11) and (A2),

$$\begin{pmatrix} I^* \\ Q^* \\ U^* \\ V^* \end{pmatrix} =$$

$$\frac{1}{\delta}\begin{pmatrix} \underline{a} & \underline{b}c & \underline{b}s & 0 \\ \underline{b}c & \underline{a}c^2+\underline{e}s^2 & (\underline{a}-\underline{e})sc & 0 \\ \underline{b}s & (\underline{a}-\underline{e})sc & \underline{a}s^2+\underline{e}c^2 & 0 \\ 0 & 0 & 0 & \underline{e} \end{pmatrix}$$

$$\times \begin{pmatrix} a\underline{a}+b\underline{b}C & \underline{ab}c+\underline{b}(acC-usS) & \underline{ab}s+\underline{b}(asC+ucS) & -bvS \\ \underline{b}c+\underline{a}b(acC+asS) & \cdot & \cdot & \cdot \\ \underline{b}s+\underline{a}b(asC-ucS) & \cdot & \cdot & \cdot \\ 0 & \cdot & \cdot & \cdot \end{pmatrix} \begin{pmatrix} I \\ 0 \\ 0 \\ 0 \end{pmatrix}$$

where $c = \cos 2\phi$ $\quad C = \cos 2(\phi'-\alpha)$

$s = \sin 2\phi$ $\quad S = \sin 2(\phi'-\alpha)$

$\underline{c} = \cos 2\phi'$

$\underline{s} = \sin 2\phi'$

$$\frac{\delta I^*}{\underline{a}^2 aI} = (1+\beta\underline{\beta}C)+\underline{\beta}\left[(\underline{\beta}c+\underline{\beta}\underline{c}C-\underline{\gamma}\underline{s}S\underline{\beta})\cos 2\phi+(\underline{\beta}\underline{s}+\underline{\beta}\underline{s}C+\underline{\gamma}\underline{c}S\underline{\beta})\sin 2\phi\right]$$

$$= (1+\beta\underline{\beta}\cos 2(\phi'-\alpha))+\underline{\beta}(\underline{\beta}+\beta\cos 2(\phi'-\alpha))\cos 2(\phi'-\phi)+\gamma\beta\underline{\beta}\sin 2(\phi'-\alpha)\sin 2(\phi'-\phi)$$

(B5)

where $\beta = b/a$, $\quad \underline{\beta} = \underline{b}/\underline{a}$

and $\gamma = u/a$, $\sqrt{1-\beta^2}\cos\delta$

(v)

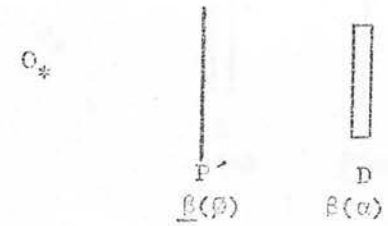

O - polarized object, p(0)

P' - partial polarizer

D - partial polarizer and retarder

$$\begin{pmatrix} I^* \\ Q^* \\ U^* \\ V^* \end{pmatrix} = \{D\}\{P'\}\begin{pmatrix} I \\ Q \\ U \\ 0 \end{pmatrix}$$

where $Q = p\cos 2\theta$

and $U = p\sin 2\theta$

Using (A8),

$$\begin{pmatrix} I^* \\ Q^* \\ U^* \\ V^* \end{pmatrix} = \tfrac{1}{4} \begin{pmatrix} a\underline{a}+b\underline{b}C & ab\underline{c}+b(\underline{a}c\underline{C}+e\underline{e}S) & ab\underline{s}+b(\underline{a}s\underline{C}-e\underline{c}S) & 0 \\ \cdot & \cdot & \cdot & 0 \\ \cdot & \cdot & \cdot & 0 \\ \cdot & \cdot & \cdot & 0 \end{pmatrix} \begin{pmatrix} I \\ Ipc \\ Ips \\ 0 \end{pmatrix}$$

where $\underline{c} = \cos 2\phi$ $\qquad c = \cos 2\theta$

$\underline{s} = \sin 2\phi$ $\qquad s = \sin 2\theta$

$C = \cos 2(\phi-\alpha)$

$S = \sin 2(\phi-\alpha)$

$$\frac{\partial I^*}{a\underline{a}I} = (1+\beta\underline{\beta}C)+p\left[(\underline{\beta}c+\underline{\beta}\underline{c}C+\sqrt{1-\underline{\beta}^2}\,\underline{s}S\beta)\cos 2\theta+(\underline{\beta}\underline{s}+\beta\underline{s}C-\sqrt{1-\underline{\beta}^2}\,\underline{c}S\beta)\sin 2\theta\right]$$

$$= (1+p\underline{\beta}\cos 2(\phi-\theta))+\beta(\underline{\beta}+p\cos 2(\phi-\theta))\cos 2(\phi-\alpha)$$

$$+ \sqrt{1-\underline{\beta}^2}\,\beta p \sin 2(\phi-\theta)\sin 2(\phi-\alpha) \qquad (B8)$$

where $\beta = b/a$, $\quad \underline{\beta} = \underline{b}/\underline{a}$

and $\underline{e}/\underline{a} = \sqrt{1-\underline{\beta}^2}$

(vi)

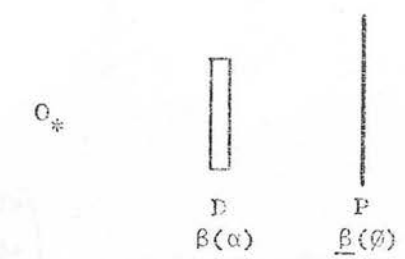

O - polarized object, p(θ)

P′ - partial polarizer

D - partial polarizer and retarder

$$\begin{pmatrix} I^* \\ Q^* \\ U^* \\ V^* \end{pmatrix} = \{P'\}\{D\} \begin{pmatrix} I \\ Q \\ U \\ 0 \end{pmatrix}$$

where $Q = p \cos 2\theta$,

and $U = p \sin 2\theta$

Using (A11),

$$\begin{pmatrix} I^* \\ Q^* \\ U^* \\ V^* \end{pmatrix} = \tfrac{1}{2} \begin{pmatrix} aa+bb\underline{C} & ab\underline{c}+b(ac\underline{C}-us\underline{S}) & ab\underline{s}+b(as\underline{C}+uc\underline{S}) & b\underline{v}S \\ \cdot & \cdot & \cdot & \cdot \\ \cdot & \cdot & \cdot & \cdot \\ 0 & \cdot & \cdot & \cdot \end{pmatrix} \begin{pmatrix} I \\ Ip\underline{c} \\ Ip\underline{s} \\ 0 \end{pmatrix}$$

where $c = \cos 2\alpha$ $\quad \underline{c} = \cos 2\theta$

$s = \sin 2\alpha$ $\quad \underline{s} = \sin 2\theta$

$C = \cos 2(\phi-\alpha)$

$S = \sin 2(\phi-\alpha)$

$$\frac{4I^*}{aa\underline{I}} = (1+\beta\underline{\beta}C)+p\left[(\beta c+\underline{\beta}cC-\gamma sS\underline{\beta})\cos 2\theta+(\beta s+\underline{\beta}sC+\gamma cS\underline{\beta})\sin 2\theta\right]$$

$$= (1+\beta p\cos 2(\theta-\alpha))+\underline{\beta}(\beta+p\cos 2(\theta-\alpha))\cos 2(\phi-\alpha)+\gamma p\underline{\beta}\sin 2(\theta-\alpha)\sin 2(\phi-\alpha) \quad (B7)$$

where $\beta = b/a$, $\quad \underline{\beta} = \underline{b}/\underline{a}$

and $\gamma = u/a = \sqrt{1-\beta^2}\cos\delta$

(vii)

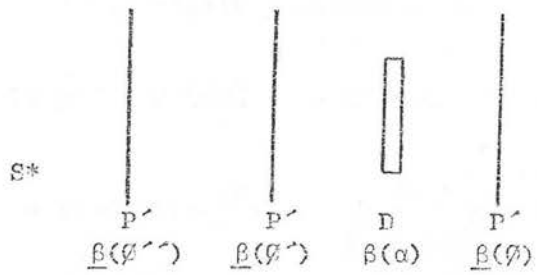

S - unpolarized source

P´- partial polarizer

D - partial polarizer and retarder

$$\begin{pmatrix} I^* \\ Q^* \\ U^* \\ V^* \end{pmatrix} = \{P'\}\{D\}\{P'\}\{P'\} \begin{pmatrix} I \\ 0 \\ 0 \\ 0 \end{pmatrix}$$

Using (A7) and (A11),

$$\begin{pmatrix} I^* \\ Q^* \\ U^* \\ V^* \end{pmatrix} =$$

$$\frac{1}{16}\begin{pmatrix} \underline{a}\underline{a}+\underline{b}\underline{b}C & \underline{a}\underline{b}c'+\underline{b}(ac'C-u's'S) & \underline{a}\underline{b}s'+\underline{b}(as'C+u'c'S) & \underline{b}v'S \\ . & . & . & . \\ . & . & . & . \\ 0 & . & . & . \end{pmatrix}$$

$$\times\begin{pmatrix} \underline{a}^2+\underline{b}^2C' & . & . & . \\ \underline{a}\underline{b}c(1+C')+\underline{e}\underline{b}sS & . & . & . \\ \underline{a}\underline{b}s(1+C')-\underline{e}\underline{b}cS & . & . & . \\ 0 & . & . & . \end{pmatrix} \qquad (B8)$$

where $C' = \cos 2(\phi'-\phi'')$, $S' = \sin 2(\phi'-\phi'')$, $C = \cos 2(\phi-\alpha)$, $S = \sin 2(\phi-\alpha)$, $c = \cos 2\phi''$, $s = \sin\phi''$, $c' = \cos 2\alpha$, $s' = \sin 2\alpha$.

a) If $\phi'' = \phi'$, $\rightarrow C' = 1$, $S' = 0$

$$\frac{16I^*}{\underline{a}^3 a I} = (1+\beta\underline{\beta}C)+2\underline{\beta}\left\{(\beta c+\underline{\beta}cC-\gamma sS\underline{\beta})\cos 2\phi'+(\beta s+\underline{\beta}sC+\gamma cS\underline{\beta})\sin 2\phi'\right\}$$

$$= (1+2\beta\underline{\beta}\cos 2(\phi''-\alpha))+\underline{\beta}(\beta+2\underline{\beta}\cos 2(\phi''-\alpha))\cos 2(\phi-\alpha)$$

$$+ 2\gamma\underline{\beta}^2\sin 2(\phi''-\alpha)\sin 2(\phi-\alpha) \qquad (B9)$$

b) If $\phi'' = \phi' \pm 90^\circ$ $\rightarrow C' = -1$, $S' = 0$

$$\frac{16I^*}{\underline{a}^3 a I} = (1+\beta\underline{\beta}C)(1-\underline{\beta}^2) \; ; \quad \frac{16I^*}{\underline{a}^3 a I(1-\underline{\beta}^2)} = 1+\beta\underline{\beta}\cos 2(\phi-\alpha) \qquad (B10)$$

APPENDIX C

The coefficients of the least squares fit to the instrumental test scans are derived, and from them the 21 instrumental parameters of the telescope and polarimeter. The function of interest is $I(\phi) = K(1+A_2\cos2(\phi-\alpha)+B_2\sin2(\phi-\alpha))$ and the coefficients fitted are A_2 and B_2.

(i) Assume a perfect analyzer. This assumption is accurate to <0.1% in the J and H wavebands. Using (B1),

$$I(\phi) = (1+\beta\cos2(\phi-\alpha))(1+\beta'\cos2(\phi-\omega)) \qquad (B1)$$

Giving,

$$I(\phi) = (1+\frac{\beta\beta'}{2}\cos2(\alpha-\omega))+(\beta\cos2\alpha+\beta'\cos2\omega)\cos2\phi$$

$$+(\beta\sin2\alpha+\beta'\sin2\omega)\sin2\omega$$

Fit this function by $I(\phi) = 1+A_2\cos2\phi+B_2\sin2\phi$,

$$A_2 = \frac{\beta\cos2\alpha+\beta'\cos2\omega}{1+\frac{\beta\beta'}{2}\cos2(\alpha-\omega)} \quad , \quad B_2 = \frac{\beta\sin2\alpha+\beta'\sin2\omega}{1+\frac{\beta\beta'}{2}\cos2(\alpha-\omega)} \qquad (C1)$$

It is known that $\beta < 1$ and $\beta' \ll 1$, therefore $\beta\beta'/2 \ll 1$. For photometer cage in first position,

$$A_2^{(1)} = \beta\cos2\alpha+\beta'\cos2\omega \quad , \quad B_2^{(1)} = \beta\sin2\alpha+\beta'\sin2\omega \qquad (C2)$$

Rotating by 90°, $\omega \rightarrow \omega \pm 90^\circ$,

$$A_2^{(2)} = \beta\cos2\alpha- \beta'\cos2\omega \quad , \quad B_2^{(2)} = \beta\sin2\alpha-\beta'\sin2\omega \qquad (C3)$$

Therefore,

$$\beta'_{J,H} = \tfrac{1}{2}\left\{(A_2^{(1)}-A_2^{(2)})^2 + (B_2^{(1)}-B_2^{(2)})^2\right\}^{\frac{1}{2}} \qquad (C4)$$

and

$$\omega_{J,H} = \tfrac{1}{2}\arctan\left\{(B_2^{(1)}-B_2^{(2)})/(A_2^{(1)}-A_2^{(2)})\right\} \qquad (C5)$$

For a partial polarizer measured in the K waveband, the appropriate equation is (B6) with p replaced by β' and θ replaced by ω,

$$I(\phi) = (1+\beta'\underline{\beta}\cos2(\phi-\omega))+\beta(\underline{\beta}+\beta'\cos2(\phi-\omega))\cos2(\phi-\alpha)$$

$$+\sqrt{1-\underline{\beta}^2}\,\beta\beta'\sin2(\phi-\omega)\sin2(\phi-\alpha) \qquad (C6)$$

It can be seen that if $\underline{\beta} = 1$, (C6) reduces to (E1).

(ii) For either the {P'}{D} or {D}{P'} configuration, from (B2),

$$I(\phi) = 1+\underline{\beta}\beta\cos2\alpha\cos2\phi+\underline{\beta}\beta\sin2\alpha\sin2\phi \qquad (C7)$$

Fit this function by $I(\phi) = 1+A_2\cos2\phi+B_2\sin2\phi$,

$$A_2 = \underline{\beta}\beta\cos2\alpha, \qquad B_2 = \underline{\beta}\beta\sin2\alpha \qquad (C8)$$

Therefore,

$$\beta_{J,H,K} = \sqrt{A_2^2+B_2^2}/\underline{\beta}_{J,H,K} \qquad (C9)$$

$$\alpha_{J,H,K} = \tfrac{1}{2}\arctan\,(B_2/A_2) \qquad (C10)$$

(iii) From (B4),

$$I(\phi) = (1+\beta\underline{\beta}\cos2(\phi'-\alpha))+\underline{\beta}(\beta+\underline{\beta}\cos2(\phi'-\alpha))\cos2(\phi-\alpha)$$

$$+\gamma\underline{\beta}^2\sin2(\phi'-\alpha)\sin2(\phi-\alpha)$$

Fit this function by $I(\phi) = 1+A_2\cos2(\phi-\alpha)+B_2\sin2(\phi-\alpha)$,

$$A_2 = \frac{\underline{\beta}(\beta+\underline{\beta}\cos2(\phi'-\alpha))}{(1+\beta\underline{\beta}\cos2(\phi'-\alpha))}, \qquad B_2 = \frac{\gamma\underline{\beta}^2\sin2(\phi'-\alpha)}{(1+\beta\underline{\beta}\cos2(\phi'-\alpha))} \qquad (C11)$$

Therefore,

$$\gamma_{J,H,K} = \left(\frac{B_2}{A_2}\right)\frac{(\beta+\underline{\beta}\cos 2(\phi'-\alpha))}{\underline{\beta}\sin 2(\phi'-\alpha)} \qquad (C12)$$

(iv) From (B5),

$$I(\phi) = (1+\beta\underline{\beta}\cos 2(\phi'-\alpha))+\underline{\beta}(\underline{\beta}+\beta\cos 2(\phi'-\alpha))\cos(\phi'-\phi)$$

$$+\gamma\beta\underline{\beta}\sin 2(\phi'-\alpha)\sin 2(\phi'-\phi)$$

Fit this function by $I(\phi) = 1+A_2\cos 2(\phi'-\phi)+B_2\sin 2(\phi'-\phi)$,

$$A_2 = \frac{\underline{\beta}(\underline{\beta}+\beta\cos 2(\phi'-\alpha))}{(1+\beta\underline{\beta}\cos 2(\phi'-\alpha))} \quad , \quad B_2 = \frac{\gamma\beta\underline{\beta}\sin 2(\phi'-\alpha)}{(1+\beta\underline{\beta}\cos 2(\phi'-\alpha))} \qquad (C13)$$

Therefore,

$$\underline{\beta}_{J,H,K} = \frac{\beta\cos 2(\phi'-\alpha) \pm \{\beta^2\cos^2(\phi'-\alpha)-4A_2\}^{\frac{1}{2}}}{2} \qquad (C14)$$

As a check, from (C11) at maximum of curve where $\sin 2(\phi'-\alpha) = 1$,

$$\underline{\beta}_{J,H,K} = \sqrt{B_2/\gamma_{J,H,K}} \qquad (C15)$$

(v) From (B6),

$$I(\phi) = (1+p\underline{\beta}\cos 2(\phi-\theta))+\beta(\underline{\beta}+p\cos 2(\phi-\theta))\cos 2(\phi-\alpha)$$

$$+ \sqrt{1-\underline{\beta}^2}\,\beta p\sin 2(\phi-\theta)\sin 2(\phi-\alpha)$$

Expanding into terms in 2ϕ and 4ϕ,

$$I(\phi) = 1+p\underline{\beta}\cos 2(\phi-\theta)+\beta\underline{\beta}\cos 2(\phi-\alpha)+\frac{\beta p}{2}(1+\sqrt{1-\underline{\beta}^2})\cos 2(\alpha-\theta) + \text{order } (4\phi) \qquad (C16)$$

Modulation at 4ϕ is aliassed by the sampling interval (45°), so fit this function by $I(\phi) = 1+A_2\cos 2\phi+B_2\sin 2\phi$,

$$A_2 = \frac{\underline{\beta}(p\cos 2\theta + \beta\cos 2\alpha)}{1+\frac{\beta p}{2}(1+\sqrt{1-\underline{\beta}^2})\cos 2(\alpha-\theta)} \quad , \quad B_2 = \frac{\underline{\beta}(p\sin 2\theta + \beta\sin 2\alpha)}{1+\frac{\beta p}{2}(1+\sqrt{1-\underline{\beta}^2})\cos 2(\alpha-\theta)} \tag{C17}$$

Let $p\cos 2\theta = p_1$, $\beta\cos 2\alpha = \beta_1$, $\frac{1+\sqrt{1-\underline{\beta}^2}}{2} = R$

$p\sin 2\theta = p_2$ $\beta\sin 2\alpha = \beta_2$

$$A_2 = \frac{\underline{\beta}(p_1+\beta_1)}{1+R(p_1\beta_1+p_2\beta_2)} \quad , \quad B_2 = \frac{\underline{\beta}(p_2+\beta_2)}{1+R(p_1\beta_1+p_2\beta_2)} \tag{C18}$$

Solving for the object's Stokes parameters,

$$p_1 = \frac{A_2-\beta_1\underline{\beta} - \frac{R\beta_2}{2}(A_2\beta_2-B_2\beta_1)}{(\underline{\beta} - \frac{R}{2}(B_2\beta_2+A_2\beta_1))} \qquad p_2 = \frac{B_2-\beta_2\underline{\beta} - \frac{R\beta_1}{2}(B_2\beta_1-A_2\beta_2)}{(\underline{\beta} - \frac{R}{2}(B_2\beta_2+A_2\beta_1))} \tag{C19}$$

Therefore,

$$p = \sqrt{p_1^2+p_2^2} \tag{C20}$$

$$\theta = \tfrac{1}{2}\arctan(p_2/p_1) \tag{C21}$$

(vi) From (B7)

$$I(\phi) = (1+\beta p\cos 2(\theta-\alpha)) + \underline{\beta}(\beta+p\cos 2(\theta-\alpha))\cos 2(\phi-\alpha) + \gamma p\underline{\beta}\sin 2(\theta-\alpha)\sin 2(\phi-\alpha)$$

Fit this function by $I(\phi) = 1+A_2\cos 2(\phi-\alpha)+B_2\sin 2(\phi-\alpha)$,

$$A_2 = \frac{\underline{\beta}(\beta+p\cos 2(\theta-\alpha))}{(1+\beta p\cos 2(\theta-\alpha))} \quad , \quad B_2 = \frac{\gamma p\underline{\beta}\sin 2(\theta-\alpha)}{(1+\beta p\cos 2(\theta-\alpha))} \tag{C22}$$

If the object has a known polarization

$$\gamma_{J,H,K} = \frac{B_2(1+\beta p\cos 2(\theta-\alpha))}{p\underline{\beta}\sin 2(\theta-\alpha)} \tag{C23}$$

Let $p_1 = p\cos 2(\theta-\alpha)$,

$p_2 = p\sin 2(\theta-\alpha)$

$$p_1 = \frac{A_2-\underline{\beta}\beta}{(\underline{\beta}-A_2\beta)} \quad , \quad p_2 = \frac{B_2(1-\beta^2)}{\gamma(\underline{\beta}-A_2\beta)} \tag{C24}$$

Hence, $$p = \sqrt{p_1^2 + p_2^2} \tag{C25}$$

$$\theta = \tfrac{1}{2}\arctan(p_2/p_1) + \alpha \tag{C26}$$

(vii) From (B9),

$$I(\phi) = (1+2\beta\underline{\beta}\cos 2(\phi'-\alpha))+\underline{\beta}(\beta+2\underline{\beta}\cos 2(\phi'-\alpha))\cos 2(\phi-\alpha)$$

$$+ 2\gamma\underline{\beta}^2\sin 2(\phi'-\alpha)\sin 2(\phi-\alpha)$$

Fit this function by $I(\phi) = 1+A_2\cos 2(\phi-\alpha)+B_2\sin 2(\phi-\alpha)$,

$$A_2 = \frac{\underline{\beta}(\beta+2\underline{\beta}\cos 2(\phi'-\alpha))}{(1+2\beta\underline{\beta}\cos 2(\phi'-\alpha))} \quad , \quad B_2 = \frac{2\gamma\underline{\beta}^2\sin 2(\phi'-\alpha)}{(1+2\beta\underline{\beta}\cos 2(\phi'-\alpha))} \tag{C27}$$

Therefore,

$$\gamma_{J,H,K} = \left(\frac{B_2}{A_2}\right)\frac{(\beta+2\underline{\beta}\cos 2(\phi'-\alpha))}{2\beta\sin 2(\phi'-\alpha)} \tag{C28}$$

APPENDIX D

The dichroic mirror used in these observations was manufactured by OCLI Laboratory Inc. with the specification of reflecting infrared radiation longward of 1μm and transmitting visible light to the T.V. System. Such a device is conventionally called a "hot mirror". The dichroic consists of a glass substrate vacuum deposited with 20nm of Silver and then coated with an optical anti-reflection coating. The mechanism of interest is therefore metallic reflection. In general, electromagnetic radiation reflecting from a metal will suffer amplitude attenuation and a relative phase change between the E vectors parallel and perpendicular to the surface. These two quantities are similar to the partial polarizance and retardance introduced by the reflection, and the two parameters are highly sensitive to the thickness and composition of the reflecting surface and the frequency of the incident light. In fact, the whole field of Ellipsometry exists to probe the properties of thin films by their polarizing characteristics. There are extra complications because of the fact that the film may not be uniform or pure. Visual inspection of the UKIRT dichroic shows it to have a mottled appearance possibly caused by oxidation from the anti-reflection coating material. Imperfect as the dichroic is, it is important to have a theoretical expectation of its properties as well as measuring them on the telescope.

Electromagnetic radiation in a conductor propagates according to the following wave equation

$$\nabla^2 \underline{E} = \varepsilon\mu \frac{\delta^2 E}{\delta t^2} + \sigma\mu \frac{\delta E}{\delta t} \qquad (D1)$$

where the two terms represent wave propagation and diffusion in the material. The attenuation of the transmitted wave generates Joule heating in the conductor. For a wave travelling in the z direction a solution is,

$$\underline{E} = E_o \exp(i(wt+\delta-\alpha z))\exp(-\beta z) \qquad (D2)$$

where ε,μ are permettivity, permeability of incident medium

β is the damping constant

α is the wave vector

and it can be shown that,

$$k^2 = \omega^2 \varepsilon\mu\left(1 + \frac{i\sigma}{\omega\varepsilon}\right) \tag{D3}$$

or

$$k = \alpha + i\beta \tag{D4}$$

The complex refractive index indicates the attenuation of the wave. In eqn. (D4), β represents the damping constant or distance into the material when the amplitude of the E vector falls by e^{-1}, and α is the wave vector representing the phase velocity of the wave. Metals (and semiconductors) have a lattice of fixed ions and electrons and a freely circulating population of conduction electrons. Two assumptions can be made about the motion of these electrons under the application of an external field. First, the resonant frequency of the bound electrons lies far into the ultraviolet so the refractive index for these electrons is near unity and their contribution to the dispersion relation can be ignored. Second, for a good conductor the conduction current is much larger than the displacement current and the diffusion part of the wave equation dominates.

$$\frac{\underline{J}}{\delta\underline{D}/\delta t} >> 1 \qquad (\underline{J} = \sigma\underline{E}, \quad \underline{D} = \varepsilon\underline{E}) \tag{D5}$$

Therefore,

$$\left|\frac{i\sigma}{\omega\varepsilon}\right| >> 1 \tag{D6}$$

Substituting into (D3),

$$k = (1+i)\sqrt{\frac{\omega\mu\sigma}{2}} \tag{D7}$$

Thus

$$\alpha = \beta = \frac{1}{\delta} = \sqrt{\frac{\sigma\omega\mu}{2}} \tag{D8}$$

Where δ is the characteristic penetration distance of the wave into the conductor, known to electrical engineers as the "skin depth". Since $\alpha/\beta \sim 1$, the wave falls off to e^{-1} of its initial amplitude in a fraction of a wavelength and can hardly be called a wave at all. In the conductor,

$$\tan \delta = \frac{\beta}{\alpha} = 1 \; ; \quad \delta = \pi/4 \tag{D9}$$

Therefore $\underline{E}$ and $\underline{H}$ are out of phase by 45°, in contrast to a good dielectric or a vacuum when $\underline{E}$ and $\underline{H}$ are in phase. At high frequencies, ω, σ and ϵ are functions of frequency and this must be taken into account.

The action of conduction in metals can be understood in terms of the simple Drude model, which describes the way conduction electrons move under an applied electric field. The acceleration due to the field is balanced by collisions with lattice ions at a rate of v per second, where v is the electron velocity. This leads to an equation of motion,

$$\frac{d^2\underline{s}}{dt^2} + v\frac{d\underline{s}}{dt} = \frac{q}{m_e}\underline{\varepsilon} \tag{D10}$$

Solution of (D10) gives a conductivity,

$$\sigma(\omega) = \frac{Nq^2}{m_e}\frac{1}{(v+i\omega)} \qquad (\text{ohm-m})^{-1} \tag{D11}$$

The low frequency behaviour shows that σ is independent of frequency. For silver, $v \sim 3 \times 10^{12}$ sec^{-1} so the layer exhibits real conductivity for frequencies below $\sim 2 \times 10^{12}$ Hz, which is in the far infrared. In the near infrared and visible regions, $\omega >> v$ giving

$$\sigma(\omega) = \frac{-iNq^2}{m_e\omega} \qquad (\text{ohm-m})^{-1} \tag{D12}$$

Inserting this into dispersion relation (D2),

$$k^2c^2 = \omega^2 - \frac{Nq^2}{m_e\varepsilon} = \omega^2 - \omega_p^2 \tag{D13}$$

where $\omega_p = \sqrt{Nq^2/m_e\varepsilon}$

ω_p is the plasma frequency, and plays a role similar to the cut-off frequency for propagation in a waveguide. For silver, $\omega_p/2\pi = 2.2 \times 10^{15}$ Hz corresponding to $\lambda_p = 2\pi C_p/\omega_p = 139$nm. At frequencies $\omega > \omega_p$, the metal transmits free waves without attenuation and acts like a transparent dielectric rather than a mirror. In the range $\nu << \omega < \omega_p$ (which contains the near infrared/optical region), the phase velocity $v = \omega/k$ goes to infinity, the group velocity $V_g = \delta\omega/\delta k$ goes to zero and waves do not propagate. The wave is cut-off and the electric and magnetic fields decay exponentially with distance from the surface; there is no energy transmission. In the third regime, $\omega >> \nu$, the wave is damped but does have an oscillatory component. Therefore, in the near infrared/optical bands, Drude theory predicts no transmission of EM waves through silver and the action of the dichroic as a "hot mirror" must be understood in terms of the thickness of the silver coating (see Fig. D.1).

In the optical/infrared regions, silver has a D.C. conductivity of $\sigma = 6.14 \times 10^7$ $(\text{ohm.m})^{-1}$. For the wavelengths of interest, we can calculate the skin depth δ, and tabulate the ratio of skin depth to film thickness (t) and hence the proportion of light transmitted at that wavelength,

λ	δ	δ/t	t/δ	$T(\lambda)$
0.5μm	20nm	1.0	1.0	0.36
1.0μm	29nm	1.5	0.67	0.23
2.0μm	41nm	2.1	0.48	0.13
3.0μm	50nm	2.5	0.40	0.02

The intensity of transmitted radiation is determined by the amplitude of the exponentially decaying amplitude after a thickness t = 20nm of silver. As the wavelength of radiation increases, the ratio of thickness to skin depth increases and the film behaves more and more like a perfect reflector. Over the range of the J, H and K wavebands, the dichroic is 70%-80% efficient at reflecting the infrared radiation. This reflectivity is sensitive to thickness variations across the film. The antireflection coating is tuned to 550nm, so that very little optical radiation is reflected by the dichroic.

The reflection coefficients for waves incident on metal are given by,

$$r_s = \frac{-k_2\cos\theta_i - k_1\cos\theta_t}{k_2\cos\theta_i + k_1\cos\theta_t} \tag{D14}$$

$$r_p = \frac{k_1\cos\theta_i - k_2\cos\theta_t}{k_1\cos\theta_i + k_2\cos\theta_t} \tag{D15}$$

where θ_i, θ_t are incident and transmitted angles

k_1, k_2 are reflection indices of incident and transmitting media.

As has been shown, k_2 is complex therefore θ_t will be complex. In addition to the Fresnel equation, Snell's Law defines a relationship between θ_t and θ_i,

$$\frac{\sin\theta_i}{\sin\theta_t} = \frac{k_1}{k_2} \tag{D16}$$

The parallel (r_s) and perpendicular (r_p) components are therefore reflected with a phase difference between them not generally equal to 0 or $\pi/2$, given by

$$r_s = |r_s| e^{i\delta_s} \tag{D17}$$

$$r_p = |r_p| e^{i\delta_p} \tag{D18}$$

and the intensity reflection coefficients are given by,

$$R_{s,p} = r_{s,p}\, r_{s,p}^* \tag{D19}$$

If k_0 is the refractive index of the incident medium, and $k_1 = \alpha + i\beta$ is the complex refractive index of the metal, then

$$R_s = \frac{(\alpha - k_1/\cos\theta_i)^2 + \beta^2}{(\alpha + k_1/\cos\theta_i)^2 + \beta^2} \tag{D20}$$

$$R_p = \frac{(\alpha - k_1\cos\theta_i)^2 + \beta^2}{(\alpha + k_1\cos\theta_i)^2 + \beta^2} \tag{D21}$$

For the thin anti-reflection coating made of MgF_2, $k_1 = 1.6$; and $\theta_i = 45^o$. For Silver, $\alpha = 0.177$ and $\beta = 20.65$, confirming the approximation $\beta >> \alpha$ as a good conductor (@ λ5893). These curves are shown in Figure B.2.

$$\therefore \quad R_s = 0.9963, \quad R_p = 0.9931 \rightarrow \beta_{in} = \frac{R_p - R_s}{R_p + R_s} \tag{D22}$$

However, the so-called optical constants in fact vary with frequency, so for silver at 2.0μm, $\alpha = 2.3$ and $\beta = 16.5$.

$$R_s = 0.9530, \quad R_p = 0.9760$$

$$\therefore \beta_{in} = 0.012 = 1.2\% \tag{D23}$$

This is an estimate of the instrumental polarization due to the dichroic reflection. The position angle of this linear polarization is given by the component perpendicular to the plane of incidence, which corresponds to the E-W line on the dichroic as it is mounted in the telescope. Therefore, if the dichroic is chopping N-S, the position angle in the sky frame of reference will be,

$$\alpha = 90^o \tag{D24}$$

To calculate the third parameter, the retardance, use Abelès' method to define effective indices for the absorbing material,

$$\eta_{2s} = a - ib \tag{D25}$$

$$\eta_{2p} = c - id \tag{D26}$$

where,

$$a^2 - b^2 = \alpha^2 - \beta^2 - k_1^2\sin^2\theta_i \tag{D27}$$

$$ab = \alpha\beta \tag{D28}$$

$$c = a(1 + k_1^2\sin^2\theta_i/(a^2 + b^2)) \tag{D29}$$

$$d = b(1 - k_1^2\sin^2\theta_i/(a^2 + b^2)) \tag{D30}$$

For the incident, dielectric medium define

$$\eta_{1s} = k_1 \mathrm{Cos}\theta_i \tag{D31}$$

$$\eta_{1p} = k_1 / \mathrm{Cos}\theta_i \tag{D32}$$

It follows that,

$$r_s = \frac{\eta_{1s} - \eta_{2s}}{\eta_{1s} + \eta_{2s}}$$

$$r_p = \frac{\eta_{1p} - \eta_{2p}}{\eta_{1p} + \eta_{2p}} \tag{D34}$$

From (D34),

$$\tan\delta_s = \frac{2\eta_{1s} b}{\eta_{1s}^2 - a^2 - b^2} \tag{D35}$$

$$\tan\delta_p = \frac{-2\eta_{1p} d}{c^2 + d^2 - \eta_{1p}^2} \tag{D36}$$

where a,b,c and d are defined by (D27)-(D30) and eqn. (D36) holds for non-normal incidence. $(\delta_p - \delta_s)$ can be estimated graphically to be $\sim 20^\circ$ (Fig. D.3).

$$\therefore \gamma = \sqrt{1-\beta^2}\, \cos(\delta_p - \delta_s) \approx 0.966 \tag{D37}$$

Equations (D23), (D24) and (D37) give expectation values for the instrumental parameters β_{in}, α and γ assuming that the dichroic is a perfectly uniform dielectric-metal layer on a glass substrate and assuming that the silver coating behaves like a vacuum-evaporated film. The parameters have been calculated for radiation at 2.0μm, but the wavelength dependence of β_{in} and γ can be estimated. From (D4), α is the wave vector of the oscillating part of the wave, and for shorter wavelengths α increases and β_{in} will increase as calculated in (D22). Therefore, the instrumental polarization is expected to increase towards shorter wavelengths. The metal behaves more like a dielectric at lower frequencies (i.e. α increasing corresponds to α/β increasing $\equiv \frac{\delta D}{\delta t} / J$ increasing), therefore the deviation of the graph of $(\delta_p - \delta_s)$ vs. θ_i from the dielectric case will be smallest for short wavelengths.

Therefore γ will decrease at shorter wavelengths, but because of the contribution of α in equations (D27)-(D30) γ is only very weakly wavelength dependent from 1-2 microns.

The assumption that the metallic film is a uniform, unblemished layer of silver is likely to be the most serious deviation of this discussion from the properties of the actual dichroic. After a period of time in air, a thin oxide film 20-25 $\mathring{A}$ thick will grow on a fresh aluminium surface. Although the silver in this case is protected by a dielectric anti-reflection coating, the degree of exposure and age of the dichroic material make it likely that an oxide layer is responsible for the mottled appearance. The simplest way to model an imperfect dichroic is to consider that surface blemishes will make the film behave less like a pure metal. Impurities in a conductor will lower the conductivity by providing impedence to the passage of free electrons. The difference between the "perfect" and "real" dichroics can be modelled as a change in σ, decreasing to σ'.

From (D3) and (D4),

$$k'^2 = \omega^2 \varepsilon\mu\left(1 + \frac{i\sigma'}{\omega\varepsilon}\right), \quad k' = \alpha + i\beta' \qquad (D32)$$

where $\beta' < \beta$

In equations (D20), (D21) as β'/α decreases β_{in} increases. The dichroic acts more like a poor conductor and the instrument polarisation rises because of the larger difference between R_s and R_p. Once again, γ is relatively insensitive to changes in β', but decreases slowly as β' increases. Numerically, with $k_1 = 1.6$, $\theta_i = 45^o$, $\alpha_o = 2.3$ and $\beta_o = 16.5$,

α	β'	$(\delta_p - \delta_s)$
α_o	β_o	15^o
$\alpha_{o/2}$	β_o	18^o
$2\alpha_o$	β_o	18^o
α_o	$\beta_{o/2}$	13^o
α_o	$2\beta_o$	21^o

To summarize, the dichroic mirror can be considered to be an imperfect metallic reflector. The instrumental linear polarization is expected to be only a few percent, at a position angle of 90° in the sky frame. The values of β and α can be measured by observing an unpolarized star. The retardance is predicted to be 10°-20°, and because $\gamma \propto \cos(\delta_p - \delta_s)$, γ is relatively insensitive to changes of a few degrees in δ. Over the range of values of α and β calculated above, γ only varies by ~3% and because it is a multiplicator factor on the $\sin 2(\beta-\alpha)$ term of eqn. (C22) the calculated polarization will be affected by <1%. Only a small amount of demodulation of the $\sin 2(\beta-\alpha)$ term is predicted because $\gamma \sim 1$.

References

Bennett, J.M. & Bennett, H.E. (1978). Handbook of Optics (McGraw-Hill), 10.

Born, M. & Wolfe, E. (1959). Principles of Optics (Pergamon Press), 612.

Burge, D.K. & Bennett, H.E. (1964). J.Opt.Soc.Am. 54, 1428.

Haas, G. & Hadley, L.N. (1972). American Institute of Physics Handbook (McGraw-Hill), 6,

Hadley, L.N. & Dennison, D.M. (1947). J.Opt.Soc.Am. 37, 451.

Hadley, L.N. & Dennison, D.M. (1948). J.Opt.Soc.Am. 38, 483.

Jackson, J.D. (1962). Classical Electrodynamics (Wiley and Sons).

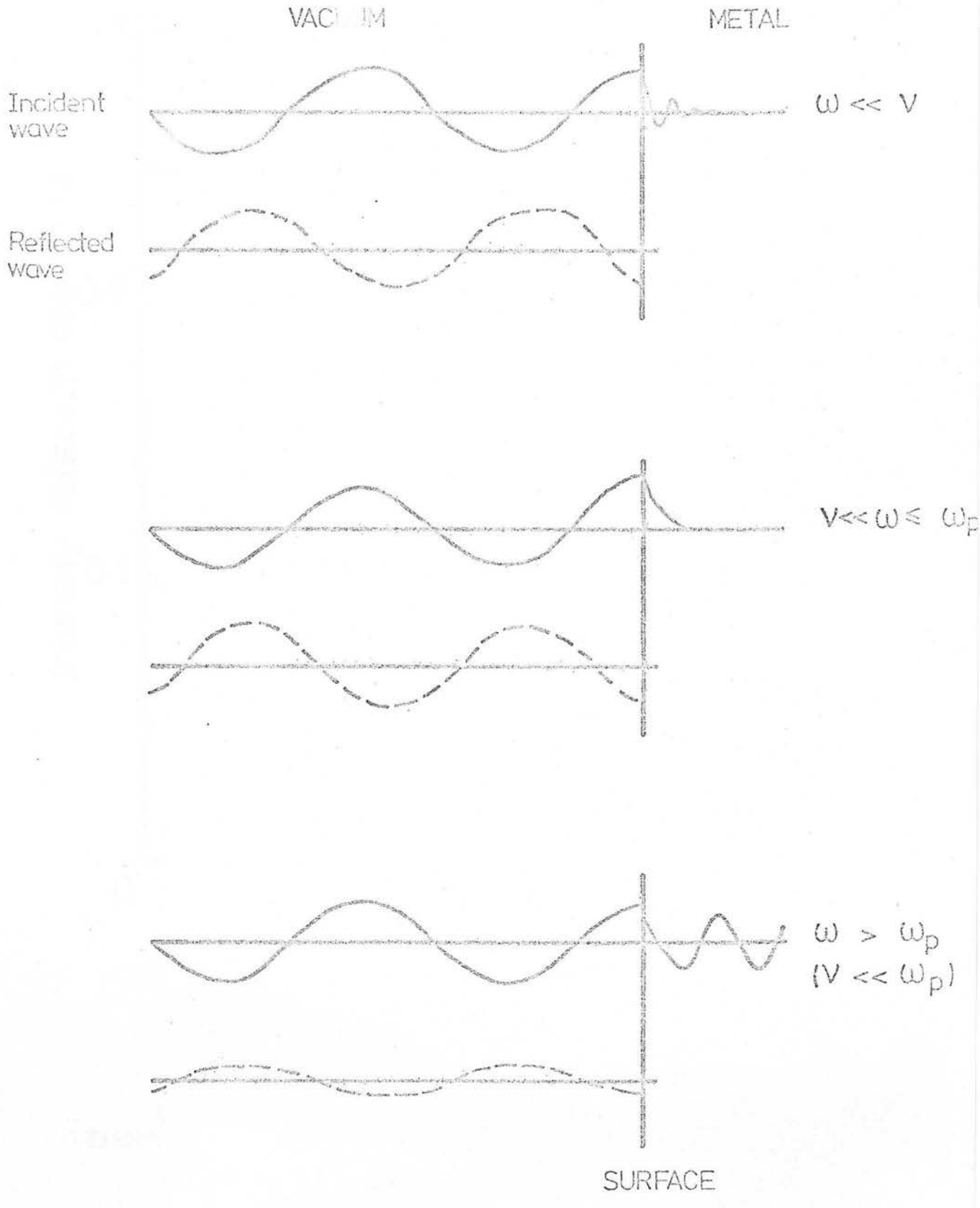

Figure D1. Behaviour of waves in a metal. When $\omega \ll \nu$, almost all of the energy is reflected (the transmitted component is dissipated as heat in electron-lattice ion collisions). When $\nu \ll \omega \lesssim \omega_p$ all the incident energy is reflected - there are exponentially decaying fields in the metal but no wave. When $\omega > \omega_p$ the metal is transparent and behaves like a good dielectric.

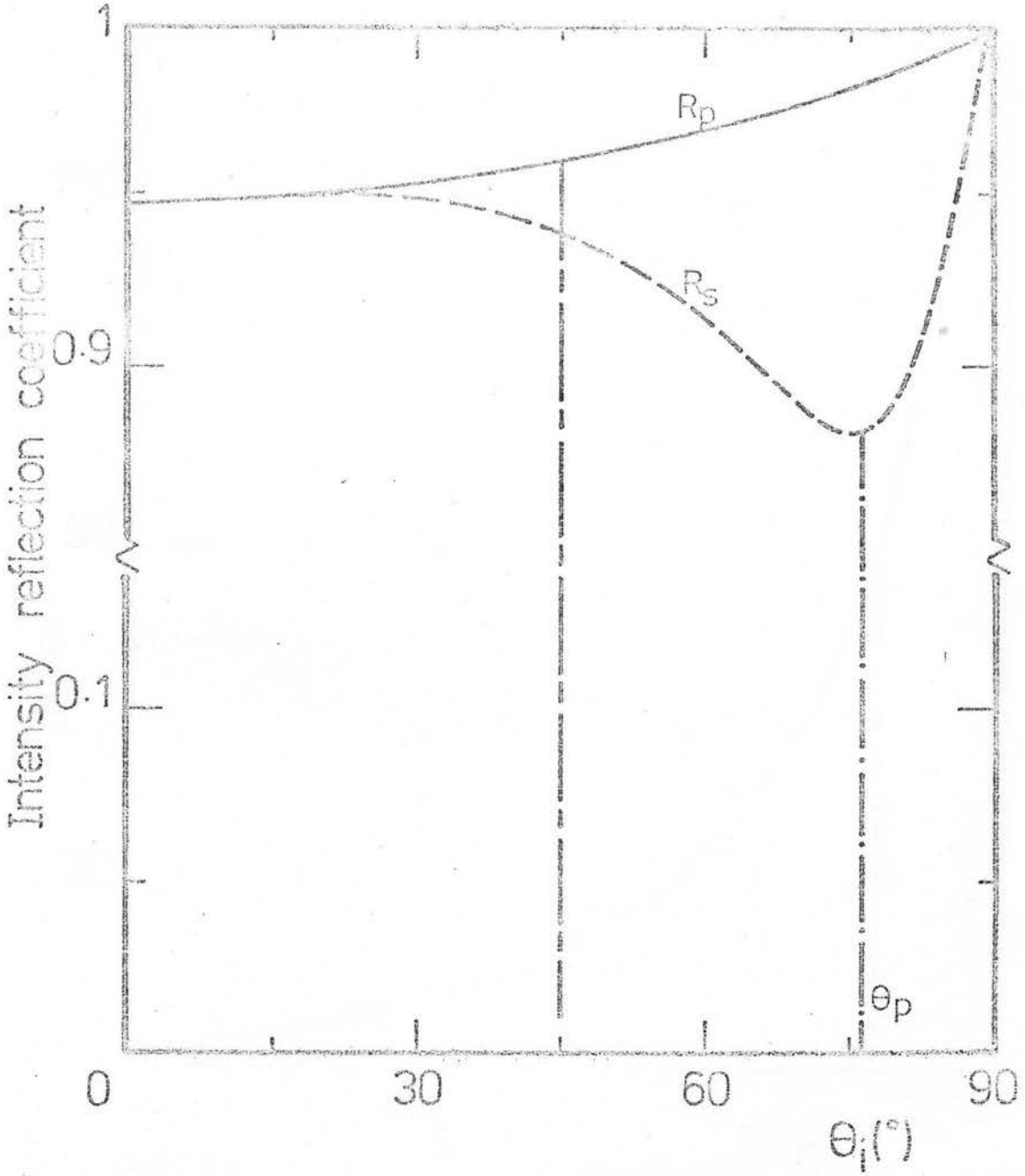

Figure D2. Variation of intensity reflection coefficients with angle of incidence for a conductor (drawn for Silver at 2.0μm with α=2.3, β=16.5 and θ_p=75.6°).

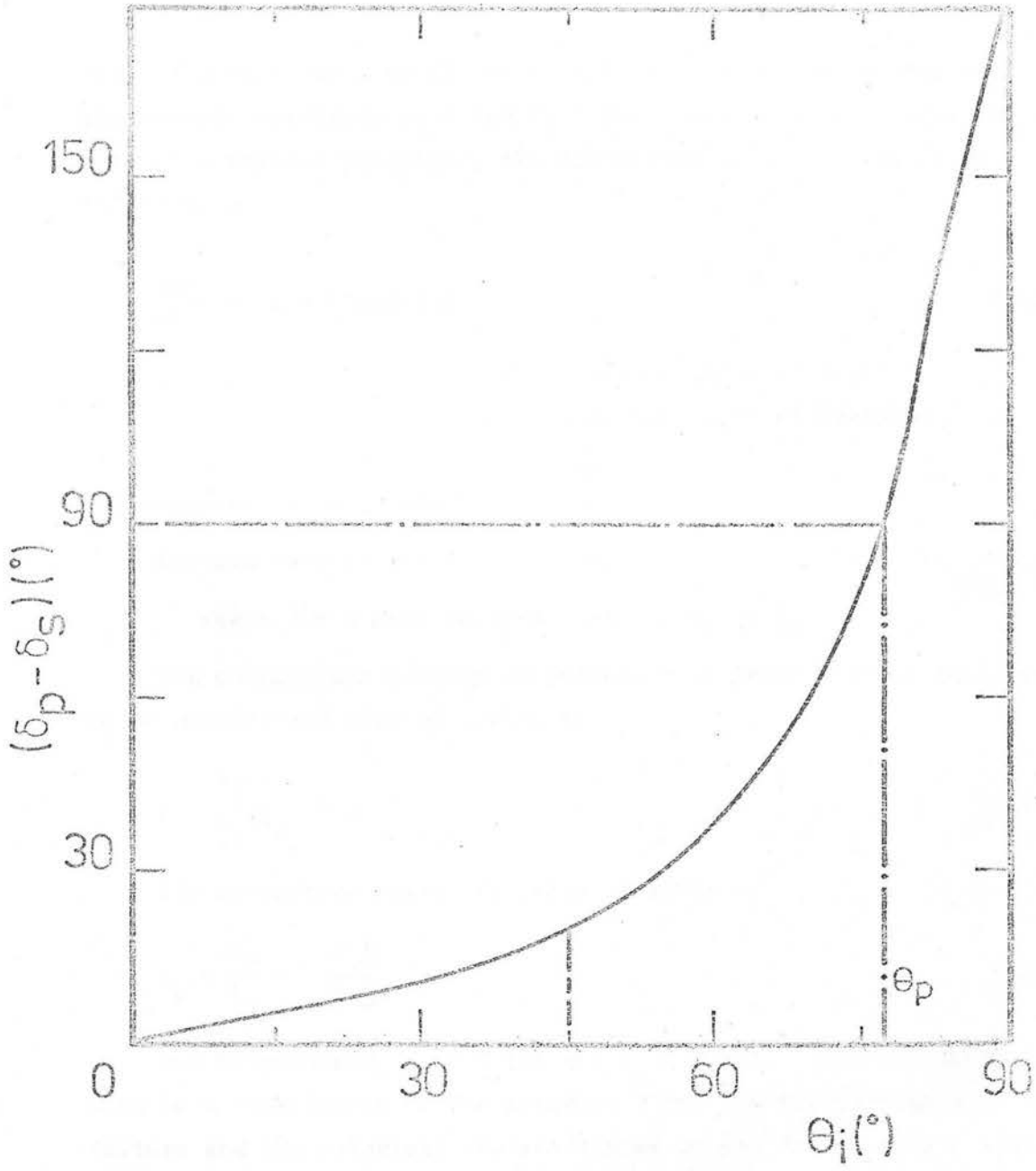

Figure D3. Variation of phase change of reflected wave with angle of incidence for a conductor (drawn for Silver at 2.0μm with α=2.3, β=16.5 and θ_p=75.6).

APPENDIX E

(i) The efficiency of HR polaroid is calculated in each of the photometric wavebands J, H and K. For plane polarized light incident on a partial polarizer, the transmitted intensity is given by Malus' Law,

$$\frac{dI^*}{a\underline{l}} = 1 + \underline{\beta}\text{Cos}2(\theta-\phi) \tag{E1}$$

θ - position angle of light

ϕ - position angle of analyzer

$\underline{\beta}$ - $\underline{b/a}$

Maximum transmittance = $1+\underline{\beta} = k_1$

Minumum transmittance = $1-\underline{\beta} = k_2$

where for a near perfect analyzer $k_1 >> k_2$.

The polarizance (degree of polarization introduced by analyzer in an unpolarized beam of light) is

$$p = \frac{k_1-k_2}{k_1+k_2} = \underline{\beta} \tag{E2}$$

The extinction ratio (Fig. E1) is given by

$$\rho_p = \frac{k_2}{k_1} = \frac{1-\underline{\beta}}{1+\underline{\beta}} \tag{E3}$$

For HR polaroid, $k_1 = f_1(\lambda)$ and $k_2 = f_2(\lambda)$. The transmitted flux is a convolution of the incident flux, the transmittance of the filters and the principal transmittances of the analyzer as a function of wavelength.

$$\begin{pmatrix} I^*(\lambda) \\ Q^*(\lambda) \\ U^*(\lambda) \\ V^*(\lambda) \end{pmatrix} = I(\lambda) \begin{pmatrix} \underline{a} \\ \underline{bc} \\ \underline{bs} \\ 0 \end{pmatrix} \tag{E4}$$

$$\therefore \quad I^*_{TOT}(\lambda) = \underline{a}(\lambda)I(\lambda) \ , \quad I^*_{POL}(\lambda) = \underline{b}(\lambda)I(\lambda) \tag{E5}$$

$$p^*(\lambda) = \frac{\underline{b}(\lambda)}{\underline{a}(\lambda)} = \underline{\beta}(\lambda) \tag{E6}$$

The measured polarization, $p_\lambda = T(\lambda)\underline{\beta}(\lambda)$

where $T(\lambda)$ is the filter transmission function.

$$\therefore I_p^*(\lambda) = \frac{\int_{\lambda_2}^{\lambda_1} T(\lambda)\underline{\beta}(\lambda)I(\lambda)\,d\lambda}{\int_{\lambda_2}^{\lambda_1} d\lambda} \qquad (E7)$$

where $0 < T(\lambda) < 1$

and $0 < \underline{\beta}(\lambda) < 1$

In series form,

$$I_p^*(\lambda) = \frac{1}{(\lambda_2-\lambda_1)}\left[T(\lambda_1)\underline{\beta}(\lambda_1)I(\lambda_1)\Delta\lambda + T(\lambda_1+\Delta\lambda)\underline{\beta}(\lambda_1+\Delta\lambda)I(\lambda_1+\Delta\lambda)\Delta\lambda + \ldots . T(\lambda_2)\underline{\beta}(\lambda_2)I(\lambda_2)\right]$$

Choose a resolution of $\Delta\lambda = 0.02\mu m$.

J			H			K		
$\lambda(\mu m)$	$\underline{\beta}$	T	$\lambda(\mu m)$	$\underline{\beta}$	T	$\lambda(\mu m)$	$\underline{\beta}$	T
1.04	0.997	0.005	1.38	0.9997	0.008	1.90	0.9987	0.005
1.06	0.998	0.07	1.42	0.9997	0.01	1.94	0.998	0.015
1.08	0.998	0.26	1.46	0.9997	0.03	1.98	0.998	0.20
1.10	0.998	0.50	1.50	0.9997	0.31	2.02	0.997	0.68
1.12	0.998	0.63	1.54	0.9997	0.62	2.06	0.996	0.73
1.14	0.998	0.70	1.58	0.9997	0.66	2.10	0.994	0.72
1.16	0.9987	0.71	1.62	0.9997	0.79	2.14	0.990	0.76
1.18	0.9990	0.66	1.66	0.9996	0.87	2.18	0.980	0.79
1.20	0.9992	0.70	1.70	0.9996	0.88	2.22	0.969	0.84
1.22	0.9994	0.74	1.74	0.9996	0.87	2.26	0.945	0.84
1.24	0.9994	0.65	1.78	0.9994	0.83	2.30	0.905	0.76
1.26	0.9995	0.77	1.82	0.9993	0.[illegible]	2.34	0.818	0.75
1.28	0.9995	0.80	1.86	0.9991	0.61	2.38	0.70	0.68
1.30	0.9996	0.70	1.90	0.9989	0.005	2.42	0.52	0.30
1.32	0.9996	0.49				2.46	0.332	0.03
1.34	0.9996	0.61						
1.36	0.9997	0.75						
1.38	0.9997	0.42						
1.40	0.9997	0.14						
1.42	0.9997	0.02						
1.44	0.9997	0.005						

The expectation value of $\underline{\beta}$,

$$\langle\underline{\beta}\rangle = \frac{\int_{\lambda_2}^{\lambda_1} T(\lambda)I(\lambda)\underline{\beta}(\lambda)d\lambda}{\int_{\lambda_2}^{\lambda_1} T(\lambda)I(\lambda)d\lambda} \approx \frac{\sum_{\lambda_2}^{\lambda_1} T(\lambda)I(\lambda)\underline{\beta}(\lambda)\Delta\lambda}{\sum_{\lambda_2}^{\lambda_1} T(\lambda)I(\lambda)\Delta\lambda} \tag{E8}$$

(a) $I(\lambda) = I_o$ (const.)

$$\langle\underline{\beta}\rangle_J = 0.9986, \quad \langle\underline{\beta}\rangle_H = 0.9996, \quad \langle\underline{\beta}\rangle_K = 0.916 \tag{E9}$$

The assumption of $\underline{\beta}_{J,H} = 1$ is valid to 0.1% for any incident flux distribution. At K, consider power law flux distributions also.

(b) $I(\lambda) = I_o\nu^{-\alpha} = I_o(\frac{\lambda_o}{\lambda})^{-\alpha}$ (E10)

α	$\langle\underline{\beta}\rangle$
0.5	0.913
1.0	0.910
2.0	0.905
3.0	0.899

For "leaky" polaroid, the spectral shape of the incident flux distribution affects the value of $\underline{\beta}$ calculated. The unpolarized stars used in the crossed polaroid tests are early type without infrared excess and have a characteristic temperature of 5000-6000K. $\underline{\beta}$ will be changed by <0.5% between this case and the case where $I = I_o$. The polarized source BN has a rising flux across the K band. The table above shows that it is sufficient to assume the constant flux case. Even for the most extreme BL Lac object ($\alpha = 2.5$), the difference in $\underline{\beta}$ is only 1%. In the equations derived in Appendix C, $\underline{\beta}$ is always a multiplicative factor on the calculated polarization. Therefore the dispersion in possible values of $\underline{\beta}$ corresponds only to a 0.1% error in the polarization of an object.

(ii) The absolute spectral flux calibration listed in Table 2.1 is based on the model atmosphere calculation by Schild et al. (1971) of Vega (α Lyr). The infrared extrapolation of their scanner data is formed by fitting a Planck function with an effective temperature of 9650K and is accurate to ∿3% out to 5μm. The flux distribution of all BL Lac objects in the near infrared is very different from an early type (A0 V) star like Vega. Across each of the broad bands there will be a correction to the calibrated flux due to the redness of the BL Lac object. In addition the choice of standards affects the calibration. There is a lack of moderately faint (K > 4), well-established standards in the near infrared, and those listed in Table 2.2 cover a range of spectral types from A2 to K0. The presence of absorption lines in the spectra of the calibration objects may also change the broad band colours. The early type stars will have Paschen and Brackett absorption lines, later spectral types (F-G) will be nearly featureless and well-fitted by a blackbody of ∿7000K, and even later types out to K0 will begin to show CO and CN absorption.

To calculate the correction the infrared spectrophotometric fluxes of stars of different spectral types are required. Strecker et al. (1979) have published airborne spectrophotometry from 1.2 - 5.5μm for 13 stars earlier than M3. They also interpolated the numerical results of Schild et al. (1971) for α Lyr to higher resolution, although the absolute spectrophotometry of their data still depends on the model atmosphere calculation of α Lyr. The incident intensity $I(\lambda)$ is convolved with the transmission of the HF Polaroid $T_p(\lambda)$, the filter transmission function $T(\lambda)$ and the InSb spectral response $S(\lambda)$ (taken from Hall et al., 1978). Sensitivity and transmission are normalized to the effective wavelength of each filter bandpass.

$$I^*(\lambda) = I(\lambda)T(\lambda)T_p(\lambda)S(\lambda) \qquad (E11)$$

and the fractional change in measured intensity due to two different flux distributions $I_1(\lambda)$ and $I_2(\lambda)$ is,

$$\Delta I = \frac{I_1^*(\lambda)}{I_2^*(\lambda)} = \frac{\int_{\lambda_2}^{\lambda_1} I_1(\lambda)T(\lambda)T_p(\lambda)S(\lambda)d\lambda}{\int_{\lambda_2}^{\lambda_1} I_2(\lambda)T(\lambda)T_p(\lambda)S(\lambda)d\lambda} \qquad (E12)$$

Choose two different flux distributions to mimic the photometric standards: the data on αCMa (A1 V) and β Gem(K0 III) in Strecker et al. (1979). Also choose three different power law slopes to represent the range covered by the BL Lac objects: $\alpha = 0.5, 1.0, 2.0$. As before, the resolution is $\Delta\lambda = 0.02\mu m$.

J

λ(μm)	T	T_p	S	$J_{1,2}$ αCMa	βGem
1.04	0.005	0.71	0.27	186	152
1.06	0.07	0.71	0.28	174	145
1.08	0.26	0.72	0.29	164	138
1.10	0.50	0.72	0.30	153	132
1.12	0.63	0.72	0.31	144	126
1.14	0.70	0.73	0.32	136	120
1.16	0.71	0.73	0.33	128	115
1.18	0.66	0.73	0.34	121	111
1.20	0.70	0.72	0.34	115	107
1.22	0.74	0.72	0.35	109	104
1.24	0.65	0.72	0.35	103	102
1.26	0.77	0.71	0.36	97	98
1.28	0.80	0.71	0.36	88	96
1.30	0.70	0.71	0.37	87	93
1.32	0.49	0.72	0.37	83	91
1.34	0.61	0.72	0.38	78	88
1.36	0.75	0.72	0.38	74	86
1.38	0.42	0.73	0.39	70	83
1.40	0.14	0.73	0.40	67	81
1.42	0.02	0.74	0.40	64	78
1.44	0.005	0.74	0.41	60	76

H

1.38	0.005	0.73	0.39	183	140
1.42	0.01	0.74	0.40	166	132
1.46	0.03	0.74	0.42	150	124
1.50	0.31	0.75	0.43	136	119
1.54	0.62	0.75	0.44	123	114
1.58	0.66	0.74	0.45	114	109
1.62	0.79	0.74	0.47	108	105
1.66	0.87	0.73	0.48	97	98
1.70	0.88	0.73	0.49	91	92
1.74	0.87	0.73	0.50	80	85
1.78	0.83	0.74	0.52	76	79
1.82	0.06	0.75	0.54	68	74
1.86	0.01	0.76	0.55	63	68
1.90	0.005	0.77	0.57	60	64

K

λ(μm)	T	T_p	S	$I_{1,2}$ αCMa	βGem
1.90	0.005	0.77	0.57	175	168
1.94	0.015	0.77	0.57	154	157
1.98	0.20	0.77	0.58	149	145
2.02	0.68	0.75	0.58	138	135
2.06	0.73	0.73	0.59	128	127
2.10	0.72	0.71	0.59	119	118
2.14	0.76	0.69	0.60	108	111
2.18	0.79	0.67	0.60	101	104
2.22	0.84	0.65	0.61	97	96
2.26	0.84	0.63	0.61	90	90
2.30	0.76	0.61	0.62	85	84
2.34	0.76	0.25	0.63	80	78
2.38	0.68	0.29	0.63	75	71
2.42	0.30	0.32	0.64	71	67
2.46	0.03	0.28	0.65	67	64

The expectation value of the transmitted intensity is,

$$\langle I^* \rangle = \frac{\int_{\lambda_2}^{\lambda_1} I(\lambda)T(\lambda)T_p(\lambda)S(\lambda)d\lambda}{\int_{\lambda_2}^{\lambda_1} T(\lambda)T_p(\lambda)S(\lambda)d\lambda} \qquad \text{(E13)}$$

Using $I(\lambda_{eff}) = 100$ for each filter, the integrated values of I* are,

Waveband	αCMa	βGem	I* α = 0.5	α = 1.0	α = 2.0
J	105.3	103.3	99.8	99.5	99.4
H	97.9	96.7	100.4	100.9	102.1
K	100.2	105.7	98.4	99.1	99.6

The difference between using calibration stars of different spectral types is small; at J it is only 2% and at K only 0.5%. However there is a significant correction to be applied to the flux because of the difference between the falling thermal flux of the standard and the rising non-thermal flux of the object across the filters. In the J and K wavebands the standard flux is measured too high and the object flux too low, so the correction is upwards; in the H waveband it is downwards. Since the dispersion in I* is small for different values of spectral index, the mean of the three values listed will be used. The mean of the I* for the two standards will be taken also. The corrections therefore are,

Waveband	I_1^*/I_2^*	
J	+4.6%	± 1%
H	-3.8%	
K	+7.0%	

Knowing the infrared spectral index from the uncorrected fluxes, it is possible to correct each object according to its own spectral shape. However the corrections applied unilaterally are accurate to ∿1%, at which level they are dominated by other contributions to the error. The corrected fluxes in mJ are listed in Table 3.4.

(iii) Interstellar Extinction. The correction due to interstellar extinction in our Galaxy can be quite uncertain for any particular object due to the inhomogeneous interstellar medium. Heiles (1976) has shown that the variable gas-to-dust ratio in the Galaxy makes the cosec $|b^{II}|$ parameter an imperfect indicator of extinction. More consistent results have been achieved by Burstein and Heiles (1978) using galaxy counts and HI column densities. These problems are considerably reduced in this work because the objects are generallyat high galactic latitude and extinction in the near infrared is considerably reduced.

As an estimate, the method of Sandage (1972) will be used. The extension of the extinction law into the infrared was done by Johnson (1968) using the work of van der Hulst (1949). The selective extinction coefficients used are:

$$A_K/A_V = 0.09, \quad A_H/A_V = 0.13, \quad A_J/A_V = 0.23 \qquad (F9)$$

Only 6 out of the sample of 17 have $|b^{II}| < 40^o$; for those with $|b^{II}| > 40^o$, $A_V < 0.10$ and the corrections in the infrared will be very small and well within the uncertainty in the photometry. Therefore no correction is applied to those sources. For the remaining six BL Lac objects (O'Dell et al., 1978b)

Object	b^{II}	A_V	A_K	A_H	A_J
0235 + 164	-39^o	0.10	0.01	0.01	0.02
0735 + 178	+18	0.46	0.04	0.06	0.11
0754 + 101	+21	0.40	0.04	0.05	0.09
0851 + 202	+38	0.13	0.01	0.02	0.03
1652 + 398	+37	0.10	0.01	0.01	0.02
1727 + 503	+34	0.15	0.01	0.02	0.03

Because of the fundamental uncertainty in the corrections and the limited precision of the photometry, corrections less than 1% at K (2.2μm), 2% at H (1.65μm) and 3% at J (1.25μm) were not applied. Therefore the only two objects where the correction has been made are 0735+178 and 0851+202.

References

Burstein,D. & Heiles, C. (1978). Astrophys.J., 225, 40.

Hall, D.B., Aikens, R.S., Joyce, R. & McCurrin, T.W. (1978). KPNO preprint.

Heiles, C. (1976). Astrophys.J., 204, 379.

van der Hulst, H.C. (1949). Rech.astr.Obs.Utrecht, 11, 1.

Johnson, H.L. (1968). Stars and Stellar Systems VII. (Univ. of Chicago), 167.

O'Dell, S.L., Puschell, J.J., Stein, W.A. & Warner, J.W. (1978b). Astrophys.J. Suppl., 38, 267.

Sandage, A. (1972). Astrophys.J., 178, 1.

Schild, R., Peterson, D.M. & Oke, J.B. (1971). Astrophys.J., 166, 95.

Strecker, D.W., Erickson, E.F. & Witteborn, F.C. (1979). Astrophys. J.Suppl., 41, 501.

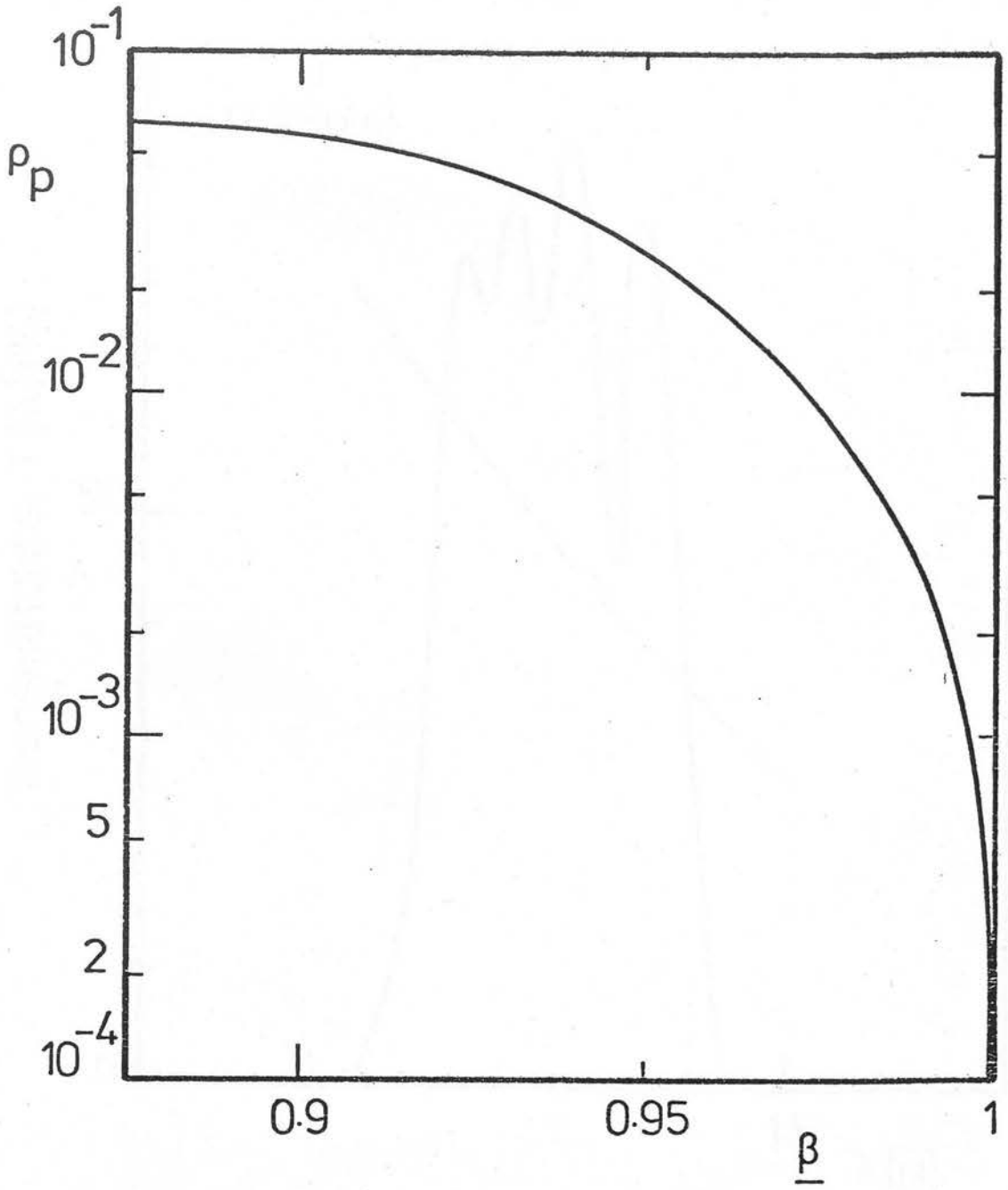

Figure E1. Relation between extinction ratio (ρ_p) and efficiency of HR Polaroid ($\underline{\beta}$).

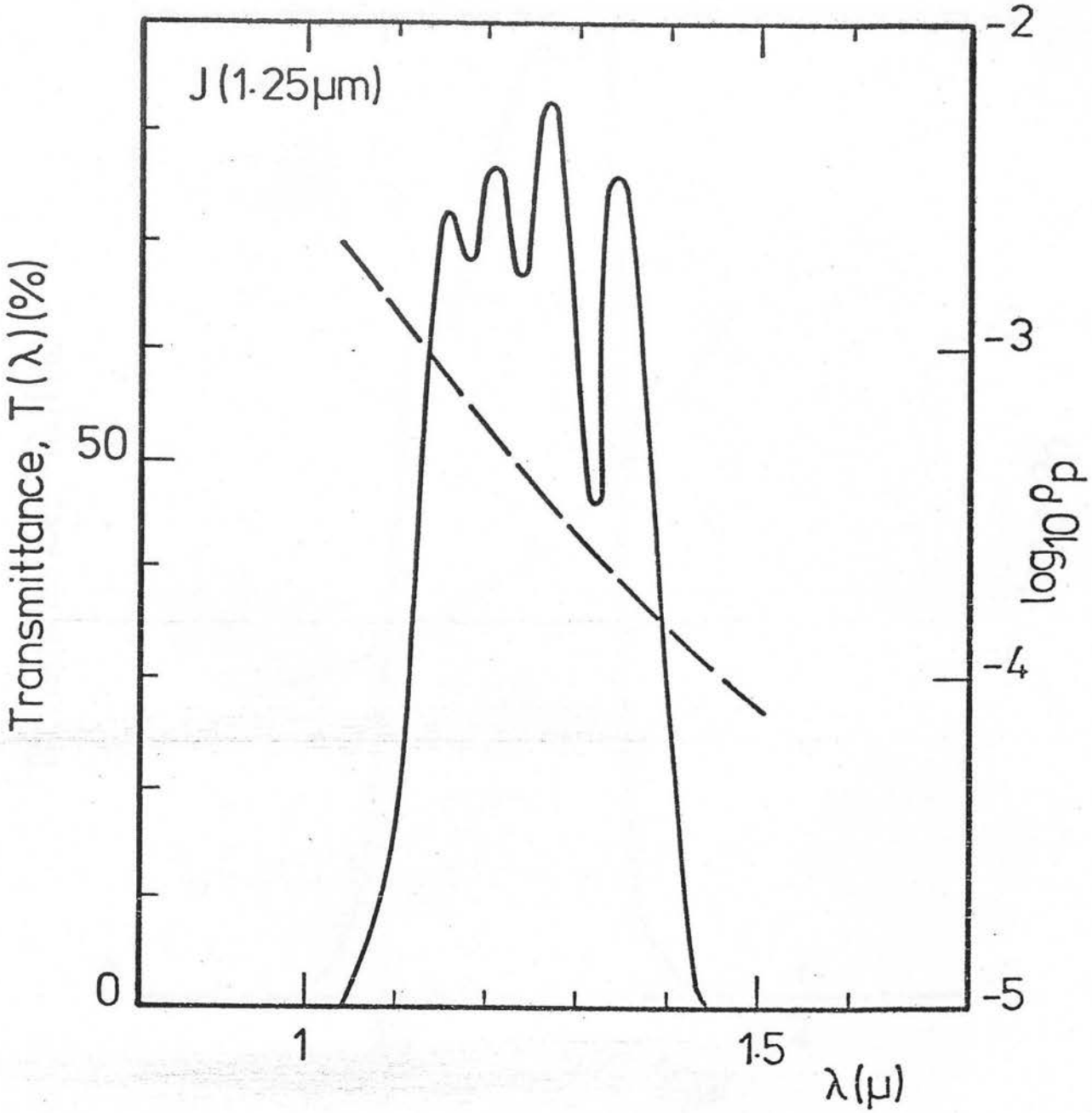

Figure E2. Filter transmission against wavelength (data from OCLI Optical Coatings Ltd.) and polaroid extinction ratio against wavelength (data from Polaroid Corporation UK Ltd.).

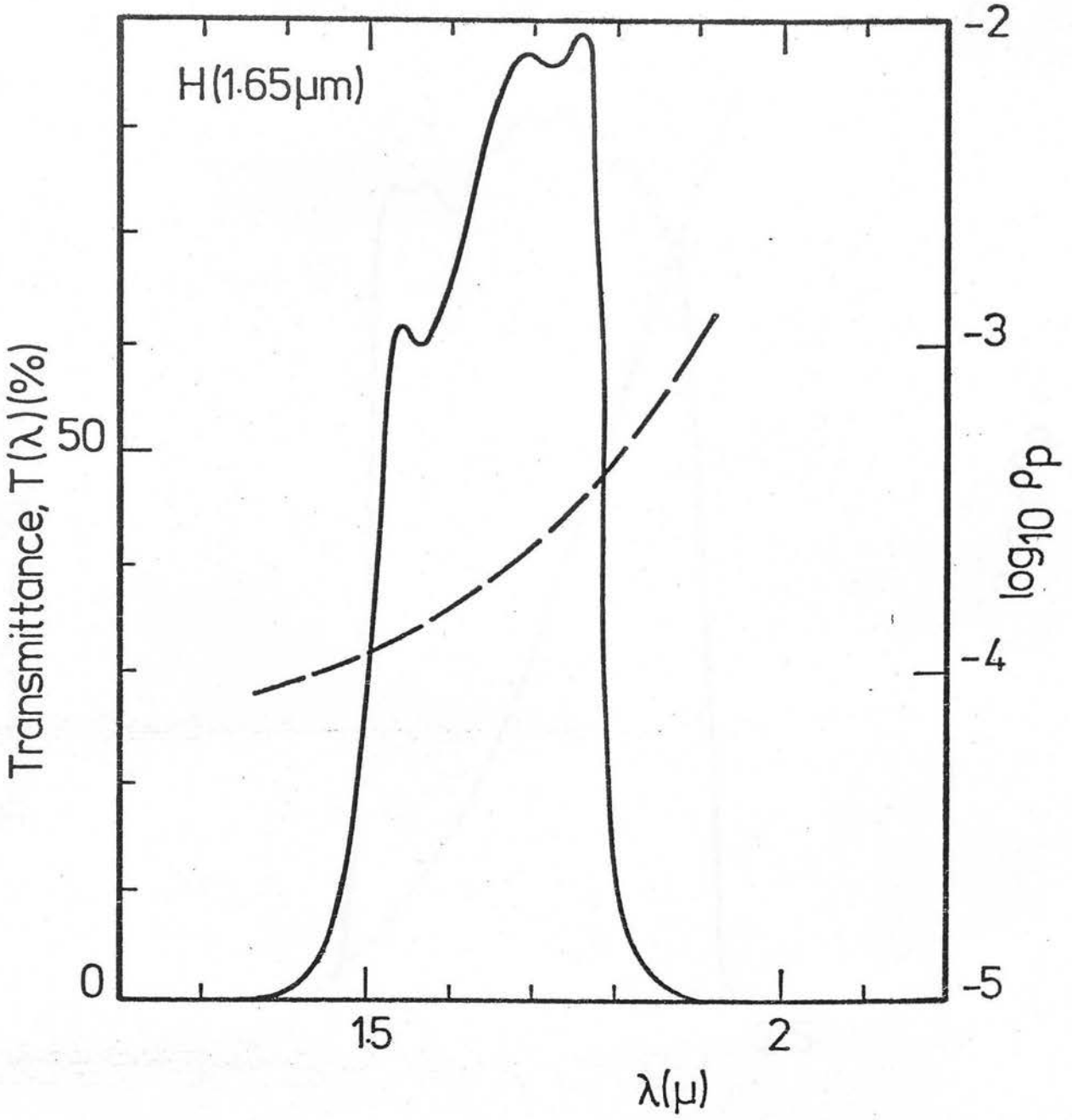

Figure E3. Filter transmission against wavelength (data from OCLI Optical Coatings Ltd.) and polaroid extinction ratio against wavelength (data from Polaroid Corporation UK Ltd.).

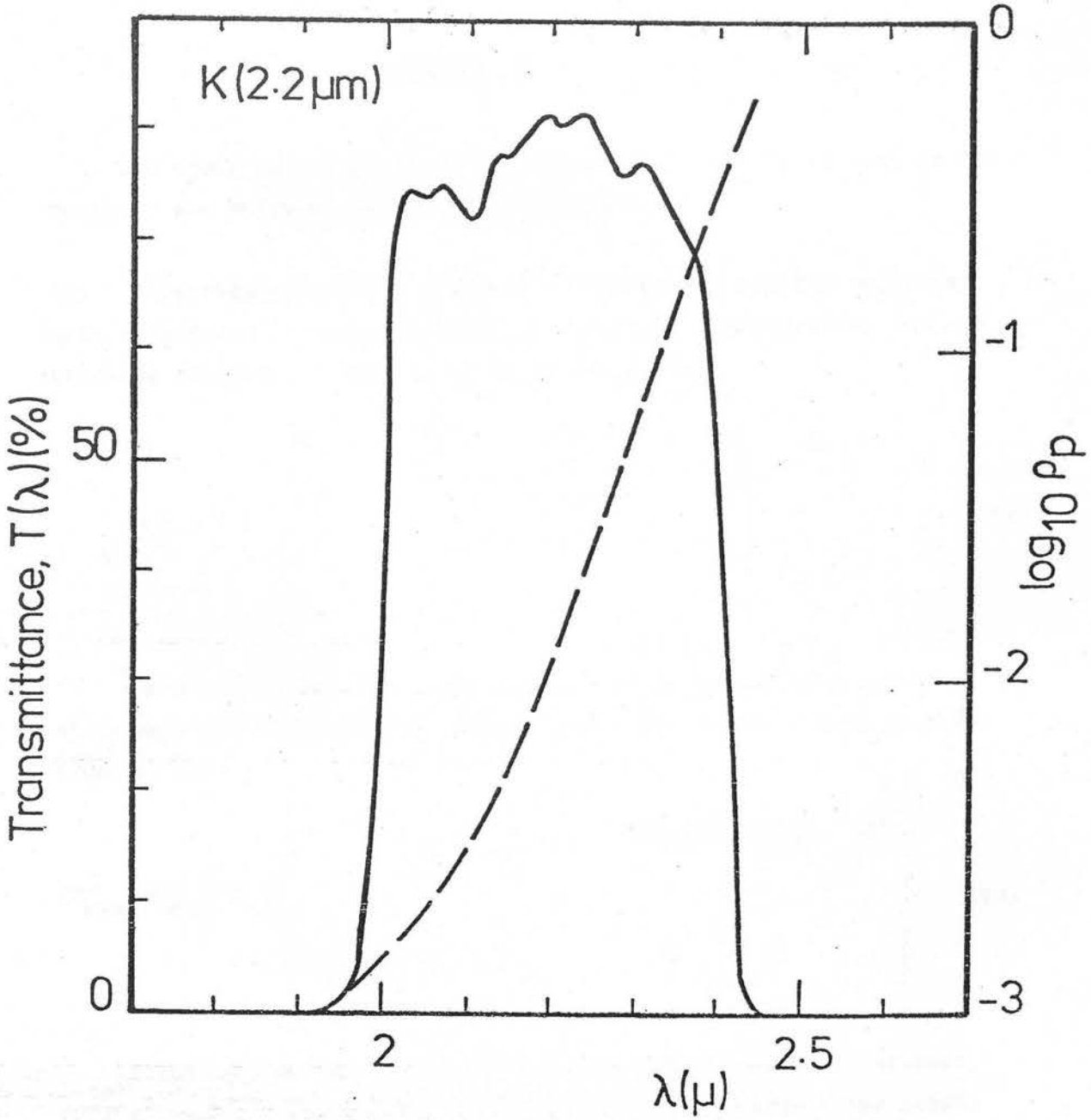

Figure E4. Filter transmission against wavelength (data from OCLI Optical Coatings Ltd.) and polaroid extinction ratio against wavelength (data from Polaroid Corporation UK Ltd.).

APPENDIX F

The order of magnitude of two possible systematic effects in the analysis are derived, and shown to be small,

(i) Birefringence of the analyzer. Consider a partial polarizer with retardance δ, where the axes of principal transmittance and retardance coincide. The matrix is given by (A4),

$$\{P'_E\} = \tfrac{1}{2}\begin{pmatrix} a & bc & bs & 0 \\ bc & ac^2+us^2 & (a-u)sc & -vs \\ bs & (a-u)sc & as^2+uc^2 & vc \\ 0 & vs & -vc & u \end{pmatrix} \qquad \text{(F1)}$$

where $u = e\cos\delta$, $v = e\sin\delta$. For crossed polaroids, the only difference the birefringence makes to the top row is a term in $\sin\delta$ (compare with A7),

$$\{P'_{B-\alpha}\}\{P'_{B-\beta}\}=\tfrac{1}{4}\begin{pmatrix} a^2+b^2C & ab\underline{c}(1+C)-eb\underline{s}S & ab\underline{s}(1+C)+eb\underline{c}S & vbS \\ \cdot & \cdot & \cdot & \cdot \\ \cdot & \cdot & \cdot & \cdot \\ \cdot & \cdot & \cdot & \cdot \end{pmatrix} \qquad \text{(F2)}$$

It is easy to see that the other two combinations of interest, $\{P'_B\}\{D\}$ and $\{D\}\{P'_B\}$, take a similar form to (F2) because the matrix form for the dichroic is identical to the matrix form of a birefringent analyzer. The difference is that the dichroic is a weak polarizer and the analyzer is a strong polarizer with $b/a \sim 0.89$ at 2.2μm. Consider first the experimental configurations (i), (ii), (v) and (vi) in Appendix B, which are all of the form,

$$\{P'_B\}\{P'_B\}\begin{pmatrix} I \\ 0 \\ 0 \\ 0 \end{pmatrix} \quad ; \quad \{P'_B\}\{D\}\begin{pmatrix} I \\ Q \\ U \\ 0 \end{pmatrix} \quad ; \quad \{D\}\{P'_B\}\begin{pmatrix} I \\ Q \\ U \\ 0 \end{pmatrix} \qquad \text{(F3)}$$

Since only the 4th element of the top row of any of these combinations is altered by the birefringence, the reduction formulae are unchanged. However, in the set-ups described by (iii), (iv) and (vii) the combinations act on elliptically polarized light and there is a mixing of U and V caused by the birefringence of the analyzer. Therefore all the elements in (F2) are important, and are different from the non-birefringent case by terms of order,

$$V_D V_P = (e\sin\delta)_D (e\sin\delta)_P \tag{F4}$$

where subscripts P and D represent polaroid and dichroic respectively. For δ_P very small ($\delta_o \sim 15^o$), $V_D V_P << 1$ and the matrices reduce to the non-birefringent case. Also, $U_p \to e$ and $V_p \to 0$, so (F1) reduces to (A2). However, with no a priori knowledge of the size of δ_p, it must be included in the analysis. Therefore, in terms of (A9),

$$\{D\}\{P'_B\} = \{D\}\{P'\} + \tfrac{1}{4}\begin{pmatrix} 0 & 0 & 0 & b\underline{v}S \\ 0 & -v\underline{v}ss & v\underline{v}sc & . \\ 0 & v\underline{v}cs & -v\underline{v}cc & . \\ 0 & \underline{u}vs & -\underline{u}vc & . \end{pmatrix} \tag{F5}$$

where $\underline{v},\underline{u}$ refer to the analyzer, and v, u refer to the dichroic. Now using equation (A11),

$$\{P'_B\}\{D\} = \{P'\}\{D\} + \tfrac{1}{4}\begin{pmatrix} 0 & 0 & 0 & b\underline{v}S \\ 0 & -v\underline{v}ss & v\underline{v}cs & -\underline{u}vs \\ 0 & v\underline{v}sc & -v\underline{v}cc & \underline{u}vc \\ -b\underline{v}S & \underline{u}vs & -\underline{u}vc & 0 \end{pmatrix} \tag{F6}$$

and using (F2),

$$\{P'_{B-\alpha}\}\{P'_{B-\beta}\} = \{P'_\alpha\}\{P'_\beta\} + \tfrac{1}{2}\begin{pmatrix} 0 & 0 & 0 & b\underline{v}S \\ 0 & \underline{v}^2ss & \underline{v}^2cs & -\underline{u}vs \\ 0 & \underline{v}^2sc & -\underline{v}^2cc & \underline{u}vc \\ -b\underline{v}S & \underline{u}vs & -\underline{u}vc & \underline{v}^2S+\underline{u}^2-\underline{e}^2 \end{pmatrix} \tag{F7}$$

Now (iii), (iv) and (vii) are of the form (Appendix B),

$$\{P_B'\}(\{D\}\{P_B'\})\begin{pmatrix}I\\0\\0\\0\end{pmatrix}\quad;\quad \{P_B'\}(\{P_B'\}\{D\})\begin{pmatrix}I\\0\\0\\0\end{pmatrix};\quad (\{P_B'\}\{D\})(\{P_B'\}\{P_B'\})\begin{pmatrix}I\\0\\0\\0\end{pmatrix} \qquad (F8)$$

Therefore only the 1st term in the top row of the preceding matrix is relevant. The extra contributions to the modulation from the birefringence aregiven by using the second terms of (F5) - (F7) in (F8). These extra terms are zero except for configuration (vii) where there is a term $-bbv^2S^2$ which corresponds to a modulation $\beta\beta\gamma^2$. Typically, $\gamma \simeq 1$, $\beta \simeq 0.9$ and $\beta \simeq 0.05$, so this one experimental test may have a spurious birefringent effect of order <5%. The important result is that the analyzer birefringence, whatever its magnitude, does not affect the derivations of reduction formulae.

(ii) Circular polarization in the source. It has been implicit in all the derivations that none of the sources observed have any intrinsic circular polarization. The only component is assumed to be due to linear-to-circular conversion at the dichroic mirror. The only source with non-zero circular polarization was the BN object, which has a level of ∿1% at 2.2μm (Lonsdale et al., 1980). The polarimeter configuration had the dichroic upstream of the analyzer, therefore using (A11),

$$\begin{pmatrix}I^*\\Q^*\\U^*\\V^*\end{pmatrix}=\tfrac{1}{2}\begin{pmatrix}a\underline{a}+b\underline{b}C & \underline{a}bC+b(acC-usS) & \underline{a}bs+\underline{b}(asC+usS) & \underline{b}vS\\ . & . & . & .\\ . & . & . & .\\ 0 & . & . & .\end{pmatrix}\begin{pmatrix}I\\Ipc\\Ips\\Iq\end{pmatrix} \qquad (F9)$$

which leads to an extra term $\beta\gamma qS$ in the expression for the transmitted intensity. The circular polarization introduces a modulating term of amplitude <1% which will lead to an error of ∿1% in the value

of linear polarization of BN. For BL Lac objects, $q < 0.1\%$ and the precision in the measurement of p is not affected. Note that if the analyzer is upstream of the dichroic, circular polarization in the source does not modulate the transmitted flux,

$$\begin{pmatrix} I^* \\ Q^* \\ U^* \\ V^* \end{pmatrix} = \tfrac{1}{4} \begin{pmatrix} \underline{a}\underline{a}+b\underline{b}C & \underline{a}bC+b(\underline{a}cC+\underline{e}\underline{s}S) & \underline{a}\underline{b}\underline{s}+b(\underline{a}\underline{s}C-\underline{e}cS) & 0 \\ \cdot & \cdot & \cdot & 0 \\ \cdot & \cdot & \cdot & 0 \\ \cdot & \cdot & \cdot & 0 \end{pmatrix} \begin{pmatrix} I \\ Ipc \\ Ips \\ Iq \end{pmatrix} \qquad \text{(F10)}$$

Reference

Lonsdale C.J., Dyck H.M., Capps R.W. & Wolstencroft R.D., 1980.

Astrophys.J., 238, L3.

Acknowledgments

My sincere thanks are due to my supervisors, Peter Brand and Ray Wolstencroft, for their help and encouragement throughout this project. Ray first introduced me to the mysteries of polarimetry and BL Lac objects, and set me on the course for this thesis. Peter has been a close friend and advisor during an alternately exhirirating and frustrating observing campaign. His insight has been a great influence on my thinking, and my many discussions with him have been the most important part of my education as a scientist.

I have been fortunate to use many of the facilities connected with the Observatory, and many people have advised me during the course of this research. In particular, I would like to thank:

Terry Lee and the UKIRT staff for magnificent support under difficult condition, and for coping with the ever-changing demands of the infrared polarimeter. It has been a priviledge to use such a powerful tool as UKIRT in the exciting early days of its development.

John Dawe and the UKST staff for much assistance during the testing and commissioning of the polaroid filter, and for teachimg me the fundamentals of astronomical photography.

Ron Beetles for his able assistance with the design of both the optical and infrared polarimeters, and Joe Matthews and the workshop staff for continually producing the impossible on demand. Mike Eccles and Bill Cormack generously supplied vital components for the infrared polarimeter.

My computing and handling of COSMOS data has drawn on the considerable expertise of Ralph Martin and Bernard McNally. I also wish to thank Steve Heathcote and Paul Hewett for their assistance.

In the early stages of this work, I benefitted considerably from the encouragement and help of George Coyne and Santiago Tapia. Many of my ideas have been moulded by discussions with Santiago, and also with Cyril Hazard.

Special thanks go to Jackie Bogie for her skill in typing a long and difficult manuscript with speed and precision, and to Marjorie Fretwell for her immaculate drawings.

Finally, this work would not have been possible without the continued support of PATT and the Science Research Council.

References

Abramowicz, M. & Stegun, I.A., 1970. Handbook of Mathematical Functions (Dover).

Abramowicz, M.A., Calvani, M. & Nobili, L., 1980. Astrophys.J., 242, 772.

Agrawal, P.C. & Riegler, G.R., 1979. Astrophys.J., 231, L25.

Allen, C.W., 1973. Astrophysical Quantities (Athlone Press).

Aller, H.D. & Ledden, J.E., 1978. Pittsburgh Conference on BL Lac Objects, ed. Wolfe, A.M. (Univ. of Pittsburgh), 53.

Aller, H.D., Aller, M.F. & Hodge, P.E., 1980. Univ. of Michigan preprint.

Altschuler, D.R. & Wardle, J.F.C., 1975. Nature 255, 306.

Altschuler, D.R. & Wardle, J.F.C., 1976. Mem.R.astr.Soc., 82, 1.

Altschuler, D.R. & Wardle, J.F.C., 1977. Mon.Not.R.astr.Soc., 179, 153.

Andrew, B.H., MacLeod, J.M., Locke, J.L., Medd, W.J. & Purton, C.R., 1969. Nature, 223, 598.

Angel, J.R.P., Boroson, T.A., Adams, M.T., Duerr, R.E., Giampapa, M.S., Gresham, M.S., Gural, P.S., Hubbard, E.N., Kopriva, D.A., Moore, R.L., Peterson, B.M., Schmidt, G.D., Turnshek, D.A., Wilkerson, M.S., Zotov, N.V., Maza, J. & Kinman, T.D., 1978. Pittsburgh Conference on BL Lac Objects, ed. Wolfe, A.M. (Univ. of Pittsburgh), 117.

Angel, J.R.P. & Stockman, H.S., 1980. Ann.Rev.Astron. & Astrophys., 18, 321.

Angione, R.J. & Smith, H.J., 1972. I.A.U. Symposium 41, 171.

Auer, L.H. & van Altena, W.F., 1978. Astron.J., 83, 531.

Axford, W.I., Leer, E. & Skadron, G., 1977. 15th International Cosmic Ray Conference, Bulgaria.

Baade, W., 1956a. Bull.Astron.Inst.Neth., 12, 312.

Baade, W., 1956b. Astrophys.J., 123, 550.

Bailey, M.E., 1979. Ph.D. Thesis, Edinburgh (Univ. of Edinburgh).

Baker, A.E., 1925. Proc.Roy.Soc. Edinburgh, 45, 166.

Baldwin, J.A., Wampler, E.J., Burbidge, E.M., O'Dell, S.L., Smith, H.E., Hazard, C., Nordsieck, K.H., Pooley, G. & Stein, W.A., 1977. Astrophys.J., 215, 408.

Balonek, T.J. & Dent, W.A., 1980. Astrophys.J., 240, L3.

Beckwith, S., Evans, N.J.III, Becklin, E.E. & Neugebauer, G., 1976. Astrophys.J., 208, 390.

Begelman, M.C. & Rees, M.J., 1978. Mon.Not.R.astr.Soc., 185, 847.

Bell, A.R., 1977. Mon.Not.R.astr.Soc., 179, 573.

Bennett, J.M. & Bennett, H.E., 1978. Handbook of Optics (McGraw-Hill), 10.

Biraud, F. & Veron, P., 1968. Nature, 219, 254.

Blandford, R.D. & Rees, M.J., 1974. Mon.Not.R.astr.Soc., 169, 395.

Blandford, R.D. & McKee, C.F., 1976. Bull.Am.astr.Soc., 8, 539.

Blandford, R.D. & McKee, C.F., 1977. Mon.Not.R.astr.Soc., 180, 343.

Blandford, R.D., McKee, C.F. & Rees, M.J., 1977. Nature, 267, 211.

Blandford, R.D. & Ostriker, J.P., 1978. Astrophys.J., 221, L29.

Blandford, R.D. & Rees, M.J., 1978a. Physica Scripta, 17, 265.

Blandford, R.D. & Rees, M.J., 1978b. Pittsburgh Conference on BL Lac Objects, ed. Wolfe, A.M. (Univ. of Pittsburgh), 328.

Blandford, R.D., 1979. Active Galactic Nuclei, eds. Hazard & Mitton (CUP), 241.

Blandford, R.D. & Königl, A., 1979. Astrophys.J., 232, 34.

Blumenthal, G.R. & Gould, R.J., 1970. Rev.Mod.Phys., 42, 237.

Bonoli, F., Braccesi, A., Federici, L., Zitelli, V. & Formiggini, L., 1979. Astron. & Astrophys., Suppl., 35, 391.

Born, M. & Wolf, E., 1959. Principles of Optics (Pergamon Press).

Boyd, T.S.M. & Sanderson, J.J., 1969. Plasma Dynamics (Nelson).

Braccesi, A., Formiggini, L. & Gandolfi, E., 1970. Astron.& Astrophys., 5, 264.

Braccesi, A., Zitelli, V., Bonoli, F. & Formiggini, L., 1980. Astron. & Astrophys., 85, 80.

Brand, P.W.J.L., 1971. Optica Acta, 18, 403.

Brandie, G.W. & Bridle, A.H., 1974. Astron.J., 79, 903.

Burbidge, E.M., Caldwell, R.D., Smith, H.E., Liebert, J. & Spinrad, H., 1976. Astrophys.J., 205, L117.

Burbidge, G.R. & Stein, W.A., 1970. Astrophys.J., 160, 573.

Burbidge, G.R., Jones, T.W. & O'Dell, S.L., 1974. Astrophys.J., 193, 43.

Burbidge, G.R., Crowne, A.H. & Smith, H.E., 1977. Astrophys.J. Suppl., 33, 113.

Burge, D.K. & Bennett, H.E., 1964. J.Opt.Soc.Am., 54, 1428.

Burn, B.J., 1975. Astron.& Astrophys., 45, 435.

Burstein, D. & Heiles, C., 1978. Astrophys.J., 225, 40.

Canterna, R. & Flower, P.J., 1977. Astrophys.J., 212, L57.

Capps, R.W. & Knacke, R.F., 1978. Astrophys.Lett., 19, 113.

Carney, B.W., 1979. Astron.J., 84, 515.

Carswell, R.F., Strittmatter, P.A., Williams, R.E., Kinman, T.D. & Serkowski, K., 1974. Astrophys.J., 190, L101.

Carter, B., 1978. Active Galactic Nuclei, eds. Hazard & Mitton (CUP), 273.

Cavaliere, A., Morrison, P. & Pacini, F., 1970. Astrophys.J., 162, L133.

Cavaliere, A. & Morrison, P., 1980. Astrophys.J., 238, L63.

Charles, P., Thorstensen, J. & Bowyer, S., 1979. Nature, 281, 285.

Chertoprud, V.E., Gudzenko, L.I. & Ozernoi, L.M., 1973. Astrophys. J., 182, L53.

Chevalier, R.A., 1977. Ann.Rev.Astron.& Astrophys., 15, 175.

Christiansen, W.A., Scott, J.S. & Vestrand, W.T., 1978. Astrophys. J., 223, 13.

Clarke, D. & Grainger, J.F., 1971. Polarized Light & Optical Measurement (Pergamon).

Cohen, M.H., Kellerman, K.I., Shaffer, D.B., Linfield, R.P., Moffet, A.T., Romney, J.D., Seielstad, G.A., Pauliny-Toth, I.I.K., Preuss, E., Witzel, A., Schilizzi, R.T. & Geldzahler, B.J., 1977. Nature, 268, 405.

Colgate, S.A., 1967. Astrophys.J., 150, 163.

Colgate, S.A., Lee, E.P. & Rosenbluth, M.N., 1970. Astrophys.J., 162, 649.

Colgate, S.A., Colvin, J.D. & Petschek, A.G., 1975. Astrophys.J., 197, L105.

Colla, G., Fanti, C., Fanti, R., Gioia, I., Lari, C., Lequeux, J., Lucas, R. & Ulrich, M.H., 1975. Astron.& Astrophys., 38, 209.

Condon, J.J. & Jauncey, D.L., 1974. Astron.J., 79, 437.

Condon, J.J., Hicks, P.D. & Jauncey, D.L., 1977. Astron.J., 82, 692.

Condon, J.J., 1978. Pittsburgh Conference on BL Lac Objects, ed. Wolfe, A.M. (Univ. of Pittsburgh), 21.

Condon, J.J., Jauncey, D.L. & Wright, A.E., 1978. Astron.J., 83, 1036.

Condon, J.J., Ledden, J.E., O'Dell, S.L. & Dennison, B., 1979. Astron.J., 84, 1.

Condon, J.J., Condon, M.A., Jauncey, D.L., Smith, M.G., Turtle, A.J. & Wright, A.E., 1980a. NRAO preprint.

Condon, J.J., O'Dell, S.L., Puschell, J.J. & Stein, W.A., 1980b. Nature, 283, 357.

Cooke, B.A., Ricketts, M.J., Maccacaro, T., Pye, J.P., Elvis, M., Watson, M.G., Griffiths, R.E., Pounds, K.A., McHardy, I., Maccagni, D., Seward, F.D. & Turner, M.J.L., 1978. Mon.Not.R.astr.Soc., 182, 489.

Cotton, W.D., Wittels, J.J., Shapiro, I.I., Marcaide, J., Owen, F.N., Spangler, S.R., Rius, A., Angulo, C., Clark, T.A. & Knight, C.A., 1980. Astrophys.J., 238, L123.

Couch, W.J. & Newell, E.B., 1980. Mount Stromlo & Siding Spring Observatories preprint.

Craine, E.R., Johnson, K. & Tapia, S., 1975. Pub.astr.Soc.Pac., 87, 123.

Craine, E.R., Duerr, R. & Tapia, S., 1978. Pittsburgh Conference on BL Lac Objects, ed. Wolfe, A.M. (Univ. of Pittsburgh), 99.

Davis, L., 1956. Phys.Rev., 101, 351.

Davis, M.M., 1977. I.A.U. Symposium, 74, 104.

Dent, W.A. & Balonek, T.J., 1980. Nature, 283, 747.

Disney, M.J., Peterson, B.A. & Rodgers, A.W., 1974. Astrophys.J., 194, L79.

Dodd, R.J., MacGillivray, H.T. & Smith, G.M., 1979. Image Processing in Astronomy, eds. Sedmak, G., Capaccioli, M. & Allen, R.J. (Trieste).

Dombrovski, V.A., 1954. Dokl.Akad.Nauk.SSSR., 94, 1021.

Dressler, A., 1980. Astrophys.J., 240, L11.

Driscoll, W.G. & Vaughan, W., 1978. Handbook of Optics (McGraw-Hill).

Dungey, J.W., 1953. Phil.Mag., 44, 725.

DuPuy, D., Schmitt, J., McClure, R., van den Bergh, S. & Racine, R. 1969. Astrophys.J., 156, L135.

Dwight, H.B., 1961. Tables of Integrals and other Mathematical Data (Macmillan).

Eachus, L.J. & Liller, W., 1975. Astrophys.J., 200, L61.

Elias, J.H., Ennis, D.J., Gezari, D.Y., Hauser, M.G., Houck, J.R., Lo, K.Y., Matthews, K., Nadeau, D., Neugebauer, G., Werner, M.W. & Westbrook, W.E., 1978. Astrophys. J., 220, 25.

Elliot, J.L. & Shapiro, S.L., 1974. Astrophys.J., 192, L3.

Epstein, E.E., Fogarty, W.G., Hackney, K.R., Hackney, R.L., Leacock, R.J., Pomphrey, R.B., Scott, R.L., Smith, A.G., Gary, B.L., Penston, M.V., Tritton, K.P., Bertaud, Ch., Veron, M.P., Wlèrick, G., Bernard, A., Bigay, J.H., Merlin, P., Durand, A., Sause, G., Beddin, E.E., Neugebauer, G. & Wynn-Williams, 1972. Astrophys.J., 178, L51.

Epstein, R.I. & Feldman, P.A., 1967. Astrophys.J., 150, L109.

Epstein, R.I., 1973. Astrophys.J., 183, 593.

Ericson, W.B. & Bazer, J., 1959. Astrophys.J., 129, 758.

Fabian, A.C., Maccagni, D., Rees, M.J. & Stoeger, W.F., 1976. Nature, 260, 583.

Fahlman, G.G. & Ulrich, T.J., 1975. Astrophys.J., 201, 277.

Fahlman, G.G., 1977. Astrophys.J., 211, 649.

Fanaroff, B.L. & Longair, M.S., 1973. Mon.Not.R.astr.Soc., 161, 393.

Fanti, R., Formiggini, L., Lari, C., Padrielli, L., Katgert-Merkelijn, J.K. & Katgert, P., 1973. Astron. & Astrophys. 23, 161.

Fanti, R., Ficarra, A., Mantovani, F., Padrielli, L. & Weiler, K., 1979. Astron. & Astrophys.Suppl., 36, 359.

Fermi, E., 1954. Astrophys.J., 119, 1.

Fisk, L.A., 1971. J.Geophys.Res., 76, 1662.

Frank, J., 1979. Mon.Not.R.astr.Soc., 187, 883.

Frogel, J.A., Persson, S.E., Aaronson, M. & Matthews, K., 1978. Ap.J.,220,25

Giacconi, R., Murray, S. et al, 1974. Astrophys.J.Suppl., 27, 37.

Gieiseking, F., 1977. AAS Photobulletin, 14, 18.

Gilmore, G., 1979. Ph.D. Thesis, Canterbury (Univ. of Canterbury).

Gilmore, G., 1980a. Nature, 287, 612.

Gilmore, G., 1980b. Mon.Not.R.astr.Soc., 190, 649.

Ginzburg, V.L. & Syrovatskii, S.A., 1964. The Origin of Cosmic Rays (Pergamon).

Ginzburg, V.L. & Syrovatskii, S.A., 1965. Ann.Rev.Astron. & Astrophys., 3, 297.

Ginzburg, V.L. & Ozernoi, L.M., 1977. Astrophys. & Sp.Sci., 50, 23.

Grandi, S.A. & Tifft, W.G., 1974. Pub.astr.Soc.Pac., 86, 873.

Grasdalen, G.L., 1980. I.A.U. Symposium 92, 269.

Griffiths, R.E., Briel, U., Chaisson, L., Davis, M., Doxsey, R.E., Hjellming, R., Schwartz, D.A. & Tapia, S., 1980. Harvard Astrophysics preprint.

Gursky, H., 1973. Pub.Am.Astronaut.Soc., 28, 255.

Haas, G. & Hadley, L.N., 1972. American Institute of Physics Handbook (McGraw-Hill).

Hadley, L.N. & Dennison, D.M., 1947. J.Opt.Soc.Am., 37, 451.

Hadley, L.N. & Dennison, D.M., 1948. J.Opt.Soc.Am., 38, 483.

Hagen-Thorn, V.A., 1972. Astron.Tsirk., 714, 5.

Hagen-Thorn, V.A., 1974. Astrofizika, 10, 79.

Hall, D.B., Aikens, R.S., Joyce, R. & McCurnin, T.W., 1980. KPNO preprint.

Heiles, C., 1976. Astrophys.J., 204, 379.

Heitler, W., 1954. The Quantum Theory of Radiation (Oxford).

Hewitt, A. & Burbidge, G.R., 1980. Astrophys.J.Suppl., 43, 57.

von Hoerner, S. & Saslaw, W.C., 1976. Astrophys.J., 206, 917.

Högbom, J.A., 1979. Astron. & Astrophys. Suppl., 36, 173.

Hoyle, F., 1949. Some Recent Advances in Solar Physics (CUP).

Hoyle, F. & Fowler, W.A., 1963. Mon.Not.R.astr.Soc., 125, 169.

van der Hulst, W.C., 1949. Rech.astr.Obs.Utrecht, 11, 1.

Hunstead, R.W., 1972. Astrophys.Lett., 12, 193.

Hyland, A.R. & Schwartz, M.P., 1977. Proc. A.S.A., 3, 137.

Icke, V., 1977. Nature, 266, 699.

Jackson, J.D., 1962. Classical Electrodynamics (Wiley).

Jaroszyński, M., Abramowicz, M.A. & Paczyński, B., 1980. Acta Astronomica, 30, 1.

Jeffreys, H. & Jeffreys, B.A., 1956. Methods of Mathematical Physics (CUP).

Johnson, H.L., 1968. Stars and Stellar Systems VII (Univ. of Chicago), 167.

Jones, F.C., 1968. Phys.Rev., 167, 1159.

Jones, T.W. & Kellogg, P.J., 1972. Astrophys.J., 172, 283.

Jones, T.W. & O'Dell, S.L., 1974. Nature, 250, 472.

Jones, T.W., O'Dell, S.L. & Stein, W.A., 1974. Astrophys.J., 188, 353.

Jones, T.W. & O'Dell, S.L., 1977a. Astrophys.J., 214, 522.

Jones, T.W. & O'Dell, S.L., 1977b. Astrophys.J., 215, 236.

Jones, T.W. & O'Dell, S.L., 1977c. Astron.& Astrophys., 61, 291.

Jones, T.W. & Tobin, W., 1977. Astrophys.J., 215, 474.

Kantrowitz, A. & Petschek, H.E., 1966. Plasma Physics in Theory and Application, ed. Kunkel, W.B. (McGraw-Hill).

Karachentsev, I.D., 1980. I.A.U. Symposium, 92, 17.

Kardeshev, N.S., 1965. Soviet Astron., 8, 643.

Katgert, P., Katgert-Merkelijn, J.K., Le Poole, R.S. & van der Laan, H., 1973. Astron.& Astrophys., 23, 171.

Katz, J.J., 1976. Astrophys.J., 206, 910.

Kaye, A.L., 1977. Mon.Not.R.astr.Soc., 180, 147.

Kellerman, K.I. & Pauliny-Toth, I.I.K., 1968. Astrophys.J., 152, L169.

Kellerman, K.I. & Pauliny-Toth, I.I.K., 1969. Astrophys.J., 155, L71.

Kellerman, K.I., 1978. Physica Scripta, 17, 257.

Kellerman, K.I., 1980. Ann.N.Y. Acad.Sci., 336, 1.

Kemp, J.C., Wolstencroft, R.D. & Swedlund, J.B., 1972. Astrophys. J., 173, L113.

Khachikian, E.Ye. & Weedman, D.W., 1974. Astrophys.J., 189, L99.

Kikuchi, S., Mikami, Y., Konno, M. & Inoue, M., 1976. Pub.astr. Soc.Jap., 28, 117.

Kinman, T.D., Lamla, E., Ciurla, T., Harlan, E. & Wirtanen, C.A., 1968. Astrophys.J., 152, 357.

Kinman, T.D., Wardle, J.F.C., Conklin, E.K., Andrew, B.H., Harvey, G.A., MacLeod, J.M. & Medd, W.J., 1974. Astron.J., 79, 349.

Kinman, T.D., 1976. Astrophys.J., 205, 1.

Kinman, T.D., 1977. Nature, 267, 798.

Kinman, T.D., 1978. Pittsburgh Conference on BL Lac Objects, ed. Wolfe, A.M. (Univ. of Pittsburgh), 82.

Kiplinger, A.P., 1974. Astrophys.J., 191, L109.

Knacke, R.F., Capps, R.W. & Johns, M., 1976. Astrophys.J., 210, L69.

Knacke, R.F., Capps, R.W. & Johns, M., 1979. Nature, 280, 215.

Korchakov, A.A. & Syrovatskii, S.I., 1961. Astron.Zh., 38, 885.

Korchakov, A.A. & Syrovatskii, S.I., 1962. Soviet Astron., 5, 678.

Kron, R.G., 1980. Astrophys.J.Suppl., 43, 305.

Kronberg, P.P., Reinhardt, M. & Simard-Normandin, M., 1977. Astron. & Astrophys., 61, 771.

Kulsrud, R.M. & Pearce, W.P., 1969. Astrophys.J., 156, 445.

Kulsrud, R.M. & Ferrari, A., 1971. Astrophys.& Sp.Sci., 12, 302.

Laing, R.A., 1980a. Mon.Not.R.astr.Soc., 193, 439.

Laing, R.A., 1980b. Mon.Not.R.astr.Soc., 193, 427.

Landau, L.D. & Lifshitz, E.M., 1975. Classical Theory of Fields (Pergamon).

Landau, R., Epstein, E.E. & Rather, J.D.G., 1980. Astron.J., 85, 363.

Landau, R., 1980. Astron.J., 85, 363.

Landstreet, J.D. & Angel, J.R.P., 1972. Astrophys.J., 174, L127.

Leacock, R.J., Smith, A.G., Edwards, P.L., Pollock, J.T., Scott, R.L., Gearhart, M.R., Pacht, E., & Kraus, J.D., 1976. Astrophys.J., 206, L87.

Ledden, J.E., Aller, H.D. & Dent, W.A., 1976. Nature, 260, 752.

Ledden, J.E. & Aller, H.D., 1978. Pittsburgh Conference on BL Lac Objects, ed. Wolfe, A.M. (Univ. of Pittsburgh), 60.

Ledden, J.E. & Aller, H.D., 1979. Astrophys.J., 229, L1.

Ledden, J.E., O'Dell, S.L., Stein, W.A. & Wisniewski, W.Z., 1980. Astrophys.J., in press.

Liller, M.H. & Liller, W., 1975. Astrophys.J., 199, L133.

Liller, W., 1976. I.A.U. Circular 2939.

Lonsdale, C.J., Dyck, H.M., Capps, R.W. & Wolstencroft, R.D., 1980. Astrophys.J., 238, L31.

Lynden-Bell, D., 1969. Nature, 233, 690.

Lynden-Bell, D., 1978. Physica Scripta, 17, 185.

Lynn, P.A., 1973. The Analysis and Processing of Signals (Macmillan).

MacLeod, J.M. & Andrew, B.H., 1968. Astrophys.Lett., 1, 243.

Marchant, J.C. & Millikan, A.G., 1965. J.Opt.Soc.Am., 55, 907.

Margon, B., & Ostriker, J.P., 1973. Astrophys.J., 186, 91.

Marscher, A.P., 1980. Astrophys.J., 235, 386.

Martin, P.G., 1979. Cosmic Dust (Oxford: Clarendon Press).

Martin, R. & Lutz, R.K., 1979. Image Processing in Astronomy, eds. Sedmak, G., Capaccioli, M., & Allen, R.J. (Trieste).

Masson, C.R. & Wall, J.V., 1977. Mon.Not.R.astr.Soc., 180, 193.

Mathewson, D.S. & Ford, V.L., 1970. Mem.Roy.astr.Soc., 74, 1.

Matthews, W.G., 1972. Astrophys.J., 174, 161.

Mattig, W., 1958. Astr.Nach., 284, 109.

Maza, J., Martin, P.G. & Angel, J.R.P., 1978. Astrophys.J., 224, 368.

Maza, J., 1979. Ph.D. thesis, Toronto (Univ. of Toronto).

Maza, J., Martin, P.G. & Angel, J.R.P., 1979. preprint.

McAdam, W.B., 1979. I.A.U. Asian-Pacific Regional Meeting, 343.

McIlwraith, B.K. & Stannard, D., 1980. Mon.Not.R.astr.Soc., 192, 798.

Mees, C.E.K. & James, T.H., 1966. The Theory of the Photographic Process (Macmillan).

Menzies, J.W., Banfield, R.M. & Laing, J.D., 1980. SAAO Circular 1, 5.

Meuller, J., 1948. J.Opt.Sci.Am., 38, 661.

Miller, H.R., Clonts, S.L. & Folsom, G.H., 1974. Astron.J., 79, 1352.

Miller, H.R., 1977. Astrophys.J., 212, L53.

Miller, H.R., 1978. Astrophys.J., 223, L67.

Miller, J.S., 1975. Astrophys.J., 200, L55.

Miller, J.S., 1978. Comm.Astrophys. & Sp.Sci., 7, 175.

Miller, J.S. & French, H.B., 1978. Pittsburgh Conference on BL Lac Objects, ed. Wolfe, A.M. (Univ. of Pittsburgh), 228.

Miller, J.S., French, H.B. & Hawley, S.A., 1978a. Astrophys.J., 219, L85.

Miller, J.S., French, H.B. & Hawley, S.A., 1978b. Pittsburgh Conference on BL Lac Objects, ed. Wolfe, A.M. (Univ. of Pittsburgh), 176.

Moore, R.L. & Stockman, H.S., 1980. Steward Observatory preprint.

Moore, R.L., Angel, J.R.P., Rieke, G.H., Lebofsky, M.J., Wisniewski, W.Z., Mufson, S.L., Vrba, F.J., Miller, H.R., McGimsey, B.Q. & Williamson, R.M., 1980. Astrophys. J., 235, 717.

Morrison, P., 1969. Astrophys.J., 153, L73.

Morse, P.M. & Feschbach, H., 1953. Methods of Theoretical Physics (McGraw-Hill).

Murdoch, H.S. & Crawford, D.F., 1977. Mon.Not.R.astr.Soc., 180, 41P.

Ness, N.F., Scearce, C.S. & Seek, J.B., 1964. J.Geophys.Res., 69, 3531.

Neugebauer, G., Oke, J.B., Becklin, E.E. & Matthews, K., 1979. Astrophys.J., 230, 79.

Nordsieck, K.H., 1972. Astrophys.Lett., 12, 69.

Nordsieck, K.H., 1976. Astrophys.J., 209, 653.

O'Dell, S.L. & Sartori, L., 1970. Astrophys.J., 162, L37.

O'Dell, S.L., Puschell, J.J. & Stein, W.A., 1977a. Astrophys.J., 213, 351.

O'Dell, S.L., Puschell, J.J., Stein, W.A. & Warner, 1977b. Astrophys. J., 214, L105.

O'Dell, S.L., Puschell, J.J., Stein, W.A., Owen, F., Porcas, R.W., Mufson, S., Moffett, T.J. & Ulrich, M.-H., 1978a. Astrophys.J., 224, 22.

O'Dell, S.L., Puschell, J.J., Stein, W.A. & Warner, J.W., 1978b. Astrophys.J. Suppl., 38, 267.

Öhman, V., 1941. Stockholm Obs.Ann., 13, 11.

Öhman, V., 1947. Stockholm Obs.Ann., 15, 2.

Oke, J.B., 1966. Astrophys.J., 147, 901.

Oke, J.B., Neugebauer, G. & Becklin, E.E., 1969. Astrophys.J., 156, L41.

Oke, J.B. & Schild, R.E., 1970. Astrophys.J., 161, 1015.

Oke, J.B., 1978. Astrophys.J., 219, L97.

Olsen, E.T., 1969. Nature, 224, 1008.

Owen, F.N. & Mufson, S.L., 1977. Astron.J., 82, 776.

Owen, F.N., Procas, R.W., Mufson, S.L. & Moffett, T.J., 1978. Astron. J., 83, 685.

Ozernoi, L.M., 1966. Astron.Zh., 43, 300.

Ozernoi, L.M. & Usov, V.V., 1977. Astron.& Astrophys., 56, 163.

Ozernoi, L.M., Chertoprud, V.E. & Gudzenko, L.I., 1977. Astrophys. J., 216, 237.

Pacholczyk, A.G., 1970. Radio Astrophysics (Freeman).

Pacht, E., 1976. Astron.J., 81, 574.

Parker, E.N., 1972. Astrophys.J., 174, 499.

Parker, E.N., 1973. Astrophys.J., 180, 247.

Pauliny-Toth, I.I.K. & Kellerman, K.I., 1972. Astron.J., 77, 797.

Peebles, P.J.E., 1972. Astrophys.J., 178, 371.

Penny, A.J., 1978. Users Guide to the RGO PDS Machine.

Penston, M.V. & Cannon, R.D., 1970. R.Obs.Bull., 159, 85.

Perley, R.A., Bridle, A.H., Willis, A.G. & Fomalont, E.B., 1980. Astron.J., 85, 499.

Peterson, B.A., Bolton, J.G. & Shimmins, A.J., 1973. Astrophys. Lett., 15, 109.

Petschek, A.G., Colgate, S.A. & Colvin, J.D., 1976. Astrophys.J., 209, 356.

Petschek, H.E., 1964. The Physics of Solar Flares, AAS-NASA Symposium (NASA SP-50), 425.

Pica, A.J., Smith, A.G. & Pollock, J.T., 1980a. Astrophys.J., 236, 84.

Pica, A.J., Pollock, J.T., Smith, A.G., Leacock, R.J., Edwards, P.L. & Scott, R.L., 1980b. Astron.J., 85, 1442.

Pickering, E.C., 1891. Ann.astr.Obs.Harvard, 26, 14.

Pollock, J.T., Pica, A.J., Smith, A.G., Leacock, R.J., Edwards, P.L. & Scott, R.L., 1979. Astron.J., 84, 1658.

Pomphrey, R.B., Smith, A.G., Leacock, R.J., Olsson, C.N., Scott, R.L., Pollock, J.T., Edwards, P. & Dent, W.A., 1976. Astron.J.,81, 489.

Pratt, N.M., 1968. Pub. ROE, 6, 4.

Pratt, N.M., 1977. Vistas in Astronomy, 21, 1.

Press, W.H., 1978. Comm.Astrophys. & Sp.Sci., 7, 103.

Pringle, J.E., Rees, M.J. & Pacholczyk, A.G., 1973. Astron. & Astrophys., 29, 179.

Prokof'eva, V.V., 1979. AAS Photobulletin, 20, 14.

Puschell, J.J., Stein, W.A., Jones, T.W., Warner, J.W., Owen, F., Rudnick, L., Aller, H. & Hodge, P., 1979. Astrophys.J., 227, L11.

Puschell, J.J. & Stein, W.A., 1980. Astrophys.J., 237, 331.

Racine, R., 1969. Astron.J., 74, 1073.

Readhead, A.C.S., Cohen, M.H. & Blandford, R.D., 1978. Nature, 272, 131.

Rees, M.J., 1971. Nature Phys.Sci., 230, 55.

Rees, M.J., Ruffini, R. & Wheeler, J.A., 1974. Black Holes, Gravitational Waves and Cosmology (Gordon & Breach).

Rees, M.J., 1977. Ann.N.Y.Acad.Sci., 302, 613.

Rees, M.J., 1978a. Mon.Not.R.astr.Soc., 184, 61P.

Rees, M.J., 1978b. Physica Scripta, 17, 193.

Rieke, G.H. & Kinman, T.D., 1974. Astrophys.J., 192, L115.

Rieke, G.H., Grasdalen, G.L., Kinman, T.D., Hintzen, P., Wills, B.J. & Wills, D., 1976. Nature, 260, 754.

Rieke, G.H., Lebofsky, M.J., Kemp, J.C., Coyne, G.V. & Tapia, S., 1977. Astrophys.J., 218, L37.

Rieke, G.H. & Lebofsky, M.J., 1979. Ann.Rev.Astron. & Astrophys., 17, 477.

Rieke, G.H., Lebofsky, M.J. & Kinman, T.D., 1979. Astrophys.J., 223, L151.

Rieke, G.H. & Weekes, T.C., 1969. Astrophys.J., 155, 429.

Rieke, G.H. & Lebofsky, M.J., 1980. I.A.U. Symposium 92, 263.

Robersts, M.S., Brown, R.L., Brundage, W.D., Rots, A.H., Haynes, M.P. & Wolfe, A.M., 1976. Astron.J., 81, 293.

Rudnick, L., Owen, F.N., Jones, T.W., Puschell, J.J. & Stein, W.A., 1978. Astrophys.J., 225, L5.

Rybicki, G.B. & Lightman, A.P., 1979. Radiative Processes in Astrophysics (Wiley).

Ryter, C., 1979. Extragalactic High Energy Astrophysics, 9th Course of Swiss Society of Astron. & Astrophys., 73.

Saltpeter, E.E., 1971. Nature Phys.Sci., 233, 5.

Sandage, A., 1972. Astrophys.J., 178, 1.

Sargent, W.L.W., 1974. High Energy Astrophysics and its Relation to Elementary Particle Physics (MIT), 455.

Sargent, W.L.W., Young, P.J., Boksenberg, A., Shortridge, K., Lynds, C.R. & Hartwick, F.D.A., 1978. Astrophys.J., 221, 731.

Saslaw, W.C., 1973. Pub.Astr.Soc.Pac., 85, 5.

Scheuer, P.A.G., 1974. Mon.Not.R.astr.Soc., 166, 513.

Scheuer, P.A.G., 1976. Mon.Not.R.astr.Soc., 177, 1P.

Scheuer, P.A.G. & Readhead, A.C.S., 1979. Nature, 277, 182.

Schild, R., Peterson, D.M. & Oke, J.B., 1971. Astrophys.J., 166, 95.

Schmidt, M., 1977. I.A.U. Symposium, 74, 259.

Schmitt, J., 1968. Nature, 218, 663.

Schoening, W.E., 1976. AAS Photobulletin, 11, 8.

Schwartz, D.A., Doxsey, R.E., Griffiths, R.E., Johnston, M.D. & Schwarz J., 1979. Astrophys.J., 229, L53.

Seielstad, G.A. & Berge, G.L., 1975. Astron.J., 80, 271.

Serkowski, K., 1960. Acta Astronomica, 10, 227.

Serkowski, K., 1974a. Methods of Experimental Physics, 12A, 36 (Academic Press).

Serkowski, K., 1974b. Planets, Stars and Nebulae Studied with Photopolarimetry, ed. Gehrels, T. (Univ. of Arizona), 135.

Serkowski, K. & Tapia, S., 1975. Bull.Am.astr.Soc., 7, 499.

Setti, G. & Woltjer, L., 1977. Astrophys.J., 218, L33.

Setti, G., 1978. Pittsburgh Conference on BL Lac Objects, ed. Wolfe, A.M. (Univ. of Pittsburgh), 385.

Shaffer, D.B., 1978a. Pittsburgh Conference on BL Lac Objects, ed. Wolfe, A.M. (Univ. of Pittsburgh), 68.

Shaffer, D.B., 1978b. Astron.J., 83, 109.

Shakura, N.I. & Sunyaev, R.A., 1973. I.A.U. Symposium 55, 155.

Shapiro, P.S., 1975. Astrophys.J., 201, 151.

Shields, G.A. & Wheeler, J.C., 1976. Astrophys. Lett., 17, 69.

Shields, G.A., 1978. Pittsburgh Conference on BL Lac Objects, ed. Wolfe, A.M. (Univ. of Pittsburgh), 257.

Shklovsky, I.S., 1953. Dokl.Akad.Nauk. SSSR, 90, 983.

Shklovsky, I.S., 1961. Soviet Astron., 4, 243.

Shklovsky, I.S., 1976. Supernova Stars (Moscow).

Sim, M.E., Hawarden, T.G. & Cannon, R.E., 1976. AAS Photobulletin, 11, 3.

Sim, M.E., 1977. AAS Photobulletin, 14, 9.

Smith, A.G., Scott, R.L., Leacock, R.J., McGimsey, B.Q., Edwards, P.L., Hackney, R.L. & Hackney, K.R., 1975. Pub. astr.Soc.Pac., 87, 149.

Smith, H.E., Spinrad, H. & Smith, E.O., 1976. Pub.astr.Soc.Pac., 88, 621.

Smith, M.G. & Wright, A.E., 1980. Mon.Not.R.astr.Soc., 191, 871.

Snyder, W.A., Davidsen, A.F., Wood, K., Kinzer, R., Smathers, H., Shulman, S., Meekins, J.F., Yentis, D.J., Evans, W.D., Byram, E.T., Chubb, T.A., Friedman, H. & Margon, B., 1980. Astrophys.J., 237, L11.

Soifer, B.T. & Pipher, J.L., 1978. Ann.Rev.Astron.& Astrophys., 16, 335.

Soifer, B.T. & Neugebauer, G., 1980. I.A.U. Symposium, 96, 329.

Spinrad, H. & Smith, H.E., 1973. Astrophys.J., 201, 275.

Spitzer, L., 1971. Active Galactic Nuclei, ed. O'Connell (North-Holland), 443.

Stein, W.A., O'Dell, S.L. & Strittmatter, P.A., 1976. Ann.Rev. Astron.& Astrophys., 14, 173.

Stein, W.A., 1978. Pittsburgh Conference on BL Lac Objects, ed. Wolfe, A.M. (Univ. of Pittsburgh), 1.

Stobie, R.S., Smith, G.M., Lutz, R.K. & Martin, R., 1979. Image Processing in Astronomy, eds. Sedmak, G., Capaccioli, M. & Allen, R.J. (Trieste), 48.

Stockman, H.S., Angel, J.R.P. & Beaver, E.A., 1976. Bull.Am.astr. Soc., 8, 495.

Stockman, H.S., 1978. Pittsburgh Conference on BL Lac Objects, ed. Wolfe, A.M. (Univ. of Pittsburgh), 149.

Stockman, H.S., Angel, J.R.P. & Miley, G.K., 1979. Astrophys.J., 227, L55.

Stockman, H.S. & Angel, J.R.P., 1980. Astrophys.J., 220, L67.

Stockman, H.S., Angel, J.R.P. & Hier, R.G., 1980. Steward Observatory preprint.

Strecker, D.W., Erickson, E.F. & Witteborn, F.C., 1979. Astrophys. J.Suppl., 41, 501.

Strittmatter, P.A., Serkowski, K., Carswell, R.F., Stein, W.A., Merrill, K.M. & Burbidge, E.M., 1972. Astrophys. J., 175, L7.

Sulentic, J.W., Arp, H. & Lorre, J., 1979. Astrophys.J., 233, 44.

Swinbank, E., 1980. Mon.Not.R.astr.Soc., 193, 451.

Tananbaum, H., Avni, Y., et al., 1979. Astrophys.J., 234, L9.

Tapia, S., Craine, E.R. & Johnson, K., 1976. Astrophys.J., 203, 291.

Tapia, S., Craine, E.R., Gearhart, M.R., Pacht, E. & Kraus, J.D., 1977. Astrophys.J., 215, L71.

Thompson, I., Landstreet, J.D., Stockman, H.S., Angel, J.R.P. & Beaver, E.A., 1980. Mon.Not.R.astr.Soc., 192, 53.

Toptyghin, I.N., 1980. Space Science Reviews, 26, 157.

Treanor, P.J., 1967. Observatory, 95, 7.

Tripp, W., 1956. Z.Ap., 41, 84.

Tucker, W.H., 1975. Radiation Processes in Astrophysics (MIT).

Tyson, J.A. & Jarvis, J.F., 1979. Instrumentation in Astronomy III, 172, 422.

Ulrich, M.-H., Kinman, T.D., Lynds, C.R., Rieke, G.H. & Ekers, R.D., 1975. Astrophys.J., 198, 261.

Usher, P.D., 1975. Astrophys.J., 198, L57.

Usher, P.D., 1978. Astrophys.J., 220, 40.

Usher, P.D. & Mitchell, K.J., 1978. Astrophys.J., 223, 1.

Vashakidze, M.A., 1954. V.A.Astron.Circ., 147, 11.

Vaucher, B.G. & Weedman, D.W., 1980. Astrophys.J., 240, 10.

de Vaucouleurs, G., 1968. Applied Optics, 7, 1513.

de Vaucouleurs, G. & de Vaucouleurs, A., 1968. Astron.J., 73, 858.

Veron, M.P., 1975. Astron.& Astrophys., 41, 423.

Veron, P. & Veron, M.P., 1975. Astron.& Astrophys., 39, 281.

Vinokur, M., 1965. Ann.D'Astrophys., 28, 412.

Visvanathan, N., 1969. Astrophys.J., 155, L133.

Visvanathan, N., 1973. Astrophys.J., 179, 1.

Visvanathan, N. & Elliot, J.L., 1973. Astrophys.J., 179, 721.

Visvanathan, N., 1974. Planets, Stars and Nebulae Studied with Photopolarimetry, ed. Gehrels, T. (Univ. of Arizona), 1059.

Wagoner, R.V., 1969. Ann.Rev.Astron.& Astrophys., 7, 553.

Wagoner, R.V., 1971. Highlights in Astronomy, 2, 316.

Wall, J.V., 1975. Observatory, 95, 196.

Wall, J.V., 1978. Mon.Not.R.astr.Soc., 182, 381.

Wall, J.V., 1979. Quart.J.R.astr.Soc., 20, 138.

Wall, J.V., Pearson, T.J. & Longair, M.S., 1980. Mon.Not.R.astr. Soc., in press.

Wardle, J.F.C. & Kronberg, P.P., 1974. Astrophys.J., 194, 249.

Wardle, J.F.C., 1977. Nature, 269, 563.

Wardle, J.F.C., 1978. Pittsburgh Conference on BL Lac Objects, ed. Wolfe, A.M. (Univ. of Pittsburgh), 39.

Weedman, D.W., 1976. Quart.J.R.astr.Soc., 17, 227.

Weiler, K.W. & Johnson, K.J., 1980. Mon.Not.R.astr.Soc., 190, 269.

Westfold, K.C., 1959. Astrophys.J., 130, 241.

Whitford, A.E., 1971. Astrophys.J., 169, 209.

Williams, W.L., Rich, A., Kupperman, P.N., Ionson, J.A. & Hiltner, W.A., 1972. Astrophys.J., 174, L63.

Willis, A.G., 1978. Physica Scripta, 17, 243.

Willis, A.G. & Strom, R.G., 1978. Astron.& Astrophys., 62, 375.

Wills, D. & Wills, B.J., 1976. Astrophys.J.Suppl., 31, 143.

Wilson, A.S., Ward, M.J., Axon, D.J., Elvis, M. & Meurs, E.J.A., 1979. Mon.Not.R.astr.Soc., 187, 109.

Wilson, D.B., 1980. Mon.Not.R.astr.Soc., 192, 787.

Wisniewski, W.Z., Mufson, S.L. & Pollock, J.T., 1980. I.A.U. Circular, 3500.

Wolfe, A.M., 1978. Pittsburgh Conference on BL Lac Objects, ed. Wolfe, A.M. (Univ. of Pittsburgh), 23.

Wolfe, A.M., 1980. University of Pittsburgh preprint.

Wolstencroft, R.D., Gilmore, G.F. & Williams, P.M., 1980. ROE preprint.

Yeh, T. & Axford, W.I., 1970. J.Plasma Phys., 4, 207.

Young, P.J., Westphal, J.A., Kristian, J., Wilson, C.P. & Landauer, F.P., 1978. Astrophys.J., 221, 721.

Zel'dovitch, Ya.B. & Raizer, Yu.P., 1966. Physics of Shock Waves and High-Temperature Hydrodynamic Phenomena (Academic Press).

Zwicky, F., 1956. Pub.astr.Soc.Pac., 68, 121.

APPENDIX G

Appendix G

Mon. Not. R. astr. Soc. (1981) **194**, 275–282

Measurement of linear and circular polarization using the UK Schmidt telescope

R. D. Wolstencroft *Royal Observatory Edinburgh, Blackford Hill, Edinburgh EH9 3HJ*

C. D. Impey and R. J. Smith *Department of Astronomy, Edinburgh University, Edinburgh EH9 3HJ*

Received 1980 June 10; in original form 1980 March 18

Summary. Filters for detecting linear and circular polarization have been constructed for the UK Schmidt telescope. The first plates with these filters have been taken, and are presently being reduced. In this paper, the filters are described and threshold levels for the detection of polarization are estimated using calibration objects. The calibration objects were the BL Lac object 0J 287 for linear polarization and the magnetic white dwarf LP 790 – 29 for circular polarization. The 4σ detection threshold is 10–12 per cent for both linear and circular polarization from one set of plates.

1 Introduction

The first accurate photographic study of linear polarization using a Schmidt telescope was carried out by Pratt (1968). He used a polaroid filter to observe 527 stars down to $V = 13$ in a 1° diameter field: multiple exposures were taken on the same plate at different orientations of the polaroid filter. Pratt used the Edinburgh Schmidt telescope and Ilford R40 emulsion in his study. By using the 48-inch UK Schmidt telescope and Kodak IIIaJ emulsion, the area of sky observed and limiting magnitude can be substantially increased. In this paper we describe a photographic method of measuring both linear and circular polarization of stars. This is the first photographic study of circular polarization.

2 The filters

2.1 LINEAR POLARIZATION

2.1.1 Description of the filter

The filter consists of two pieces of HN 32 polaroid vacuum-laminated between high-quality float glass (see Fig. 1). The first (A) is circular, of diameter 25.4 cm, and defines a program region of 560 cm^2 (19.4 deg^2). It rotates on a friction bearing between positions 45° apart. The second (B) is fixed; the part within the unvignetted region of the plate (shown in the

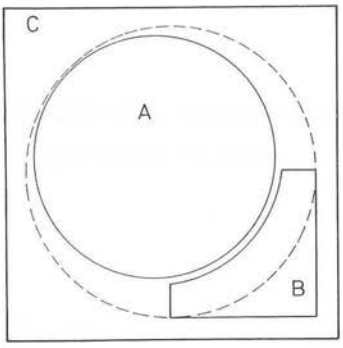

Figure 1. The linear polarization filter. A is a circular, rotatable filter which defines the program area A. It is entirely within the unvignetted field (dashed circle). B is a fixed filter: the part within the unvignetted field defines the control region. C is the opaque filter holder.

figure as a dashed circle of diameter 30.5 cm) defines the control region. The remainder of the photographic plate is occluded by the filter holder (C) and the Schmidt calibration step wedges are not visible. The filter is approximately 3 mm thick. Note that the program region is centred 2.5 cm from the centre of the unvignetted area.

2.1.2 Use of the filter

When partially linearly polarized light of intensity I and degree of polarization p is incident on the filter the transmitted intensity is

$$T_\phi I = I\left\{\left(\frac{K_1+K_2}{2}\right)+p\left(\frac{K_1-K_2}{2}\right)\cos 2(\phi-\theta)\right\}, \tag{1}$$

where ϕ and θ are the position angles of the polaroid and the polarized radiation respectively, and K_1 and K_2 are the transmission factors parallel and perpendicular to the acceptance axis of the polaroid. A set of plates is obtained by making four consecutive exposures, each taken through a different orientation of the polaroid ($\phi = 0°$, $45°$, $90°$ and $135°$). To allow for differences in exposure time, emulsion sensitivity, atmospheric transmission and other factors we write the intensity measured from the photographic plate taken at orientation ϕ as $I_\phi = C_\phi T_\phi I$. The control filter remains at a fixed orientation and thus measurements of stars in the control region of the plate can be used to determine the control factor C_ϕ for each plate of a set. The combination of polaroid filter and IIIaJ emulsion defines a passband from 4000 to 5500 Å approximately, similar to that of a Johnson B magnitude.

From the measured values of I_ϕ and C_ϕ we can obtain $T_\phi I = I_\phi/C_\phi$, and hence

$$\begin{aligned} p\sin 2\theta &= R\left(\frac{T_{45}-T_{135}}{T_{45}+T_{135}}\right)=\frac{U}{I} \\ p\cos 2\theta &= R\left(\frac{T_0-T_{90}}{T_0+T_{90}}\right)=\frac{Q}{I}, \end{aligned} \tag{2}$$

where (Q, U, I) are the Stokes parameters of the incident light and $R = (K_1+K_2)/(K_1-K_2)$ is essentially unity ($R - 1 < 0.003$). Note that in order to obtain the intensities I_ϕ from measurements of the photographic plate a photoelectric sequence is necessary. The control factors C_ϕ allow for the average plate to plate differences but cannot allow for variations

across a given plate due to any of the contributing effects mentioned above. Of these the photographic effects are potentially the most serious; they have been minimized by using IIIaJ plates taken from the same box, and by hypersensitizing and developing the plates together. Exposure through consecutive orientations have been taken in conditions of stable seeing close to the meridian. The polaroid filter material was selected to have the minimum variations in transmission across its surface; the variations are regular (frequently termed corrugations) and have been mapped both in the lab and on the telescope. In the analysis of small regions of the plate reported in this paper ($\sim 4\,\mathrm{cm}^2$) the corrugations can be ignored because of their relatively long wavelength (4.5 cm) and modest amplitude (~ 4 per cent peak to peak), but are taken into account in our analysis of the entire program region ($560\,\mathrm{cm}^2$) currently in progress.

2.2 CIRCULAR POLARIZATION

2.2.2 Description of the filter

Two filters are necessary for the detection of circular polarization. Termed the LH and RH filters respectively, both are made of HNCP37 – a carbonized butyrate lamination of a plastic quarter-wave plate and a sheet of polaroid. The waveplate exhibits a quarter-wave retardance at a wavelength close to 5600 Å, while the polaroid is similar to HN38. Each filter is cemented to a piece of commercial float glass for support, a semi-plastic polyester resin being used to avoid stress effects in the waveplate. Incoming starlight passes through the waveplate, then the polaroid and finally through the glass. In this way the quality of the glass and the properties of the cement should not affect the measurement of polarization. The filters are approximately 4 mm thick and have a clear aperture of $1156\,\mathrm{cm}^2$ (corresponding to a field of $40\,\mathrm{deg}^2$ on the UK Schmidt, including the entire unvignetted area). The calibration step wedges remain visible. The two filters differ in the orientation of the waveplate with respect to the axis of the polaroid. The LH filter produces left-handed or negative circular polarization when unpolarized light passes through from the polaroid side, as the fast axis of the waveplate in this filter is at -45° to the axis of the polaroid. The RH filter produces right-handed or positive circular polarization and has the fast axis of the waveplate at $+45^\circ$ to the axis of the polaroid. Gehrels' sign convention is used (Gehrels 1974).

2.2.2 Use of the filter

Using the Mueller calculus (see e.g. Clarke & Grainger 1971), the following expression can be given for the intensity detected by the photographic plate.

$$I'_{\pm} = C_{\pm}\left[(K_1 + K_2)I + (K_1 - K_2)\,Q\cos\delta \pm (K_1 - K_2)\,V\sin\delta\right], \tag{3}$$

where (I, Q, U, V) are the Stokes parameters of the incoming starlight, I'_+ and I'_- are the intensities of the light emerging from the RH and LH filters respectively, K_1 and K_2 are as before the principal intensity transmission coefficients of the polaroid, C_+ and C_- are the transmission scale factors to account for different integration times, plate sensitivities, atmospheric transmission, etc. and δ is the retardance of the waveplate.

Photographic plates are obtained with each filter in turn. The Kodak IIIaF emulsion is used giving a bandpass of approximately 4000–7000 Å. Since $\geqslant 99$ per cent of all stars on the plate are effectively unpolarized, almost every star image can be used to define the transformation between the two plates. As in the linear case, intensities are derived using a calibration sequence. In this way, the factors C_+ and C_- can be determined and the measured

degree of circular polarization obtained from

$$q' = \frac{(I'_+/C_+) - (I'_-/C_-)}{(I'_+/C_+) + (I'_-/C_-)} . \tag{4}$$

If $K_2 = 0$ (perfect polarizer) and $\delta = 90°$ (perfect waveplate), q' would be equal $q = V/I$. However, we find from (3) that

$$q' = \frac{V}{I} \frac{\sin\delta}{(K_1 + K_2)/(K_1 - K_2) + (Q\cos\delta/I)} = \frac{V\gamma}{I} . \tag{5}$$

Note that the detection efficiency for circular polarization drops off at wavelengths far from 5600 Å, and also that linearly polarized flux can affect the measurement. Using typical values for K_1 and K_2 and the relation $\delta = 90° \times 5600/\lambda$ (λ in Å) we obtain

	γ		
λ(Å)	Q/I = 10 per cent	Q/I = 30 per cent	
4000	0.844	0.962	
4500	0.945	1.024	
5000	0.983	1.022	$K_1 = 0.8$
5500	0.985	0.991	$K_2 = 0.007$
6000	0.967	0.948	
6500	0.940	0.902	
7000	0.907	0.857	

3 Calibration object

3.1 LINEAR POLARIZATION

3.1.1 Detection

A set of short exposure (10 min) plates of the BL Lac object 0J 287 were obtained in 1979 March. This object has a history of strong and variable liner polarization with a maximum level of 29 per cent (Kinman 1976). An independent determination of the polarization was needed to give accurate information on the detection level using the Schmidt plates. Six days

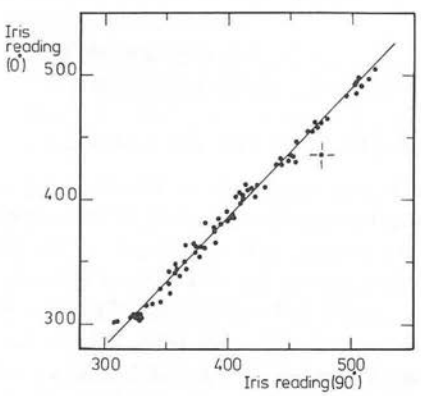

Figure 2. The photographic detection of the linearly polarized BL Lac object 0J 287. Readings of the Iris Diaphragm Photometer for the 0° and 90° orientations of the filter for stars in the field (4 cm²) are plotted against each other (with 0J 287) (indicated by a cross). The best fitting straight line is shown.

before the plates were taken 0J 287 was observed by S. Tapia at the University of Arizona with the 'Minipol' polarimeter. The photoelectric measurement of polarization was $p = 16.6 \pm 0.9$ per cent at position angle $\theta = 85°.7 \pm 1°.6$.

Using the Becker Iris Photometer at ROE, 86 stars around 0J 287 were measured on each of the four plates. The stars covered an area of approximately 4 cm^2. Thirteen faint stars were discarded because they were close to the plate limit. Iris readings were plotted for the two orthogonal pairs: 0° and 90°, 45° and 135°. In both cases the plots were fitted with a straight line by linear regression with a correlation coefficient of greater than 0.99. The 1σ dispersion for 0° versus 90° was 4.4 iris units, and for 45° versus 135° it was 3.4 iris units. The Becker measurement error is only 1 unit. 0J 287 was displaced from the best-fit straight line on the 0° versus 90° plot by 5.6σ (Fig. 2), but was not at all displaced from the 45° versus 135° best fit line. Note that the line in Fig. 2 does not pass through the origin because of slight differences in the background density of the plate.

3.1.1 Calculation

A magnitude calibration is needed to derive a measure of the degree of polarization. Penston & Wing (1973) have published a photoelectric sequence for 0J 287. Only four members of the sequence could be used, because when observed, 0J 287 was at the faint end of its magnitude range. It should be noted that the variable star in the sequence was not used (Schaeffer 1979). To calculate an interpolated magnitude for 0J 287 on each of the four plates, it was assumed that over a small magnitude range ($\Delta B < 0.5$) there is a linear relationship between iris reading and magnitude. Any polarization of the standard stars is accounted for in the error of the magnitude calibration, given that the position angles are randomly orientated.

The error on the magnitude of 0J 287 at each of the position angles was calculated from the iris reading error, the photoelectric error on the sequence stars and a linear regression straight line fit. From equations (2),

$$p = \left\{\left(\frac{1 - T_{135}/T_{45}}{1 + T_{135}/T_{45}}\right)^2 + \left(\frac{1 - T_{90}/T_0}{1 + T_{90}/T_0}\right)^2\right\}^{1/2},$$

$$\theta = \tfrac{1}{2} \arctan\left\{\left(\frac{1 - T_{135}/T_{45}}{1 + T_{135}/T_{45}}\right) \Big/ \left(\frac{1 - T_{90}/T_0}{1 + T_{90}/T_0}\right)\right\}. \tag{6}$$

The quantities T_{90}/T_0 and T_{135}/T_{45} are calculated from the magnitude difference between images at orthogonal positions of the polaroid. p and θ are calculated by (6), with $\sigma(p)$ and $\sigma(\theta)$ being derived from the propagation of errors through equations (6).

The results for the polarization of 0J 287 are:

Photographic $p = 16.5$ per cent $\pm$ 5.0 per cent at $87° \pm 18°$,

Photoelectric $p = 16.6$ per cent $\pm$ 0.9 per cent at $85.7° \pm 1.6°$.

3.1.3 Comments

The photoelectric and photographic determinations agree to well within the errors. Since some BL Lac objects have variable polarization on a time-scale of days, and the two observations were separated by six nights, the close agreement may be fortuitous. However, the extensive monitoring of 0J 287 by Angel *et al.* (1978) failed to turn up night-to-night polarization changes; all the large movements were over periods of weeks or months. The present four exposures were taken within the space of one hour.

For relatively bright objects at high galactic latitude the assumption of unpolarized or randomly polarized standard stars is acceptable. The extension of this technique to deeper fields may entail the use of photometric standards with appreciable interstellar polarization. Our reduction procedure effectively subtracts the mean polarization of the field stars from the polarization of the program object. Measurements of two field stars close to 0J 287 (Serkowski 1980, private communication) show polarizations of less than 2 per cent, a level which will not significantly affect our results. Thus objects with anomalous polarization will be readily detected even if the measured values of the polarization are subject to this uncertainty.

When the method is used as a discovery technique, only the threshold of detection is important. BL Lac objects are rare, but 2/3 of those known have maximum polarization of more than 12 per cent (Stein *et al.* 1976), and their numbers are expected to increase with limiting magnitude. As large areas of a deep survey plate containing 10^5 images are studied, errors are likely to increase. Since this is a photographic process, a high-σ tail might be expected. It should be noted that polarization of field stars (Craine *et al.* 1978) will contribute to the scatter in Fig. 2. To give a manageable sample of objects for closer examination, a detection threshold of 4σ can be set corresponding to $p = 12$ per cent for one set of plates.

3.2 CIRCULAR POLARIZATION

3.2.1 Detection

Two sets of short exposure plates on IIIaF emulsion were obtained of the magnetic white dwarf LP 790 – 29 (Liebert *et al.* 1978). This object is reported to have a surface magnetic field in excess of 10^8 G, and to have strong continuum polarization which does not vary with time. The spectrum is dominated by a large depression extending from 4300 to 5600 Å. A circular polarization spectrum shows a similar dip, with polarization of about + 7.5 per cent in the blue, +10 to 12 per cent in the red, and practically zero in the depression. The circular polarization in the filter/emulsion passband is difficult to calculate as the degree of polarization is not well determined at the wavelength of maximum sensitivity of the emulsion. We estimate it to be $+10 \pm 2$ per cent.

Using the Iris Becker photometer at ROE, 107 stars around LP 790 – 29 were measured on each of the four plates, and also on two plates taken without a filter. The stellar images lay in an area of approximately 1 cm^2. Each plate was measured twice and the results averaged. Stars for which the two measures were discordant were discarded. Plots were then made of iris reading between RH and LH plates of each set (Fig. 3) and between the two unfiltered plates. A straight line was fitted to the centre of the range (covering about 30 stars). The average 1σ dispersion for the filtered set of plates was 2.5 iris units, being worse on one of the sets of plates. Note that Fig. 3 shows both a non-zero intercept and a slope which differs from unity. These effects arise mainly from the way in which the Becker was set up to measure each plate. They do not signify gross differences in either the transmissions of the two filters or in the integration times for which the two plates were exposed.

3.2.2 Calibration

Unfortunately, no suitable photoelectric sequence exists for this region of sky. Accordingly, no photographic measure of the degree of polarization is possible. However, if the method is merely to be a discovery technique, then only the threshold of detection is important. The white dwarf was detected on both plates at an average of 4σ. Combining the two sets of

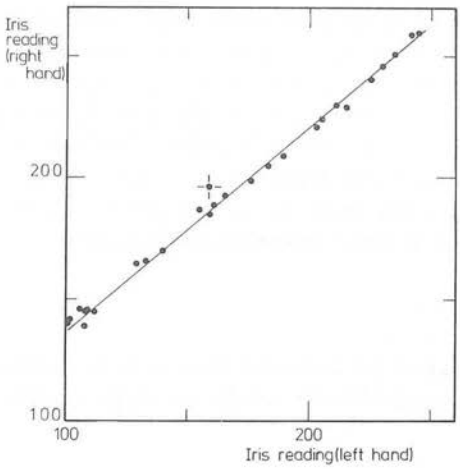

Figure 3. The photographic detection of the circularly polarized magnetic white dwarf LP 790 – 29. Readings of the Iris Diaphragm Photometer for objects on plates taken through the left hand and right hand filters are plotted against each other (the white dwarf is indicated by a cross). Sky background was significantly different between the two plates and only the linear portion of the graph is shown.

plates gave a detection of almost 6.5σ. Comparison between the two unfiltered plates showed no variation in the integrated light from the white dwarf to have occurred, within the errors.

3.2.3 Comment

Magnetic white dwarfs are not common, and examples with as high a polarization as LP 290 – 29 are particularly rare. If a deep survey plate containing 10^5 images is to be searched, the detection threshold must be set considerably higher than 3σ because of the expected high-σ tail. The data discussed here suggests that a combination of two sets of plates would give a 4σ detection of circular polarization of 6–8 per cent.

4 Future work

The filter to detect linear polarization is being used to search for BL Lac and related objects at high galactic latitude. BL Lac objects have been discovered almost exclusively from radio source identifications. Optical searches for quasars have been successful, but BL Lac objects do not have the same characteristics of strong emission lines or an ultraviolet excess. In the Schmidt survey we are looking for the strong linear polarization which these objects display (the highest recorded degree of polarization to date is 48 per cent). These levels of polarization pose severe problems for all conventional models of synchrotron-emitting active nuclei. A radio-independent search for BL Lac objects will determine whether there are analogues to the radio-quiet quasars, and help to discriminate between current models of active nuclei. The circular polarization filters are being used to search for magnetic white dwarfs at medium to high galactic latitude. The number of known magnetic white dwarfs, both in and out of binary systems, is currently 17: it is hoped that this number would be increased very substantially with this technique. In a high latitude Schmidt field containing about 2×10^5 stars (in 40 square degrees) down to $V = 21$, the number of detectable magnetic white dwarfs

can be estimated very approximately to be between 5 and 50. For a given magnetic field strength the largest polarizations (up to 35 per cent) occur in the magnetic white dwarfs in binary systems for which the relevant field (in the accretion column) is well ordered, rather than in the isolated magnetic white dwarfs for which the field must be integrated over the entire photosphere. Assuming that the distribution of field strengths are the same for the isolated and binary objects, the survey will detect the binary objects principally. The periods of these objects are only a few hours but a sequence of exposures at intervals of about 15 min should be sufficient to detect these objects efficiently.

Acknowledgments

We acknowledge with pleasure the assistance given to us by members of the Schmidt Unit, especially John Dawe. CDI and RJS acknowledge the support of SRC Research Studentships.

References

Angel, J. P. R. *et al.*, 1978. *Pittsburgh BL Lac Conference*, p. 117, University of Pittsburgh.
Clarke, D. & Grainger, J. F., 1971. *Polarized Light and Optical Measurement*, Pergamon Press, Oxford.
Craine, E. R., Duerr, R. & Tapia, S., 1978. *Pittsburgh BL Lac Conference*, p. 99, University of Pittsburgh.
Gehrels, T. (ed.), 1974. *Planets, Stars and Nebulae Studied with Photopolarimetry*, p. 52, University of Arizona.
Kinman, T. D., 1976. *Astrophys. J.*, **205**, 1.
Liebert, J., Angel, J. R. P., Stockman, H. S. & Beaver, E. A., 1978. *Astrophys, J.*, **225**, 181.
Penston, M. V. & Wing, R. F., 1973. *Observatory*, **93** 149.
Pratt, N. M., 1968. *Publs R. Obs. Edinb.*, **6**, No. 4.
Schaeffer, B. E., 1979. *Publs astr. Soc. Pacif.*, **91**, 670.
Stein, W. A., O'Dell, S. L. & Strittmatter, P. A., 1976. *A. Rev. Astr. Astrophys.*, **14**, 173.